frontiers | Research Topics

Pattern formation in biology

Edited by
Luis Diambra, Pau Formosa-Jordan and David M. Holloway

Published in
Frontiers in Physics
Frontiers in Systems Biology
Frontiers in Cell and Developmental Biology

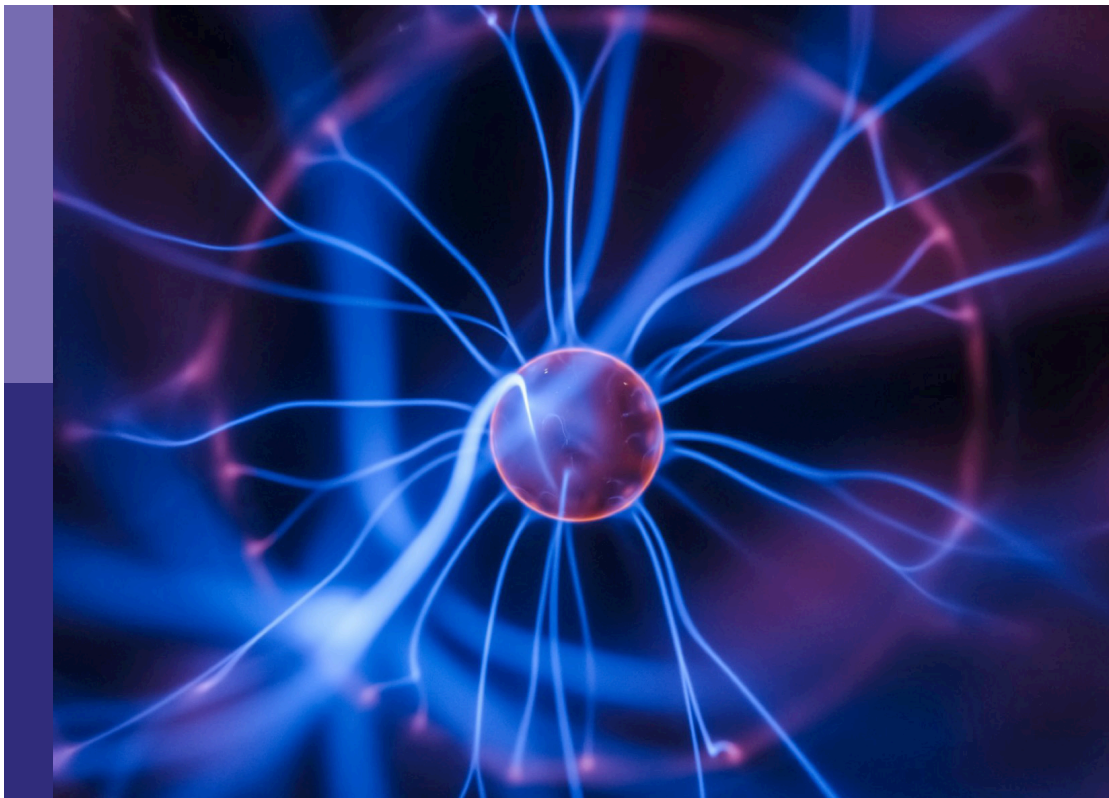

ISSN 1664-8714
ISBN 978-2-8325-2568-5
DOI 10.3389/978-2-8325-2568-5

About Frontiers

Frontiers is more than just an open access publisher of scholarly articles: it is a pioneering approach to the world of academia, radically improving the way scholarly research is managed. The grand vision of Frontiers is a world where all people have an equal opportunity to seek, share and generate knowledge. Frontiers provides immediate and permanent online open access to all its publications, but this alone is not enough to realize our grand goals.

Frontiers journal series

The Frontiers journal series is a multi-tier and interdisciplinary set of open-access, online journals, promising a paradigm shift from the current review, selection and dissemination processes in academic publishing. All Frontiers journals are driven by researchers for researchers; therefore, they constitute a service to the scholarly community. At the same time, the *Frontiers journal series* operates on a revolutionary invention, the tiered publishing system, initially addressing specific communities of scholars, and gradually climbing up to broader public understanding, thus serving the interests of the lay society, too.

Dedication to quality

Each Frontiers article is a landmark of the highest quality, thanks to genuinely collaborative interactions between authors and review editors, who include some of the world's best academicians. Research must be certified by peers before entering a stream of knowledge that may eventually reach the public - and shape society; therefore, Frontiers only applies the most rigorous and unbiased reviews. Frontiers revolutionizes research publishing by freely delivering the most outstanding research, evaluated with no bias from both the academic and social point of view. By applying the most advanced information technologies, Frontiers is catapulting scholarly publishing into a new generation.

What are Frontiers Research Topics?

Frontiers Research Topics are very popular trademarks of the *Frontiers journals series*: they are collections of at least ten articles, all centered on a particular subject. With their unique mix of varied contributions from Original Research to Review Articles, Frontiers Research Topics unify the most influential researchers, the latest key findings and historical advances in a hot research area.

Find out more on how to host your own Frontiers Research Topic or contribute to one as an author by contacting the Frontiers editorial office: frontiersin.org/about/contact

Pattern formation in biology

Topic editors

Luis Diambra — National University of La Plata, Argentina

Pau Formosa-Jordan — Department of Plant Developmental Biology, Max Planck Institute for Plant Breeding Research, Germany

David M. Holloway — British Columbia Institute of Technology, Canada

Citation

Diambra, L., Formosa-Jordan, P., Holloway, D. M., eds. (2023). *Pattern formation in biology*. Lausanne: Frontiers Media SA. doi: 10.3389/978-2-8325-2568-5

Table of contents

frontiers | Frontiers in Physics

TYPE Editorial
PUBLISHED 20 February 2023
DOI 10.3389/fphy.2023.1161890

OPEN ACCESS

EDITED AND REVIEWED BY
Ralf Metzler,
University of Potsdam, Germany

*CORRESPONDENCE
Pau Formosa-Jordan,
pformosa@mpipz.mpg.de
David M. Holloway,
David_Holloway@bcit.ca
Luis Diambra,
ldiambra@gmail.com

SPECIALTY SECTION
This article was submitted to Biophysics, a section of the journal Frontiers in Physics

RECEIVED 08 February 2023
ACCEPTED 10 February 2023
PUBLISHED 20 February 2023

CITATION
Formosa-Jordan P, Holloway DM and Diambra L (2023), Editorial: Pattern formation in biology.
Front. Phys. 11:1161890.
doi: 10.3389/fphy.2023.1161890

Editorial: Pattern formation in biology

Pau Formosa-Jordan[1,2]*, David M. Holloway[3]* and Luis Diambra[4]*

[1]Department of Plant Developmental Biology, Max Planck Institute for Plant Breeding Research, Cologne, Germany, [2]Cluster of Excellence on Plant Science (CEPLAS), Max Planck Institute for Plant Breeding Research, Cologne, Germany, [3]Mathematics Department, British Columbia Institute of Technology, Burnaby, BC, Canada, [4]Centro Regional de Estudios Genómicos, UNLP-CONICET, La Plata, Argentina

KEYWORDS

patterning, Turing patterns, biological patterns, morphodynamics, segmentation, morphogenesis, modelling, nonlinear dynamics

Editorial on the Research Topic
Pattern formation in biology

Cells can self-organize in time and space forming biological patterns [1]. Examples of pattern formation in biology are very diverse and can be found in a wide variety of tissues and organisms. For instance, the segmentation process along the longitudinal axes of vertebrates and invertebrates [2, 3], the fine-grained mixtures of different cell types appearing in both plant and animal tissues [4], the regular arrangement of organs along the plant shoot [5], and the cell polarity patterns appearing in multiple cell types [6], among many others. Pattern formation arises from the coordination and interplay of several mechanisms and processes across molecular, cellular and tissue scales. At the cellular level, growth, cell fate specification, migration and cell–cell interactions can be important and influence each other during the formation of a tissue. All these processes are finely orchestrated in space and time by gene expression, which in turn can also be affected by these processes. Over the past two decades, the study of pattern formation in biology has attracted the attention of many scientists from diverse fields, ranging from developmental biology, cell biology and synthetic biology, to physics, mathematics and computer science. Quantitative and interdisciplinary approaches have become essential for understanding these challenging phenomena [7, 8].

This Research Topic contains a collection of articles and reviews that use quantitative and interdisciplinary perspectives to understand the underlying mechanisms driving biological pattern formation. Modeling morphogenetic processes, gene regulatory network dynamics and morphogen gradients link the articles of this Research Topic, with a focus on three research areas: 1) underlying mechanisms of patterning processes; 2) cross-talk of morphogenetic and pattern formation processes, and 3) mathematical methods for modeling and quantifying biological patterning and morphogenesis. Below, each of the present Research Topic papers is briefly discussed.

One of the most celebrated mechanisms to explain self-organizing spatial structures is known as the Turing instability [9–13]. Lacalli's review provides a history of the application of Turing's ideas in developmental biology, which he has been a part of since the 1970's. In particular, Lacalli emphasizes the progress that can be made by investigating and understanding the role of such physicochemical systems that can make patterns *de novo* within the context of evolved biochemical or gene regulatory networks and that confer some degree of "programmatic assembly" on developmental phenomena. Lacalli details ways in which the relative contribution of *de novo* and programmatic elements may manifest in the generation of robust body and brain structures, including consciousness.

Certainly, although today there are no doubts about the Turing instability as a source of symmetry breaking in biological patterning, the molecular mechanisms behind Turing

remain difficult to validate experimentally, as many of the kinetic parameters cannot be reliably assessed in biological tissues.

Experiments and modeling have continued to reveal new extensions or alternatives to Turing for periodic pattern formation. The spatial patterns driven by Turing instabilities are stable structures historically associated with stable fixed points of the system [9–12]. However, exploring a known morphogenetic model [14], Guisoni and Diambra find that Turing patterns can also exist associated to unstable fixed points, enabling in this case the emergence of transient and also metastable spatial patterns.

In line with Turing ideas, Casanova-Ferrer et al. describe former and more recent quantitative modeling studies of heterocyst patterning in filamentous cyanobacteria in an in-depth review. In this case, in addition to an activator-inhibitor system, a particular type of Turing system, there exists another inhibitor gen, hetN, whose production is restricted to the heterocysts. This cell–cell scale inhibition provides an additional dynamics in the pattern formation, extending the diffusion-based Turing mechanism.

Iber and Mederacke offer a detailed state-of-the-art report on tracheal ring formation, reviewing recently elucidated molecular regulatory interactions. Despite these advances, the mechanism forming periodic rings in the trachea remains poorly understood. In this regard, the authors describe several putative mechanisms that could be better explored, such as chemotaxis, differential adhesion, and differential growth of two adjacent tissue layers, in addition to Turing instabilities.

A classic example of patterning is the periodic structure formed during somitogenesis resulting from the interplay of oscillatory gene expression and a maturation wavefront [2]. Carraco et al. provide an extensive bibliography on the embryonic clock of vertebrates over the last 25 years, with special emphasis on the understanding of species-specific oscillation periods, where similar gene architectures produce different periods in different contexts. Fernández Arancibia et al. propose a modified reaction wavefront model [15] which sequentially produces segments in the zebrafish notochord in a periodic manner, even in the presence of noise. In particular, the new model adds a reaction wavefront that sequentially activates the chemical reactions of the FitzHugh–Nagumo model [12].

Besides mechanisms based on biochemical interactions, there is a great deal of interest in how mechanical cues also drive biological patterning [16, 17]. Song et al. study the formation of the gastrovascular canal network in jellyfish through a combination of anatomical studies and mechanical modeling. The authors propose that mechanical stress acts as a trigger of differential growth of the canal network. Contraction during swimming is different for different parts of the tissue, and depends on the stiffness of the canal network itself. In this way, differential stiffness influences the growth direction of the canals and biases the connectivity of the canal network, affecting morphogenesis.

In addition, Moreno and Alonso address the interaction between pattern formation and locomotion at the cellular level. They performed a numerical analysis of a model of amoeboid cell morphology dynamics proposed in [18] and found that polarization, based on bistability, is sensitive to changes in parameter values. The authors introduce mass conservation constraints to increase the robustness of the model.

How cells are geometrically organized and packed in space is crucial in the formation of tissues and organs. Iber and Vetter review and discuss the physical principles driving 3D cellular organization and packing in tissues, focusing on the case of pseudostratified epithelia, a type of epithelia found in animal tissues where nuclei are positioned along the apical–basal axis. The authors propose a new geometrical shape, which they term "punakoid", whose irregular shape is reminiscent of the rocks at the beach of Punakaiki in New Zealand.

Finally, adequate mathematical tools and methodologies are critical for ensuring robust and reliable predictions from biological patterning models. From a more methodological and theoretical perspective, Mjolsness presents a fundamental study about dynamical graph grammars. In this work, the author extends the framework introduced in [19] and proposes a general expression that reduces products of rewrite rule operators to sums of such operators, resulting in two theorems that comprise a general modeling framework. Mjolsness presents an application of this multiscale mathematical method for modeling microtubule dynamics of the cytoskeleton in plant cells.

The spatial patterns of Min proteins on bacterial cells have been extensively studied with respect to pattern-formation mechanisms [20]. However, the transient and irregular nature of these patterns makes image processing and extraction of pattern quantities, such as wavelength, challenging. Meindlhumer et al. introduce a new analysis pipeline that quantifies temporal and spatial information from data images, which could provide a more reliable support for model development.

Pattern formation has been classically modeled and simulated in systems that are continuous in space [9, 10]. Yet, it has been increasingly important to have computational frameworks that can simulate biological pattern formation taking into account the underlying cellular spatial structure [7, 21] a feature that is limited in continuous models. In the last few years, several agent-based modeling frameworks have emerged, in which cells are treated as individual agents whose dynamics are governed by rules. Pleyer and Fleck discuss the use of agent-based modeling on cellular systems and multicellular pattern formation, and review different available computational frameworks of interest.

We hope this Research Topic will stimulate further studies from mathematical biologists and theoreticians interested in modeling biological patterning.

Author contributions

LD, PF-J, and DH conceived and wrote the editorial.

Acknowledgments

We would like to thank all the authors in the articles of this Research Topic for their contributions, all the reviewers for their constructive comments and Jizeng Wang for participating as guest Editor. PF-J acknowledges for being funded by the Deutsche Forschungsgemeinschaft (DFG, German Research Foundation) under Germany's Excellence Strategy—EXC-2048/1—project ID 390686111 and by the Max Planck Society (Germany), DH acknowledges the support of BCIT and NSERC Canada, and LD acknowledges the support by CONICET (Argentina).

Conflict of interest

The authors declare that the research was conducted in the absence of any commercial or financial relationships that could be construed as a potential conflict of interest.

Publisher's note

References

1. Gilbert SF. *Developmental biology*. 9th ed. United States: Sinauer Associates (2010).

2. Oates AC, Morelli LG, Ares S. Patterning embryos with oscillations: Structure, function and dynamics of the vertebrate segmentation clock. *Development* (2012) 139: 625–39. doi:10.1242/dev.063735

3. Clark E, Peel AD, Akam M. Arthropod segmentation. *Development* (2019) 146: dev170480. doi:10.1242/dev.170480

4. Torii KU. Two-dimensional spatial patterning in developmental systems. *Trends Cell Biology* (2012) 22:438–46. doi:10.1016/j.tcb.2012.06.002

5. Kuhlemeier C. Phyllotaxis. *Trends Plant Science* (2007) 12:143–50. doi:10.1016/j.tplants.2007.03.004

6. Asnacios A, Hamant O. The mechanics behind cell polarity. *Trends Cell Biology* (2012) 22:584–91. doi:10.1016/j.tcb.2012.08.005

7. Formosa-Jordan P, Teles J, Jönsson H. Single-cell approaches for understanding morphogenesis using computational morphodynamics. In: RJ Morris, editor. *Mathematical modelling in plant biology*. Cham: Springer International Publishing (2018). p. 87–106. doi:10.1007/978-3-319-99070-5_6

8. Negrete J, Oates AC. Towards a physical understanding of developmental patterning. *Nat Rev Genet* (2021) 22:518–31. doi:10.1038/s41576-021-00355-7

9. Turing AM. The chemical basis of morphogenesis. *Phil Trans R Soc Lond B, Biol Sci* (1952) 237:37–72.

10. Gierer A, Meinhardt H. A theory of biological pattern formation. *Kybernetik* (1972) 12:30–9. doi:10.1007/bf00289234

11. Cross MC, Hohenberg PC. Pattern formation outside of equilibrium. *Rev Mod Phys* (1993) 65:851–1112. doi:10.1103/revmodphys.65.851

12. Murray JD. *Mathematical biology II: Spatial models and biomedical applications*. New York: Springer (2003). doi:10.1007/b98869

13. Kondo S. The present and future of Turing models in developmental biology. *Development* (2022) 149:dev200974. doi:10.1242/dev.200974

14. Diambra L, Senthivel VR, Menendez DB, Isalan M. Cooperativity to increase Turing pattern space for synthetic biology. *ACS Synth Biol* (2015) 4:177–86. doi:10.1021/sb500233u

15. Forero LL, Narayanan R, Huitema LF, VanBergen M, Apschner A, Peterson-Maduro J, et al. Segmentation of the zebrafish axial skeleton relies on notochord sheath cells and not on the segmentation clock. *Elife* (2018) 7:e33843. doi:10.7554/eLife.33843

16. Brinkmann F, Mercker M, Richter T, Marciniak-Czochra A. Post-Turing tissue pattern formation: Advent of mechanochemistry. *PLoS Comput Biol* (2018) 14: e1006259. doi:10.1371/journal.pcbi.1006259

17. Villa C, Chaplain MA, Gerisch A, Lorenzi T. Mechanical models of pattern and form in biological tissues: The role of stress–strain constitutive equations. *Bull Math Biol* (2021) 83:80. doi:10.1007/s11538-021-00912-5

18. van Haastert PJ, Keizer-Gunnink I, Kortholt A. Coupled excitable Ras and F-actin activation mediates spontaneous pseudopod formation and directed cell movement. *Mol Biol Cel* (2017) 28:922–34. doi:10.1091/mbc.E16-10-0733

19. Mjolsness E. Prospects for declarative mathematical modeling of complex biological systems. *Bull Math Biol* (2019) 81:3385–420. doi:10.1007/s11538-019-00628-7

20. Wettmann L, Kruse K. The Min-protein oscillations in *Escherichia coli*: An example of self-organized cellular protein waves. *Phil Trans R Soc B: Biol Sci* (2018) 373: 20170111. doi:10.1098/rstb.2017.0111

21. Deutsch A, Dormann S. *Mathematical modeling of biological pattern formation*. Berlin, Germany: Springer (2005). doi:10.1007/0-8176-4415-6_3

frontiers | Frontiers in Cell and Developmental Biology

MINI REVIEW
published: 25 April 2022
doi: 10.3389/fcell.2022.900447

Tracheal Ring Formation

Dagmar Iber[1,2]* *and Malte Mederacke*[1,2]

[1]Department of Biosystems Science and Engineering, ETH Zurich, Basel, Switzerland, [2]Swiss Institute of Bioinformatics, Basel, Switzerland

The trachea is a long tube that enables air passage between the larynx and the bronchi. C-shaped cartilage rings on the ventral side stabilise the structure. On its esophagus-facing dorsal side, deformable smooth muscle facilitates the passage of food in the esophagus. While the symmetry break along the dorsal-ventral axis is well understood, the molecular mechanism that results in the periodic *Sox9* expression pattern that translates into the cartilage rings has remained elusive. Here, we review the molecular regulatory interactions that have been elucidated, and discuss possible patterning mechanisms. Understanding the principles of self-organisation is important, both to define biomedical interventions and to enable tissue engineering.

Keywords: trachea, cartilage rings, symmetry break, SOX9, Turing pattern, chemotaxis, differential adhesion, differential growth

1 INTRODUCTION

The trachea is a long (6 mm in mice, 10–15 cm in human), almost cylindrical tube that serves as a passage of air to the bronchial system Kishimoto and Morimoto (2021). Its wide diameter (1.5 mm in mice, 2–3 cm in human) poses little resistance to air flow. C-shaped cartilage rings on its ventral side prevent the collapse or obstruction of the tube (**Figure 1A**). Smooth muscle on the dorsal side allows for the expansion of the adjacent esophagus during the consumption of food or liquid. The separation into distinct domains that form cartilage and smooth muscles, and the subsequent emergence of cartilage rings reflects two separate symmetry breaks. While the first one is well understood, the molecular mechanism behind the second has remained elusive. In the following, we will discuss the regulatory interactions that are involved in these symmetry breaks.

2 DORSAL-VENTRAL POLARITY

The separation of cartilage and smooth muscles domains follows the already established dorsal-ventral polarity. Fibroblastic growth factor (FGF) from the cardiac mesoderm induces the *Nkx2.1*-expressing lung field on the ventral side of the mouse foregut Serls et al. (2005). Bone morphogenetic protein 4 (*Bmp4*) expression is restricted to the ventral foregut from early stages (E8.5) Li et al. (2008), and the BMP antagonist NOGGIN is secreted from the dorsally located notochord Fausett et al. (2014). BMP4 signalling surpresses SRY (sex determining region Y)-box transcription factor (*Sox*)2 expression in the ventral foregut Domyan et al. (2011). Mutual repression between NKX2.1, which is restricted to the ventral foregut endoderm, and SOX2, which is expressed in the dorsal foregut endoderm, defines the border between the trachea, and the future esophagus Que et al. (2007). NKX2.1 directly represses *Efnb2*, which establishes an EPH/EPHRIN boundary that results in the physical separation of tracheal and esophageal cells Lewis et al. (2022). *Nkx2.1* null mice, and endodermal mutants for the BMP type I receptor genes *Bmpr1a* and *Bmpr1b* upregulate *Sox2* and form a continuous ring of smooth muscle and no cartilage rings Que et al. (2007); Minoo et al. (1999);

OPEN ACCESS

Edited by:
David M. Holloway,
British Columbia Institute of Technology, Canada

Reviewed by:
Shigeru Kondo,
Osaka University, Japan

***Correspondence:**
Dagmar Iber
iberd@ethz.ch

Specialty section:
This article was submitted to Morphogenesis and Patterning, a section of the journal Frontiers in Cell and Developmental Biology

Received: 20 March 2022
Accepted: 05 April 2022
Published: 25 April 2022

Citation:
Iber D and Mederacke M (2022) Tracheal Ring Formation. Front. Cell Dev. Biol. 10:900447. doi: 10.3389/fcell.2022.900447

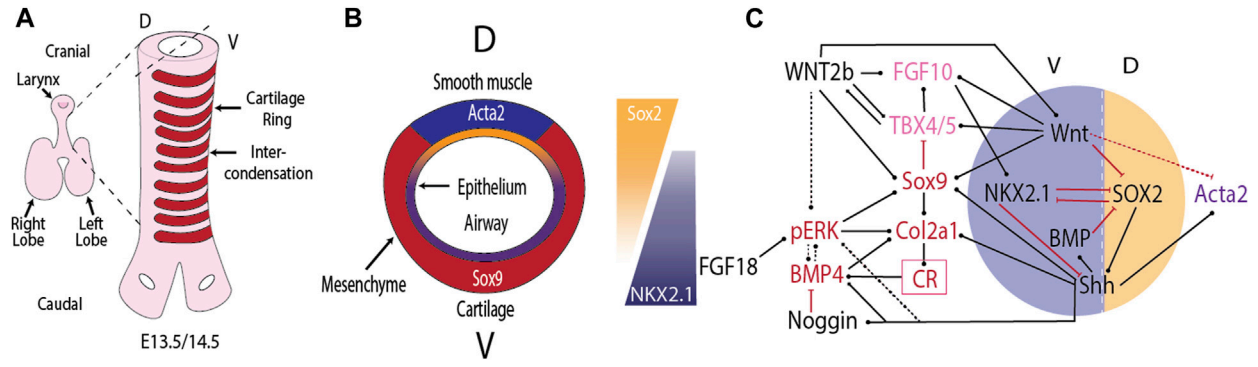

FIGURE 1 | Tracheal cartilage ring formation. **(A)** Cartilage rings (red) emerge in the mesenchyme on the ventral (V) side of the trachea. **(B)** Cross-section of the developing trachea. **(C)** Regulatory interactions that control the emergence of cartilage rings (CR) in the ventral and airway smooth muscle in the dorsal (D) tracheal mesenchyme. Black arrows indicate positive regulation, red arrows negative regulation. For details see text.

Yuan et al. (2000); Li et al. (2008); Domyan et al. (2011). Conditional ablation of *Bmp4* from the foregut endoderm from E8.5 and from the mesenchyme by E9.5 does not prevent the ventral expression of *Nkx2.1* at E9.5, but by E12.5 *Nkx2.1* is absent, and expression of the cartilage marker Collagen Type II Alpha 1 Chain (*Col2a1*) is not observed Li et al. (2008).

Once the trachea has split from the future esophagus, it maintains the dorsal-ventral polarity, with *Nkx2.1* expression restricted to the ventral side, and *Sox2* and Sonic Hedgehog (*Shh*) expression higher on the dorsal side (**Figure 1B**). This polarity is observed also in mutants (*Noggin* null) that fail to split the tubes Que et al. (2006). The epithelial dorsal–ventral polarity translates into a mesenchymal polarity. Mesenchymal cells derived from the splanchnic mesoderm, positioned ventral to the developing tracheal tube express the transcription factor *Sox9* as early as E10.5 Hines et al. (2013). From E11.5, dorsal mesenchymal cells express *Acta2*, a smooth muscle marker Hines et al. (2013). Removal of *Sox9* or a key smooth muscle gene does not alter the expression domain of the other in the trachea Hines et al. (2013). The spatial restriction is thus not maintained by mutual repression between SOX9 and smooth muscle genes. Rather, signals from the tracheal epithelium appear important for the spatial restriction in the mesenchyme. Blockage of WNT secretion from the tracheal epithelium in *Wls* conditional mutants blocks *Sox9* expression and results in smooth muscle formation also on the ventral side Snowball et al. (2015); Kishimoto et al. (2020). Epithelial WNT secretion thus seems to be required in translating the epithelial polarity to the mesenchyme. Canonical WNT signalling appears to be important in both layers as conditional removal of β-catenin in either the epithelium (*Shh-Cre* driven) or mesenchyme (*Dermo1-Cre* driven) results in loss of mesenchymal expression of the chondrogenic factor *Tbx4* Kishimoto et al. (2020). In *Shh* null mice, the ventral restriction of *Sox9* expression is lost, and until E13.5, *Sox9* is transiently weakly expressed in a circumferential expression pattern on both the dorsal and ventral sides Park et al. (2010). Even though *Shh* is expressed more strongly dorsally, overexpression of *Shh* does not affect the relative cartilage and smooth muscle domains Sala et al. (2011). Addition of BMP4 or Noggin to lung explant cultures induces patches of cartilage formation and *Sox9* and *Bmp4* expression around the entire tracheal epithelium Park et al. (2010).

In summary, the separation of the smooth muscle and cartilage domains along the dorsal-ventral axis is controlled by the already existing embryonic dorsal-ventral polarity. The dorsal-ventral polarity is first induced along the epithelial tube, and later translated to the mesenchyme via diffusible morphogens.

3 EMERGENCE OF PERIODIC PATTERNS ALONG THE TRACHEA

The positions of the future cartilage rings in the ventral tracheal mesenchyme first become apparent between embryonic day (E) 12.75 and E13 as periodic patterns in *Sox9* and type II collagen (*Col2a1*) expression Miller et al. (2004); Elluru et al. (2009); Park et al. (2010); Sala et al. (2011); Hines et al. (2013); Turcatel et al. (2013); Boucherat et al. (2014); Young et al. (2020). Lineage tracing experiments with Col2a1-mTmG mice show that *Col2a1*-expressing cells do not transdifferentiate into non-cartilage cells Young et al. (2020). Rather, the *Col2a1*-expressing cells condense in the cartilage rings, and the intervening space becomes filled by other mesenchymal cells. The *Col2a1* gene encodes the pro-alpha1 (II) chain component of type II collagen, which is primarily found in cartilage. At E11.5, collagen type II is restricted to the lamina propria on the ventral side of the trachea Sala et al. (2011). By E12.5, collagen type II has spread into the ventral mesenchyme, but no staining is observed in the ventral half of the ventral mesenchyme. By E13.5, collagen type II-positive condensations are observed. At the same time, phosphorylated extracellular signal-regulated kinase (ERK) is found mainly on the boundary of the cartilage condensations and at lower levels between the condensations, and is largely absent from the condensations Yoshida et al. (2020). Expression of the SHH receptor *Ptch1* appears to be restricted to the nascent

cartilage condensations from E13.5 Miller et al. (2004). In parallel, the expression of *Shh* assumes a periodic pattern on the ventral, but not on the dorsal side of the tracheal epithelial tube Sala et al. (2011). Around E13.5 or slightly after, *Tbx5* disappears from the cartilage condensations Tiozzo et al. (2009); Arora et al. (2012). From E14.5, *Fgf10* expression becomes restricted in between the nascent cartilage condensations, but its receptor *Fgfr2b* remains uniformly expressed in the epithelial tube Sala et al. (2011). The cartilage condensations secrete BMP4 by E17.5 Park et al. (2010); it is not known at what time the spatial restriction of *Bmp4* emerges.

4 MUTANTS WITHOUT CARTILAGE RINGS

Functional genetics can help to identify the components of the core mechanism as their null mutations should result in the loss of cartilage rings. In the following, we will focus on mutants that do not show any periodic *Sox9*/*Col2a1* expression patterns or tracheal cartilage ring formation, even though the trachea forms with correct dorsal-ventral polarity. This analysis thus necessarily excludes potential core components that are involved also in processes upstream of periodic pattern formation as their contribution to periodic patterning cannot be evaluated by this approach. The following mouse mutants have so far been reported that lack tracheal cartilage rings, even though the trachea forms with correct dorsal-ventral polarity: *Shh* null Miller et al. (2004); Park et al. (2010), *Sox9* null Hines et al. (2013); Turcatel et al. (2013), mesenchymal *Mek1*/*Mek2* removal Boucherat et al. (2014), and endodermal *Wls* removal Snowball et al. (2015). Finally, in mouse double mutants of R-spondin2 and lipoprotein receptor related protein 6 (*Rspo2Tg/Tg;Lrp6*$^{-/-}$) tracheal rings were absent on the shortened tracheal structure Bell et al. (2008), and *Dermo1-Cre*-driven conditional removal of β-catenin, a core component of canonical WNT signalling, result in loss of mesodermal *Tbx4*, impaired mesenchymal growth, and lack of cartilage rings at E16.5 Kishimoto et al. (2020). A mutation in human FGFR2 (S351C) prevents visible tracheal ring formation, but the cartilaginous tracheal sleeve still forms Gonzales et al. (2005). Alternative mRNA splicing in one of the extracellular immunoglobulin (Ig)-like domains results in different FGF receptor isoforms, known as FGFR (IIIb), and FGFR (IIIc) Johnson and Williams (1993). The isoforms differ in their ligand specificity and expression pattern. FGFR2(IIIb) is produced predominantly in epithelial cells and binds to FGF7 and FGF10, while FGFR2(IIIc) is found in the mesenchyme. *Fgfr2b* and *Fgf10* null mice have a different phenotype from that reported for human FGFR2 (S351C) in that they develop shorter tracheas with 6–8 distorted cartilage rings Min et al. (1998); Sekine et al. (1999); Sala et al. (2011), suggesting that the phenotype of human FGFR2 (S351C) results from defects in the mesenchymal isoform. Ectopic mesenchymal expression of *FgfR2b* in *FgfR2c* heterozygous mouse mutants results in overgrowth of the tracheal rings and absence of noncartilaginous mesenchyme Tiozzo et al. (2009).

BMP4 and its antagonist NOGGIN can both rescue cartilage formation as well as *Sox9* and *Bmp4* expression in *Shh* null lung explants, but cartilage formation is then no longer restricted to the ventral side; it has not been reported whether periodic patterns are obtained Park et al. (2010). BMP4 and Noggin induce additional cartilage formation also in wildtype lungs, and cartilage then forms also on the dorsal side. In *Bmp4* conditional mutants, *Nkx2.1* is restricted to the ventral side at E9.5, but is lost by E12.5, and no *Col2a1* expression and cartilage ring formation is observed Li et al. (2008). Mice with inactivated *Bmpr1b* and *Sox2*, and a SHH-driven endodermal conditional knockout of *Bmpr1a* develop a ventral NKX2.1 domain that forms disorganized isolated cartilage pieces/nodules, but not rings at later stages Domyan et al. (2011). Epithelial BMP signalling thus appears not to be necessary for the emergence of the periodic cartilage pattern. It is unclear whether mesenchymal BMP signalling is required for periodic cartilage formation as a combined mesenchymal knockout of *Bmpr1a* and *Bmpr1b* has so far not been reported.

While perturbations in many other pathways affect tracheal ring formation or tracheal growth, no other pathway has been described that is necessary for cartilage ring formation once the tracheal mesenchyme has emerged Iber (2021).

5 CONTROL OF CARTILAGE RING FORMATION

SOX9 controls all steps of the cartilage differentiation process, and is a necessary factor for cartilage ring formation such that cartilage rings are absent in mesenchymal *Sox9* knockout mice Hines et al. (2013); Turcatel et al. (2013). If doxycycline-driven *Sox9* removal is stopped at E13.5, then some cartilage nodules are observed by E18.5 in the most proximal part Turcatel et al. (2013). Progressively more distal nodules are observed if doxycycline induction is stopped already at E12.5 or E11.5 Turcatel et al. (2013). Secretion of endodermal WNT via WLS is required for mesenchymal *Sox9* expression Snowball et al. (2015), and *Sox9* expression appears strongly reduced or absent in *Rspo2Tg/Tg* mutant tracheal mesenchyme Bell et al. (2008). More generally, epithelial WNT ligands including WNT7b and WNT5a activate WNT/β-catenin in the mesenchyme of the developing trachea to influence expression of chondrogenic factors including *Tbx4*, *Tbx5*, *Msx1*, *Msx2*, *Sox9*, and *Col2a1* Snowball et al. (2015); Kishimoto et al. (2020). SHH signalling induces the expression of *Wnt5a* and its receptor *Ror2*, and ablation of *Wnt5a* or its receptor *Ror2* results in shorter trachea with fewer cartilage rings Li et al. (2002); Oishi et al. (2003). Deletion of *Wnt7b*, expressed by the respiratory epithelium and known to mediate Wnt/β-catenin signaling, does not affect trachea length or width, but results in incomplete cartilaginous rings Rajagopal et al. (2008). Deletion of *Wnt4* does not affect tracheal length, but results in 12 distorted rather than 14 tracheal rings, and results in reduced *Sox9* and increased *Fgf10* expression at 13.5 Caprioli et al. (2015).

SOX9 is a direct regulator of *Col2a1* expression (**Figure 1C**), a necessary factor for cartilage formation Rockich et al. (2013); Boucherat et al. (2014). Despite the direct regulation, the expression of *Sox9* and *Col2a1* is largely independently

regulated. Thus, *Col2a1* rings emerge in *Tbx4*/*Tbx5* conditional mutants even though *Sox9* expression is rather weak, and *Sox9* rings are barely visible Arora et al. (2012). Vice versa, *Col2a1* is absent in *Shh* null mice, even though *Sox9* is expressed until E13.5 Park et al. (2010). While *Sox9* is weakly expressed in *Shh* null mice until E13.5, the ventral restriction of *Sox9* expression is lost, and *Sox9* expression is completely lost by E15 Pepicelli et al. (1998); Park et al. (2010). One group reported disorganised cartilage ring formation in *Shh* null mice Pepicelli et al. (1998), but other groups failed to observe cartilage rings Park et al. (2010); Miller et al. (2004).

A study in chondrocytes showed that SOX9-GLI directly and cooperatively regulate many genes such as *Sox9*, *Col2a1*, *Ptch1*, *Gli1*, *Gli2*, *Fgfr3*, *Igf1r,* and *Bmp6* Tan et al. (2018). SHH signalling may thus engage in a positive feedback with SOX9. SHH signalling represses *Fgf10* expression, and *Fgf10* disappears from the mesenchymal condensations by E14.5 Bellusci et al. (1997); Park et al. (1998); Abler et al. (2009). In the absence of *Sox9*, the expression of *Fgf10*, *Tbx4*, and *Tbx5* remains uniform Turcatel et al. (2013). Conditional removal of *Tbx4*, and *Tbx5* has similar effects on trachea development as removal of *Fgf10*, but, even though TBX4/5 promote *Fgf10* expression Cebra-Thomas et al. (2003); Sakiyama et al. (2003), they appear to act also independently of FGF10 during trachea development Arora et al. (2012). *Bmp4*, *Wnt2/2b*, and *Sox9* are strongly reduced in *Tbx4/5* conditional mutants, but *Col2a1* levels appear normal.

Mesenchymal removal of *Mek1*/*Mek2* results in a thinner trachea with continuous, but lower *Sox9* expression at E14.5 and without cartilage rings by E18.5 Boucherat et al. (2014). Epithelial removal of *Mek1*/*Mek2* results in a shorter trachea with fewer cartilage rings. Culturing lung explants with PD0325901, an inhibitor for MEK, results in increased *Col2a1* expression and a widening of the cartilage condensations, but has no impact on *Sox9* expression Yoshida et al. (2020). This is consistent with reports in other systems that show that mesenchymal phosphorylated ERK (a kinase downstream of MEK) opposes cartilage formation Oh et al. (2000); Ibarra et al. (2021). The differences between the culture experiments and the mesenchymal knockouts likely reflect differences in dosage and spatial restriction.

Despite its importance for cartilage ring formation, the upstream regulators of the MEK/ERK cascasde have remained elusive. FGFs signal via ERK, and overexpression of *Fgf18* results in abnormal tracheal cartilage formation Elluru et al. (2009), but the knockout of *Fgf18* does not result in a tracheal phenotype Usui et al. (2004). The FGF10 receptor, FGFR2b, is restricted to the tracheal epithelium Sala et al. (2011), and can therefore not trigger mesenchymal ERK activation. BMP4 appears to be the main inducer of ERK1/2 activation in the E9.25 ventral endoderm and mesoderm Li et al. (2008), but it is not known whether it remains so also at later stages when mesenchymal condensations form (E12.5-E13.5). A cell culture study concluded that BMP2 induces *Sox9* transcription mainly via p38 MAP Kinase (MAPK), while regulating SOX9 transcription factor activity via pSMAD1/5/8 and p38 Pan et al. (2008). A number of other mechanisms has been found to activate ERK in other contexts. For one, mesenchymal WNT signalling has recently been shown to activate pERK in the cranial mesenchyme, which then blocks *Sox9* and *Col2a* expression and cartilage formation Ibarra et al. (2021). Non-canonical SHH signaling has been suggested to trigger calcium-induced extracellular signal-regulated kinases (ERK) activation Robbins et al. (2012); Carballo et al. (2018). ERK may also respond to pressure and/or curvature, as reported for the lung epithelium Hirashima and Matsuda (2021). In epithelial cells from the mammary gland, ERK activity has been found sensitive to the stiffness of the surrounding matrix Farahani et al. (2021). Whether any of this plays a role in the tracheal mesenchyme is not known.

Interestingly, upon conditional removal of Myorcardin, the cartilage rings fail to expand towards the dorsal side, and the trachael lumen is reduced Young et al. (2020). Considering that smooth muscles and peristalsis are undetectable, and the expression of two BMP inhibitors is decreased and pSMAD signalling is increased in the mutants, this could be the consequence of either mechanical and/or signalling defects.

In summary, WNT signalling (WLS, R-spondin2/LRP6) is essential for mesenchymal *Sox9* expression, and SOX9 is essential for cartilage formation. *Sox9* is still expressed weakly in *Shh* and mesenchymal *Mek1*/*Mek2* mutants, but fails to organise into rings. As such, SHH and MEK1/2 are either part of the core mechanism that results in periodic *Sox9* patterning, or periodic patterning fails because *Sox9* expression is too weak in those mutants. Myocardin, a master regulatory of smooth muscle differentiation, is necessary for the dorsal expansion of the nascent cartilage rings to their characteristic C-shape. But what leads to the periodic *Sox9* pattern?

6 CANDIDATE MECHANISMS FOR PERIODIC PATTERN FORMATION

A wide range of chemical and/or mechanical instabilities can result in biological pattern formation. The Swift-Hohenberg equation has been shown to recapitulate the complex tracheal cartilage pattern also at the tracheobranchial juncture, if coupled with a gradient to achieve the correct stripe orientation Kingsley et al. (2018). While the Swift-Hohenberg equation can be derived from fundamental equations for the Rayleigh-Benard convection in an heated fluid Swift and Hohenberg (1977), it has remained difficult to find a mechanistic explanation for the forth-order spatial derivative in biology Oza et al. (2016). Given its patterning versatility, Turing mechanisms Turing (1952) (**Figure 2A**) have been proposed for a large number of biological patterning processes, including tracheal cartilage ring formation Sala et al. (2011); Kingsley et al. (2018). While the mathematical properties of Turing mechanisms are well understood Murray (2003), and Turing patterns have been confirmed in chemical reaction systems Horvath et al. (2009), the molecular mechanism behind biological Turing mechanisms remains unknown. The experimental validation of proposed molecular implementations of Turing mechanisms remains impossible as kinetic parameters cannot be measured reliably in biological tissues and pattern likeness is insufficient proof. As such, only the experimental rejection of Turing mechanisms is possible to date. A well-known example are the stripes in the *Drosophila*

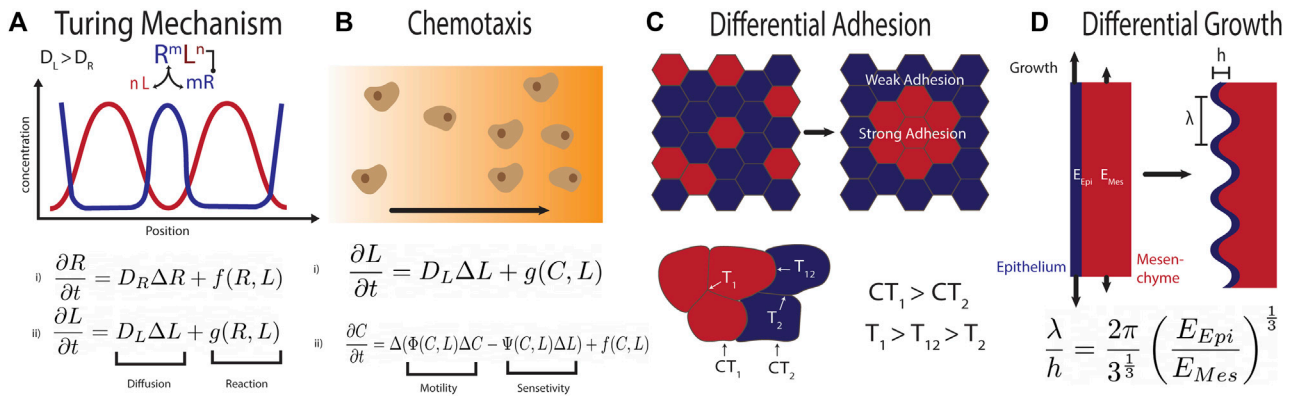

FIGURE 2 | (A) Repetitive patterns can emerge via a Turing mechanism when two regulatory factors that diffuse at different speeds engage in a negative feedback Turing (1952). In case of the ligand-receptor based Turing mechanism, the binding of the rapidly diffusing ligand (L) to the slowly diffusing receptor (R) results in up-regulation of the receptor and removal of the ligand. This system can be modelled with two coupled partial differential reaction diffusion equations. This system can yield a large variety of patterns, dependent on the reaction parameters and the tissue geometry. **(B)** Chemotaxis can result in periodic patterning when motile cells (C) produce and consume the diffusible chemoattractant or chemorepellent (*L*), as modelled for instance by the Keller-Segel model Keller and Segel (1971). **(C)** Differential adhesion between the blue and the red cells can result in periodic pattern formation. The mixture of cells is dependent on their relative surface tension (CT_1 for the red, CT_2 for the blue population). This results in three different relative surface tensions (T_1 between red cells, T_2 between blue and T_{12} between the two populations) Canty et al. (2017). To achieve separation in the displayed form CT_1 must be larger than CT_2 and T_1 larger than T_{12} which is larger than T_2. **(D)** Differential growth of two adjacent tissue layers can result in buckling. The wavelength λ of the periodic pattern depends on the thickness, *h*, of the expanding epithelial layer (blue layer), and the relative Young modulus E_{Epi}/E_{Mes} of epithelium (blue) and mesenchyme (red) Sultan and Boudaoud (2008).

blastoderm, which were initially accounted to a Turing mechanism, but have since been shown to result from cross-repressive transcription factor cascades downstream of opposing morphogen gradients Meinhardt (1986); Lacalli et al. (1988); Akam (1989); Jaeger (2011). In many other complex, stereotypic patterning systems, Turing models have remained the only candidate mechanism that is consistent with the experimental data. In its simplest form, Turing patterns require a negative feedback between at least two components that diffuse at different speed. Turing patterns can be obtained also with a single morphogen or growth factor if its binding to the cell-bound receptor upregulates the receptor concentration (**Figure 2A**), as is the case for SHH, FGF10, and BMP Menshykau et al. (2012); Badugu et al. (2012); Celliere et al. (2012); Kurics et al. (2014); Menshykau et al. (2014). Candidate networks for Turing models that yield periodic cartilage patterns have been studied extensively in limb development, where the cartilage condensations mark future digits and phalanges Iber and Germann (2014). The patterns in wildtype and perturbed conditions could be explained with a variety of biological mechanisms, including a 3-node network composed of BMP, SOX9, and WNT Raspopovic et al. (2014), a negative feedback between TGF-β and either the extracellular matrix (ECM) or TGF-β antagonists Zhu et al. (2010), and the interaction between BMPs and its receptor Badugu et al. (2012). These mechanisms have so far not been explored in the trachea. Mesodermal β-catenin appears necessary also for tracheal *Sox9* expression Kishimoto et al. (2020), but this makes it difficult to assess the role of WNT signalling in the subsequent periodic patterning of SOX9. In case of a ligand-receptor-based Turing mechanism, the receptor would have to be upregulated in the tracheal cartilage condensations. This has indeed been reported for the SHH receptor PTCH1 Miller et al. (2004). The expression patterns of *Bmpr1a* and *Bmpr1b* are not known. Unlike in lung branching morphogenesis Menshykau et al. (2014); Kurics et al. (2014), FGF10 is unlikely to be part of the core Turing mechanism as its receptor remains uniformly expressed in the tracheal epithelium, and periodic collagen type II patterns are still observed in *Fgf10* mice, if delayed and less uniformly shaped compared to the wildtype Sala et al. (2011). In case of a SHH-based ligand-receptor-based Turing mechanism, uniform SHH signalling on the dorsal side of the trachea could be explained with the higher *Shh* expression levels Que et al. (2009) that can take the regulatory system out of Turing parameter space and thereby ensure uniform patterns Kurics et al. (2014). The one-day patterning delay observed in *Fgf10* null mice Sala et al. (2011) may then reflect a delay in the ventral downregulation of *Shh* expression. Apart from chemical signalling, cell-cell interactions can also result in Turing instabilities Watanabe and Kondo (2015). Given the movement and aggregation of *Col2a1*-expressing cells Young et al. (2020), the periodic pattern could, in principle, also arise from chemotaxis Keller and Segel (1971); Hillen and Painter (2009) (**Figure 2B**), or differential adhesion of cartilage progenitors in the ventral mesenchyme, though additional mechanisms would need to be in place to ensure reproducible stripe formation from noisy initial conditions Armstrong et al. (2006); Canty et al. (2017); Carrillo et al. (2019) (**Figure 2C**). Finally, differential growth of the ventral epithelium and mesenchyme (**Figure 2D**) could result in periodic patterning Sultan and Boudaoud (2008); Marin-Riera et al. (2018); Carrillo et al. (2019); Tozluoglu and Mao (2020). Expansion of a thin, incompressible layer with elastic modulus E_{Epi} and thickness h relative to a thick, incompressible substrate with modulus E_{Mes} results in buckling with wavelength $\lambda = 2\pi h(\frac{E_{Epi}}{3E_{Mes}})^{1/3}$ Sultan and

Boudaoud (2008). To obtain the ratio of patterning wavelength, λ, and epithelial thickness, h, that is observed in the trachea Yoshida et al. (2020), the Young moduli of epithelium, E_{Epi}, and mesenchyme, E_{Mes}, would need to be similar. However, even if the epithelial folds arise from epithelial buckling, they may well be a consequence rather than a driver of mesenchymal condensations. After all, mesenchymal condensations reduce spatial expansion. Given this wide range of possibilities, more quantitative experimental studies and mathematical modelling are required to delineate the mechanism by which the cartilage rings form.

7 CONCLUSION AND OUTLOOK

Despite the simplicity of the pattern and the importance of the structure, tracheal cartilage ring formation remains poorly understood. Conditional mutants in combination with explant cultures, organoids, quantitative imaging, and mathematical modelling may help to unravel this patterning mechanism.

AUTHOR CONTRIBUTIONS

DI wrote the text; MM created the figures.

FUNDING

This work was funded by SNF Sinergia grant CRSII5_170930 to DI. Open access funding provided by ETH Zürich.

ACKNOWLEDGMENTS

We thank members of the CoBi group for discussions.

REFERENCES

Abler, L. L., Mansour, S. L., and Sun, X. (2009). Conditional Gene Inactivation Reveals Roles for Fgf10 and Fgfr2 in Establishing a normal Pattern of Epithelial Branching in the Mouse Lung. *Dev. Dyn.* 238, 1999–2013. doi:10.1002/dvdy.22032

Akam, M. (1989). Drosophila Development: Making Stripes Inelegantly. *Nature* 341, 282–283. doi:10.1038/341282a0

Armstrong, N. J., Painter, K. J., and Sherratt, J. A. (2006). A Continuum Approach to Modelling Cell-Cell Adhesion. *J. Theor. Biol.* 243, 98–113. doi:10.1016/j.jtbi.2006.05.030

Arora, R., Metzger, R. J., and Papaioannou, V. E. (2012). Multiple Roles and Interactions of Tbx4 and Tbx5 in Development of the Respiratory System. *Plos Genet.* 8, e1002866. doi:10.1371/journal.pgen.1002866

Badugu, A., Kraemer, C., Germann, P., Menshykau, D., and Iber, D. (2012). Digit Patterning during Limb Development as a Result of the Bmp-Receptor Interaction. *Sci. Rep.* 2, 991. doi:10.1038/srep00991

Bell, S. M., Schreiner, C. M., Wert, S. E., Mucenski, M. L., Scott, W. J., and Whitsett, J. A. (2008). R-Spondin 2 Is Required for normal Laryngeal-Tracheal, Lung and Limb Morphogenesis. *Development* 135, 1049–1058. doi:10.1242/dev.013359

Bellusci, S., Grindley, J., Emoto, H., Itoh, N., and Hogan, B. L. (1997). Fibroblast Growth Factor 10 (Fgf10) and Branching Morphogenesis in the Embryonic Mouse Lung. *Development* 124, 4867–4878. doi:10.1242/dev.124.23.4867

Boucherat, O., Nadeau, V., Bérubé-Simard, F.-A., Charron, J., and Jeannotte, L. (2014). Crucial Requirement of Erk/mapk Signaling in Respiratory Tract Development. *Development* 141, 3197–3211. doi:10.1242/dev.110254

Canty, L., Zarour, E., Kashkooli, L., François, P., and Fagotto, F. (2017). Sorting at Embryonic Boundaries Requires High Heterotypic Interfacial Tension. *Nat. Commun.* 8, 157. doi:10.1038/s41467-017-00146-x

Caprioli, A., Villasenor, A., Wylie, L. A., Braitsch, C., Marty-Santos, L., Barry, D., et al. (2015). Wnt4 Is Essential to normal Mammalian Lung Development. *Dev. Biol.* 406, 222–234. doi:10.1016/j.ydbio.2015.08.017

Carballo, G. B., Honorato, J. R., de Lopes, G. P. F., and Spohr, T. C. L. d. S. e. (2018). A Highlight on Sonic Hedgehog Pathway. *Cell Commun. Signal* 16, 11. doi:10.1186/s12964-018-0220-7

Carrillo, J. A., Murakawa, H., Sato, M., Togashi, H., and Trush, O. (2019). A Population Dynamics Model of Cell-Cell Adhesion Incorporating Population Pressure and Density Saturation. *J. Theor. Biol.* 474, 14–24. doi:10.1016/j.jtbi.2019.04.023

Cebra-Thomas, J. A., Bromer, J., Gardner, R., Lam, G. K., Sheipe, H., and Gilbert, S. F. (2003). T-box Gene Products Are Required for Mesenchymal Induction of Epithelial Branching in the Embryonic Mouse Lung. *Dev. Dyn.* 226, 82–90. doi:10.1002/dvdy.10208

Cellière, G., Menshykau, D., and Iber, D. (2012). Simulations Demonstrate a Simple Network to Be Sufficient to Control branch point Selection, Smooth Muscle and Vasculature Formation during Lung Branching Morphogenesis. *Biol. Open* 1, 775–788. doi:10.1242/bio.20121339

Domyan, E. T., Ferretti, E., Throckmorton, K., Mishina, Y., Nicolis, S. K., and Sun, X. (2011). Signaling through Bmp Receptors Promotes Respiratory Identity in the Foregut via Repression of Sox2. *Development* 138, 971–981. doi:10.1242/dev.053694

Elluru, R. G., Thompson, F., and Reece, A. (2009). Fibroblast Growth Factor 18 Gives Growth and Directional Cues to Airway Cartilage. *Laryngoscope* 119, 1153–1165. doi:10.1002/lary.20157

Farahani, P. E., Lemke, S. B., Dine, E., Uribe, G., Toettcher, J. E., and Nelson, C. M. (2021). Substratum Stiffness Regulates Erk Signaling Dynamics through Receptor-Level Control. *Cel. Rep.* 37, 110181. doi:10.1016/j.celrep.2021.110181

Fausett, S. R., Brunet, L. J., and Klingensmith, J. (2014). Bmp Antagonism by Noggin Is Required in Presumptive Notochord Cells for Mammalian Foregut Morphogenesis. *Dev. Biol.* 391, 111–124. doi:10.1016/j.ydbio.2014.02.008

Gonzales, M., Heuertz, S., Martinovic, J., Delahaye, S., Bazin, A., Loget, P., et al. (2005). Vertebral Anomalies and Cartilaginous Tracheal Sleeve in Three Patients with Pfeiffer Syndrome Carrying the S351c Fgfr2 Mutation. *Clin. Genet.* 68, 179–181. doi:10.1111/j.1399-0004.2005.00477.x

Hillen, T., and Painter, K. J. (2009). A User's Guide to PDE Models for Chemotaxis. *J. Math. Biol.* 58, 183–217. doi:10.1007/s00285-008-0201-3

Hines, E. A., Jones, M.-K. N., Verheyden, J. M., Harvey, J. F., and Sun, X. (2013). Establishment of Smooth Muscle and Cartilage Juxtaposition in the Developing Mouse Upper Airways. *Proc. Natl. Acad. Sci. U.S.A.* 110, 19444–19449. doi:10.1073/pnas.1313223110

Hirashima, T., and Matsuda, M. (2021). Erk-mediated Curvature Feedback Regulates Branching Morphogenesis in Lung Epithelial Tissue. *bioRxiv*. doi:10.1101/2021.07.11.451982

Horváth, J., Szalai, I., and De Kepper, P. (2009). An Experimental Design Method Leading to Chemical Turing Patterns. *Science* 324, 772–775. doi:10.1126/science.1169973

Ibarra, B., Beatriz, A., Machen, C., Radhika, P., and Atit (2021). Wnt-Dependent Activation of ERK Mediates Repression of Chondrocyte Fate during Calvarial Development. *J. Developm. Biol.* 9 (3), 23. doi:10.3390/jdb9030023

Iber, D., and Germann, P. (2014). How Do Digits Emerge? - Mathematical Models of Limb Development. *Birth Defect Res. C* 102, 1–12. doi:10.1002/bdrc.21057

Iber, D. (2021). The Control of Lung Branching Morphogenesis in *Current Topics in Developmental Biology* Editors M. Affolter. Academic Press 143, 205–237. doi:10.1016/bs.ctdb.2021.02.002

Jaeger, J. (2011). The gap Gene Network. *Cell. Mol. Life Sci.* 68, 243–274. doi:10.1007/s00018-010-0536-y

Johnson, D. E., and Williams, L. T. (1993). Structural and Functional Diversity in the Fgf Receptor Multigene Family. *Adv. Cancer Res.* 60, 1–41. doi:10.1016/s0065-230x(08)60821-0

Keller, E. F., and Segel, L. A. (1971). Model for Chemotaxis. *J. Theor. Biol.* 30, 225–234. doi:10.1016/0022-5193(71)90050-6

Kingsley, E. P., Eliason, C. M., Riede, T., Li, Z., Hiscock, T. W., Farnsworth, M., et al. (2018). Identity and novelty in the Avian Syrinx. *Proc. Natl. Acad. Sci. U.S.A.* 115, 10209–10217. doi:10.1073/pnas.1804586115

Kishimoto, K., and Morimoto, M. (2021). Mammalian Tracheal Development and Reconstruction: Insights from *In Vivo* and *In Vitro* Studies. *Development* 148, dev198192. doi:10.1242/dev.198192

Kishimoto, K., Furukawa, K. T., Luz-Madrigal, A., Yamaoka, A., Matsuoka, C., Habu, M., et al. (2020). Bidirectional Wnt Signaling between Endoderm and Mesoderm Confers Tracheal Identity in Mouse and Human Cells. *Nat. Commun.* 11, 4159. doi:10.1038/s41467-020-17969-w

Kurics, T., Menshykau, D., and Iber, D. (2014). Feedback, Receptor Clustering, and Receptor Restriction to Single Cells Yield Large Turing Spaces for Ligand-Receptor-Based Turing Models. *Phys. Rev. E Stat. Nonlin Soft Matter Phys.* 90, 022716. doi:10.1103/PhysRevE.90.022716

Lacalli, T. C., Wilkinson, D. A., and Harrison, L. G. (1988). Theoretical Aspects of Stripe Formation in Relation to drosophila Segmentation. *Development* 104, 105–113. doi:10.1242/dev.104.1.105

Lewis, A. E., Kuwahara, A., Franzosi, J., and Bush, J. O. (2022). Tracheal Separation Is Driven by Nkx2-1-Mediated Repression of Efnb2 and Regulation of Endodermal Cell Sorting. *Cel Rep.* 38, 110510. doi:10.1016/j.celrep.2022.110510

Li, C., Xiao, J., Hormi, K., Borok, Z., and Minoo, P. (2002). Wnt5a Participates in Distal Lung Morphogenesis. *Dev. Biol.* 248, 68–81. doi:10.1006/dbio.2002.0729

Li, Y., Gordon, J., Manley, N. R., Litingtung, Y., and Chiang, C. (2008). Bmp4 Is Required for Tracheal Formation: a Novel Mouse Model for Tracheal Agenesis. *Dev. Biol.* 322, 145–155. doi:10.1016/j.ydbio.2008.07.021

Marin-Riera, M., Moustakas-Verho, J., Savriama, Y., Jernvall, J., and Salazar-Ciudad, I. (2018). Differential Tissue Growth and Cell Adhesion Alone Drive Early Tooth Morphogenesis: An *Ex Vivo* and In Silico Study. *Plos Comput. Biol.* 14, e1005981. doi:10.1371/journal.pcbi.1005981

Meinhardt, H. (1986). Hierarchical Inductions of Cell States: a Model for Segmentation in drosophila. *J. Cel Sci Suppl.* 1986, 357–381. doi:10.1242/jcs.1986.supplement_4.20

Menshykau, D., Kraemer, C., and Iber, D. (2012). Branch Mode Selection during Early Lung Development. *Plos Comput. Biol.* 8, e1002377. doi:10.1371/journal.pcbi.1002377

Menshykau, D., Blanc, P., Unal, E., Sapin, V., and Iber, D. (2014). An Interplay of Geometry and Signaling Enables Robust Lung Branching Morphogenesis. *Development* 141, 4526–4536. doi:10.1242/dev.116202

Miller, L.-A. D., Wert, S. E., Clark, J. C., Xu, Y., Perl, A.-K. T., and Whitsett, J. A. (2004). Role ofSonic Hedgehog in Patterning of Tracheal-Bronchial Cartilage and the Peripheral Lung. *Dev. Dyn.* 231, 57–71. doi:10.1002/dvdy.20105

Min, H., Danilenko, D. M., Scully, S. A., Bolon, B., Ring, B. D., Tarpley, J. E., et al. (1998). Fgf-10 Is Required for Both Limb and Lung Development and Exhibits Striking Functional Similarity to drosophila Branchless. *Genes Dev.* 12, 3156–3161. doi:10.1101/gad.12.20.3156

Minoo, P., Su, G., Drum, H., Bringas, P., and Kimura, S. (1999). Defects in Tracheoesophageal and Lung Morphogenesis inNkx2.1(−/−) Mouse Embryos. *Dev. Biol.* 209, 60–71. doi:10.1006/dbio.1999.9234

Murray, J. D. (2003). "Mathematical Biology," in : *Mathematical Biology: II. Spatial Models and Biomedical Applications*. 3rd edition (Springer), 2.

Oh, C.-D., Chang, S.-H., Yoon, Y.-M., Lee, S.-J., Lee, Y.-S., Kang, S.-S., et al. (2000). Opposing Role of Mitogen-Activated Protein Kinase Subtypes, Erk-1/2 and P38, in the Regulation of Chondrogenesis of Mesenchymes. *J. Biol. Chem.* 275, 5613–5619. doi:10.1074/jbc.275.8.5613

Oishi, I., Suzuki, H., Onishi, N., Takada, R., Kani, S., Ohkawara, B., et al. (2003). The Receptor Tyrosine Kinase Ror2 Is Involved in Non-canonical Wnt5a/jnk Signalling Pathway. *Genes Cells* 8, 645–654. doi:10.1046/j.1365-2443.2003.00662.x

Oza, A. U., Heidenreich, S., and Dunkel, J. (2016). Generalized swift-hohenberg Models for Dense Active Suspensions. *Eur. Phys. J. E* 39, 97. doi:10.1140/epje/i2016-16097-2

Pan, Q., Yu, Y., Chen, Q., Li, C., Wu, H., Wan, Y., et al. (2008). Sox9, a Key Transcription Factor of Bone Morphogenetic Protein-2-Induced Chondrogenesis, Is Activated through Bmp Pathway and a Ccaat Box in the Proximal Promoter. *J. Cel. Physiol.* 217, 228–241. doi:10.1002/jcp.21496

Park, W. Y., Miranda, B., Lebeche, D., Hashimoto, G., and Cardoso, W. V. (1998). Fgf-10 Is a Chemotactic Factor for Distal Epithelial Buds during Lung Development. *Dev. Biol.* 201, 125–134. doi:10.1006/dbio.1998.8994

Park, J., Zhang, J. J. R., Moro, A., Kushida, M., Wegner, M., and Kim, P. C. W. (2010). Regulation of Sox9 by Sonic Hedgehog (Shh) Is Essential for Patterning and Formation of Tracheal Cartilage. *Dev. Dyn.* 239, 514–526. doi:10.1002/dvdy.22192

Pepicelli, C. V., Lewis, P. M., and McMahon, A. P. (1998). Sonic Hedgehog Regulates Branching Morphogenesis in the Mammalian Lung. *Curr. Biol.* 8, 1083–1086. doi:10.1016/s0960-9822(98)70446-4

Que, J., Choi, M., Ziel, J. W., Klingensmith, J., and Hogan, B. L. M. (2006). Morphogenesis of the Trachea and Esophagus: Current Players and New Roles for Noggin and Bmps. *Differentiation* 74, 422–437. doi:10.1111/j.1432-0436.2006.00096.x

Que, J., Okubo, T., Goldenring, J. R., Nam, K.-T., Kurotani, R., Morrisey, E. E., et al. (2007). Multiple Dose-dependent Roles for Sox2 in the Patterning and Differentiation of Anterior Foregut Endoderm. *Development* 134, 2521–2531. doi:10.1242/dev.003855

Que, J., Luo, X., Schwartz, R. J., and Hogan, B. L. M. (2009). Multiple Roles for Sox2 in the Developing and Adult Mouse Trachea. *Development* 136, 1899–1907. doi:10.1242/dev.034629

Rajagopal, J., Carroll, T. J., Guseh, J. S., Bores, S. A., Blank, L. J., Anderson, W. J., et al. (2008). Wnt7b Stimulates Embryonic Lung Growth by Coordinately Increasing the Replication of Epithelium and Mesenchyme. *Development* 135, 1625–1634. doi:10.1242/dev.015495

Raspopovic, J., Marcon, L., Russo, L., and Sharpe, J. (2014). Digit Patterning Is Controlled by a Bmp-Sox9-Wnt Turing Network Modulated by Morphogen Gradients. *Science* 345, 566–570. doi:10.1126/science.1252960

Robbins, D. J., Fei, D. L., and Riobo, N. A. (2012). The Hedgehog Signal Transduction Network. *Sci. Signal.* 5, re6. doi:10.1126/scisignal.2002906

Rockich, B. E., Hrycaj, S. M., Shih, H. P., Nagy, M. S., Ferguson, M. A. H., Kopp, J. L., et al. (2013). Sox9 Plays Multiple Roles in the Lung Epithelium during Branching Morphogenesis. *Proc. Natl. Acad. Sci. U.S.A.* 110, E4456–E4464. doi:10.1073/pnas.1311847110

Sakiyama, J.-i., Yamagishi, A., and Kuroiwa, A. (2003). Tbx4-Fgf10system Controls Lung Bud Formation during Chicken Embryonic Development. *Development* 130, 1225–1234. doi:10.1242/dev.00345

Sala, F. G., Del Moral, P.-M., Tiozzo, C., Alam, D. A., Warburton, D., Grikscheit, T., et al. (2011). Fgf10 Controls the Patterning of the Tracheal Cartilage Rings via Shh. *Development* 138, 273–282. doi:10.1242/dev.051680

Sekine, K., Ohuchi, H., Fujiwara, M., Yamasaki, M., Yoshizawa, T., Sato, T., et al. (1999). Fgf10 Is Essential for Limb and Lung Formation. *Nat. Genet.* 21, 138–141. doi:10.1038/5096

Serls, A. E., Doherty, S., Parvatiyar, P., Wells, J. M., and Deutsch, G. H. (2005). Different Thresholds of Fibroblast Growth Factors Pattern the Ventral Foregut into Liver and Lung. *Development* 132, 35–47. doi:10.1242/dev.01570

Snowball, J., Ambalavanan, M., Whitsett, J., and Sinner, D. (2015). Endodermal Wnt Signaling Is Required for Tracheal Cartilage Formation. *Dev. Biol.* 405, 56–70. doi:10.1016/j.ydbio.2015.06.009

Sultan, E., and Boudaoud, A. (2008). The Buckling of a Swollen Thin Gel Layer Bound to a Compliant Substrate. *ASME. J. Appl. Mech.* 75 (5), 051002. doi:10.1115/1.2936922

Swift, J., and Hohenberg, P. C. (1977). Hydrodynamic Fluctuations at the Convective Instability. *Phys. Rev. A.* 15, 319–328. doi:10.1103/PhysRevA.15.319

Tan, Z., Niu, B., Tsang, K. Y., Melhado, I. G., Ohba, S., He, X., et al. (2018). Synergistic Co-regulation and Competition by a Sox9-Gli-Foxa Phasic Transcriptional Network Coordinate Chondrocyte Differentiation Transitions. *Plos Genet.* 14, e1007346. doi:10.1371/journal.pgen.1007346

Tiozzo, C., Langhe, S. D., Carraro, G., Alam, D. A., Nagy, A., Wigfall, C., et al. (2009). Fibroblast Growth Factor 10 Plays a Causative Role in the Tracheal Cartilage Defects in a Mouse Model of Apert Syndrome. *Pediatr. Res.* 66, 386–390. doi:10.1203/PDR.0b013e3181b45580

Tozluoglu, M., and Mao, Y. (2020). On Folding Morphogenesis, a Mechanical Problem. *Philos. Trans. R. Soc. B: Biol. Sci.* 375, 20190564. doi:10.1098/rstb.2019.0564

Turcatel, G., Rubin, N., Menke, D. B., Martin, G., Shi, W., and Warburton, D. (2013). Lung Mesenchymal Expression of Sox9plays a Critical Role in Tracheal Development. *BMC Biol.* 11, 117. doi:10.1186/1741-7007-11-117

Turing, A. M. (1952). The Chemical Basis of Morphogenesis. *Phil. Trans. Roy. Soc. Lond.* B237, 37–72.

Usui, H., Shibayama, M., Ohbayashi, N., Konishi, M., Takada, S., and Itoh, N. (2004). Fgf18 Is Required for Embryonic Lung Alveolar Development. *Biochem. Biophys. Res. Commun.* 322, 887–892. doi:10.1016/j.bbrc.2004.07.198

Watanabe, M., and Kondo, S. (2015). Fish Pigmentation. Comment on "local Reorganization of Xanthophores fine-tunes and Colors the Striped Pattern of Zebrafish. *Science* 348, 297. doi:10.1126/science.1261947

Yoshida, T., Matsuda, M., and Hirashima, T. (2020). Incoherent Feedforward Regulation via Sox9 and Erk Underpins Mouse Tracheal Cartilage Development. *Front. Cel Dev. Biol.* 8, 585640. doi:10.3389/fcell.2020.585640

Young, R. E., Jones, M. K., Hines, E. A., Li, R., Luo, Y., Shi, W., et al. (2020). Smooth Muscle Differentiation Is Essential for Airway Size, Tracheal Cartilage Segmentation, but Dispensable for Epithelial Branching. *Dev. Cel.* 53, 73–85.e5. doi:10.1016/j.devcel.2020.02.001

Yuan, B., Li, C., Kimura, S., Engelhardt, R. T., Smith, B. R., and Minoo, P. (2000). Inhibition of Distal Lung Morphogenesis innkx2.1(?/?) Embryos. *Dev. Dyn.* 217, 180–190. doi:10.1002/(sici)1097-0177(200002)217:2<180::aid-dvdy5>3.0.co;2-3

Zhu, J., Zhang, Y.-T., Alber, M. S., and Newman, S. A. (2010). Bare Bones Pattern Formation: a Core Regulatory Network in Varying Geometries Reproduces Major Features of Vertebrate Limb Development and Evolution. *PLoS ONE* 5, e10892. doi:10.1371/journal.pone.0010892

Conflict of Interest: The authors declare that the research was conducted in the absence of any commercial or financial relationships that could be construed as a potential conflict of interest.

Publisher's Note: All claims expressed in this article are solely those of the authors and do not necessarily represent those of their affiliated organizations, or those of the publisher, the editors and the reviewers. Any product that may be evaluated in this article, or claim that may be made by its manufacturer, is not guaranteed or endorsed by the publisher.

frontiers | Frontiers in Physics

ORIGINAL RESEARCH
published: 28 April 2022
doi: 10.3389/fphy.2022.881885

Mass-Conservation Increases Robustness in Stochastic Reaction-Diffusion Models of Cell Crawling

*Eduardo Moreno and Sergio Alonso**

Department of Physics, Universitat Politècnica de Catalunya, Barcelona, Spain

The process of polarization determines the head and tail of single cells. A mechanism of this kind frequently precedes the subsequent cell locomotion and it determines the direction of motion. The process of polarization has frequently been described as a reaction-diffusion mechanism combined with a source of stochastic perturbations. We selected a particular model of amoeboid cell crawling for the motion of *Dictyostelium discoideum* and studied the interplay between pattern formation and locomotion. Next, we integrated the model in a two-dimensional domain considering the shape deformations of the cells in order to characterize the dynamics. We observed that the condition of pattern formation is finely tuned and we propose a modification based on the use of a mass-conservation constraint to substantially increase the robustness of the mathematical model.

Keywords: bistability, stochastic partial differential equations, pattern formation, *Dictyostelium discoideum*, cell polarization, amoeboid motion

OPEN ACCESS

Edited by:
Luis Diambra,
National University of La Plata, Argentina

Reviewed by:
Satoshi Sawai,
The University of Tokyo, Japan
M. N. Kuperman,
Bariloche Atomic Centre (CNEA), Argentina

****Correspondence:***
Sergio Alonso
s.alonso@upc.edu

Specialty section:
This article was submitted to Biophysics, a section of the journal Frontiers in Physics

Received: *23 February 2022*
Accepted: *12 April 2022*
Published: *28 April 2022*

Citation:
Moreno E and Alonso S (2022) Mass-Conservation Increases Robustness in Stochastic Reaction-Diffusion Models of Cell Crawling. Front. Phys. 10:881885. doi: 10.3389/fphy.2022.881885

1 INTRODUCTION

An intensive use of physical and mathematical theories on pattern formation in extended systems [1, 2], gave rise to valuable arguments to explain the formation of certain biological structures. Such mathematical mechanisms have permitted the modeling of processes on very different spatial and temporal scales: from the formation of the skin in fishes [3], to the definition of the direction in embryonic developing [4]. Such mechanisms have to be robust to small changes of parameters in order to be reliable. Robustness is a generic feature of living cells. It ensures that specific cellular functions are maintained despite external and internal change on the conditions. System control and feedback control are some of the characteristic mechanisms that allow robustness [5, 6].

Cell migration is an example of robust phenomenon that is present both in prokaryotic and eukaryotic cells. Living cells migrate to perform different tasks such as food targeting, wound healing and immune response. Independently of the presence of an external signal, before moving, cells need to define the direction to follow. To do so, they first define the front and the back of the cell. The process of formation of a polar direction inside a single cell is commonly known as cell polarization [7] and it is a typical example of pattern formation at the cellular level [8].

Several mathematical models have been developed to explain polarization of single eukaryotic cells [9–11]. Some models rely on a local excitation, which, combined with global inhibition makes the cell respond to external gradients [12], others rely on the accumulation of a certain biochemical components to guide the motion of the single cells [13]. The accumulation responsible for this second mechanism is frequently combined with a conservation constraint because the process of polarization is fast in comparison to the production of new biochemical components. With this

restriction, the mechanism of pattern formation inside living cells, together with the constraint of mass conservation, is analogous to a process of coarsening of the initial nucleus of components [14] and gives rise to phase separation [15] and to models of pattern formation [16]. Several simple models of intracellular pattern formation have appeared including the conservation restriction [13, 17, 18].

Once the axes and direction of movement are defined in amoeboid cells, small projections (defined as protrusions) are formed at the membrane of the cells [19]. These projections, which extend and retract periodically, are responsible for pushing the cell, and therefore, to move in the typical amoeboid motion. *Dictyostelium discoideum* is a species of soil-dwelling amoeba, frequently employed to characterize amoeboid locomotion. Inside the amoeba several signaling events are triggered, for example the activation of the Ras proteins and PI3K enzymes and accumulation of PIP_3 at the front of the cell, while activation of PTEN and myosin occur at the rear of the cell [20, 21]. Membrane areas where the protrusion activity is greater are typically characterized by the presence of Ras-GTP protein patches [22]. The appearance of Rac regions around the membrane with high protrusion activity [23, 24] has been observed in the slime mold organism *Dictyostelium discoideum*, where it is related to cytoskeletal dynamics [25].

A reaction-diffusion model with bistable dynamics is one of the common models of cell motility and particularly employed for *Dictyostelium discoideum*. Some dimensional bistable models are based on the formation of a finite lifetime and localized patches of high protein concentration [26, 27] while others are based on membrane dynamics of moving connected points [28]. Bistable conditions for cellular processes can be obtained by the coupling of a mass control regulating condition in the biochemical components present around the cytosol and the membrane of the cell, for example proteins, phospholipids and enzymes [13, 16, 29].

A common technique to model pattern formation inside a cell and the shape evolution of the membrane is the addition of a phase field with a sharp interface to distinguish the interior and exterior of the cell. This field maintains the correct boundary conditions while the borders are moving [30]. Some studies have applied phase field modeling to study keratocyte motility [31–33] and amoeboid motility [34] which can be divided into diffuse and persistent migration depending on the starvation level [35, 36]. There are also some intermediate cases observed in *Dictyostelium discoideum* cells for certain types of genetic variants [37] which have also been modelled with a phase field and variation of some parameters [38–40]. Other properties of *Dictyostelium discoideum* cells modeled employing a phase field are the viscoelasticity of the cells [41] and cell division [42]. Finally, we would like to mention that interactions among cells can also be considered for keratocyte [43, 44] and amoeboid cells [45].

Here, first, we transform a one dimensional model of the polarization at the membrane of a single *Dictyostelium discoideum* cell [23] into a two-dimensional domain for the waves in the basal membrane, in contact with the surface, using an additional phase field for the shape of the cell. We observe a strong dependence of the numerical dynamics on the explicit

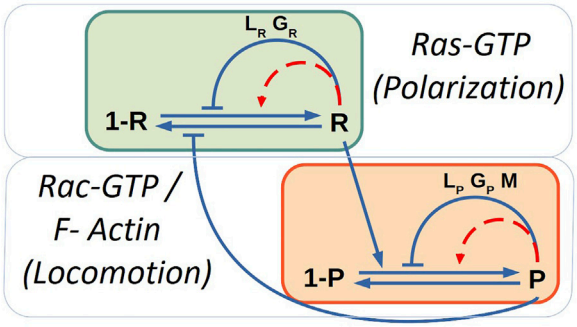

FIGURE 1 | Sketch of the biochemical model of polarization due to chemotaxis and locomotion modules. Blue solid lines corresponds to the interactions and red dashed lines to auto-catalytic processes. The mass-conservation constrains control the auto-catalytic interactions.

parameter values of the original model. Cell motion occurs only in a small window of parameter values, which indicates that the model is not robust to small variations of the parameters. Therefore, we propose a constraint on the conservation of a component of the signal pathway, controlling the autocatalytic mechanism, in order to increase the robustness of the model in representing changes in parameter values [46]. Similar types of conservation have previously been employed in other models of motion of *Dictyostelium discoideum* cells [34, 38, 47, 48], and we show here that a constraint of this kind is an useful and reasonable condition to systematically increase the robustness of the crawling mechanism, increasing the window of parameter values allowing cell migration.

2 MATERIALS AND METHODS

2.1 Biochemical Model for Ras Activation and Pseudopod Extension

Biochemical components inside the *Dictyostelium discoideum* amoeba self-organized to follow chemical signals in the exterior by the accumulation of Ras-GTP in the front of the cell. Next, F-actin molecules accumulates also at the front triggering push of the cytoskeleton and the motion of the amoeba.

We investigate a simple reaction-diffusion model [23] for Ras-GTP (R) patches that consists on the next partial differential equation:

$$\frac{\partial R}{\partial t} = (1-R)\left(k_0 + k_1 S + \frac{k_2 R^{n_1}}{R^{n_1} + K_R^{n_1}} - k_3 G_R - k_4 L_R\right) - \frac{k_5 R}{1 + k_6 P} + D_R \nabla^2 R + \xi_R(\mathbf{x}, t), \tag{1}$$

where we have a basal production, the stimulation production R by local occupied receptor S, an autocatalytic stimulation of R, an inhibition R by global and local inhibitors (G_R and L_R), the degradation of R, the diffusion of R and, a Gaussian spatio-temporal distributed white noise $\xi_R(\mathbf{x}, t)$ with zero mean $\langle \xi_R(\mathbf{x}, t) \rangle = 0$ and correlation $\langle \xi_R(\mathbf{x}, t) \xi_R(\mathbf{x}', t') \rangle = 2\sigma_R \delta(\mathbf{x} - \mathbf{x}')\delta(t - t')$. The external S can

significantly increase the response of Ras [23], see diagram in **Figure 1**, therefore, we keep here $S = 0$.

The variables L_R and G_R correspond, respectively, to local and global inhibitors of R:

$$\frac{\partial G_R}{\partial t} = k_7\bar{R} - k_9 G_R, \tag{2}$$

$$\frac{\partial L_R}{\partial t} = (1 - L_R)k_{10}R - k_{11}L_R + D_{LR}\nabla^2 L_R; \tag{3}$$

where both are produced by R and degrade, and only the local inhibitor diffuses. Note that the quantity $\bar{R}$ corresponds to the spatial average in the whole space of the field R.

At the same time we included a quantity related to the formation of protrusions (P) such as F-actin and Rac-GTP molecules; see diagram in **Figure 1**. This variable P was coupled with its respective inhibitors:

$$\frac{\partial P}{\partial t} = (1 - P)\left(k_{12} + k_{13}R + \frac{k_{14}P^{n_2}}{P^{n_2} + K_P^{n_2}} + \frac{k_{15}M^{n_3}}{M^{n_3} + K_M^{n_3}} - k_{16}G_P - k_{17}L_P\right) - k_{18}P + D_P\nabla^2 P + \xi_P(\mathbf{x}, t), \tag{4}$$

where we have a basal production, the stimulation production by R, an autocatalytic stimulation of P, a production by an extra term M, an inhibition of P by global and local inhibitors (G_P and L_P), the degradation of P, the diffusion of P and, a Gaussian spatio-temporal distributed white noise $\xi_P(\mathbf{x}, t)$ with zero mean $\langle\xi_P(\mathbf{x}, t)\rangle = 0$ and correlation $\langle\xi_P(\mathbf{x}, t)\xi_P(\mathbf{x}', t')\rangle = 2\sigma_P\delta(\mathbf{x} - \mathbf{x}')\delta(t - t')$.

Similar to the previous set of equations, the variables L_P and G_P correspond, respectively, to local and global inhibitors of P:

$$\frac{\partial G_P}{\partial t} = k_{19}\bar{P} - k_{20}G_P, \tag{5}$$

$$\frac{\partial L_P}{\partial t} = (1 - L_P)k_{21}P - k_{22}L_P + D_{LP}\nabla^2 L_P; \tag{6}$$

where both are produced by P and degrade, and only the local inhibitor diffuses. Note that the quantity $\bar{P}$ corresponds to the spatial average in the whole space of the field P.

Finally, the model takes into account the inclusion of a variable of memory (M) which is coupled with P; this variable stimulates the formation of new protrusion zones and represents the results observed in some experiments:

$$\frac{\partial M}{\partial t} = k_{23}P - k_{24}M + D_M\nabla^2 M. \tag{7}$$

which is produced by P, degrades and diffuses. The memory term is related to the probability of identifying when and where the signaling cascade is activated to generate new pseudopods. At a molecular level, such term is identified with the mechanisms of how information is collected, stored and used to bias future pseudopods [49, 50].

A more exhaustive description of the model is shown in the original study [23]. However, note that the noise description in the original study was different and we have adapted to an equivalent description based on physical derivations of stochastic fluctuations [51]; for more details see **Supplementary Material**.

One dimensional simulations were made using periodic boundary conditions in a grid of 120 points. The cell was considered as circular and having a radius of 6.25 μm. The pixel size for this case was set at $\Delta x = 0.32\,\mu m$ and the time step $\Delta t = 0.03\,s$. The definition and the value of the parameters of the model can be found in **Supplementary Table S1**.

2.2 Physical Phase Field Model for Cell Shape Deformations

The original model did not include deformable cells. Therefore, we expanded the model to 2D geometry and introduced an auxiliary phase field ϕ with the purpose of describing the evolution of the cell shape. The use of a phase field permits a smooth variation between the values of $\phi = 1$ inside and $\phi = 0$ outside of the cell.

The phase field equation is the result of a force balance involving several types of forces of different origins acting in the cell body. The equation for the phase field is as follows

$$\tau\frac{\partial\phi}{\partial t} = \gamma\left(\nabla^2\phi - \frac{G'(\phi)}{\epsilon^2}\right) - \beta\left(\int\phi\,dA - A_0\right)|\nabla\phi| + \alpha\,\phi\,P|\nabla\phi|, \tag{8}$$

The first term on the right side in **Eq. 8** is related to the surface energy of the cell membrane, where γ is the surface tension and $G(\phi) = 18\phi^2(1 - \phi)^2$ is a double well potential. The second term keeps the area close to the value of A_0. And the third term represents the active force generated by the Rac-GTP (P) molecules when pushing on the cell membrane [34]. The inclusion of the phase field permits to mimic the shape of the ventral membrane of crawling cells.

We consider a deformable cell of 122 μm^2 in area corresponding to a circle with radius equal to 6.25μm. The pixel size used was the half as in the 1D case $\Delta x = \Delta y = 0.16\,\mu m$. Also, to increase accuracy, the time discretization was reduced to $\Delta t = 0.003s$. We integrated **Eqs 1–8** using periodic boundary conditions and standard finite differences. The rest of parameters are as displayed in **Supplementary Table S1**.

2.3 Mathematical Description of the Mass-Conservation Constraint

The mathematical model represented in **Eqs 1–7** has several conservation terms which affect the dynamics of the system; see for example **Eqs.2–5**. However, we further modify the original model to include a new feedback through parameters k_{14} to create a more robust model by the control of the bistable properties, which are discussed in following sections. Therefore, the parameter k_{14} is dynamically controlled depending on the total amount of the protein of the inducer P at the cell. A new control term related to k_{14} is incorporated, following previous similar approaches in simple models [32, 38, 47]:

$$k_{14} = k_{14}^* + \eta(\bar{P} - C_P), \tag{9}$$

where k_{14}^* is a new constant that take the values of the original value of k_{14}. It is important to note that the new constrain

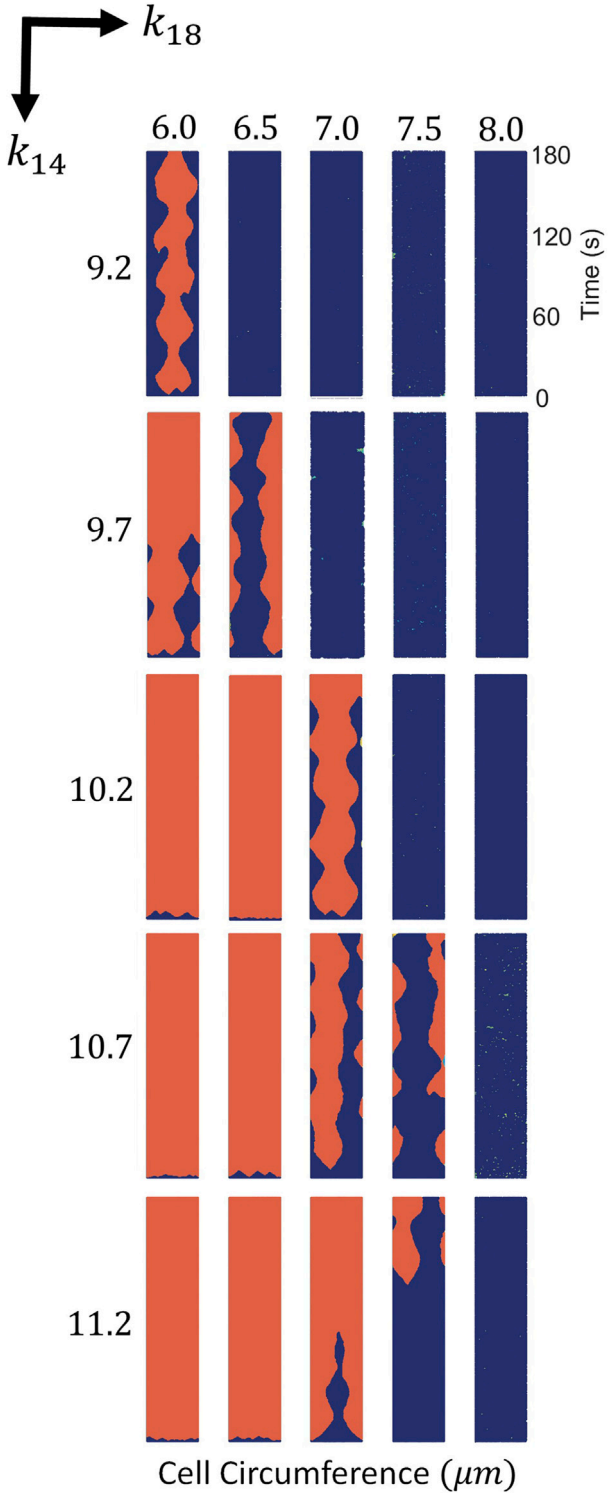

FIGURE 2 | Spatio-temporal plots of P (in red) for different values of k_{14} and k_{18}. For each panel times goes from bottom to top and horizontal direction corresponds to membrane position in the cell circumference. Variances of noise intensity were fixed at $\sigma_R = 0.04$ and $\sigma_P = 0.025$.

precludes the cell to be fully covered with the component P or emptying of the component P. Both extreme conditions are rare during cell crawling.

Parameter C_P is the target value of the fraction of the cell area occupied by patches of pseudopod inducer *P*. When, the total concentration $\bar{P}$ is larger (lower) than C_p the parameter value of k_{14} is larger (lower) than k_{14}^* and the bistable conditions implies the reduction (increase) of the $\bar{P}$. It corresponds to a feedback control of the parameter to keep a particular stable solution in **Eq. 9**. Note that for $\eta = 0$ we recover the original model.

3 RESULTS

3.1 Mechanism of Cell Motion in the Mathematical Model Is Based in Stochastic Generation of Patches

In a one-dimensional system, mimicking the membrane of a crawling cell, the generation of a single local patch of high biochemical concentration is equivalent to cell polarization. A stable domain in a specific location of the membrane is related with actin accumulation and produces persistent motion of the cell in that direction. The random appearance and disappearance of small domains is related with amoeboid motion, where two or three pseudopods compete for a certain time. The alternation of direction gives rise to random motion of the virtual cell.

Stochastic reaction-diffusion equations, as in **Eqs 1**–**7**, and previously developed [23], can be numerically integrated into a one-dimensional domain as in the original study, where kymographs are shown for a certain window of parameter values.

If we vary the parameters k_{14} and k_{18}, we obtain the phase diagram; see **Figure 2**. For large values of k_{14} and small values of k_{18} the membrane is completely covered by P, while for small values of k_{14} and large values of k_{18} the concentration of P strongly decreases. Locomotion is, therefore, expected for intermediate values of these two parameters as shown in **Figure 2**. For the evaluation of the mechanism of the simulations shown in **Figure 2**, we fixed the stochastic source of perturbations of the additive noises in **Eqs 1**–**7** to $\sigma_R = 0.04$ and $\sigma_P = 0.025$.

3.2 Mechanism of Cell Motion Is Based in Bistability

For the evaluation of the mechanism of pattern formation we found the stationary solutions for the deterministic version of **Eqs 1**–**7** by removing the additive noise. We have slowly increased the parameter k_{14} by small intervals ($0.05\ s^{-1}$) and integrated the model for a considerable amount of time to permit the model reach the equilibrium (180 *s*). Subsequent increase of the parameter permits the observation of the evolution of the stationary value of P by obtaining a value for P in every interval in k_{14}; see **Figure 3A**. Once the system of equations

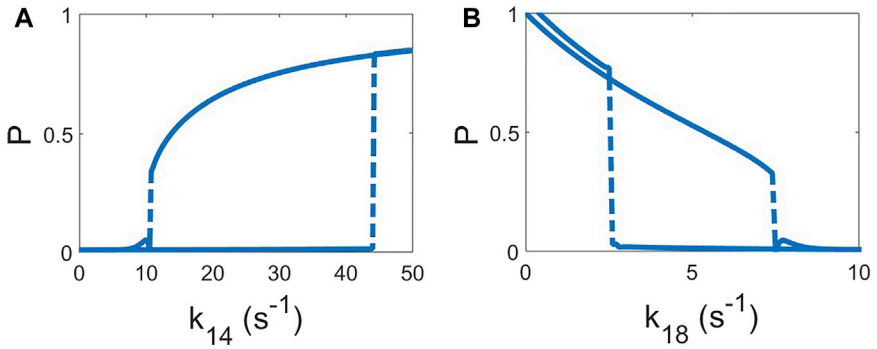

FIGURE 3 | Hysteresis curves of the deterministic model ($\sigma_R = 0$ and $\sigma_P = 0$). The value of the homogeneous solution of P is shown as function of the parameter increasing and, subsequently, decreasing of k_{14}, keeping $k_{18} = 7\ s^{-1}$ **(A)** and k_{18} keeping $k_{14} = 10.2\ s^{-1}$ **(B)**. Increase and decrease of the both parameters are done by steps of 0.05 s^{-1} and, after each step, permitting to relax to the new solution for 180 s.

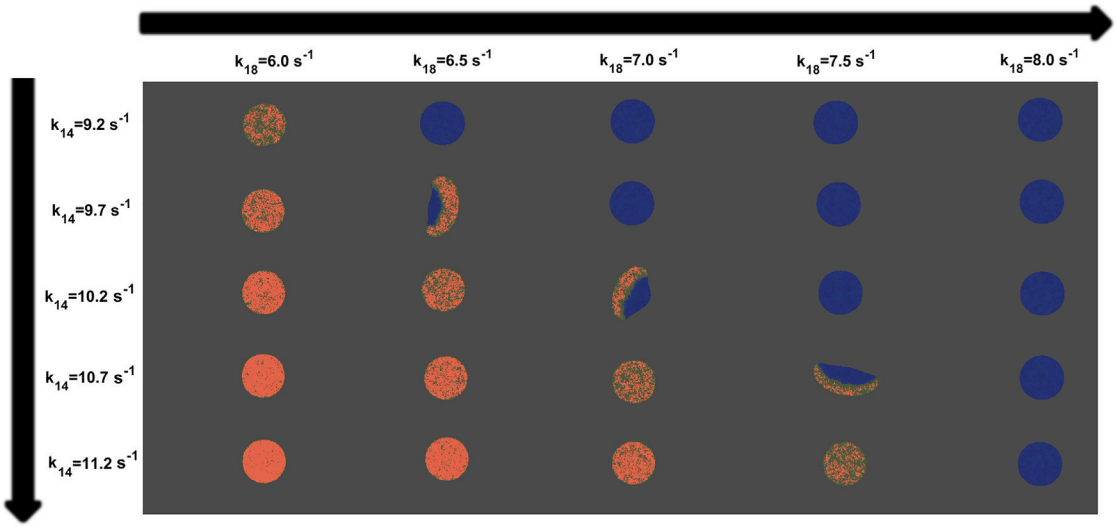

FIGURE 4 | Snapshots of the virtual cells showing P (in red) obtained from computer simulations and applying the phase field technique to the model for different values of k_{14} and k_{18}. Variances of noise intensity were fixed at $\sigma_R = 0.04$ and $\sigma_P = 0.025$. The rest of them are consistent with **Supplementary Table S1**.

saturated to a certain value of $P \sim 0.75 - 0.80$ we stopped and reduced the value of k_{14}, giving rise to a hysteresis cycle; see **Figure 3A**. The hysteresis cycle shows that the system actually is bistable for certain window of parameter values. Equivalent dynamics of P can be observed under a similar change in k_{18}; see **Figure 3B**. Therefore for low and large values of k_{14} and k_{18} there is a single stable solution and for intermediate values the model shows bistability.

It is known that the combination of a bistable dynamics with an appropriate noise intensity produces the formation of localized patches in reaction-diffusion equations [52, 53]. This formation is the mechanism responsible for the formation of localized domains of P. The localized pattern observed in **Figure 2** is not due to excitable dynamics but rather to a delicate equilibrium between bistable dynamics and noise.

3.3 Stochastic Bistability Provides a Mechanism of Cell Crawling Motion in Two Dimensional Systems

For the coupling of the polarization mechanism to the cell motion we used a phase field. This additional field is employed for the definition of the interior of the cell. In this case, the two dimensional phase field permits the use of different biochemical concentrations in the ventral membrane of a crawling cell.

The extension of the stochastic reaction-diffusion described in the previous section to two dimensions permits numerical simulations of the shape of the crawling cell and the corresponding motion responding to the dynamics of the patches. In **Figure 4** we showed snapshots of the *in silico* cells with the parameter values corresponding to the values shown in **Figure 2**. We reproduced the dynamics expected from the one

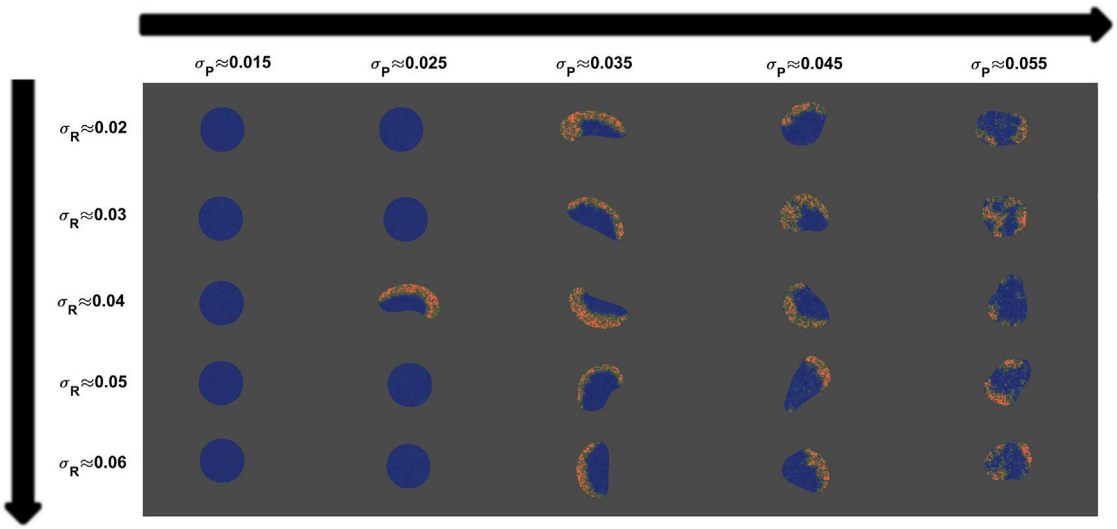

FIGURE 5 | Map of snapshots of the virtual cell taken from different variance values of noise intensity for the original model [23]. For each column, snapshots indicate P distribution (red) inside the cell. The value of the parameter of the simulations are k_{14} = 10.2 s^{-1} and k_{18} = 7 s^{-1}. The rest of them are consistent with **Supplementary Table S1**.

dimensional simulations, and the crawling dynamics can be clearly studied. Again, for high values of parameter k_{14} and small values of k_{18} the concentration of P is mostly high and homogeneously distributed along the membrane; see **Figure 4**. On the other hand, in the opposite limit, for small values of k_{14} and high values of k_{18} the concentration of P disappears from the ventral membrane. However, for a small window of values of the parameters the cell moves and inspects the surrounding region. The shape of the resulting cell depends on the particular realization and the parameter values; in the snapshots shown in **Figure 4** we obtain fan-shaped cells, a typical mode of *Dictyostelium discoideum* cell crawling [37].

The dependence of locomotion on the parameters k_{14} and k_{18} is strong as shown in **Figure 4**. Persistent motion is observed only for an intermediate window of values of the two parameters. For very small or very large amounts of $\bar{P}$ cells do not move. Such quantity is determined by the parameters k_{14} and k_{18}, and small changes on their values prevent the cell motion, making the whole model non-robust.

3.4 Noise Intensities Determine the Type of Motion

The variation of the type of cell motion is determined by the intensity of the noise. Low levels of both noises do not permit the formation of the domains of P needed to give rise to cell movement; see **Figure 5**. As we increase the amplitude of noise for P, we reach a single domain that fills the front part of the cell and persistent motion is shown; see middle column and right hand snapshots in **Figure 5**. This type of motion is reminiscent of the fan-shaped amoeboid cells previously reported [37] and also reproduced with simpler models [38]. An increase in the noise intensity produces an increase in the appearance and disappearance of pseudopods and therefore a transition to amoeboid movement; see fifth column in **Figure 5** for higher noise intensities. There are some noise intensities which produce patterns and dynamics similar to the characteristic patterns observed in the experiments, however, as previously mentioned, and shown in **Figure 4**, small variations in the parameter values k_{14} and k_{18} may completely change the movement dynamics.

3.5 Inclusion of Mass-Conservation Constrain Qualitatively Increases Robustness

In order to reduce the high sensitivity of the appearance of motion on the parameter values, we included a conservation constraint on the total inducer P, see **Eq. 9**, in the biochemical rates responsible for the bistable transition in **Eq. 4**. Following similar previous approaches [34, 47], we included this conservation as a global feedback condition in the reaction-diffusion equations of the model, see **Section 2.3**.

In **Figure 6**, we show several realizations incorporating the conservation constraint of P proteins, for different k_{14} and k_{18} parameter. A direct comparison can be made with the results displayed in **Figure 4** showing the effects of the inclusion of the mass conservation feedback. Results in **Figure 6** show that for a wide range of parameter values, the variation of the parameters does not affect either the bistability of the model or the quantity of inducer P inside the cell phase field, which was kept constant. The inclusion of this global condition permits the use of a larger range of parameter values, increasing the robustness of the mechanism in comparison with the original model.

The shape and type of motion were affected by the noise intensity. Using the same parameters of **Figure 5** we studied the effects of varying the noise variance in the new mass-conserved model. When the noise intensity related to the pseudopod inducer P increases, changes the shape from persistent fan-

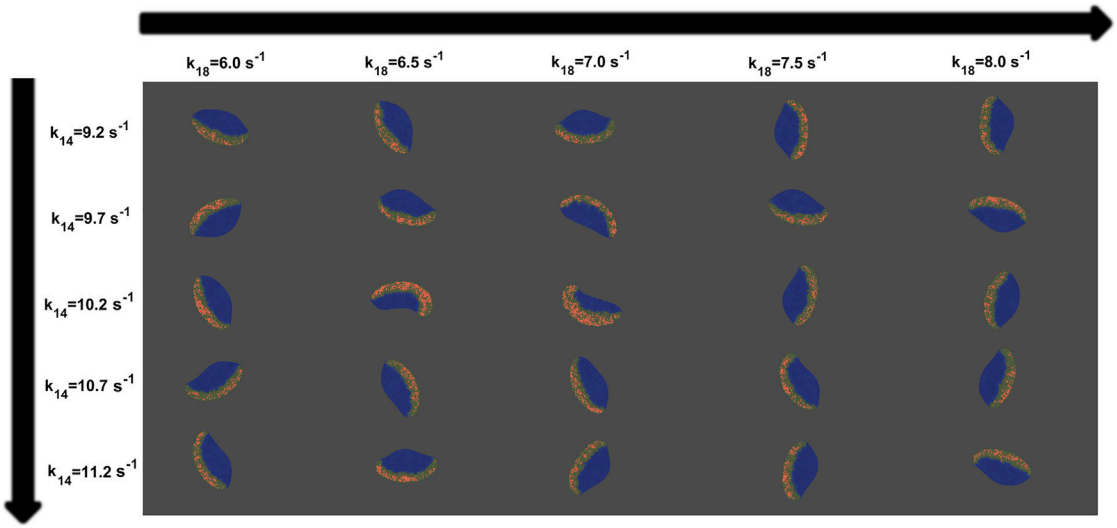

FIGURE 6 | Map of snapshots of the virtual cell taken from different values of k_{14} and k_{18} for the new mass-conserved model. For each column, snapshots indicate P distribution (red) inside the cell. Variances of noise intensity were fixed at $\sigma_R = 0.04$ and $\sigma_P = 0.025$. The rest of them are consistent with **Supplementary Table S1**.

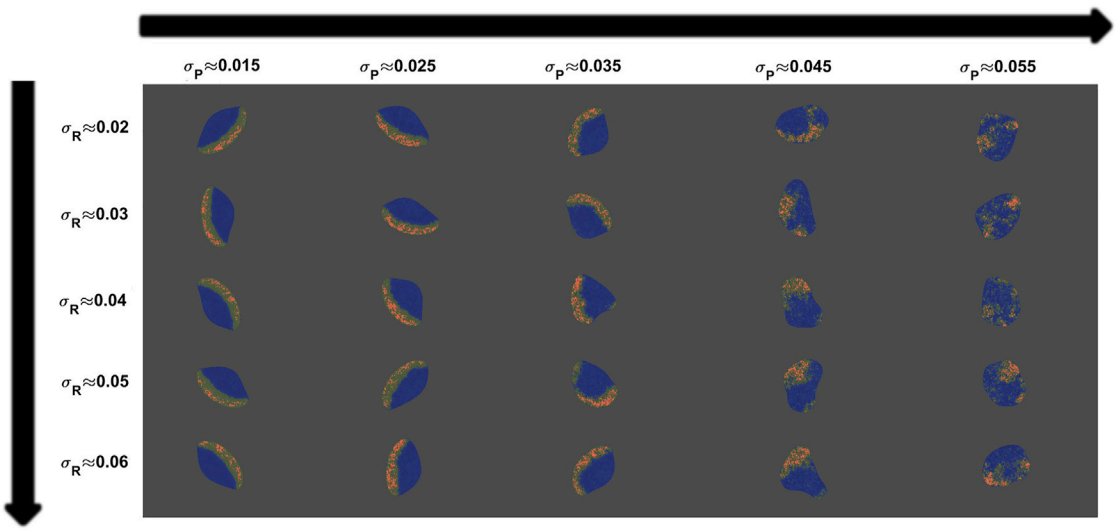

FIGURE 7 | Map of snapshots of the virtual cell taken from different variance values of noise intensity for the new mass-conserved model. For each column, snapshots indicate P distribution (red) inside the cell. The value of the parameter of the simulations are $k_{14} = 10.2\ s^{-1}$ and $k_{18} = 7\ s^{-1}$. The rest of them are consistent with **Supplementary Table S1**.

shape to random amoeboid phenotype, see **Figure 7**. This change is present because while small values of σ_P generates less blurred patches, an increment of σ_P drives the opposite effect, the appearance of more blurred and distributed patches for P.

3.6 Inclusion of Mass-Conservation Constrain Quantitatively Increases Robustness

We measured the speed of the resulting cells for different parameter conditions for the original and the new mass-conserved models. We observed that the dynamics of the simulated cells are more robust for the mass-conserved version of the equations; see **Figure 8**.

For the original model the speed and shape drastically changes when varying the parameters, and only a particular combination of parameters gives rise to cell crawling (see **Figure 4**). On the other hand, for the new mass-conserved version both velocities and shapes are more similar to each other for a much larger window of parameter values, as we can see in the speeds calculated in **Figure 8**. Such results were obtained by changing k_{18} to correspond to simulations shown in the third row of

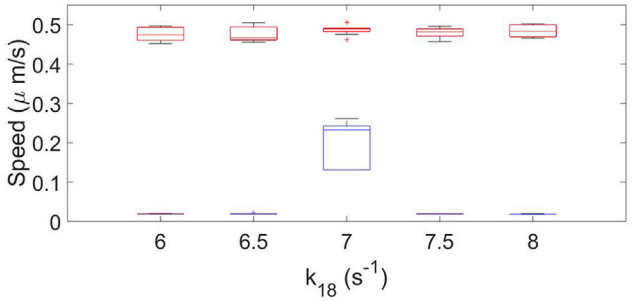

FIGURE 8 | Box plot representation for the cell speed of the original model (blue color) and the new mass-conserved model (red color). Results are for when k_{18} is varied. using a fixed value of $k_{14} = 10.2\ s^{-1}$, $\sigma_R = 0.04$ and $\sigma_P = 0.025$. Ten realizations for each case were performed.

Figure 4 for the no mass conservation case and for **Figure 6** for the mass-conservation system.

In **Figure 9** we show the dependency of the speed on the noise σ_P for different values of σ_R. The speed of the cells employed for the calculation comes from the dynamics shown in **Figures 5**, **7**. We observe that the speed obtained from both conditions decreases for greater noise intensities. However, for the original model almost null velocities appear for low noise magnitude. As we increase the noise intensity, values of the speed are more similar.

4 DISCUSSION

We studied the dynamics of a one-dimensional *Dictyostelium Discoideum* cell model consisting in the stochastic dynamics of Ras activation (R) and pseudopod inducer (P). The deterministic version of the model reveals the emergence of bistability. This conclusion appears from the visible hysteresis transition under the change of the parameters. In contrast, the stochastic version of the model permits the transition between two stable regimes. The extension of the model into two dimensions with the use of the addition of a phase field, allowing cell deformation, shows similar dependence on the parameters, in agreement with [23].

Since for typical experimental conditions the total concentration barely changes despite environmental perturbations, we chose to incorporate global feedback for the pseudopod inducer inside the cell. Such inclusion increases the robustness of the model and expands the parameter range where cell motion is observed without affecting the shape and dynamics.

The idea behind the approach is to dynamically control the velocity of the border between the clusters of P (orange domains) and the empty region. When the size of the orange domain is above (below) a certain threshold the border contracts (expands) keeping the global size of the domain of P and therefore the polarization of the cell. Such control does not substantially depend on the rest of the parameters because it is defined to maintain the size of the domain close to a certain value, and ensures that small modifications of the parameter do not destroy the structure of the domains and the polarization. Therefore, the described mechanism is more robust that a pure parameter fitting.

A bistable dynamics together with diffusion typically produces the motion of a front in reaction-diffusion equations. Under certain fine tuned parameter values, the front velocity becomes zero [54]. If we consider such bistable variable the concentration at the membrane and we, therefore, couple its dynamics with a

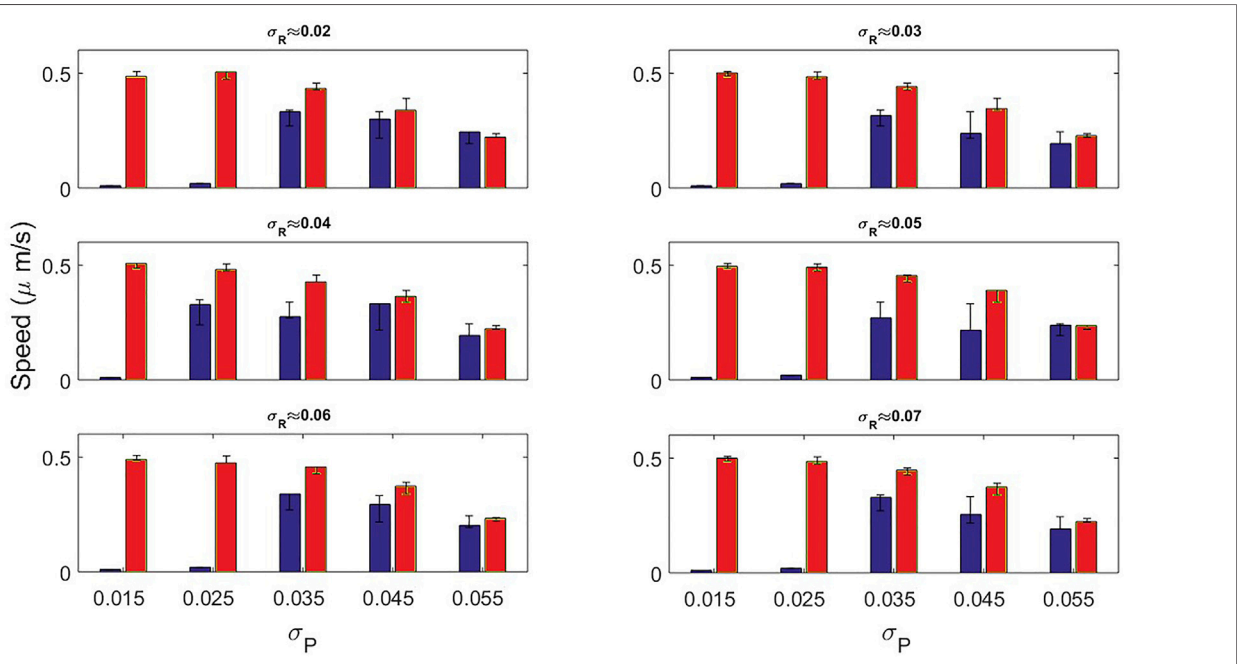

FIGURE 9 | Speed bar plots measured by the original model (blue bars) and the new mass-conserved model (red bars) by varying the noise variance σ_P. In each panel the variance associated to σ_R was fixed for different values.

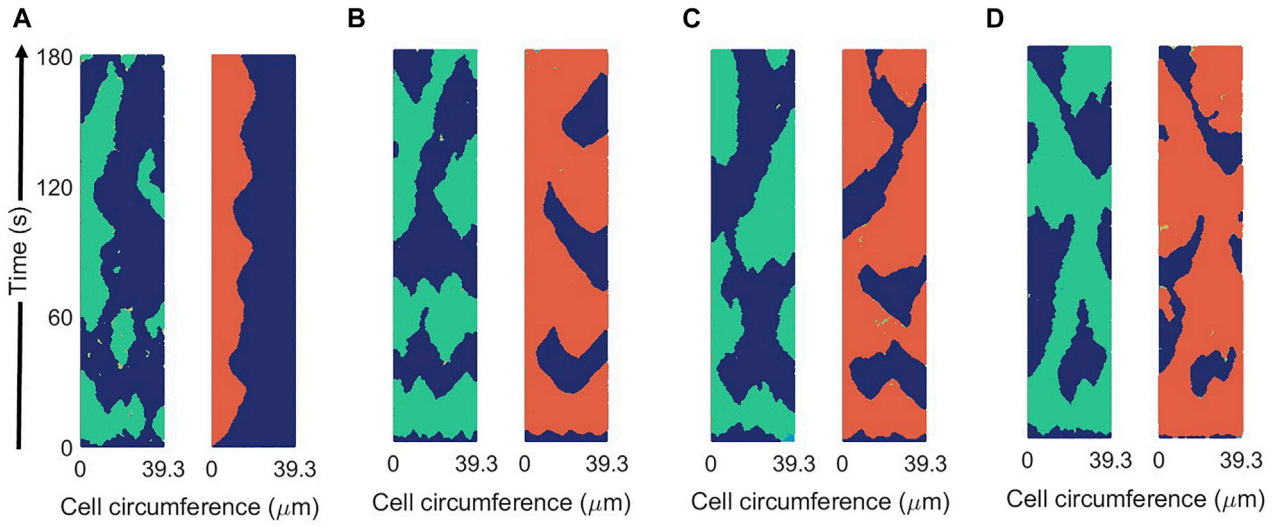

FIGURE 10 | Spatio-temporal plots of R (in green) and P (in red) for different values of the coupling parameter between R and P: $k_{13} = 0.1\ s^{-1}$ **(A)**, $k_{13} = 0.5\ s^{-1}$ **(B)**, $k_{13} = 1\ s^{-1}$ **(C)**, and $k_{13} = 2\ s^{-1}$ **(D)** in the new mass-conserved model. Results are for a fixed values of $\sigma_R = 0.04$ and $\sigma_P = 0.025$.

second variable, related with the concentration of the same protein in the cytosol, where diffusion is faster, the condition of zero velocity spontaneously appears, and the front is frozen at a particular position giving rise to wave pinning [13, 29]. Such a pinned condition appears because the coordinated balance between the membrane and the cytosol concentrations maintains constant the total amount of the protein inside the cell. Therefore, some other new models consider only a single variable for the membrane together with a global feedback to account for the mass-conservation condition for a single concentration [17, 32, 38]. When the dynamics of the concentration at the membrane is combined with other membrane concentrations more complex models including also excitable signalling networks are developed [39, 47, 48, 55]. In contrast with such models, in this study we chose an existing complex model where the condition of bistability is finely tuned [23] and add the global feedback condition to account for the conservation of the protein. Such modification highly increases the robustness of the model and, therefore, its applicability to other conditions.

Two of the parameters k_{14} and k_{18} can show hysteresis loops in the concentration of P, see **Figure 3**. We have employed the global feedback in the condition of parameter k_{14}, see **Eq. 9**, however we could have employed a similar condition for parameter k_{18} or any other parameter which exhibits a hysteresis behavior on the concentration P. Actually, note that other global feedback were already considered in the original version of the model [23]; see the dynamics of the global inhibitors, defined by G_R and G_P in **Eqs 2–5** respectively, similarly to other models of the motion of *Dictyostelium discoideum* cells based on global cytosolic quantities [12, 48]. The addition of global control quantities which can determine the available concentration inside the cell has previously been employed in other models [32, 38, 47].

Instant speed was measured, highlighting that for the original model a considerable set of parameters driven to velocities of close to zero, while for the set of parameters for the new mass-conserved model the speed remained almost constant around $0.45\ \mu m/s$.

Note that we have shown that the original model is based on a bistable conditions with the appropriate noise intensity. We have previously used simple stochastic bistable models for the description of the motion of *Dictyostelium discoideum* cells [34, 38] based on the same concept together with a mass-conservation constraint. There are also other models based on similar constraints [24, 40, 47] where some of the key differences relies in the inherent oscillatory dynamics of the models, the specific parameters that need to be change to generate different types of cell motion (e.g., amoeboid or keratocyte) without affecting the biochemical signaling dynamics; apart from the number of membrane concentrations involved in the cell dynamics as already mentioned. Therefore, the addition of a mass conservation constraint is a convenient mechanism to increase robustness in the delicate equilibrium between stochastic fluctuations and a bistable condition.

The coupling of the Ras activation R on the pseudopod inducer P is weak. The coupling is produced by the term proportional to k_{13} and it increases the probability of the generation of patches of P. A chemotactic concentration can enhance R and, therefore, polarize the field P and direct the locomotion [23]. In the absence of chemotaxis the coupling is small, while more physiological conditions may require larger couplings. In **Figure 10** we increased parameter k_{13} to demonstrate the increase in the coupling of both field R and P through the parameter. Intermediate values can be compared with experimental measures to fit an appropriate value; however such evaluation is outside the scope of this work.

An extension of the new mass-conserved model is possible with the inclusion of an external chemo-attractant gradient to analyze the response, known as chemotaxis and already considered in the original model [23]. Future simulations should study the relation of the chemotactic motion of *Dictyostelium discoideum* cells with the stochastic fluctuations and the rest of the parameters. They should also measure the effects on the shape and speed caused by the gradient.

In summary, we have shown that the inclusion of a mass-conservation constraint in the correct position substantially increases the robustness of a computational model of a crawling cell.

DATA AVAILABILITY STATEMENT

The original contributions presented in the study are included in the article/**Supplementary Material**, further inquiries can be directed to the corresponding author.

AUTHOR CONTRIBUTIONS

EM performed the numerical simulations; EM and SA contributed to the design and implementation of the research, to the analysis of the results and to the writing of the manuscript.

ACKNOWLEDGMENTS

We thank grant PGC2018-095456-B-I00 funded by MCIN/AEI/10.13039/501100011033 and by "ERDF A way of making Europe," by the "European Union." E.M. acknowledges also financial support from CONACYT.

SUPPLEMENTARY MATERIAL

The Supplementary Material for this article can be found online at: https://www.frontiersin.org/articles/10.3389/fphy.2022.881885/full#supplementary-material

REFERENCES

1. Cross MC, Hohenberg PC. Pattern Formation outside of Equilibrium. *Rev Mod Phys* (1993) 65:851–1112. doi:10.1103/revmodphys.65.851
2. Koch AJ, Meinhardt H. Biological Pattern Formation: from Basic Mechanisms to Complex Structures. *Rev Mod Phys* (1994) 66:1481–507. doi:10.1103/revmodphys.66.1481
3. Kondo S, Miura T. Reaction-diffusion Model as a Framework for Understanding Biological Pattern Formation. *science* (2010) 329:1616–20. doi:10.1126/science.1179047
4. Gross P, Kumar KV, Goehring NW, Bois JS, Hoege C, Jülicher F, et al. Guiding Self-Organized Pattern Formation in Cell Polarity Establishment. *Nat Phys* (2019) 15:293–300. doi:10.1038/s41567-018-0358-7
5. Kitano H. Biological Robustness. *Nat Rev Genet* (2004) 5:826–37. doi:10.1038/nrg1471
6. Whitacre JM. Biological Robustness: Paradigms, Mechanisms, and Systems Principles. *Front Gene* (2012) 3:67. doi:10.3389/fgene.2012.00067
7. Mogilner A, Allard J, Wollman R. Cell Polarity: Quantitative Modeling as a Tool in Cell Biology. *Science* (2012) 336:175–9. doi:10.1126/science.1216380
8. Camley BA, Rappel W-J. Physical Models of Collective Cell Motility: from Cell to Tissue. *J Phys D: Appl Phys* (2017) 50:113002. doi:10.1088/1361-6463/aa56fe
9. Rappel W-J, Edelstein-Keshet L. Mechanisms of Cell Polarization. *Curr Opin Syst Biol* (2017) 3:43–53. doi:10.1016/j.coisb.2017.03.005
10. Jilkine A, Edelstein-Keshet L. A Comparison of Mathematical Models for Polarization of Single Eukaryotic Cells in Response to Guided Cues. *Plos Comput Biol* (2011) 7:e1001121. doi:10.1371/journal.pcbi.1001121
11. Beta C, Kruse K. Intracellular Oscillations and Waves. *Annu Rev Condens Matter Phys* (2017) 8:239–64. doi:10.1146/annurev-conmatphys-031016-025210
12. Xiong Y, Huang C-H, Iglesias PA, Devreotes PN. Cells Navigate with a Local-Excitation, Global-Inhibition-Biased Excitable Network. *Proc Natl Acad Sci U.S.A* (2010) 107:17079–86. doi:10.1073/pnas.1011271107
13. Mori Y, Jilkine A, Edelstein-Keshet L. Wave-pinning and Cell Polarity from a Bistable Reaction-Diffusion System. *Biophysical J* (2008) 94:3684–97. doi:10.1529/biophysj.107.120824
14. Bergmann F, Zimmermann W. On System-Spanning Demixing Properties of Cell Polarization. *PloS one* (2019) 14:e0218328. doi:10.1371/journal.pone.0218328
15. Brauns F, Halatek J, Frey E. Phase-space Geometry of Mass-Conserving Reaction-Diffusion Dynamics. *Phys Rev X* (2020) 10:041036. doi:10.1103/physrevx.10.041036
16. Halatek J, Frey E. Rethinking Pattern Formation in Reaction-Diffusion Systems. *Nat Phys* (2018) 14:507–14. doi:10.1038/s41567-017-0040-5
17. Alonso S, Bär M. Phase Separation and Bistability in a Three-Dimensional Model for Protein Domain Formation at Biomembranes. *Phys Biol* (2010) 7:046012. doi:10.1088/1478-3975/7/4/046012
18. Trong PK, Nicola EM, Goehring NW, Kumar KV, Grill SW. Parameter-space Topology of Models for Cell Polarity. *New J Phys* (2014) 16:065009. doi:10.1088/1367-2630/16/6/065009
19. Bosgraaf L, Van Haastert PJM. The Ordered Extension of Pseudopodia by Amoeboid Cells in the Absence of External Cues. *PloS one* (2009) 4:e5253. doi:10.1371/journal.pone.0005253
20. Kae H, Lim CJ, Spiegelman GB, Weeks G. Chemoattractant-induced Ras Activation duringDictyosteliumaggregation. *EMBO Rep* (2004) 5:602–6. doi:10.1038/sj.embor.7400151
21. Etzrodt M, Ishikawa HCF, Dalous J, Müller-Taubenberger A, Bretschneider T, Gerisch G. Time-resolved Responses to Chemoattractant, Characteristic of the Front and Tail ofDictyosteliumcells. *FEBS Lett* (2006) 580:6707–13. doi:10.1016/j.febslet.2006.11.031
22. Sasaki AT, Janetopoulos C, Lee S, Charest PG, Takeda K, Sundheimer LW, et al. G Protein-independent Ras/PI3K/F-Actin Circuit Regulates Basic Cell Motility. *J Cel Biol* (2007) 178:185–91. doi:10.1083/jcb.200611138
23. van Haastert PJM, Keizer-Gunnink I, Kortholt A. Coupled Excitable Ras and F-Actin Activation Mediates Spontaneous Pseudopod Formation and Directed Cell Movement. *MBoC* (2017) 28:922–34. doi:10.1091/mbc.e16-10-0733
24. Shi C, Huang C-H, Devreotes PN, Iglesias PA. Interaction of Motility, Directional Sensing, and Polarity Modules Recreates the Behaviors of Chemotaxing Cells. *Plos Comput Biol* (2013) 9:e1003122. doi:10.1371/journal.pcbi.1003122
25. Huang C-H, Tang M, Shi C, Iglesias PA, Devreotes PN. An Excitable Signal Integrator Couples to an Idling Cytoskeletal Oscillator to Drive Cell Migration. *Nat Cel Biol* (2013) 15:1307–16. doi:10.1038/ncb2859
26. Hecht I, Kessler DA, Levine H. Transient Localized Patterns in Noise-Driven Reaction-Diffusion Systems. *Phys Rev Lett* (2010) 104:158301. doi:10.1103/physrevlett.104.158301
27. Hecht I, Skoge ML, Charest PG, Ben-Jacob E, Firtel RA, Loomis WF, et al. Activated Membrane Patches Guide Chemotactic Cell Motility. *Plos Comput Biol* (2011) 7:e1002044. doi:10.1371/journal.pcbi.1002044
28. Neilson MP, Veltman DM, van Haastert PJM, Webb SD, Mackenzie JA, Insall RH. Chemotaxis: a Feedback-Based Computational Model Robustly Predicts Multiple Aspects of Real Cell Behaviour. *Plos Biol* (2011) 9:e1000618. doi:10.1371/journal.pbio.1000618

29. Otsuji M, Ishihara S, Co C, Kaibuchi K, Mochizuki A, Kuroda S. A Mass Conserved Reaction-Diffusion System Captures Properties of Cell Polarity. *Plos Comput Biol* (2007) 3:e108. doi:10.1371/journal.pcbi.0030108
30. Camley BA, Zhao Y, Li B, Levine H, Rappel W-J. Periodic Migration in a Physical Model of Cells on Micropatterns. *Phys Rev Lett* (2013) 111:158102. doi:10.1103/physrevlett.111.158102
31. Shao D, Levine H, Rappel W-J. Coupling Actin Flow, Adhesion, and Morphology in a Computational Cell Motility Model. *Proc Natl Acad Sci U.S.A* (2012) 109:6851–6. doi:10.1073/pnas.1203252109
32. Camley BA, Zhao Y, Li B, Levine H, Rappel WJ. Crawling and Turning in a Minimal Reaction-Diffusion Cell Motility Model: Coupling Cell Shape and Biochemistry. *Phys Rev E* (2017) 95:012401. doi:10.1103/PhysRevE.95.012401
33. Nickaeen M, Novak IL, Pulford S, Rumack A, Brandon J, Slepchenko BM, et al. A Free-Boundary Model of a Motile Cell Explains Turning Behavior. *Plos Comput Biol* (2017) 13:e1005862. doi:10.1371/journal.pcbi.1005862
34. Alonso S, Stange M, Beta C. Modeling Random Crawling, Membrane Deformation and Intracellular Polarity of Motile Amoeboid Cells. *PloS one* (2018) 13:e0201977. doi:10.1371/journal.pone.0201977
35. Stankevicins L, Ecker N, Terriac E, Maiuri P, Schoppmeyer R, Vargas P, et al. Deterministic Actin Waves as Generators of Cell Polarization Cues. *Proc Natl Acad Sci U.S.A* (2020) 117:826–35. doi:10.1073/pnas.1907845117
36. Ecker N, Kruse K. Excitable Actin Dynamics and Amoeboid Cell Migration. *Plos one* (2021) 16:e0246311. doi:10.1371/journal.pone.0246311
37. Miao Y, Bhattacharya S, Edwards M, Cai H, Inoue T, Iglesias PA, et al. Altering the Threshold of an Excitable Signal Transduction Network Changes Cell Migratory Modes. *Nat Cel Biol* (2017) 19:329–40. doi:10.1038/ncb3495
38. Moreno E, Flemming S, Font F, Holschneider M, Beta C, Alonso S. Modeling Cell Crawling Strategies with a Bistable Model: From Amoeboid to Fan-Shaped Cell Motion. *Physica D: Nonlinear Phenomena* (2020) 412:132591. doi:10.1016/j.physd.2020.132591
39. Cao Y, Ghabache E, Miao Y, Niman C, Hakozaki H, Reck-Peterson SL, et al. A Minimal Computational Model for Three-Dimensional Cell Migration. *J R Soc Interf* (2019) 16:20190619. doi:10.1098/rsif.2019.0619
40. Cao Y, Ghabache E, Rappel WJ. Plasticity of Cell Migration Resulting from Mechanochemical Coupling. *Elife* (2019) 8:e48478. doi:10.7554/eLife.48478
41. Moure A, Gomez H. Phase-field Model of Cellular Migration: Three-Dimensional Simulations in Fibrous Networks. *Comput Methods Appl Mech Eng* (2017) 320:162–97. doi:10.1016/j.cma.2017.03.025
42. Flemming S, Font F, Alonso S, Beta C. How Cortical Waves Drive Fission of Motile Cells. *Proc Natl Acad Sci U.S.A* (2020) 117:6330–8. doi:10.1073/pnas.1912428117
43. Löber J, Ziebert F, Aranson IS. Collisions of Deformable Cells lead to Collective Migration. *Scientific Rep* (2015) 5:9172.
44. Kulawiak DA, Camley BA, Rappel W-J. Modeling Contact Inhibition of Locomotion of Colliding Cells Migrating on Micropatterned Substrates. *Plos Comput Biol* (2016) 12:e1005239. doi:10.1371/journal.pcbi.1005239
45. Moreno E, Grossmann R, Beta C, Alonso S. From Single to Collective Motion of Social Amoebae: A Computational Study of Interacting Cells. *Front Phys* (2022) 9:750187. doi:10.3389/fphy.2021.750187
46. Kitano H. Towards a Theory of Biological Robustness. *Mol Syst Biol* (2007) 3:137. doi:10.1038/msb4100179
47. Imoto D, Saito N, Nakajima A, Honda G, Ishida M, Sugita T, et al. Comparative Mapping of Crawling-Cell Morphodynamics in Deep Learning-Based Feature Space. *Plos Comput Biol* (2021) 17:e1009237. doi:10.1371/journal.pcbi.1009237
48. Taniguchi D, Ishihara S, Oonuki T, Honda-Kitahara M, Kaneko K, Sawai S. Phase Geometries of Two-Dimensional Excitable Waves Govern Self-Organized Morphodynamics of Amoeboid Cells. *Proc Natl Acad Sci U.S.A* (2013) 110:5016–21. doi:10.1073/pnas.1218025110
49. Cooper RM, Wingreen NS, Cox EC. An Excitable Cortex and Memory Model Successfully Predicts New Pseudopod Dynamics. *PloS one* (2012) 7:e33528. doi:10.1371/journal.pone.0033528
50. van Haastert PJM. Short- and Long-Term Memory of Moving Amoeboid Cells. *PloS one* (2021) 16:e0246345. doi:10.1371/journal.pone.0246345
51. García-Ojalvo J, Sancho J. *Noise in Spatially Extended Systems*. Berlin, Germany: Springer Science & Business Media (2012).
52. Hanggi P, Mroczkowski TJ, Moss F, McClintock PVE. Bistability Driven by Colored Noise: Theory and experiment. *Phys Rev A* (1985) 32:695–8. doi:10.1103/physreva.32.695
53. Kramers HA. Brownian Motion in a Field of Force and the Diffusion Model of Chemical Reactions. *Physica* (1940) 7:284–304. doi:10.1016/s0031-8914(40)90098-2
54. Beta C, Amselem G, Bodenschatz E. A Bistable Mechanism for Directional Sensing. *New J Phys* (2008) 10:083015. doi:10.1088/1367-2630/10/8/083015
55. Saito N, Sawai S. Three-dimensional Morphodynamic Simulations of Macropinocytic Cups. *Iscience* (2021) 24:103087. doi:10.1016/j.isci.2021.103087

Conflict of Interest: The authors declare that the research was conducted in the absence of any commercial or financial relationships that could be construed as a potential conflict of interest.

frontiers | Frontiers in Cell and Developmental Biology

REVIEW
published: 03 May 2022
doi: 10.3389/fcell.2022.871950

Patterning, From Conifers to Consciousness: Turing's Theory and Order From Fluctuations

Thurston C. Lacalli *

Biology Department, University of Victoria, Victoria, BC, Canada

This is a brief account of Turing's ideas on biological pattern and the events that led to their wider acceptance by biologists as a valid way to investigate developmental pattern, and of the value of theory more generally in biology. Periodic patterns have played a key role in this process, especially 2D arrays of oriented stripes, which proved a disappointment in theoretical terms in the case of *Drosophila* segmentation, but a boost to theory as applied to skin patterns in fish and model chemical reactions. The concept of "order from fluctuations" is a key component of Turing's theory, wherein pattern arises by selective amplification of spatial components concealed in the random disorder of molecular and/or cellular processes. For biological examples, a crucial point from an analytical standpoint is knowing the nature of the fluctuations, where the amplifier resides, and the timescale over which selective amplification occurs. The answer clarifies the difference between "inelegant" examples such as *Drosophila* segmentation, which is perhaps better understood as a programmatic assembly process, and "elegant" ones expressible in equations like Turing's: that the fluctuations and selection process occur predominantly in evolutionary time for the former, but in real time for the latter, and likewise for error suppression, which for *Drosophila* is historical, in being lodged firmly in past evolutionary events. The prospects for a further extension of Turing's ideas to the complexities of brain development and consciousness is discussed, where a case can be made that it could well be in neuroscience that his ideas find their most important application.

Keywords: pattern formation, reaction-diffusion theory, irreversible processes, neurocircuit assembly, error suppression in evolution and development

OPEN ACCESS

Edited by:
David M Holloway, British Columbia Institute of Technology, Canada

Reviewed by:
Luciano Marcon, Spanish National Research Council (CSIC), Spain
Jeremy B.A. Green, King's College London, United Kingdom

***Correspondence:**
Thurston C. Lacalli
lacalli@uvic.ca

Specialty section:
This article was submitted to Morphogenesis and Patterning, a section of the journal Frontiers in Cell and Developmental Biology

Received: *08 February 2022*
Accepted: *11 March 2022*
Published: *03 May 2022*

Citation:
Lacalli TC (2022) Patterning, From Conifers to Consciousness: Turing's Theory and Order From Fluctuations. Front. Cell Dev. Biol. 10:871950. doi: 10.3389/fcell.2022.871950

INTRODUCTION

As graduate students in the early 1970s, we were aware of Turing's reaction-diffusion theory of pattern formation, but it was at that time more a curiosity than a part of mainstream developmental thinking. Fifty years on, Turing's ideas have been successfully applied to a number of developmental systems (Maini et al., 2006; 2012; Othmer et al., 2009; Kondo and Miura, 2010; Davidson and Baum, 2012; Chatterjee et al., 2020; Green, 2021), though the mechanistic details often differ from his original proposal, with chemical autocatalysis being replaced by other self-enhancing molecular or cellular processes, and distance effects by other means of material transport, or by mechanochemical effects (for the latter, see Murray and Oster, 1984; Howard et al., 2011; Brinkmann et al., 2018; Veerman et al., 2021). For theorists, there have been disappointments along the way, in that patterns that appeared to match theoretical prediction were shown to arise by other mechanisms. But despite this, the theoretical enterprise has now reached a healthy middle age, with expectations of a vigorous and productive future. This review is

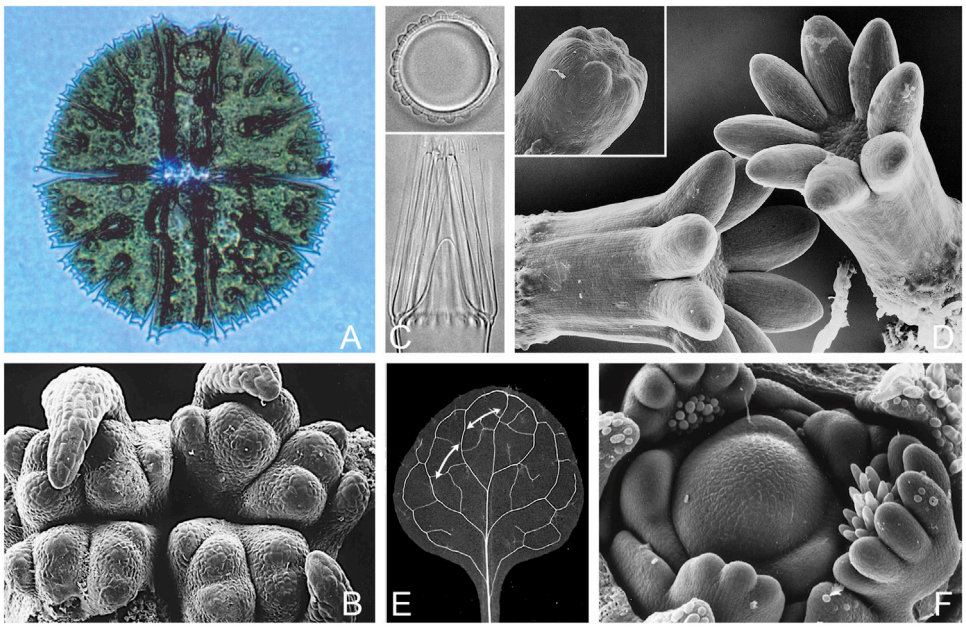

FIGURE 1 | Turing-type patterns in plants: branching and whorl formation in uni- and multicellular examples, and leaf venation. **(A)**. Dichotomous branching in one dimension: the freshwater desmid *Micrasterias rotata*, (cell diameter 230 μm) where form is generated following cell division by branching tip growth along the edge of the expanding semicell. The effective pattern scale (wavelength) declines during this process from ca. 30 μm at the beginning to 5 μm for the distal branches; see Lacalli & Harrison (1987) for quantitative details. **(B)**. Alternating dichotomous branching in two dimensions: the shoot apex of *Psilotum nudum*, a basal fern whose simple aerial shoots originate through repeated dichotomous branching and only elongate, together, secondarily. Distance between adjacent primordia at this stage is in the 150–200 μm range (Takiguchi et al., 1997), but the pattern wavelength has not been measured through the branching sequence, and could well vary; specimen supplied by T. A. Steeves. **(C)**. Whorl formation in a single cell: the pattern of hair initials (top) and their outgrowth (bottom) in the dasyclad alga *Acetabularia*. The distance between initials, typically 20 μm in culture, can range between 16 and 28 μm in a predictable way depending on temperature and calcium concentration, and from this one can make useful inferences about the mechanism; see Harrison & Hillier (1985), Dumais & Harrison (2000) for details. **(D)**. Whorl formation in conifers: the cotyledons (primary needles) of cultured white spruce embryos; stem diameter is ca. 750 μm compared with 400 μm when the initials are first evident (inset), with a spacing of ca. 95 μm (Fowke et al., 1994). The most detailed statistical information available on cotyledon spacing is for larch, where the pattern wavelength has been measured precisely, at 98 ± 4 μm (Harrison & von Aderkas, 2004; Holloway et al., 2018). **(E)**. Leaf venation in a young *Arabidopsis* leaf, where distance between secondary veins (arrows) in part reflects a spacing mechanism that acts along the leaf margin as the primordium develops. The leaf blade is ca. 2 mm long at the stage shown, but the first secondary veins appear when it is 20-fold smaller (100–120 μm long) with an effective wavelength between secondaries as they develop in the 20 μm range, down to a few cell diameters (10–15 μm) in some instances (Scarpella et al., 2006, Wenzel et al., 2007, Verna et al., 2019; see Holloway & Wenzel, 2021 for relevant modeling). The mechanistic basis of the discrepancy between vascular patterning at this scale and that of primordia across the apical meristem is as yet unresolved. **(F)**. The shoot apical meristem of lupin (*Lupinus polyphyllus*), one of the largest among the angiosperms, with a central dome ca. 250 μm across at its base. The overall pattern of primordia, typical of angiosperms (with some exceptions, e.g., of decussate pattern), is one of spiral phyllotaxy, but the leaves are palmate, developing as partial whorls as can be seen here in three examples, where spacing would appear to be on a scale somewhere below 30 μm; see Runions et al. (2017) for a further discussion of leaf shape in relation to spacing mechanisms acting along the leaf margin. Photo credits: (A, B) T. C. Lacalli, (C) Jacques Dumais, (D) L. C. Fowke, (E) Enrico Scarpella, (F) V. K. Sawhney.

designed as a broad survey with a focus less on mechanistic details than on what I consider the main turning points in the acceptance of Turing's insight regarding the kinetic basis of pattern selection, whether specifically by reaction and diffusion, or via other means of self-enhancement and action over distance. While my account of the subject is retrospective, the intent is not, as my interest is in part to consider how Turing's ideas might be extended in future, notably to neuroscience, as a way of accounting for the precise construction of the neurocircuitry required to support consciousness in the brain (Lacalli, 2020; Lacalli, 2021). Among scientific problems in search of a solution, this must surely be among the most daunting, and it remains a distinct possibility that the acknowledged importance of Turing to computer science (De Mol, 2021) will be equaled or surpassed in biology should his ideas on patterning prove applicable to the problem of biological consciousness.

EARLY DAYS

The publication of Turing's paper on morphogenesis (Turing, 1952) resulted in a brief period of interest among biologists, due in part to the efforts of C. W. Wardlaw, then Professor of Cryptogamic Botany at Manchester University (Wardlaw, 1953). Wardlaw would have been familiar with diverse examples of whorl formation and dichotomous branching in algae, ferns and the like, and that comparable patterns occur at both the unicellular and multicellular level (**Figure 1**). This latter feature probably accounts, at least in part, for the greater willingness of developmental botanists, in contrast to their zoological counterparts, to consider pattern as an entity in its own right irrespective of mechanistic details. So, for example, one can study whorl formation in a single cell, like the dasyclad alga *Acetabularia*,

where distance effects are likely due to diffusion (Dumais et al., 2000), or in the apical meristem of conifers (Harrison and von Aderkas, 2004), where distance effects arise through polar transport of auxin between cells (Reinhardt et al., 2003; Shi and Vernoux, 2019). Auxin transport can also produce patterns suitable for explaining both phyllotaxis (Jönsson et al., 2006) and leaf veins (Mitchison, 1981; Scarpella et al., 2006; Biedroń and Banasiak, 2018) where, for the latter, regularity of spacing along the leaf margin appears to play an important role (Holloway and Wenzel, 2021; Lavania et al., 2021). Yet for all these examples, the mathematical and computational problems of dealing with material flow, growth and mechanistic redundancy will be much the same.

Developmental zoologists, faced with a more diverse range of patterning situations, have tended to focus more on identifying the proximate causal agents in each case than on the general features of broadly based theories like Turing's. And in any case, the conventional wisdom in the early days, expressed by C. H. Waddington (see Waddington, 1956; page 423), was that a reaction-diffusion mechanism, being "inherently chancy" could at most account for the dapplings and mottlings filling otherwise unimportant spaces. It did not help that the specific equations Turing devised did not always produce regular patterns (Bard and Lauder, 1974), or that the one 2D pattern Turing included in his 1952 paper (his **Figure 2**) was itself rather irregular. But that example was computed for what Turing himself considered the least interesting case [his case *(a)*, stationary waves of moderate wavelength being case *(d)*], and his preliminary attempts to document the formation of regular 2D patterns were unpublished at his death (Dawes, 2016). Hence, by default, it was left largely to physical chemists to explore Turing's ideas more fully, and the energy-dissipative, far-from-equilibrium thermodynamics they embody. This was carried forward initially by Illya Prigogine and his Brussels research group (Prigogine and Lefever, 1968; Nicolis and Prigogine, 1977), using a hypothetical reaction system, the Brusselator, that was subsequently widely used and adapted by others (Tyson and Light, 1973; Harrison, 1987; Subramanian and Murray, 2021). On the experimental side, there was increasing interest in the Belousov-Zhabotinsky reaction, renowned for the production of oscillations and moving waves (Field and Burger, 1985; Zhabotinsky, 2007), a phenomenon so striking at the time as to be met frequently by disbelief among chemists when first encountered. This led, on the theoretical side, to an interest in model reaction systems that produced periodic oscillations that could be used to model biological processes, notably circadian rhythms (Winfree, 1980), segmentation (Cooke and Zeeman, 1976; Newman, 1993; Pourquié, 2003), and the mitotic oscillator, where Tyson has continued to make important contributions (e.g., see Tyson and Novák, 2015).

Interest in Turing's ideas was reignited among developmental zoologists by two developments, first the work of Gierer and Meinhardt (1972) modeling pattern formation and regeneration in hydra, and second, by Murray's comparatively well-received (for theory) account of animal coat patterns (Murray, 1981; Murray, 1988). Neither of these efforts, however, led immediately to a reassessment of the relevance of Turing's theory to a wider range of developmental examples. This was perhaps in part because a role in specifying coat patterns reinforced the existing notion that the theory was applicable only to irregular surface patterns, but also because the Gierer-Meinhardt model, designed to amplify an existing prepattern rather than generating well-controlled patterns *ab initio*, was not at first widely recognized for being a Turing model in disguise. There was also, for a time, a degree of suspicion verging on hostility towards Turing's theory on the part of some proponents of other mechanisms, where it should have been obvious from the start that Turing-type mechanisms could well be acting in concert with, for example, position-specific signaling, but at a different stage in the patterning process, as has proved to be the case (Miura, 2013; Green and Sharpe, 2015; Newman et al., 2018).

Even so, the main impediment to wider acceptance of Turing's ideas among biologists has always been, and remains, a matter of expectations: that theory was to be judged in strictly reductionist terms, as to whether it either does, or does not provide a route towards identifying the proximate entity responsible for the pattern in question, be this a gene, a diffusible morphogen, or something else. This is different from the biomathematical focus, towards anything in biology that yields interesting mathematics, and from preconception of the physical chemistry community, that progress is first and foremost a matter of understanding principles and process, a point of view well represented in Harrison's account of the subject (Harrison, 1987; Harrison, 1993). Here the details matter less than identifying the range of possible classes of explanation and establishing ground rules for distinguishing between them. Harrison identifies three such classes, of kinetics, self-assembly, and equilibrium, where Turing's model belongs to the first. But among the broad class of kinetic processes, the subset of importance to patterning are those able to act as selective amplifiers, extracting a signal from the statistical noise of real-time molecular behavior. This is in fact the essence of Turing's conception, explicit in the form of the solutions, and it precisely on this point, the form of the solutions, that he begins his mathematical account (Turing, 1952, pg. 39). The issue of the sensitivity (i.e., instability) of the un-patterned, homogeneous situation to fluctuations is then raised at various points in the text (e.g., pp. 56–57), using oscillatory electrical circuits as a point of reference. It is this feature I want specifically to highlight as distinguishing Turing's theory (here Turing-type models or, in Harrison's usage, kinetic theory and the kinetic preconception more broadly, or the "Turing problem" referred to by Kang et al., 2012), from other ways of accounting for biological pattern. And, for macro-scale biological pattern, kinetic mechanisms with the properties described by Turing would seem to have a distinct edge: "but what else could do it?" Harrison quotes a colleague as saying. The question here is rhetorical, and I return to it below (see section *Inelegance and Ratchets, Error Suppression and Time*) because, when it is indeed something else that "does it", that something else needs to be characterized and understood. Applying the order-from-fluctuations principle more generally, there are three things to consider when distinguishing classes of patterning models in terms of what they do and how they do it: the nature of the fluctuations, the identity of the amplifier, and the time scale on which these both operate, where more than one notion of what we mean by "time" may be required.

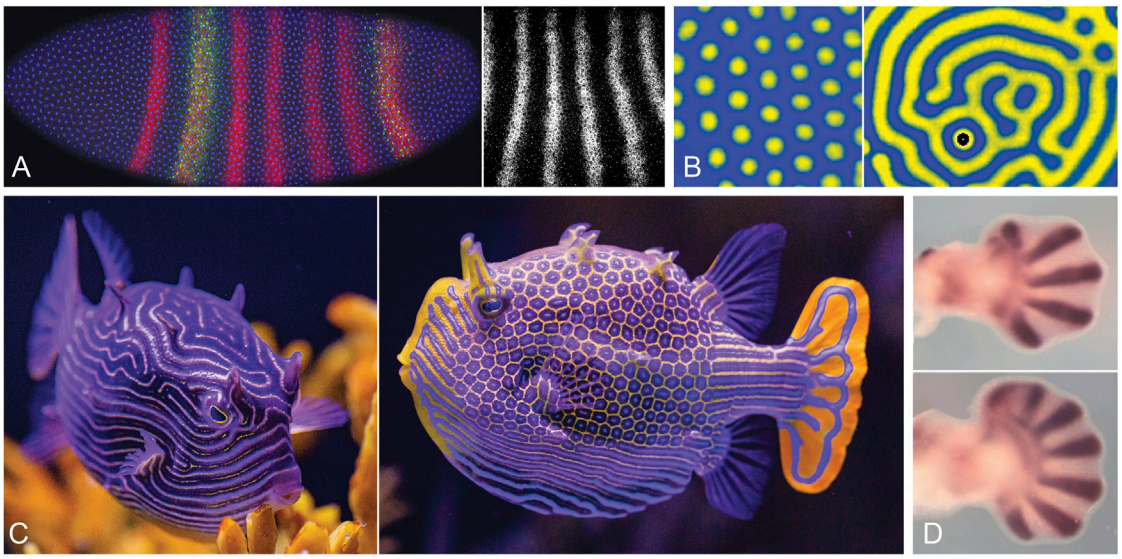

FIGURE 2 | Selected animal and chemical patterns: stripes, spots, and digits. **(A)**. The *Drosophila* pair-rule pattern. Left: an embryo at stage 5 (length 505 μm, anterior to the left), nearing the completion of cellularization; nuclei in blue, even-skipped (*eve*) protein in red, with an enhancer tag (green) showing specificity for some stripes rather than others, a clear demonstration of stripe-specific control over *eve* expression. Right: detail of the *eve* transcript pattern; stripe spacing (centre-to-centre distance) is ca. 40 μm. **(B)**. Chemical patterns, showing arrays of spots (left) and labyrinthine stripes (right) produced by the TuIS (thiourea-iodate-sulfite) reaction in a gel medium, a variant of the better known CIMA reaction. Spacing between pattern elements is ca. 2 mm; see Horvath et al. (2009) for details. **(C)**. The ornate boxfish, *Aracana ornata*, native to waters off South Australia; female (left) and male (right) showing mixed stripe and spotted patterns characteristic of boxfishes, which often vary between the sexes despite, presumably, a common underlying mechanism. **(D)**. Digit development in mouse embryos, showing patterns of the marker *Sox9* in wild type limb (top) and the expanded fan of digits produced by the homozygous *Gli3* null mutant (bottom). The pattern here is realized as a series of cartilaginous elements, but is a result of a one-dimensional periodicity along the limb margin that lays down a two-dimensional pattern as the limb grows (Hiscock et al., 2017), a 1D to 2D transition comparable to that seen in *Micrasterias*. The number of digits increases further in *Hox11/13* mutants, but the underlying pattern results from Turing-type interactions between the protein products of *Bmp*, *Sox9* and *Wnt* genes; see Raspopovic et al. (2014) for details; Onimaru et al. (2016), Stewart et al. (2017), Newman et al. (2018) for evolutionary perspectives. Photo credits: (A, left) Thomas Gregor, (A, right) Erik Clark, (B) Istvan Szalai, (C) the Birch Aquarium at Scripps, (D) Rushikesh Sheth and Marian Ros.

FLEXIBILITY IN PATTERN SELECTION: SPOTS, STRIPES AND IN-BETWEEN

Of various inaccurate notions about Turing's theory, the first that needs addressing is Waddington's objection, that it accounts only for irregular dapplings and mottlings. To do more than this, what is needed is a mechanism that is sufficiently flexible in the patterns it produces that it can be adapted by evolution as required. So, for example, on a two-dimensional surface the Gierer-Meinhardt model produces an irregular array of peaks frozen in place, which is not particularly useful for producing regular patterns of spots or stripes, let alone anything more elaborate. But the Gierer-Meinhardt model is rather idiosyncratic in this respect, because other models, including the Brusselator, generate regular hexagonal arrays of spots with ease. Turing's own notes show preliminary calculations approaching this result, where there were parallels with contemporary observations in fluid dynamics (Dawes, 2016), but the first fully developed computational examples using reaction-diffusion equations, so far as I am aware, came from my own work on pattern in unicellular algae (Lacalli, 1981). The ability to produce a modulated, well-controlled pattern in two and three dimensions means also the ability to respond to changing influences throughout the non-linear phase of pattern development, including boundary conditions, imposed gradients and the presence of neighboring pattern elements (Hiscock and Megason, 2015), as well as the ability to subdivide cell and tissue domains in an orderly way (Lacalli and Harrison, 1978; Hunding, 1984). In stark contrast to Waddington's view, and depending on the mechanistic details, boundary conditions and the like, a Turing model can in principle produce almost any pattern one cares to choose, and will do so in a reliable and reproducible fashion: "bespoke" patterning to borrow a phrase from Woolley et al. (2021), with evolution as the customer.

The ability to generate orderly patterns of stripes, in particular, quickly became a focus of attention with the discovery of the pair-rule pattern that precedes the formation of morphologically distinct segments in *Drosophila* embryos (Hafen et al., 1984 for the *fushi-tarazu* gene; see also Pick, 2016). The precision of this pattern at the cellular level (**Figure 2A**), with multiple stripes appearing essentially simultaneously, was astonishing at the time, and was interpreted by some, including myself, as strong circumstantial evidence for the involvement of a kinetic mechanism. The link between Turing and *Drosophila* stripes proved to be a bridge too far, as position-specific molecular events involving complex assemblages of transcriptional modulators responsive to graded signals along the length of the embryo were soon thereafter shown to be the means by which pattern was specified (Štanojević et al., 1989; Struhl et al., 1989, Struhl et al., 1992; Rivera-Pomar and Jäckle, 1996). This has

been characterized as an inelegant solution to the patterning problem (Akam, 1989), in contrast to simplicity of global control over pattern, with pattern landmarks being preset by the action of maternal and gap genes (Diaz-Cuadros et al., 2021). A greater degree of hierarchical control is thereby imposed over what was previously, in more basal arthropods, a self-organizing process of sequential segmentation relying, as in vertebrates, on molecular clocks and moving wavefronts (Salazar-Ciudad et al., 2001; Pourquié, 2003; Hunding and Baumgartner, 2017). A sequential mode of segmentation is characteristic of basal arthropods and short germ band insects like the beetle *Tribolium*, and there are plausible scenarios for linking this to the *Drosophila* condition through a complicated series of transitional steps (Clark et al., 2019; Clark, 2021). If there is elegance here, it is well hidden.

Even though the *Drosophila* pair-rule pattern proved not to depend on a Turing-type mechanism, the striking regularity of the pattern was a significant spur to theorists to understand the conditions under which model systems would generate stripes as opposed to spots or other patterns, in other words, to define the rules for pattern selection. This was first addressed in two nearly simultaneous publications, by Lyons and Harrison (1991) and Ermentrout (1991), making it immediately clear why symmetry features of the non-linear phase of pattern development are important, in that matched positive and negative departures from the steady state favored stripes (Lyons and Harrison, 1992). Further fueled by interest among chemists in the CIMA reaction (Lengyel and Epstein, 1991; Abdelmalek and Bendoukhu, 2020), which forms regular arrays of spots, stripes, and intermediate reticulate or labyrinthine patterns (**Figure 2B**), a burgeoning experimental literature appeared on pattern in chemical reaction systems (e.g. Ouyang and Swinney, 1991; Boissonade et al., 1995; Konow et al., 2021), with parallel advances in the theory (e.g. Dufiet and Boissonade, 1992; De Wit, 1999; Cross and Greenside, 2009). On the biological side, striking observations on fish pattern by Kondo and Asai (1995) made the likely involvement of a Turing-type mechanism of some kind increasingly hard to deny. And, while fish patterns arise through dynamics operating at the cellular level rather than diffusing reactants (Kondo et al., 2021), this does not matter when the point of the exercise is to validate the theory for kinetic processes as a class. Zebrafish have proven a useful model system here as well (Singh and Nüsslein-Volhard, 2015; Kondo et al., 2021), and even more dramatic patterns, combining arrays of spots, stripes and reticulate intermediates, are seen in coral reef fishes, amongst which boxfishes are noteworthy examples (**Figure 2C**; see Pearson, 1993, and Othmer et al., 2009 to compare with a range of computed examples). Combining these observations with more recent work on digit patterns (**Figure 2D**; see Newman and Frisch, 1979; Sheth et al., 2012; Raspopovic et al., 2014; Newman et al., 2018; and Chatterjee et al., 2020 for the basic theoretical case), it appears that two of the main objections to Turing's ideas as applied to animal systems have been answered, at least for vertebrates, that 1) kinetic theory is perfectly capable of explaining a range of surface patterns that are regular, highly controlled and flexible in their adaptive capabilities, and 2) not only surface pattern, but skeletal patterns lodged within the body depend at least in part on Turing-type mechanisms (see Painter et al., 2021 for other examples of internal patterning).

A final, perennial objection to Turing's reaction-diffusion mechanism is a supposed lack of robustness, that pattern formation depends on the parameters being adjusted within a narrow range. While this is true to a degree of 2-component models, more recent work has shown that having more components, especially if some are non-diffusing (Marcon et al., 2016; Diego et al., 2018; Landge et al., 2020; Krause et al., 2021), and discrete rather than continuous systems (Leyshon et al., 2021), yields models far more robust than previously supposed possible, and there is now a better understanding of how pattern stability is maintained in the non-linear regime (Subramanian and Murray, 2021). The burden of past misconceptions concerning kinetic theories has thus now, in large part, been removed.

INELEGANCE AND RATCHETS, ERROR SUPPRESSION AND TIME

The idea of the inelegance of the mechanisms underlying developmental pattern captures both a superficial truth and a deeper one. On the one hand, inelegance in this context refers to the complexity of developmental phenomena at the molecular level, which verges on the illogical (Lewin, 1984). Elegance equates to simplicity, in that patterning by a Turing-type mechanism can be encapsulated in a few lines of mathematical symbols, whereas accounting for the pair-rule pattern requires a detailed inventory of molecular components and their myriad functional interactions. But while the *Drosophila* stripe issue was resolved largely in favor of inelegance, the failure of theory, as often in science, proved a more interesting and informative result than success. In this instance, it led to a new appreciation of the problem of achieving a reliable developmental result in the face of the random noise that characterizes molecular events in the real world (Rao et al., 2002; Balázsi et al., 2011). The question was first posed in theoretical terms (Holloway and Harrison, 1999; Kang et al., 2012), and then addressed experimentally in considerable detail using *Drosophlia*, initially in work carried out by Eric Wieschaus and collaborators (e.g., Houchmandzadeh et al., 2002). This was part an emerging trend that has since made biomolecular science more quantitative (Maddox, 1992; Davidson and Baum, 2012; Gregor et al., 2014), and there is now both a much increased appreciation of the importance of error suppression in developmental systems at the molecular level, with the production of the *Drosophila* pair-rule pattern as a key model (Petkova et al., 2019; Bauer et al., 2021), and a far better understanding of how this is achieved.

Conceptually, the questions that need addressing, of precision, reliability and robustness, are more general than any one example, or any one pattern. And, if a Turing-type mechanism is not involved, we return to the chemist's question, above, but now applied to error suppression: "but what else could do it?" The answer from *Drosophila* is that we have left the realm of microscopically reversible kinetic processes, where Turing models reside, but neither is this structural self-assembly of a jigsaw-puzzle type, e.g., of a virus particle. Instead,

the *Drosophila* pair-rule pattern depends on macromolecular complexes that decode and implement a set of genetic instructions, and are assembled in a series of steps that are, in effect, thermodynamically irreversible (Carey, 1998; Poss et al., 2013). At the level of transcriptional control, this involves multiple enhancer elements that act at the level of the gene in a combinatorial way to optimize the response to graded inputs that convey information on cell position (Chen et al., 2018; Furlong and Levine, 2018; Petkova et al., 2019; Bauer et al., 2021), but there are strategies at all levels of the process, from the shape of the gradients (Song and Hyeon, 2021) to mechanisms for sharpening the stripes (Munteanu et al., 2014), that have been likewise optimized by evolution to ensure that patterning proceeds in a way that minimizes errors. To emphasize the programmatic aspect of the molecular assembly part of the process, I suggest the term "programmatic assembly", which is also ratchet-like, to use a mechanical analogy (Oster, 2002), while being both combinatorial and synergistic, and there is a graph-theoretical formulation, of micro-states linked by unidirectional edges representing the irreversible assembly steps (Ahsendorf et al., 2014; Martinez-Corral et al., 2021) that is especially promising as an analytical methodology going forward. Implicitly all such approaches face the same problem, that, to quote from Ahsendorf et al., "history cannot be ignored away from thermodynamic equilibrium", where by history, we mean the sequence of steps by which the machinery in question is assembled and operates. But there is a second history, and a second time scale, of the evolutionary sequence by which the machinery itself was refined and perfected over many generations, with all the contingency that implies. Taking the molecular level equivalents of coding and decoding as an example (e.g., Jarzynski, 2008; 2011), fully accounting for the thermodynamic driving forces behind each step in such cases is a complex and sometimes counterintuitive exercise. The same is true at a more abstract level, for a concept like positional information, since a device able to read and interpret such information will necessarily, like a human reader, be an energy dissipative product of evolution operating irreversibly far from equilibrium.

To go yet further, to the level of physics, the issue becomes one of time, of whether, in the terminology of Cortês and Smolin (2014), one is dealing with passive time or generative time. Passive time in this context is the "t" that appears in a typical set of equations, whether for Turing's mechanism or for calculating a ballistic trajectory, and solving such equations yields the same answer each time. *Drosophila* segments also form the same way each time, but there is a difference. To see this, consider error suppression yet again, and how a developmental outcome can be produced as precisely realized as a pair-rule stripe. For a Turing mechanism, error suppression depends on feedback steps in the mechanism that amplify fluctuations and, together with diffusion, select one pattern over all others, including over background noise, doing so in real time as the pattern develops. For the transcriptional machinery employed in *Drosophila* segmentation, in contrast, the feedback step is evolution itself, in its role as a generator of gene sequences for the enhancers and transcriptional regulators required to produce the pattern in question, and to suitably refine their interactions. So in this case error suppression is in large part historical, that is, *it has already occurred*. And, because it is then embedded in the codes and structures that implement the genetic program, it does not appear explicitly in equations that model change in real time. Similarly, if we think about the fluctuations on which the amplifier acts, for a programmatic assembly process these are not spatial in character, but arise from genetic variation at the population level, because different individuals will vary as to the precision with which they replicate pattern, and it is by eliminating the more error-prone individuals, generation by generation, that the genome evolves in ways that reduce developmental errors for the population as a whole. It is then this mix of time scales and of history-dependent and history-independent features, which in analytical terms must be dealt with separately, rather than complexity *per se*, that precludes an elegant solution. From an error-suppression standpoint, this means that the problem of statistical noise at the level of positional cues can be dealt with analytically in a straightforward way (as by Tkačik and Gregor, 2021), but reliability and accuracy at the level of the interpreter cannot, as the evolutionary steps by which that interpreter was conjured into existence are inescapably part of the story. This also means, for the experimentalist, that quantitative tests of reliability for examples of programmatic assembly are less a measure of the physical limits of a given class of mechanisms, than they are of the effectiveness of evolution in its choice of an error-suppression strategy for each step in the assembly process.

A further lesson from *Drosophila* is, or would seem to be, that where evolution has replaced one mechanism by another, the transition is more likely than not to be in the direction of increased reliance on programmatic control, so that development becomes more complex, and hence inelegant, over time. For *Drosophila* in particular, the proximate advantage of making this change can be measured in the developmental time saved, as segment specification is significantly faster in *Drosophila* than in basal arthropods and short germ-band insects. This is a distinct advantage for insects like fruit flies, whose larvae compete with fungi and nematodes for a rapidly depleting food resource. But there is a potential cost in the loss of one key feature of oscillatory, clock-based segmentation mechanisms, in that errors accumulated from past steps in the developmental program are no longer overwritten by the new pattern and reset to zero. That this cost is not paid in reduced developmental reliability in *Drosophila* shows that programmatic assembly solves the problem of error suppression by other means, namely through structural innovations and enhanced specificity in the molecular machinery that implements the developmental program. This then begs the question of whether this same solution has been employed in the past, perhaps repeatedly, in multiple development pathways as a means of speeding the overall process of embryogenesis. Germ layer specification, for example, depends on highly complex gene regulatory networks (Loose and Patient, 2004; Kiecker et al., 2016), and is hence a good candidate for having imposed a programatic overlay on simpler, more purely kinetic ancestral mechanisms in order to achieve the same result more rapidly. There are implications here also on the botanical side, in providing a rationale for why mechanisms for plant patterning are generally more conserved across taxa than is typical of animals: that growth and patterning are tightly integrated in plants (Dumais and Kwiatkowska, 2002; Harashima and Schnittge, 2010; Rebocho et al., 2017), and so long as it is growth rather than patterning that is rate-limiting, there is little to be gained by reducing the time required to specify pattern. Ancestral

mechanisms are then more likely to be retained rather than being replaced.

CONCLUSIONS, AND SOME FINAL THOUGHTS, ON THOUGHT

It has been gratifying, over the last 2 decades, to see Turing's ideas gaining acceptance and proving their worth in specific biological situations. But this is only part of a larger enterprise, in the past a concern mainly of the more physico-chemically minded, but now more widely recognized, which is to better understand the essential underlying features of kinetic mechanisms as a class. A key concept here, featured in Turing's own account, is the idea of generating order from fluctuations, that is, of extracting a meaningful signal from the underlying noise of the system, which can be at a molecular, subcellular or cellular level. The issue has relevance across a range of examples: from purely chemical systems, such as the CIMA reaction, to hybrid ones, like *Drosophila*, relying more on programmatic assembly than simple kinetics. Examples of programmatic assembly are then inherently less elegant than purely kinetic mechanisms because real time events play a lesser role than evolutionary ones. So, for example, achieving a precise outcome reliably depends on processes unfolding largely in real time for a kinetic mechanism like Turing's, but for programmatic assembly these are embedded in the past, in the evolutionary sequence that produced the machinery that executes the program. Programmatic assembly cannot therefore be fully understood except in the context of an extended sequence of evolutionary events, which begs an analytical question, of how to deal in practice with events unfolding in two mutually exclusive time scales.

A final point I want to address is whether we have been missing what is potentially the most important application of Turing's ideas, to controlling the assembly of neural circuits in the developing brain. If we consider the various cellular level activities needed to correctly configure the neural circuitry underpinning complex brain functions, there are many opportunities for competitive dynamics of the kind envisioned by Turing, but played out at a structural level, of cells, synapses and dendrites, rather than diffusing molecules (Lacalli, 2020). Turing himself had considered this issue, as is evident from a letter to J. Z. Young in February of 1951 (see Hodges, 1983, pg. 436), and his ideas have potential application to the period of synaptic remodeling that occurs in the neonatal nervous system, including in the cortex, whereby excess neurons and synaptic connections are removed in an activity-dependent way in response to sensory feedback (Le Bé and Markram, 2006; Low and Cheng, 2006; Kano and Hashimoto, 2009). But this is also the period when the newborn begins to develop a conscious awareness of its surroundings (Lagercrantz and Changeux, 2010), and for the circuits responsible for the basic sensations of phenomenal consciousness, i.e. qualia in most formulations, there is a problem. To illustrate this, consider a newborn hearing a sound, or experiencing pain, for the first time. The problem here is the absence of feedback mechanisms to correct any errors that may occur in the quality and character of the sensation evoked by the neural circuitry to which this task has been assigned. In other words, if the circuits evoking a particular sensation, of pain for example, or sound or light, have been incorrectly assembled in the embryonic period, the resulting sensations, whether they are the correct sensations or not, simply become the nature of experience for that individual. The brain thus faces the same problem that an insect does in correctly forming its segments, that it has one chance to get it right. The developmental options for doing so should then also be the same: to develop in a programmatic way to yield what is essentially a deterministic result, as in *Drosophila*, or to instead employ a Turing-type process of dynamic competition, either during the initial phase of circuit development or later remodeling, to amplify some circuitry variants at the expense of others. There may in fact be no single answer, as mechanisms by which brain circuitry is assembled will undoubtedly vary across taxa, from being more programmatic in the brains of small rapidly-developing invertebrates, to less programmatic in the brains of larger animals showing more flexible modes of learning and behavior, most notably cephalopods and vertebrates. For the circuits responsible for consciousness more specifically, there could in fact be a sequence, similar to that in insect segmentation, with global kinetic mechanisms being the ancestral way of generating the circuits responsible for phenomenal sensations as these first emerged in evolution, with more streamlined, programmatic ways of achieving the same result evolving secondarily.

We have, in sum, three options as to how the neural circuitry responsible for conscious sensation is assembled: that 1) it originated and remains a product of a global Turing-type patterning system operating at a structural, neurocircuitry level, or 2) like insect segmentation, it began that way but has since been converted, as in *Drosophila*, to some form of programmatic assembly, or 3) that the efficiencies inherent in programmatic assembly were themselves an essential part of the ability to evolve consciousness in the first place. It may be a mammalian bias to suppose that flexibility in behavior depends on more flexible, non-programmatic modes of development than is typically encountered in small invertebrates like *Drosophila*, but the general point remains valid in any case: that there are multiple scenarios under which mechanisms like those devised by Turing would lie at the very root of consciousness, and hence of the abilities of members of our species to engage in such activities as meaningful speech, logical thought and, not least, formulating and solving equations like Turing's.

AUTHOR CONTRIBUTIONS

The author confirms being the sole contributor of this work and has approved it for publication.

FUNDING

Funds to support this work were received from the Lionel G. Harrison Research Trust.

ACKNOWLEDGMENTS

I thank those acknowledged in the figure legends, along with Patrick von Aderkas and Carol Wenzel, for images and/or additional information on the examples illustrated, Stuart Newman and the two reviewers for helpful comments on the

manuscript, and Riley Lacalli for preparing the figures. The botanical portion of this paper is dedicated in memory of Taylor Steeves, the most kindly and helpful colleague one could wish to have. His connection with Turing is at one remove, through his work in Wardlaw's lab in the mid 1950s. Apologies also to authors whose reviews on specific examples of pattern formation are not included due to space limitations. Completeness here is less a problem than it once would have been, as the literature on developmental pattern formation, like embryonic development itself, has now achieved a degree of robustness through redundancy.

REFERENCES

Abdelmalek, S., and Bendoukha, S. (2020). "The Lengyel-Epstein Reaction Diffusion System," in *Applied Mathematical Analysis: Theory, Models, and Applications*. Editors H. Dutta and J. F. Peters (New York: Springer), 311–351. doi:10.1007/978-3-319-99918-0_10

Ahsendorf, T., Wong, F., Eils, R., and Gunawardena, J. (2014). A Framework for Modelling Gene Regulation Which Accommodates Non-Equilibrium Mechanisms. *BMC Biol.* 12, 102. doi:10.1186/s12915-014-0102-4

Akam, M. (1989). Making Stripes Inelegantly. *Nature* 341, 282–283. doi:10.1038/341282a0

Balázsi, G., van Oudenaarden, A., and Collins, J. J. (2011). Cellular Decision Making and Biological Noise: From Microbes to Mammals. *Cell* 144, 910–925. doi:10.1016/j.cell.2011.01.030

Bard, J., and Lauder, I. (1974). How Well Does Turing's Theory of Morphogenesis Work? *J. Theor. Biol.* 45, 501–531. doi:10.1016/0022-5193(74)90128-3

Bauer, M., Petkova, M. D., Gregor, T., Wieschaus, E. F., and Bialek, W. (2021). Trading Bits in the Readout from a Genetic Network. *Proc. Natl. Acad. Sci. U.S.A.* 118, e2109011118. doi:10.1073/pnas.2109011118

Biedroń, M., and Banasiak, A. (2018). Auxin-Mediated Regulation of Vascular Patterning in *Arabidopsis thaliana* Leaves. *Plant Cel Rep* 37, 1215–1229. doi:10.1007/s00299-018-2319-0

Boissonade, J., Dulos, E., and De Kepper, P. (1995). "Turing Patterns: From Myth to Reality," in *Chemical Waves and Patterns*. Editors R. Kapral and K. Showalter (Dordrecht, NL: Kluwer Academic), 221–268. doi:10.1007/978-94-011-1156-0_7

Brinkmann, F., Mercker, M., Richter, T., and Marciniak-Czochra, A. (2018). Post-Turing Tissue Pattern Formation: Advent of Mechanochemistry. *PLoS Comput. Biol.* 14, e1006259. doi:10.1371/journal.pcbi.1006259

Carey, M. (1998). The Enhanceosome and Transcriptional Synergy. *Cell* 92, 5–8. doi:10.1016/S0092-8674(00)80893-4

Chatterjee, P., Glimm, T., and Kaźmierczak, B. (2020). Mathematical Modeling of Chondrogenic Pattern Formation during Limb Development: Recent Advances in Continuous Models. *Math. Biosci.* 322, 108319. doi:10.1016/j.mbs.2020.108319

Chen, H., Levo, M., Barinov, L., Fujioka, M., Jaynes, J. B., and Gregor, T. (2018). Dynamic Interplay between Enhancer-Promoter Topology and Gene Activity. *Nat. Genet.* 50, 1296–1303. doi:10.1038/s41588-018-0175-z

Clark, E. (2021). Time and Space in Segmentation. *Interf. Focus.* 11, 20200049. doi:10.1098/rsfs.2020.0049

Clark, E., Peel, A. D., and Akam, M. (2019). Arthropod Segmentation. *Development* 146, dev170480. doi:10.1242/dev.170480

Cooke, J., and Zeeman, E. C. (1976). A Clock and Wavefront Model for Control of the Number of Repeated Structures during Animal Morphogenesis. *J. Theor. Biol.* 58, 455–476. doi:10.1016/S0022-5193(76)80131-2

Cortês, M., and Smolin, L. (2014). The Universe as a Process of Unique Events. *Phys. Rev. D* 90, 084007. doi:10.1103/PhysRevD.90.084007

Cross, M., and Greenside, H. (2009). *Pattern Formation and Dynamics in Nonequilibrium Systems*. Cambridge, UK: Cambridge University Press.

Davidson, L. A., and Baum, B. (2012). Making Waves: The Rise and Fall and Rise of Quantitative Developmental Biology. *Development* 139, 3065–3069. doi:10.1242/dev.080093

Dawes, J. H. P. (2016). After 1952: The Later Development of Alan Turing's Ideas on the Mathematics of Pattern Formation. *Historia Mathematica* 43, 49–64. doi:10.1016/j.hm.2015.03.003

De Mol, L. (2021). "Turing Machines," in *The Stanford Encyclopedia of Philosophy (Winter 2021 Edition)*. Editor E. N. Zalta. Available at: https://plato.stanford.edu/asrchives/win2021/entries/turing-machine/.

De Wit, A. (1999). Spatial Patterns and Spatiotemporal Dynamics in Chemical Systems. *Adv. Chem. Phys.* 109, 435–513. doi:10.1002/9780470141687.ch5

Diaz-Cuadros, M., Pourquié, O., and El-Sherif, E. (2021). Patterning with Clocks and Genetic Cascades: Segmentation and Regionalization of Vertebrate versus Insect Body Plans. *PLoS Genet.* 17, e1009812. doi:10.1371/journal.pgen.1009812

Diego, X., Marcon, L., Müller, P., and Sharpe, J. (2018). Key Features of Turing Systems Are Determined Purely by Network Topology. *Phys. Rev. X* 8, 021071. doi:10.1103/PhysRevX.8.021071

Dufiet, V., and Boissonade, J. (1992). Conventional and Unconventional Turing Patterns. *J. Chem. Phys.* 96, 664–673. doi:10.1063/1.462450

Dumais, J., and Harrison, L. G. (2000). Whorl Morphogenesis in the Dasycladalean Algae: The Pattern Formation Viewpoint. *Phil. Trans. R. Soc. Lond. B* 355, 281–305. doi:10.1098/rstb.2000.0565

Dumais, J., and Kwiatkowska, D. (2002). Analysis of Surface Growth in Shoot Apices. *Plant J.* 31, 229–241. doi:10.1046/j.1365-313X.2001.01350.x

Dumais, J., Serikawa, K., and Mandoli, D. F. (2000). *Acetabularia*: A Unicellular Model for Understanding Subcellular Localization and Morphogenesis during Development. *J. Plant Growth Regul.* 19, 253–264. doi:10.1007/S003440000035

Ermentrout, B. (1991). Stripes or Spots? Nonlinear Effects in Bifurcation of Reaction-Diffusion Equations on the Square. *Proc. R. Soc. Lond. A.* 434, 413–417. doi:10.1098/rspa.1991.0100

Field, R. J., and Burger, M. (1985). *Oscillations and Traveling Waves in Chemical Systems*. New York: John Wiley & Sons.

Fowke, L., Attree, S., and Rennie, P. (1994). Scanning Electron Microscopy of Hydrated and Desiccated Mature Somatic Embryos and Zygotic Embryos of White Spruce (*Picea glauca* [Moench] Voss.). *Plant Cel Rep.* 13, 612–618. doi:10.1007/BF00232931

Furlong, E. E. M., and Levine, M. (2018). Developmental Enhancers and Chromosome Topology. *Science* 361, 1341–1345. doi:10.1126/science.aau0320

Gierer, A., and Meinhardt, H. (1972). A Theory of Biological Pattern Formation. *Kybernetik* 12, 30–39. doi:10.1007/BF00289234

Green, J. B. A. (2021). Computational Biology: Turing's Lessons in Simplicity. *Biophysical J.* 120, 4139–4141. doi:10.1016/j.bpj.2021.08.041

Green, J. B. A., and Sharpe, J. (2015). Positional Information and Reaction-Diffusion: Two Big Ideas in Developmental Biology Combine. *Development* 142, 1203–1211. doi:10.1242/dev.114991

Gregor, T., Garcia, H. G., and Little, S. C. (2014). The Embryo as a Laboratory: Quantifying Transcription in *Drosophila*. *Trends Genet.* 30, 364–375. doi:10.1016/j.tig.2014.06.002

Hafen, E., Kuroiwa, A., and Gehring, W. J. (1984). Spatial Distribution of Transcripts from the Segmentation Gene *fushi tarazu* during Drosophila Embryonic Development. *Cell* 37, 833–841. doi:10.1016/0092-8674(84)90418-5

Harashima, H., and Schnittger, A. (2010). The Integration of Cell Division, Growth and Differentiation. *Curr. Opin. Plant Biol.* 13, 66–74. doi:10.1016/j.pbi.2009.11.001

Harrison, L. G. (1987). What is the Status of Reaction-Diffusion Theory Thirty-Four Years after Turing? *J. Theor. Biol.* 125, 369–384. doi:10.1016/s0022-5193(87)80208-4

Harrison, L. G. (1993). *Kinetic Theory of Living Pattern*. Cambridge, UK: Cambridge University Press.

Harrison, L. G., and Hillier, N. A. (1985). Quantitative Control of *Acetabularia* Morphogenesis by Extracellular Calcium: A Test of Kinetic Theory. *J. Theor. Biol.* 114, 177–192. doi:10.1016/S0022-5193(85)80261-7

Harrison, L. G., and von Aderkas, P. (2004). Spatially Quantitative Control of the Number of Cotyledons in a Clonal Population of Somatic Embryos of Hybrid Larch *Larix x leptoeuropaea*. *Ann. Bot.* 93, 423–434. doi:10.1093/aob/mch061

Hiscock, T. W., and Megason, S. G. (2015). Orientation of Turing-Like Patterns by Morphogen Gradients and Tissue Anisotropies. *Cel Syst.* 1, 408–416. doi:10.1016/j.cels.2015.12.001

Hiscock, T. W., Tschopp, P., and Tabin, C. J. (2017). On the Formation of Digits and Joints during Limb Development. *Developmental Cel* 41, 459–465. doi:10.1016/j.devcel.2017.04.021

Hodges, A. (1983). *Alan Turing: The Enigma*. 1st edn. London: Hutchinson, Burnett Books.

Holloway, D. M., and Harrison, L. G. (1999). Suppression of Positional Errors in Biological Development. *Math. Biosciences* 156, 271–290. doi:10.1016/S0025-5564(98)10070-6

Holloway, D. M., Rozada, I., and Bray, J. J. H. (2018). Two-Stage Patterning Dynamics in Conifer Cotyledon Whorl Morphogenesis. *Ann. Bot.* 121, 525–534. doi:10.1093/aob/mcx185

Holloway, D. M., and Wenzel, C. L. (2021). Polar Auxin Transport Dynamics of Primary and Secondary Vein Patterning in Dicot Leaves. *in silico Plants* 3, diab030. doi:10.1093/insilicoplants/diab030

Horváth, J., Szalai, I., and De Kepper, P. (2009). An Experimental Design Method Leading to Chemical Turing Patterns. *Science* 324, 772–775. doi:10.1126/science.1169973

Houchmandzadeh, B., Wieschaus, E., and Leibler, S. (2002). Establishment of Developmental Precision and Proportions in the Early *Drosophil*a Embryo. *Nature* 415, 798–802. doi:10.1038/415798a

Howard, J., Grill, S. W., and Bois, J. S. (2011). Turing's Next Steps: The Mechanochemical Basis of Morphogenesis. *Nat. Rev. Mol. Cel. Biol.* 12, 392–398. doi:10.1038/nrm3120

Hunding, A. (1984). Bifurcations of Nonlinear Reaction-Diffusion Systems in Oblate Spheroids. *J. Math. Biol.* 19, 249–263. doi:10.1007/BF00277098

Hunding, A., and Baumgartner, S. (2017). Ancient Role of *ten-m/odz* in Segmentation and the Transition from Sequential to Syncytial Segmentation. *Hereditas* 154, 8. doi:10.1186/s41065-017-0029-1

Jarzynski, C. (2008). The Thermodynamics of Writing a Random Polymer. *Proc. Natl. Acad. Sci. U.S.A.* 105, 9451–9452. doi:10.1073/pnas.0805209105

Jarzynski, C. (2011). Equalities and Inequalities: Irreversibility and the Second Law of Thermodynamics at the Nanoscale. *Annu. Rev. Condens. Matter Phys.* 2, 329–351. doi:10.1146/annurev-conmatphys-062910-140506

Jönsson, H., Heisler, M. G., Shapiro, B. E., Meyerowitz, E. M., and Mjolsness, E. (2006). An Auxin-Driven Polarized Transport Model for Phyllotaxis. *Proc. Natl. Acad. Sci. U.S.A.* 103, 1633–1638. doi:10.1073/pnas.0509839103

Kang, H.-W., Zheng, L., and Othmer, H. G. (2012). The Effect of the Signalling Scheme on the Robustness of Pattern Formation in Development. *Interf. Focus.* 2, 465–486. doi:10.1098/rsfs.2011.0116

Kano, M., and Hashimoto, K. (2009). Synapse Elimination in the Central Nervous System. *Curr. Opin. Neurobiol.* 19, 154–161. doi:10.1016/j.conb.2009.05.002

Kiecker, C., Bates, T., and Bell, E. (2016). Molecular Specification of Germ Layers in Vertebrate Embryos. *Cell. Mol. Life Sci.* 73, 923–947. doi:10.1007/s00018-015-2092-y

Kondo, S., and Asai, R. (1995). A Reaction-Diffusion Wave on the Skin of the Marine Angelfish *Pomacanthus*. *Nature* 376, 765–768. doi:10.1038/376765a0

Kondo, S., and Miura, T. (2010). Reaction-Diffusion Model as a Framework for Understanding Biological Pattern Formation. *Science* 329, 1616–1620. doi:10.1126/science.1179047

Kondo, S., Watanabe, M., and Miyazawa, S. (2021). Studies of Turing Pattern Formation in Zebrafish Skin. *Phil. Trans. R. Soc. A.* 379, 20200274. doi:10.1098/rsta.2020.0274

Konow, C., Dolnik, M., and Epstein, I. R. (2021). Insights From Chemical Systems into Turing-Type Morphogenesis. *Phil. Trans. R. Soc. A.* 379, 20200269. doi:10.1098/rsta.2020.0269

Krause, A. L., Gaffney, E. A., Maini, P. K., and Klika, V. (2021). Modern Perspectives on Near-Equilibrium Analysis of Turing Systems. *Phil. Trans. R. Soc. A.* 379, 20200268. doi:10.1098/rsta.2020.0268

Lacalli, T. C. (1981). Dissipative Structures and Morphogenetic Pattern in Unicellular Algae. *Phil. Trans. R. Soc. Lond. B* 294, 547–588. doi:10.1098/rstb.1981.0118

Lacalli, T. (2020). Evolving Consciousness: Insights from Turing, and the Shaping of Experience. *Front. Behav. Neurosci.* 14, 598561. doi:10.3389/fnbeh.2020.598561

Lacalli, T. (2021). Consciousness as a Product of Evolution: Contents, Selector Circuits, and Trajectories in Experience Space. *Front. Syst. Neurosci.* 15, 697129. doi:10.3389/fnsys.2021.697129

Lacalli, T. C., and Harrison, L. G. (1978). The Regulatory Capacity of Turing's Model for Morphogenesis, with Application to Slime Moulds. *J. Theor. Biol.* 70, 273–295. doi:10.1016/0022-5193(78)90377-6

Lacalli, T. C., and Harrison, L. G. (1987). Turing's Model and Branching Tip Growth: Relation of Time and Spatial Scales in Morphogenesis, with Application to *Micrasterias*. *Can. J. Bot.* 65, 1308–1319. doi:10.1139/b87-184

Lagercrantz, H., and Changeux, J.-P. (2010). Basic Consciousness of the Newborn. *Semin. Perinatology* 34, 201–206. doi:10.1053/j.semperi.2010.02.004

Landge, A. N., Jordan, B. M., Diego, X., and Müller, P. (2020). Pattern Formation Mechanisms of Self-Organizing Reaction-Diffusion Systems. *Developmental Biol.* 460, 2–11. doi:10.1016/j.ydbio.2019.10.031

Lavania, D., Linh, N. M., and Scarpella, E. (2021). Of Cells, Strands, and Networks: Auxin and the Patterned Formation of the Vascular System. *Cold Spring Harb Perspect. Biol.* 13, a039958. doi:10.1101/cshperspect.a039958

Le Bé, J.-V., and Markram, H. (2006). Spontaneous and Evoked Synaptic Rewiring in the Neonatal Neocortex. *Proc. Natl. Acad. Sci. U.S.A.* 103, 13214–13219. doi:10.1073/pnas.0604691103

Lengyel, I., and Epstein, I. R. (1991). Modeling of Turing Structures in the Chlorite-Iodide-Malonic Acid-Starch Reaction System. *Science* 251, 650–652. doi:10.1126/science.251.4994.650

Lewin, R. (1984). Why is Development So Illogical? *Science* 224, 1327–1329. doi:10.1126/science.6374894

Leyshon, T., Tonello, E., Schnoerr, D., Siebert, H., and Stumpf, M. P. H. (2021). The Design Principles of Discrete Turing Patterning Systems. *J. Theor. Biol.* 531, 110901. doi:10.1016/j.jtbi.2021.110901

Loose, M., and Patient, R. (2004). A Genetic Regulatory Network for *Xenopus* Mesendoderm Formation. *Developmental Biol.* 271, 467–478. doi:10.1016/j.ydbio.2004.04.014

Low, L. K., and Cheng, H.-J. (2006). Axon Pruning: An Essential Step Underlying the Developmental Plasticity of Neuronal Connections. *Phil. Trans. R. Soc. B* 361, 1531–1544. doi:10.1098/rstb.2006.1883

Lyons, M. J., and Harrison, L. G. (1991). A Class of Reaction-Diffusion Mechanisms Which Preferentially Select Striped Patterns. *Chem. Phys. Lett.* 183, 158–164. doi:10.1016/0009-2614(91)85117-F

Lyons, M. J., and Harrison, L. G. (1992). Stripe Selection: An Intrinsic Property of Some Pattern-Forming Models with Nonlinear Dynamics. *Dev. Dyn.* 195, 201–215. doi:10.1002/aja.1001950306

Maddox, J. (1992). Is Molecular Biology yet a Science? *Nature* 355, 201. doi:10.1038/355201a0

Maini, P. K., Baker, R. E., and Chuong, C.-M. (2006). The Turing Model Comes of Molecular Age. *Science* 314, 1397–1398. doi:10.1126/science.1136396

Maini, P. K., Woolley, T. E., Baker, R. E., Gaffney, E. A., and Lee, S. S. (2012). Turing's Model for Biological Pattern Formation and the Robustness Problem. *Interf. Focus.* 2, 487–496. doi:10.1098/rsfs.2011.0113

Marcon, L., Diego, X., Sharpe, J., and Müller, P. (2016). High-Throughput Mathematical Analysis Identifies Turing Networks for Patterning with Equally Diffusing Signals. *eLife* 5, e14022. doi:10.7554/eLife.14022

Martinez-Corral, R., Park, M., Biette, K., Friedrich, D., Scholes, C., Khalil, A. S., et al. (2021). Transcriptional Kinetic Synergy: A Complex Landscape Revealed by Integrating Modelling and Synthetic Biology. *bioRxiv preprint.* doi:10.1101/2020.08.31.276261

Mitchison, G. J. (1981). The Polar Transport of Auxin and Vein Patterns in Plants. *Phil. Trans. R. Soc. Lond. B* 295, 461–471. doi:10.1098/rstb.1981.0154

Miura, T. (2013). Turing and Wolpert Work Together during Limb Development. *Sci. Signal.* 6, pe14. doi:10.1126/scisignal.2004038

Munteanu, A., Cotterell, J., Solé, R. V., and Sharpe, J. (2014). Design Principles of Stripe-Forming Motifs: The Role of Positive Feedback. *Sci. Rep.* 4, 5003. doi:10.1038/srep05003

Murray, J. D. (1981). A Pre-Pattern Formation Mechanism for Animal Coat Markings. *J. Theor. Biol.* 88, 161–199. doi:10.1016/0022-5193(81)90334-9

Murray, J. D. (1988). How the Leopard Gets its Spots. *Sci. Am.* 258, 80–87. doi:10.1038/scientificamerican0388-80

Murray, J. D., and Oster, G. F. (1984). Cell Traction Models for Generating Pattern and Form in Morphogenesis. *J. Math. Biol.* 19, 265–279. doi:10.1007/BF00277099

Newman, S. A. (1993). Problems and Paradigms: Is Segmentation Generic? *BioEssays* 15, 277–283. doi:10.1002/bies.950150409

Newman, S. A., and Frisch, H. L. (1979). Dynamics of Skeletal Pattern Formation in Developing Chick Limb. *Science* 205, 662–668. doi:10.1126/science.462174

Newman, S. A., Glimm, T., and Bhat, R. (2018). The Vertebrate Limb: An Evolving Complex of Self-Organizing Systems. *Prog. Biophys. Mol. Biol.* 137, 12–24. doi:10.1016/j.pbiomolbio.2018.01.002

Nicolis, G., and Prigogine, I. (1977). *Self-Organization in Non-Equilibrium Systems: From Dissipative Structures to Order through Fluctuations* (New York: John Wiley & Sons).

Onimaru, K., Marcon, L., Musy, M., Tanaka, M., and Sharpe, J. (2016). The Fin-To-Limb Transition as the Re-Organization of a Turing Pattern. *Nat. Commun.* 7, 11582. doi:10.1038/ncomms11582

Oster, G. (2002). Brownian Ratchets: Darwin's Motors. *Nature* 417, 25. doi:10.1038/417025a

Othmer, H. G., Painter, K., Umulis, D., and Xue, C. (2009). The Intersection of Theory and Application in Elucidating Pattern Formation in Developmental Biology. *Math. Model. Nat. Phenom.* 4, 3–82. doi:10.1051/mmnp/20094401

Ouyang, Q., and Swinney, H. L. (1991). Transition from a Uniform State to Hexagonal and Striped Turing Patterns. *Nature* 352, 610–612. doi:10.1038/352610a0

Painter, K. J., Ptashnyk, M., and Headon, D. J. (2021). Systems for Intricate Patterning of the Vertebrate Anatomy. *Phil. Trans. R. Soc. A.* 379, 20200270. doi:10.1098/rsta.2020.0270

Pearson, J. E. (1993). Complex Patterns in a Simple System. *Science* 261, 189–192. doi:10.1126/science.261.5118.189

Petkova, M. D., Tkačik, G., Bialek, W., Wieschaus, E. F., and Gregor, T. (2019). Optimal Decoding of Cellular Identities in a Genetic Network. *Cell* 176, 844–855. doi:10.1016/j.cell.2019.01.007

Pick, L. (2016). Hox Genes, Evo-Devo, and the Case of the *ftz* Gene. *Chromosoma* 125, 535–551. doi:10.1007/s00412-015-0553-6

Poss, Z. C., Ebmeier, C. C., and Taatjes, D. J. (2013). The Mediator Complex and Transcription Regulation. *Crit. Rev. Biochem. Mol. Biol.* 48, 575–608. doi:10.3109/10409238.2013.840259

Pourquié, O. (2003). The Segmentation Clock: Converting Embryonic Time into Spatial Pattern. *Science* 301, 328–330. doi:10.1126/science.1085887

Prigogine, I., and Lefever, R. (1968). Symmetry Breaking Instabilities in Dissipative Systems. II. *J. Chem. Phys.* 48, 1695–1700. doi:10.1063/1.1668896

Rao, C. V., Wolf, D. M., and Arkin, A. P. (2002). Control, Exploitation and Tolerance of Intracellular Noise. *Nature* 420, 231–237. doi:10.1038/nature01258

Raspopovic, J., Marcon, L., Russo, L., and Sharpe, J. (2014). Digit Patterning is Controlled by a Bmp-Sox9-Wnt Turing Network Modulated by Morphogen Gradients. *Science* 345, 566–570. doi:10.1126/science.1252960

Rebocho, A. B., Southam, P., Kennaway, J. R., Bangham, J. A., and Coen, E. (2017). Generation of Shape Complexity through Tissue Conflict Resolution. *eLife* 6, e20156. doi:10.7554/elife.20156

Reinhardt, D., Pesce, E.-R., Stieger, P., Mandel, T., Baltensperger, K., Bennett, M., et al. (2003). Regulation of Phyllotaxis by Polar Auxin Transport. *Nature* 426, 255–260. doi:10.1038/nature02081

Rivera-Pomar, R., and Jäckle, H. (1996). From Gradients to Stripes in *Drosophila* Embryogenesis: Filling in the Gaps. *Trends Genet.* 12, 478–483. doi:10.1016/0168-9525(96)10044-5

Runions, A., Tsiantis, M., and Prusinkiewicz, P. (2017). A Common Developmental Program Can Produce Diverse Leaf Shapes. *New Phytol.* 216, 401–418. doi:10.1111/nph.14449

Salazar-Ciudad, I., Sole, R. V., and Newman, S. A. (2001). Phenotypic and Dynamical Transitions in Model Genetic Networks II. Application to the Evolution of Segmentation Mechanisms. *Evol. Dev.* 3, 95–103. doi:10.1046/j.1525-142x.2001.003002095.x

Scarpella, E., Marcos, D., Friml, J., and Berleth, T. (2006). Control of Leaf Vascular Patterning by Polar Auxin Transport. *Genes Dev.* 20, 1015–1027. doi:10.1101/gad.1402406

Sheth, R., Marcon, L., Bastida, M. F., Junco, M., Quintana, L., Dahn, R., et al. (2012). *Hox* Genes Regulate Digit Patterning by Controlling the Wavelength of a Turing-Type Mechanism. *Science* 338, 1476–1480. doi:10.1126/science.1226804

Shi, B., and Vernoux, T. (2019). Patterning at the Shoot Apical Meristem and Phyllotaxis. *Curr. Top. Dev. Biol.* 131, 81–107. doi:10.1016/bs.ctdb.2018.10.003

Singh, A. P., and Nüsslein-Volhard, C. (2015). Zebrafish Stripes as a Model for Vertebrate Colour Pattern Formation. *Curr. Biol.* 25, R81–R92. doi:10.1016/j.cub.2014.11.013

Song, Y., and Hyeon, C. (2021). Cost-Precision Trade-Off Relation Determines the Optimal Morphogen Gradient for Accurate Biological Pattern Formation. *eLife* 10, e70034. doi:10.7554/eLife.70034

Štanojević, D., Hoey, T., and Levine, M. (1989). Sequence-Specific DNA-Binding Activities of the Gap Proteins Encoded by Hunchback and Krüppel in *Drosophila*. *Nature* 341, 331–335. doi:10.1038/341331a0

Stewart, T. A., Bhat, R., and Newman, S. A. (2017). The Evolutionary Origin of Digit Patterning. *EvoDevo* 8, 21. doi:10.1186/s13227-017-0084-8

Struhl, G., Johnston, P., and Lawrence, P. A. (1992). Control of *Drosophila* Body Pattern by the Hunchback Morphogen Gradient. *Cell* 69, 237–249. doi:10.1016/0092-8674(92)90405-2

Struhl, G., Struhl, K., and Macdonald, P. M. (1989). The Gradient Morphogen *bicoid* is a Concentration-Dependent Transcriptional Activator. *Cell* 57, 1259–1273. doi:10.1016/0092-8674(89)90062-7

Subramanian, S., and Murray, S. M. (2021). Pattern Selection in Reaction Diffusion Systems. *Phys. Rev. E* 103, 012215. doi:10.1103/PhysRevE.103.012215

Takiguchi, Y., Imaichi, R., and Kato, M. (1997). Cell Division Patterns in the Apices of Subterranean Axis and Aerial Shoot of *Psilotum nudum* (Psilotaceae): Morphological and Phylogenetic Implications for the Subterranean Axis. *Am. J. Bot.* 84, 588–596. doi:10.2307/2445894

Tkačik, G., and Gregor, T. (2021). The Many Bits of Positional Information. *Development* 148, dev176065. doi:10.1242/dev.176065

Turing, A. M. (1952). The Chemical Basis of Morphogenesis. *Phil. Trans. R. Soc. Lond. B* 237, 37–72. doi:10.1098/rstb.1952.0012

Tyson, J. J., and Light, J. C. (1973). Properties of Two-component Bimolecular and Trimolecular Chemical Reaction Systems. *J. Chem. Phys.* 59, 4164–4173. doi:10.1063/1.1680609

Tyson, J. J., and Novák, B. (2015). Models in Biology: Lessons from Modeling Regulation of the Eukaryotic Cell Cycle. *BMC Biol.* 13, 46. doi:10.1186/s12915-015-0158-9

Veerman, F., Mercker, M., and Marciniak-Czochra, A. (2021). Beyond Turing: Far-From-Equilibrium Patterns and Mechano-Chemical Feedback. *Phil. Trans. R. Soc. A.* 379, 20200278. doi:10.1098/rsta.2020.0278

Verna, C., Ravichandran, S. J., Sawchuk, M. G., Linh, N. M., and Scarpella, E. (2019). Coordination of Tissue Cell Polarity by Auxin Transport and Signaling. *eLife* 8, e51061. doi:10.7554/eLife.51061

Waddington, C. H. (1956). *Principles of Embryology*. New York: Macmillan.

Wardlaw, C. W. (1953). A Commentary on Turing's Diffusion-Reaction Theory of Morphogenesis. *New Phytol.* 52, 40–47. doi:10.1111/j.1469-8137.1953.tb05203.x

Wenzel, C. L., Schuetz, M., Yu, Q., and Mattsson, J. (2007). Dynamics of MONOPTEROS and PIN-FORMED1 Expression during Leaf Vein Pattern Formation in *Arabidopsis thaliana*. *Plant J.* 49, 387–398. doi:10.1111/j.1365-313X.2006.02977.x

Winfree, A. T. (1980). *The Geometry of Biological Time*. 1st edn. New York: Springer-Verlag.

Woolley, T. E., Krause, A. L., and Gaffney, E. A. (2021). Bespoke Turing Systems. *Bull. Math. Biol.* 83, 41. doi:10.1007/s11538-021-00870-y

Zhabotinsky, A. (2007). Belousov-Zhabotinsky Reaction. *Scholarpedia* 2, 1435. doi:10.4249/scholarpedia.1435

Conflict of Interest: The author declares that the research was conducted in the absence of any commercial or financial relationships that could be construed as a potential conflict of interest.

Publisher's Note: All claims expressed in this article are solely those of the authors and do not necessarily represent those of their affiliated organizations, or those of the publisher, the editors and the reviewers. Any product that may be evaluated in this article, or claim that may be made by its manufacturer, is not guaranteed or endorsed by the publisher.

frontiers | Frontiers in Physics

PERSPECTIVE
published: 12 May 2022
doi: 10.3389/fphy.2022.898160

3D Organisation of Cells in Pseudostratified Epithelia

Dagmar Iber[1,2]* *and Roman Vetter*[1,2]*

[1]Department of Biosystems Science and Engineering (D-BSSE), ETH Zürich, Basel, Switzerland, [2]Swiss Institute of Bioinformatics (SIB), Basel, Switzerland

Pseudostratified epithelia have smooth apical and basal surfaces, yet along the apical-basal axis, cells assume highly irregular shapes, which we introduce as punakoids. They interact dynamically with many more cells than visible at the surface. Here, we review a recently developed new perspective on epithelial cell organisation. Seemingly random at first sight, the cell packing configurations along the entire apical-basal axis follow fundamental geometrical relationships, which minimise the lateral cell-cell contact energy for a given cross-sectional cell area variability. The complex 3D cell neighbour relationships in pseudostratified epithelia thus emerge from a simple physical principle. This paves the way for the development of data-driven 3D simulation frameworks that will be invaluable in the simulation of epithelial dynamics in development and disease.

Keywords: epithelial organisation, cell shape, neighbour number, computational model, physical principle, punakoid

OPEN ACCESS

Edited by:
Pau Formosa-Jordan, Max Planck Institute for Plant Breeding Research, Germany

Reviewed by:
ClaudeEdouard Hannezo, Institute of Science and Technology Austria (ISTA), Austria
Pilar Guerrero, Universidad Carlos III de Madrid, Spain

***Correspondence:**
Dagmar Iber
dagmar.iber@bsse.ethz.ch
Roman Vetter
vetterro@ethz.ch

Specialty section:
This article was submitted to Biophysics, a section of the journal Frontiers in Physics

Received: *17 March 2022*
Accepted: *21 April 2022*
Published: *12 May 2022*

Citation:
Iber D and Vetter R (2022) 3D Organisation of Cells in Pseudostratified Epithelia. Front. Phys. 10:898160. doi: 10.3389/fphy.2022.898160

INTRODUCTION

Epithelia are common to all animals and plants, and play a key structural role in tissue morphogenesis and the development of organ shapes. With more than 90% of cancers being of epithelial origin [1], there is an urgent need to uncover the principles of epithelial organisation and understand the basis for epithelial integrity and homeostasis. Epithelia achieve their structural function *via* their polarity (**Figure 1A**). On the outward-facing apical side, cells form a virtually impermeable barrier *via* a cadherin-based adhesion belt and tight junctions, while, on their basal side, they bind tightly to the basal lamina, a thin sheet composed of extracellular matrix (ECM) proteins [2–5]. Additional cell-cell junction complexes along the lateral sides provide further mechanical stabilisation. Recent advances in imaging provide insight into the physical principles according to which cell connectivity is organised in epithelia, and how it changes during morphogenesis and concomitant cell shape transitions.

3D Epithelial Cell Shapes

Since the advent of light microscopy, epithelial surfaces have been studied in great detail, and this has revealed tight cell packing in polygonal lattices along the entire apical-basal axis [6–19]. As 3D segmentation of cells has become possible only very recently [17, 18, 20–25], 3D cell shapes have long been depicted as prisms, which retain the same size and neighbour relationship along the entire apical-basal axis (**Figure 1B**). Cells in curved epithelial monolayers are commonly pictured as frusta (also termed bottle cells) as the apical and basal areas must differ. Differences in neighbour arrangements between the apical and basal side point to neighbour changes along the apical-basal axis in a range of epithelia [26]. Prismatoids accommodate the neighbour change at either surface. If the neighbour relationships change somewhere in between (**Figure 1C**), the cell shape is reminiscent of that formed by beetle scutum, scutellum and wings (**Figure 1D**), which led to the new term *scutoid* [15]. With up to 14 neighbour changes along the apical-basal axis [18], pseudostratified

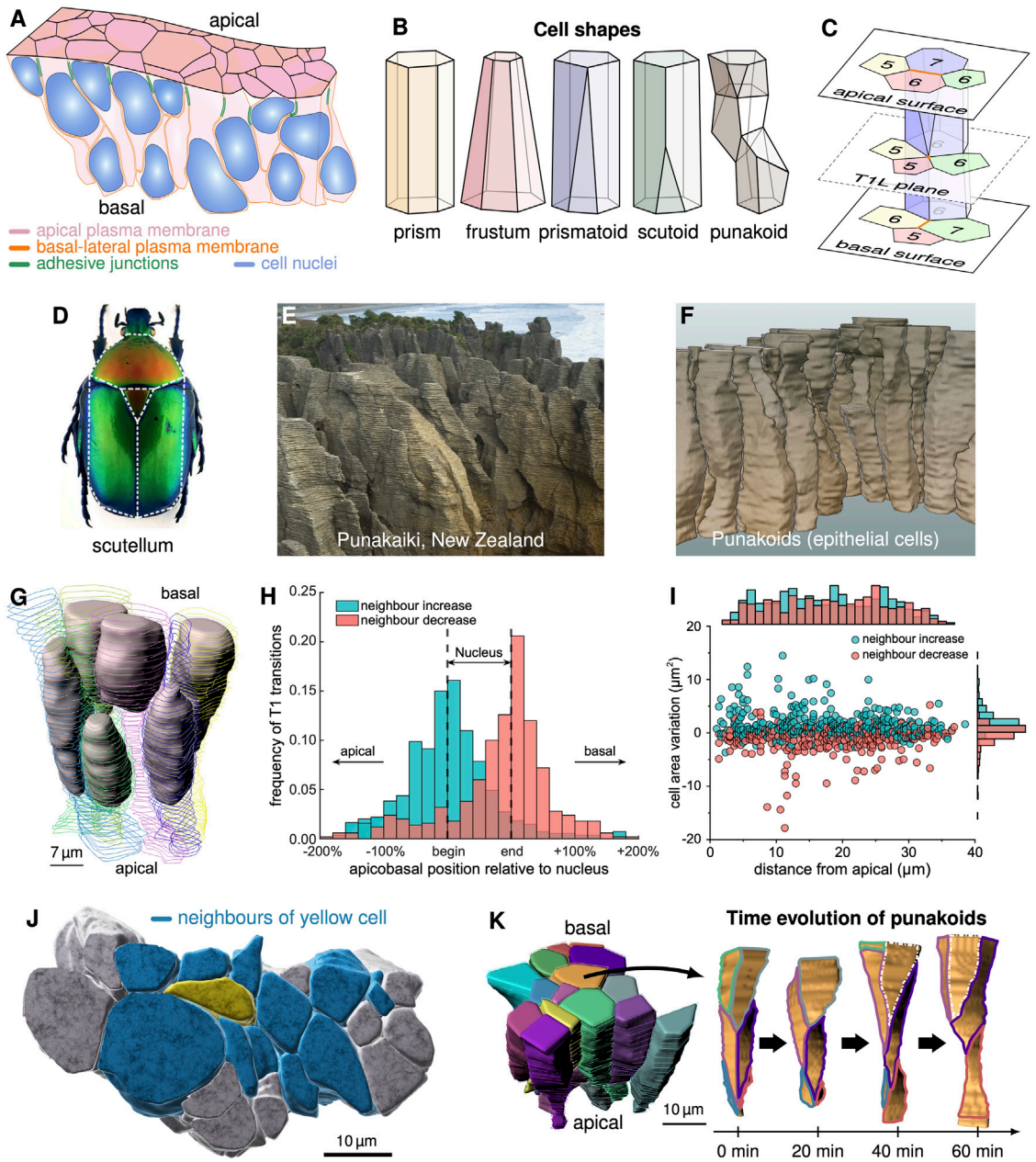

FIGURE 1 | 3D epithelial cell shapes. **(A)** Pseudostratified epithelium with cell boundaries wrapping around wider nuclei. **(B)** Schematic depiction of cell shapes. **(C)** Cells alter their neighbour arrangements *via* T1L processes along the apical-basal axis. In a T1L process, two vertices that share an edge (orange) merge and decompose in a different direction such that neighbour relationships change. **(D)** The term scutoid was coined based on the shape of beetle scutum, scutellum and wings. **(E)** Pancake rocks at the beach of Punakaiki, NZ. **(F)** 3D segmented cells in the developing pseudostratified mouse lung epithelium (E12.5) resemble the Punakaiki rocks. **(G)** 3D shapes of 6 cells and their nuclei in an E12.5 pseudostratified mouse lung epithelium. **(H)** Neighbour relationships change predominantly at the apical and basal limits of the nuclei. **(I)** The lateral T1L processes are largely uniformly distributed along the apical-basal axis. Neighbour numbers tend to increase as cross-sectional cell area variation increases, and vice versa. **(J)** 3D cell neighbourship extends further than apparent on the surface. **(K)** Time evolution of the contact areas between the central cell (orange) and its neighbours in a patch of 15 epithelial cells (left) over 60 min of explant culture. **(A, G–K)** reproduced with modifications from [18], panel D from [15], published under the Creative Commons Attribution Non-Commercial 4.0 International License (CC BY-NC 4.0; https://creativecommons.org/licenses/by-nc/4.0/). Further reproduction of these panels would need to comply with the terms of this license.

epithelial cells in developing mouse lungs, however, resemble more the pancake rock formations in Punakaiki at New Zealand's west coast (**Figure 1E**) than the back of beetles (**Figure 1D**). This novel complex geometry may therefore better be referred to as *punakoid* (**Figure 1F**). The defining characteristics of punakoids are 1) a quasi-polygonal surface, 2) a well-defined cell axis (in the pseudostratified epithelia reviewed here, the apical-basal axis), and 3) multiple neighbour changes along the axis. Like scutoids,

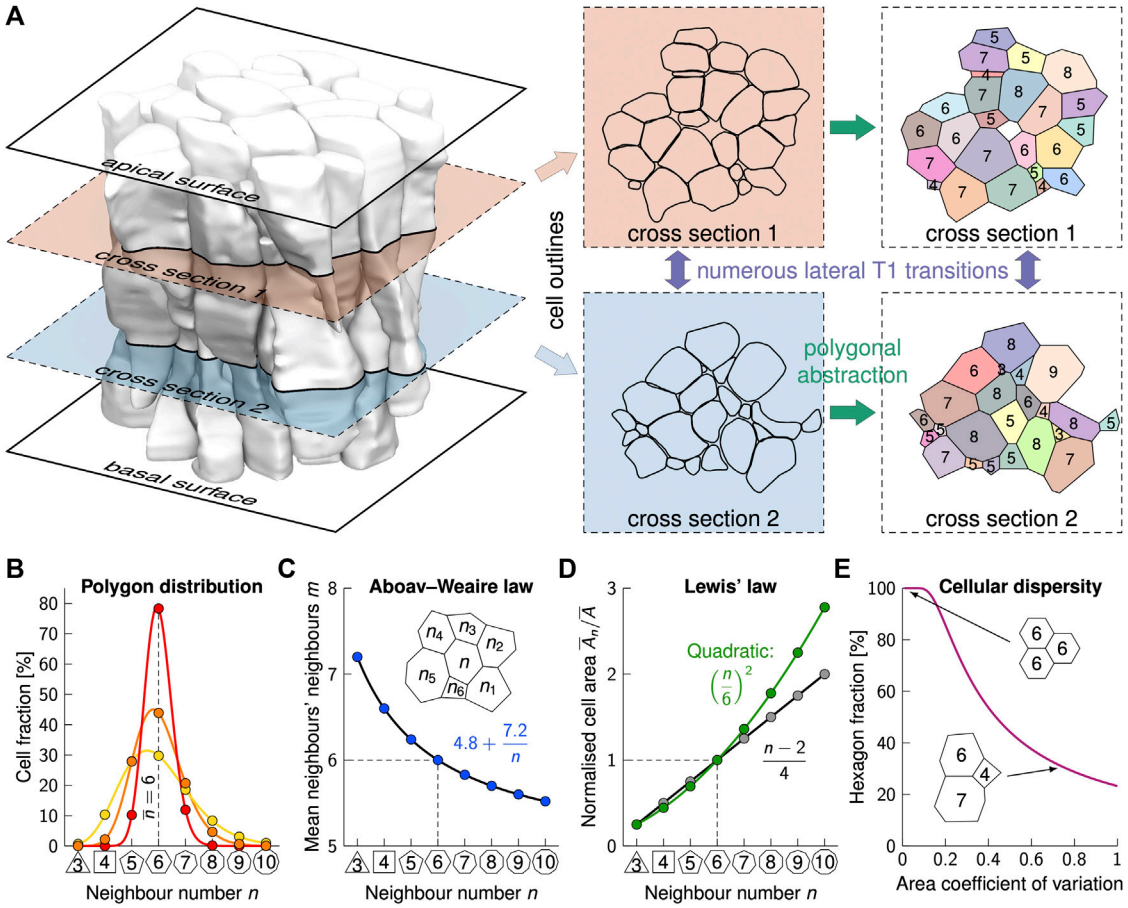

FIGURE 2 | Phenomenological laws in epithelial cell arrangements. **(A)** Slicing through a mouse embryonic lung epithelium (shaded cells [18]) repeatedly along the apical-basal axis reveals the complex shape and packing structure of punakoids. Even over short distances, numerous T1L transitions occur, leading to vastly different cell neighbourships. Colours in the last column indicate cell identity, values are cross-sectional neighbour numbers. **(B)** The average neighbour number, $\bar{n}$, is (close to) six in all epithelia, even though the hexagon fraction and the neighbor number distribution vary. **(C)** All quantified epithelial tissues follow Aboav-Weaire's law. **(D)** All quantified epithelial tissues follow either Lewis' law (grey line), or the quadratic law (green line), or lie in between. **(E)** The hexagon frequency declines for increasing area variability according to the magenta curve.

the faces of punakoids are not necessarily planar, the edges not necessarily straight, and the entire shape not necessarily convex. So far, punakoids were found in the embryonic mouse lung, and their prevalence in other pseudostratified epithelia, although likely, remains to be demonstrated.

As characteristic for pseudostratified epithelia [27], nuclei are found distributed along the entire apical-basal axis (**Figure 1G**) [18]. Neighbour changes occur mainly at the limits of the nuclei (**Figure 1H**), where the cross-sectional area changes the most [18]. An increase in the cross-sectional area correlates with a neighbour increase, and vice versa (**Figure 1I**). If the number of cells remains the same, neighbour relationships change *via* so-called T1 processes [28] (also referred to as rosette formation if more than four cells are involved [29]). We will refer to a neighbour transition along the apical-basal axis as lateral T1 process (T1L for short) (**Figure 1C**). The potentially large number of neighbour intercalations along their long axis lets the cells be in physical contact with others that, on the apical or basal surface, appear to be several cell diameters apart (**Figure 1J**). Cell-cell signalling can thus spread further than previously anticipated, and cells can read and average morphogen gradients over distances that were previously expected to require cell protrusions [30–33]. Much as on the apical surface [34], cell neighbour relationships further change dynamically over time along the entire apical-basal axis [17, 18] (**Figure 1K**), thereby further increasing the distance over which signals can be sensed, exchanged, and averaged. But what leads to these unexpectedly complex and dynamic 3D cell shapes, and what determines cell neighbour relationships?

Surface Area Minimisation

Epithelial cells are often compared to soap bubbles. Soap bubbles famously minimise their surface area and assume a spherical shape in isolation. Motivated by the tight packing of soap bubbles in foams, there has been a long-standing interest in optimal packing solutions that minimise the overall surface area. In the 19th century, Lord Kelvin proposed that tetrakaidekahedra minimise the overall surface area if all soap bubbles have the

same volume. Flattened 14-sided tetrakaidecahedra with hexagonal apical and basal surfaces are found in the multi-layered, stratified *epidermis* of the skin [22]. However, a more efficient packing of equally sized cells has since been described [35], and the complex shapes of cells in single-layered pseudostratified epithelia (**Figure 2A**) certainly do not minimise the overall surface area for the given cell volume. What then governs their shape and neighbour relationships?

Striking Regularities in Cell Arrangements

The 3D cell neighbour relationships can be understood by considering single 2D planes, perpendicular to the apical-basal cell axis [18]. In the following, we will therefore first discuss the neighbour relationships in these 2D planes (**Figure 2**).

Striking regularities that have long been known and that are found on *all* apical and basal surfaces studied to date [6–16, 19], have recently been reported also in all planes along the apical-basal axis (**Figure 2A**), even though neighbour relationships change between individual cells [18]. First and foremost, cells in any 2D plane have on average (close to) six neighbours, albeit the neighbour number distributions (**Figure 2B**) differ significantly among epithelia and between planes. This can be accounted to topological constraints in 2D contiguous polygonal lattices, and follows directly from Euler's polyhedron formula [10, 36]. If three edges meet at each junction, the mean neighbour number in infinite lattices is exactly six, $\bar{n} = 6$. The average declines as the number of edges per vertex increases, to $\bar{n} = 4$ if four edges meet in each junction. Locally, the average deviates from six in epithelia (**Figure 2C**) and follows a phenomenological relationship known as Aboav-Weaire's law [37],

$$m = \frac{1}{n}\sum_{i=1}^{n} n_i = a + \frac{b}{n} \tag{1}$$

which relates the number of neighbours, n, of a central cell to the average one of its neighbours, m (Figure 3C, inset). In epithelia, the parameter values fall into the range $a \in [4.5, 5.5]$ and $b \in [4.5, 9.5]$ [38]. Finally, the relative average apical area, $\overline{A_n}$, of cells with n neighbours with respect to the average area of all cells, $\bar{A}$, linearly increases with n (**Figure 2D**, black line), a phenomenological relation termed Lewis' law [6],

$$\frac{\overline{A_n}}{\bar{A}} \approx \frac{(n-2)}{4}. \tag{2}$$

Initially, Lewis' law has been accounted to entropy maximisation [36], but this has subsequently been ruled out [39, 40]. Many other hypotheses have been explored to explain epithelial organisation. According to topological arguments, sequential cell division results in the observed frequencies of neighbour numbers (**Figure 2B**) [10, 41]. However, this argument does not explain the emergence of cells with less than five neighbours, and predicts proliferative epithelial tissues to have about 45% hexagons. The hexagon frequencies, however, decrease with increasing variability in the cell cross-sectional areas (**Figure 2E**), and reported values range from 30 to 80% [14]. Contrary to the assumptions of the topological model, cells rearrange their boundaries until they reach a mechanical equilibrium [9]. By altering the relative cell-cell adhesion strength and cortical tension, the full range of neighbour relationships can be reproduced in vertex models and similar model setups [9, 14, 41–46]. In a small subset of the parameter space, Lewis' law emerges [9, 43, 44]. Lewis' law and the entire range of measured neighbour frequencies can be reproduced also using Voronoi tessellations, but again only for the subset of the parameter space that yields the right level of tessellation irregularity [13, 47]. So, why do all epithelia follow those two phenomenological laws?

Minimisation of the Lateral Cell-Cell Contact Energy Determines Cell Neighbour Relationships

As cells reach the mechanical equilibrium quickly (in less than a minute [9]), the polygonal lattices that one observes when cutting the epithelium in any plane (**Figure 2A**) represent a mechanical equilibrium, i.e., a state of minimal energy. At first sight, the highly irregular shapes of epithelial cells may appear inconsistent with surface energy minimisation, as observed in foam. However, by following Lewis' law and Aboav-Weaire's law, epithelial cells still minimise the lateral surface area for the given irregular cell volume distribution [14, 38]. Thus, in each plane along the apical-basal axis (**Figure 2A**), cells minimise the total perimeter for the enclosed cross-sectional areas.

As regular polygons have the smallest perimeter per enclosed area, a lattice composed of regular polygons will have the smallest total perimeter. If all cells had the same cross-sectional area, a regular hexagonal lattice would be most favourable. However, cellular processes constantly alter the cross-sectional areas, and the combined cell-cell contact surface energy is lower with mixed cross-sectional cell areas [14]. Even the hexagonal ommatidia in the *Drosophila* eye are each composed of 21 differently-sized apical cell areas, which are predominantly not hexagonal [48]. The arrangement into hexagonal ommatidia relies on the careful adjustment of cell adhesion, cortical tension, and cell dilation [49–51]. As mixed cross-sectional cell areas are most favourable, epithelial cells easily disperse from a clone with smaller cells, while they remain clustered without such a cell size difference relative to the surrounding tissue, potentially facilitating the spreading of tumour cells [16].

For the distribution of cross-sectional cell areas found in epithelial tissues, perfectly regular contiguous lattices cannot form. By following Aboav-Weaire's law, the internal angles of the polygons are closest to those of a regular polygon while still adding up to 360° at each junction [38]. By following Lewis' law, the side lengths are most similar [14]. Equal side lengths are obtained if the cross-sectional cell areas follow a quadratic relation (Figure 3D, green line) of the form

$$\frac{\overline{A_n}}{\bar{A}} \approx \frac{n}{6}\frac{\tan(\pi/6)}{\tan(\pi/n)} \approx \left(\frac{n}{6}\right)^2. \tag{3}$$

The quadratic relationship, however, emerges only at a high area variability, as found on the apical side of embryonic lung tubes [14, 18]. Finally, a novel relationship that all epithelia follow

emerges from the drive to the most regular polygonal shape, and relates the fraction of hexagons to the apical area variability, measured by the coefficient of variation (CV = std/mean) (**Figure 2E**) [14]. Interestingly, even puzzle cells in plants, which derive their name from their highly irregular shape, reminiscent of puzzle pieces, follow Lewis' law [52]. This is still consistent with a minimisation of the cell perimeter because the puzzle shape emerges in an effort to minimise stress in large cross-sections only after the cells have stopped dividing and the neighbour relationships have been fixed by the rigid cell walls [53]. In summary, the minimisation of lateral cell-cell contact energy defines the polygonal shape of each cell cross-section, and thus the cell neighbour relationships. Changes in the relative cross-sectional areas along the apical-basal axis or over time drive cell neighbour changes [14, 18]. But why do the cross-sectional areas change–or differently put, what defines the 3D cell shape?

Impact of Tissue Curvature on Cell Neighbour Relationships

If the two principal curvatures of the tissue surface change differently along the apical-basal axis, such as in sufficiently thick epithelial tubes, then the cell aspect ratio changes along the apical-basal axis. To maintain a regular polygonal cross-sectional cell shape, neighbour relationships have to change. This curvature effect has been proposed to result in scutoid cell shapes in epithelial tubes [15]. Curvature-driven T1L processes should then on average occur more frequently, i.e., for lesser curvature fold-changes κ_2/κ_1, the higher the cell neighbour number, n, in local cross sections [18]:

$$\frac{\kappa_2}{\kappa_1}(n) = \left(1 - \frac{\alpha\,(2+\cos\alpha)}{n\sin\alpha\,(1+2\cos\alpha)}\right)^{\pm\frac{\pi}{2}},\ \alpha = \frac{2\pi}{n}. \qquad (4)$$

In the tubular embryonic mouse lung epithelium, no such systematic n-dependency is observed [18]. Moreover, in planar monolayers and in spherically shaped epithelia, where the principal curvatures change equally, T1L transitions are nonetheless still found [15, 18, 19]. Effects other than tissue curvature must thus dominate in these epithelia.

Determinants of 3D Cell Shape and Neighbour Relationships

The shape of cells in single-layered epithelia can range from a cuboidal to highly elongated columns with large aspect ratio, and apical or basal constriction can further affect the cell shape [20, 21, 54]. In highly elongated cells, the diameter of a spherical nucleus would be larger than the diameter of a cylindrical cell. Accordingly, both the cells and the nuclei deform [55]. The cell is wider where the nucleus is present, and the remaining part of the cell is necessarily much thinner (**Figure 1G**). At the apical and basal limits of the nucleus, there is a sharp change in the cell cross-sectional areas, and most changes in neighbour relationships are found in this transition zone (**Figure 1H**). Epithelia with an average cell diameter smaller than the maximal nuclear diameter can thus be expected to have many more neighbour changes than those with wider cells.

Given the narrow columnar shape, there is insufficient space to accommodate all nuclei simultaneously in the same plane. Accordingly, the nuclei of neighbouring cells are found at different positions along the apical-basal axis (**Figures 1A,G**) [18], a configuration referred to as pseudostratification [27]. As mitosis is restricted to the apical side [27, 56], nuclei actively move towards the apical side during the G2 phase, and are pushed towards the basal side as the cell exits mitosis, in a process called interkinetic nuclear migration (IKNM) [55, 57, 58]. As the nuclei translocate between the apical and basal side during the cell cycle, the cell cross-sectional areas and connectivities continuously change (**Figure 1K**). An increase in the cross-sectional area increases the chance of a neighbour increase and vice versa (**Figure 1I**). Neighbour changes are less frequent close to the basal surface of tube segments, where cells remain wider throughout the cell cycle, but are otherwise uniformly distributed along the apical-basal axis [18]. Consistent with a stochastic basis to the 3D organisation of epithelial cells, the number of T1L per cell is Poisson-distributed [18].

But why would epithelial cells adopt such an elongated cell shape? Independent of the increased number of dynamically changing cell contacts, a smaller cell diameter can increase the precision of morphogen-based patterning [30]. Interestingly, several diffusible morphogens and growth factors, including Fibroblastic Growth Factor (FGF), Sonic Hedgehog (SHH), Bone Morphogenetic Protein (BMP)/transforming growth factor-beta (TGF-β), and WNT, have been observed to affect cell height, presumably *via* an effect on cell tension and/or cell-cell adhesion [59–65]. Epithelial pseudostratification may thus have evolved to enable higher developmental patterning precision.

Discussion: Towards 3D Cell-Based Tissue Simulations of Epithelial Dynamics

As the complex, dynamic 3D organisation of cells in growing epithelia is governed by simple physical concepts, computer simulations present powerful tools to understand the emergent properties of epithelia [66], including IKNM and its effects [67–71]. Cellular Potts models, which represent a generalisation of the Ising model to cells, have long been used to simulate complex 3D cell shapes [72–74]. Vertex models have been developed to specifically represent epithelia in 3D, but without resolving the complex irregular shapes of epithelial cells [64, 75–77]. In 2D, several vertex-based models with higher cell boundary resolution have been developed to enable more complex cell shapes [78–82], and to represent individual cell boundaries and the interstitial volume [83–86]. A recent hybrid version between a spheroid and a vertex model allows for a 3D vertex model with an intermediate vertex that enables a neighbour transition along the apical-basal axis [87]. To make full use of the available 3D imaging data, efficient, high-resolution vertex-based simulation frameworks are now required. A first such simulation framework that represents cells by individual, deformable meshes has recently been developed [88, 89]. In combination with quantitative 3D imaging data, this now paves the way to a more detailed understanding of epithelial cell

dynamics in development and disease. Vice versa, cell shape data can be used to infer force fields and to predict bias in cell division as cells divide perpendicular to the longest axis of their apical surface [41, 90–94]. With such tools at hand, it may become feasible to address open questions regarding the maintenance and loss of epithelial integrity and cell polarity, for instance in tumour growth and mesenchymal-to-epithelial transitions.

DATA AVAILABILITY STATEMENT

Publicly available datasets were analyzed in this study. The data is available via openBIS: https://openbis-data-repo.ethz.ch/openbis/webapp/eln-lims/?user=observer&pass=openbis as dataset 2021_Gomez_3D_Cell_Neighbour_Dynamics.

AUTHOR CONTRIBUTIONS

DI and RV wrote the review, RV generated the figures.

FUNDING

This work was funded by SNF Sinergia grant CRSII5_70930. Open access funding provided by ETH Zürich.

ACKNOWLEDGMENTS

We thank Harold F. Gómez, and Steve Runser for assistance in creating **Figures 1F**, **2A**, respectively.

REFERENCES

1. Hinck L, Näthke I. Changes in Cell and Tissue Organization in Cancer of the Breast and colon. *Curr Opin Cel Biol* (2014) 26:87–95. doi:10.1016/j.ceb.2013.11.003
2. Shin K, Margolis B. ZOning Out Tight Junctions. *Cell* (2006) 126:647–9. doi:10.1016/j.cell.2006.08.005
3. Drubin DG, Nelson WJ. Origins of Cell Polarity. *Cell* (1996) 84:335–44. doi:10.1016/s0092-8674(00)81278-7
4. Rodriguez-Boulan E, Macara IG. Organization and Execution of the Epithelial Polarity Programme. *Nat Rev Mol Cel Biol* (2014) 15:225–42. doi:10.1038/nrm3775
5. Walma DAC, Yamada KM: The extracellular matrix in development. *Development.* (2020) 147:dev175596.doi:10.1242/dev.175596
6. Lewis FT. The Correlation between Cell Division and the Shapes and Sizes of Prismatic Cells in the Epidermis of Cucumis. *Anat Rec* (1928) 38:341–76. doi:10.1002/ar.1090380305
7. Classen A-K, Anderson KI, Marois E, Eaton S. Hexagonal Packing of Drosophila wing Epithelial Cells by the Planar Cell Polarity Pathway. *Develop Cel* (2005) 9:805–17. doi:10.1016/j.devcel.2005.10.016
8. Escudero LM, da F. Costa L, Kicheva A, Briscoe J, Freeman M, Babu MM. Epithelial Organisation Revealed by a Network of Cellular Contacts. *Nat Commun* (2011) 2:526. doi:10.1038/ncomms1536
9. Farhadifar R, Röper J-C, Aigouy B, Eaton S, Jülicher F. The Influence of Cell Mechanics, Cell-Cell Interactions, and Proliferation on Epithelial Packing. *Curr Biol* (2007) 17:2095–104. doi:10.1016/j.cub.2007.11.049
10. Gibson MC, Patel AB, Nagpal R, Perrimon N. The Emergence of Geometric Order in Proliferating Metazoan Epithelia. *Nature* (2006) 442:1038–41. doi:10.1038/nature05014
11. Heller D, Hoppe A, Restrepo S, Gatti L, Tournier AL, Tapon N, et al. EpiTools: An Open-Source Image Analysis Toolkit for Quantifying Epithelial Growth Dynamics. *Develop Cel* (2016) 36:103–16. doi:10.1016/j.devcel.2015.12.012
12. Etournay R, Popović M, Merkel M, Nandi A, Blasse C, Aigouy B, et al. Interplay of Cell Dynamics and Epithelial Tension during Morphogenesis of the Drosophila Pupal wing. *Elife* (2015) 4:e07090. doi:10.7554/eLife.07090
13. Sánchez-Gutiérrez D, Tozluoglu M, Barry JD, Pascual A, Mao Y, Escudero LM. Fundamental Physical Cellular Constraints Drive Self-Organization of Tissues. *EMBO J* (2016) 35:77–88. doi:10.15252/embj.201592374
14. Kokic M, Iannini A, Villa Fombuena G, Casares F, Iber D. Minimisation of Surface Energy Drives Apical Epithelial Organisation and Gives Rise to Lewis' Law. *bioRxiv* (2019). doi:10.1101/590729
15. Gómez-Gálvez P, Vicente-Munuera P, Tagua A, Forja C, Castro AM, Letrán M, et al. Scutoids Are a Geometrical Solution to Three-Dimensional Packing of Epithelia. *Nat Commun* (2018) 9:2960. doi:10.1038/s41467-018-05376-1
16. Ramanathan SP, Krajnc M, Gibson MC. Cell-Size Pleomorphism Drives Aberrant Clone Dispersal in Proliferating Epithelia. *Develop Cel* (2019) 51:49–61. doi:10.1016/j.devcel.2019.08.005
17. Rupprecht J-F, Ong KH, Yin J, Huang A, Dinh H-H -Q, Singh AP, et al. Geometric Constraints Alter Cell Arrangements within Curved Epithelial Tissues. *MBoC* (2017) 28:3582–94. doi:10.1091/mbc.e17-01-0060
18. Gómez HF, Dumond MS, Hodel L, Vetter R, Iber D. 3D Cell Neighbour Dynamics in Growing Pseudostratified Epithelia. *Elife* (2021) 10. doi:10.7554/eLife.68135
19. Condic ML, Fristrom D, Fristrom JW. Apical Cell Shape Changes during Drosophila Imaginal Leg Disc Elongation: a Novel Morphogenetic Mechanism. *Development* (1991) 111:23–33. doi:10.1242/dev.111.1.23
20. Krueger D, Tardivo P, Nguyen C, De Renzis S. Downregulation of Basal Myosin-II Is Required for Cell Shape Changes and Tissue Invagination. *EMBO J* (2018) 37. doi:10.15252/embj.2018100170
21. Gelbart MA, He B, Martin AC, Thiberge SY, Wieschaus EF, Kaschube M. Volume Conservation Principle Involved in Cell Lengthening and Nucleus Movement during Tissue Morphogenesis. *Proc Natl Acad Sci U.S.A* (2012) 109:19298–303. doi:10.1073/pnas.1205258109
22. Yokouchi M, Atsugi T, Logtestijn MV, Tanaka RJ, Kajimura M, Suematsu M, et al. Epidermal Cell Turnover across Tight Junctions Based on Kelvin's Tetrakaidecahedron Cell Shape. *Elife* (2016) 5. doi:10.7554/eLife.19593
23. Sun Z, Amourda C, Shagirov M, Hara Y, Saunders TE, Toyama Y. Basolateral Protrusion and Apical Contraction Cooperatively Drive Drosophila Germ-Band Extension. *Nat Cel Biol* (2017) 19:375–83. doi:10.1038/ncb3497
24. Cao J, Guan G, Ho VWS, Wong M-K, Chan L-Y, Tang C, et al. Establishment of a Morphological Atlas of the *Caenorhabditis elegans* Embryo Using Deep-Learning-Based 4D Segmentation. *Nat Commun* (2020) 11:6254. doi:10.1038/s41467-020-19863-x
25. Guignard L, Fiúza UM, Leggio B, Laussu J, Faure E, Michelin G, et al. Contact Area-dependent Cell Communication and the Morphological Invariance of Ascidian Embryogenesis. *Science* (2020) 369:369. doi:10.1126/science.aar5663
26. Gómez-Gálvez P, Vicente-Munuera P, Anbari S, Buceta J, Escudero LM. The Complex Three-Dimensional Organization of Epithelial Tissues. *Development* (2021) 148:148. doi:10.1242/dev.195669
27. Norden C. Pseudostratified Epithelia - Cell Biology, Diversity and Roles in Organ Formation at a Glance. *J Cel Sci* (2017) 130:1859–63. doi:10.1242/jcs.192997
28. Weaire D, Rivier N. Soap, Cells and Statistics-Random Patterns in Two Dimensions. *Contemp Phys* (1984) 25:59–99. doi:10.1080/00107518408210979
29. Harding MJ, McGraw HF, Nechiporuk A. The Roles and Regulation of Multicellular Rosette Structures during Morphogenesis. *Development* (2014) 141:2549–2558. doi:10.1242/dev.101444
30. Adelmann JA, Vetter R, Iber D. Impact of Cell Size on Morphogen Gradient Precision. *bioRxiv* (2022). doi:10.1101/2022.02.02.478800
31. Hadjivasiliou Z, Hunter GL, Baum B. A New Mechanism for Spatial Pattern Formation via Lateral and Protrusion-Mediated Lateral Signalling. *J R Soc Interf* (2016) 13. doi:10.1098/rsif.2016.0484
32. Cohen M, Georgiou M, Stevenson NL, Miodownik M, Baum B. Dynamic Filopodia Transmit Intermittent Delta-Notch Signaling to Drive Pattern

Refinement during Lateral Inhibition. *Develop Cel* (2010) 19:78–89. doi:10.1016/j.devcel.2010.06.006
33. Kornberg TB. Distributing Signaling Proteins in Space and Time: the Province of Cytonemes. *Curr Opin Genet Develop* (2017) 45:22–7. doi:10.1016/j.gde.2017.02.010
34. Curran S, Strandkvist C, Bathmann J, de Gennes M, Kabla A, Salbreux G, et al. Myosin II Controls Junction Fluctuations to Guide Epithelial Tissue Ordering. *Develop Cel* (2017) 43:480–92. doi:10.1016/j.devcel.2017.09.018
35. Weaire D, Phelan R. A Counter-example to Kelvin's Conjecture on Minimal Surfaces. *Phil Mag Lett* (1994) 69:107–10. doi:10.1080/09500839408241577
36. Rivier N, Lissowski A. On the Correlation between Sizes and Shapes of Cells in Epithelial Mosaics. *J Phys A: Math Gen* (1982) 15:L143–L148. doi:10.1088/0305-4470/15/3/012
37. Aboav DA. The Arrangement of Grains in a Polycrystal. *Metallography* (1970) 3:383–390. doi:10.1016/0026-0800(70)90038-8
38. Vetter R, Kokic M, Gomez H, Hodel L, Gjeta B, Iannini A, et al. Aboave-Weaire's Law in Epithelia Results from an Angle Constraint in Contiguous Polygonal Lattices. *bioRxiv* (2019). doi:10.1101/591461
39. Chiu SN. A Comment on Rivier's Maximum Entropy Method of Statistical Crystallography. *J Phys A: Math Gen* (1995) 28:607–15. doi:10.1088/0305-4470/28/3/015
40. Chiu SN. Aboav-Weaire's and Lewis' Laws-A Review. *Mater Characterization* (1995) 34:149–65. doi:10.1016/1044-5803(94)00081-u
41. Gibson WT, Veldhuis JH, Rubinstein B, Cartwright HN, Perrimon N, Brodland GW, et al. Control of the Mitotic Cleavage Plane by Local Epithelial Topology. *Cell* (2011) 144:427–38. doi:10.1016/j.cell.2010.12.035
42. Naveed H, Li Y, Kachalo S, Liang J. Geometric Order in Proliferating Epithelia: Impact of Rearrangements and Cleavage Plane Orientation. *Annu Int Conf IEEE Eng Med Biol Soc* (2010) 2010:3808–11. doi:10.1109/IEMBS.2010.5627601
43. Aegerter-Wilmsen T, Smith AC, Christen AJ, Aegerter CM, Hafen E, Basler K. Exploring the Effects of Mechanical Feedback on Epithelial Topology. *Development* (2010) 137:499–506. doi:10.1242/dev.041731
44. Sahlin P, Jönsson H. A Modeling Study on How Cell Division Affects Properties of Epithelial Tissues under Isotropic Growth. *PLoS One* (2010) 5:e11750. doi:10.1371/journal.pone.0011750
45. Tanaka S, Sichau D, Iber D. LBIBCell: a Cell-Based Simulation Environment for Morphogenetic Problems. *Bioinformatics* (2015). doi:10.1093/bioinformatics/btv147
46. Conrad L, Runser SVM, Fernando Gómez H, Lang CM, Dumond MS, Sapala A, et al. The Biomechanical Basis of Biased Epithelial Tube Elongation in Lung and Kidney Development. *Development* (2021) 148:148. doi:10.1242/dev.194209
47. Zhu HX, Thorpe SM, Windle AH. The Geometrical Properties of Irregular Two-Dimensional Voronoi Tessellations. *Philosophical Mag A* (2001) 81:2765–83. doi:10.1080/01418610010032364
48. Carthew RW. Pattern Formation in the Drosophila Eye. *Curr Opin Genet Develop* (2007) 17:309–13. doi:10.1016/j.gde.2007.05.001
49. Käfer J, Hayashi T, Marée AFM, Carthew RW, Graner F. Cell Adhesion and Cortex Contractility Determine Cell Patterning in the Drosophila Retina. *Proc Natl Acad Sci U.S.A* (2007) 104:18549–54. doi:10.1073/pnas.0704235104
50. Hilgenfeldt S, Erisken S, Carthew RW. Physical Modeling of Cell Geometric Order in an Epithelial Tissue. *Proc Natl Acad Sci U.S.A* (2008) 105:907–11. doi:10.1073/pnas.0711077105
51. Gallagher KD, Mani M, Carthew RW. Emergence of a Geometric Pattern of Cell Fates from Tissue-Scale Mechanics in the Drosophila Eye. *eLife* (2022) 11:11. doi:10.7554/eLife.72806
52. Carter R, Sánchez-Corrales YE, Hartley M, Grieneisen VA, Marée AFM. Pavement Cells and the Topology Puzzle. *Development* (2017) 144:4386–97. doi:10.1242/dev.157073
53. Sapala A, Runions A, Routier-Kierzkowska AL, Das Gupta M, Hong L, Hofhuis H, et al. Why Plants Make Puzzle Cells, and How Their Shape Emerges. *Elife* (2018) 7, e32794. doi:10.7554/eLife.32794
54. Iber D. The Control of Lung Branching Morphogenesis. In: *CTDB: Cellular Networks in Development*, Vol. 143. Elsevier[Affolter M Series Editor (2021). p. 205–37. doi:10.1016/bs.ctdb.2021.02.002
55. Lele TP, Dickinson RB, Gundersen GG. Mechanical Principles of Nuclear Shaping and Positioning. *J Cel Biol* (2018) 217:3330–42. doi:10.1083/jcb.201804052
56. Gundersen GG, Worman HJ. Nuclear Positioning. *Cell* (2013) 152:1376–89. doi:10.1016/j.cell.2013.02.031
57. Meyer EJ, Ikmi A, Gibson MC. Interkinetic Nuclear Migration Is a Broadly Conserved Feature of Cell Division in Pseudostratified Epithelia. *Curr Biol* (2011) 21:485–91. doi:10.1016/j.cub.2011.02.002
58. Yanakieva I, Erzberger A, Matejčić M, Modes CD, Norden C. Cell and Tissue Morphology Determine Actin-dependent Nuclear Migration Mechanisms in Neuroepithelia. *J Cel Biol* (2019) 218:3272–89. doi:10.1083/jcb.201901077
59. Gritli-Linde A, Bei M, Maas R, Zhang XM, Linde A, McMahon AP. Shh Signaling within the Dental Epithelium Is Necessary for Cell Proliferation, Growth and Polarization. *Development* (2002) 129:5323–37. doi:10.1242/dev.00100
60. Widmann TJ, Dahmann C. Dpp Signaling Promotes the Cuboidal-To-Columnar Shape Transition of Drosophila wing Disc Epithelia by Regulating Rho1. *J Cel Sci* (2009) 122:1362–73. doi:10.1242/jcs.044271
61. Kadzik RS, Cohen ED, Morley MP, Stewart KM, Lu MM, Morrisey EE. Wnt ligand/Frizzled 2 Receptor Signaling Regulates Tube Shape and branch-point Formation in the Lung through Control of Epithelial Cell Shape. *Proc Natl Acad Sci U.S.A* (2014) 111:12444–9. doi:10.1073/pnas.1406639111
62. Kondo T, Hayashi S. Mechanisms of Cell Height Changes that Mediate Epithelial Invagination. *Develop Growth Differ* (2015) 57:313–323. doi:10.1111/dgd.12224
63. Hirashima T, Matsuda M. ERK-mediated Curvature Feedback Regulates Branching Morphogenesis in Lung Epithelial Tissue. *bioRxiv* (2021). doi:10.1101/2021.07.11.451982
64. Bielmeier C, Alt S, Weichselberger V, La Fortezza M, Harz H, Jülicher F, et al. Interface Contractility between Differently Fated Cells Drives Cell Elimination and Cyst Formation. *Curr Biol* (2016) 26:563–74. doi:10.1016/j.cub.2015.12.063
65. Storgel N, Krajnc M, Mrak P, Strus J, Ziherl P. Quantitative Morphology of Epithelial Folds. *Biophys J* (2016) 110:269–77. doi:10.1016/j.bpj.2015.11.024
66. Tanaka S. Simulation Frameworks for Morphogenetic Problems. *Computation* (2015) 3:197–221. doi:10.3390/computation3020197
67. Kosodo Y, Suetsugu T, Suda M, Mimori-Kiyosue Y, Toida K, Baba SA, et al. Regulation of Interkinetic Nuclear Migration by Cell Cycle-Coupled Active and Passive Mechanisms in the Developing Brain. *EMBO J* (2011) 30:1690–704. doi:10.1038/emboj.2011.81
68. Azizi A, Herrmann A, Wan Y, Buse SJ, Keller PJ, Goldstein RE, et al. Nuclear Crowding and Nonlinear Diffusion during Interkinetic Nuclear Migration in the Zebrafish Retina. *Elife* (2020) 9. doi:10.7554/eLife.58635
69. Shinoda T, Nagasaka A, Inoue Y, Higuchi R, Minami Y, Kato K, et al. Elasticity-based Boosting of Neuroepithelial Nucleokinesis via Indirect Energy Transfer from Mother to Daughter. *Plos Biol* (2018) 16:e2004426. doi:10.1371/journal.pbio.2004426
70. Carroll TD, Langlands AJ, Osborne JM, Newton IP, Appleton PL, Näthke I. Interkinetic Nuclear Migration and Basal Tethering Facilitates post-mitotic Daughter Separation in Intestinal Organoids. *J Cel Sci* (2017) 130:3862–3877. doi:10.1242/jcs.211656
71. Guerrero P, Perez-Carrasco R, Zagorski M, Page D, Kicheva A, Briscoe J, et al. Neuronal Differentiation Influences Progenitor Arrangement in the Vertebrate Neuroepithelium. *Development* (2019) 146. doi:10.1242/dev.176297
72. Hirashima T, Rens EG, Merks RMH. Cellular Potts Modeling of Complex Multicellular Behaviors in Tissue Morphogenesis. *Develop Growth Differ* (2017) 59:329–39. doi:10.1111/dgd.12358
73. Starruss J, de Back W, Brusch L, Deutsch A. Morpheus: a User-Friendly Modeling Environment for Multiscale and Multicellular Systems Biology. *Bioinformatics* (2014) 30:1331–2. doi:10.1093/bioinformatics/btt772
74. Swat MH, Thomas GL, Belmonte JM, Shirinifard A, Hmeljak D, Glazier JA. Multi-scale Modeling of Tissues Using CompuCell3D. *Methods Cel Biol* (2012) 110:325–66. doi:10.1016/b978-0-12-388403-9.00013-8
75. Honda H, Tanemura M, Nagai T. A Three-Dimensional Vertex Dynamics Cell Model of Space-Filling Polyhedra Simulating Cell Behavior in a Cell Aggregate. *J Theor Biol* (2004) 226:439–53. doi:10.1016/j.jtbi.2003.10.001
76. Rozman J, Krajnc M, Ziherl P. Collective Cell Mechanics of Epithelial Shells with Organoid-like Morphologies. *Nat Commun* (2020) 11:3805. doi:10.1038/s41467-020-17535-4

77. Rauzi M, Hočevar Brezavšček A, Ziherl P, Leptin M. Physical Models of Mesoderm Invagination in Drosophila Embryo. *Biophysical J* (2013) 105:3–10. doi:10.1016/j.bpj.2013.05.039
78. Palmieri B, Bresler Y, Wirtz D, Grant M. Multiple Scale Model for Cell Migration in Monolayers: Elastic Mismatch between Cells Enhances Motility. *Sci Rep* (2015) 5:11745. doi:10.1038/srep11745
79. Kourouklis AP, Nelson CM. Modeling Branching Morphogenesis Using Materials with Programmable Mechanical Instabilities. *Curr Opin Biomed Eng* (2018) 6:66–73. doi:10.1016/j.cobme.2018.03.007
80. Svoboda D, Necasova T, Tesarova L, Simara P. Tubular Network Formation Process Using 3D Cellular Potts Model. *Lecture Notes Comput Sci* (2018). doi:10.1007/978-3-030-00536-8_10
81. Brown PJ, Green JEF, Binder BJ, Osborne JM. A Rigid Body Framework for Multicellular Modeling. *Nat Comput Sci* (2021) 1:754–66. doi:10.1038/s43588-021-00154-4
82. Kim S, Pochitaloff M, Stooke-Vaughan GA, Campàs O. Embryonic Tissues as Active Foams. *Nat Phys* (2021) 17:859–66. doi:10.1038/s41567-021-01215-1
83. Tanaka S, Sichau D, Iber D. LBIBCell: a Cell-Based Simulation Environment for Morphogenetic Problems. *Bioinformatics* (2015) 31:2340–2347. doi:10.1093/bioinformatics/btv147
84. Conradin R, Coreixas C, Latt J, Chopard B. PalaCell2D: A Framework for Detailed Tissue Morphogenesis. *J Comput Sci* (2021) 53. doi:10.1016/j.jocs.2021.101353
85. Boromand A, Signoriello A, Lowensohn J, Orellana CS, Weeks ER, Ye F, et al. The Role of Deformability in Determining the Structural and Mechanical Properties of Bubbles and Emulsions. *Soft Matter* (2019) 15:5854–65. doi:10.1039/c9sm00775j
86. Boromand A, Signoriello A, Ye F, O'Hern CS, Shattuck MD, Jamming of Deformable Polygons. *Phys Rev Lett* (2018) 121:248003. doi:10.1103/physrevlett.121.248003
87. Ioannou F, Dawi MA, Tetley RJ, Mao Y, Muñoz JJ. Development of a New 3D Hybrid Model for Epithelia Morphogenesis. *Front Bioeng Biotechnol* (2020) 8:405. doi:10.3389/fbioe.2020.00405
88. Van Liedekerke P, Neitsch J, Johann T, Warmt E, Gonzàlez-Valverde I, Hoehme S, et al. A Quantitative High-Resolution Computational Mechanics Cell Model for Growing and Regenerating Tissues. *Biomech Model Mechanobiol* (2020) 19:189–220. doi:10.1007/s10237-019-01204-7
89. Hoehme S, Boettger J, Hammad S, Begher-Tibbe B, Bucur P, Vibert E, et al. *A Predictive Computational Model Shows that Biomechanical Cell Cycle Progression Control Can Explain Liver Regeneration after Partial Hepatectomy* (2021). *hal-03136097f*.
90. Hertwig O. Das Problem der Befruchtung und der Isotropie des Eies. Eine Theorie der Vererbung. *Jenaische Z Naturwissenschaft* (1884) 18:274.
91. Bosveld F, Markova O, Guirao B, Martin C, Wang Z, Pierre A, et al. : Epithelial Tricellular Junctions Act as Interphase Cell Shape Sensors to orient Mitosis. *Nature* (2016) 530:495–8. doi:10.1038/nature16970
92. Minc N, Burgess D, Chang F. Influence of Cell Geometry on Division-Plane Positioning. *Cell* (2011) 144:414–426. doi:10.1016/j.cell.2011.01.016
93. Tang Z, Hu Y, Wang Z, Jiang K, Zhan C, Marshall WF, et al. Mechanical Forces Program the Orientation of Cell Division during Airway Tube Morphogenesis. *Dev Cel* (2018). doi:10.1016/j.devcel.2017.12.013
94. Roffay C, Chan CJ, Guirao B, Hiiragi T, Graner F. Inferring Cell junction Tension and Pressure from Cell Geometry. *Development* (2021) 148:148. doi:10.1242/dev.192773

Conflict of Interest: The authors declare that the research was conducted in the absence of any commercial or financial relationships that could be construed as a potential conflict of interest.

frontiers | Frontiers in Physics

TYPE Original Research
PUBLISHED 22 July 2022
DOI 10.3389/fphy.2022.927152

OPEN ACCESS

EDITED BY
Jizeng Wang,
Lanzhou University, China

REVIEWED BY
Pablo Padilla,
National Autonomous University of Mexico, Mexico
Alexandre Rosas,
Federal University of Paraíba, Brazil

*CORRESPONDENCE
Nara Guisoni,
naraguisoni@conicet.gov.ar
Luis Diambra,
ldiambra@gmail.com

SPECIALTY SECTION
This article was submitted to Biophysics, a section of the journal Frontiers in Physics

RECEIVED 23 April 2022
ACCEPTED 27 June 2022
PUBLISHED 22 July 2022

CITATION
Guisoni N and Diambra L (2022), Transient Turing patterns in a morphogenetic model.
Front. Phys. 10:927152.
doi: 10.3389/fphy.2022.927152

Transient Turing patterns in a morphogenetic model

Nara Guisoni* and Luis Diambra*

Centro Regional de Estudios Genómicos, Universidad Nacional de La Plata (UNLP)–CONICET, La Plata, Argentine

One of the most surprising mechanisms to explain the symmetry breaking phenomenon linked to pattern formation is known as Turing instabilities. These patterns are self-organising spatial structures resulting from the interaction of at least two diffusive species in specific conditions. The ideas of Turing have been used extensively in the specialised literature both to explain developmental patterns, as well as synthetic biology design. In the present work we study a previously proposed morphogenetic synthetic circuit consisting of two genes controlled by the same regulatory system. The spatial homogeneous version of this simple model presents a rich phase diagram, since it has a saddle-node bifurcation, spirals and limit cycle. Linear stability analysis and numerical simulations of the complete model allow us to determine the conditions for the development of Turing patterns, as well as transient patterns. We found that the parameter region where Turing patterns are found is much smaller than the region where transient patterns occur. We observed that the temporal evolution towards Turing patterns can present one or two different length scales, depending on the initial conditions. Further, we found a parameter region where the persistence time of the transient patterns depends on the distance between the parameters values on which the system is operating and the boundary of Turing patterns. This persistence time has a singularity at a critical distance that gives place to metastable patterns. To the best of our knowledge, transient and metastable patterns associated with Turing instabilities have not been previously reported in morphogenetic models.

KEYWORDS

Turing instability, biological pattern, morphogenesis, transient pattern, metastable pattern, saddle-node bifurcation, morphogenetic modelling, synthetic biology

1 Introduction

Pattern formation in morphogenetic system is one of the central problems in developmental biology. One of the best-known mechanism of autonomous pattern formation is the Turing instability. This symmetry breaking mechanism was introduced in 1952 by Alan Turing in the context of models for morphogenesis [1]. The basic idea is that Turing instability arises from the coupling between diffusion and reaction which can destabilize spatially homogenous equilibrium and lead to the formation of patterns. The minimum biological system able to present Turing

instabilities consists in only two interacting diffusible components: an activator with a slow diffusion rate and an inhibitor with a fast diffusion rate [2].

There is a large body of literature focused on the mechanism proposed by Turing to explain the patterns of self-organization during the animal development [3–11]. However, the identification of the molecular agents driving Turing patterns remains an unsolved issue in most cases.

Thanks to recent progress in synthetic genetic circuit engineering, several researchers have embarked on the implementation of Turing ideas on cell culture [12–17]. To engineer such biological systems, one needs to know the mandatory properties and genetic circuit that support the biological patterning process. It is well known that two key factors underlying the Turing model are the differential diffusion between activator and inhibitor, and also the non-linearity in the reactive terms. In addition, it has been shown that the latter can be as important as the differential diffusion [18, 19]. In this sense, a Turing model has been proposed where the activator and inhibitor are under the control of the same promoter, a simplification that can be exploited in the design of synthetic morphogenetic circuits. This biological simplification allows a mathematical analysis which has highlighted the role of cooperative regulation as source of non-linearity [18]. However, beyond this contribution, the single-promoter model has not been explored to its full potential in either theoretical or experimental studies. In this paper we present a deep theoretical analysis of this simple model and report that it has a rich phase diagram that include: saddle-node, limit cycles and Turing patterns. We also observe transient patterns, driven by Turing instability, which hereafter will be referred to as transient Turing patterns. Previous reports about transient Turing patterns have been done in the context of closed systems, when chemical species are being consumed [20–22] and for noise-driven stochastic patterns in a multicellular cyanobacterial organism [23]. Moreover, out of the reaction-diffusion context, transient Turing patterns have been reported in a neural field model of working memory [24]. Except for the last case, the reaction-diffusion systems associated with transient Turing patterns are composed by several species, which posses the additional challenge to derive analytical predictions or to associate a phase diagram to study them. On the other hand, the present model can be associated with biological systems [25, 26] and the analysis of the associated reaction-diffusion equations are feasible for some values of the Hill exponent of regulatory function. The present results show that in this model the transient patterns are due to the presence of a saddle node which have associated spatial modes with no-null amplification rate. Patterns initiated around this steady state can experiment a transition to Turing pattern associated with a stable steady state, or disappear. The existence of transient patterns brings with it the question of their persistence. This question is especially important given that in the biological context Turing patterns are associated with spatial distributions of molecules that induce morphogenetic processes whose time scales must be finely orchestrated. Interestingly, we observe that the persistence time of the transient patterns suffers a critical transition when parameters values approaches at a critical distance of the boundary that separate Turing stable patterns. This critical distance defines a region for metastable patterns, where the spatial pattern remains stable over large time scales while no disturbances operate. Metastable transient patterns have been previously reported in the context of 1D reaction-diffusion systems [27, 28]. To the best of our knowledge, metastable Turing patterns are a novel feature as far as morphogenetic models are concerned, because are related to unstable nodes, which have not been considered in previous studies on Turing instability.

2 The morphogenetic model

The minimum biological system able to present Turing instabilities consists of two interacting diffusible proteins, named morphogens. In the case of the model considered here, the self-activating morphogen A also activates the morphogen H, which in turn inhibits both morphogens (see the sketch in Figure 1A). The activator and the inhibitor morphogens are coupled through the regulatory functions associated with the genes that encode them. The regulatory functions describe mathematically how the protein synthesis rate depends on the concentration of activators and inhibitors. A morphogenetic model was recently introduced which considers that both morphogens are regulated by the same promoter [18]. That means that regulatory functions that control the synthesis rate of both morphogens will be the same. Thus, in this case, the temporal evolution of the system is described by a couple of reaction-diffusion equations of the form.

$$\frac{\partial a}{\partial t} = D_a \nabla^2 a + \rho_a f(a,h) - \mu_a a \tag{1}$$

$$\frac{\partial h}{\partial t} = D_h \nabla^2 h + \rho_h f(a,h) - \mu_h h, \tag{2}$$

Where a (x, t) and h (x, t) denote the concentration of the activator A and the inhibitor H, respectively, as a function of spatial position and time. The last term on the right hand side of each equation describes the degradation process and was assumed to be linear. The function f corresponds to the regulatory function that controls the expression of both activator and inhibitor. As in the previous study [18], we consider a sigmoidal regulatory function where activator and inhibitor compete for the same regulatory site in the form:

$$f(a,h) = \frac{a^{n_H}}{1 + (h/k_h)^{n_H} + (a/k_a)^{n_H}}, \tag{3}$$

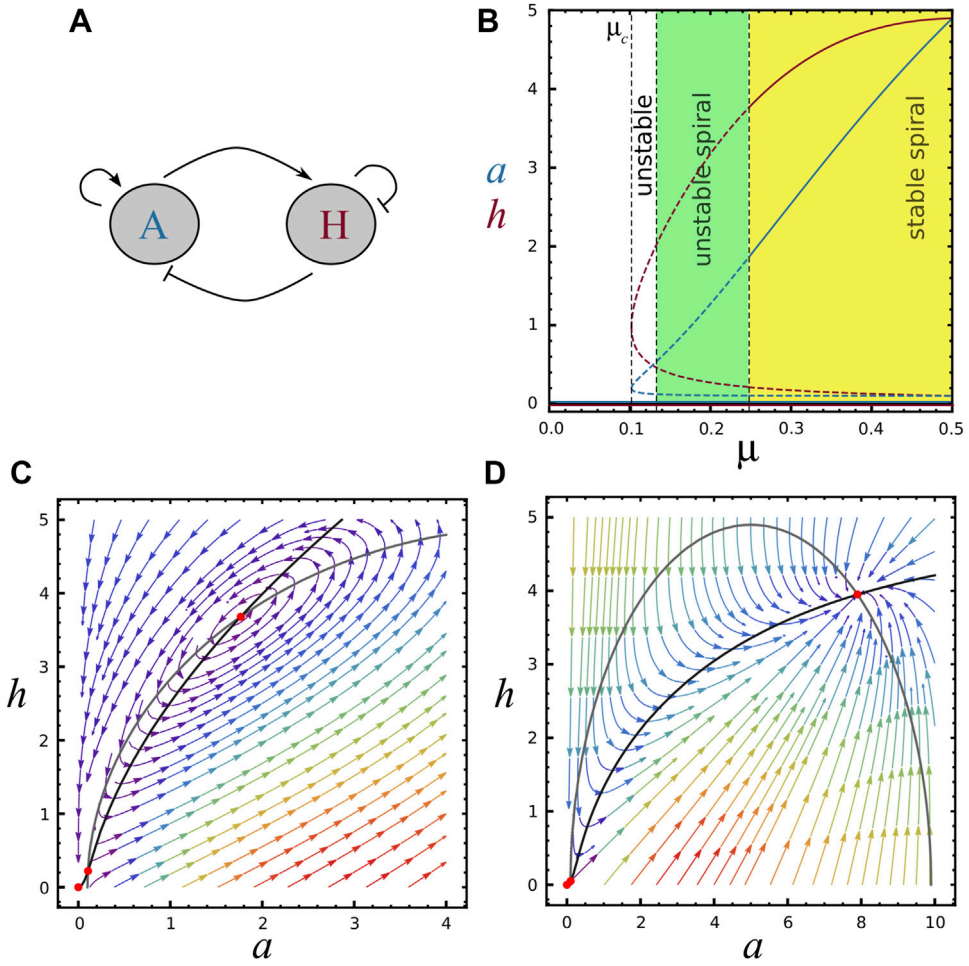

FIGURE 1
Bifurcation diagram and nullclines, **(A)** Schematic representation of the two-component system, A is the activator morphogene (activates both reactants), H is the inhibitor morphogene (inhibits both reactants). **(B)** Bifurcation diagram showing the behavior of concentrations *a* (blue) and *h* (red) as a function of μ, with r_a =10 and r_h =5. The trivial fixed point S_0=(0,0) is present for all μ values. The saddle-node bifurcation at $\mu = \mu_c \approx 0.10$ marks the emergence of two new fixed points (S_1 and S_2). Continuous and dashed curves represent respectively regions of stable and unstable steady state solutions. Black vertical dashed lines refer to μ_c and the stability of steady-state S_2, indicating regions of unstable node (white area, where Tr**A** <0, det **A** >0 and Δ >0), unstable spiral (green area, where Tr**A** <0, det **A** >0 and Δ <0) and stable spiral (yellow area, where Tr**A** >0, det **A** >0 and Δ <0). For $\mu = \mu_2$ the system displays a limit cycle (Tr**A** =0 and det **A** >0). For visualisation in the phase diagram, see horizontal line in Supplementary Figure S1B. **(C)** Black and grey curves represent *F* and *G* functions (nullclines) for the parameters value (μ, r_a, r_h)=(0.24,10,5) (S_2 is an unstable spiral). **(D)** Nullclines for the parameters value (μ, r_a, r_h)=(1,10,5) (S_2 is a stable node). Red points represent fixed points.

where n_H is the Hill exponent that describes the steepness of the sigmoidal function (considered equal for both activator and inhibitor), while k_a and k_h are related to the effective dissociation constant for the activator and inhibitor, respectively. However, non-competitive regulatory function can also be used [29, 30]. At this point it is convenient to introduce dimensionless variables for time $\hat{t}$, position $\hat{x}$, and the concentrations $\hat{a}$ and $\hat{h}$ as follow:

$$\hat{x} = x\sqrt{\mu_a / D_h}, \qquad \hat{t} = t\mu_a, \qquad \hat{a} = a \Big/ k_a, \qquad \hat{h} = h \Big/ k_h.$$

To simplify the notation we introduced the abbreviations $d = D_a / D_h$, $\mu = \mu_h / \mu_a$, $r_a = \rho_a k_a^{n-1} / \mu_a$ and $r_h = \rho_h k_a^n / (\mu_a k_h)$. Thus, Eqs. 1, 2 can be rewritten as:

$$\frac{\partial \hat{a}}{\partial t} = d\nabla^2 \hat{a} + F\left(\hat{a}, \hat{h}\right), \tag{4}$$

$$\frac{\partial \hat{h}}{\partial t} = \nabla^2 \hat{h} + G\left(\hat{a}, \hat{h}\right). \tag{5}$$

Where.

$$F\left(\hat{a}, \hat{h}\right) = r_a f\left(\hat{a}, \hat{h}\right) - \hat{a}, \tag{6}$$

$$G\left(\hat{a}, \hat{h}\right) = r_h f\left(\hat{a}, \hat{h}\right) - \mu\hat{h}. \tag{7}$$

Next, we carried out a detailed mathematical analysis of local stability of this dimensionless model for the case without diffusion. After that, we presented the Turing-instability conditions. From now on we will write new variables without the

hat in order to simplify the notation. The Hill exponent on the regulatory function f is usually associated with the number of regulatory sites in the promoter, but as a consequence of the finite free energy involved in the interaction between regulators molecules [31, 32], the exponent is not an integer number. Despite that, hereafter we set $n_H = 2$ for mathematical convenience since it allows the derivation of analytical expressions which will help to obtain the results on the next Section.

3 Results

3.1 Stability analysis for the non-spatial model

In order to determine the general conditions for diffusion-driven instabilities, it is necessary to study the temporal evolution of the diffusion-less system:

$$\frac{\partial a}{\partial t} = F(a,h), \tag{8}$$

$$\frac{\partial h}{\partial t} = G(a,h). \tag{9}$$

The homogeneous steady states $S = (a_{ss}, h_{ss})$ system of (Eqs. 8, 9) are the positive solutions of equations $F(a_{ss}, h_{ss}) = 0$ and $G(a_{ss}, h_{ss}) = 0$. The system can present up to three fixed points: the trivial solution $S_0 = (0, 0)$, and two non-trivial solutions, identified as $S_1 = (a_1, h_1)$ and $S_2 = (a_2, h_2)$ with.

$$a_1 = \frac{\mu^2 r_a^3 - \mu r_a \sqrt{\mu^2 r_a^4 - 4(\mu^2 r_a^2 + r_h^2)}}{2(\mu^2 r_a^2 + r_h^2)}, \qquad h_1 = a_1 \frac{r_h}{\mu r_a}, \tag{10}$$

$$a_2 = \frac{\mu^2 r_a^3 + \mu r_a \sqrt{\mu^2 r_a^4 - 4(\mu^2 r_a^2 + r_h^2)}}{2(\mu^2 r_a^2 + r_h^2)}, \qquad h_2 = a_2 \frac{r_h}{\mu r_a}. \tag{11}$$

The non-trivial steady-states, S_1 and S_2, are real in a parameter region defined by

$$\mu^2 r_a^4 - 4(\mu^2 r_a^2 + r_h^2) > 0. \tag{12}$$

Hence, $\mu_c^2 r_a^4 - 4(\mu_c^2 r_a^2 + r_h^2) = 0$ defines a surface in the parameter space where a saddle-node bifurcation is found. In that way, for fixed values of r_a and r_h, it is possible to define a critical value for μ

$$\mu_c = \frac{2r_h}{r_a}\sqrt{\frac{1}{r_a^2 - 4}} \qquad \text{with} \qquad r_a > 2. \tag{13}$$

For $\mu > \mu_c$ the three steady-states are real, while for $\mu < \mu_c$ only the trivial one is found. For $\mu = \mu_c$ the two non-trivial solutions merge together (see Figure 1B). Similarly, we can obtain analytical expressions for critical values of r_a and r_h as a function of the remaining parameters.

In Figure 1B it is possible to appreciate the activator and inhibitor concentrations as a function of μ for the three steady states, when r_a and r_h are kept as constants. Note that $\mu = \mu_c$ is a saddle-node bifurcation and the non-trivial stead-states S_1 and S_2 are present only for $\mu > \mu_c$. Similarly, Supplementary Figure S1A shows a and h as a function of r_h keeping constants μ and r_a. Supplementary Figure S1B depicts a stability phase diagram for S_2 in the plane μ-r_h with $r_a = 10$, where the different regions of stability are indicated by colors. Horizontal dashed line shows the section of the parameter region explored in Figure 1B ($r_a = 10$ and $r_h = 5$), with dots indicating the dashed lines of Figure 1B. Vertical dashed line shows the section of the parameter region explored in Supplementary Figure S1A.

Typical phase planes can be seen in Figures 1C,D, for different values of μ. Note that increasing μ brings S_0 and S_1 closer together, as it can also be seen in Figure 1B.

Linearising the system about the steady-states $S = (a_{ss}, h_{ss})$ it is possible to determine the stability of each state S. Therefore, we define

$$\mathbf{v} = \begin{pmatrix} a - a_{ss} \\ h - h_{ss} \end{pmatrix}. \tag{14}$$

For the case of $|\mathbf{v}|$ small, it is possible to approximate Eqs. 8 and 9 as

$$\frac{\partial \mathbf{v}}{\partial t} = \mathbf{A}\mathbf{v}, \qquad \mathbf{A} = \begin{pmatrix} F_a & F_h \\ G_a & G_h \end{pmatrix}_{a_{ss},h_{ss}} \tag{15}$$

where $\mathbf{A}$ is the Jacobian matrix, with $F_a = \frac{\partial F}{\partial a}$, $F_h = \frac{\partial F}{\partial h}$, $G_a = \frac{\partial G}{\partial a}$ and $G_h = \frac{\partial G}{\partial h}$. Where the partial derivatives of F and G are evaluated at the steady-state $S = (a_{ss}, h_{ss})$ under consideration. For each steady state, the eigenvalues are given by

$$\lambda_{1,2} = \frac{1}{2}\left[\mathrm{Tr}\mathbf{A} \pm \sqrt{\Delta}\right], \tag{16}$$

with $\Delta = (\mathrm{Tr}\mathbf{A})^2 - 4\det\mathbf{A}$. Following Routh–Hurwitz criterion, a fixed point is linearly stable if the real part of the eigenvalues of the associated Jacobian matrix $\mathbf{A}$ are negative. According to Eq. 16 this is guaranteed if

$$\mathrm{Tr}\mathbf{A} < 0 \quad \text{and} \quad \det\mathbf{A} > 0. \tag{17}$$

The trivial steady-state S_0 is always a stable node, whereas S_1 is an unstable saddle-point for the parameter region delimited by the inequality (Eq. 12). S_2 has a more intricate behaviour, as it is discussed below.

The stability of S_2 depends on the values of r_a, r_h and μ, as shown in Figure 2A. As it can be seen, the region where S_2 is stable becomes smaller as the inhibitor production rate r_h increases. On the other hand, this region rises with the activator production rate r_a and the relative degradation rate μ. We observe that a and h concentrations in S_2 can present oscillations, which can be stable or unstable (see Figure 2B). Interestingly, in the region of unstable spirals (where $\mathrm{Tr}\mathbf{A} > 0$ and $\Delta < 0$), oscillations drive the system to the trivial steady-state S_0 (see Figure 2C and the phase-plane of Figure 1C). Otherwise,

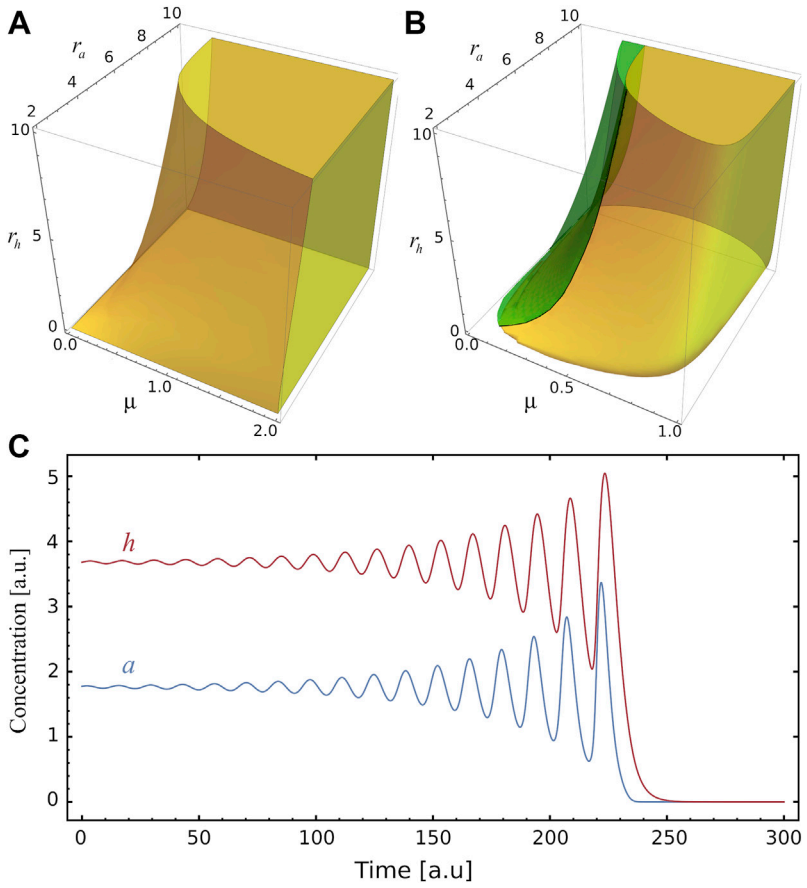

FIGURE 2
Stability and instability of the fixed point S_2. **(A)** Yellow volume delimits, in the parameters space (μ, r_a, r_h), the region where the steady state S_2 is stable. **(B)** The green region corresponds to the values of the parameters where the system develops a spiral source behaviour in the steady state S_2 (see panel C), while in the yellow region there is a spiral sink behaviour at S_2. Only at the interface of these two regions does the system exhibit a limit cycle. **(C)** Example illustrating of unstable oscillatory behaviour for a and h, as function of time, for (μ, r_a, r_h)=(0.24,10,5), the amplitudes increase until they reach the stable trivial fixed point S_0.

when Tr$\mathbf{A}$ < 0 (with Δ < 0) the stable spirals around S_2 are damped until the system reaches the stable steady-state (see Supplementary Figure S1C). On the boundary of unstable and stable spirals, when Reλ = 0 and Im$\lambda \neq 0$ (Tr$\mathbf{A}$ = 0 and det $\mathbf{A}$ > 0), a stable limit circle is found, as shown in Supplementary Figure S1D. The rich behaviour of the system around S_2 can also be seen in the μ-r_h phase diagram of Supplementary Figure S1B: four regions indicate when S_2 is an unstable node, unstable spiral, stable spiral or stable node. Besides, the saddle-node bifurcation line and the limit-circle line are shown.

In Figure 1B the stability of S_2 for increasing μ is presented: it changes from an unstable node to unstable and stable oscillations. In the phase-plane of Figure 1C, S_2 is an unstable spiral while for Figure 1D it is a stable node. The stability of S_2 as a function of r_h is shown in Supplementary Figure S1A. In this case, greater values of r_h lead the system towards instability. The points $\mu = \mu_c$ and $r_h = r_{hc}$ shown respectively in Figure 1B and Supplementary Figure S1A, where $S_1 = S_2$, are saddle points.

3.2 Conditions for Turing patterns

As it was mentioned in the previous section, the fixed point S_2 is stable in a region of the parameter space. The addition of diffusive terms to the system of (Eqs. 8, 9) can destabilise the spatially homogeneous equilibrium and lead to the formation of patterns, known as Turing patterns. To obtain the mathematical conditions for Turing instability let us consider a one-dimensional version of Eq. 15, that includes the diffusive process,

$$\frac{\partial \mathbf{v}}{\partial t} = \mathbf{A}\,\mathbf{v} + \mathbf{D}\frac{\partial^2 \mathbf{v}}{\partial x^2}, \qquad \mathbf{D} = \begin{pmatrix} d & 0 \\ 0 & 1 \end{pmatrix}, \tag{18}$$

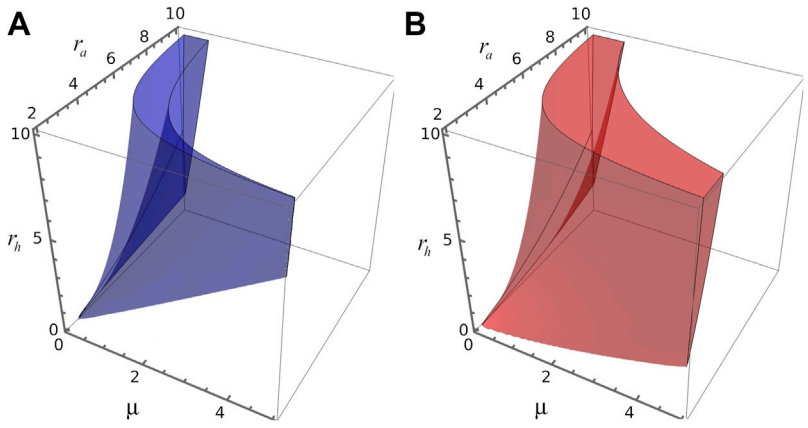

FIGURE 3
3D parameters space. **(A)** Blue volume delimits, in the space spanned by parameters (μ, r_a, r_h), the region where the four Turing conditions are verified for steady state S_2. **(B)** Red volume delimits, in the space spanned by parameters (μ, r_a, r_h), the region where $k^2>0$ and $\omega>0$ for the steady state S_1.

and the boundary conditions. We are interested in the zero-flux boundary condition, i.e., that morphogens cannot diffuse beyond the boundaries [0,L]. This implies that the wave number k of solutions of Eq. 18 takes discrete values $k_n = n\pi/L$, with $n = 0, 1, 2, \ldots$. As usual, the steady solution S is perturbed with $\boldsymbol{\delta}_n(x,t) = (\delta_a, \delta_h)e^{(\omega t - ik_n x)}$. Substituting $\mathbf{v} = \boldsymbol{\delta}_n(x,t)$ in Eq. 18 we obtain

$$\omega\boldsymbol{\delta}_n = \mathbf{A}\boldsymbol{\delta}_n - \mathbf{D}k_n^2\boldsymbol{\delta}_n. \tag{19}$$

The perturbation $\boldsymbol{\delta}_n(x,t)$ can be different from zero (non-trivial solution), if and only if

$$\det\left(\omega I - \mathbf{A} + \mathbf{D}k_n^2\right) = 0. \tag{20}$$

Therefore, for the stable homogeneous state to become unstable upon perturbation $\boldsymbol{\delta}_n$ it is required that $\mathrm{Re}(\omega) > 0$. This is fulfilled if any of the conditions below are satisfied

$$\mathrm{Tr}\left(\mathbf{A} - k_n^2\mathbf{D}\right) > 0 \tag{21}$$

$$\det\left(\mathbf{A} - k_n^2\mathbf{D}\right) < 0 \tag{22}$$

As (Eq. 21) is never true for a stable fixed point, the only necessary condition is (Eq. 22). Taking into account that $\det\mathbf{A} > 0$ on stable fixed point, condition (Eq. 22) implies in

$$F_a + d\ G_h > 0. \tag{23}$$

The condition for a non-trivial solution Eq. 20 leads to the relation of the eigenvalues as function of the wave number k, knows as dispersion relation

$$\omega^{\pm}(k) = \frac{-\alpha(k) \pm \sqrt{\alpha(k)^2 - 4\beta(k)}}{2}, \tag{24}$$

where $\alpha(k)$ and $\beta(k)$ are functions of k^2 and given by

$$\alpha(k) = (d+1)k^2 - \mathrm{Tr}\mathbf{A}, \tag{25}$$

$$\beta(k) = d\ k^4 - (F_a + d\ G_h)k^2 + \det\ \mathbf{A}, \tag{26}$$

where the partial derivatives of F and G are evaluated at the steady-state S under consideration. In the following we will consider only the dispersion relation ω^+ because ω^- is negative in the parameter region of interest.

Furthermore, we are looking for positive k^2 such that $\beta(k) < 0$ for some nonzero k. Thus it is necessary that the minimum of β be negative. By differentiating with respect to k^2 we obtain that the minimum of β is at $k^2_{\min} = (F_a + d\ G_h)/2d$, and the condition for β negative can be written as:

$$(F_a + d\ G_h)^2 > 4d\ \det\mathbf{A}. \tag{27}$$

Thus, the necessary and sufficient conditions for Turing instability can be summarised by the conditions for the existence of a stable homogeneous state in the absence of diffusion (Eq. 17), and conditions (Eq. 23) and (Eq. 27). These four conditions determine that the system will develop Turing patterns when a stable fixed point is disturbed by a perturbation with a certain wave number.

Figure 3A depicts the region of the parameter space spanned by parameters μ, r_a and r_h where the reaction-diffusion system of (Eqs. 8, 9) satisfies the conditions for Turing instabilities for $d = 0.01$. However, we observe that some perturbations can also propagate even when the fixed point in question is unstable, given rise in this case to transient patterns, or transitions between spatial patterns with different wave numbers. To analyse this aspect lets us remark that the temporal evolution of a spatial perturbation is dominated by the value of the wave number associated with the largest amplification rate, i.e., k value which maximises $\omega^+(k)$. This wave number, denoted here by $k_{\max}$, is related to

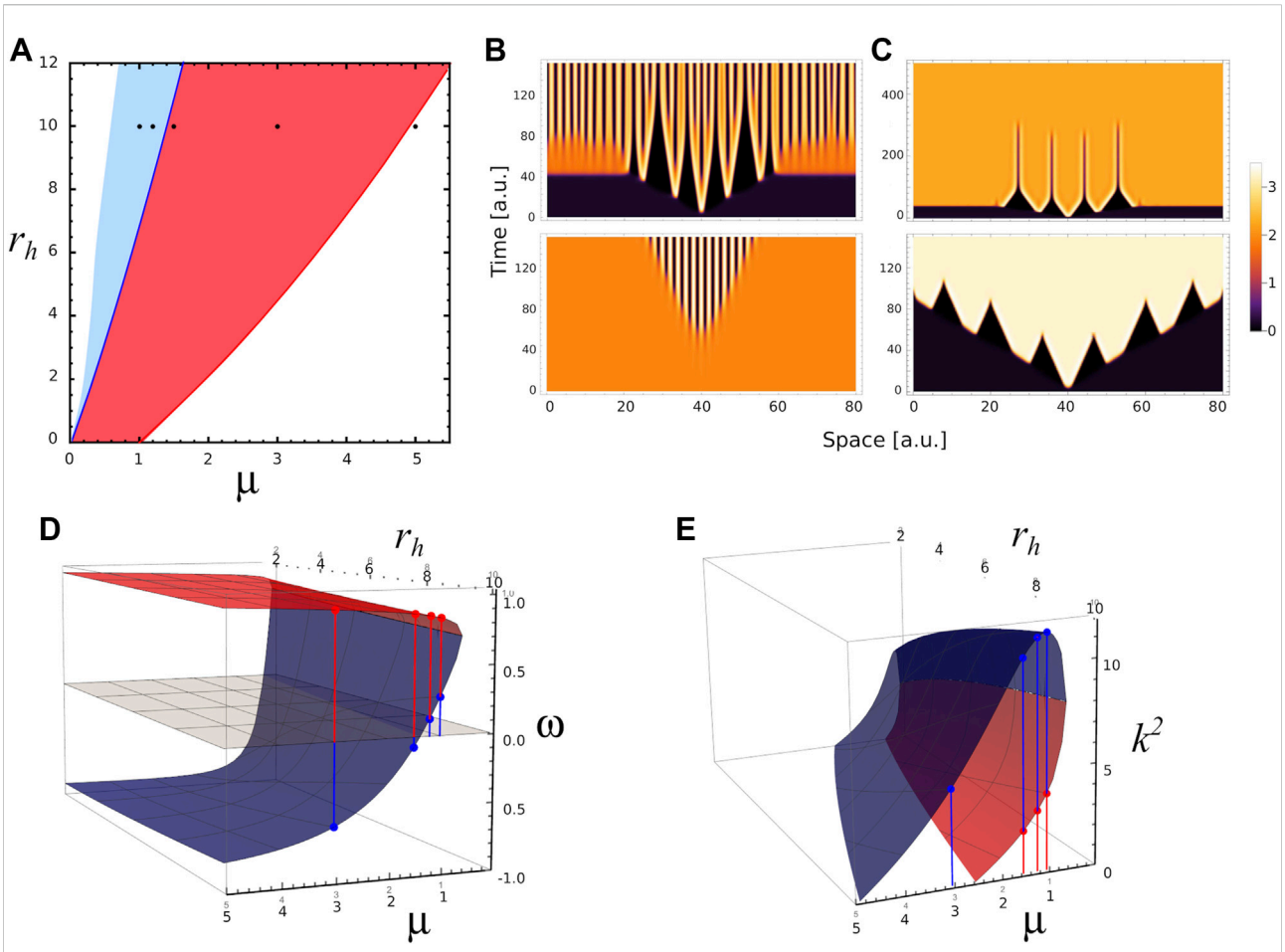

FIGURE 4
Different spatial scales. **(A)** 2D phase diagram shows the parameters region where the system presents stable Turing patterns (blue area) and unstable or transient Turing patterns (red area) for r_a=6.0. Black dots correspond to different triplet of parameters values (μ, r_a, r_h) where numerical simulation were performed: P_1=(1.0,6,10), P_2=(1.2,6,10) in the Turing pattern region, P_3=(1.5,6,10), P_4=(3.0,6,10) in the transient Turing pattern region, and P_5=(5.0,6,10) in the region for uniform distributions. **(B)** 1-D numerical simulations showing the temporal evolution of activator concentration distribution a for parameters value P_2 with two different initial conditions. Top (bottom) panel corresponds to the temporal evolution when fixed point S_1 (S_2) is perturbed by a small perturbation at x =40, note the different spatial scales of patterns on the panels. The temporal evolution of a for parameters values P_1, P_3 and P_5 are shown in Supplementary Figure S2. **(C)** 1-D numerical simulations showing the temporal evolution of a for parameters values P_3 (top panel) and P_4 (bottom panel) when the same fixed point S_1 is perturbed at x = 40. **(D)** Red and blue surfaces correspond to ω-value as function of μ and r_h associated with fixed points S_1 and S_2, respectively. **(E)** k^2-values as function of μ and r_h associated with S_1 (red surface) and S_2 (blue surface). In both panels D and E, r_a =6.0, and the red and blue dots indicate ω and k^2 values for P_1, P_2, P_3 and P_4 in each case.

the size of the emergent pattern, and the characteristic pattern size is given by $\pi/k_{\max}$. Note that spatial patterns will be developed when $k^2_{\max}$ and $\omega^+(k_{\max})$ are positive. In fact, these conditions are implicit in the derivation of Turing conditions (Eq. 23) and (Eq. 27). Therefore, referring to the stable fixed point S_2, the parameter region where $k^2_{\max}$ and $\omega^+(k_{\max})$ are positive is the same that the region where the four Turing conditions are verified, and will be denoted by R_2 (Figure 3A). On the other hand, the parameter region where $k^2_{\max}$ and $\omega^+(k_{\max})$ are positive for the unstable saddle-point S_1, gives a finite region showed in Figure 3B, and will be called R_1. In region of overlap between R_1 and R_2, there are two characteristic pattern sizes related to the unstable and stable fixed points S_1 and S_2, respectively. Depending on the initial conditions, unidirectional transitions between spatial patterns with different wave numbers are expected. Furthermore, in the region of R_1 that extends beyond of R_2, we expect to observe transient patterns related to the unstable fixed point S_1. In the next subsection we will exemplify these possibilities by numerical simulations considering a diffusion rate value of d = 0.01 in all cases. For the sake of simplifying the notation, hereafter, the expression $\omega^+(k_{\max})$ computed over steady state S_i will be denoted by $\omega(S_i)$.

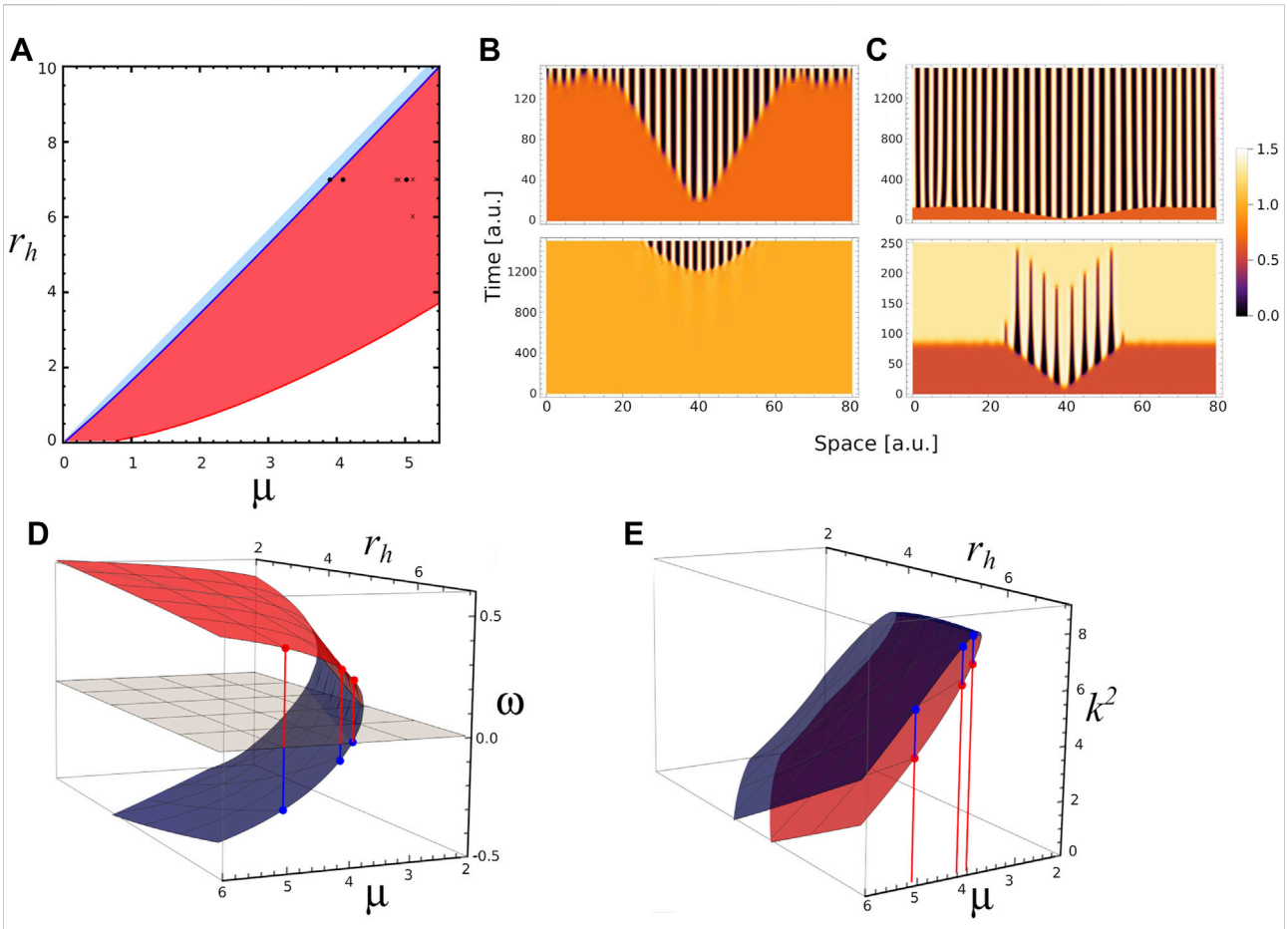

FIGURE 5
Different time scales. **(A)** 2D phase diagram shows the parameters region where the system presents stable Turing patterns (narrow blue area) and unstable or transient Turing patterns (blue area) for r_a =2.5. Black dots correspond to different triplet of parameters values (μ, r_a, r_h) where numerical simulation were performed: P_1=(3.9,2.5,7), in the Turing pattern region, P_2=(4.1,2.5,7) and P_3=(5.0,2.5,7) in the transient Turing pattern region. The crosses indicate parameters values used on Figure 6. **(B)** 1-D numerical simulations showing the temporal evolution of activator concentration distribution *a* for parameters value P_1 with two different initial conditions. Top (bottom) panel corresponds to the temporal evolution when fixed point S_1 (S_2) is perturbed by a small perturbation at x =40, note the different timescales on the panels. **(C)** 1-D numerical simulations showing the temporal evolution of *a* for parameters values P_2 (top panel) and P_3 (bottom panel) when the same fixed point S_1 is perturbed at x =40, note the different timescales on the panels. **(D)** Red and blue surfaces correspond to ω-value as function of μ and r_h (r_a =2.5) associated with fixed points S_1 and S_2, respectively. **(E)** k^2-values as function of μ and r_h associated with S_1 (red surface) and S_2 (blue surface). Red and blue dots indicate k^2 values for P_1, P_2 and P_3 in each case.

3.3 Stable and transient Turing patterns

To illustrate some features of stable and transient Turing patterns, we perform 1D simulations of the reaction-diffusion equations at different values of the parameters μ, r_a and r_h. In Figure 4A we superpose Figures 3A,B on the plane spanned by parameters μ and r_h for r_a = 6. In this way, we identify the region where stable Turing patterns are found (overlap between R_1 and R_2, light blue); and the region where only transient patterns are observed (R_2, red). Black points in the plane correspond to parameter values used in different numerical simulations. Figure 4B depicts the Turing patterns developed by the activator, for parameters (μ, r_a, r_h) = (1, 6, 10). In both simulations the spatial perturbation is the same, $\propto \exp[-(x-40)^2/0.25]$, however the simulations differ in the initial spatial distribution to be perturbed. The top panel of Figure 4B corresponds to a perturbation of homogeneous distribution associated with the fixed point S_1 (saddle node), while the bottom panel corresponds to a perturbation of homogeneous distribution associated with the stable fixed point S_2. In the first case the system develops quickly a central pattern, with small wave number. Over time, the ridges split in two, increasing the wave number of the pattern. These splits evidence the transition to a stable Turing pattern with the same wave number as that observed in the bottom panel. We also see in Figure 4B that the amplification

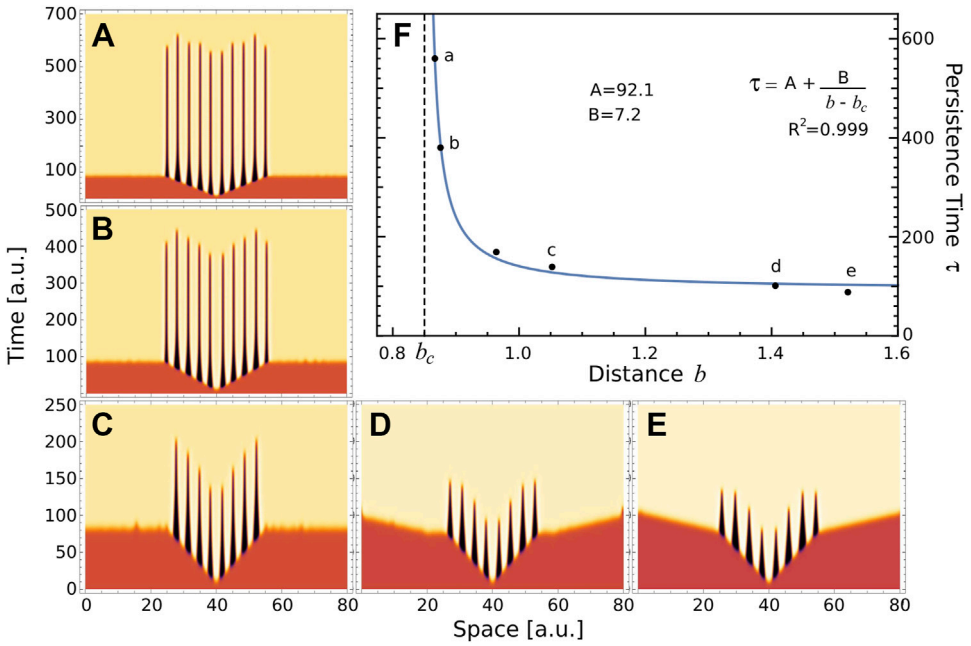

FIGURE 6
Persistence time. **(A–E)** These panels depict the temporal evolution of a, when the uniform distribution associated with fixed point S_1 is perturbed at x =40, for different values of the parameters (μ, r_a, r_h)=(4.89,2.5,7) **(A)** (4.9, 2.5,7) **(B)** (5.1,2.5,7) **(C)** (5.5,2.5,7) **(D)** and (5.1,2.5,6) **(E)**. These parameters values were indicated by crosses on 5A. **(F)** Raster-plot of persistence time τ and distance b for the numerical simulations **(A–E)** and also P_3=(5.0,2.5,7) depicted in bottom panel of 5C. Blue line corresponds to the rational function $A+ B/(b - b_c)$, where the value of parameters were obtained by nonlinear fitting (A =92.1, B =7.2 and b_c =0.85). Letters a-e indicated the corresponding panel.

rate of the perturbation of S_2 is lower than in the case where S_1 is perturbed.

We also perform numerical simulations in the region of transient patterns for μ = 1.5 and 3.0 (top and bottom panels of Figure 4C), when a small perturbation is applied on fixed point S_1. In these cases the system makes a transition to a stable homogeneous distribution associated with state S_2. These transitions occur in a spatially heterogeneous manner, as long as $\omega(S_1)$ and $k^2_{\max}$ computed over S_1 are positive. One can also note in Figure 4C that the decay times to homogeneous state S_2 in top panel is lower than in bottom panel. This aspect will be discussed in the next section. Illustrative simulations, corresponding to the points μ = 1.2 and 5.0, showed in the parameter space Figure 4A, can be appreciated in Supplementary Figure S2. Figure 4D shows ω as function of μ and r_h with r_a = 6.0, computed for steady states S_1 (red sheet) and S_2 (blue sheet). Similarly, Figure 4E depicts $k^2_{\max}$ for these steady states, for the same parameters. The points/bars at μ = 1.0, 1.2, 1.5 and 3.0 indicate the values at which numerical simulations were performed. For all cases, we can see that $\omega(S_1) \geq \omega(S_2)$. Further, $\omega(S_2)$ can present positive and negative values, while $\omega(S_1)$ is always positive. Thus, only simulations for μ = 1.0 and 1.2 fall in the region of stable Turing patterns, since $\omega(S_2) > 0$ is required. Transient Turing patterns are observed for μ = 1.5 and 3.0, i.e., when $\omega(S_1) > 0$ and $\omega(S_2) < 0$ (red region of Figure 4A). In addition, we can also note in Figure 4E that $k^2_{\max}(S_1) \leq k^2_{\max}(S_2)$, indicating that the characteristic size of the initial pattern is greater than that one related to the stable Turing pattern, which agrees with the simulations shown in panels of Figure 4B.

3.4 Metastable spatial patterns

In an effort to further understand the transient patterns exhibited by our model, Figure 5 depicts analyses and simulations for r_a = 2.5 where there is a narrow region for Turing instabilities (light blue region) and a large region for transient Turing patterns (red region). In this case, the $k^2_{\max}$ is highly folded and the predicted wave number values associated with S_1 and S_2 are very close. However, the rate $\omega(S_1)$ has a higher dynamic range than in the case shown in Figure 4. Figure 5B depicts numerical simulations in the region of stable Turing patterns, near the stable-transient patterns interface (P_1 = (3.9, 2.5, 7)). Patterning is reached quickly when the unstable fixed point S_1 is perturbed (top panel of Figure 5B), while a very long transient is observed when the same perturbation is applied to the stable steady state S_2 (bottom panel). Figure 5C depicts numerical

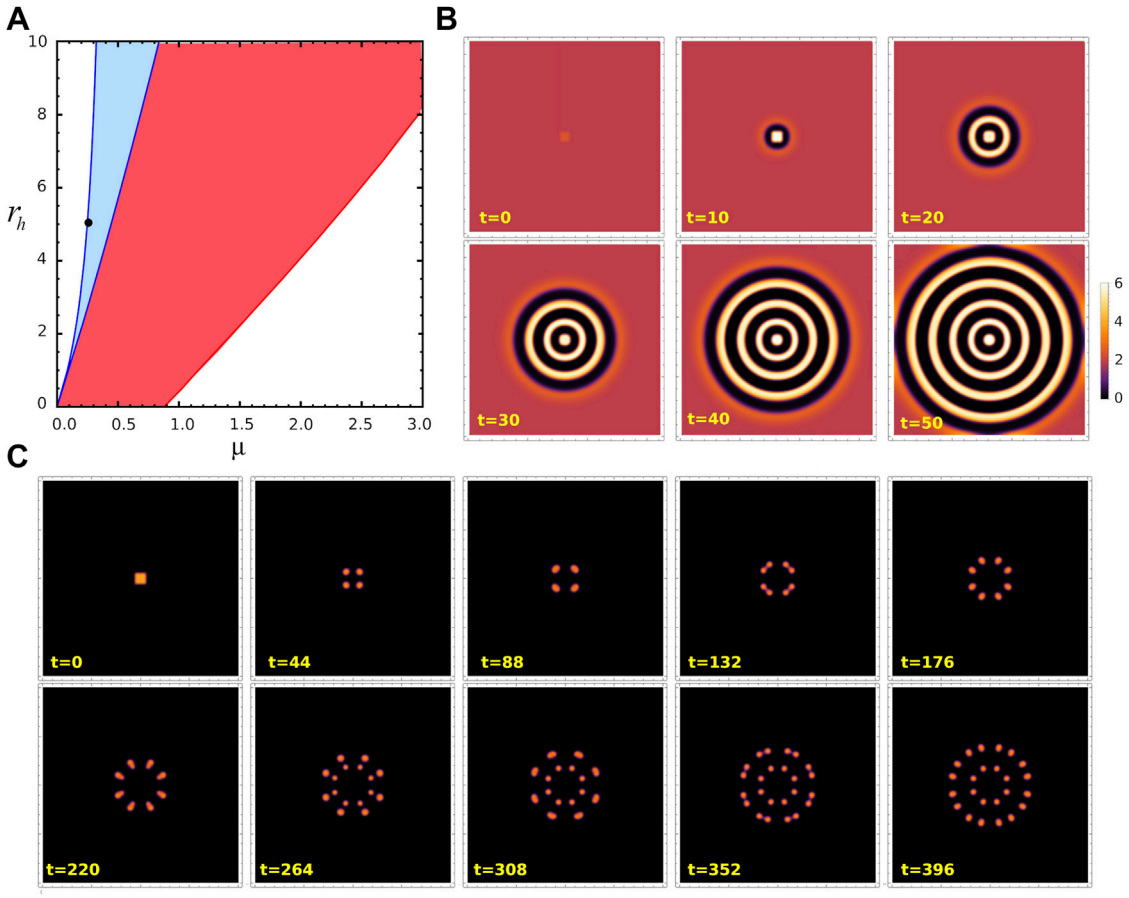

FIGURE 7
Turing patterns in 2D. **(A)** Parameter region where stable Turing patterns (blue) and unstable Turing patterns (red) can be found, for r_a =10. Black dot corresponds to (μ, r_a, r_h)=(0.25,10,5)= P_1, in the stable Turing pattern region. **(B)** Snapshots from space-temporal 2D simulations showing activator concentration pattern for parameters value P_1 at different time t. These panels corresponds to the case when fixed point S_2 is perturbed by a small perturbation at the centre of the field. **(C)** Snapshots from space-temporal 2D simulations showing a for the same parameters value, when uniform distribution associated to fixed point S_1 is perturbed by the same perturbation. The region considered is 40×40 with periodic conditions. Animated Movies associated to these simulations are available as Supplementary Movies S1 and S2.

simulations for P_2 = (4.1, 2.5, 7) (top panel) and P_3 = (5, 2.5, 7) (bottom panel), both in the region of transient Turing patterns, when a small perturbation is applied on homogeneous distribution at S_1. In the first case, the system develops a spatial pattern that does not end on the course of simulation, while the bottom panel shows a short-lived pattern that finishes in the homogeneous distribution associated with the steady state S_2. The time to reach the patterns showed in Figures 5B,C, and also their sizes, are in agreement with the functions ω and k^2 (see Figures 5D,E). However, they do not provide information on what determines the duration of the transient patterns.

Regarding the pattern on Figure 5C, we hypothesise that when the parameter values approach to the boundary between regions of stable and transient Turing patterns (blue line in Figure 5A), the resulting transient patterns would be associated with larger half-lives. Let us define the persistence time of a transient pattern, τ, as the duration of the central ridge, that is before it merges with the neighbours ones; and b as the Euclidean distance from actual parameters value to the boundary between regions of stable and transient Turing patterns. Following our *ansatz*, we compute the persistence time τ on several transient patterns, depicted on panels A–E of Figure 6, obtained for r_a = 2.5, and different values of r_h and μ. Also, Figure 6F depicts the persistence time as function of the distance b. Interestingly, the plot suggests that near Turing-patterns boundary the persistence time exhibits a singularity at b_c. This means that, in this region of the parameters space (r_a = 2.5 and $r_h \approx 7.0$), a system operating with parameters value corresponding to b smaller than b_c will present patterns with infinite persistence time, i.e. metastable patterns. This is the case of the top panel of Figure 5C. This could be a particular characteristic of this region, since no metastable patterns were observed in the parameter region

studied in Figure 4 (r_a = 6), where transient patterns were also observed.

These results suggest the existence of a new interface separating two types of transients Turing patterns associated to S_1: those with finite τ and the metastable patterns. Although establishing the mechanisms that determine this interface is beyond the scope of this work, we believe that the morphogenetic model proposed by Diambra *et al.* could be suitable for such study. To the best of our knowledge, transient and metastable patterns arising from Turing instability mechanism have not been previously reported.

3.5 Turing patterns in 2D

As noticed in the previous subsections, the trajectory of the system upon perturbation depends on whether the system is initially on state S_1 or S_2, however the final states after a transient are the same (as shown in Figure 4B, Figure 5B). We wonder if this also happens in two dimensions. And to answer this question we performed numerical simulations of Eqs. 4 and 5 in a 2D region $\Omega = [0, 40] \times [0, 40]$ with periodic boundary conditions. In order to solve the equations, we discretized space and time using NDSolve routine in Mathematica 12.1, in which we take $\Delta x = \Delta y = 0.01$. The temporal step size used is adaptative so that the estimated error in the numerical solution is lower than 10^{-6}. We consider the same perturbation $\exp[-((x-20)^6 + (y-20)^6))/1.5]$ at the centre of Ω applied to two different initial conditions: 1) uniform distributions of a and h, at concentrations fixed by steady point S_2; and 2) in a similar fashion but considering the steady point S_1. The parameters value used in this numerical experiment are $(\mu, r_a, r_h) = (0.25, 10, 5)$ which fall in the region of stable Turing patterns (blue region in Figure 7A). Figure 7B depicts the density plots of a at different times when the stable steady point S_2 is perturbed. In this case the perturbation propagates from the centre, forming radial stripes (Supplementary Movie S1B). On the other hand, when the initial condition corresponds to the steady point S_1, the system develops a pattern based on spots with splitting dynamics. In this case, the initial perturbation first divides in four spots, each of which in turn splits tangentially into two other spots. Each of the resulting eight spots split again, but now in radial manner. The spots are distributed in a circular shape with the same radius as the circular bands of the previous case (Supplementary Movie S2). The stripes (spots) stabilise after formation (splitting) and the activity concentrate at expanding Frontier. Although the characteristic sizes are preserved, the resulting 2D patterns are different depending on whether the initial condition is close to S_1 or S_2.

4 Discussion and conclusion

In this paper we have analysed a two-gen reaction–diffusion system that operates under only one regulatory function, as previously proposed by [18]. The non-diffusive model presents three fixed points. One of them corresponds to the trivial solution and is referred to as S_0, while the other two non-trivial solutions, identified as S_1 and S_2, are originated in a saddle-node bifurcation. We obtain analytically that the saddle-node bifurcation defines a surface in the 3D parameter space. The trivial solution S_0 is a stable node and S_1 is an unstable saddle-point for all the parameter region studied. On the other hand, S_2 is stable for a certain region of the parameter space and when perturbed can also present oscillations and a stable limit circle. In the region of unstable spirals of S_2, oscillations drive the system to the trivial steady-state S_0, while stable spirals are damped until the perturbed system reaches S_2.

To derive the Turing-instability conditions, one requires an stable homogeneous steady state, like S_2, to guarantee that instabilities will be solely spatially dependent. However, diffusion-driven patterns can also raise up from an unstable steady state, like S_1. In fact, by linearizing the spatial version of the model around these steady states we found that both points have associated a dispersion relation where $\omega > 0$ and $k > 0$, indicating the presence of a spatial patterns. We denote the parameter region where S_1 has $\omega > 0$ and $k > 0$ as R_1. Similarly, in R_2 the steady state S_2 has $\omega > 0$ and $k > 0$. We observe that R_1 is greater than R_2 and R_2 is included in R_1.

The final state of the system, when a small spatial perturbation is applied to S_1 or S_2 fixed points, depends on where the parameters value falls relative to R_1 or R_2. As expected, we observe that a spatial perturbation of the S_2 state, for parameters values belong to R_2, leads to stable Turing patterns. On the other hand, if S_2 is perturbed for parameters values outside R_2, no pattern will be developed. When S_1 is perturbed for parameter values that are in the intersection region of R_1 and R_2, then a spatially heterogeneous transition to stable Turing patterns with sizes typical of the S_2 state develops. In this sense we have seen examples where the initial peaks with typical size of the state S_1 split. But if the values of the parameters fall outside R_2 and inside R_1, the system develops in the face of disturbance a transient spatial pattern whose typical size is predicted by the dispersion relation in S_1. In the region of the parameter space with low r_a-value, the system can present transitory patterns, as well as metastable patterns. In the former case, we observed that the persistence time of these transitory patterns is related to the distance between the value of the system parameters and the boundary between regions of stable and transient Turing patterns. We found that this dependence has a singularity which delimits a new boundary between metastable patterns and transient patterns with finite time life. However, the present analysis did not allow to

determines the boundary, in the parameters space, separating metastable patterns and short transients.

Furthermore, in the synthetic patterning endeavour is critical the range of kinetic parameters, Hill coefficient and diffusion ratio between activator and inhibitor, that support Turing patterns development [18]. Consequently, alternatives to reduce the requirement for differential diffusion are always welcomed. The present results show that transient patterns can expand the parameter space for an initial breaking-symmetry. These initial patterns, although transient, could induce other gene regulatory circuits able to stabilise patterning but without breaking-symmetry ability. In this manner, transient patterns could play a role in developmental biology as breaking-symmetry triggers rather than to be responsible for the whole patterning process. We believe that the current findings open the door to further theoretical studies which can offer new insights into the nature of patterning mechanisms in developmental biology.

Data availability statement

The original contributions presented in the study are included in the article/Supplementary Material, further inquiries can be directed to the corresponding authors.

Author contributions

LD conceived the paper. NG and LD developed the structure and design of the manuscript. NG and LD developed the analysis, and algorithms and wrote the manuscript. Both NG and LD revised the manuscript and approved the final version.

Funding

This research was supported by CONICET, Argentine (PIP N° 0597 and PIP N° 1748).

Acknowledgments

NG and LD are reasearchers at the CONICET (Argentine). We are thankful for Karina Mazzitello's judicious comments on the manuscript, and Celina Guisoni's help in preparing graphics.

Conflict of interest

The authors declare that the research was conducted in the absence of any commercial or financial relationships that could be construed as a potential conflict of interest.

Publisher's note

Supplementary material

The Supplementary Material for this article can be found online at: https://www.frontiersin.org/articles/10.3389/fphy.2022.927152/full#supplementary-material

References

1. Turing AM. The chemical basis of morphogenesis. *Philos Trans R Soc B* (1952) 237:37. doi:10.1098/rstb.1952.0012

2. Meinhardt H, Gierer A. Applications of a theory of biological pattern formation based on lateral inhibition. *J Cel Sci* (1974) 15:321. doi:10.1242/jcs.15.2.321

3. Asai R, Taguchi E, Kume Y, Saito M, Kondo S. Zebrafish leopard gene as a component of the putative reaction-diffusion system. *Mech Dev* (1999) 89:87–92. doi:10.1016/s0925-4773(99)00211-7

4. Painter KJ, Maini PK, Othmer HG. Stripe formation in juvenile pomacanthus explained by a generalized Turing mechanism with chemotaxis. *Proc Natl Acad Sci U S A* (1999) 96:5549–54. doi:10.1073/pnas.96.10.5549

5. Diambra L, Costa LDF. Pattern formation in a gene network model with boundary shape dependence. *Phys Rev E* (2006) 73:031917. doi:10.1103/PhysRevE.73.031917

6. Yamaguchi M, Yoshimoto E, Kondo S. Pattern regulation in the stripe of zebrafish suggests an underlying dynamic and autonomous mechanism. *Proc Natl Acad Sci U S A* (2007) 104:4790–3. doi:10.1073/pnas.0607790104

7. Kondo S, Miura T. Reaction-diffusion model as a framework for understanding biological pattern formation. *Science* (2010) 329:1616–20. doi:10.1126/science.1179047

8. Salazar-Ciudad I, Jernvall J. A computational model of teeth and the developmental origins of morphological variation. *Nature* (2010) 464:583–6. doi:10.1038/nature08838

9. Sheth R, Marcon L, Bastida MF, Junco M, Quintana L, Dahn R, et al. Hox genes regulate digit patterning by controlling the wavelength of a Turing-type mechanism. *Science* (2012) 338:1476–80. doi:10.1126/science.1226804

10. Economou AD, Ohazama A, Porntaveetus T, Sharpe PT, Kondo S, Basson MA, et al. Periodic stripe formation by a Turing mechanism operating at growth zones in the mammalian palate. *Nat Genet* (2012) 44:348–51. doi:10.1038/ng.1090

11. Inaba M, Chuong CM. Avian pigment pattern formation: developmental control of macro-(across the body) and micro-(within a feather) level of pigment patterns. *Front Cel Dev Biol* (2020) 8:620. doi:10.3389/fcell.2020.00620

12. Basu S, Gerchman Y, Collins CH, Arnold FH, Weiss R. A synthetic multicellular system for programmed pattern formation. *Nature* (2005) 434:1130–4. doi:10.1038/nature03461

13. Kämpf MM, Engesser R, Busacker M, Hörner M, Karlsson M, Zurbriggen MD, et al. Rewiring and dosing of systems modules as a design approach for synthetic mammalian signaling networks. *Mol Biosyst* (2012) 8:1824. doi:10.1039/c2mb05509k

14. Karig D, Martini KM, Lu T, DeLateur NA, Goldenfeld N, Weiss R, et al. Stochastic Turing patterns in a synthetic bacterial population. *Proc Natl Acad Sci U S A* (2018) 115:6572–7. doi:10.1073/pnas.1720770115

15. Konow C, Somberg NH, Chavez J, Epstein IR, Dolnik M. Turing patterns on radially growing domains: experiments and simulations. *Phys Chem Chem Phys* (2019) 21:6718–24. doi:10.1039/c8cp07797e

16. Santos-Moreno J, Schaerli Y. Using synthetic biology to engineer spatial patterns. *Adv Biosyst* (2019) 3:1800280. doi:10.1002/adbi.201800280

17. Luo N, Wang S, You L. Synthetic pattern formation. *Biochemistry* (2019) 58: 1478–83. doi:10.1021/acs.biochem.8b01242

18. Diambra L, Senthivel VR, Menendez DB, Isalan M. Cooperativity to increase Turing pattern space for synthetic biology. *ACS Synth Biol* (2015) 4:177–86. doi:10.1021/sb500233u

19. Marcon L, Diego X, Sharpe J, Müller P. High-throughput mathematical analysis identifies Turing networks for patterning with equally diffusing signals. *Elife* (2016) 5:e14022. doi:10.7554/elife.14022

20. Lengyel I, Kádár S, Epstein IR. Transient Turing structures in a gradient-free closed system. *Science* (1993) 259:493–5. doi:10.1126/science.259.5094.493

21. Kadar S, Lengyel I, Epstein IR. Modeling of transient Turing-type patterns in the closed chlorine dioxide-iodine-malonic acid-starch reaction system. *J Phys Chem* (1995) 99:4054–8. doi:10.1021/j100012a028

22. Szalai I, De Kepper P. Turing patterns, spatial bistability, and front instabilities in a reaction-diffusion system. *J Phys Chem A* (2004) 108:5315–21. doi:10.1021/jp049168n

23. Di Patti F, Lavacchi L, Arbel-Goren R, Schein-Lubomirsky L, Fanelli D, Stavans J, et al. Robust stochastic Turing patterns in the development of a one-dimensional cyanobacterial organism. *Plos Biol* (2018) 16:e2004877. doi:10.1371/journal.pbio.2004877

24. Elvin AJ, Laing CR, Roberts MG. Transient Turing patterns in a neural field model. *Phys Rev E* (2009) 79:011911. doi:10.1103/PhysRevE.79.011911

25. Carvalho A, Menendez DB, Senthivel VR, Zimmermann T, Diambra L, Isalan M, et al. Genetically encoded sender-receiver system in 3D mammalian cell culture. *ACS Synth Biol* (2014) 3:264–72. doi:10.1021/sb400053b

26. Senthivel VR, Sturrock M, Piedrafita G, Isalan M. Identifying ultrasensitive hgf dose-response functions in a 3d mammalian system for synthetic morphogenesis. *Sci Rep* (2016) 6:39178. doi:10.1038/srep39178

27. Carr J, Pego RL. Metastable patterns in solutions of $u_t = \varepsilon^2 u_{xx} - f(u)$. *Commun Pure Appl Math* (1989) 42:523–76. doi:10.1002/cpa.3160420502

28. Folino R, Plaza RG, Strani M. Metastable patterns for a reaction-diffusion model with mean curvature-type diffusion. *J Math Anal Appl* (2021) 493:124455. doi:10.1016/j.jmaa.2020.124455

29. Sick S, Reinker S, Timmer J, Schlake T. WNT and DKK determine hair follicle spacing through a reaction-diffusion mechanism. *Science* (2006) 314:1447–50. doi:10.1126/science.1130088

30. Scholes NS, Schnoerr D, Isalan M, Stumpf MP. A comprehensive network atlas reveals that Turing patterns are common but not robust. *Cel Syst* (2019) 9: 243–2574. doi:10.1016/j.cels.2019.07.007

31. Gutierrez PS, Monteoliva D, Diambra L. Role of cooperative binding on noise expression. *Phys Rev E* (2009) 80:011914. doi:10.1103/physreve.80.011914

32. Gutierrez PS, Monteoliva D, Diambra L. Cooperative binding of transcription factors promotes bimodal gene expression response. *PLoS ONE* (2012) 7:44812. doi:10.1371/journal.pone.0044812

frontiers | Frontiers in Physics

TYPE Methods
PUBLISHED 03 August 2022
DOI 10.3389/fphy.2022.930811

OPEN ACCESS

EDITED BY
David M Holloway,
British Columbia Institute of Technology, Canada

REVIEWED BY
Petra Schwille,
Max Planck Society, Germany
Eldon Emberly,
Simon Fraser University, Canada

*CORRESPONDENCE
Cees Dekker,
c.dekker@tudelft.nl

SPECIALTY SECTION
This article was submitted to Biophysics, a section of the journal Frontiers in Physics

RECEIVED 28 April 2022
ACCEPTED 30 June 2022
PUBLISHED 03 August 2022

CITATION
Meindlhumer S, Kerssemakers J and Dekker C (2022), Quantitative analysis of surface wave patterns of Min proteins. *Front. Phys.* 10:930811.
doi: 10.3389/fphy.2022.930811

Quantitative analysis of surface wave patterns of Min proteins

Sabrina Meindlhumer, Jacob Kerssemakers and Cees Dekker*

Department of Bionanoscience, Kavli Institute of Nanoscience Delft, Delft University of Technology, Delft, Netherlands

The Min protein system is arguably the best-studied model system for biological pattern formation. It exhibits pole-to-pole oscillations in *E. coli* bacteria as well as a variety of surface wave patterns in *in vitro* reconstitutions. Such Min surface wave patterns pose particular challenges to quantification as they are typically only semi-periodic and non-stationary. Here, we present a methodology for quantitatively analysing such Min patterns, aiming for reproducibility, user-independence, and easy usage. After introducing pattern-feature definitions and image-processing concepts, we present an analysis pipeline where we use autocorrelation analysis to extract global parameters such as the average spatial wavelength and oscillation period. Subsequently, we describe a method that uses flow-field analysis to extract local properties such as the wave propagation velocity. We provide descriptions on how to practically implement these quantification tools and provide Python code that can directly be used to perform analysis of Min patterns.

KEYWORDS

min proteins, pattern formation, image analysis, surface protein waves, quantification, python

1 Introduction

Pattern formation is a fascinating basic phenomenon that occurs across many scales, from galaxy formation all the way down to embryology and beyond. In chemistry and biology, self-organizing patterns emerge from the combination of specific intermolecular interactions and molecular transport processes [1]. Acting together, reaction and diffusion can result in inhomogeneous concentrations of molecules that constitute spatiotemporal patterns. Such patterns provide useful functions as they impose directional or positional preferences on processes in cells and tissues [2–5]. Indeed, pattern formation is of vital importance for the description of a multitude of biological phenomena, ranging from bacterial and eukaryotic cell division [4], to embryonic development of multicellular organisms [3, 5], up to entire ecosystems [6].

For example, in *E. coli* bacteria, a pattern-forming mechanism acts to determine the central position of the rod-shaped cell, ensuring that the required protein-machinery is guided to the correct location to start a fully symmetric division into daughter cells. This particular pattern-forming system, formed by the Min proteins, relies on a reaction-diffusion mechanism and is widely considered to be the best-studied model system for intracellular pattern formation [4, 7]. As the moment of cell division approaches, Min proteins will periodically bind and unbind the inner membrane at the poles of the

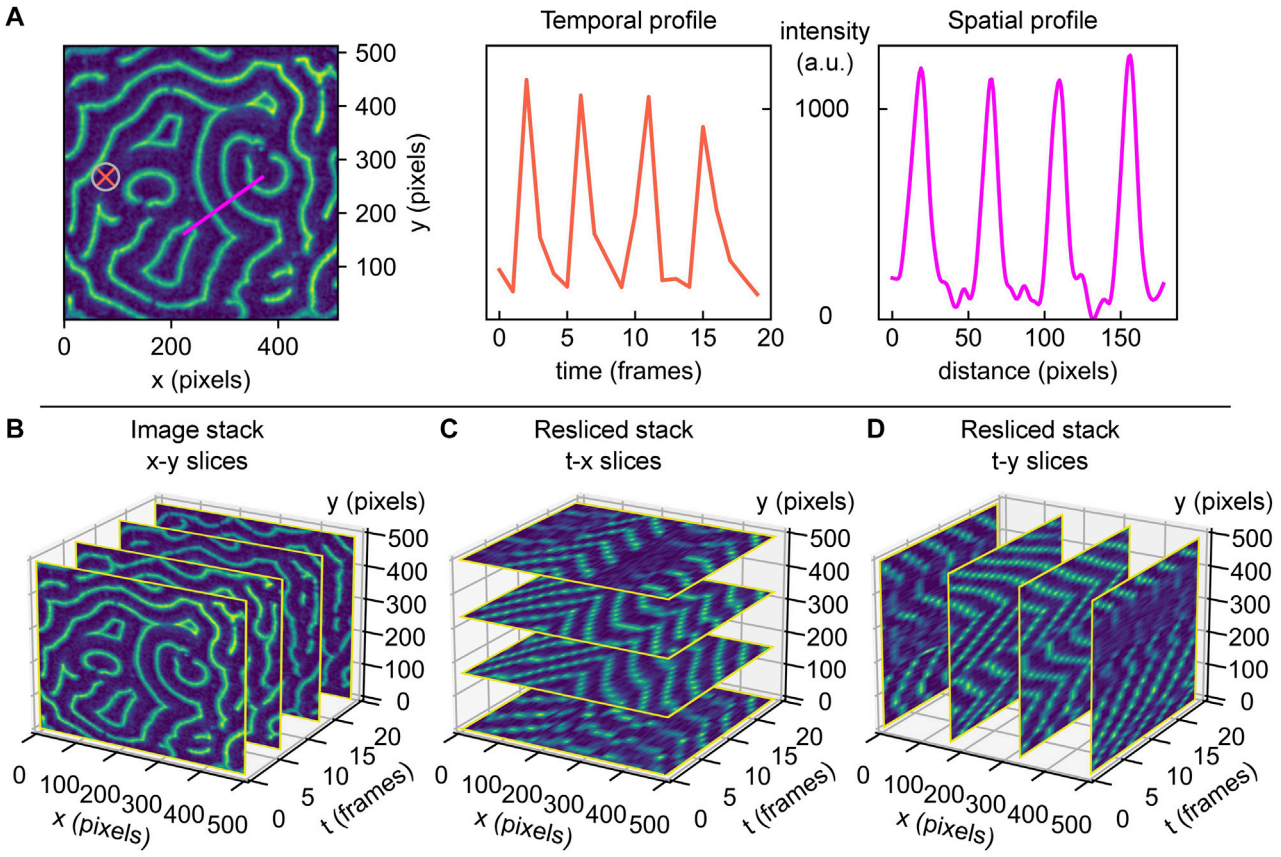

FIGURE 1
Min protein surface patterns are dynamic in space and time. Min pattern acquisitions are 3D (*x*, *y*, *t*) matrices, containing the measured fluorescence intensity values for different coordinates. The information contained within this matrix can be accessed and visualized differently, dependent on what parameters are of interest. **(A)** Left: example of a real MinE protein surface pattern. Middle: fluorescence intensity over time at the surface position highlighted by orange cross in the image, for an image stack comprising of 20 frames. Right: fluorescence intensity trace along surface cross-section highlighted in magenta in the image. **(B)** 3D view of a Min protein acquisition stack with four example images (standard *x*-*y* slices) shown for demonstration. **(C)** 3D view of slice from A, resliced along constant *y*-directions, creating *t*-*x* slices. **(D)** 3D view of slice from A, resliced along constant *x*-directions, creating *t*-*y* slices.

bacterium. When visualized by fluorescent labelling, the Min proteins are observed to oscillate from pole to pole with a period of approximately 1 minute. As a result, their temporally averaged concentration is minimized at the mid-cell location. One component of the Min system, MinC, exerts an inhibitory effect on a component of the cell division machinery. As the lowest concentration of MinC is found at mid-cell, the proteins that facilitate cell division will preferably bind there, and the cell gets divided evenly [8].

While MinC is important for this downstream process, the pattern as such is formed by only two proteins, MinD and MinE. MinD is an ATPase that upon binding ATP can attach to the membrane, while MinE is its ATPase activator. MinE can bind to the membrane upon recruitment by membrane-bound MinD and subsequently facilitate MinD's ATP-consuming membrane detachment [7, 9–11]. The Min proteins thus constitute a pattern-forming model system with only 2 essential components, which is appealingly simple for both theoretical and experimental studies. A wide range of experiments have been reported that explore particular features of the Min system [9, 12, 13]. A multitude of Min protein models [14, 15] have been proposed, and continue to be developed as new molecular details are discovered [10, 16–18].

Arguably, the most iconic images of Min protein patterns present themselves in *in vitro* studies of these proteins. Such experiments typically reconstitute Min proteins on supported lipid bilayers on a glass slide, with a fraction of Min proteins carrying a fluorescent label [9]. Min proteins exhibit mesmerizing dynamic membrane patterns in such an artificial *in vitro* environment: Over a wide range of concentrations, one encounters characteristic patterns such as rotating spirals or travelling planar wave fronts, with typical wavelengths in the order of tens of micrometers [9, 12]. An example is given in Figure 1A, showing a snapshot image for labelled MinE.

Examination of this image reveals various features that are typical for Min patterns. For example, Min proteins exhibit planar waves, but these occur only locally and become less correlated on longer length scales. Min patterns thus organize in surface domains with one dominating type of pattern, such as spiral or planar wave fronts travelling in a certain direction. Boundaries between domains are recognizable by phase shifts.

Thorough quantitative analysis of Min patterns is nontrivial. While visual inspection is often sufficient to deduce the basic Min pattern, quantitative information is required to extract trends in the patterns' characteristic parameters, such as the average or local wavelength, oscillation period, or propagation velocity. For perfectly periodic Min patterns with only one type of pattern with a set orientation over the entire imaged surface, analysis can easily be achieved by Fourier analysis. However, this is most often not possible due to the fact that real Min patterns are usually a patchwork of domains separated by phase-shift boundaries. The semi-periodic nature of Min patterns makes image analysis challenging, and so far there are no clear guidelines or standards on how to realise this without user bias. Extraction of quantitative parameters is typically performed by manual selection of individual surface positions [19], line traces [20], or rectangular regions-of-interest [12, 21]. Plotting of fluorescence intensity along a defined axis allows to determine the pattern's local wavelength. Similarly, the temporal characteristics such as its oscillation period and wave propagation velocity can be measured by monitoring the intensity versus time at one spot [19], see Figure 1A for an illustration of these possible practices.

While these approaches are widely used, such manual selection is cumbersome, prone to user bias, and it underuses the vast amount of data in videos of Min patterns that could improve data accuracy. In the example given in Figure 1A, the intensity profile of denoted line trace (magenta) shows approximately equidistant peaks that indicate the wavelength. However, selection of another spot or a slightly different trace that is not perpendicular to the wave fronts would have led to a deviating result. Furthermore, note how extending the trace over the region of the spiral domain would erroneously lead to the inclusion of shorter or longer wavelengths. Notably, these domain boundaries do not always remain stationary over the time of acquisition, and hence line traces would have to be carefully adapted for every single frame so as to adapt to possible reorientations of wave fronts (compare for example the domain variation over time in Supplementary Figure S1A). In view of all these limitations, we conclude that an automated user-independent analysis of large regions is preferable, as it allows to obtain solid statistics on the patterns' characteristic features.

In this paper, we present a methodology for analysing Min patterns that aims for thorough quantitation, easy usage, reproducibility, and user independence. We start by briefly proposing strategies for image cleaning. After that, we proceed to presenting strategies for global and local analysis of Min protein surface patterns. For extracting global parameters, we rely on calculating autocorrelation maps to examine the average periodic features of Min patterns, following other groups [16] as well as our own [18]. We treat a Min pattern acquisition stack as a threedimensional matrix containing information in space and time (x, y, t), and we propose strategies on how to efficiently access this information. Subsequently, we introduce an analysis pipeline which allows to quantify local properties of Min patterns, such as the wave propagation speed and direction of propagation. The approach we present here relies on the identification of individual wave crest points and their movement from one frame to the next. While other tools have been used to extract the directional preferences of Min surface wave propagation [22], our approach allows not only for obtaining large distributions of parameters, but also for accessing multiple parameters at the same time. For both global and local analysis, we offer guidance to researchers who would like to implement similar strategies for their own applications. Code is openly available and provided in Python 3 [23].

2 Image processing methodology

Min patterns are phenomena that occur at lipid membranes. Accordingly, the most suitable forms of microscopy for *in vitro* experiments are those that acquire an image along the membrane-coated surface. Examples are total internal reflection fluorescence (TIRF) microscopy [12, 16, 19, 24], laser scanning confocal microscopy [20–22, 25] or spinning disc confocal microscopy [18, 26]. Epifluorescence microscopy [27] is generally not suitable as it leads to high background signal from the fluorescent molecules in the bulk, significantly reducing the pattern's quality or even making it unrecognizable.

"Image cleaning" includes procedures and operations performed on microscope data that improve the overall quality of the image by making the features of interest better recognizable, while not distorting or removing essential components. Good image cleaning, where background and spurious contributions are removed, is important for successful quantitative analysis of Min protein patterns, as insufficient cleaning can lead the algorithms to fail to recognize the pattern as such. There are multiple imaging artefacts that need to be corrected. For example, local fluorescent impurities such as protein aggregates may give a static signal that is not part of the Min pattern. Depending on the microscope, illumination is typically inhomogeneous across the field-of-view. In many cases, researchers are interested in the time-dependent behavior of Min patterns, and for this, they acquire images at the same spatial positions at regular time intervals ranging from seconds to minutes. Consequently, Min proteins may bleach due to prolonged imaging [18]. Flow-cell setups with constant bulk flow may pose additional challenges in the form of objects entering and passing through the field-of-view or adhering to and spontaneously detaching from the surface [26]. We empirically found that the

occurrence of imaging artefacts can vary strongly, depending on the experimental setup (specifically, the type of sample chamber and the surface preparation), protein concentration (higher concentrations may result in more aggregates), and experiment duration (the longer, the more aggregates occur).

With image cleaning, we aim to tackle all of these issues. Here, we propose a sequence of standard actions that we found to yield overall good results for a time series (several frames of the same sample position saved sequentially in an image stack) of images I_{movie} of *in vitro* Min surface patterns. Our protocol involves the following steps:

– Correct for fluorescence bleaching by normalizing each frame to its mean intensity value.
– Create an 'illumination correction map' I_{illum} by smoothing and averaging all movie images, and normalizing the images to their maximum intensity.
– Create a static background image I_{stat} by averaging over all the moving (surface pattern) features of all images in the stack. This background image then only contains static fluorescent features such as local specks, holes, and scratches.
– Correct each image via the following image operation: $I_{cor} = (I_{movie} - I_{stat})/I_{illum}$.
– At this point, there may still be some artefacts left, for example, those that appeared during the acquisition time and might thus not have been included in the static background image. Therefore, remaining bright or dark artefacts can be removed manually or by thresholding.
– Images can finally be slightly smoothed to diminish effect of sharp edges and artefacts from the latter cropping.

In cases where it is required to explore Min patterns across very large areas, it may furthermore be of interest to stitch multiple fields-of-view of Min patterns into larger images [26, 28]. If the microscope's software does not offer an automatized solution for this, stitching can be achieved by good bookkeeping and a few lines of code. When planning to stitch images, it can be helpful to choose individual field-of-views in such a way that there is a bit of an overlap (e.g. 5% of the width) between adjacent areas, as this makes it easier to correctly reassemble the full image afterwards. Note that in general, adjoining areas may not have exactly the same median intensity. Therefore, differences in median intensity levels between individual field-of-views need to be corrected for when assembling the stitched image. This way, the resulting large image will appear more homogeneous in brightness and stitching borders will be less visible.

3 Pattern analysis strategies

3.1 Global parameters

In many cases, researchers are interested in quantifying parameters such as the average spatial wavelength and oscillation period of a Min pattern. For this purpose, they acquire image stacks of Min patterns at a certain surface region (x, y in pixel or distance units) and at regular time-intervals (t in time units or frames). However, the existence of domains within and dynamics of patterns make manual extraction of these parameters a laborsome task, and the results of such analyses (cf. Figure 1A) may suffer from poor statistics and user bias. Here, it is important to realize that what we are interested in are essentially global, image-averaged parameters. In this section, we describe how quantification of such global parameters can be achieved by performing autocorrelation analysis [29] for different slices along time or space coordinates (x-y frames such as in Figure 1B, t-x slices such as in Figure 1C or t-y slices as in Figure 1D). We start with spatial autocorrelation, aiming to quantify the wavelength, and then continue to present how temporal autocorrelation can be used to quantify the oscillation period of a pattern.

3.1.1 Global wavelength

Spatial autocorrelation analysis of an image essentially compares each pixel to other pixels around it, quantifying their (dis)similarity as a function of distance [29]. Starting from a single image frame as shown in Figure 2A, an autocorrelation map can be calculated using routines from scientific libraries provided for most programming languages. Before performing these operations, the image should be normalized by a series of actions (subtraction of minimum intensity, division by summed-up total intensity and subtraction of mean intensity). Using standard functions supplied within most environments, a twodimensional autocorrelation map *crmx* can be calculated for an image frame *image* by the transformation

$$crmx = \mathrm{real}\left(\mathrm{ifft2}\left(\mathrm{fft2}\left(image\right) \cdot \mathrm{conj}\left(\mathrm{fft2}\left(image\right)\right)\right)\right) \quad (1)$$

with *fft2* calculating a two-dimensional discrete Fourier Transformation, *ifft2* calculating its inverse and *real* and *conj* returning the real part and complex conjugate of the input, respectively. The four quadrants of the autocorrelation map can be re-arranged so as to place the position ($\Delta x = 0$, $\Delta y = 0$) in the center of the image, rather than having four partial peaks in the corners.

Close examination of the autocorrelation map in Figure 2B reveals a general speckled pattern as well as a ring-shaped feature that is present around the center, which is characterized by a peak in intensity. As this central peak corresponds to a distance of zero, its high intensity is a consequence of the self-correlation of each pixel with itself. Moving radially outward from the center, one observes a decrease in intensity (negative autocorrelation) followed by a peak (positive autocorrelation). An easy way to extract the pattern's dominant wavelength is to perform an angular averaging of the profile around the central peak, where the radial line profiles are averaged over all angles, as illustrated by the red arrow in panel Figure 2B. This leads to a

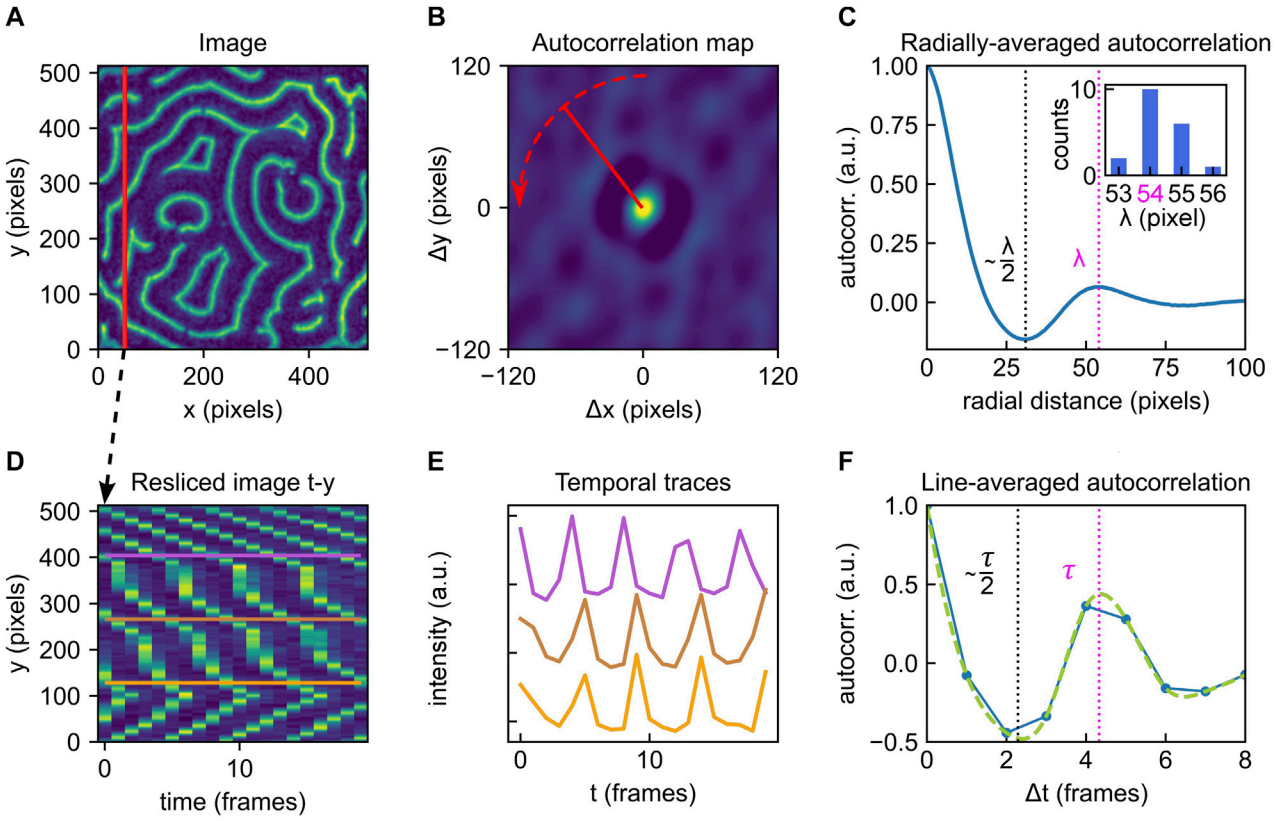

FIGURE 2
Overview of the autocorrelation analysis pipeline to obtain global parameters. **(A)** Example of a Min protein surface pattern, single frame. Color brightness indicates fluorescence intensity (a.u.). **(B)** Autocorrelation map of the frame shown in A. Color brightness indicates intensity. Red dashed line indicates radial averaging. **(C)** Averaged radial profile for the autocorrelation map shown in B. The first maximum after the central peak at distance zero is a measure of the patterns global characteristic wavelength. The identified wavelength λ is highlighted by the magenta dashed line. The first valley is positioned at approximately $\lambda/2$ (black dashed line). Inset: the analysis presented in **(A–C)** can be performed for all individual frames within an image stack. Here, the collected results for 20 consecutive frames (image stack also represented in Figure 1B) are shown in a histogram. A λ of 54 pixels is deduced. **(D)** Resliced image for fixed x; same as shown in Figure 1D. **(E)** Selected temporal traces for the y-positions indicated in D. All point-traces shown in the kymograph in D will be included in the autocorrelation trace shown in F. **(F)** Line-averaged autocorrelation trace from point-traces (such as shown in E) in blue, cubic spline fit used for peak-detection in green. The first maximum after the central peak at $\Delta t = 0$ measures the average characteristic oscillation period of the pattern. The identified global oscillation of $\tau = 4$ frames is highlighted by the magenta dashed line. The first valley is positioned approximately at $\tau/2$ (black dashed line). The analysis pipeline illustrated in **(D-F)** can be performed for multiple slices (fixed x or y) of the image stack.

profile as shown in Figure 2C. Here, the first peak after the central peak identifies the pattern's global wavelength λ (magenta dashed line). The first minimum corresponds to the dark value from the autocorrelation map. The valley in fact corresponds to $\sim \lambda/2$ (black dashed line). Note that this value is not exactly half the wavelength, since Min profiles are typically somewhat asymmetrical (cf. Figure 1A).

If, as often is the case, Min patterns display steady-state dynamics, then multiple time frames can be used to provide better statistics in estimating the global wavelength. Min patterns are routinely acquired at constant time intervals, which provides a series of sequential image frames, as represented in Figure 1B. Calculating and analysing autocorrelation maps for several frames within such an image stack allows to collect a distribution of wavelengths, such as the histogram shown in the inset in Figure 2C, summarising results for 20 consecutive frames. Indeed, for dynamic patterns, we recommend performing this analysis strategy for multiple (e.g. 10) frames and averaging the results to obtain a reliable value for the pattern's spatial wavelength. As Min patterns are typically dynamic, it is also possible that their wavelengths change over time, e.g. due to changes in external parameters. The spatial autocorrelation analysis presented here is however equally applicable to static patterns.

Identifying the peaks shown in Figures 2C,F, see following section) is trivial to the human eye, but not necessarily

straightforward to automate. For our data, we achieved this via a simple algorithm that identifies the second local maximum of the trace. In doing so, we implicitly assume that the trace is fine enough to achieve sufficient accuracy and upsampling is not required. While a curve such as shown in Figure 2C looks smooth to the eye, the original image data had a finite resolution, and accordingly, this curve contains small rags which an algorithm may erroneously detect as a local maximum. In many cases, this issue can be solved by smoothing the curve slightly before subjecting it to peak analysis. This can be achieved by applying a smoothing kernel stretching over a few pixels, for example a small fraction of the image dimension.

To avoid erroneous results, it is recommendable to plot at least one example trace (for one frame) and inspect whether the detected (averaged) wavelength position correctly co-localizes with the valley position. If no clear valley can be identified (characterized by a small or even vanishing intensity difference between the local minimum and maximum), the pattern may lack a recognizable periodicity, which could be an intrinsic property of the given pattern. Alternatively, this issue can also be encountered if insufficient image cleaning has been applied to the stack before analysis and the pattern is superimposed with too many artefacts, resulting in low autocorrelation. However, we find that this method is generally quite robust towards noise, as shown in Supplementary Figure S2B.

Further, the ratio between image size and spatial wavelength is of importance. In Supplementary Figure S3, a large-scale image stack is sequentially cropped to smaller sizes and global autocorrelation analysis as presented here is performed on randomly selected areas. Based on these results, we find that the standard deviation increases as the image sizes gets smaller, and estimate that the image dimension should be large enough to contain at least 5–10 full wavelengths for the presented algorithm to provide reliable results.

3.1.2 Global oscillation period

Another global property of interest is the average oscillation period. This parameter describes how at any given point within the imaged region, the membrane protein density (which is proportional to the fluorescence intensity) can be expected to change over time. We quantify the global oscillation period of a Min pattern following a strategy that closely resembles the one presented for obtaining the global wavelength in the preceding section.

To obtain quantitative information on the temporal dynamics of Min patterns, they are typically acquired as time series. A time series such as the one shown in Figure 1B is essentially a threedimensional (x, y, t) matrix, containing information on fluorescence intensity as a function of space and time. Notably, for temporal analysis to be reliable, image data has to be acquired at a rate above the Nyquist rate. Min patterns are characterized by point-wise temporal periodicity (compare the time evolution at a random sample position in Figure 1A). Hence, when acquiring a time series, intervals have to be chosen short enough to ensure the acquisition of enough data to adequately depict the pattern's temporal dynamics. If consecutive acquisition times in a series are chosen very far apart, the pattern may even appear to travel towards the opposite direction. According to Nyquist theorem, for patterns of an oscillation period τ, consecutive images in a series have to be acquired at intervals spaced no longer than $\tau/2$ apart. In principle, the shorter these intervals are, the better the temporal dynamics can be characterized. Min protein patterns in lipid bilayer reconstitutions will typically exhibit wave propagation velocities of several 100 nm s^{-1} [12] and wavelengths around 50 µm [9]. This leads to an expected oscillation period in the order of minutes. Acquiring sufficient images to fulfill Nyquist theorem should therefore not be an issue in most microscope setups. In practice, finding the optimal imaging rate is a trade-off between achieving a high temporal resolution and minimizing fluorescence bleaching.

Upon analysing a given Min pattern stack with respect to its temporal characteristics, we found that reslicing the stack along fixed spatial coordinates simplifies data processing and makes it more straightforward to access the temporal information contained within the stack. Figure 2D shows a (t, y) slice through our example image stack at fixed pixel position x. These t-x or t-y slices are collections of kymographs for all points along the cross-section at the fixed spatial coordinate. In Figure 2E, we show example traces of these kymographs along selected y positions, which then correspond to individual surface locations (x, y) on the field-of-view shown in Figure 2A. Analogous to the strategy presented for spatial global analysis, Eqn. 1. can be used to obtain an autocorrelation map for this slice (cf. Supplementary Appendix *DEMO_MinDE_global_analysis*). To extract the pattern's global oscillation period, we consider the autocorrelation map's trace at $\Delta y = 0$ for $\Delta t \geq 0$, plotted in Figure 2F. Including the $\Delta t \leq 0$ trace (going back in time) of the curve would not yield additional resolution, as it contains the same information as the positive trace. This profile then immediately provides the averaged temporal autocorrelation trace for all points along one fixed spatial coordinate (as indicated for fixed x by the vertical line in Figure 2A). If the line-averaged autocorrelation trace does not provide sufficiently high resolution to identify a minimum indicative of the oscillation period, imaging over a longer time and/or at shorter intervals could be necessary.

The first maximum of this curve beyond the central peak again identifies the predominant global oscillation period τ (magenta dashed line), while the first minimum is located at approximately $\tau/2$ (black dashed line). Statistics on τ can be collected by performing the analysis pipeline illustrated in Figures 2D–F for multiple cross-sections at fixed y or x, that is, for multiple resliced frames as shown in Figures 1C,D. Compared to the traces obtained from spatial autocorrelation,

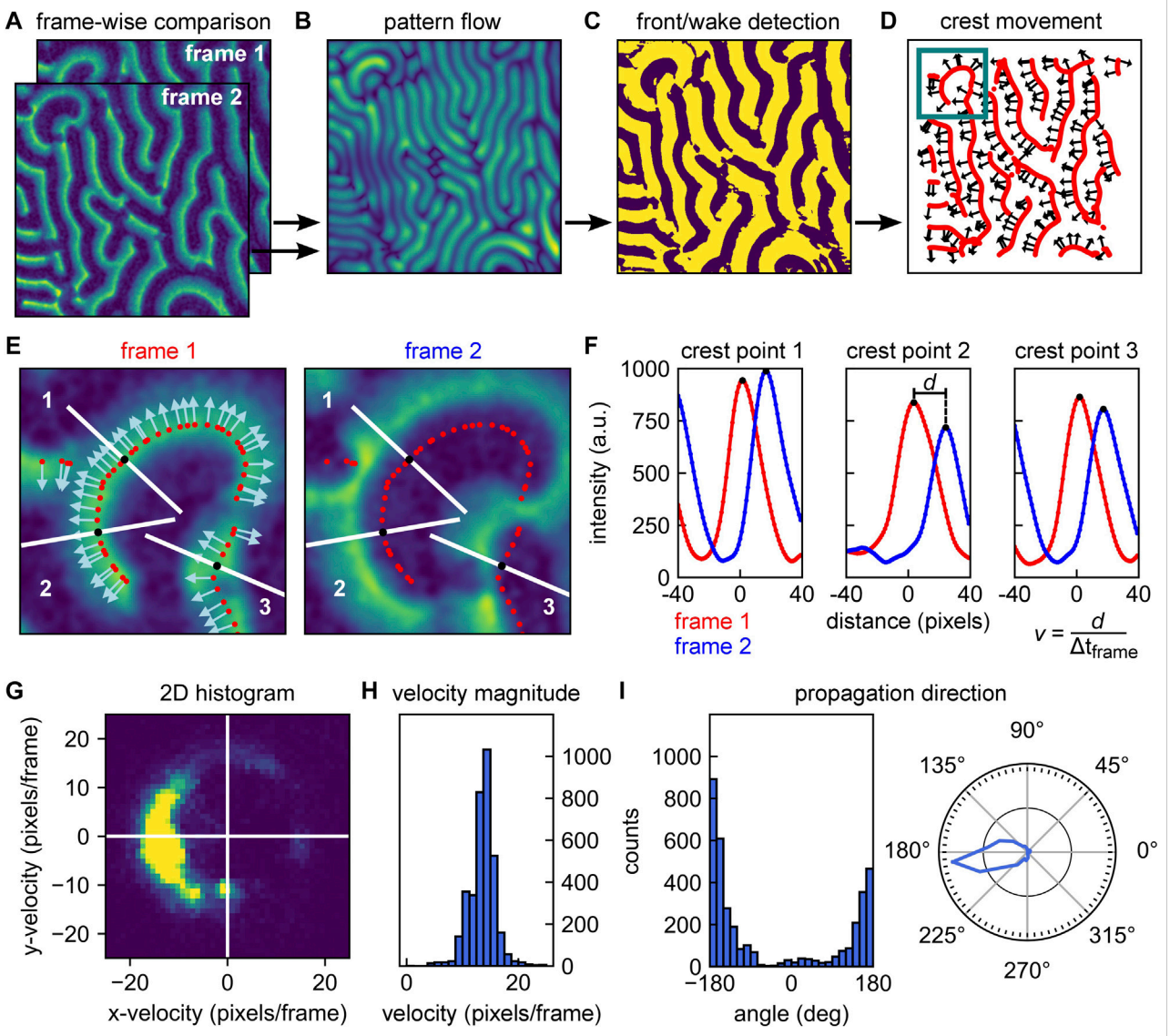

FIGURE 3
Overview of analysis pipeline for determining local wave propagation velocities. **(A)** Local analysis relies on sequential pairwise comparison of frames within an image stack. Example frames are here referred to as frame 1 and frame 2. **(B)** The Horn-Schunck algorithms is used to compute optical flow of the image pair (from frame 1 to frame 2) These return one vector per pixel, indicating the shift. Brightness indicates the vector magnitude. **(C)** Phase image of frame 1. The phase is determined by whether the wave intensity goes up ("front" of the wave, bright color) or down ("wake" of the wave, dark color) following the direction of the vector obtained from the optical flow analysis. **(D)** Wave crests can be identified by the transitions from front to wake as denoted in panel C. Red lines show the identified wave crest locations. Selected arrows indicate the direction of movement of the crests as determined from the optical flow. **(E)** Left: Zoom-in of frame 1 at the location highlighted in panel D. Wave crest points are indicated by red dots; direction of movement as identified by optical flow analysis are indicated by arrows. Right: Zoom-in of frame 2 at the same location. Crest points of frame 1 are indicated by red dots. In both images, 3 crest point positions are highlighted by white line traces parallel to the direction of propagation at these points (i.e., normal to the wave fronts). **(F)** Intensities versus distance along the white lines in panel E. Starting from the crests identified for frame 1 (red dots), intensities are sampled at discrete sub-pixel positions perpendicular to the wave front. Smoothed intensity traces are shown in red for frame 1 and in blue for frame 2. The translocation d of each crest position is then determined from the peak shift, allowing to calculate a velocity vector with magnitude v. Wave crest velocities can be calculated for each crest and each sequential pair of frames in an image stack. **(G)** Velocity distribution of a pattern can be visualized as a 2D histogram. **(H)** Velocity histogram that provides the average velocity magnitude v as well as the distribution of velocities within a given pattern. **(I)** Histogram of angles of the wave propagation vector (left) and an angular diagram denoting the occurrence of various pattern velocities (right). From the list of velocity vectors, we have immediate access to the propagation directions present within a pattern, the occurrence of which can be visualized in a histogram (left). The information can be represented as a polar histogram (right).

which are calculated via radial averaging, these temporal autocorrelation traces may appear rather coarse. A more advanced peak detection can be performed with cubic-spline fitting and subsequent extreme point analysis. Further, the presented method for temporal autocorrelation analysis is less robust towards noise than spatial autocorrelation, as shown in Supplementary Figure S2C Adequate image preprocessing and cleaning is again of high importance. Image smoothing was found to slightly increase the detected oscillation period, albeit not above the error margins obtained for unsmoothed images, as shown in Supplementary Figure S4.

Note furthermore that the propagation speed of a pattern may depend on the concentrations of all components, and may change over time. Therefore, for very long time series, it can make sense to split the stack up into multiple stacks of shorter total duration and perform analysis for subsequent sub-stacks (compare Supplementary Figure S8). However, we estimate that an image stack needs to span the duration of a minimum length of 3 oscillation periods for the presented method to yield reliable results (cf. Supplementary Figure S4).

3.2 Local parameters

In this section, we present an analysis strategy that aims to quantify local parameters of Min patterns. These parameters include the local wave propagation velocity or characteristic local distances such as the distance between MinD and MinE wave crests. As we will describe in more detail, local parameters can be quantified by implementing two steps: 1) identification of wave crests for each frame within an image stack, and 2) comparison of intensities at and around the identified crest points from one frame to the next.

3.2.1 Local wave propagation velocity

The local wave propagation velocity is determined as the shift of individual crest points from one frame to the next. To calculate the local velocity, we first need to identify these crest points, and then determine their positional difference. We achieve this by applying optical flow analysis. Optical flow is defined by how brightness patterns move from one image to another [30, 31]. For our Min patterns, we estimate an optical flow vector field using Horn-Schunck algorithm [30, 32]. This algorithm works on a pair of sequential image frames (see Figure 3A for example data, recorded for MinE) and returns a vector field, describing the estimated optical flow for each pixel from the first to the second frame. Figure 3B shows the magnitude (indicated by image brightness) of the optical flow vectors obtained for our example image pair from Figure 3A. Note that the collected optical flow vectors do not necessarily represent the local wave propagation velocities. The relation between the two measures will depend on the wave shape, making it hard to generalize.

As a first step to identifying the positions of the wave crests within the first frame, we use the information obtained from optical flow analysis to create a phase image. This phase image is essentially a binary map over the whole image, which indicates whether at any given point we are at the “front” (‘ahead of the wave’) or “wake” region of the wave (‘behind the wave’). These regions are characterized by a decrease or increase in fluorescence intensity, respectively, along the direction of movement. If we consider any specific surface location and its corresponding vector obtained from optical flow, we can follow the direction of that vector over a short distance (say 3 pixels) within the same frame, and determine whether the fluorescence intensity is decreasing or increasing. The outcome of this procedure for our example frames is shown in Figure 3C. Using this phase image, we can identify those positions in the image that make up the wave crests – which form the backbone structure of the pattern. Wave crests are identified by the positions at which a transition from the front to a wake region occurs. Figure 3D shows the wave crests identified for the first frame in red. Subsequently, we need to determine the direction of wave propagation for these individual crest points. While we have a set of vectors available for distinct (x, y) positions from optical flow analysis, their directions will in general not be exactly normal to the wave crests due to noise. Therefore, we calculate vectors which are perpendicular to the lines of wave crests, and determine their correct directionality (pointing towards the front of the wave) using the information already present in the phase image. In Figure 3D the direction of propagation is indicated by vectors at distinct crest points throughout the image for illustration. Following the procedure outlined here and in Figures 3A–D, we thus effectively obtained 1) a list of positions, identifying the wave crest point positions, and 2) a list of vectors, describing their direction of movement from the current to the next frame.

The next step is to quantify how far these crest points moved during the transition from the current to the next frame. Upon quantifying this positional shift, the velocity magnitude is given by this distance divided by the time that passed between the acquisition of subsequent frames. The procedure is illustrated in Figures 3E,F for three example crest points. For each crest point, we considered the fluorescence intensity traces along the direction of movement at the given position (i.e., perpendicular to the wave front). Starting from the crest position, we plotted this trace up to a distance corresponding to roughly half the (global) wavelength of the pattern. Choosing this distance should ensure that the next frame’s peak is still within the sampling range (provided that the time resolution of the acquisition stack is sufficiently high, cf. Section 3.1.2). In Figure 3E, the example traces along which intensities are plotted are highlighted in white. For sampling positions along this trace that are located off the pixel grid, intensities can be estimated by interpolation. This yields an intensity trace at sub-pixel resolution. This intensity trace will have a maximum located very close to the center of the originally determined crest position, with a small offset that can be attributed to the

additional smoothing step performed before optical flow analysis, and is generally not significant (cf. Supplementary Figure S5 and adjoined table).

Next, we performed exactly the same procedure at the same positions on the next frame. As shown in Figure 3E and Figure 3F, these positions are now no longer centered around the maximum of the intensity trace, but offset from them by a certain distance. This distance is the positional shift that we need to obtain for quantification of the local wave propagation velocity. Performing peak fitting allows to identify the two traces' peak values and measure the shift d in crest peak position at sub-pixel resolution.

Performing this analysis for all identified crest points along all sequential pairs of frames in an stack eventually yielded a list of velocity vectors with components (v_x, v_y) at frame n for a wave crest at position (x, y). Image smoothing is an important technical aspect of the local analysis presented here. We first perform a light image smoothing (with a limited initial smoothing kernel) to de-noise the image and to simplify peak detection such as shown in Figure 3F. For optical flow analysis (Figure 3B), we perform an additional smoothing step with a more extensive secondary smoothing kernel. The effect of different initial smoothing kernels is illustrated in Supplementary Figure S6, the effect of increasing image noise in Supplementary Figure S2D,E. Further, applying Horn-Schunck algorithm [30] requires setting a few parameters, particularly the regularization constant and the number of iterations. Here, we determined their values by trial-and-error from evaluating simulated as well as real Min protein pattern data and kept both constant from then on.

Depending on what kind of information is of interest, the obtained distribution of velocity vectors can be represented in different ways. A representation that combines information on the magnitude and directional preference is a 2D histogram such as the one shown in Figure 3G for an example image stack of MinE data. If the magnitude of the wave propagation velocity is most important, the velocity magnitudes v can be plotted in a histogram to visualize their distribution and peak value, as shown in Figure 3H. In other cases, the directional information may be of prime interest, for example, when studying the influence of an external bulk flow [26] or physical environmental parameters on the pattern [22]. For each vector component, an angle α can be calculated that corresponds to the wave crest point's direction of movement with respect to the direction of applied flow. The occurrence of different directions can then be plotted in a regular or polar histogram, as shown in Figure 3I. As shown Supplementary Figure S7, the method can be applied to a wide range of image sizes. Decreasing the area on which analysis is performed generally leads to smaller standard deviation in velocity magnitude distribution, which is linked to a loss in directional information. The full local velocity pipeline is also presented in the Supplementary Appendix *DEMO_MinDE_local_analysis*.

3.2.2 Local MinD/MinE crest shift

When studying Min protein patterns, researchers routinely acquire data in two channels, for fluorescently-labelled MinD and MinE, respectively. Both these proteins exhibit a peak in their surface density, but these two peaks do not coincide in space and time (an example is given in Figure 4A).

To determine these differences, the analysis pipeline presented in Section 3.2.1 for obtaining wave propagation velocity between sequential frames can be slightly adapted for measuring the difference in crest position between MinD and MinE waves. This can be achieved by first performing crest detection (analysis pipeline shown in Figures 3A–D) for one stack, e.g. the MinD stack. The crest points attributed to the MinD stack can then be compared to the corresponding frame of the MinE stack, analogous to the comparison shown in Figure 3E. The collected peak shifts d can be visualized in a histogram, such as shown in Figure 4B for our example data.

4 Discussion

In this paper, we proposed protocols that can be applied to analyse data on *E. coli* Min protein surface patterns with respect to quantitative parameters such as the spatial wavelength, oscillation period, or wave crest propagation velocities. Our primary goal was to develop user-independent and largely automatized strategies for pattern analysis in order to 1) improve comparability of results obtained from different studies and research groups, and 2) provide tools for quantification of experimental data for comparing results to theoretical studies. We presented global and local analysis methods which both can be valuable depending on what kind of pattern information is of interest. All of the routines that we suggested and described can be further modified to better fit the requirements posed by a particular research question – thus providing a framework that others can build upon.

The methodology we describe can be combined with many of the aspects and practices of Min pattern analysis which we did not cover here. For example, in studies investigating absolute or relative local concentrations or concentration gradients of MinD and MinE on the surface, fluorescence calibration can be important. Calibration allows to relate fluorescence intensity to the local membrane protein density [12, 16, 19, 21]. However, in many cases the patterns as such – their shapes, domains, wavelength, or dynamics – can be studied without this step, using the acquired fluorescence intensity data in arbitrary units, and this is what we focused on in this paper.

The global analysis that was presented here provides parameters averaged over entire image frames (spatial analysis) or slices along fixed spatial coordinates (temporal analysis). We found that for well-cleaned images, spatial autocorrelation robustly quantifies the main dominant wavelength within an image frame,

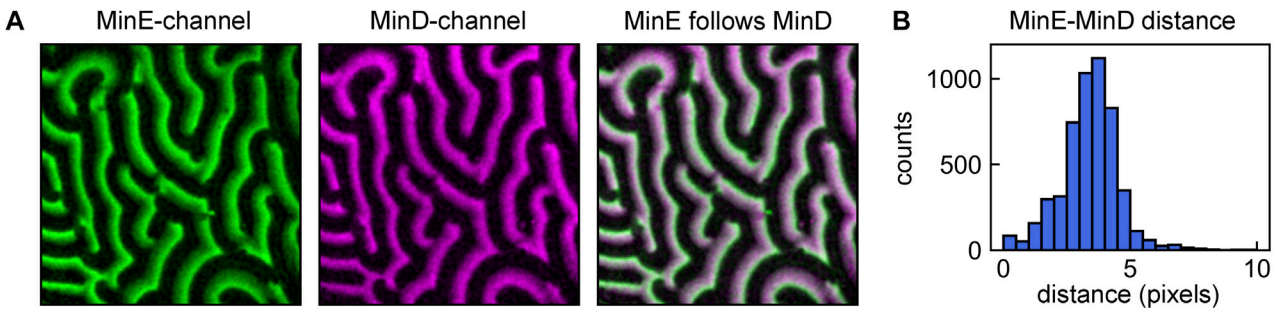

FIGURE 4
Using the local analysis pipeline to determine local MinE-MinD crest positions shifts. **(A)** MinD (magenta) and MinE (green) patterns. The pipeline for local analysis shown in Figures 3A–F can be used to quantify other properties of the pattern, such as the MinE-MinD crest point distance in a simultaneous dual-channel acquisition. Here, crest point detection was performed for each frame of the MinD stack. Subsequently, the intensity traces at these positions were compared to those of the corresponding MinE frame. **(B)** Distribution of MinE-MinD crest point distances.

as identified by the distance at which maximum self-correlation is present. This yielded results that are very comparable to those obtained by manual quantification, albeit with higher statistical reliability (see Supplementary Figure S1 for an example comparison of manual and automatic analysis). For temporal autocorrelation, we recommend re-orienting the image stack into slices of fixed x- or y-coordinates and calculating autocorrelation-maps along sets of kymographs, as described. We found this to be an efficient way to access large parts of the information provided within the image stack. Pixelwise analysis of intensity traces at distinct surface location, autocorrelation thereof and subsequent averaging is a more straightforward approach. However, we found that taking this detour via reslicing as presented in this paper reduces computational time by about two orders of magnitude, and hence, allows for easier processing of large amounts of data (cf. SI).

In many cases, parameters obtained from spatial and temporal analysis can be averaged for several frames/slices. However, whether this is justified depends on the time evolution of the pattern over the course of the acquisition. Supplementary Figure S8 shows the temporal autocorrelation results for an example image stack which shows a decline in oscillation period over time. This is visible from the spreading of peaks in the resliced image (cf. Supplementary Figure S8A) as well as in the variation in the shape of the $\Delta x = 0$ traces (cf. Supplementary Figure S8B). In such a case, averaging is only justified over the part of the stack that shows a constant temporal periodicity. If required, the routines can be expanded to include peak analysis of single traces in the kymograph set and automatically determine up to which point averaging is permitted.

Local analysis, in contrast to global analysis, directly provides large-number distributions of parameters even when analysing only two consecutive images. Our approach to local analysis relies on the identification of wave crests and quantification of the positional shift thereof from one frame to the next. The first step can in principle be achieved by various strategies. For example, one could implement an algorithm that relies on thresholds of fluorescence intensity to identify peaks. Here, we presented a strategy that relies on established algorithms for optical flow analysis, as it offers certain advantages, in particular access to directional information. We have already successfully used this local analysis methodology to examine and quantify the response of Min protein patterns to hydrodynamic bulk flow [26]. Numerous other applications can be imagined, in which a surface pattern is either exposed to an external stimulus and responds to it, or in which the time evolution of its characteristic properties is relevant. Using the local analysis pipeline presented here (or modifications thereof) allows to systematically quantify properties of interest with proper statistics rather than relying on qualitative description alone.

As our local analysis routine essentially offers a way to acquire a high number of intensity traces that are locally perpendicular to the wave fronts, it opens up possibilities for further in-depth analysis. Our brief illustration of a MinD-MinE crest distance detection is only one example of a parameter that can be extracted using an optical-flow-based routine. For example, it is imaginable to modify our local analysis pipeline such that it facilitates fast visualization of local fluorescence intensity profiles for both MinD and MinE waves. Upon fluorescence calibration, the fluorescence intensity can be converted to membrane protein density, and hence the relative peak heights can be connected to the protein ratio at the surface. Further, information obtained from local and global analysis can be combined, and local velocity analysis can provide an alternative to global methods if their requirements are not met. For example, while we found that a certain minimum number of entire oscillations is required for global temporal analysis to yield results (cf. Supplementary Figure S4), local analysis can already be performed on only two consecutive frames, and can be combined with global spatial analysis to serve as an alternative route to determining the predominant oscillation period.

Finally, we note that the general strategies presented within this paper are not restricted to application to the analysis of *E. coli* Min protein surface patterns. Min protein patterns have some properties that are very specific to them – such as their quasi-

periodic nature, dynamic oscillatory behavior, and their organization within domains – and our routines are designed for these specific properties. However, the routines presented here may very well be modifiable and applicable to quantify other types of semi-periodic surface patterns, biological or not, for example to the fascinating reaction-diffusion patterns of chemical systems like the BZ-AOT system [33]. We hope that our analysis toolbox will help to further disentangle the intriguing mechanisms that underlie pattern formation.

Data availability statement

The code created for this study as well as example data are openly available and can be found on Zenodo at zenodo.org/record/6724666 (second release). Please refer to the Supplementary Material for further information on how to access and use the analysis tools.

Author contributions

SM performed experiments with Min proteins, contributed to the provided image analysis tools and their representation, created the figures and co-wrote the paper. JK identified suitable image analysis methods, developed the majority of the provided tools and co-wrote the paper. CD co-developed the underlying methodology and co-wrote the paper.

Funding

Financial support was provided by the Netherlands Organisation for Scientific Research (NWO/OCW) as part of the NanoFront and BaSyC programs, as well as by ERC Advanced Grant no. 883684.

Acknowledgments

We thank Grzegorz Pawlik for providing example Min data, Julian Hofer for support with Python coding, and Alberto Blanch Jover, Angeliki Goutou, Ashmiani van den Berg, Eli van der Sluis, Erwin Frey, Fridtjof Brauns, Jaco van der Torre, Jernej Rudi Finžgar and Nicola De Franceschi for helpful discussions.

Conflict of interest

The authors declare that the research was conducted in the absence of any commercial or financial relationships that could be construed as a potential conflict of interest.

Publisher's note

Supplementary material

The Supplementary Material for this article can be found online at: https://www.frontiersin.org/articles/10.3389/fphy.2022.930811/full#supplementary-material

References

1. Turing A. The chemical basis of morphogenesis. *Philos Trans R Soc Lond Ser B, Biol Sci* (1952) 237:37–72. doi:10.1098/rstb.1952.0012

2. Bois JS, Jülicher F, Grill SW. pattern formation in active fluids. *Phys Rev Lett* (2011) 106:028103. doi:10.1103/PhysRevLett.106.028103

3. Kondo S, Miura T. Reaction-diffusion model as a framework for understanding biological pattern formation. *Science* (2010) 329:1616–20. doi:10.1126/science.1179047

4. Halatek J, Brauns F, Frey E. Self-organization principles of intracellular pattern formation. *Phil Trans R Soc B* (2018) 373:20170107. doi:10.1098/rstb.2017.0107

5. Schweisguth F, Corson F. Self-organization in pattern formation. *Develop Cel* (2019) 49:659–77. doi:10.1016/j.devcel.2019.05.019

6. Rietkerk M, van de Koppel J. Regular pattern formation in real ecosystems. *Trends Ecol Evol* (2008) 23:169–75. doi:10.1016/j.tree.2007.10.013

7. Ramm B, Heermann T, Schwille P. The *E. coli* MinCDE system in the regulation of protein patterns and gradients. *Cell Mol Life Sci* (2019) 76:4245–73. doi:10.1007/s00018-019-03218-x

8. Kretschmer S, Schwille P. Pattern formation on membranes and its role in bacterial cell division. *Curr Opin Cel Biol* (2016) 38:52–9. doi:10.1016/j.ceb.2016.02.005

9. Mizuuchi K, Vecchiarelli AG. Mechanistic insights of the Min oscillator via cell-free reconstitution and imaging. *Phys Biol* (2018) 15:031001. doi:10.1088/1478-3975/aa9e5e

10. Wettmann L, Kruse K. The min-protein oscillations in *Escherichia coli* : An example of self-organized cellular protein waves. *Phil Trans R Soc B* (2018) 373:20170111. doi:10.1098/rstb.2017.0111

11. Frey E, Halatek J, Kretschmer S, Schwille P. Protein pattern formation. In: Bassereau P, Sens P, editors. *Physics of biological membranes*. Cham: Springer International Publishing (2018). p. 229–60. doi:10.1007/978-3-030-00630-3_10

12. Vecchiarelli AG, Li M, Mizuuchi M, Mizuuchi K. Differential affinities of MinD and MinE to anionic phospholipid influence Min patterning dynamics *in vitro*: Flow and lipid composition effects on Min patterning. *Mol Microbiol* (2014) 93:453–63. doi:10.1111/mmi.12669

13. Heermann T, Steiert F, Ramm B, Hundt N, Schwille P. Mass-sensitive particle tracking to elucidate the membrane-associated MinDE reaction cycle. *Nat Methods* (2021) 18:1239–46. doi:10.1038/s41592-021-01260-x

14. Meinhardt H, de Boer PAJ. pattern formation in *Escherichia coli*: A model for the pole-to-pole oscillations of min proteins and the localization of the division site. *Proc Natl Acad Sci U S A* (2001) 98:14202–7. doi:10.1073/pnas.251216598

15. Kruse K, Howard M, Margolin W. An experimentalist's guide to computational modelling of the Min system. *Mol Microbiol* (2007) 63:1279–84. doi:10.1111/j.1365-2958.2007.05607.x

16. Vecchiarelli AG, Li M, Mizuuchi M, Hwang LC, Seol Y, Neuman KC, et al. Membrane-bound MinDE complex acts as a toggle switch that drives Min oscillation coupled to cytoplasmic depletion of MinD. *Proc Natl Acad Sci U S A* (2016) 113:E1479–E1488. doi:10.1073/pnas.1600644113

17. Denk J, Kretschmer S, Halatek J, Hartl C, Schwille P, Frey E, et al. MinE conformational switching confers robustness on self-organized Min protein patterns. *Proc Natl Acad Sci U S A* (2018) 115:4553–8. doi:10.1073/pnas.1719801115

18. Brauns F, Pawlik G, Halatek J, Kerssemakers J, Frey E, Dekker C, et al. Bulk-surface coupling identifies the mechanistic connection between Min-protein patterns *in vivo* and *in vitro*. *Nat Commun* (2021) 12:3312. doi:10.1038/s41467-021-23412-5

19. Ivanov V, Mizuuchi K. Multiple modes of interconverting dynamic pattern formation by bacterial cell division proteins. *Proc Natl Acad Sci U S A* (2010) 107:8071–8. doi:10.1073/pnas.0911036107

20. Ramm B, Glock P, Mücksch J, Blumhardt P, García-Soriano DA, Heymann M, et al. The MinDE system is a generic spatial cue for membrane protein distribution *in vitro*. *Nat Commun* (2018) 9:3942. doi:10.1038/s41467-018-06310-1

21. Loose M, Fischer-Friedrich E, Herold C, Kruse K, Schwille P. Min protein patterns emerge from rapid rebinding and membrane interaction of MinE. *Nat Struct Mol Biol* (2011) 18:577–83. doi:10.1038/nsmb.2037

22. Zieske K, Schweizer J, Schwille P. Surface topology assisted alignment of Min protein waves. *FEBS Lett* (2014) 588:2545–9. doi:10.1016/j.febslet.2014.06.026

23. Van Rossum G, Drake FL. *Python 3 reference manual*. Scotts Valley, CA: CreateSpace (2009).

24. Vecchiarelli AG, Li M, Mizuuchi M, Ivanov V, Mizuuchi K. MinE recruits, stabilizes, releases, and inhibits MinD interactions with membrane to drive oscillation. *Microbiology* (2017). doi:10.1101/109637

25. Ramm B, Goychuk A, Khmelinskaia A, Blumhardt P, Eto H, Ganzinger KA, et al. A diffusiophoretic mechanism for ATP-driven transport without motor proteins. *Nat Phys* (2021) 17:850–8. doi:10.1038/s41567-021-01213-3

26. Meindlhumer S, Brauns F, Finžgar J, Kerssemakers J, Dekker C, Frey E. Directing min protein patterns with advective bulk flow. *BioRxiv* (2021). doi:10.1101/2021.12.23.474007

27. Caspi Y, Dekker C. Mapping out Min protein patterns in fully confined fluidic chambers. *eLife* (2016) 5:e19271. doi:10.7554/eLife.19271

28. Würthner L, Brauns F, Pawlik G, Halatek J, Kerssemakers J, Dekker C, et al. Bridging scales in a multiscale pattern-forming system. *arXiv:2111.12043 [nlin, physics:physics]* (2021). ArXiv: 2111.12043.

29. Robertson C. Theory and practical recommendations for autocorrelation-based image correlation spectroscopy. *J Biomed Opt* (2012) 17:080801. doi:10.1117/1.JBO.17.8.080801

30. Horn BKP, Schunck BG. Determining optical flow. *Artif Intelligence* (1981) 17:185–203. doi:10.1016/0004-3702(81)90024-2

31. Mesbah M. Gradient-based optical flow: A critical review. In: *Isspa '99. Proceedings of the fifth international symposium on signal processing and its applications (IEEE cat. No.99EX359)*, 1. Brisbane: Queensland Univ. Technol (1999). p. 467–70. doi:10.1109/ISSPA.1999.818213

32. [Dataset] Michael I. *scivision/pyoptflow: update implementation, compare 3 implementations* (2021). doi:10.5281/zenodo.5574844

33. Vanag VK, Epstein IR. Pattern formation mechanisms in reaction-diffusion systems. *Int J Dev Biol* (2009) 53:673–81. doi:10.1387/ijdb.072484vv

frontiers | Frontiers in Cell and Developmental Biology

TYPE Review
PUBLISHED 11 August 2022
DOI 10.3389/fcell.2022.944016

OPEN ACCESS

EDITED BY
David M. Holloway,
British Columbia Institute of Technology, Canada

REVIEWED BY
Nick Monk,
The University of Sheffield, United Kingdom
Muhammed Fethullah Simsek,
Cincinnati Children's Hospital Medical Center, United States

*CORRESPONDENCE
Raquel P. Andrade,
rgandrade@ualg.pt

†These authors have contributed equally to this work

SPECIALTY SECTION
This article was submitted to Morphogenesis and Patterning, a section of the journal Frontiers in Cell and Developmental Biology

RECEIVED 14 May 2022
ACCEPTED 11 July 2022
PUBLISHED 11 August 2022

CITATION
Carraco G, Martins-Jesus AP and Andrade RP (2022), The vertebrate Embryo Clock: Common players dancing to a different beat.
Front. Cell Dev. Biol. 10:944016.
doi: 10.3389/fcell.2022.944016

The vertebrate Embryo Clock: Common players dancing to a different beat

Gil Carraco[1,2†], Ana P. Martins-Jesus[1†] and Raquel P. Andrade[1,2,3*]

[1]ABC-RI, Algarve Biomedical Center Research Institute, Faro, Portugal, [2]Faculdade de Medicina e Ciências Biomédicas (FMCB), Universidade do Algarve, Campus de Gambelas, Faro, Portugal, [3]Champalimaud Research Program, Champalimaud Center for the Unknown, Lisbon, Portugal

Vertebrate embryo somitogenesis is the earliest morphological manifestation of the characteristic patterned structure of the adult axial skeleton. Pairs of somites flanking the neural tube are formed periodically during early development, and the molecular mechanisms in temporal control of this early patterning event have been thoroughly studied. The discovery of a molecular Embryo Clock (EC) underlying the periodicity of somite formation shed light on the importance of gene expression dynamics for pattern formation. The EC is now known to be present in all vertebrate organisms studied and this mechanism was also described in limb development and stem cell differentiation. An outstanding question, however, remains unanswered: what sets the different EC paces observed in different organisms and tissues? This review aims to summarize the available knowledge regarding the pace of the EC, its regulation and experimental manipulation and to expose new questions that might help shed light on what is still to unveil.

KEYWORDS

temporal control, embryo clock, somitogenesis, negative feedback regulation, notch signalling, HES

1 Highlights

- The vertebrate Embryo Clock oscillates with species-specific periodicity
- Embryo Clock periodicity is tissue-specific within the same organism
- A comprehensive concept of the Embryo Clock is presented

2 The somitogenesis Embryo Clock

Vertebrate embryo development comprises several processes that are highly regulated in time. One such process is somitogenesis, which is characterized by the periodic formation of metameric structures, the somites, along the anterior-to-posterior (A-P) axis of the early embryonic body. Somites are formed in pairs from the anterior-most portion of the presomitic mesoderm (PSM), on each side of the neural tube, and they are the first morphological manifestation of the characteristic segmented structure of the adult

TABLE 1 Time of somite formation in different vertebrate organisms.

Organism	Time	References
Human	4—5 h	Müller and O'Rahilly, (1986)
Mouse	2–3 h	Tam, (1981)
Chicken	90 min	Palmeirim et al. (1997)
Quail	90 min	Packard, (1980)
Emu	100—110 min	Nagai et al. (2011)
Zebrafish	30 min	Kimmel et al. (1995)
Medaka	60 min	Iwamatsu, (2004)
Xenopus	40 min	Cooke and Zeeman (1976)
House snake	60 min	Gomez et al. (2008)
Corn snake	100 min	
Whiptail lizard	4 h	

vertebrate axial skeleton. In fact, somites not only give rise to the axial skeleton and skeletal musculature, but also impose the segmented organization of the peripheral nervous system (Keynes and Stern, 1988). Most importantly to the subject of this review, somite pairs are formed sequentially, over time, while the embryonic body is elongating in an A-P direction. This is characteristic of all vertebrates, although the pace at which somites are formed varies among species (Table 1).

In 1976, Cooke and Zeeman proposed a theoretical model that aimed to explain the formation of periodic structures during vertebrate development. In their *Clock and Wavefront* model (Cooke and Zeeman, 1976), the authors proposed the existence of two players: a molecular oscillator (*clock*), responsible for the rhythmic generation of a cell responsive state, and a maturation *wavefront*, moving slowly in an anterior-to-posterior direction. Exposure of a clock-induced cell population to the wavefront signal would promote a rapid change in cell properties, leading to the formation of a somite. Together, these two components would translate temporal information into a spatial pattern. According to this model, somite size and number are jointly determined by the period of the clock's oscillations and the speed of the moving wavefront (Cooke and Zeeman, 1976; Oates et al., 2012). However, breakthroughs regarding the identity of the molecules comprising the *Clock* and the *Wavefront* were only made 20 years later.

The Embryo Clock (EC)—or the *developmental clock,* as it was first termed–arose from the discovery that the mRNA of chick *hairy1* (now termed *hes4*), a member of the Hairy Enhancer of Split (HES) transcription factor family, oscillated in the chicken embryo PSM with a 90 min periodicity, concomitant with the formation of a new pair of somites (Palmeirim et al., 1997). In their study, the authors first observed that chicken embryos with the same number of somites (i.e., within the same developmental stage) displayed very different patterns of *hairy1* expression, leading them to hypothesize that its expression could be cyclic. Indeed, by bisecting the embryo, and culturing one half for a given time while the other was immediately fixed, *hairy1* expression recapitulated after 90 min. Moreover, *hairy1* oscillations in the PSM were found to be an intrinsic property of the system, as they were maintained even when the PSM was sectioned in smaller pieces or isolated from the surrounding tissues (Palmeirim et al., 1997). Since then, many genes that display an oscillatory behaviour during somitogenesis have been identified in multiple organisms, evidencing that the EC underlying somitogenesis is a conserved mechanism among vertebrates (Krol et al., 2011).

The first evidence for a *Wavefront* in control of somite formation was provided soon after (Dubrulle et al., 2001 in chick; Sawada et al., 2001 in zebrafish). A gradient of *fgf8* mRNA (chick) and signalling activity (zebrafish) was described, with high levels at the embryo tail bud decreasing towards the anterior PSM. Local inhibition of FGF8 signalling in the anterior PSM resulted in longer somites, suggesting an instructive role for FGF signalling in positioning the somitic boundary (Dubrulle et al., 2001; Sawada et al., 2001). This was consistent with what was previously proposed for the *wavefront* activity (Cooke and Zeeman, 1976). Further studies elucidated that the chick *fgf8* mRNA gradient resulted from the production of stable mRNA transcripts in the tail bud region alone, that degraded over time as the embryo elongated posteriorly, leading to less mRNA levels in the anterior PSM relative to the posterior region (Dubrulle and Pourquié, 2004). Graded Wnt activity and an opposing, anterior-to-posterior gradient of retinoic acid signalling were further shown to have *wavefront* activity in defining somite boundary positioning (reviewed in Resende et al., 2014).

This review reunites and summarizes key findings on Embryo Clock operation over the last 25 years, since *hes4* oscillations in the chicken embryo were first described (Palmeirim et al., 1997). Originally termed "developmental clock" (Palmeirim et al., 1997), then "segmentation clock" (McGrew et al., 1998) and "somitogenesis clock" (Leimeister et al., 2000), herein we employ a more comprehensive concept of "Embryo Clock," since oscillations in clock gene expression have been described in cells and developmental stages that are not associated with embryo somite formation (discussed below). We propose the term Embryo Clock to refer to the system of molecular oscillators operating in embryonic cells undergoing temporally controlled morphogenetic processes and/or cell fate specification. These genetic (or, in some cases, biochemical) oscillators exhibit periodic alterations (in contrast to stochastic pulses) that are maintained by negative feedback regulation. Due to the extensive and growing number of studies performed on the subject, we have focused our attention on the temporal dynamics of the EC. We aim to provide an overview of the main factors contributing to the exquisite temporal properties of this

TABLE 2 Periodicity of gene expression oscillations.

Organism	Gene	Tissue/cell line	Period	Technique	References
Human	*HES1*	UCB1 Mesenchymal stem cells	5 h	qPCR/Microarray	William et al. (2007)
	HES7	iPSC	5 h	Live imaging	Diaz-Cuadros et al. (2020)
		PSM-like cells derived from iPSC	~5 h	Luciferase reporter assay	Matsuda et al. (2020b)
			5.37 h	Luciferase reporter assay	Matsuda et al. (2020a)
		ESC	~5 h	Luciferase reporter assay	Chu et al. (2019)
Mouse	Axin2	PSM	2 h	*In situ* hybridization (ISH)	Aulehla et al. (2003)
	Dact1	PSM	2 h	ISH	Suriben et al. (2006)
	Dll1	PSM	2 h	ISH	Bone et al., 2014; Maruhashi et al., 2005
		NPC	2 h	Live imaging	Shimojo et al. (2008)
	Dusp4	PSM	2 h	ISH	Niwa et al. (2007)
	Hes1	Myoblasts, fibroblasts, neuroblastoma and teratocarcinoma cells	2 h	qPCR	Hirata et al. (2002)
		C2C12 myoblasts	2 h	qPCR/Microarray	William et al. (2007)
		Fibroblasts (C3H 10T1/2)	2.03 h	Bioluminescence imaging	Masamizu et al. (2006)
		PSM	2.67 h		
		Dissociated PSM cells	2.58 h		
		NPC	2—3 h	Live imaging	Shimojo et al. (2008)
		ESC (MG1.19 cell line)	3—5 h	Live imaging	Kobayashi et al. (2009)
	Hes5	Spinal cord cells	3.3 h	Live imaging	Manning et al. (2019)
	Hes7	PSM	2 h	ISH	Bessho et al. (2001)
		Induced PSM from ESC	2.5–3 h	Live imaging	Matsumiya et al. (2018)
		PSM-derived cells form iPSC	2.03 h	Luciferase reporter assay	Matsuda et al. (2020a)
	Lfng	PSM	2 h	ISH	Aulehla and Johnson, 1999
					Forsberg et al. (1998)
	Nkd1	PSM	2 h	ISH	Ishikawa et al. (2004)
	Notch1	PSM	2 h	ISH	Bone et al. (2014)
	Nrarp	PSM	2 h	ISH	Sewell et al. (2009)
	Smad6	Fibroblasts (C3H 10T1/2)	2 h	qPCR	Yoshiura et al. (2007)
	Snail1	PSM	2 h	ISH	Dale et al. (2006)
	Sprouty4	PSM	2 h	ISH	Hayashi et al. (2009)
	[a]	PSM	[a]	qPCR/microarray	Dequéant et al. (2006)
	[a]	PSM	[a]	qPCR/microarray	Krol et al. (2011)
Chicken	*hairy2*	PSM	1.5 h	ISH	Jouve et al. (2000)
		Limb bud	6 h		Pascoal et al. (2007)
	HES4	limb bud micromass cells	6 h	qPCR	Bhat et al. (2019)
	HES4	PSM	1.5 h	ISH	Palmeirim et al. (1997)
	snail2	PSM	1.5 h	ISH	Dale et al. (2006)
	HEY2	PSM	1.5 h	ISH	Leimeister et al. (2000)
	LFNG	PSM	1.5 h	ISH	McGrew et al. (1998)
	NRARP	PSM	1.5 h	ISH	Wright et al. (2009)
	[a]	PSM	[a]	qPCR/microarray	Krol et al. (2011)
Medaka	*her1/11*	PSM	1 h	ISH	Gajewski et al. (2006)
	her5	PSM	1 h	ISH	
	her7	PSM	1 h	ISH	Elmasri et al. (2004)
Xenopus	*hes5.5*	PSM	0.67 h	ISH	Li et al. (2003)
	hes9.1	PSM	0.67 h	ISH	
Zebrafish	*DeltaC*	PSM	0.5 h	ISH	Jiang et al. (2000)
	her1	PSM	0.5 h	ISH	Holley et al. (2000)
	her7	PSM	0.5 h	ISH	Oates and Ho, (2002)
	her11	PSM	0.5 h	ISH	Sieger et al. (2004)
	her12	PSM	0.5 h	ISH	Gajewski et al. (2006)
					Shankaran et al. (2007)

(Continued on following page)

TABLE 2 (*Continued*) Periodicity of gene expression oscillations.

Organism	Gene	Tissue/cell line	Period	Technique	References
	her15	PSM	0.5 h	ISH	Shankaran et al. (2007)
	hey1	PSM	0.5 h	ISH	Winkler et al. (2003)
	nrarp-a	PSM	0.5 h	ISH	Wright et al. (2009)
	[a]	PSM	[a]	qPCR/microarray	Krol et al. (2011)

[a]High throughput study (please refer to original paper for complete gene list); iPSC, induced Pluripotent Stem Cells; ESC, embryonic stem cells; ISH, *in situ* hybridization; PSM, presomitic mesoderm; NPC, neural progenitor cells.

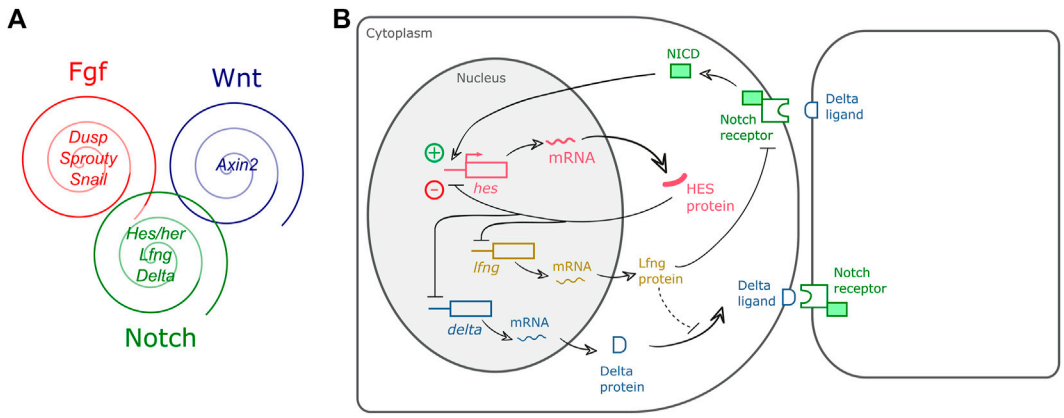

FIGURE 1
Embryo Clock (EC) gene expression oscillations. **(A)** The EC encompasses oscillatory genes belonging to the Fgf, Wnt and Notch signalling pathways (representative genes are indicated); **(B)** Negative feedback regulation of hairy-enhancer-of-split (HES) oscillations. In PSM cells, *hes* transcription is induced by pulses of intercellular Notch-Delta signalling, leading to HES protein production. HES protein enters the nucleus and represses its own promoter. HES protein and mRNA are rapidly degraded allowing for a new cycle of expression. HES also inhibits *delta* and *lfng* expression ensuring coupled oscillations in neighbour cells of the tissue. Dashed line represents a delay imposed on Delta integration in the cell membrane (Yoshioka-Kobayashi et al., 2020). NICD: Notch intracellular domain.

biological oscillator and anticipate this will be a useful roadmap for researchers interested in this increasingly exciting scientific field.

3 Gene expression oscillations

3.1 Embryo Clock genes in the PSM

After the description of the first segmentation clock gene, *hairy1*, in the chicken embryo (Palmeirim et al., 1997), similar oscillatory patterns of expression were identified for other genes, and in multiple organisms (Table 2). The use of genome-wide approaches identified a wide range of genes with oscillatory gene expression during somitogenesis and evidenced that the embryo clock is an intricate oscillatory genetic network, that comprises genes belonging to multiple signalling pathways, notably, Notch, Wnt and FGF (Dequéant et al., 2006; Krol et al., 2011) (Figure 1A). These include Wnt-dependent *Axin2*, FGF signalling pathway genes *Dusp1/2/4/6*, *Snail1/2*, *Spry2/4*, and Notch pathway genes of the Already defined earlier. HES family, *Lfng* and Nrarp, among others. Strikingly, only two genes–the *Hes1* and *Hes5* orthologs–were conserved in mouse, chicken and zebrafish. Otherwise, the identity of the pathway-specific oscillating genes varied considerably, evidencing evolutionary plasticity of the conserved oscillations in signalling pathway activity (Krol et al., 2011). Several studies have shown that these intercellular communication pathways cooperate during embryo body segmentation. Niwa et al. (2007), (2011) showed that the onset of *Hes7* expression in the mouse tailbud is FGF-dependent, while its maintenance and propagation throughout the PSM requires Notch signalling. A gradient of nuclear Wnt-related β-catenin was shown to control key features of PSM maturation and somite formation (Aulehla et al., 2008). Notch- and Wnt-dependent gene expression oscillations are coupled in the PSM and undergo a phase shift towards the anterior PSM. Inhibition of this phase shift in an *in vitro* setting delayed the arrest of EC waves and impaired tissue

TABLE 3 Periodicity of cyclic protein expression.

Organism	Protein	Tissue/cell line	Period	Technique	References
Mouse	Delta1	PSM	2 h	Immunohistochemistry	Bone et al. (2014)
			2.45 h	Live imaging	Shimojo et al. (2016)
		NPC	2.38 h	Live imaging	
		Pancreas	~1.5 h	Live imaging	Seymour et al. (2020)
	Dusp4	PSM	2 h	Immunohistochemistry	Niwa et al. (2007), (2011)
	Hes1	Myoblasts	2 h	Western Blot	Hirata et al. (2002)
		NPC	2.5 h	Live imaging	Imayoshi et al. (2013)
		Pancreas	~1.5 h	Live imaging	Seymour et al. (2020)
	Hes5	NPC	2.5 h	Live imaging	Imayoshi et al. (2013)
	Hes7	PSM	2 h	Immunohistochemistry	Bessho et al. (2003)
	NICD	PSM	2 h	Immunohistochemistry	Huppert et al. (2005)
					Niwa et al. (2011)
	Notch1	PSM	2 h	Immunohistochemistry	Bone et al. (2014)
					Morimoto et al. (2005)
	p-ERK	Fibroblasts (CH3 10T1/2)	2 h	Western Blot	Nakayama et al. (2008)
		PSM		Immunohistochemistry	Niwa et al. (2011)
	p-Smad1/5/8	Fibroblasts (CH3 10T1/2)	2 h	Western Blot	Yoshiura et al. (2007)
	Ascl	NPC	2.92 h	Live imaging	Imayoshi et al. (2013)
	Olig2	NPC	6.26 h	Live Imaging	
	Smad6	Fibroblasts (CH3 10T1/2)	2.5 h	Western Blot	Yoshiura et al. (2007)
Chicken	LFNG	PSM	1.5 h	Western Blot	Dale et al. (2003)
Zebrafish	DeltaC	PSM	0.5 h	Immunohistochemistry	Giudicelli et al. (2007)
	Her6	Neural progenitors	1.2–1.4 h	Live imaging	Soto et al. (2020)
	Hes6	PSM	0.5 h	Immunohistochemistry	Schröter et al. (2012)
	Tbx6	PSM	0.5 h	Immunohistochemistry	Wanglar et al. (2014)

PSM, presomitic mesoderm; NPC, neural progenitor cells.

segmentation (Sonnen et al., 2018). Identification of EC oscillatory dynamics at the protein level has lagged behind, mostly due to the lack of appropriate antibodies and because it is technically more challenging than the well-established *in situ* hybridization protocols for RNA detection. However, corresponding cycles of protein expression with the same periodicity have been reported and are summarized in Table 3.

3.2 Negative feedback regulation

Several studies have identified negative feedback regulation as a fundamental feature of EC oscillations (Hirata et al., 2002; Bessho et al., 2003; Lewis, 2003; Chen et al., 2005). Figure 1B presents a simplified view of the negative feedback regulatory mechanisms underlying HES gene expression oscillations, whereby *hes* oscillations are maintained by an inhibitory action of the HES protein on its own promoter. HES also inhibits *delta* expression and/or expression of the Notch-modulator Lunatic fringe–*Lfng*, which contributes to synchronized oscillations of Notch-dependent gene expression in neighbour cells. Rapid degradation of the molecular products produced, mRNAs and proteins, ensures propagation of the oscillatory behaviour (reviewed in Kageyama et al., 2012).

Using mathematical modelling, Lewis (2003), Monk (2003) and Jensen et al. (2003) independently postulated that oscillations in gene expression are influenced by delays in the various steps of the regulatory negative feedback loop. Indeed, further experimental evidence showed that the EC mechanism depends on Delayed Negative Feedback loops and that the temporal delays are introduced in multiple steps of the process. Namely:

3.2.1 Transcriptional delay

Lewis (2003) proposed that the time it takes to synthesize a transcript was one of the major accountants for transcriptional delay, so one would assume lengthier genes would have larger transcriptional delays. Elongation was, however, not found to have a major contribution to these delays–RNA polymerase II elongation rate measured in intact zebrafish embryos showed that the time needed to transcribe *her1* and *her7* is negligible and elongation kinetics of *Hes7* and *Lfng* determined using mouse

cells also occurred at a fast rate (Hanisch et al., 2013; Hoyle and Ish-Horowicz, 2013). Besides the elongation rate, however, there are other factors that significantly influence the transcriptional delay, namely mRNA nuclear export and mRNA splicing. Giudicelli et al. (2007) experimentally observed a delay from nuclear mRNA production to mature mRNA detection in the cytoplasm of *her1*, *her7* and *deltaC*–zebrafish's key clock components. Takashima et al. (2011) addressed the contribution of mRNA splicing to gene expression oscillations. They used transgenic mice carrying all or none of *Hes7* introns, together with a luciferase reporter, and assessed the time of *Hes7* transcription and protein production in both conditions. Mice carrying all *Hes7* introns showed a delay of approximately 19 min in *Hes7* expression, when compared to the intron-null mice. When abolishing this delay in a mathematical model, *Hes7* oscillations were abolished, and this was confirmed in the mutant animals. Hoyle and Ish-Horowicz (2013) corroborated that mRNA splicing and nuclear export account for most of the EC transcriptional delay. Additionally, they compared the splicing and export delays in mouse, chicken and zebrafish, and concluded that organisms that have longer delays in these processes also present longer clock periods.

3.2.2 mRNA degradation delay

Another aspect to take into consideration are the half-life times of EC mRNAs and proteins. Due to the inhibitory action of EC products on their own transcription, the time required for their clearance from the cell will directly impact the rate at which a new cycle of gene expression is initiated. Multiple factors that contribute to differential mRNA stability were experimentally assessed for their involvement in EC regulation. These include the mRNA 3′ untranslated region (3′UTR), polyA tail length and microRNA-mediated degradation.

While studying the mechanisms that control segmental gene expression in *Xenopus*, Davis et al. (2001) found that *hes4* (formerly known as *hairy2a*) expression dynamics was influenced by its 3′UTR sequence. When the 3′UTR of *hes4* was substituted by the 3′UTR of other *hes* genes (either from *Xenopus* or other vertebrate species), *hes4* expression retained its characteristic striped pattern in the PSM, unlike what happened when the 3′UTR of constitutively expressed genes was used. The authors further identified a phylogenetically conserved 25 bp sequence in the 3′UTR of EC genes which was necessary and sufficient to confer instability to these transcripts (Davis et al., 2001). Similar findings were reported by Hilgers and colleagues (2005) using an *in vivo* inducible system to halt transcription and measure mRNA degradation rate in the chicken embryo. They clearly showed that the 3′UTR of the EC gene *Lfng* promoted rapid mRNA decay, while the 3′UTR of *fgf8* mRNA contributed to stabilization of the reporter mRNA (Hilgers et al., 2005), which is compatible with *fgf8* graded expression pattern in the PSM (Dubrulle and Pourquié, 2004). Similar findings were reported for zebrafish EC genes (Fujino et al., 2018), evidencing that 3′UTR-mediated regulation of EC gene expression oscillations is a conserved feature in vertebrates. The Amacher lab went on to specify that mRNA decay of both zebrafish *her1* and *deltaC* relies on the Pumilio response- and AU-rich-elements present in their distal 3′UTRs, in a Pnrc2-dependent manner (Gallagher et al., 2017; Tietz et al., 2020).

Different EC genes with the same periodicity in the PSM can nevertheless present very different expression patterns. Nitanda *et al.* (2014) explored this feature focussing on *Hes7* and *Lfng* in the mouse PSM. After bisecting the PSM and culturing one half in actinomycin D to inhibit transcription, while the other was immediately fixed, quantitative PCR analysis showed that *Lfng* mRNA is less stable than *Hes7* mRNA. This was attributed to the 3′UTR, as demonstrated using cells transfected with a reporter vector containing either *Hes7* or *Lfng* 3′UTRs and monitoring mRNA degradation. The authors then generated transgenic mice lines, both containing a reporter gene driven by the *Hes7* promoter, but with different 3′UTRs–one from *Hes7,* and another from *Lfng*. The transgenic line with the *Lfng* 3′UTR showed a severe reduction in reporter mRNA, further confirming the role of the 3′UTR in promoting rapid mRNA decay. Importantly, the reporter mRNA presented the same expression pattern as its 3′UTR-donor gene, i.e., the *Lfng* 3′UTR-reporter displayed the same pattern as endogenous *Lfng*, and this was also true for the *Hes7* 3′UTR-transgene (Nitanda et al., 2014). These results strongly suggest that 3′UTR-mediated mRNA stability defines both the temporal and spatial properties of EC oscillations in the PSM.

Fujimuro et al. (2014) showed that *Hes7* 3′UTR is also required for the production of proper amounts of Hes7 protein to maintain oscillations. In the absence of the 3′UTR, *Hes7* mRNA no longer displayed cyclic expression patterns. The authors found that transcription levels of *Hes7* mRNA were reduced, and that Hes7 protein was hardly detectable in the mouse PSM, compared to wild-type embryos. As expected, since the protein was not being correctly produced, *Hes7* transcription inhibition was impaired, which compromised the maintenance of the oscillations (Fujimuro et al., 2014).

Work performed by Fujino and colleagues (2018) suggested that poly(A) tail length could also be important for EC mRNA rapid turnover. These authors measured the lengths of the poly(A) tails of zebrafish *her1*, *her7* and *hes6*, and observed that the first two genes, that display cyclic expression in the PSM, have shorter poly(A) tails, while *hes6* that is expressed in a gradient has a longer one. Through the inhibition of the deadenylase complex CCR4-NOT, the authors were able to lengthen the poly(A) tails of *her1* and *her7,* and this resulted in a 2-3-fold increase in mRNA levels, indicating an increase in mRNA stability (Fujino et al., 2018).

Finally, EC mRNA degradation rate is also regulated by microRNAs (miRNAs). Xie et al. (2007) were the first to theoretically propose a role for miRNAs in EC delayed

negative feedback regulation. Experimental evidence for oscillatory gene modulation by miRNAs was provided by Bonev et al. (2012), who reported that mouse *Hes1* mRNA is a direct target of microRNA-9 (miR-9). *Hes1* oscillations were dampened either when mir-9 was overexpressed or its binding to *Hes1* was inhibited, suggesting that *Hes1* oscillations are maintained within a certain range of miR-9 levels. This is ensured by negative feedback of Hes1 on the production of miR-9 primary transcripts, generating a double-negative feedback loop. Although the pri-miR-9 and pre-miR-9 are processed and cleared at a fast rate, the same is not true for the mature miR-9 which accumulates in the cell over time. Hence, a self-limiting oscillator model was proposed, whereby when miR-9 levels reach a certain threshold, *Hes1* is permanently downregulated and NPC differentiation occurs (Bonev et al., 2012). Similar findings were further reported in zebrafish hindbrain development. Here, miR-9 acts on *her6* to ensure robust oscillatory expression during neural progenitor cell differentiation (Soto et al., 2020).

During somitogenesis, miR-125a-5p is expressed in the chicken PSM where it targets the *Lfng* 3′UTR (Riley et al., 2013). Inhibition of chicken miR-125a-5p activity resulted in abnormal somite segmentation, resembling the phenotype obtained when *Lfng* was ubiquitously expressed in the chicken PSM (Dale et al., 2003). This is consistent with a role for miR-125a-5p in promoting *Lfng* mRNA decay. Moreover, *Lfng* and *hairy1* lost their oscillatory expression pattern, further evidencing that miRNA-mediated regulation is necessary for EC gene expression oscillations (Riley et al., 2013). A regulatory action of miR-125a-5p on *Lfng* mRNA degradation and expression dynamics was also documented in the mouse embryo (Wahi et al., 2017). Mathematical modelling performed by Jing et al. (2015) provided important insights regarding miRNA role in the segmentation clock. Their work suggests that the interaction between *Lfng* and miR-125a-5p affects both the amplitude and period of the oscillations, thus acting as a fine-tuning mechanism to Notch activity during somitogenesis.

Despite the established importance of miRNAs for mRNA decay, the extent of their relevance for EC oscillations is still unclear. Recent work from our group showed that different miRNA species are expressed in the PSM and in the forelimb distal cyclic domain. These tissues have very different EC periodicities (discussed below), which suggests that miRNAs may play a role in establishing different paces of the EC (Duarte et al., 2022).

3.2.3 Protein turnover delay

Even though translational delays are not accounted to influence oscillations (Hoyle and Ish-Horowicz, 2013), protein stability plays a crucial role. Hirata et al. (2004) addressed what would happen if Hes7 protein half-life time increased from 20 min (wild-type conditions) to 30 min and found that this provokes a dampening in both Hes7 mRNA and protein oscillations over time. Interestingly, lysine residues were found to play a key role in Hes7 protein stability. The authors generated Hes7 protein mutants, by introducing lysine-to-arginine mutations for each of the seven lysine residues in Hes7 sequence and found that different mutations gave rise to proteins with a half-life that differed from the wild-type. Ishii et al. (2008) reported that some of the lysine mutants lost transcriptional repressor activity, although they were more stable than the wild-type counterpart, thus evidencing the role of these lysine residues in Hes7 protein stability. Studies done by Lewis (2003) and Giudicelli et al. (2007) also stated that *her* protein half-life time should be short, compared to the zebrafish's segmentation clock pace. Mathematical modelling performed by Ay et al. (2013) reiterated the finding that proteins with a short half-life time are an essential requirement for the maintenance of the period of oscillations in the wild-type zebrafish segmentation clock. They further confirmed this by determining that Her7 protein has a half-life time ~10 times inferior to the zebrafish segmentation clock period (Ay et al., 2013).

3.3 Cell autonomous *vs*. tissue level oscillations

Embryo Clock gene expression oscillations are a cell autonomous property. This was first hinted by dissecting the chicken PSM in multiple portions and observing that the overall expression pattern of *hes4* (Palmeirim et al., 1997) and *Lfng* (Maroto et al., 2005) remained intact. The same was observed in dissected mouse PSMs (Masamizu et al., 2006). Cyclic *Lfng* gene expression even persisted in dissociated chicken PSM cells, but it occurred asynchronously among cells, evidencing the need for cell-cell contact to ensure synchrony and establish robust cyclic expression patterns at the tissue level (Maroto et al., 2005). In dissociated mouse PSM cells, *Hes1* oscillations also occur cell-autonomously (Masamizu et al., 2006) and Webb et al. (2016) further reported that zebrafish *her1* gene retains oscillatory expression in isolated tailbud cells. In this case, oscillations in individual cells presented a longer period and were less robust, compared with the intact tissue. Altogether, these results suggest that cell-cell communication is a key requirement for oscillations to be in phase within the vertebrate PSM tissue. This was corroborated by the work of Tsiairis and Aulehla (2016), that showed that a re-aggregation of mouse PSM cells is able to synchronize oscillations. Cell-autonomous EC gene expression oscillations have also been described in other cell types, such as mouse embryonic stem cells (ESC) (Kobayashi et al., 2009), individual fibroblasts (Masamizu et al., 2006) and neural progenitor cells (Shimojo et al., 2008; Bonev et al., 2012; Manning et al., 2019). These can be synchronized *in vitro* by the application of a serum shock or by Notch activation (Hirata et al., 2002). However, cell-specific distinct phases of EC oscillations may also play important roles *in vivo*. This will be discussed further below.

EC synchronization between PSM cells is required for proper somite formation. Local synchrony within the PSM tissue is achieved through Delta-Notch signalling (Jiang et al., 2000; Horikawa et al., 2006; Riedel-Kruse et al., 2007), which also functions to overcome the effect of "noise" introduced by other biological processes, such as cell division (Horikawa et al., 2006; Riedel-Kruse et al., 2007). Riedel-Kruse and colleagues found that EC synchrony in the zebrafish embryo is achieved by simultaneous (Notch-independent) activation immediately prior to gastrulation and is then maintained by Notch-dependent self-organized synchronization. The latter was elegantly shown by incubating embryos with the Notch-inhibitor DAPT until complete EC desynchronization. Then, DAPT washout alone was sufficient to completely restore both *dlc* oscillations and somite formation (Riedel-Kruse et al., 2007). Delaune et al. (2012) applied single cell live-imaging of *her1* expression in zebrafish wild-type and mutant embryos for *deltaC*, *deltaD* and *notch1a* to study the role of Delta-Notch signalling in EC synchronization. In the mutants, *her1* dynamics persisted in PSM neighbour cells, but in different oscillation phases (Delaune et al., 2012). Interestingly, *deltaC* and *deltaD* work together to ensure synchrony of the zebrafish segmentation clock in distinct portions of the PSM. While *deltaD* is responsible for the onset of the oscillations at the tailbud level, *deltaC* plays in role in maintaining and amplifying the oscillations in adjacent cells along the PSM tissue (Mara et al., 2007).

Soza-Ried et al. (2014) provided conclusive evidence for the role of oscillations of Notch-Delta signalling in maintaining the EC synchronized in neighbour cells for somite segmentation. Using a *deltaC* zebrafish mutant line, the authors were able to rescue both *her1* oscillations and somite formation by applying short artificial pulses of *deltaC* expression, evidencing that Notch signalling is indeed maintaining cell synchrony during somitogenesis. Accordingly, longer intervals between *deltaC* pulses generated larger somites (Soza-Ried et al., 2014). This was confirmed by Isomura et al. (2017) who developed an optogenetics-based system to monitor Notch-Delta signalling dynamics in neighbour cells. Light-induced *Dll1* pulses in sender cells were able to generate synchronized oscillations of *Hes1* expression in receiver cells. Furthermore, they were able to determine the time from the induction of *Dll1* to the cleavage of NICD, which was ~50.9 min, followed by an additional ~77 min until maximum *Hes1* levels were reached (Isomura et al., 2017). More recently, Yoshioka-Kobayashi et al. (2020) used this system to show that LFNG in sender cells introduces a 15 min-delay in the transport of Dll1 protein to the cell membrane, without which HES7 oscillations are severely dampened in individual cells of the PSM. These studies corroborate the importance of delays in cell-cell communication for EC oscillations and illustrate the power of optogenetics-based tools for dissecting these intricate regulatory mechanisms.

Notch-Delta signalling was shown to require non-muscle myosin II (NM II)-dependent contractility in both signal-sending and -receiving cells (Hunter et al., 2019). Recently, our lab evaluated the importance of fibronectin (FN) extracellular matrix assembly and signalling through the integrin-ROCK-NM II axis for somite segmentation and EC oscillations in chick PSM. We found that experimental treatments targeting FN matrix assembly, cell-FN interactions and actomyosin contractility significantly perturbed somite formation and EC gene expression, highlighting the importance of the PSM tissue's mechanical properties for EC oscillations (Gomes de Almeida et al., 2022).

Hes7 and *her1* oscillations slowdown in the anterior PSM in mouse (about 1.5-fold) (Niwa et al., 2011) and in zebrafish (Giudicelli et al., 2007; Delaune et al., 2012). Shih et al. (2015) corroborated these findings using live imaging in a transgenic zebrafish line with a her1-venus reporter. They saw that the periodicity of the segmentation clock increases by 1.5-fold in the anterior PSM, comparatively to the posterior PSM. SSoroldoni et al. (2014) had previously described this as a Dynamic Wavelength effect that, together with a Doppler effect resulting from the relative motion of the anterior PSM towards the posterior end due to tissue shortening over time, explains the rhythm of embryo body segmentation. To better understand the dynamics of EC deacceleration in the anterior PSM, Shih et al. (2015) assessed her1-venus reporter expression in cells that would form either side of a somite boundary. Within the same presumptive somite, clock oscillations were arrested in a posterior-to-anterior direction, i.e., cells that were incorporated in a posterior somite boundary ceased oscillations prior to cells that were incorporated in the anterior boundary of the same somite. Moreover, the authors reported that cells at a one-somite distance are initially synchronized in the posterior PSM and, as the clock slows down in the anterior PSM, they assume opposite phases of EC expression (Shih et al., 2015).

Another important alteration that cells experience as they transition from the posterior to anterior PSM is the relative timing of Notch- and Wnt-dependent EC oscillators (Sonnen et al., 2018). In fact, *Lfng* (Notch) and *Axin2* (Wnt) oscillated out-of-phase in the posterior PSM and were progressively coupled towards the anterior PSM, where their synchronization was critical for somite segmentation. This was shown using an ingenious microfluidics-based system, which allowed for precise manipulation of gene expression oscillations by applying temporally controlled pulses of Wnt/Notch-specific activator molecules (Sonnen et al., 2018). Recently, it was shown that the distinct levels of FGF signalling experienced in the anterior and posterior regions of the PSM could underlie the differences in EC dynamics observed in these cells (Diaz Cuadros et al., 2020; Yaman et al., 2022). Yaman et al. (2022) further reported that the posterior-to-anterior FGF gradient in the PSM, classically solely associated with the *wavefront* activity, is also

controlling the anterior propagation of the EC oscillations (Yaman et al., 2022).

There is also evidence of significant spatiotemporal metabolic changes along the PSM axis. Microarray analysis performed in PSM and tailbud samples of zebrafish embryos revealed that cell cycle/DNA metabolic functions are enriched in the posterior PSM, while translation/oxidative metabolism is enriched in anterior PSM and somites. The authors also reported a 2-fold increase in ATP content, as well as 2.5-fold decrease of Cytochrome C oxidase activity in the posterior PSM compared to anterior tissues (Özbudak et al., 2010). A posterior-to-anterior gradient of glycolytic activity was also linked to presomitic mesoderm development in mouse (Bulusu et al., 2017) and chicken (Oginuma et al., 2017) embryos. To test the functional relevance of these metabolic differences, PSM explants were cultured in glucose- or pyruvate-supplemented medium. While explants cultured in glucose supplemented medium developed normally, pyruvate-cultured explants displayed several defects concomitantly with loss of *Lfng* gene expression in the posterior PSM. Using a genetically encoded sensor for pyruvate to monitor metabolic transitions during PSM differentiation in real-time, the authors reported that pyruvate levels, i.e., glycolytic activity, decreased as cells transited towards an anterior PSM-like, more differentiated, state. Consistent with these findings, chicken embryos treated with 2-deoxy-D-glucose (2DG), a competitive inhibitor of the glycolytic enzyme hexokinase, displayed severe elongation defects, even though somite formation occurred normally. On the other hand, embryos treated with sodium azide (NaN_3)—a respiration inhibitor, had impaired somite segmentation (Oginuma et al., 2017).

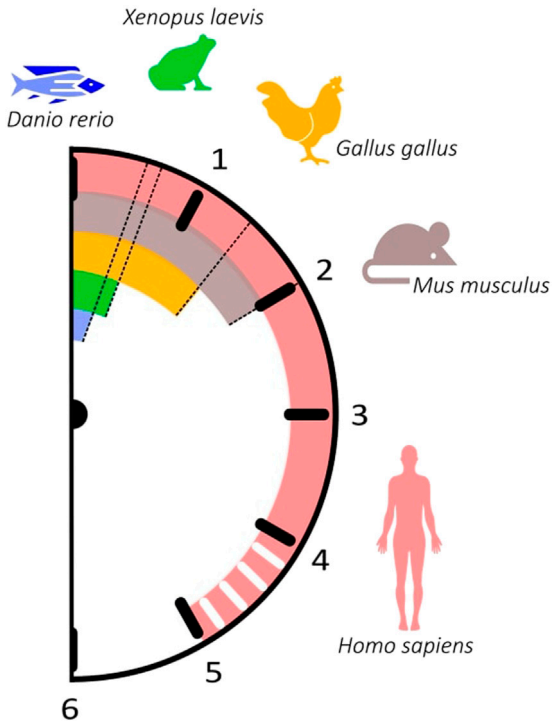

FIGURE 2
The somitogenesis clock ticks with different paces among vertebrates. The periodicity of somitogenesis clock gene expression in different organisms correlates with somite formation time. *Danio rerio*: 30 min (blue); *Xenopus laevis:* 40 min (green); *Gallus gallus*: 90 min (orange); *Mus musculus*: 120 min (brown); *Homo sapiens*: ~5 h (pink).

4 Embryo clock periodicity

4.1 Different species

The time each pair of somites takes to form is species-specific and displays great variability between organisms, ranging from 30 min in zebrafish to approximately 5 h in Human (Table 1). Similarly, the expression of segmentation clock genes oscillates with a periodicity characteristic of each species, which closely matches the time of somite formation (Figure 2; Table 2). The signalling pathways that comprise these genes are conserved; however, data suggests that cyclic genes display an evolutionary plasticity, since the specific genes involved in each pathway differ in the studied organisms (Krol et al., 2011).

A curious aspect of somite formation time is that the size of the organism does not significantly influence the time a pair of somites takes to form. For instance, somites have a relatively similar time of formation in the chicken and the emu, although dimension-wise these two birds are very distinct (Nagai et al., 2011). Likewise, the time of somite formation does not depend on phylogenetic relationships, since vertebrates belonging to different phyla can have the same somitogenesis period: 60 min for medaka and the house snake (Gomez et al., 2008).

Recent work started shedding light into the molecular mechanisms underlying divergent EC periodicity among organisms. Using *in vitro* models to compare EC gene expression dynamics in mouse *vs.* human cells, two independent studies found that the near 2-fold difference in oscillation periodicity could be explained by the different speeds in biochemical reactions within human and mouse cells, in particular mRNA and/or protein decay rates (Matsuda et al., 2020a; Rayon et al., 2020). This was documented in different cell types, which suggests that global temporal scaling mechanisms are a cell-autonomous property of the organism (Rayon and Briscoe, 2021).

4.2 Different axial levels of the same organism

EC oscillations underlying the formation of somites positioned at different A-P levels of the vertebrate body axis

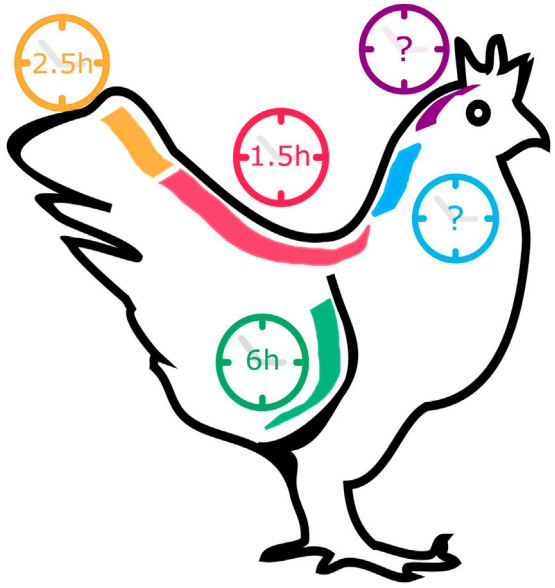

FIGURE 3
The pace of *Gallus gallus* Embryo Clock (EC) oscillations in different tissues. During somitogenesis (red and orange), the EC pace ranges from 1.5 to 2.5 h, while during forelimb development (green) a cycle lasts 6 h. EC dynamics in the early stages of somitogenesis (blue) and in neural development (purple) remain unknown.

have different periodicities. In the chicken embryo, somitogenesis and EC oscillations occur with a 90 min-periodicity for somites 15–20 (HH12-13^{+}) (Palmeirim et al., 1997). However, the final 5-8 somites (HH23) form with a periodicity of 150 min, matched by correspondingly slower cycles of *Lfng* gene expression (Gibb et al., 2009; Tenin et al., 2010) (Figure 3). In the opposite end, knowledge on the EC in the formation of the anterior-most somites is scarce. Rodrigues et al. (2006) characterized the expression of Notch-related EC genes in somites 1–10 and reported that, while they were dynamically expressed in the PSM, they did not present somite A-P polarity, as occurs in caudal somites. The EC was proposed to already be active even earlier in development, during gastrulation. In fact, Jouve et al. (2002) reported the existence of pulses of gene expression of *hairy2* and *Lfng* in the prospective PSM of early chicken embryos. In zebrafish gastrulation stages, the EC already oscillates with 30-min periodicity (Riedel-Kruse et al., 2007) and in mouse, with a ~2-h period (Falk et al., 2022). What triggers the onset of the Embryo Clock, and the existence of a clear periodicity in the early developmental stages of chick development, however, remains elusive.

Differences regarding segmentation clock operation in anterior and posterior regions of the zebrafish body axis have also been described (Choorapoikayil et al., 2012; Schröter et al., 2012; Hanisch et al., 2013). Although the double-mutant and -morphant for *her1* and *her7* exhibit defects throughout the entire body axis (Henry et al., 2002; Oates and Ho, 2002; Lleras-Forero et al., 2018), disrupting *her1* or *her7* gene expression has a different impact depending on the somites that are being formed. In fact, segmentation defects in *her1* mutants are restricted to the anterior trunk, while in *her7* mutants somites become defective only posterior to somite 8 (Choorapoikayil et al., 2012; Schröter et al., 2012; Hanisch et al., 2013).

4.3 Different tissues of the same organism

Throughout development, the same gene regulatory networks can be employed in different tissues to produce multiple outcomes. Besides the segmentation of the axial vertebrate body plan, EC oscillations also participate in other developmental processes, where their dynamics differs from the one presented in the PSM during somitogenesis.

Embryonic stem cells (ESC) differentiate into cell types belonging to all three germ layers–mesoderm, endoderm and ectoderm. Evidence that oscillatory gene expression played an important role in ESC differentiation was first provided by Kobayashi et al. (2009). The authors identified unsynchronized cycles of *Hes1* gene expression in mouse ESCs with a periodicity of 3–5 h–longer than the 2-h *Hes1* period described for other cell types from this organism (see Table 2). Under the same culture conditions, Hes1-high cells differentiated more efficiently into mesodermal cells, while Hes1-low cells into neurons, suggesting that unsynchronized gene expression oscillations might potentiate heterogeneous cell fate specification within the same population of cells (Kobayashi et al., 2009).

Oscillatory EC expression was also described in mouse neural progenitor cells (NPC). Using real-time imaging, *Hes5* and *Dll1* mRNA were determined to oscillate with a 2 h-periodicity (Imayoshi et al., 2013; Shimojo et al., 2008, 2016), and for *Hes1* this period was 2–3 h (Shimojo et al., 2008; Imayoshi et al., 2013) (Table 2). Likewise, Hes1 and Delta1 proteins display an identical period of oscillation (Table 3; Imayoshi et al., 2013). Studies performed in mouse NPCs reiterated the importance of gene expression oscillations for cell fate determination. During neurogenesis, the NPC population is maintained due to the repression of neural fate determination factors, such as *Neurogenin2*, *Ascl1/Mash1* and *Olig2* by *Hes1* and *Hes5* oscillatory expression levels. As a consequence, *Neurogenin2* and *Ascl1* also display oscillatory mRNA expression (Shimojo et al., 2008; Imayoshi et al., 2013). Unlike somitogenesis, oscillations during neural development are asynchronous. While undergoing differentiation, neural cells impede their neighbours to differentiate into the same cell type through lateral inhibition mediated by the Notch signalling pathway. Imayoshi et al. (2013) reported that the expression level of gene oscillations plays an important role in

NPC differentiation. Upon segregating NPC according to their levels of expression of *Hes1*, *Ascl1* and *Olig2* and culturing them in differentiation medium, the authors found that high or low EC expression levels dictated different differentiation outcomes. For instance, Hes1-high NPCs differentiated into an astrocyte lineage, while Hes1-low NPCs into neurons (Imayoshi et al., 2013).

Similar to what is observed during neural development, *Hes1* expression is required for the maintenance of multipotency in pancreatic progenitors, and undifferentiated neighbour cells undergo a mechanism of lateral inhibition to give rise to different cell types (de Lichtenberg et al., 2018). Even though pancreas development shares common players with somitogenesis and neural development, it was unknown if they displayed an oscillatory behaviour in this tissue. Recently, Seymour and colleagues (2020) reported that *Hes1* and *Dll1* proteins oscillate with a 90-min periodicity in cultured mouse pancreatic explants, and that this stimulates progenitor proliferation. The periodicity is different from the average 150 min period of Hes1 oscillations in NPC, which could be explained by lower levels of Notch activation in pancreatic progenitors. Importantly, extending the Hes1 oscillation period to ~120 min by inhibiting NICD degradation altered cell fate specification (Seymour et al., 2020).

Oscillatory gene expression was also reported during chicken limb development (Pascoal et al., 2007) (Figure 3). Oscillations of *hairy2* expression were first described in the chicken PSM, with the same periodicity as somite formation–90 min (Jouve et al., 2000). To study *hairy2* expression dynamics in the developing chick forelimb, Pascoal et al. (2007) microsurgically removed one limb from HH22-26 embryos *in ovo* and reincubated the embryo for different periods of time. *hairy2* expression was then assessed in each limb pair using *in situ* hybridization, revealing that *hairy2* has very dynamic expression in the distal limb field, that is recapitulated every 6 h. The authors then determined that the time required to form a new autopod skeletal element is 12 h, suggesting that the limb chondrogenic precursor cells undergo two cycles of *hairy2* expression for the formation of each autopod segmented element (Pascoal et al., 2007). This was the first evidence that a molecular clock is operating during limb development, a process where temporal control is also fundamental. *hes4* is also expressed in the distal mesenchyme of the avian limb (Vasiliauskas et al., 2003) and recent work suggests that its expression is also cyclic during limb development Bhat et al. (2019). cultured cells from chicken pre-cartilage leg mesenchyme and observed oscillations of *hes4* expression with a period of 6 h, suggesting that EC periodicity is a tissue-specific property.

The cases mentioned above clearly exemplify that the EC can play very distinct roles in different cells and tissues. For the formation of segmented structures such as somites and autopod limb elements, cells need to be synchronized to aggregate and give rise to a new segment. In multipotent cells, such as ESC, NPC and pancreatic progenitors, asynchronous EC oscillations function to allow heterogeneous cell fate responses of the population to a differentiation signal, ensuring the simultaneous specification of multiple cell types required for normal development.

5 Experimental manipulation of the Embryo Clock

Many attempts have been made to manipulate EC gene expression levels and/or temporal dynamics in order to obtain a clear understanding of the mechanisms underlying ultradian biological rhythms and their impact on embryo development. Although EC periodicity can be significantly altered throughout the developmental program (Figure 3)–chicken *hairy2* oscillates with a periodicity of 90 min in embryos with 48 h (PSM) (Palmeirim et al., 1997) and 6 h in the forelimb of older embryos (4–5 days) (Pascoal et al., 2007)–it has been extremely challenging to produce such significant alterations in an experimental setting. Most of the attempts to date completely disrupted EC expression or oscillatory dynamics (Table 4). In the most cases, only slight alterations to its rhythmicity were obtained (Table 5). The knowledge gained by such approaches, however, has been invaluable, and is patent in the topics described in the previous sections of this review.

Genetic manipulation of EC genes and associated intercellular signalling pathways provided the main framework of what we know today. Figure 4 offers a graphical overview of the alterations to EC gene expression imposed by genetic manipulation in the mouse and zebrafish models (references listed in Tables 4, 5). An interesting observation is that manipulation of Notch-dependent EC genes has limited impact on the dynamics of oscillatory genes associate with the FGF or Wnt signalling pathways, while the other Notch-EC genes are significantly altered. The major effects on FGF clock genes were observed when *Hes7* or *Lfng* were expressed at constant levels and only the latter altered Wnt-related *Axin2* oscillations. On the contrary, modulation of key components of FGF and Wnt pathways significantly impacted the expression of EC genes pertaining to all signalling pathways (Figure 4). The available information in zebrafish regards only to Notch-pathway EC genes and provides complementary knowledge to what is described for mouse. As can be easily perceived from Figure 4, many more studies are required to make full sense of the information gathered to date and to allow a clear inter-species comparison of the EC mechanism. It is worth highlighting that conclusive evidence for the functional relevance of the dynamic nature of EC gene expression, in opposition to EC expression levels, was provided by Shimojo et al. (2016). These authors succeeded in abolishing *Dll1* oscillations while ensuring physiological expression levels of the protein and this led to defective somitogenesis.

TABLE 4 Experimental disruption of Embryo Clock dynamics.

Organism	Tissue	Manipulation	Somitogenesis phenotype	Altered gene expression	References
Mouse	Embryo	Hes7 KO	Segmentation and skeletal patterning defects	Hes1, Hey2, Lfng, Sprouty4, Nrarp and Nkd1 disrupted oscillations. Steady expression of NICD and MESP2	Besho et al. (2001), Besho et al. (2003); Hayashi et al. (2009), Ferjentsik et al. (2009), Ishikawa et al. (2004), Niwa et al. (2007), (2011)
	Embryo	Hes7 overexpression	n/a	Sprouty4 absent in the posterior PSM and static expression in the anterior PSM	Hayashi et al. (2009)
	PSM	hes7 ± and Mesp2$^{+/-}$mutants in mild hypoxia	Segmentation and skeletal patterning defects	Notch pathway and FGF are downregulated	Sparrow et al. (2012)
	Embryo	Hes7 intron deletion	Fused somites and skeletal patterning defects	Sustained Hes7 expression	Takashima et al. (2011)
	Embryo	Hes7 3′UTR insertion of 5, 10 or 20 kb	Segmentation and skeletal patterning defects	LFNG and Hes7 dampened oscillations	Fujimuro et al. (2014)
	Embryo	Dll1 KO	Segmentation and skeletal patterning defects	Lfng and Hes7 expression absent	Barrantes et al. (1999), Chen et al. (2005), Niwa et al. (2007), Zhang et al. (2002)
	Embryo	Dll1 gene shortening/elongation	Fused somites	Steady Dll1 protein expression and dampened oscillations of Hes1 and Hes7	Shimojo et al. (2016)
	Embryo	Dll3 KO	Severe segmentation defects	Lfng, Hes1 and Hes5 absent expression. Steady Hes7 and Nrarp expression	Chen et al. (2005), Dunwoodie et al. (2002), Sewell et al. (2009)
	Embryo	RBPJκ KO	n/a	Lfng expression absent	Barrantes et al. (1999)
	Tailbud explants	Uncoupled notch and wnt oscillations	Halted segmentation	Delayed arrest of oscillations	Sonnen et al. (2018)
	Embryo	Lfng KO	Somite defects and axial strutures defects	Hes7, NICD and Nrarp with disrupted oscillatory expression	Chen et al. (2005), Ferjentsik et al. (2009), Morimoto et al. (2005),Niwa et al. (2007), (2011), Sewell et al. (2009), Shifley et al. (2008)
	Embryo	Lfng overexpression	Segmentation and skeletal patterning defects	Steady Hes7 expression	Serth et al. (2003)
	Embryo	LFNG dominant alele (RLFNG) resistant to Golgi degradation and non secreted	Absent or disorganized intersomitic boundaries	Abolished Dll1, Notch and Hes7 oscillations	Williams et al. (2016)
	Embryo	wnt3a vt mutant	Segmentation and skeletal patterning defects	Axin2 and Nrarp expression absent. Lfng and Hes7 oscillations abolished	Aulehla et al. (2003), Nakaya et al. (2005), Niwa et al. (2007), Sewell et al. (2009)
	Embryo	Ctnnb1 KO	Defective somites and boundaries	Axin, Dusp6/Mkp3, Spry2, Lfng and Hes7 with very low or no expression	Dunty et al. (2008)
	Embryo	Fgfr1 cKO (driven by T promoter)	Segmentation and skeletal patterning defects	Hes7 expression absent; Lfng steady expression; Dusp4, Sprouty4, Axin2 and Snail1 are downregulated	Niwa et al., 2007; Wahl et al., 2007
	Embryo	Psen1 KO; Psen2 KO	Do not form any somites	NICD, Snail1 and Sprouty2 with absent expression; Hes7, Axin2 and Dusp6 are expressed only in the tailbud	Ferjentsik et al. (2009)
Chicken	Embryo	Mir-125-5p manipulation (target protection assay)	Absent or disorganized intersomitic boundaries	Steady hairy1 expression and absent Lfng expression	Riley et al. (2013)
	Forelimb	Abrogate FGF signaling via AER ablation or inhibiting drugs	n/a	Absent hairy2 expression in the Distal Cyclic Domain	Sheeba et al. (2012)
	Forelimb	Abrogate Shh signaling via ZPA ablation or inhibiting drugs	n/a	Absent hairy2 expression in the Distal Cyclic Domain	

(Continued on following page)

TABLE 4 (*Continued*) Experimental disruption of Embryo Clock dynamics.

Organism	Tissue	Manipulation	Somitogenesis phenotype	Altered gene expression	References
Medaka	Embryo	Pharmacological modulation of ROS levels (NAC and DPI treatment)	Defective somites and boundaries	her4 and hey1 downregulated	Ventre et al. (2015)
Zebrafish	Embryo	her1 MO	Somite boundary defects	Steady deltaC, her7 and mesp2 expression	Gajewski et al. (2003), Sieger et al. (2004), Shankaran. (2007); Holley et al. (2002)
	Embryo	her7 MO	Somite boundary defects	Steady deltaC, her1, her 11, her12, her 15 and mesp2 expression	Gajewski et al. (2003), Sieger et al. (2004), Shankaran et al. (2007), Trofka et al. (2012)
	Embryo	her1 and her7 double mutant	Defective somite shape	Constant deltaC expression in the anterior PSM	Lleras-Forero et al. (2018)
	Embryo	her1, her7 and hes6 triple mutant	Defective somite shape	Constant deltaC expression in the anterior PSM	
	Embryo	her1, her7 and Tbx6 triple mutant	Defective somite shape	Constant deltaC expression throughout the PSM	
	Embryo	her1 and her7 double MO	Defective somites and boundaries	deltaD, Mesp2 and Notch expression disrupted	Henry et al. (2002), Oates and Ho (2002)
	Embryo	her1 mutant	disrupts the three anterior-most somite borders	Steady deltaC, her1, her7 and mesp2 expression	Choorapoikayil et al. (2012), Schröter et al. (2012), Hanisch et al. (2013)
	Embryo	her7 mutant	somite border defects from somite 8 to 17	Steady deltaC, her1, her7 and mesp2 expression	
	Embryo	her1 and deltaC double mutant	Defective somites and boundaries	Her7 expression through all PSM	Choorapoikayil et al. (2012)
	Embryo	deltaC MO	Defective somites and boundaries	Constant Her1 expression	Holley et al. (2002)
	Embryo	deltaC mutant (*bea*)	Defective somites and boundaries	Constant Her1 expression	Choorapoikayil et al. (2012), Holley et al. (2000),(2002)
	Embryo	deltaD mutant (*aei*)	Defective somites and boundaries	her12 and her15 absent expression. her1 and her11 with static expression	Sieger et al. (2004), Shankaran et al. (2007), Holley et al. (2000)
	Embryo	her12 overexpression	Defective somites and boundaries	Constant her1, her7 and deltaC expression	Shankaran et al. (2007)
	Embryo	her15 overexpression	Defective somites and boundaries	Constant her1, her7 and deltaC expression	
	Embryo	her12 MO	n/a	Constant her1, her7 and deltaC expression	
	Embryo	Notch1 mutant (des)	Defective somites and boundaries	her12 and her15 downregulation. Static her1, her7 and her11 expression	Sieger et al. (2004), Shankaran et al. (2007), Holley et al. (2000)
	Embryo	NICD activation	Somite boundary defects	difuse her1 and her7 expression	Ozbudak and Lewis. (2008)
	Embryo	Su (H) MO	Defective somites and boundaries	her12 and her15 downregulation. Static her1, her7 and her11 expression	Sieger et al. (2003), (2004) Shankaran et al. (2007)
	Embryo	Greb1 MO	Defective somites and boundaries	Downregulated her7	Prajapati et al. (2020)
	Embryo/ hindbrain	Mutation of the miR-9 target site on her6 3′UTR	n/a	Stabilized her6 levels	Soto et al. (2020)
	Embryo	her1/her7 disrupted chromossomal linkage	Defective somites and boundaries	Constant her1 and her7 expression	Zinani et al. (2021)

Besides genetic manipulation, other factors, such as environmental hypoxia or alterations to reactive oxygen species (ROS) levels, can impact EC operation in the PSM. Exposure of pregnant mice to mild hypoxia disrupted EC oscillations and induced vertebral malformations in heterozygous pups for *Hes7* or *Mesp2*, which otherwise developed normally (Sparrow et al., 2012). Ventre et al. (2015) suggested that this effect could be mediated by ROS, since pharmacological modulation of ROS levels in Medaka (*Oryzias latipes*) impaired somite formation and

TABLE 5 Embryo Clock pace manipulation.

Organism	Manipulation	wt pace	Altered pace	Δ pace	References
Mouse	Deletion of Hes7 introns 1 and 2	123 min	112 min	(-) 8,94%	Harima et al. (2013)
	Hes1 type-1 mutant (NPC)	173.5 ± 4.4 min	159.9 ± 2.6 min	(-) 7,8%	Ochi et al. (2020)
	Hes1 type-2 mutant (NPC)		187.0 ± 4.3 min	(+) 7,8%	
	Hes7 K14R mutation (HES7 prot half-life increase from 20 to 30 min)	121.4 min	131.6 min	(+) 8,4%	Hirata et al. (2004)
	KO of Nrarp	106 min	111 min	(+) 4,5%	Kim el al. (2011)
	LiCl 20 mM treatment	2.5 h	2.9 h	(+) 16%	González et al. (2013)
	LiCl 40 mM treatment	2.5 h	3.6 h	(+) 44%	
	CKI-7 100 μM treatment	2.5 h	3.3 h	(+) 32%	
	pancreatic dorsal bud, MLN4924 treatment (NICD stabilization)	~90 min	~120 min	(+) 33%	Seymore et al. (2020)
	PSM-like tissue (iPSM)	159.6 min	[a] 123.3–203.3 min	[a] (-) 22.7% - (+) 25.7%	Yoshioka-Kobayashi et al. (2020)
Zebrafish	Damascus mutant (~100 deltaD copies)	24.7 ± 0.6 min	23.1 ± 0.8 min	(-) 6.4%	Liao et al. (2016)
	MO hes6	n/a	n/a	(-) 6.5% ± 1.2%	Schroter and Oates. (2010)
	Mib1 mutant	n/a	n/a	(+) 19%	Herrgen et al. (2010)
	aei/deltaD mutant	n/a	n/a	(+) 23%	
	des/notch1a mutant	n/a	n/a	(+) 7%	
	Notch inhibition with saturating DAPT concentrations (R 40 mM)	n/a	n/a	(+) 18%	
	Her7 hetero:hes6 mutant	n/a	n/a	(+) 6%	Schröter et al. (2012)
	Her7 Mutant:hes6 mutant	n/a	n/a	(+) 5%	
Chicken	CKI-7 100 μM treatment	90 min	115–120 min	(+) 33%	Gibb et al. (2009)
	Shh inhibition/notochord removal	90 min	~2 h 45 min	(+) 85%	Resende et al. (2010)
	Blebbistatin 50 μM treatment	90 min	120 min	(+) 33%	Gomes de Almeida et al. (2022)

n/a: data not available.
[a]Chemical library screening; maximum range is indicated (please refer to original paper for complete list and respective alterations).

downregulated *her4* and *hey1,* two EC genes in this organism (Ventre et al., 2015). Recent studies using *in vitro*-derived PSM-like tissues showed that graded levels of Fgf ligands are required to ensure the EC dynamics (pace, amplitude and phase) (Diaz Cuadros et al., 2020; Yaman et al., 2022) and directionality of EC oscillation waves in the PSM (Yaman et al., 2022).

Sheeba et al. (2014) studied the regulation of *hairy2* oscillations in the chick distal forelimb. When the Apical Ectodermal Ridge (AER) or the Zone of Polarizing Activity (ZPA), the key sources of FGF and Shh, respectively, were surgically removed from developing limbs, *hairy2* expression was abolished from the distal cyclic domain. This suggested that the EC could represent a functional intersection of these key molecules for limb proximal-distal outgrowth and patterning.

5.1 Strategies for accelerating/delaying the Embryo Clock

As described above, most attempts to modify the EC led to a complete disruption of the oscillations. However, an increasing number of experimental approaches have succeeded in altering the pace of the EC, which is key to understanding how this biological oscillator is regulated and the functional significance of its temporal dynamics (Table 5).

Following the work of by Takashima et al. (2011), Harima and colleagues generated a mouse mutant lacking only the first two introns of the Hes7 gene. This resulted in Hes7 oscillations with an 11 min-faster periodicity than the WT mice. This shorter cycle did not abolish EC oscillations nor somite formation. As predicted by the Clock and Wavefront model, since the EC presented a faster pace, this culminated in more and smaller somites (Harima et al., 2013). Recently, a similar approach was used to modify the tempo of *Hes1* oscillations in NPCs (Ochi et al., 2020). Deleting all the introns of the mouse *Hes1* gene accelerated expression oscillations by 13.6 min. On the other hand, by substantially increasing the primary transcript length the authors obtained exactly the opposite result, delayed EC in 13.5 min (Ochi et al., 2020). These are powerful examples of how transcriptional delays of EC genes can be modulated to tinker gene expression dynamics.

In the EC negative feedback regulatory loop, HES proteins are imported to the nucleus and repress their own transcription. Repression is lifted upon protein degradation, allowing a new

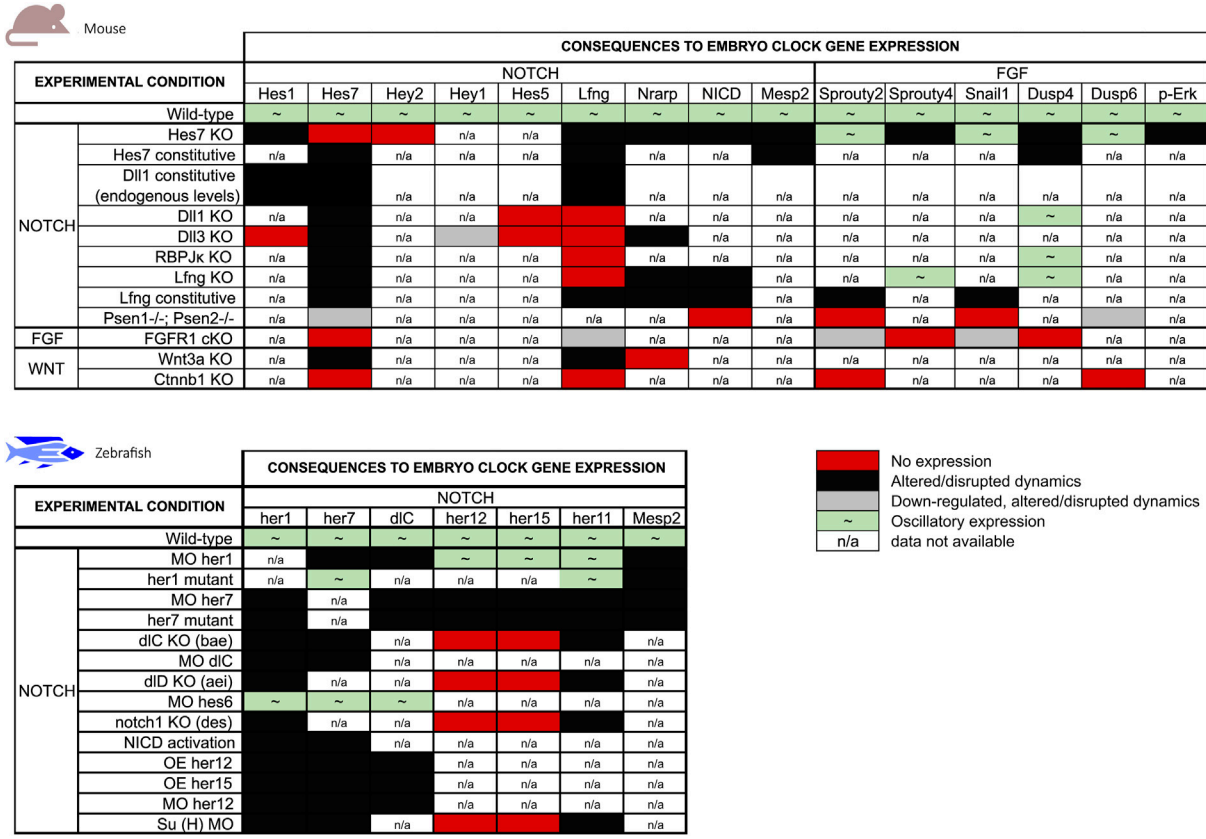

FIGURE 4
Summary of the effects of genetic manipulation on mouse and zebrafish EC gene expression. EC genes were grouped by the main signalling pathways they are associated with.

transcription cycle to begin. Hence, by changing protein stability the repressive time on the gene promoter also changes, culminating in an overall alteration in the *tempo* of the EC. Through replacement of a Lysine for an Arginine in position 14, Hirata and colleagues were able to increase the half-life of the HES7 protein by 10 min, which led to an increase of 10,2 min in the global pace of the Embryo Clock (Hirata et al., 2004). A similar approach was applied by Kim et al. (2011) by knocking-out Nrarp, a negative effector of Notch signalling. This approach, suggested to delay NICD turnover, extended the EC pace by 5 min and resulted in the formation of fewer and defective vertebrae (Kim et al., 2011). Wiedermann et al. (2015) also accomplished to delay EC oscillations by stabilising NICD in the chick embryo, further corroborating these findings.

A wealth of knowledge on EC pace manipulation has also been provided using the zebrafish model. The Oates lab produced mutants in genes belonging to the Notch signalling pathway that displayed slower EC oscillations (Herrgen et al., 2010; Schröter and Oates, 2010). Knock-out of *notch1a*, *mib1*, and *deltaD* slowed the EC pace by 7%, 19%, and 23%, respectively (Herrgen et al., 2010), and mutating *hes6* delayed the EC by 6.5% (Schröter and Oates, 2010). Finally, chemical inhibition of the notch signalling pathway using DAPT delayed the EC by 18% (Herrgen et al., 2010). Corresponding delays in somitogenesis periodicity and a reduced final somite number corroborated the importance of Delta-Notch coupled oscillations for timely embryo body segmentation. Accordingly, elevation of Delta-Notch signalling accelerated EC oscillations and somite formation (Liao et al., 2016). Liao et al. (2016) created fish lines with 7 (*Dover*) or 100 (*Damascus*) extra copies of *deltaD*. Only the Damascus mutant displayed alterations to the EC, where oscillations were 1.6 min (6.4%) faster than in the wild-type. This increased the number of trunk segments by 7,6% and, despite the dramatic overexpression of *deltaD*, segmentation defects were rarely observed (Liao et al., 2016).

Other intercellular communication pathways contribute to the proper timing of the Embryo Clock. Sonic hedgehog (Shh) was shown to participate in EC *tempo* regulation. By comparing chicken PSM explants cultured with and without a source of Shh (notochord tissue and/or SHH-expressing cells), Resende et al. (2010) showed that the absence of Shh significantly delayed both EC oscillations and somite formation. Absence of Shh signalling

led to an 85% increase of the EC period, from 90 min to approximately 2 h and 45 min. Similar experimental approaches showed that Wnt pathway inhibition by CKI-7 extended the EC pace from 90 to 120 min (Gibb et al., 2009). Comparable results were further obtained in the mouse model. Here, both CKI-7 treatment and activation of Wnt signalling using LiCl delayed *Hes7* oscillations (González et al., 2013). Using PSM-like tissues induced from mouse ESC, Yoshioka-Kobayashi et al. (2020) performed a high throughput chemical library screening and identified multiple small compounds capable of altering the period of *Hes7* oscillations by up to 40 min (Yoshioka-Kobayashi et al., 2020). These included modulators of a wide range of cellular processes and signalling pathways and further characterization of these alterations will surely improve our knowledge on EC operation.

Recently, we showed that the fibronectin-integrin-ROCK-NM II signalling axis regulates EC dynamics in the chicken PSM. Importantly, inhibition of actomyosin-mediated contractility delayed the period of *hairy1* (*hes4*) oscillations from 90 to 120 min (Gomes de Almeida et al., 2022), unveiling a previously unappreciated biomechanical regulation of the EC periodicity.

6 Pressing questions and future perspectives

Great attention has classically been dedicated to studying the molecular mechanisms involved in correct spatial positioning of cells/tissues/organs during embryo development, while the dynamics of gene expression over time was an under-represented concern. The discovery of a molecular Embryo Clock underlying somite formation gave way to a dramatic shift in this trend. Since it was first described in 1997, the EC has been characterized in multiple vertebrate species, evidencing a phylogenetically conserved mechanism. However, there are two aspects that differ depending on the organism: the pace of the EC and the specific oscillatory genes, although common signalling pathways are involved. The EC biological function has been tightly correlated with the segmentation of paraxial mesoderm, and mutations in Human EC genes give rise to severe congenital malformations of the axial skeleton, such as the phenotypes associated with spondylocostal dysostosis (Sparrow et al., 2012; Nobrega et al., 2021).

There is great interest in clarifying the EC clock dynamics and regulatory mechanisms in tissues other than the paraxial mesoderm and in different species, since this should help evidence what constitutes the central mechanism(s) of the clock, and which components are species/tissue-specific. Hairy-enhancer-of-split oscillatory expression is conserved in all species and tissues analysed, which has suggested their role as "core" members of the EC, but conclusive evidence for such fundamental clock components remains elusive. Studies on the mechanism(s) associated with the onset of gene expression oscillations during development might help elucidate whether EC operation is the output of a limited set of "core" clock genes or if it is an emergent property of the developing biological system, reverberating the oscillatory nature of the very first events during fertilization (e.g., Ca^{2+} oscillations induced upon sperm-oocyte fusion).

For many years, only *hairy2* was described to have cyclic expression in the chicken limb bud. More recently, Bhat et al. (2019) reported oscillations of *hes4* expression in chick limb micromass cultures. Here, *hes4* oscillates with a 6 h periodicity (Bhat et al., 2019), which matches the rate of limb *hairy2* oscillations *in vivo* (Pascoal et al., 2007). This suggests that the expression dynamics of both *hairy2* and *hes4* may be regulated by common mechanisms in the developing limb, further reinforcing the existence an EC-like mechanism operating during limb development (Sheeba et al., 2016). However, it is still unknown if this is conserved in other vertebrates and if altering *hairy2* or *hes4* expression may impact limb outgrowth and patterning. Clues arise from recent work evidencing that *Hes1* is a critical downstream effector of the Shh/Gli3 pathway in mouse limb development, where it regulates mesenchymal cell proliferation (Sharma et al., 2021). Importantly, *Hes1* overexpression promoted supernumerary digit formation and the authors concluded that *Hes1* regulates anterior boundary formation for digit development. Together, these studies suggest that synchronized *Hes* oscillations in the distal limb field could be functioning to prepattern the tissue for segment (digit) formation, which is reminiscent of the EC function in the PSM. Hence, the developing limb bud represents an additional extraordinary model system to further study EC regulation and function.

Despite the effort put into characterizing the EC, many fundamental questions remain unanswered. What triggers the onset of EC oscillations? What sets the *tempo* of the clock? What is the functional relevance of EC oscillations in different cell types and embryonic tissues? Is there a core component common to all vertebrates? Answering these and other pressing questions would allow us to understand how TIME is set and perceived for pattern formation during embryo development. Currently, there is a growing number of researchers employing novel experimental *in vitro* model systems that bring great promise to dissecting the EC mechanism in ways that have been hindered *in vivo* (reviewed in Diaz-Cuadros and Pourquié, 2021). These include the recently described Human *somitoids* derived from induced pluripotent stem cells (iPSC), which display segment formation and *Hes7* gene expression oscillations with the same periodicity as that previously describe for Human somitogenesis: ~5 h (Sanaki-Matsumiya et al., 2022). After 25 years since the somitogenesis Embryo Clock was first described, the scientific community is more aware than ever of the existing knowledge gaps, but is also more equipped than ever to tackle the challenges ahead.

Author contributions

GC, AM-J, and RPA conceptualized, wrote, and revised the manuscript. GC and AM-J created figures and tables. RPA provided supervision and guidance on the manuscript organization.

Funding

This study was supported by the Portuguese Fundação para a Ciência e Tecnologia (FCT) (scholarships SFRH/BD/101609/2014 and PTDC/BEX-BID/5410/2014 to GC and AM-J, respectively) and by AD-ABC and Município de Loulé to RPA.

Acknowledgments

The authors are grateful for the careful analysis and critical discussion with the reviewers that greatly improved our final manuscript. We also acknowledge Letícia Leite and Betina Silva for their contributions to Figure 1 construction.

Conflict of interest

The authors declare that the research was conducted in the absence of any commercial or financial relationships that could be construed as a potential conflict of interest.

Publisher's note

All claims expressed in this article are solely those of the authors and do not necessarily represent those of their affiliated organizations, or those of the publisher, the editors and the reviewers. Any product that may be evaluated in this article, or claim that may be made by its manufacturer, is not guaranteed or endorsed by the publisher.

References

Aulehla, A., and Johnson, R. L. (1999). Dynamic expression of lunatic fringe suggests a link between notch signaling and an autonomous cellular oscillator driving somite segmentation. *Dev. Biol.* 207, 49–61. doi:10.1006/dbio.1998.9164

Aulehla, A., Wehrle, C., Brand-Saberi, B., Kemler, R., Gossler, A., Kanzler, B., et al. (2003). Wnt3a plays a major role in the segmentation clock controlling somitogenesis. *Dev. Cell* 4, 395–406. doi:10.1016/s1534-5807(03)00055-8

Aulehla, A., Wiegraebe, W., Baubet, V., Wahl, M. B., Deng, C., Taketo, M., et al. (2008). A β-catenin gradient links the clock and wavefront systems in mouse embryo segmentation. *Nat. Cell Biol.* 10, 186–193. doi:10.1038/ncb1679

Ay, A., Knierer, S., Sperlea, A., Holland, J., and Özbudak, E. M. (2013). Short-lived her proteins drive robust synchronized oscillations in the Zebrafish segmentation clock. *Development* 140, 3244–3253. doi:10.1242/dev.093278

Barrantes, I. D. B., Elia, A. J., Wünsch, K., De Angelis, M. H., Mak, T. W., Rossant, J., et al. (1999). Interaction between Notch signalling and Lunatic fringe during somite boundary formation in the mouse. *Curr. Biol.* 9, 470–480. doi:10.1016/S0960-9822(99)80212-7

Bessho, Y., Hirata, H., Masamizu, Y., and Kageyama, R. (2003). Periodic repression by the bHLH factor Hes7 is an essential mechanism for the somite segmentation clock. *Genes Dev.* 17, 1451–1456. doi:10.1101/gad.1092303

Bessho, Y., Sakata, R., Komatsu, S., Shiota, K., Yamada, S., Kageyama, R., et al. (2001). Dynamic expression and essential functions of Hes7 in somite segmentation. *Genes Dev.* 15, 2642–2647. doi:10.1101/gad.930601

Bhat, R., Glimm, T., Linde-medina, M., Cui, C., and Newman, S. A. (2019). Synchronization of Hes1 oscillations coordinates and refines condensation formation and patterning of the avian limb skeleton. *Mech. Dev.* 156, 41–54. doi:10.1016/j.mod.2019.03.001

Bone, R. A., Bailey, C. S. L., Wiedermann, G., Ferjentsik, Z., Appleton, P. L., Murray, P. J., et al. (2014). Spatiotemporal oscillations of Notch1, Dll1 and NICD are coordinated across the mouse PSM. *Development* 141, 4806–4816. doi:10.1242/dev.115535

Bonev, B., Stanley, P., and Papalopulu, N. (2012). MicroRNA-9 modulates hes1 ultradian oscillations by forming a double-negative feedback loop. *Cell Rep.* 2, 10–18. doi:10.1016/j.celrep.2012.05.017

Bulusu, V., Prior, N., Snaebjornsson, M. T., Schultz, C., Sauer, U., Aulehla, A., et al. (2017). Spatiotemporal analysis of a glycolytic activity gradient linked to mouse embryo mesoderm development. *Dev. Cell* 40, 331–341. doi:10.1016/j.devcel.2017.01.015

Chen, J., Kang, L., and Zhang, N. (2005). Negative feedback loop formed by lunatic fringe and Hes7 controls their oscillatory expression during somitogenesis. *Genesis* 43, 196–204. doi:10.1002/gene.20171

Choorapoikayil, S., Willems, B., Ströhle, P., and Gajewski, M. (2012). Analysis of her1 and her7 mutants reveals a spatio temporal separation of the somite clock module. *PLoS One* 7, e39073. doi:10.1371/journal.pone.0039073

Chu, L.-F., Mamott, D., Ni, Z., Bacher, R., Liu, C., Swanson, S., et al. (2019). An *in vitro* human segmentation clock model derived from embryonic stem cells. *Cell Rep.* 28, 2247–2255. e5. doi:10.1016/j.celrep.2019.07.090

Cooke, J., and Zeeman, E. C. (1976). A clock and wavefront model for control of the number of repeated structures during animal morphogenesis. *J. Theor. Biol.* 58, 455–476. doi:10.1016/S0022-5193(76)80131-2

Dale, J. K., Malapert, P., Chal, J., Vilhais-Neto, G., Johnson, T., Maroto, M., et al. (2006). Oscillations of the Snail genes in the presomitic mesoderm coordinate segmental patterning and morphogenesis in vertebrate somitogenesis. *Dev. Cell* 10, 355–366. doi:10.1016/j.devcel.2006.02.011

Dale, J. K., Maroto, M., Dequeant, M. L., Malapert, P., McGrew, M., Pourquie, O., et al. (2003). Periodic Notch inhibition by lunatic fringe underlies the chick segmentation clock. *Nature* 421, 275–278. doi:10.1038/nature01244

Davis, R. L., Turner, D. L., Evans, L. M., and Kirschner, M. W. (2001). Molecular targets of vertebrate segmentation: Two mechanisms control segmental expression of Xenopus hairy2 during somite formation. *Dev. Cell* 1, 553–565. doi:10.1016/S1534-5807(01)00054-5

De Lichtenberg, K. H., Seymour, P. A., Jørgensen, M. C., Kim, Y.-H., Grapin-Botton, A., Magnuson, M. A., et al. (2018). Notch controls multiple pancreatic cell fate regulators through direct hes1-mediated repression. bioRxiv, 336305. doi:10.1101/336305

Delaune, E. A., François, P., Shih, N. P., and Amacher, S. L. (2012). Single-cell-resolution imaging of the impact of notch signaling and mitosis on segmentation clock dynamics. *Dev. Cell* 23, 995–1005. doi:10.1016/j.devcel.2012.09.009

Dequéant, M.-L., Glynn, E., Gaudenz, K., Wahl, M., Chen, J., Mushegian, A., et al. (2006). A complex oscillating network of signaling genes underlies the mouse segmentation clock. *Sci. (80-.)* 314, 1595–1598. doi:10.1126/science.1133141

Diaz-cuadros, M., and Pourquie, O. (2021). *In vitro* systems: A new window to the segmentation clock. *Dev. Growth Differ.* 63, 140–153. doi:10.1111/dgd.12710

Diaz-cuadros, M., Wagner, D. E., Budjan, C., Hubaud, A., Tarazona, O. A., Donelly, S., et al. (2020). *In vitro* characterization of the human segmentation clock. *Nature* 580, 113–118. doi:10.1038/s41586-019-1885-9

Duarte, I., Carraco, G., de Azevedo, N. T. D., Benes, V., and Andrade, R. P. (2022). gga-miRNOME, a microRNA-sequencing dataset from chick embryonic tissues. *Sci. Data* 9, 29. doi:10.1038/s41597-022-01126-7

Dubrulle, J., Mcgrew, M. J., and Pourquié, O. (2001). FGF signaling controls somite boundary position and regulates segmentation clock control of spatiotemporal hox gene activation. *Cell* 106, 219–232. doi:10.1016/S0092-8674(01)00437-8

Dubrulle, J., and Pourquie, O. (2004). fgf8 mRNA decay establishes a gradient that couples axial elongation to patterning in the vertebrate embryo. *Nature* 427, 419–422. doi:10.1038/nature02216

Dunty, W. C., Jr, Biris, K. K., Chalamalasetty, R. B., Taketo, M. M., Lewandoski, M., Yamaguchi, T. P., et al. (2008). Wnt3a/beta-catenin signaling controls posterior body development by coordinating mesoderm formation and segmentation. *Development* 135, 85–94. doi:10.1242/dev.009266

Dunwoodie, S. L., Clements, M., Sparrow, D. B., Sa, X., Conlon, R. A., Beddington, R. S. P., et al. (2002). Axial skeletal defects caused by mutation in the spondylocostal dysplasia/pudgy gene Dll3 are associated with disruption of the segmentation clock within the presomitic mesoderm. *Development* 129, 1795–1806. doi:10.1242/dev.129.7.1795

Elmasri, H., Liedtke, D., Lücking, G., Volff, J. N., Gessler, M., Winkler, C., et al. (2004). Her7 and hey1, but not lunatic fringe show dynamic expression during somitogenesis in medaka (*Oryzias latipes*). *Gene Expr. Patterns* 4, 553–559. doi:10.1016/j.modgep.2004.02.003

Falk, H. J., Tomita, T., Mönke, G., McDole, K., and Aulehla, A. (2022). Imaging the onset of oscillatory signaling dynamics during mouse embryo gastrulation. *Development* 149 (13), 1027–1030. doi:10.1242/dev.200083

Ferjentsik, Z., Hayashi, S., Dale, J. K., Bessho, Y., Herreman, A., De Strooper, B., et al. (2009). Notch is a critical component of the mouse somitogenesis oscillator and is essential for the formation of the somites. *PLoS Genet.* 5, e1000662. doi:10.1371/journal.pgen.1000662

Forsberg, H., Crozet, F., and Brown, N. A. (1998). Waves of mouse Lunatic fringe expression, in four-hour cycles at two-hour intervals, precede somite boundary formation. *Curr. Biol.* 8, 1027–1030. doi:10.1016/S0960-9822(07)00424-1

Fujimuro, T., Matsui, T., Nitanda, Y., Matta, T., Sakumura, Y., Saito, M., et al. (2014). Hes7 3'UTR is required for somite segmentation function. *Sci. Rep.* 4, 6462. doi:10.1038/srep06462

Fujino, Y., Yamada, K., Sugaya, C., Ooka, Y., Ovara, H., Ban, H., et al. (2018). Deadenylation by the CCR4-NOT complex contributes to the turnover of hairy-related mRNAs in the zebrafish segmentation clock. *FEBS Lett.* 592, 3388–3398. doi:10.1002/1873-3468.13261

Gajewski, M., Elmasri, H., Girschick, M., Sieger, D., and Winkler, C. (2006). Comparative analysis of her genes during fish somitogenesis suggests a mouse/chick-like mode of oscillation in medaka. *Dev. Genes Evol.* 216, 315–332. doi:10.1007/s00427-006-0059-6

Gajewski, M., Sieger, D., Alt, B., Leve, C., Hans, S., Wolff, C., et al. (2003). Anterior and posterior waves of cyclic her1 gene expression are differentially regulated in the presomitic mesoderm of zebrafish. *Development* 130, 4269–4278. doi:10.1242/dev.00627

Gallagher, T. L., Tietz, K. T., Morrow, Z. T., Mccammon, J. M., Goldrich, M. L., Derr, N. L., et al. (2017). Pnrc2 regulates 3'UTR-mediated decay of segmentation clock-associated transcripts during zebrafish segmentation. *Dev. Biol.* 429, 225–239. doi:10.1016/j.ydbio.2017.06.024

Gibb, S., Zagorska, A., Melton, K., Tenin, G., Vacca, I., Trainor, P., et al. (2009). Interfering with Wnt signalling alters the periodicity of the segmentation clock. *Dev. Biol.* 330, 21–31. doi:10.1016/j.ydbio.2009.02.035

Giudicelli, F., Özbudak, E. M., Wright, G. J., and Lewis, J. (2007). Setting the tempo in development: An investigation of the zebrafish somite clock mechanism. *PLoS Biol.* 5, e150. doi:10.1371/journal.pbio.0050150

Gomes de Almeida, P., Rifes, P., Martins-Jesus, A. P., Pinheiro, G. G., Andrade, R. P., Thorsteinsdóttir, S., et al. (2022). Cell-fibronectin interactions and actomyosin contractility regulate the segmentation clock and spatio-temporal somite cleft formation during chick embryo somitogenesis. *Cells* 11, 2003. doi:10.3390/cells11132003

Gomez, C., Özbudak, E. M., Wunderlich, J., Baumann, D., Lewis, J., Pourquié, O., et al. (2008). Control of segment number in vertebrate embryos. *Nature* 454, 335–339. doi:10.1038/nature07020

González, A., Manosalva, I., Liu, T., and Kageyama, R. (2013). Control of Hes7 expression by Tbx6, the Wnt pathway and the chemical Gsk3 inhibitor LiCl in the mouse segmentation clock. *PLOS ONE* 8, e53323. doi:10.1371/journal.pone.0053323

Hanisch, A., Holder, M. V., Choorapoikayil, S., Gajewski, M., Özbudak, E. M., Lewis, J., et al. (2013). The elongation rate of RNA polymerase II in zebrafish and its significance in the somite segmentation clock. *Development* 453, 444–453. doi:10.1242/dev.077230

Harima, Y., Takashima, Y., Ueda, Y., Ohtsuka, T., and Kageyama, R. (2013). Accelerating the tempo of the segmentation clock by reducing the number of introns in the Hes7 gene. *Cell Rep.* 3, 1–7. doi:10.1016/j.celrep.2012.11.012

Hayashi, S., Shimoda, T., Nakajima, M., Tsukada, Y., Sakumura, Y., Dale, J. K., et al. (2009). Sprouty4, an FGF inhibitor, displays cyclic gene expression under the control of the notch segmentation clock in the mouse PSM. *PloS One* 4, e5603. doi:10.1371/journal.pone.0005603

Henry, C. A., Urban, M. K., Dill, K. K., Merlie, J. P., Page, M. F., Kimmel, C. B., et al. (2002). Two linked hairy/Enhancer of split-related zebrafish genes, her1 and her7, function together to refine alternating somite boundaries. *Development* 129, 3693–3704. doi:10.1242/dev.129.15.3693

Herrgen, L., Ares, S., Morelli, L. G., Schroter, C., Julicher, F., Oates, A. C., et al. (2010). Intercellular coupling regulates the period of the segmentation clock. *Curr. Biol.* 20, 1244–1253. doi:10.1016/j.cub.2010.06.034

Hilgers, V., Pourquié, O., and Dubrulle, J. (2005). *In vivo* analysis of mRNA stability using the Tet-Off system in the chicken embryo. *Dev. Biol.* 284, 292–300. doi:10.1016/j.ydbio.2005.05.021

Hirata, H., Bessho, Y., Kokubu, H., Masamizu, Y., Yamada, S., Lewis, J., et al. (2004). Instability of Hes7 protein is crucial for the somite segmentation clock. *Nat. Genet.* 36, 750–754. doi:10.1038/ng1372

Hirata, H., Yoshiura, S., Ohtsuka, T., Bessho, Y., Harada, T., Yoshikawa, K., et al. (2002). Oscillatory expression of the BHLH factor Hes1 regulated by a negative feedback loop. *Science* 298, 840–843. doi:10.1126/science.1074560

Holley, S. A., Geisler, R., and Nüsslein-Volhard, C. (2000). Control of her1 expression during zebrafish somitogenesis by a Delta-dependent oscillator and an independent wave-front activity. *Genes Dev.* 14, 1678–1690. doi:10.1101/gad.14.13.1678

Holley, S. A., Julich, D. R., Rauch, G.-J. R., Geisler, R., and Nüsslein-Volhard, C. (2002). her1 and the notch pathway function within the oscillator mechanism that regulates zebrafish somitogenesis. *Development* 129, 1175–1183. doi:10.1242/dev.129.5.1175

Horikawa, K., Ishimatsu, K., Yoshimoto, E., Kondo, S., and Takeda, H. (2006). Noise-resistant and synchronized oscillation of the segmentation clock. *Nature* 441, 719–723. doi:10.1038/nature04861

Hoyle, N. P., and Ish-Horowicz, D. (2013). Transcript processing and export kinetics are rate-limiting steps in expressing vertebrate segmentation clock genes. *Proc. Natl. Acad. Sci. U. S. A.* 110, E4316–E4324. doi:10.1073/pnas.1308811110

Hunter, G. L., He, L., Perrimon, N., Charras, G., Giniger, E., Baum, B., et al. (2019). A role for actomyosin contractility in Notch signaling. *BMC Biol.* 17 (1), 12. doi:10.1186/s12915-019-0625-9

Huppert, S. S., Ilagan, M. X. G., De Strooper, B., and Kopan, R. (2005). Analysis of notch function in presomitic mesoderm suggests a γ-secretase-independent role for presenilins in somite differentiation. *Dev. Cell* 8, 677–688. doi:10.1016/j.devcel.2005.02.019

Imayoshi, I., Isomura, A., Harima, Y., Kawaguchi, K., Kori, H., Miyachi, H., et al. (2013). Oscillatory control of factors determining multipotency and fate in mouse neural progenitors. *Science* 342, 1203–1208. doi:10.1126/science.1242366

Ishii, A., Kobayashi, T., and Kageyama, R. (2008). Requirement of multiple lysine residues for the transcriptional activity and the instability of Hes7. *Biochem. Biophys. Res. Commun.* 372, 142–146. doi:10.1016/j.bbrc.2008.05.015

Ishikawa, A., Kitajima, S., Takahashi, Y., Kokubo, H., Kanno, J., Inoue, T., et al. (2004). Mouse Nkd1, a Wnt antagonist, exhibits oscillatory gene expression in the PSM under the control of Notch signaling. *Mech. Dev.* 121, 1443–1453. doi:10.1016/j.mod.2004.08.003

Isomura, A., Ogushi, F., Kori, H., and Kageyama, R. (2017). Optogenetic perturbation and bioluminescence imaging to analyze cell-to-cell transfer of oscillatory information. *Genes Dev.* 31, 524–535. doi:10.1101/gad.294546.116

Iwamatsu, T. (2004). Stages of normal development in the medaka *Oryzias latipes*. *Mech. Dev.* 121, 605–618. doi:10.1016/j.mod.2004.03.012

Jensen, M. H., Sneppen, K., and Tiana, G. (2003). Sustained oscillations and time delays in gene expression of protein Hes1. *FEBS Lett.* 541, 176–177. doi:10.1016/S0014-5793(03)00279-5

Jiang, Y.-J., Aerne, B. L., Smithers, L., Haddon, C., Ish-Horowicz, D., Lewis, J., et al. (2000). Notch signalling and the synchronization of the somite segmentation clock. *Nature* 408, 475–479. doi:10.1038/35044091

Jing, B., Yuan, J., Yin, Z., Lv, C., Lu, S., Xiong, H., et al. (2015). Dynamic properties of the segmentation clock mediated by microRNA. *Int. J. Clin. Exp. Pathol.* 8, 196–206.

Jouve, C., Iimura, T., and Pourquié, O. (2002). Onset of the segmentation clock in the chick embryo: Evidence for oscillations in the somite precursors in the primitive streak. *Development* 129, 1107–1117. doi:10.1242/dev.129.5.1107

Jouve, C., Palmeirim, I., Henrique, D., Beckers, J., Gossler, A., Ish-Horowicz, D., et al. (2000). Notch signalling is required for cyclic expression of the hairy-like gene HES1 in the presomitic mesoderm. *Development* 127, 1421–1429. doi:10.1242/dev.127.7.1421

Kageyama, R., Niwa, Y., Isomura, A., González, A., and Harima, Y. (2012). *Oscillatory gene expression and somitogenesis*, 1. Wiley Interdiscip Rev Dev Biol, 629–641. doi:10.1002/wdev.46

Keynes, R. J., and Stern, C. D. (1988). Mechanisms of vertebrate segmentation. *Development* 103, 413–429. doi:10.1242/dev.103.3.413

Kim, W., Matsui, T., Yamao, M., Ishibashi, M., Tamada, K., Takumi, T., et al. (2011). The period of the somite segmentation clock is sensitive to Notch activity. *Mol. Biol. Cell* 22, 3541–3549. doi:10.1091/mbc.E11-02-0139

Kimmel, C. B., Ballard, W. W., Kimmel, S. R., Ullmann, B., and Schilling, T. F. (1995). Stages of embryonic development of the zebrafish. *Dev. Dyn.* 203, 253–310. doi:10.1002/aja.1002030302

Kobayashi, T., Mizuno, H., Imayoshi, I., Furusawa, C., Shirahige, K., Kageyama, R., et al. (2009). The cyclic gene Hes1 contributes to diverse differentiation responses of embryonic stem cells. *Genes Dev.* 23, 1870–1875. doi:10.1101/gad.1823109

Krol, A. J., Roelling, D., Dequéant, M.-L., Tassy, O., Glynn, E., Hattem, G., et al. (2011). Evolutionary plasticity of segmentation clock networks. *Development* 138, 2783–2792. doi:10.1242/dev.063834

Leimeister, C., Dale, K., Fischer, A., Klamt, B., Hrabe de Angelis, M., Radtke, F., et al. (2000). Oscillating expression of c-Hey2 in the presomitic mesoderm suggests that the segmentation clock may use combinatorial signaling through multiple interacting bHLH factors. *Dev. Biol.* 227, 91–103. doi:10.1006/dbio.2000.9884

Lewis, J. (2003). Autoinhibition with transcriptional delay: A simple mechanism for the zebrafish somitogenesis oscillator. *Curr. Biol.* 13, 1398–1408. doi:10.1016/S0960-9822(03)00534-7

Li, Y., Fenger, U., Niehrs, C., and Pollet, N. (2003). Cyclic expression of esr9 gene in Xenopus presomitic mesoderm. *Differentiation.* 71, 83–89. doi:10.1046/j.1432-0436.2003.700608.x

Liao, B. K., Jorg, D. J., and Oates, A. C. (2016). Faster embryonic segmentation through elevated Delta-Notch signalling. *Nat. Commun.* 7, 11861. doi:10.1038/ncomms11861

Lleras Forero, L., Narayanan, R., Huitema, L. F., VanBergen, M., Apschner, A., Peterson-Maduro, J., et al. (2018). *Segmentation of the zebrafish axial skeleton relies on notochord sheath cells and not on the segmentation clock*, 7. doi:10.7554/eLife.33843

Manning, C. S., Biga, V., Boyd, J., Kursawe, J., Ymisson, B., Spiller, D. G., et al. (2019). Quantitative single-cell live imaging links HES5 dynamics with cell-state and fate in murine neurogenesis. *Nat. Commun.* 10, 2835. doi:10.1038/s41467-019-10734-8

Mara, A., Schroeder, J., Chalouni, C., and Holley, S. A. (2007). Priming, initiation and synchronization of the segmentation clock by deltaD and deltaC. *Nat. Cell Biol.* 9, 523–530. doi:10.1038/ncb1578

Maroto, M., Dale, J. K., Dequéant, M. L., Petit, A. C., and Pourquié, O. (2005). Synchronised cycling gene oscillations in presomitic mesoderm cells require cell-cell contact. *Int. J. Dev. Biol.* 49, 309–315. doi:10.1387/ijdb.041958mm

Maruhashi, M., Van De Putte, T., Huylebroeck, D., Kondoh, H., and Higashi, Y. (2005). Involvement of SIP1 in positioning of somite boundaries in the mouse embryo. *Dev. Dyn.* 234, 332–338. doi:10.1002/dvdy.20546

Masamizu, Y., Ohtsuka, T., Takashima, Y., Nagahara, H., Takenaka, Y., Yoshikawa, K., et al. (2006). Real-time imaging of the somite segmentation clock: Revelation of unstable oscillators in the individual presomitic mesoderm cells. *Proc. Natl. Acad. Sci. U. S. A.* 103, 1313–1318. doi:10.1073/pnas.0508658103

Matsuda, M., Hayashi, H., Garcia-ojalvo, J., Yoshioka-kobayashi, K., Kageyama, R., Yamanaka, Y., et al. (2020a). Species-specific segmentation clock periods are due to differential biochemical reaction speeds. *Science* 369, 1450–1455. doi:10.1126/science.aba7668

Matsuda, M., Yamanaka, Y., Uemura, M., Osawa, M., Saito, M. K., Nagahashi, A., et al. (2020b). Recapitulating the human segmentation clock with pluripotent stem cells. *Nature* 580, 124–129. doi:10.1038/s41586-020-2144-9

Matsumiya, M., Tomita, T., Yoshioka-Kobayashi, K., Isomura, A., and Kageyama, R. (2018). ES cell-derived presomitic mesoderm-like tissues for analysis of synchronized oscillations in the segmentation clock. *Development* 145, dev156836. doi:10.1242/dev.156836

McGrew, M. J., Dale, J. K., Fraboulet, S., and Pourquié, O. (1998). The lunatic Fringe gene is a target of the molecular clock linked to somite segmentation in avian embryos. *Curr. Biol.* 8, 979–982. doi:10.1016/S0960-9822(98)70401-4

Monk, N. A. M. (2003). Oscillatory expression of Hes1, p53, and NF-kappaB driven by transcriptional time delays. *Curr. Biol.* 13, 1409–1413. doi:10.1016/S0960-9822(03)00494-9

Morimoto, M., Takahashi, Y., Endo, M., and Saga, Y. (2005). The Mesp2 transcription factor establishes segmental borders by suppressing Notch activity. *Nature* 435, 354–359. doi:10.1038/nature03591

Müller, F., and O'Rahilly, R. (1986). Somitic-vertebral correlation and vertebral levels in the human embryo. *Am. J. Anat.* 177, 3–19. doi:10.1002/aja.1001770103

Nagai, H., Mak, S. S., Weng, W., Nakaya, Y., Ladher, R., Sheng, G., et al. (2011). Embryonic development of the emu, *Dromaius novaehollandiae*. *Dev. Dyn.* 240, 162–175. doi:10.1002/dvdy.22520

Nakaya, M. A., Biris, K., Tsukiyama, T., Jaime, S., Rawls, J. A., Yamaguchi, T. P., et al. (2005). Wnt3a links left-right determination with segmentation and anteroposterior axis elongation. *Development* 132, 5425–5436. doi:10.1242/dev.02149

Nakayama, K., Satoh, T., Igari, A., Kageyama, R., and Nishida, E. (2008). FGF induces oscillations of Hes1 expression and Ras/ERK activation. *Curr. Biol.* 18, 332–334. doi:10.1016/j.cub.2008.03.013

Nitanda, Y., Matsui, T., Matta, T., Higami, A., Kohno, K., Nakahata, Y., et al. (2014). 3′-UTR-dependent regulation of mRNA turnover is critical for differential distribution patterns of cyclic gene mRNAs. *FEBS J.* 281, 146–156. doi:10.1111/febs.12582

Niwa, Y., Masamizu, Y., Liu, T., Nakayama, R., Deng, C. X., Kageyama, R., et al. (2007). The initiation and propagation of Hes7 oscillation are cooperatively regulated by fgf and notch signaling in the somite segmentation clock. *Dev. Cell* 13, 298–304. doi:10.1016/j.devcel.2007.07.013

Niwa, Y., Shimojo, H., Isomura, A., González, A., Miyachi, H., Kageyama, R., et al. (2011). Different types of oscillations in notch and Fgf signaling regulate the spatiotemporal periodicity of somitogenesis. *Genes Dev.* 25, 1115–1120. doi:10.1101/gad.2035311

Nobrega, A., Maia-Fernandes, A. C., and Andrade, R. P. (2021). Altered cogs of the clock: Insights into the embryonic etiology of spondylocostal dysostosis. *J. Dev. Biol.* 9, 5. doi:10.3390/jdb9010005

Oates, A. C., and Ho, R. K. (2002). Hairy/E(spl)-related (Her) genes are central components of the segmentation oscillator and display redundancy with the Delta/Notch signaling pathway in the formation of anterior segmental boundaries in the zebrafish. *Development* 129, 2929–2946. doi:10.1242/dev.129.12.2929

Oates, A. C., Morelli, L. G., and Ares, S. (2012). Patterning embryos with oscillations: Structure, function and dynamics of the vertebrate segmentation clock. *Development* 139 (4), 625–639. doi:10.1242/dev.063735

Ochi, S., Imaizumi, Y., Shimojo, H., Miyachi, H., and Kageyama, R. (2020). Oscillatory expression of Hes1 regulates cell proliferation and neuronal differentiation in the embryonic brain. *Development* 147, dev182204. doi:10.1242/dev.182204

Oginuma, M., Moncuquet, P., Xiong, F., Karoly, E., Guevorkian, K., and Pourquié, O. (2017). A gradient of glycolytic activity coordinates FGF and Wnt signaling during elongation of the body Axis in amniote embryos. *Dev. Cell* 40, 342–353. doi:10.1016/j.devcel.2017.02.001

Özbudak, E. M., and Lewis, J. (2008). Notch signalling synchronizes the zebrafish segmentation clock but is not needed to create somite boundaries. *PLoS Genet.* 4, e15. doi:10.1371/journal.pgen.0040015

Özbudak, E. M., Tassy, O., and Pourquié, O. (2010). Spatiotemporal compartmentalization of key physiological processes during muscle precursor differentiation. *Proc. Natl. Acad. Sci. U. S. A.* 107, 4224–4229. doi:10.1073/pnas.0909375107

Packard, D. S. J. (1980). Somitogenesis in cultured embryos of the Japanese quail, *Coturnix coturnix* japonica. *Am. J. Anat.* 158, 83–91. doi:10.1002/aja.1001580108

Palmeirim, I., Henrique, D., Ish-Horowicz, D., and Pourquié, O. (1997). Avian hairy gene expression identifies a molecular clock linked to vertebrate segmentation and somitogenesis. *Cell* 91, 639–648. doi:10.1016/S0092-8674(00)80451-1

Pascoal, S., Carvalho, C. R., Rodriguez-León, J., Delfini, M. C., Duprez, D., Thorsteinsdóttir, S., et al. (2007). A molecular clock operates during chick autopod proximal-distal outgrowth. *J. Mol. Biol.* 368, 303–309. doi:10.1016/j.jmb.2007.01.089

Prajapati, R. S., Mitter, R., Vezzaro, A., and Ish-Horowicz, D. (2020). Greb1 is required for axial elongation and segmentation in vertebrate embryos. *Biol. Open* 9, bio047290. doi:10.1242/bio.047290

Rayon, T., and Briscoe, J. (2021). Cross-species comparisons and *in vitro* models to study tempo in development and homeostasis. *Interface Focus* 11, 20200069. doi:10.1098/rsfs.2020.0069

Rayon, T., Stamataki, D., Perez-carrasco, R., Garcia-perez, L., Barrington, C., Melchionda, M., et al. (2020). Species-specific pace of development is associated with differences in protein stability. *Science* 369, eaba7667. doi:10.1126/science.aba7667

Resende, T. P., Andrade, R. P., and Palmeirim, I. (2014). Timing embryo segmentation: Dynamics and regulatory mechanisms of the vertebrate segmentation clock. *Biomed. Res. Int.* 2014, 718683. doi:10.1155/2014/718683

Resende, T. P., Ferreira, M., Teillet, M.-A., Tavares, A. T., Andrade, R. P., Palmeirim, I., et al. (2010). Sonic hedgehog in temporal control of somite formation. *Proc. Natl. Acad. Sci. U. S. A.* 107, 12907–12912. doi:10.1073/pnas.1000979107

Riedel-Kruse, I. H., Müller, C., and Oates, A. C. (2007). Synchrony dynamics during initiation, failure, and rescue of the segmentation clock. *Science* 317 (5846), 1911–1915. doi:10.1126/science.1142538

Riley, M. F., Bochter, M. S., Wahi, K., Nuovo, G. J., and Cole, S. E. (2013). Mir-125a-5p-Mediated regulation of lfng is essential for the avian segmentation clock. *Dev. Cell* 24, 554–561. doi:10.1016/j.devcel.2013.01.024

Rodrigues, S., Santos, J., and Palmeirim, I. (2006). Molecular characterization of the rostral-most somites in early somitic stages of the chick embryo. *Gene Expr. Patterns* 6, 673–677. doi:10.1016/j.modgep.2006.01.004

Sieger, D., Tautz, D., and Gajewski, M. (2004). Her11 is involved in the somitogenesis clock in zebrafish. *Dev. Genes Evol.* 214, 393–406. doi:10.1007/s00427-004-0427-z

Sanaki-matsumiya, M., Matsuda, M., Gritti, N., Nakaki, F., Sharpe, J., Trivedi, V., et al. (2022). Periodic formation of epithelial somites from human pluripotent stem cells. *Nat. Commun.* 13, 2325. doi:10.1038/s41467-022-29967-1

Sawada, A., Shinya, M., Jiang, Y.-J., Kawakami, A., Kuroiwa, A., Takeda, H., et al. (2001). Fgf/MAPK signalling is a crucial positional cue in somite boundary formation. *Development* 128 (23), 4873–4880. doi:10.1242/dev.128.23.4873

Schröter, C., Ares, S., Morelli, L. G., Isakova, A., Hens, K., Soroldoni, D., et al. (2012). Topology and dynamics of the zebrafish segmentation clock core circuit. *PLoS Biol.* 10, e1001364. doi:10.1371/journal.pbio.1001364

Schröter, C., and Oates, A. C. (2010). Segment number and axial identity in a segmentation clock period mutant. *Curr. Biol.* 20, 1254–1258. doi:10.1016/j.cub.2010.05.071

Serth, K., Schuster-gossler, K., Cordes, R., and Gossler, A. (2003). Transcriptional oscillation of lunatic fringe is essential for somitogenesis. *Genes Dev.* 17, 912–925. doi:10.1101/gad.250603

Sewell, W., Sparrow, D. B., Smith, A. J., Gonzalez, D. M., Rappaport, F., Dunwoodie, S. L., et al. (2009). Cyclical expression of the Notch/Wnt regulator Nrarp requires modulation by Dll3 in somitogenesis. *Dev. Biol.* 329, 400–409. doi:10.1016/j.ydbio.2009.02.023

Seymour, P. A., Collin, C. A., Egeskov-madsen, A. R., Jørgensen, M. C., Shimojo, H., Imayoshi, I., et al. (2020). Jag1 modulates an oscillatory dll1-notch-hes1 signaling module to coordinate growth and fate of pancreatic progenitors. *Dev. Cell* 52, 731–747. e8. doi:10.1016/j.devcel.2020.01.015

Shankaran, S. S., Sieger, D., Schröter, C., Czepe, C., Pauly, M. C., Laplante, M. A., et al. (2007). Completing the set of h/E(spl) cyclic genes in zebrafish: her12 and her15 reveal novel modes of expression and contribute to the segmentation clock. *Dev. Biol.* 304, 615–632. doi:10.1016/j.ydbio.2007.01.004

Sharma, D., Mirando, A. J., Leinroth, A., Long, J. T., Karner, C. M., Hilton, M. J., et al. (2021). HES1 is a novel downstream modifier of the SHH-GLI3 Axis in the development of preaxial polydactyly. *PLoS Genet.* 17, e1009982. doi:10.1371/journal.pgen.1009982

Sheeba, C. J., Andrade, R. P., and Palmeirim, I. (2012). Joint interpretation of AER/FGF and ZPA/SHH over time and space underlies hairy2 expression in the chick limb. *Biol. Open* 1, 1102–1110. doi:10.1242/bio.20122386

Sheeba, C. J., Andrade, R. P., and Palmeirim, I. (2014). Limb patterning: From signaling gradients to molecular oscillations. *J. Mol. Biol.* 426, 780–784. doi:10.1016/j.jmb.2013.11.022

Sheeba, C. J., Andrade, R. P., and Palmeirim, I. (2016). Mechanisms of vertebrate embryo segmentation: Common themes in trunk and limb development. *Semin. Cell Dev. Biol.* 49, 125–134. doi:10.1016/j.semcdb.2016.01.010

Shifley, E. T., Vanhorn, K. M., Perez-balaguer, A., Franklin, J. D., Weinstein, M., Cole, S. E., et al. (2008). Oscillatory lunatic fringe activity is crucial for segmentation of the anterior but not posterior skeleton. *Development* 135, 899–908. doi:10.1242/dev.006742

Shih, N. P., Francois, P., Delaune, E. A., and Amacher, S. L. (2015). Dynamics of the slowing segmentation clock reveal alternating two-segment periodicity. *Development* 142, 1785–1793. doi:10.1242/dev.119057

Shimojo, H., Isomura, A., Ohtsuka, T., Kori, H., Miyachi, H., Kageyama, R., et al. (2016). Oscillatory control of Delta-like1 in cell interactions regulates dynamic gene expression and tissue morphogenesis. *Genes Dev.* 30, 102–116. doi:10.1101/gad.270785.115

Shimojo, H., Ohtsuka, T., and Kageyama, R. (2008). Oscillations in notch signaling regulate maintenance of neural progenitors. *Neuron* 58, 52–64. doi:10.1016/j.neuron.2008.02.014

Sieger, D., Tautz, D., and Gajewski, M. (2003). The role of Suppressor of Hairless in Notch mediated signalling during zebrafish somitogenesis. *Mech. Dev.* 120, 1083–1094. doi:10.1016/S0925-4773(03)00154-0

Sonnen, K. F., Lauschke, V. M., Uraji, J., Falk, H. J., Petersen, Y., Funk, M. C., et al. (2018). Modulation of phase shift between Wnt and notch signaling oscillations controls mesoderm segmentation. *Cell* 172, 1079–1090. e12. doi:10.1016/j.cell.2018.01.026

Soroldoni, D., Jörg, D. J., Morelli, L. G., Richmond, D. L., Schindelin, J., Jülicher, F., et al. (2014). Genetic oscillations. A Doppler effect in embryonic pattern formation. *Sci. (80-.)* 345, 222–225. doi:10.1126/science.1253089

Soto, X., Biga, V., Kursawe, J., Lea, R., Doostdar, P., Thomas, R., et al. (2020). Dynamic properties of noise and Her6 levels are optimized by miR-9, allowing the decoding of the Her6 oscillator. *EMBO J.* 39, e103558. doi:10.15252/embj.2019103558

Soza-Ried, C., Ozturk, E., Ish-Horowicz, D., and Lewis, J. (2014). Pulses of Notch activation synchronise oscillating somite cells and entrain the zebrafish segmentation clock. *Development* 141, 1780–1788. doi:10.1242/dev.102111

Sparrow, D. B., Chapman, G., Smith, A. J., Mattar, M. Z., Major, J. A., O'Reilly, V. C., et al. (2012). A mechanism for gene-environment interaction in the etiology of congenital scoliosis. *Cell* 149, 295–306. doi:10.1016/j.cell.2012.02.054

Suriben, R., Fisher, D. A., and Cheyette, B. N. R. (2006). Dact1 presomitic mesoderm expression oscillates in phase with Axin2 in the somitogenesis clock of mice. *Dev. Dyn.* 235, 3177–3183. doi:10.1002/dvdy.20968

Takashima, Y., Ohtsuka, T., González, A., Miyachi, H., and Kageyama, R. (2011). Intronic delay is essential for oscillatory expression in the segmentation clock. *Proc. Natl. Acad. Sci. U. S. A.* 108, 3300–3305. doi:10.1073/pnas.1014418108

Tam, P. P. L. (1981). The control of somitogenesis in mouse embryos. *J. Embryol. Exp. Morphol.* 65 103–128. doi:10.1242/dev.65.Supplement.103

Tenin, G., Right, D., Ferjentsik, Z., Bone, R., McGrew, M. J., Maroto, M., et al. (2010). The chick somitogenesis oscillator is arrested before all paraxial mesoderm is segmented into somites. *BMC Dev. Biol.* 10, 24. doi:10.1186/1471-213x-10-24

Tietz, K. T., Gallagher, T. L., Mannings, M. C., Morrow, Z. T., Derr, N. L., Amacher, S. L., et al. (2020). Pumilio response and AU-rich elements drive rapid decay of Pnrc2-regulated cyclic gene transcripts. *Dev. Biol.* 462, 129–140. doi:10.1016/j.ydbio.2020.03.017

Trofka, A., Schwendinger-schreck, J., Brend, T., Pontius, W., Emonet, T., Holley, S. A., et al. (2012). The Her7 node modulates the network topology of the zebrafish segmentation clock via sequestration of the Hes6 hub. *Development* 139, 940–947. doi:10.1242/dev.073544

Tsiairis, C. D., and Aulehla, A. (2016). Self-organization of embryonic genetic oscillators into spatiotemporal wave patterns. *Cell* 164, 656–667. doi:10.1016/j.cell.2016.01.028

Vasiliauskas, D., Laufer, E., and Stern, C. D. (2003). A role for hairy1 in regulating chick limb bud growth. *Dev. Biol.* 262, 94–106. doi:10.1016/S0012-1606(03)00360-9

Ventre, S., Indrieri, A., Fracassi, C., Franco, B., Conte, I., Cardone, L., et al. (2015). Metabolic regulation of the ultradian oscillator Hes1 by reactive oxygen species. *J. Mol. Biol.* 427, 1887–1902. doi:10.1016/j.jmb.2015.03.007

Wahi, K., Friesen, S., Coppola, V., and Cole, S. E. (2017). Putative binding sites for mir-125 family miRNAs in the mouse Lfng 3′UTR affect transcript expression in the segmentation clock, but mir-125a-5p is dispensable for normal somitogenesis. *Dev. Dyn.* 246, 740–748. doi:10.1002/dvdy.24552

Wahl, M. B., Deng, C., Lewandowski, M., and Pourquié, O. (2007). FGF signaling acts upstream of the NOTCH and WNT signaling pathways to control segmentation clock oscillations in mouse somitogenesis. *Development* 134, 4033–4041. doi:10.1242/dev.009167

Wanglar, C., Takahashi, J., Yabe, T., and &Takada, S. (2014). Tbx protein level critical for clock-mediated somite positioning is regulated through interaction between tbx and ripply. *PloS One* 9, e107928. doi:10.1371/journal.pone.0107928

Webb, A. B., Lengyel, I. M., Jörg, D. J., Valentin, G., Jülicher, F., Morelli, L. G., et al. (2016). Persistence, period and precision of autonomous cellular

oscillators from the zebrafish segmentation clock. *Elife* 5, e08438. doi:10.7554/eLife.08438

Wiedermann, G., Bone, R. A., Silva, J. C., Bjorklund, M., Murray, P. J., Dale, J. K., et al. (2015). A balance of positive and negative regulators determines the pace of the segmentation clock. *eLife* 4, e05842. doi:10.7554/eLife.05842

William, D. A., Saitta, B., Gibson, J. D., Traas, J., Markov, V., Gonzalez, D. M., et al. (2007). Identification of oscillatory genes in somitogenesis from functional genomic analysis of a human mesenchymal stem cell model. *Dev. Biol.* 305, 172–186. doi:10.1016/j.ydbio.2007.02.007

Williams, D. R., Shifley, E. T., Braunreiter, K. M., and Cole, S. E. (2016). Disruption of somitogenesis by a novel dominant allele of Lfng suggests important roles for protein processing and secretion. *Development* 143, 822–830. doi:10.1242/dev.128538

Winkler, C., Elmasri, H., Klamt, B., Volff, J.-N., and Gessler, M. (2003). Characterization of hey bHLH genes in teleost fish. *Dev. Genes Evol.* 213, 541–553. doi:10.1007/s00427-003-0360-6

Wright, D., Ferjentsik, Z., Chong, S.-W., Qiu, X., Yun-Jin, J., Malapert, P., et al. (2009). Cyclic Nrarp mRNA expression is regulated by the somitic oscillator but Nrarp protein levels do not oscillate. *Dev. Dyn.* 238, 3043–3055. doi:10.1002/dvdy.22139

Xie, Z. R., Yang, H., and Hwang, M. J. (2007). The role of microRNA in the delayed negative feedback regulation of gene expression. *Biochem. Biophys. Res. Commun.* 358, 722–726. doi:10.1016/j.bbrc.2007.04.207

Yaman, Y. I., Huang, R., and Ramanathan, S. (2022). Coupled organoids reveal that signaling gradients drive traveling segmentation clock waves during human axial morphogenesis. *bioRxiv* 2005, 491359. doi:10.1101/2022.05.10.491359

Yoshioka-Kobayashi, K., Matsumiya, M., Niino, Y., Isomura, A., Kori, H., Miyawaki, A., et al. (2020). Coupling delay controls synchronized oscillation in the segmentation clock. *Nature* 580 (7801), 119–123. doi:10.1038/s41586-019-1882-z

Yoshiura, S., Ohtsuka, T., Takenaka, Y., Nagahara, H., Yoshikawa, K., Kageyama, R., et al. (2007). Ultradian oscillations of Stat, Smad, and Hes1 expression in response to serum. *Proc. Natl. Acad. Sci. U. S. A.* 104, 11292–11297. doi:10.1073/pnas.0701837104

Zhang, N., Norton, C. R., and Gridley, T. (2002). Segmentation defects of Notch pathway mutants and absence of a synergistic phenotype in lunatic fringe/radical fringe double mutant mice. *Genesis* 33, 21–28. doi:10.1002/gene.10081

Zinani, O. Q. H., Keseroğlu, K., Ay, A., and Özbudak, E. M. (2021). Pairing of segmentation clock genes drives robust pattern formation. *Nature* 589, 431–436. doi:10.1038/s41586-020-03055-0

frontiers | Frontiers in Physics

TYPE Original Research
PUBLISHED 02 September 2022
DOI 10.3389/fphy.2022.933915

OPEN ACCESS

EDITED BY
Pau Formosa-Jordan,
Max Planck Institute for Plant Breeding Research, Germany

REVIEWED BY
James Cotterell,
European Molecular Biology Laboratory, Spain
Francis Corson,
UMR8023 Le Laboratoire de Physique de l'ENS, France

*CORRESPONDENCE
Luis G. Morelli,
morelli.luis.g@gmail.com

SPECIALTY SECTION
This article was submitted to Biophysics, a section of the journal Frontiers in Physics

RECEIVED 01 May 2022
ACCEPTED 29 July 2022
PUBLISHED 02 September 2022

CITATION
Fernández Arancibia SM, Oates AC, Schulte-Merker S and Morelli LG (2022), Reaction wavefront theory of notochord segment patterning. *Front. Phys.* 10:933915. doi: 10.3389/fphy.2022.933915

Reaction wavefront theory of notochord segment patterning

Sol M. Fernández Arancibia[1], Andrew C. Oates[2], Stefan Schulte-Merker[3] and Luis G. Morelli[1,4,5]*

[1]Instituto de Investigación en Biomedicina de Buenos Aires (IBioBA)—CONICET/Partner Institute of the Max Planck Society, Polo Científico Tecnológico, Buenos Aires, Argentina, [2]Institute of Bioengineering, École polytechnique fédérale de Lausanne, Lausanne, Switzerland, [3]Institute for Cardiovascular Organogenesis and Regeneration, Faculty of Medicine, WWU Münster, Münster, Germany, [4]Departamento de Física, FCEyN UBA, Ciudad Universitaria, Buenos Aires, Argentina, [5]Department of Systemic Cell Biology, Max Planck Institute for Molecular Physiology, Dortmund, Germany

The vertebrate axis is segmented into repetitive structures, the vertebrae. In fish, these segmented structures are thought to form from the paraxial mesoderm and the adjacent notochord. Recent work revealed an autonomous patterning mechanism in the zebrafish notochord, with inputs from the segmented paraxial mesoderm. The notochord pattern is established in a sequential manner, progressing from anterior to posterior. Building on this previous work, here, we propose a reaction wavefront theory describing notochord patterning in zebrafish. The pattern is generated by an activator–inhibitor reaction–diffusion mechanism. Cues from the paraxial mesoderm are introduced as a profile of inhibitor sinks. Reactions are turned on by a wavefront that advances from anterior to posterior. We show that this reaction wavefront ensures that a pattern is formed sequentially, in register with the cues, despite the presence of fluctuations. We find that the velocity and shape of the reaction wavefront can modulate the prevalence of defective patterns. Normal patterning is supported in a wide range of sink profile wavelengths, while a minimum sink strength is required for the pattern to follow the cues. The theory predicts that distinct defect types occur for small or large wavelengths. Thus, the reaction wavefront theory provides a possible scenario for notochord patterning, with testable predictions that prompt future experiments.

KEYWORDS

vertebrate segmentation, pattern formation theory, reaction–diffusion, activator–inhibitor, noise

1 Introduction

Biological pattern formation underlies the structure of tissues and organs that form during embryonic development [1]. The formation of these structures results from an interplay between gene expression patterns and cell movements [2–5]. In developing tissues, cells regulate the expression of different genes and communicate with neighboring cells by means of signals. Biochemical noise due to fluctuations in molecule number and the stochastic nature of gene expression hamper the formation of patterns [6]. However,

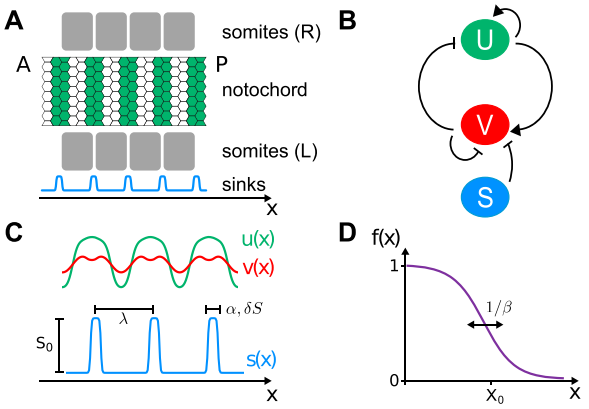

FIGURE 1
(A) Scheme showing the dorsal view of a portion of the segmented notochord (green bands) extending from anterior (A) to posterior (P). In the embryo, somites (gray squares) are located on the left and right sides relative to the notochord. The sink profile (light blue line) matches somite boundaries. **(B)** Interactions between activator *U*, inhibitor *V*, and the inhibitor sinks *S*. Pointed arrows indicate activation, and blunt-ended arrows indicate inhibition. **(C)** Activator (green line) and inhibitor (red line) activities. Inhibitor sinks profile (light blue line) of sink strength S_0, wavelength λ, steepness α, and width $2\delta S$. **(D)** Reaction wavefront profile $f(x)$ of steepness β.

embryonic development is a very reproducible process. Thus, a general question is how patterns form reliably despite the presence of biochemical fluctuations.

The vertebrate body plan is organized around the vertebral column, a structure of repetitive segments—the vertebrae—running from the head to tail. An early pattern of axial segments is laid out during somitogenesis. Somites form from the paraxial mesoderm tissue on both sides of the embryo midline. Somitogenesis occurs from anterior to posterior in a rhythmic manner and is controlled by a molecular genetic oscillator called the segmentation clock [7–11]. Later in development, the bone-forming cells derived from the somites are reorganized in a process termed re-segmentation, and this pattern is eventually translated into an array of vertebrae [12].

In some vertebrates, such as amniotes, it is thought that the segmented vertebral structure derives entirely from previously established somites [13]. However, fish mutants that have an impaired segmentation clock show normal formation of the majority of their vertebral centra [14–16]. This suggests that, at least in fish, normal somites are not required to determine the structure of the vertebral centrum. Still, a mutant which has a slower segmentation clock produces fewer vertebrae [17], indicating that vertebral structure does receive information from segmentation clock-derived somite segments.

Recently, it was shown that vertebral patterning is concomitantly driven by the notochord in zebrafish [16]. The notochord is an unsegmented cylinder formed by mesoderm cells that lie along the anteroposterior axis of the embryo and is flanked to both sides by somites (Figure 1A). In teleosts—fish with bones—the notochord comprises a layer of epithelial sheath cells, called chordoblasts, enveloping a column of large vacuolated cells that provide mechanical support [18, 19]. New evidence indicates that there is an autonomous patterning mechanism in the notochord that is influenced but not determined by the pre-existing somite pattern in the adjacent tissue [16].

Although the nature of the zebrafish notochord patterning mechanism remains unknown, an autonomous reaction–diffusion system with an activator and an inhibitor operating in the notochord sheath cells has been proposed [16]. The cues provided by the paraxial mesoderm pattern were introduced as a distribution of inhibitor sinks. Starting from an anteriorly localized perturbation, this theory proved capable of producing an autonomous pattern, sequentially adding notochord segments from anterior to posterior in register with the cues. However, this theory did not explicitly account for random perturbations and their effects on patterning.

Here, we extend this previous theory, introducing a wavefront that moves from anterior to posterior, turning on reactions in its wake. Such reaction wavefront could have a biological origin in a molecular maturation gradient invading the notochord from the anterior. Introducing measures to characterize defective patterns, we analyze the robustness of the reaction wavefront theory upon random initial perturbations and dynamic fluctuations. We explore how the shape and velocity of the reaction wavefront modulate defect rate and analyze the effects of fluctuations in the sink positions and strength.

2 Theory

Here, we describe the notochord as a one-dimensional system. To describe pattern formation in the notochord sheath cells, we propose a reaction–diffusion system with an activator U and an inhibitor V. As we do not know the molecular components involved and their interactions, here, we follow [16] and consider a generic FitzHugh–Nagumo model to describe activator and inhibitor dynamics [20].

$$\frac{\partial U}{\partial t} = D_U \frac{\partial^2 U}{\partial x^2} + k_1 U - k_3 U^3 - k_4 V + k_0 \tag{1}$$

$$\frac{\partial V}{\partial t} = D_V \frac{\partial^2 V}{\partial x^2} + k_5 U - k_6 V - SV, \tag{2}$$

where D_U and D_V are diffusion coefficients, and k_i are reaction rate constants. The effective variables $U(x, t)$ and $V(x, t)$ depend on position x and time t and represent activity levels that could be associated with actual physical concentrations through an unknown non-linear mapping.

Both species have positive linear terms for the activator and negative linear terms for the inhibitor. There is a cubic term for the activator that limits growth and enables stabilization of steady states (Figure 1B). The effect of the segmentation clock input is introduced as an additional degradation term for the inhibitor, spatially modulated by $S = S(x)$ (Figures 1A–C). This spatial modulation takes the form of an inhibitor sinks profile $S(x) = S_0 s(x)$, where S_0 is a rate constant representing the sink strength and $s(x)$ is a dimensionless profile shape.

In order to reduce the number of parameters of the model, we introduce an activity scale U_0 and a timescale T_0 and define new dimensionless variables u, v, x', and t' that verify

$$U = U_0 u, \quad V = U_0 v, \quad x = L_0 x', \quad t = T_0 t', \tag{3}$$

where L_0 is a fixed length that relates the notochord length with the dimensionless system size. We can rewrite Eqs 1, 2 in terms of the new variables. Dropping primes to simplify the notation and setting the source term $k_0 = 0$,

$$\frac{U_0}{T_0}\frac{\partial u}{\partial t} = \frac{D_U U_0}{L_0^2}\frac{\partial^2 u}{\partial x^2} + k_1 U_0 u - k_3 U_0^3 u^3 - k_4 U_0 v, \tag{4}$$

$$\frac{U_0}{T_0}\frac{\partial v}{\partial t} = \frac{D_V U_0}{L_0^2}\frac{\partial^2 v}{\partial x^2} + k_5 U_0 u - k_6 U_0 v - S_0 s(x) U_0 v. \tag{5}$$

These two equations have units of activity over time, so we multiply both by T_0/U_0 to render them dimensionless. Regrouping parameters:

$$\frac{\partial u}{\partial t} = \frac{D_U T_0}{L_0^2}\frac{\partial^2 u}{\partial x^2} + k_1 T_0\left(u - \frac{k_3 U_0^2}{k_1}u^3 - \frac{k_4}{k_1}v\right), \tag{6}$$

$$\frac{\partial v}{\partial t} = \frac{D_V T_0}{L_0^2}\frac{\partial^2 v}{\partial x^2} + k_1 T_0\left(\frac{k_5}{k_1}u - \frac{k_6}{k_1}v - \frac{S_0}{k_1}s(x)v\right). \tag{7}$$

Selecting a timescale and an activity scale through the relations

$$\frac{D_U T_0}{L_0^2} \equiv 1 \quad \text{and} \quad \frac{k_3 U_0^2}{k_1} \equiv 1 \tag{8}$$

and introducing definitions for the remaining dimensionless groups

$$\delta \equiv \frac{D_V}{D_U}, \quad \gamma \equiv \frac{k_1 L_0^2}{D_U}, \quad \kappa_i \equiv \frac{k_i}{k_1} \quad s_0 \equiv \frac{S_0}{k_1}, \tag{9}$$

we obtain

$$\frac{\partial u}{\partial t} = \frac{\partial^2 u}{\partial x^2} + \gamma\left(u - u^3 - \kappa_4 v\right), \tag{10}$$

$$\frac{\partial v}{\partial t} = \delta\frac{\partial^2 v}{\partial x^2} + \gamma\left(\kappa_5 u - \kappa_6 v - s_0 s(x) v\right). \tag{11}$$

For the inhibitor sinks profile shape $s(x)$, we choose a combination of opposing tanh (. . .) functions that compose localized peaks of steepness $\alpha = 100$ and width $2\delta s = 0.1$ separated by a wavelength λ:

$$s(x) = \frac{1}{2}\sum_i \left(-\tanh\left(\alpha\left(-x_i + x - \delta s\right)\right) + \tanh\left(\alpha\left(-x_i + x + \delta s\right)\right)\right). \tag{12}$$

A first sink is placed at $\lambda/2$, and positions x_i of consecutive sinks are determined by the wavelength λ (Figure 1C).

Starting from an anteriorly localized perturbation in otherwise uniform, vanishing initial conditions, the theory described so far is capable of producing an autonomous pattern, sequentially adding notochord segments from anterior to posterior in register with the cues [16]. However, it appears unlikely that activity values for the activator and inhibitor are perfectly uniform across the notochord. Random perturbations to the initial activities may occur, for example, due to leaky transcription causing stochastic bursts [21]. In the presence of such random initial perturbations, the theory cannot account for the observed sequential segmentation [16]. Moreover, stochasticity in gene expression may introduce noise in the dynamics of both the activator and the inhibitor [6, 22]. To account for such dynamic fluctuations, we include a white noise term

$$\frac{\partial u}{\partial t} = \frac{\partial^2 u}{\partial x^2} + \gamma\left(u - u^3 - \kappa_4 v\right) + \sigma\xi_u(x,t), \tag{13}$$

$$\frac{\partial v}{\partial t} = \delta\frac{\partial^2 v}{\partial x^2} + \gamma\left(\kappa_5 u - \kappa_6 v - s_0 s(x) v\right) + \sigma\xi_v(x,t), \tag{14}$$

where $\xi_u(x,t)$ and $\xi_v(x,t)$ are Gaussian processes with zero mean and uncorrelated in space, time, and between themselves, and σ sets the noise strength.

Here, we extend this theory to restore sequential patterning in the presence of noise in the initial condition and dynamics. With the scaling that we chose in Eq. 8, all reaction rates are weighted by the dimensionless parameter γ, which sets the relative strength of reaction terms. By allowing γ to depend on position and time, this dimensionless formulation permits a spatiotemporal control of the balance between reaction rates and diffusion. We use this feature to introduce a wavefront that moves from anterior to posterior, turning reactions on in its wake. Ahead of such wavefront, reactions are disabled and cannot trigger spontaneous patterning from random fluctuations. Behind the wavefront, reactions turn on and can generate patterns. Thus, we implement a reaction wavefront in the theory through the space and time dependence in parameter γ:

$$\frac{\partial u}{\partial t} = \frac{\partial^2 u}{\partial x^2} + \gamma(x,t)\left(u - u^3 - \kappa_4 v\right) + \sigma\xi_u(x,t), \tag{15}$$

$$\frac{\partial v}{\partial t} = \delta\frac{\partial^2 v}{\partial x^2} + \gamma(x,t)\left(\kappa_5 u - \kappa_6 v - s_0 s(x) v\right) + \sigma\xi_v(x,t), \tag{16}$$

where $\gamma(x, t)$ is a wavefront of invariant shape

$$f(x) = \frac{1}{2}\left(1 - \tanh\left(\beta\left(-X_0 + x\right)\right)\right), \tag{17}$$

TABLE 1 Reaction wavefront theory dimensionless parameters: default values and description.

Model parameters

Parameter	Value	Description
δ	100	Relative diffusion coefficient
γ_0	1,000	Relative reactions strength
κ_4	1	Reaction rate constant Eq. 15
κ_5	10	Reaction rate constant Eq. 16
κ_6	5	Reaction rate constant Eq. 16
μ	0.01	Mean initial activity of u and v
σ_0	0.01	Initial standard deviation of u and v
σ	0.1	Noise strength
v	81.77	Wavefront velocity
β	5	Wavefront steepness
X_0	0	Wavefront initial position
λ	0.57	Sink profile wavelength
$\Delta\lambda$	0	Sink position fluctuation amplitude
s_0	80	Sink strength
Δs_0	0	Sink strength fluctuation amplitude

moving from anterior to posterior with a velocity v. Thus, $\gamma(x, t) = \gamma_0 f(x - vt)$, where γ_0 is the relative strength of reactions. The wavefront profile $f(x)$ is a dimensionless sigmoidal function that takes values between 0 and 1, with front steepness β, and centered at X_0 (Figure 1D).

Next, we solve partial differential equations using a custom Python implementation of the Heun method [23]. Spatial discretization length is $\Delta x = 0.01$, and time discretization is $\Delta t = 0.9\Delta x^2/(2.10^3)$. Unless something else is specified, default parameter values are given in Table 1.

Solutions to the reaction wavefront theory with random initial conditions and noise can produce a segmented pattern sequentially (Figure 2A). Without a reaction wavefront, random perturbations are quickly amplified in the entire domain and trigger non-sequential defective pattern formation (Figure 2B and Supplementary Video S2). This suggests a possible test for the wavefront scenario that could, in principle, be implemented in an embryonic experiment. A small perturbation within the posterior region of the domain representing the notochord dies out in a reaction wavefront scenario (Figure 3A). In contrast, in the absence of a reaction wavefront, such perturbation is amplified and trigger segment formation occurs in both directions, disrupting the sequential segmentation from anterior to posterior and likely generating a defective pattern (Figure 3B and Supplementary Video S3). Thus, introducing a bead soaked in the activator within the posterior region of the unsegmented notochord would provide a test for the wavefront hypothesis. In the next section, we study how fluctuations induce pattern formation defects in the reaction wavefront theory.

3 Noise and initial conditions

A normal pattern is here defined by a one-to-one correspondence between sinks and activator peaks (Figure 2A). When this correspondence is broken, we call the pattern defective (Figure 2B). One source of defects is local pattern inversions, where a trough occurs at a sink position in place of a peak (Figure 4A). These pattern inversions occur because solutions to the partial differential Eqs. 15 and 16 have an inversion symmetry: if (u, v) is a solution, then so is $(-u, -v)$. Consequently, in the presence of noise, the pattern may switch locally between peaks and troughs at sink positions. Solutions and their inverses are separated by an unstable vanishing solution (0, 0). For initial conditions with a vanishing mean value $\mu = 0$, the resulting patterns often switch between the two solutions. Thus, the value of μ may affect the formation of normal patterns. We also expect that increasing noise strength σ will interfere with the formation of normal patterns. Thus, we first set to explore pattern robustness when these parameters change, with the aim of constructing quantitative maps that we can use to guide further exploration of the theory (Figure 4).

Two types of pattern defects occur: 1) misplaced peaks are not aligned with any inhibitor sink, and 2) unmatched sinks do not have a matching activator peak (Figure 4A). In this work, we have set a threshold distance between sinks and peaks for segments to be classified as normal or defective. When the distance between an activator peak and a sink is less than 10% of the mean distance between sinks, we consider this a match, and it is classified as a normal segment. Peaks without a match are defined as misplaced peaks, and sinks without a match are defined as unmatched sinks. The frequencies of these two defect types provide measures for the number of errors in the resulting pattern: f_{mp} is the ratio between the number of misplaced peaks and the total number of peaks in the pattern, and f_{us} is the ratio between the number of unmatched sinks and the total number of sinks. Both these measures take values between zero and one. We assess the effects of noise and initial activities on individual patterns by counting the occurrence of these defect types (Figures 4B–G). The fraction of misplaced peaks f_{mp} and unmatched sinks f_{us} increases with noise strength (Figures 4C,F). This means that individual patterns deteriorate with increasing noise. However, defect frequencies f_{mp} and f_{us} decrease with increasing initial activity μ (Figures 4D,G).

While f_{mp} and f_{us} characterize the frequency of defects in individual patterns, we are also interested in quantifying defective patterns at the population level. Thus, we introduce the fraction of defective patterns f_d as the ratio between the number of realizations that contain at least one defect to the total number of realizations. This fraction of defective patterns increases with noise strength σ and

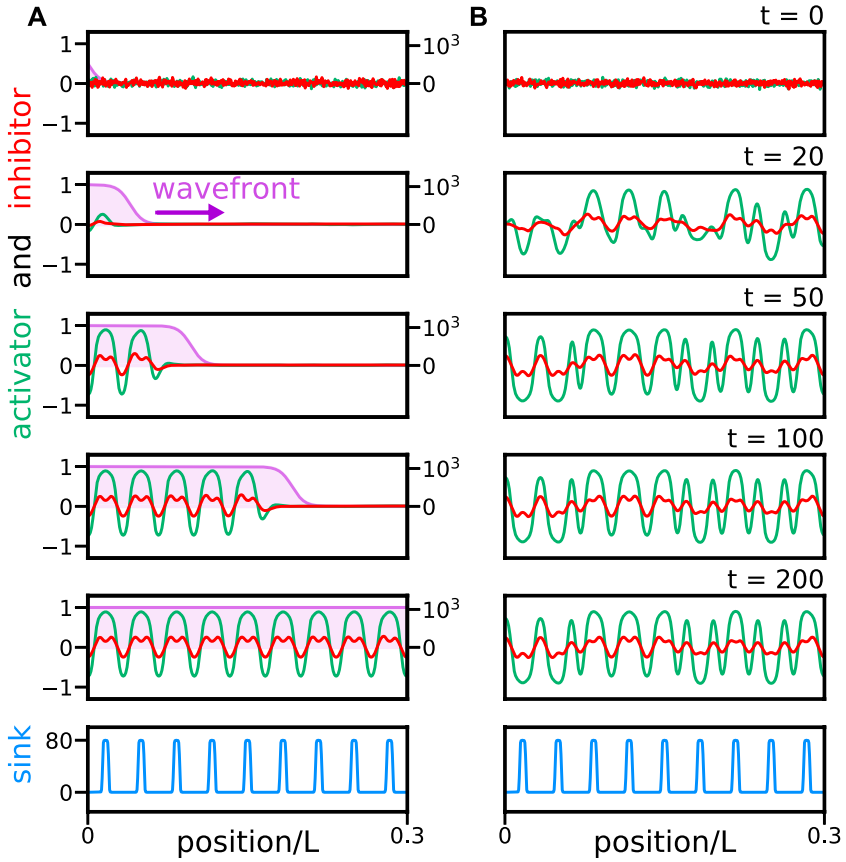

FIGURE 2
Reaction wavefront theory can produce a sequential pattern without defects in the presence of noise. Snapshots of solutions **(A)** of reaction wavefront theory Eqs 15, 16, and **(B)** Eqs 13, 14 lacking a reaction wavefront. Activator (green line) and inhibitor (red line) dimensionless activities (left axis scale) together with reaction wavefront $\gamma(x, t)$ (purple line and shade, right axis scale) at different times. The bottom panel shows the inhibitor sink profile (light blue line). Position is scaled by the dimensionless system size, $L = 30\lambda = 17.1$, which is chosen to accommodate 30 segments, similar to the 31 segments in zebrafish [17, 24]. Time is expressed in frames and 1 frame ≈ 0.0004 time units. Random initial conditions have mean $\mu = 0.01$ and standard deviation $\sigma_0 = 0.05$. Other parameters are as in Table 1.

decreases with increasing initial activity μ (Figures 4H–J). We observe that f_d can become large while f_{mp} and f_{us} remain relatively low (Figures 4B,E,H). In embryological terms, the fraction of defective patterns is a measure of phenotype penetrance at the population level, and the frequency of defects in individual patterns provides a measure of phenotype expressivity within individual embryos. While these quantities should be related to some extent, this relation is not straightforward since the occurrence of a defect in a pattern might favor further defects.

In summary, these results show how increasing noise causes more pattern defects and defective patterns. In contrast, shifting the mean of the initial condition away from the boundary of the unstable vanishing solution reduces defect prevalence (Figure 4). In the following sections, we use these maps to choose values of σ and μ to further explore other sources of noise and variability in the theory.

4 Wavefront velocity and shape

In addition to dynamic activity fluctuations, the other novel component in the theory is the reaction wavefront $\gamma(x, t)$. This reaction wavefront moves with velocity v, and its shape is determined by the wavefront profile steepness β (Eq. 17 and Figure 1D).

In the absence of noise and reaction wavefront, starting from a small anterior perturbation with otherwise vanishing initial conditions, a pattern forms sequentially, invading the unpatterned region with a natural propagation velocity v_0 [16]. To determine the value of v_0, we set a threshold activity value for the activator and determine the trajectory of the posterior-most position where the pattern activity exceeds this threshold. A linear fit of this trajectory returns the value $v_0 = 81.77$ that we use to scale velocities.

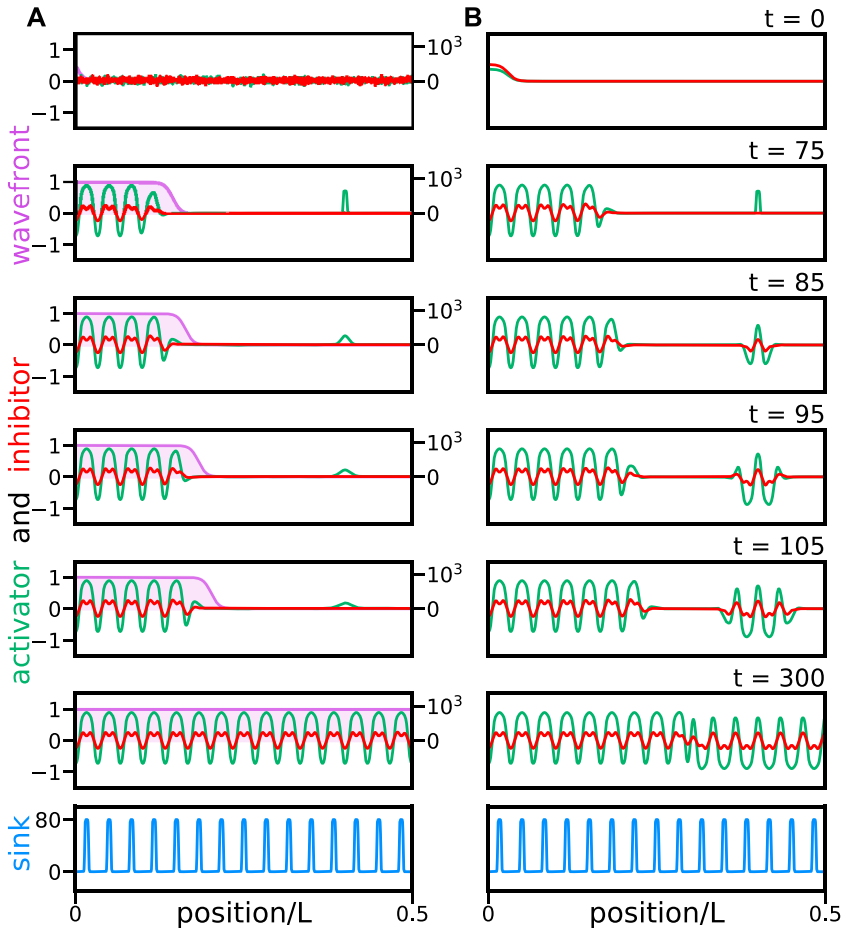

FIGURE 3
A perturbation in the posterior region of the notochord vanishes in a reaction wavefront scenario. Snapshots of solutions **(A)** of reaction wavefront theory Eqs 15, 16, and **(B)** Eqs 13, 14 with $\sigma = 0$, without a reaction wavefront. A perturbation is introduced in the activator at frame $t = 75$. Color coding and plot layout are as in Figure 2. Initial conditions are **(A)** random with mean $\mu = 0.01$ and standard deviation $\sigma_0 = 0.05$ and **(B)** vanishing except for the anterior perturbation. Other parameters are as in Table 1. Time is expressed in frames and 1 frame ≈ 0.0004 time units.

We find that decreasing the reaction wavefront velocity below $v/v_0 = 1$ can reduce the fraction of defective patterns (Figure 5A). This indicates that retarding pattern propagation may be favorable for normal pattern formation. Normal pattern formation is also affected by the shape of the reaction wavefront (Figure 5B). The fraction of defective patterns peaks around $\beta = 2$, decaying both above and below this value. However, for small β, the wavefront profile becomes too gradual and sequential pattern formation is lost, compromising a key role of the reaction wavefront (Supplementary Video S5). Thus, a steeper reaction wavefront would be beneficial for normal pattern formation.

In summary, both the velocity and shape of the reaction wavefront critically affect the fraction of defective patterns. A slower and steeper wavefront could have a dual role: 1) allowing for sequential pattern formation and 2) rendering patterning more robust in the presence of random fluctuations.

5 Sink profile wavelength and strength

The forming notochord segments should align with previously formed somites in the adjacent tissue. It is thought that the adjacent paraxial mesoderm provides signals that influence notochord segment formation to be in register with somites [16]. In the theory, paraxial mesoderm signals are introduced as an inhibitor sinks profile $s(x)$ with a characteristic wavelength and strength s_0 (Eq. 12). In the following section, we explore how the reaction wavefront theory responds to changes in this sinks profile. To decouple defects due to dynamic noise while perturbing sink wavelength and strength, we set parameters $\sigma = 0.1$ and $\mu = 0.01$ with a very low fraction of defective realizations $f_d \approx 0.02$ (Figure 4H).

Alterations to the segmentation clock can induce changes in somite length, as in the case of *hes6* mutant [17]. Therefore,

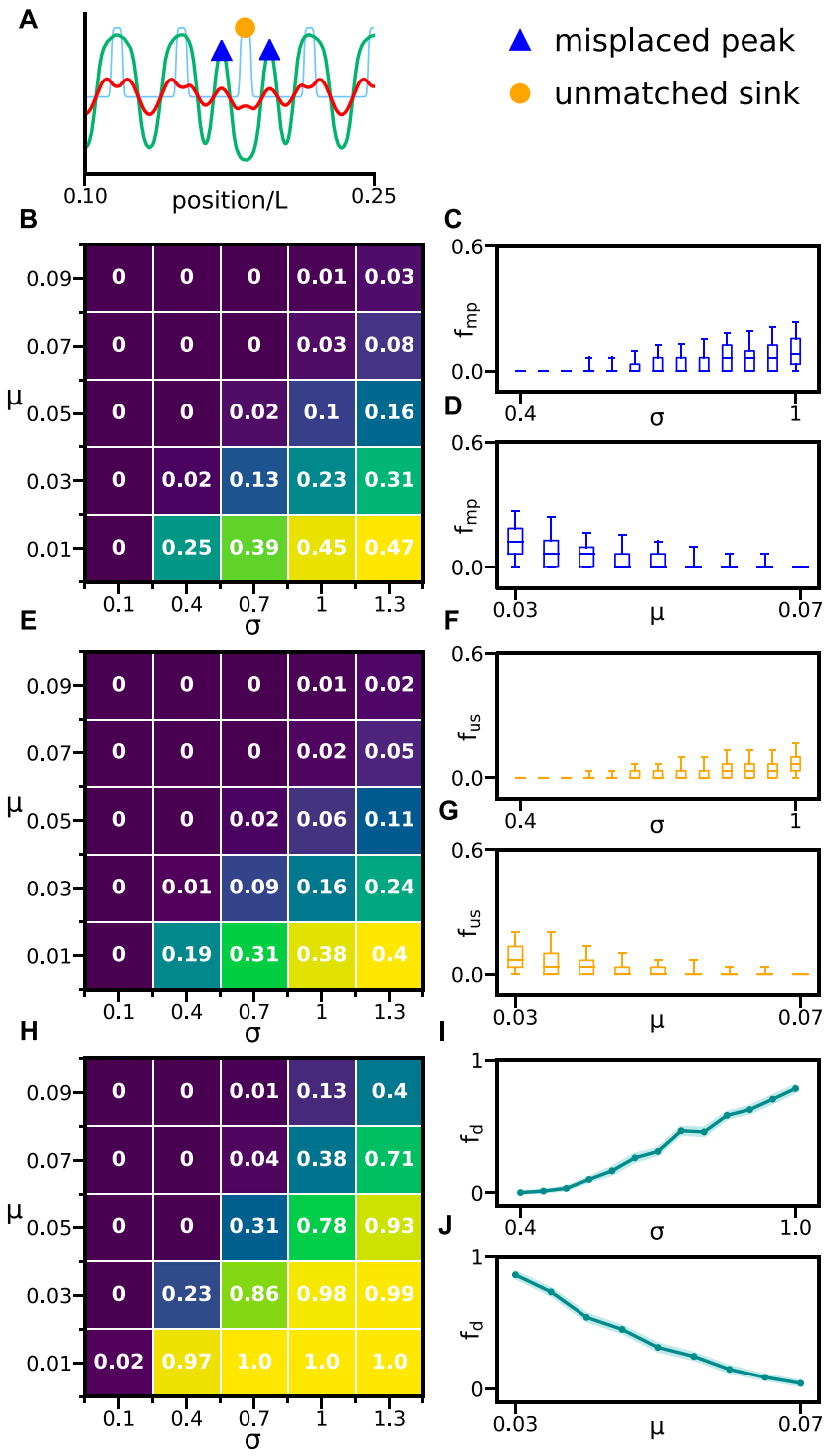

FIGURE 4
Effects of initial activity and noise in pattern formation. **(A)** Activator (green line), inhibitor (red line) patterns, and inhibitor sink profile (light blue line) showing misplaced peaks (blue triangles) and an unmatched sink (orange dot). **(B)** ⟨fmp⟩ for different values of μ and σ. **(C)** fmp vs. σ for fixed μ = 0.05. **(D)** fmp vs. μ for fixed σ = 0.7. **(E)**⟨fus⟩ for different values of μ and σ. **(F)**fus vs. σ for fixed μ = 0.05. **(G)**fus vs. μ for fixed σ = 0.7. **(H)** fd for different values of μ and σ. **(I)** fd vs. σ for fixed μ = 0.05. **(J)** fd vs. μ for fixed σ = 0.7. **(I and J)** Errors in fd (dark cyan shade) are the standard deviation determined using a statistical bootstrap. **(C,D,F, and G)** Middle line marks the median, box limits are 25 and 75 percentiles, and whiskers are 5 and 95 percentiles. Brackets ⟨.⟩ denote average over realizations. Other parameters are as in Table 1. In all cases, we performed 300 realizations for each parameter combination.

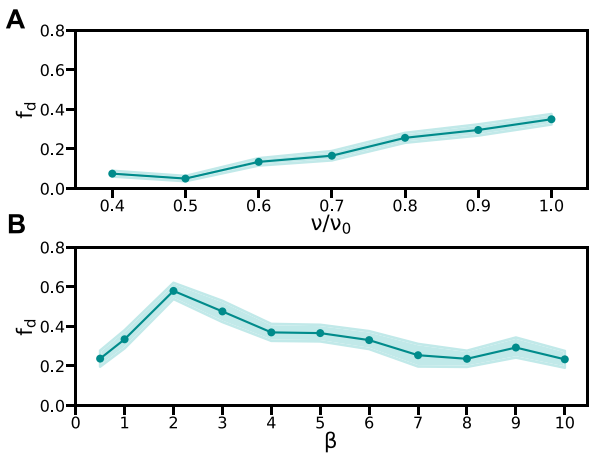

FIGURE 5
Reaction wavefront can modulate defect rates. Fraction of defective patterns f_d vs. **(A)** relative velocity ν/ν_0 and **(B)** steepness β. Errors in f_d (dark cyan shade) are the standard deviation determined using a statistical bootstrap. Other parameters are as in Table 1, except $\mu = 0.05$ and $\sigma = 0.7$. In all cases, we performed 300 realizations of each simulation.

we next explore whether pattern formation can adapt to different sink profile wavelengths. In the absence of a wavefront and noise, Eqs 10, 11, and for a vanishing sink profile $s_0 = 0$, the unforced reaction–diffusion system selects a natural wavelength $\lambda_0 = 0.398$ that is determined by parameters values (Supplementary Material). Thus, we compute defect fractions for different sink profile wavelengths λ, taking this natural wavelength as a reference (Figure 6C). We find that for small profile wavelengths, the predominant type of defect is unmatched sinks (Figures 6A,C and Supplementary Video S6A). The reason for this may be that the system often fails to produce activator peaks at the short distances imposed by the sinks. In contrast, for sufficiently large wavelengths, the predominant type of defect is misplaced peaks (Figures 6B,C and Supplementary Video S6B). Here the reason maybe that, with enough space in between sinks, the system tries to produce a segment of the shorter natural wavelength, so activator peaks are often intercalated. For intermediate profile wavelength values, we find a broad range where no defects occur (Figure 6C). It is interesting that this defect-free range is centered at $\lambda/\lambda_0 \approx 1.4$, which is away from the natural wavelength λ_0. This may result from a non-trivial interplay between sinks and the unforced reaction–diffusion system, which alters the patterning mode.

In addition to wavelength fluctuations, another possible source of sink profile variability is the sink strength s_0. To characterize the effects of sink strength on pattern formation, we first alter s_0 uniformly across the axis. For large sink strength, the fractions of defects are vanishing (Figures 6E,F). As the sink strength is reduced, defect fractions abruptly grow to large values (Figures 6D,F). When the sink strength is small, it may be insufficient to entrain the formation of a segment at that position. With this resolution, the onset of defects appears to occur at a sink strength threshold $s_0 = 30$.

Thus, segments form normally above a critical sink strength and for a wide range of sink profile wavelengths. This tolerance for different wavelengths is consistent with the *hes6* mutant phenotype. For short sink profile wavelengths, defects are predominantly unmatched sinks, while for large wavelengths, misplaced peaks dominate the defective patterns.

6 Sink profile fluctuations

So far, we have considered sink profiles with a fixed wavelength, where sink positions are regularly spaced. However, the segmentation clock that drives somite formation is subject to fluctuations that may cause segment length variability [16, 24, 25]. Thus, we next ask how the pattern responds to local fluctuations in individual sink positions. To introduce sink position fluctuations, we generate the sink profile sequentially, placing sinks at perturbed positions a distance $\lambda + \delta_\lambda$ from the previous sink. Here, δ_λ is a random variable uniformly distributed in the interval $\pm\Delta\lambda$, and $\Delta\lambda$ controls the amplitude of sink position fluctuations. We find that the reaction wavefront theory is robust against small position fluctuations (Figure 7A). Up to $\Delta\lambda/\lambda = 0.25$, we see a vanishing fraction of both defect types, which then appear to grow gradually (Figures 7B and C). Here, fluctuations in sink position are relative to a mean wavelength $\lambda = 0.57$, so $\lambda/\lambda_0 \approx 1.43$ is close to the midpoint of the defect-free region in Figure 6C. The defect-free region spans a range that extends about 20% above and below this midpoint, so fluctuations of up to 25% of the mean wavelength are mostly included in the defect-free region of Figure 6C. Thus, the observed onset of defects in Figure 7C may be due to the fact that fluctuations of about 25% can cause consecutive sinks that are either closer or further apart than the supported wavelengths in the defect-free region.

In the embryo, the information provided by the paraxial mesoderm could be variable along the segmenting axis. Thus, a relevant question is how the reaction wavefront theory responds to sink strength variability. We set individual sink strengths to $s_0 + \delta_s$, where δ_s is a random variable uniformly distributed in the interval $\pm\Delta s_0$, and Δs_0 controls the amplitude of sink strength fluctuations. The fraction of defects is vanishing or very small for a wide range of the relative fluctuations amplitude $\Delta s_0/s_0$ (Figures 7D–F). For relatively large fluctuations $\Delta s_0/s_0 = 1$, the pattern can correctly entrain to the sink profile even when individual sink strength falls way below the critical threshold for uniform profiles, asterisk in Figure 7E.

In summary, the system can buffer fluctuations in sink position up to 25%. Stronger sink position fluctuations can

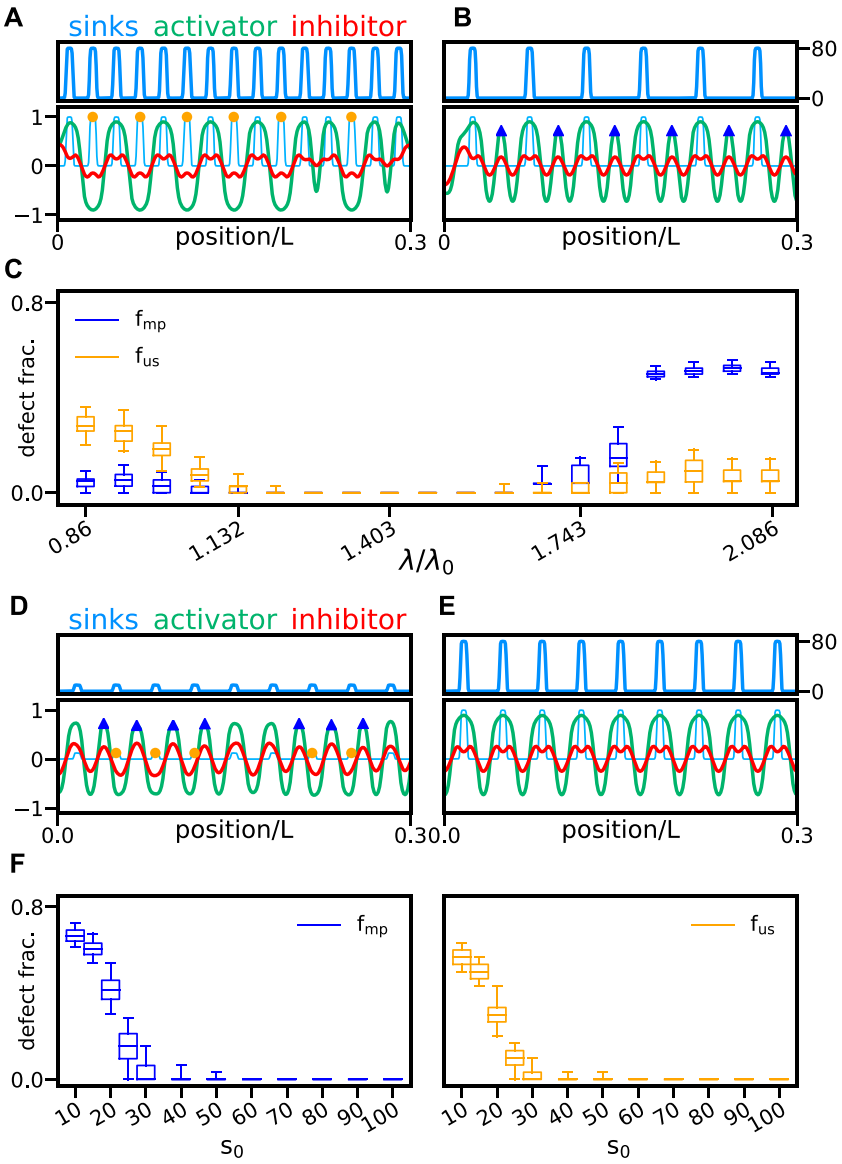

FIGURE 6
Sink profile wavelength and strength. Activator (green line) and inhibitor (red line) patterns together with the scaled sink profile (faint light blue line) are shown for sink profiles of wavelength **(A)** $\lambda/\lambda_0 = 0.86$ and **(B)** $\lambda/\lambda_0 = 2.086$. Here, $\lambda_0 = 0.398$ is the wavelength of the unforced pattern. Sink profile (light blue line) is also shown separately in the top panels for clarity. **(C)** Fraction of misplaced peaks f_{mp} (blue box plot) and unmatched sinks f_{us} (orange box plot) vs. relative sink profile wavelength λ/λ_0. Activator and inhibitor patterns for sink profiles of strength **(D)** $s_0 = 10$ and **(E)** $s_0 = 80$. Color coding and plot layout are as in panels **(A** and **B)**. **(F)** Fraction of misplaced peaks f_{mp} (blue box plot) and unmatched sinks f_{us} (orange box plot) vs. sink profile strength s_0. Box plots in **(C)** and **(F)** are as in Figure 4. Other parameters are as in Table 1. In all cases, we performed 300 realizations for each parameter combination.

disturb the patterns inducing defects of both types. Additionally, the median of defective fractions vanishes up to a relative sink strength fluctuation $\Delta s_0/s_0 = 0.85$ (Figure 7F). With this value, sinks may be as weak as $s_0 = 12$, which in uniform patterns generate large defect fractions (Figure 6F). This indicates that nonuniform sink profiles display a high tolerance for large sink strength fluctuations.

7 Discussion

We presented a reaction wavefront theory describing notochord pattern formation in zebrafish. Building on a one-dimensional activator–inhibitor reaction–diffusion system subject to external cues [16], we introduced a reaction wavefront that travels from anterior to posterior and enables reactions in its path. Although we do not know the nature of this

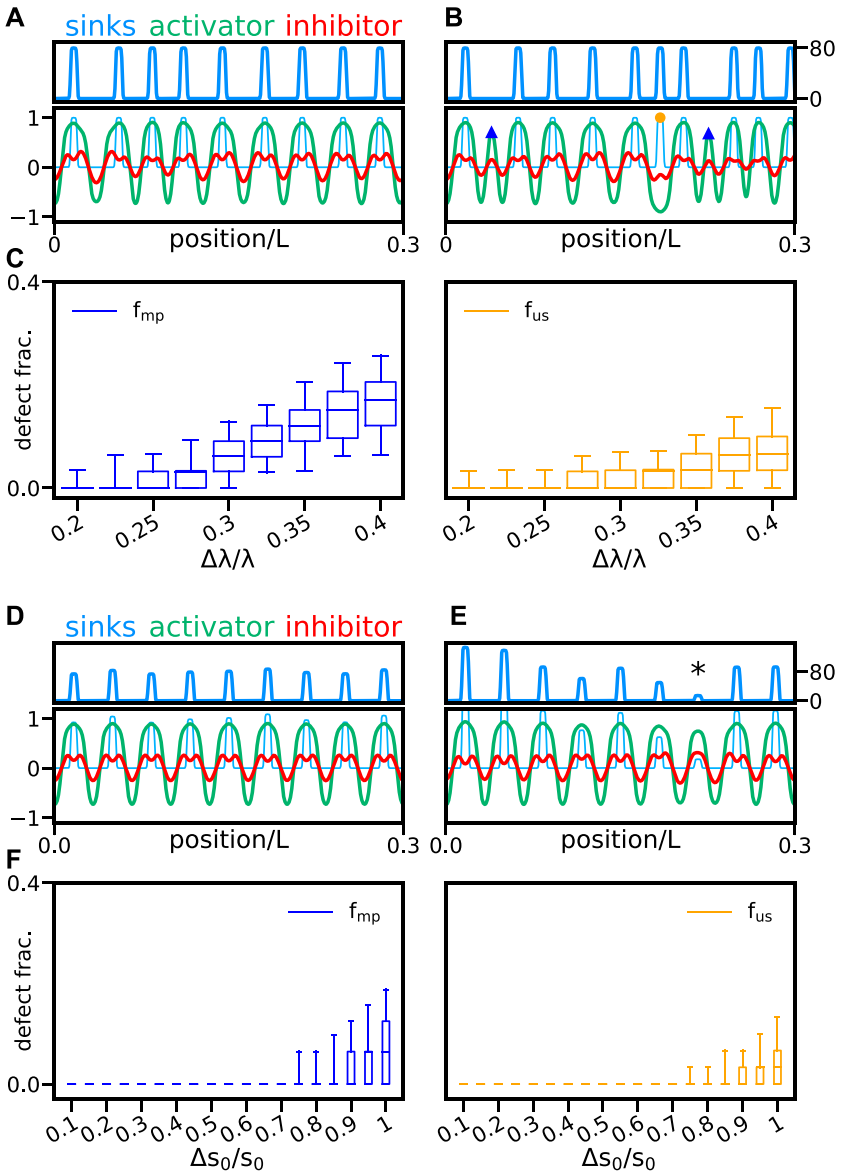

FIGURE 7
Fluctuations in sink position and strength. Activator (green line) and inhibitor (red line) patterns together with the scaled sink profile (faint light blue line) are shown for sink profiles with relative sink position fluctuation amplitudes **(A)** $\Delta\lambda/\lambda = 0.2$ and **(B)** $\Delta\lambda/\lambda = 0.4$. We choose a mean wavelength $\lambda = 0.57$, so $\lambda/\lambda_0 \approx 1.43$ is close to the center of the defect free region in Figure 6C. Sink profile (light blue line) is also shown separately in the top panels for clarity. **(C)** Fraction of misplaced peaks f_{mp} (blue box plot) and unmatched sinks f_{us} (orange box plot) vs. relative sink position fluctuation amplitudes $\Delta\lambda/\lambda$. Activator and inhibitor patterns for sink profiles with relative sink strength fluctuation amplitudes **(D)** $\Delta s_0/s_0 = 0.1$ and **(E)** $\Delta s_0/s_0 = 1$, with mean sink strength $s_0 = 80$. Color coding and plot layout are as in panels **(A** and **B)**. **(E)** Asterisk marks a sink of strength $s_0 \approx 15$. **(F)** Fraction of misplaced peaks f_{mp} (blue box plot) and unmatched sinks f_{us} (orange box plot) vs. relative sink strength fluctuation amplitude $\Delta s_0/s_0$. Box plots in **(C)** and **(F)** are as in Figure 4. Other parameters are as in Table 1. In all cases, we performed 300 realizations for each parameter combination.

reaction wavefront, we can speculate that a maturation gradient progressing posteriorly could trigger synthesis reactions. The gradient progression could control the synthesis of an adaptor molecule that binds DNA at the promoter of the activator and the inhibitor, allowing binding and action of the activator. Alternatively, the gradient could be an inhibitor of U and V that is initially present across the notochord and then gradually degraded as cells stop synthesizing it—or start degrading it actively. Such mechanisms would make the activation terms turn on when the maturation wavefront arrives at the cell. In the context of our model, this could be described effectively by parameters k_1, k_3, and k_5 in Eqs 1and 2. In the dimensionless

theory, since $\gamma \propto k_1$, the wavefront $\gamma(x, t)$ could be caused by a posteriorly decreasing synthesis rate for the activator and other coupled reactions.

First put forward by Turing [26] and later rediscovered by Gierer and Meinhardt [27], reaction diffusion systems have been applied to a variety of biological pattern formations [20]. Specific molecular components and their interactions have been proposed in some cases, such as for skin patterns in angelfish [28] and zebrafish [29] and the primary hair follicle pattern formation in the skin of vertebrates [30, 31], among other examples [32]. While the conditions for pattern formation in reaction–diffusion systems have been thought to be very restrictive, recent efforts have shown that these conditions may be relaxed in a wide range of cases. Along this line is a proposal for a synthetic circuit architecture capable of patterning with quenched oscillators that might be implemented in synthetic multicellular systems or cell aggregates [33]. In another study, the presence of a binding immobile substrate was shown to relax the constraints on reaction kinetics for diffusion-driven instability [34]. The need for constraints on diffusion rates for Turing patterns was also challenged in a study that used an automated framework to identify cell autonomous features that allow for pattern formation [35]. More recently, the plausibility of network motifs to give rise to reaction–diffusion patterns was systematically surveyed by means of graph theory [36]. Here, we have not chosen a specific network motif to implement the cell autonomous component. Instead, we choose a generic model to describe the dynamics, given that we do not know the molecular components involved and their interactions. It may be interesting future work to study how more specific networks respond to the presence of cues and a wavefront.

In this article, we have considered a theory that can generate a pattern from an unstable homogeneous state. Another possibility could be a pushed front invading a stable homogeneous state that is perturbed beyond unstable fixed points and is attracted by non-vanishing stable fixed points [37, 38]. This can occur in the context of an amplitude equation with a quintic term introducing the possibility of a subcritical bifurcation. In our theory, the only nonlinear term is the stabilizing cubic term in the activator equation, so we expect that the amplitude equation will have only up to third-order terms [39]. We expect that an additional fifth-order term in the equation that contains the cubic nonlinearity would cause a subcritical bifurcation and allow patterning from a stable homogeneous state, without requiring a wavefront. This could constitute an alternative scenario for the notochord patterning, and it would be interesting to study how this instability responds to an external input source providing the cues for the segments.

In addition to the reaction wavefront, the theory accounts for stochastic gene expression incorporating both noise in the initial condition for the activities of the components and a dynamic noise term in the differential equations. The theory describes the sequential patterning of the notochord in register with cues, from anterior to posterior, as observed in zebrafish [16], even in the presence of noise (Figure 2). A perturbation in the posterior region of the notochord should die out in the presence of a reaction wavefront but grow and generate a non-sequential defective pattern in its absence (Figure 3). Thus, the reaction wavefront hypothesis could be tested by introducing a bead soaked in the activator within the posterior notochord region.

In the embryo, the wild-type notochord segments are in register with the previously patterned paraxial mesoderm: one notochord segment is formed for each adjacent pair of somites. Thus, in the theory, we hypothesize that cues from somite boundaries instruct the notochord patterning mechanism, taking the form of a sink profile for the inhibitor. A normal pattern is defined by a one-to-one correspondence between individual activator peaks and inhibitor sinks. Two types of defects can occur in the theory: an inhibitor sink without a corresponding peak and a peak that does not have a corresponding inhibitor sink. Such defects may be amenable to observation in the embryo since somite boundaries can be seen as morphological landmarks with a bright field microscope or the DMD transgenic line [40], and notochord segment precursors can be revealed using a reporter for *entpd5* [16].

In the dimensionless theory that we considered here, the sink profile appears under the control of the wavefront $\gamma(x, t)$ (see Eq. 16). However, note that if the spatiotemporal dependence of $\gamma(x, t)$ is given by k_1 as we hypothesize above, the sink term would be time-independent, since $s_0 = S_0/k_1$ in the dimensionless theory (Eq. 9). This could be made explicit by keeping the sink term out of the wavefront in Eq. 7, by introducing an additional dimensionless parameter $\zeta = T_0 S_0$ that is constant in time and uniform in space, that is, not wavefront controlled.

Both wavefront velocity and steepness can modulate defect rate (Figure 5). We observe an interesting non-monotonic relation of the fraction of defective patterns with the wavefront steepness, peaking at $\beta = 2$. However, below this vale of β, the wavefront becomes very gradual, causing the pattern to trigger ahead of the wavefront middle point, with more than one activator peak forming simultaneously. We speculate that this might allow the reaction system to read the information of more than one sink in advance and accommodate the activator peaks more reliably. We also observe that slower wavefront velocities cause a decrease in the fraction of defective patterns, suggesting that this could be beneficial for embryonic patterning. A slower wavefront may allow the reaction system to average out fluctuations introduced by the dynamic noise source, and this may prevent defect formation. It is intriguing that while zebrafish somitogenesis takes about 12 h, notochord patterning is relatively much slower, taking about 3 weeks [16]. The theory predicts that accelerating the wavefront in a wild-type context may induce segment defects. A possible test of this prediction could be to slow down the wavefront in an experimental condition that is prone to making defects. Presumably,

transcriptional noise levels would be increased in a heterozygous mutant for a component of the notochord patterning system. In this context, the notochord pattern would be expected to make more defective segments, and we could ask whether a slower wavefront can partially rescue the phenotype.

The *hes6* mutant has larger somite segments and still patterns the notochord in register with these [17]. Consistent with this, here, we find a broad range of sink profile wavelengths where no defects occur (Figure 6C). Different defect types dominate for large and small wavelengths. For sufficiently small wavelengths, the system fails to produce peaks at such short distances, so it often misses every other sink. For large wavelengths, the pattern often intercalates a peak in between sinks. These characteristic defective patterns could be tested experimentally in conditions with altered somite lengths. Very small somites would cause notochord defects that skip adjacent somite boundaries, while large somites would cause misplaced notochord segments to happen more often. The transient modulation of Fgf or Wnt signaling during somitogenesis may provide a means to locally induce the formation of a small number of somites with altered length [41, 42], offering a way to test these predictions for segment lengths outside the range observed in the known segmentation clock period mutants.

We found an abrupt transition to defective patterns as a function of sink strength (Figure 6F). To decouple defects due to dynamic noise while perturbing sink strength, in this work, we have chosen a low dynamic noise strength $\sigma = 0.1$. There may be an interplay between sink strength and dynamic noise strength in determining both the onset and shape of this transition. This remains an interesting open question for future work.

Sink profile alterations may involve sink strength and wavelength fluctuations. There is a minimum sink strength required for the pattern to follow sink cues normally (Figure 6). However, in a sink profile with fluctuating strengths, sink strength values below the threshold do not cause pattern defects as long as they are surrounded by stronger sinks (Figure 7). Furthermore, fluctuations of up to 20% in the distance between sinks do not cause pattern defects (Figure 7). This is important because, in the embryo, we can expect some variability both in the intensity of cues provided by somite boundaries and in the distances between them [25]. We have not considered the changes to sink width and steepness, that is, sink shape fluctuations, which may be an interesting topic for future work.

The role of the notochord in vertebral column development seems to differ in different species, such as amniotes and teleosts [19]. The amniote notochord lacks the layer of epithelial cells and is formed by vacuolated cells only, surrounded by an extracellular matrix [43]. In chicks, vertebrae are thought to derive entirely from somite cells, while a cross-talk between somites and notochord ensures that the notochord contribution to vertebral discs is in register with vertebral bodies [43]. In teleosts, the inner part of the vertebral bodies derives from notochord cells [13]. In particular, zebrafish notochord sheath cells are the initial substrate for the vertebral bodies patterning and formation. A sequential ring-like pattern of *entpd5* expression is observed in the notochord sheath cells as the first sign of vertebral patterning [16]. In this work, we considered the notochord as a one-dimensional tissue for simplicity. In future work, it would be interesting to study ring pattern formation considering the notochord as a cylindrical surface. This geometry might support a richer variety of patterns, for example, helical defects.

The notochord tissue has remarkable mechanical properties. It is thought that the notochord serves as a hydrostatic scaffold during embryonic development [44, 45]. The particular structural configuration of the notochord, with the central vacuolated cells and its enveloping sheath cells, provides it with mechanical support as well as elasticity [18, 46]. Caveolae located in the vacuolated cells are essential for notochord structural integrity [47]. The arrangement of vacuolated cells is achieved by a self-organizing mechanical process and has been realized in a physical notochord model [48]. Here, we have considered a purely biochemical mechanism of notochord patterning. An interesting question for future enquiry is whether mechanical signaling has a role in providing either the sink cues or some other aspect of the patterning mechanism.

In summary, we have presented a possible scenario for an autonomous notochord patterning mechanism. The reaction wavefront theory is consistent with the observed spatiotemporal pattern in the notochord. We expect that this work will motivate future experimental designs to test the distinct predictions from this theory.

Data availability statement

The raw data supporting the conclusion of this article will be made available by the authors, without undue reservation.

Author contributions

All authors contributed to conceptualization and research design. SFA designed and implemented software, performed numerical simulations, and produced plots and figures. All authors contributed to formal analysis and validated the data and figures. All authors wrote and revised the manuscript.

Funding

This work was supported by ANPCyT grants PICT 2017 3753 and PICT 2019 0445 awarded to LGM and FOCEM-

Mercosur (COF 03/11) to IBioBA. SFA was supported by a CONICET fellowship, and LGM is a researcher of CONICET.

Acknowledgments

The authors are grateful to D. Arribas, F. Fabris, and D. Tenenbaum for their thoughtful comments on the manuscript.

Conflict of interest

The authors declare that the research was conducted in the absence of any commercial or financial relationships that could be construed as a potential conflict of interest.

Publisher's note

Supplementary material

The Supplementary Material for this article can be found online at: https://www.frontiersin.org/articles/10.3389/fphy.2022.933915/full#supplementary-material

References

1. Wolpert L, Smith J, Jessell T, Lawrence P, Robertson E, Meyerowitz E. *Principles of development*. 3rd ed. Oxford University Press (2006).

2. Howard J, Grill SW, Bois JS. Turing's next steps: The mechanochemical basis of morphogenesis. *Nat Rev Mol Cel Biol* (2011) 12:392–8. doi:10.1038/nrm3120

3. Uriu K, Morelli LG, Oates AC. Interplay between intercellular signaling and cell movement in development. *Semin Cel Dev Biol* (2014) 35:66–72. doi:10.1016/j.semcdb.2014.05.011

4. Gross P, Kumar KV, Grill SW. How active mechanics and regulatory biochemistry combine to form patterns in development. *Annu Rev Biophys* (2017) 46:337–56. doi:10.1146/annurev-biophys-070816-033602

5. Petrungaro G, Morelli LG, Uriu K. Information flow in the presence of cell mixing and signaling delays during embryonic development. *Semin Cel Dev Biol* (2019) 93:26–35. doi:10.1016/j.semcdb.2018.09.008

6. Raser JM, O'Shea EK. Noise in gene expression: Origins, consequences, and control. *Science* (2005) 309:2010–3. doi:10.1126/science.1105891

7. Palmeirim I, Henrique D, Ish-Horowicz D, Pourquié O. Avian hairy gene expression identifies a molecular clock linked to vertebrate segmentation and somitogenesis. *Cell* (1997) 91:639–48. doi:10.1016/s0092-8674(00)80451-1

8. Masamizu Y, Ohtsuka T, Takashima Y, Nagahara H, Takenaka Y, Yoshikawa K, et al. Real-time imaging of the somite segmentation clock: Revelation of unstable oscillators in the individual presomitic mesoderm cells. *Proc Natl Acad Sci U S A* (2006) 103:1313–8. doi:10.1073/pnas.0508658103

9. Soroldoni D, Jörg DJ, Morelli LG, Richmond DL, Schindelin J, Jülicher F, et al. A Doppler effect in embryonic pattern formation. *Science* (2014) 345:222–5. doi:10.1126/science.1253089

10. Pourquié O. Vertebrate segmentation: From cyclic gene networks to scoliosis. *Cell* (2011) 145:650–63. doi:10.1016/j.cell.2011.05.011

11. Oates AC, Morelli LG, Ares S. Patterning embryos with oscillations: Structure, function and dynamics of the vertebrate segmentation clock. *Development* (2012) 139:625–39. doi:10.1242/dev.063735

12. Bagnall K, Higgins SJ, Sanders E. The contribution made by a single somite to the vertebral column: Experimental evidence in support of resegmentation using the chick-quail chimaera model. *Development* (1988) 103:69–85. doi:10.1242/dev.103.1.69

13. Fleming A, Kishida MG, Kimmel CB, Keynes RJ. Building the backbone: The development and evolution of vertebral patterning. *Development* (2015) 142:1733–44. doi:10.1242/dev.118950

14. Fleming AF, Keynes R, Tannahill D. A central role for the notochord in vertebral patterning. *Development* (2004) 131:873–80. doi:10.1242/dev.00952

15. Agrawal S, Archer C, Schaffer DV. Computational models of the notch network elucidate mechanisms of context-dependent signaling. *Plos Comput Biol* (2009) 5:e1000390. doi:10.1371/journal.pcbi.1000390

16. Lleras Forero L, Narayanan R, Huitema LF, Vanbergen M, Apschner A, Peterson-Maduro J, et al. Segmentation of the zebrafish axial skeleton relies on notochord sheath cells and not on the segmentation clock. *eLife* (2018) 7:e33843. doi:10.7554/elife.33843

17. Schröter C, Oates AC. Segment number and axial identity in a segmentation clock period mutant. *Curr Biol* (2010) 20:1254–8. doi:10.1016/j.cub.2010.05.071

18. Stemple DL. Structure and function of the notochord: An essential organ for chordate development. *Development* (2005) 132:2503–12. doi:10.1242/dev.01812

19. Bagnat M, Gray RS. *Development of a straight vertebrate body axis. Development* (2020) 147:dev175794.

20. Murray JD. Mathematical biology II: Spatial models and biomedical applications. In: *Interdisciplinary applied mathematics*. 3rd ed., 18. New York: Springer (2003).

21. Chubb JR, Trcek T, Shenoy SM, Singer RH. Transcriptional pulsing of a developmental gene. *Curr Biol* (2006) 16:1018–25. doi:10.1016/j.cub.2006.03.092

22. Tsimring LS. Noise in biology. *Rep Prog Phys* (2014) 77:026601. doi:10.1088/0034-4885/77/2/026601

23. San Miguel M, Toral R. Instabilities and nonequilibrium structures VI. In: E Tirapegui, J Martínez, R Tiemann, editors. *Nonlinear phenomena and complex systems*. Kluwer Academic Publishers (2000). p. 35–130. doi:10.1007/978-94-011-4247-2

24. Gomez C, Özbudak EM, Wunderlich J, Baumann D, Lewis J, Pourquié O. Control of segment number in vertebrate embryos. *Nature (London)* (2008) 454:335–9. doi:10.1038/nature07020

25. Schröter C, Herrgen L, Cardona A, Brouhard GJ, Feldman B, Oates AC. Dynamics of zebrafish somitogenesis. *Dev Dyn* (2008) 237:545–53. doi:10.1002/dvdy.21458

26. Turing AM. The Chemical Basis of Morphogenesis. *Philosophical Trans R Soc Lond Ser B* (1952) 237:37–72.

27. Gierer A, Meinhardt H. A theory of biological pattern formation. *Kybernetik* (1972) 12:30–9. doi:10.1007/bf00289234

28. Kondo S, Asai R. A reaction–diffusion wave on the skin of the marine angelfish Pomacanthus. *Nature* (1995) 376:765–8. doi:10.1038/376765a0

29. Yamaguchi M, Yoshimoto E, Kondo S. Pattern regulation in the stripe of zebrafish suggests an underlying dynamic and autonomous mechanism. *Proc Natl Acad Sci U S A* (2007) 104:4790–3. doi:10.1073/pnas.0607790104

30. Mou C, Jackson B, Schneider P, Overbeek PA, Headon DJ. Generation of the primary hair follicle pattern. *Proc Natl Acad Sci U S A* (2006) 103:9075–80. doi:10.1073/pnas.0600825103

31. Klika V, Baker RE, Headon D, Gaffney EA. The influence of receptor-mediated interactions on reaction-diffusion mechanisms of cellular self-organisation. *Bull Math Biol* (2012) 74:935–57. doi:10.1007/s11538-011-9699-4

32. Kondo S, Miura T. Reaction-diffusion model as a framework for understanding biological pattern formation. *Science* (2010) 329:1616–20. doi:10.1126/science.1179047

33. Hsia J, Holtz WJ, Huang DC, Arcak M, Maharbiz MM. A feedback quenched oscillator produces turing patterning with one diffuser. *Plos Comput Biol* (2012) 8: e1002331. doi:10.1371/journal.pcbi.1002331

34. Korvasová K, Gaffney EA, Maini PK, Ferreira MA, Klika V. Investigating the Turing conditions for diffusion-driven instability in the presence of a binding immobile substrate. *J Theor Biol* (2015) 367:286–95. doi:10.1016/j.jtbi.2014.11.024

35. Marcon L, Diego X, Sharpe J, Müller P. High-throughput mathematical analysis identifies Turing networks for patterning with equally diffusing signals. *eLife* (2016) 5:e14022. doi:10.7554/elife.14022

36. Diego X, Marcon L, Müller P, Sharpe J. Key features of turing systems are determined purely by network topology. *Phys Rev X* (2018) 8:021071. doi:10.1103/physrevx.8.021071

37. van Saarloos W. Front propagation into unstable states. *Phys Rep* (2003) 386: 29–222.

38. Cross MC, Greenside HS. *Pattern formation and dynamics in nonequilibrium systems*. Cambridge University Press (2009).

39. Kuznetsov M, Kolobov A, Polezhaev A. Pattern formation in a reaction-diffusion system of Fitzhugh-Nagumo type before the onset of subcritical Turing bifurcation. *Phys Rev E* (2017) 95:052208. doi:10.1103/physreve.95.052208

40. Ruf-Zamojski F, Trivedi V, Fraser SE, Trinh LA. Spatio-temporal differences in dystrophin dynamics at mRNA and protein levels revealed by a novel FlipTrap line. *PLoS One* (2015) 10:e0128944. doi:10.1371/journal.pone.0128944

41. Sawada A, Shinya M, Jiang Y-J, Kawakami A, Kuroiwa A, Takeda H. Fgf/MAPK signalling is a crucial positional cue in somite boundary formation. *Development* (2001) 128:4873–80. doi:10.1242/dev.128.23.4873

42. Bajard L, Morelli LG, Ares S, Pécréaux J, Jülicher F, Oates AC. Wnt-regulated dynamics of positional information in zebrafish somitogenesis. *Development* (2014) 141:1381–91. doi:10.1242/dev.093435

43. Ward L, Pang AS, Evans SE, Stern CD. The role of the notochord in amniote vertebral column segmentation. *Developmental Biol* (2018) 439:3–18. doi:10.1016/j.ydbio.2018.04.005

44. Ellis K, Bagwell J, Bagnat M. Notochord vacuoles are lysosome-related organelles that function in axis and spine morphogenesis. *J Cel Biol* (2013) 200: 667–79. doi:10.1083/jcb.201212095

45. Bagwell J, Norman J, Ellis K, Peskin B, Hwang J, Ge X, et al. Notochord vacuoles absorb compressive bone growth during zebrafish spine formation. *eLife* (2020) 9:e51221. doi:10.7554/elife.51221

46. Adams DS, Keller R, Koehl MAR. The mechanics of notochord elongation, straightening and stiffening in the embryo of *Xenopus laevis*. *Development* (1990) 110:115–30. doi:10.1242/dev.110.1.115

47. Garcia J, Bagwell J, Njaine B, Norman J, Levic DS, Wopat S, et al. Sheath cell invasion and trans-differentiation repair mechanical damage caused by loss of caveolae in the zebrafish notochord. *Curr Biol* (2017) 27:1982–9.e3. doi:10.1016/j.cub.2017.05.035

48. Norman J, Sorrell EL, Hu Y, Siripurapu V, Bagwell JGJ, Charbonneau P, et al. Tissue self-organization underlies morphogenesis of the notochord. *Phil Trans R Soc B* (2018) 373:20170320. doi:10.1098/rstb.2017.0320

frontiers | Frontiers in Systems Biology

ORIGINAL RESEARCH
published: 09 September 2022
doi: 10.3389/fsysb.2022.898858

Explicit Calculation of Structural Commutation Relations for Stochastic and Dynamical Graph Grammar Rule Operators in Biological Morphodynamics

Eric Mjolsness *

Departments of Computer Science and Mathematics, University of California, Irvine, CA, United States

Many emergent, non-fundamental models of complex systems can be described naturally by the temporal evolution of spatial structures with some nontrivial discretized topology, such as a graph with suitable parameter vectors labeling its vertices. For example, the cytoskeleton of a single cell, such as the cortical microtubule network in a plant cell or the actin filaments in a synapse, comprises many interconnected polymers whose topology is naturally graph-like and dynamic. The same can be said for cells connected dynamically in a developing tissue. There is a mathematical framework suitable for expressing such emergent dynamics, "stochastic parameterized graph grammars," composed of a collection of the graph- and parameter-altering rules, each of which has a time-evolution operator that suitably moves probability. These rule-level operators form an operator algebra, much like particle creation/annihilation operators or Lie group generators. Here, we present an explicit and constructive calculation, in terms of elementary basis operators and standard component notation, of what turns out to be a general combinatorial expression for the operator algebra that reduces products and, therefore, commutators of graph grammar rule operators to equivalent integer-weighted sums of such operators. We show how these results extend to "dynamical graph grammars," which include rules that bear local differential equation dynamics for some continuous-valued parameters. Commutators of such time-evolution operators have analytic uses, including deriving efficient simulation algorithms and approximations and estimating their errors. The resulting formalism is complementary to spatial models in the form of partial differential equations or stochastic reaction-diffusion processes. We discuss the potential application of this framework to the remodeling dynamics of the microtubule cytoskeleton in cortical microtubule networks relevant to plant development and of the actin cytoskeleton in, for example, a growing or shrinking synaptic spine head. Both cytoskeletal systems underlie biological morphodynamics.

Keywords: dynamical graph grammar, morphodynamics, operator commutator, cortical microtubule array, actin filament network, synaptic spine head, operator algebra, stochastic graph grammar

OPEN ACCESS

Edited by:
Luis Diambra,
National University of La Plata, Argentina

Reviewed by:
Mikolaj Cieslak,
University of Calgary, Canada
Ian McQuillan,
University of Saskatchewan, Canada

***Correspondence:**
Eric Mjolsness
emj@uci.edu

Specialty section:
This article was submitted to Multiscale Mechanistic Modeling, a section of the journal Frontiers in Systems Biology

Received: *18 March 2022*
Accepted: *08 June 2022*
Published: *09 September 2022*

Citation:
Mjolsness E (2022) Explicit Calculation of Structural Commutation Relations for Stochastic and Dynamical Graph Grammar Rule Operators in Biological Morphodynamics. Front. Syst. Biol. 2:898858. doi: 10.3389/fsysb.2022.898858

1 INTRODUCTION

Many emergent, non-fundamental models of complex systems can be described naturally by the temporal evolution of spatial structures with some nontrivial discretized topology, such as a graph with suitable discrete and/or continuous state-determining parameter vectors labeling its vertices. In materials science, there can be dynamic networks of fractures or extended crystal defects. Biological examples include the network of adjacent cells in a tissue or the dynamic polymeric cytoskeleton within a single cell. Such biological examples arise in development, where one has morphodynamics (dynamics of the form) at both the tissue and cellular level, and they are interrelated. In this study, our examples will mainly be taken from the domain of graph-like structural dynamics in the cytoskeleton, in these two domains of biological pattern formation and morphodynamics (Vos et al., 2004; Hotulainen and Hoogenraad, 2010; Sampathkumar et al., 2014; Chakrabortty et al., 2018; Bonilla-Quintana et al., 2020).

In previous work [(Mjolsness, 2019a), Propositions 1 and 2], we showed that the parameterized or labeled graph rewrite rule operator semantics specified there (in two versions, one without and one with hanging edge removal) is contained within a somewhat larger operator algebra closed under addition, scalar multiplication, and operator multiplication (and hence under commutation, as in a Lie algebra).

The purpose of this study is to show explicitly and combinatorially what this operator algebra is: under either semantics (hanging edges removed or not), the vector space spanned by the graph rewrite rule operators previously defined form an operator algebra and a Lie algebra among all such graph rewrite rule operators, under an explicit formula to be presented in **Section 2.4**. In particular, the product of the state-changing portions of two such operators can be written as a sum of such operators with nonnegative integer weights, and the full product and commutator of two such operators can be written as a sum of such operators with integer weights.

These results arise within a larger scientific scope discussed at length in Mjolsness (2019a), including grammar-like or rule-based structured models of molecular complexes (Blinov et al., 2004) and of tissues with dividing cells (Mjolsness et al., 1991; Prusinkiewicz et al., 1993). Potential applications include cytoskeletal dynamics in cellular and developmental biology, neurobiology, and smart materials, as well as the dynamics of more abstract, non-spatial graphs in a wide variety of fields. We will illustrate with subcellular cortical microtubule biophysical dynamics that are important at the cellular and tissue level of plant development.

Given state-changing operators $\hat{W}_r$ for the rules in grammar, for example, as outlined in **Section 2.2**, the Master Equation for the stochastic dynamics is as follows (Mjolsness and Yosiphon, 2006):

$$\frac{dp}{dt} = W \cdot p, \quad \text{(probability flows according to } W\text{)}, \quad \text{where} \tag{1a}$$

$$W = \sum_r W_r, \quad \text{(rule operators sum up)} \tag{1b}$$

$$W_r \equiv \hat{W}_r - D_r, \quad \text{(rules conserve probability)} \tag{1c}$$

$$D_r \equiv \text{diag}\left(\mathbf{1} \cdot \hat{W}_r\right) \quad \text{(total probability outflow per state)} \tag{1d}$$

[generalizing (Doi, 1976a; Doi, 1976b; Mattis and Glasser, 1998) for stochastic chemical reaction networks], where probability is defined over a suitable Fock space for varying numbers of graph nodes (with labels) and graph edges. **Supplementary Section SC** discusses how this framework can be used to model stochastic chemical reaction networks, using the algebras of elementary and compound W_r operators.

In this study, the goal is to explicitly calculate the key operator algebra identity for such operators $\hat{W}_r$, as exhibited in **Eq. 16** of **Section 2.4**, with important corollaries in **Sections 3.4**, **3.5**, and proven in **Section 3** and **Supplementary Material SA**, and to extend it to the differential equations case. The exposition will be organized in three successive levels of detail: first a statement of the main results (**Section 2**), then a sketch of the general computations and theorems, including their corollaries (**Section 3**), then a collection of examples (**Section 3.7**), followed by **Supplementary Material**, which refines the explicit operator semantics and contains the full calculations.

2 PROBLEM STATEMENT

We first recapitulate the required operator algebra definitions and then state our problems. In **Section 2.1**, we will define graphs, labeled graphs, and graph grammars. In **Section 2.2**, we will use operator algebra to define the semantics of graph grammar rules and graph grammars. Then, in **Section 2.3**, we will state the operator algebra problems, and in **Section 2.4**, we will preview the main results of the study. The methods in this study will be purely theoretical: performing operator algebra calculations that establish concise results that solve the stated problems.

2.1 Graph Grammar Rule Syntax

The definitions of this section informally summarize the more systematic definitions of Mjolsness (2019a) (**Supplementary Material**). A graph is an unordered set V of "vertices" or "nodes," together with a set E of "edges" or "links," each of which is, or corresponds to, either 1) an unordered pair of vertices $\{u, v\}$, for an "undirected edge," 2) an ordered pair of vertices (u, v), for a "directed edge," or 3) a singleton vertex $\{v\}$ (or equivalently the ordered pair (v, v)), for a "self-edge." An unordered pair of vertices cannot have both directed and undirected edges, except in the sense that a pair of oppositely directed edges can represent an unordered edge. An "undirected graph" has only undirected edges; a "directed graph" has only directed edges; either kind can allow self-edges or not. This notion of a graph encompasses undirected graphs and directed graphs, with or without self-loops, in a way that is compatible with the computational representation of a graph as an adjacency matrix.

A labeled graph adds the extra structure of a mapping from vertices in V to labels in label set Λ. Labeled graphs (with node labels as above) can be used to encode and implement many other kinds of graphs, such as multigraphs, edge-labeled graphs

mapped to bipartite- (node-) labeled graphs, hypergraphs, and abstract cell complexes.

More technically, a numbered graph is a labeled graph in which the label set is an initial subset $\Lambda' = \{1, \ldots n\}$ of the natural numbers, and the assigned node labels are unique (so $|\Lambda'| \geq |V|$). In this case, there is an induced total ordering on the vertex set V, breaking the prima facie permutation invariance of the vertices of the graph. If all numbers in $|\Lambda'|$ are assigned (so $|\Lambda'| = |V|$ by 1-1 correspondence), then such a numbered graph can be represented uniquely by a 0/1-valued adjacency matrix recording the presence or absence of directed edges ($i = \lambda(u), j = \lambda(v)$), where i and j are integer-valued "index" labels, with undirected edges encoded by the presence of two oppositely directed edges and self-edges recorded by diagonal matrix entries. The case $|\Lambda'| > |V|$ is required just to define a consistent numbering of several graphs, not all of whose vertices can be identified across graphs.

A labeled graph can be represented (perhaps nonuniquely) by a numbered graph G together with a vector of labels $\langle\!\langle \lambda_1, \ldots \lambda_i, \ldots \lambda_n \rangle\!\rangle$ that map vertex indices i to vertex labels; the resulting labeled graph combination is denoted $G\langle\!\langle \lambda_1, \ldots \lambda_i, \ldots \lambda_n \rangle\!\rangle$. Elements λ of the label set Λ can themselves take the form of a vector or tuple with d components; if $d = 0$, then there is only one label and the labeled graph is equivalent to an unlabeled graph again.

Given these definitions, the "syntax" of a graph grammar rewrite rule takes a form involving two labeled graphs that have been decomposed into two consistently numbered graphs and their label maps:

$$G\langle\!\langle \lambda_1, \ldots \lambda_n \rangle\!\rangle \rightarrow G'\langle\!\langle \lambda'_1, \ldots \lambda'_{n'} \rangle\!\rangle \quad \textbf{with} \quad \rho(\lambda_1, \ldots \lambda_n, \lambda'_1, \ldots \lambda'_{n'}). \tag{2}$$

Such an expression represents a discrete local transformation that can act or "fire" anywhere that the left-hand side (LHS) labeled graph $G\langle\!\langle \lambda_1, \ldots \lambda_i, \ldots \lambda_n \rangle\!\rangle$ matches (occurs as a labeled subgraph, with matching edge structure and labels) within a potentially much larger system graph that comprises the current state of a system model. Of course, many rule firings may be possible for a given rule and system graph; it is up to the semantics outlined below to determine what actually happens with what probability and when. That will depend on the non-negative function ρ, the propensity, or rule firing probability per unit time. By making ρ a function of the λs, we allow that one syntactic rule, as above, can specify many grounded rules, each of which has all λs replaced with constant values, as in the integration semantics provided in the next section. The integrable measure spaces in which labels λ_i live were outlined in Mjolsness and Yosiphon (2006).

Such a graph rewrite rule is expressed in terms of a single consistent numbering of the vertices of the two numbered graphs. Therefore, vertices in G and G' that share a vertex number are regarded as "the same" vertex v, before and after rewriting, and any graph edges contacting v but not mentioned in the rewrite rule are preserved. In this way, graph rewrite rules can operate within a broader graph context. On the other hand, the particular consistent numbering chosen is arbitrary and does not matter. The semantics in the next section will be invariant with respect to permutations of the consistent numbering.

For example, **Eq. 3** below specifies a part of the refinement process for 2D triangular meshes. Each graph node bears an integer parameter l denoting a local level number for the depth of refinement. This rewrite rule is one of four that suffice to implement a standard triangular mesh refinement scheme. The other three rules handle partially refined triangle edges, an unavoidable consequence of the previous refinement of adjacent triangles. Further details are provided by Mjolsness (2019a). The labeled graph rewrite rule is

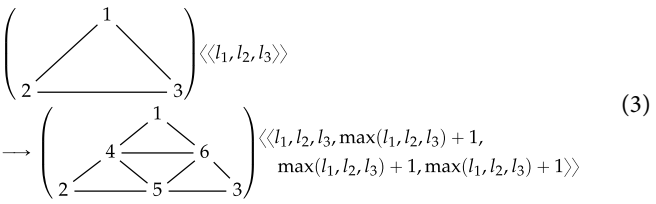

(3)

with some constant propensity ρ (omitted). Of course, it is also possible to provide a linear, textual representation of a numbered graph G, if only as a list of its edges between ordered pairs of index values.

2.2 Graph Grammar Rule Semantics

Let indices $i_1, \ldots i_k$ range over many graph nodes that can each be allocated to model the state of some object in a modeling domain.

In the following, as elaborated in Mjolsness (2010) and Mjolsness (2013), stochastic labeled graph grammar (SLGG) rule semantics with vectors $\boldsymbol{\lambda}$, $\boldsymbol{\lambda}'$ of incoming and outgoing graph node labels can be thought of as stochastic parameterized graph grammar (SPGG) semantics when the labels are taken to be functions $\boldsymbol{\lambda}(X)$ and $\boldsymbol{\lambda}'(X)$ of some vector of parameters or variables X. The rule semantics is obtained by integrating over all possible values of a vector of rule variables X that appear in the graph labels λ, λ'; as a special case, some labels and/or parameters could be constant. Then,

$$\hat{W}_r = \int d\mu_r(X) \hat{W}_r(\boldsymbol{\lambda}(X), \boldsymbol{\lambda}'(X)), \tag{4}$$

where $\mu_r(X)$ is a suitable measure that could be discrete in one or several dimensions (so, the integral becomes a sum or multiple sum) or continuous in one or several dimensions (so the integral may be a multiple integral), or a multidimensional combination of discrete and continuous components. However, any continuous measures can be approximated by discrete ones to retain the essentially combinatorial nature of the proofs below. In addition, the label functions $\boldsymbol{\lambda}(X)$ and $\boldsymbol{\lambda}'(X)$ can include extra components, which are constant, for the given rule number r. These are not to be integrated over, so they are not part of the variable X.

We provided examples of such graph grammar rules for mesh refinement in Mjolsness (2019a) and will exhibit graph grammar rules for coarse-grained models of plant cortical microtubule dynamics in **Section 3.7.1**.

Consider a graph rewrite rule expressed, in part, as $G^{r\ \mathrm{in}}(\boldsymbol{\lambda}(X)) \rightarrow G^{r\ \mathrm{out}}(\boldsymbol{\lambda}'(X))$, where $G^{r\ \mathrm{in}}$ and $G^{r\ \mathrm{out}}$ are graphs with the given vectors of labels and an arbitrary but shared numbering of their nodes. Define "$\sum_{\langle i_1,\ldots i_k\rangle_{\neq}}\ldots$" to be a sum over indices $(i_1, \ldots i_k)$ constrained so that each i_l is unequal to all the others. Then, in the simplest case (but see **Supplementary Section SA.4.3**), we define the time-evolution operator of a graph rewrite rule:

$$\begin{aligned}\hat{W}_r &= \frac{1}{C_r\left(N_{\max\,\mathrm{free}}\right)}\int d\mu_r(X)\,\rho_r\left(\boldsymbol{\lambda}(X),\boldsymbol{\lambda}'(X)\right)\\ &\times\sum_{\langle i_1,\ldots i_k\rangle_{\neq}}\hat{a}_{i_1,\ldots i_k}\left(G^{r\ \mathrm{out}}\right)a_{i_1,\ldots i_k}\left(G^{r\ \mathrm{in}}\right)\end{aligned} \tag{5}$$

where, as explained by Mjolsness (2019a), the graph grammar rule operator first annihilates all the edges and labeled nodes in the incoming "left hand side" graph $G = G^{r\ \mathrm{in}}$ and then, but uninterruptibly and with zero time delay, creates the corresponding elements of the outgoing "right-hand side" graph $G' = G^{r\ \mathrm{out}}$:

$$\begin{aligned}\hat{a}_{i_1,\ldots i_k}(G') &= \hat{a}_{i_1,\ldots i_k}(G'_{\mathrm{links}})\hat{a}_{i_1,\ldots i_k}(G'_{\mathrm{nodes}})\\ &= \left[\prod_{s',t'\in\mathrm{rhs}(r)}\left(\hat{a}_{i_{s'}i_{t'}}\right)^{g'_{s't'}}\right]\left[\prod_{\nu'\in\mathrm{rhs}(r)}\hat{a}_{i_{\nu'}\lambda'_{\nu'}}\right]\\ &= \left[\prod_{(s',t')\in G'_{\mathrm{links}}}\hat{a}_{i_{s'}i_{t'}}\right]\left[\prod_{\nu'\in G'_{\mathrm{nodes}}}\hat{a}_{i_{\nu'}\lambda'_{\nu'}}\right]\\ a_{i_1,\ldots i_k}(G) &= a_{i_1,\ldots i_k}(G_{\mathrm{links}})a_{i_1,\ldots i_k}(G_{\mathrm{nodes}}) = \left[\prod_{s,t\in\mathrm{lhs}(r)}\left(a_{i_si_t}\right)^{g_{st}}\right]\left[\prod_{\nu\in\mathrm{lhs}(r)}a_{i_\nu\lambda_\nu}\right].\\ &= \left[\prod_{(s,t)\in G_{\mathrm{links}}}a_{i_si_t}\right]\left[\prod_{\nu\in G_{\mathrm{nodes}}}a_{i_\nu\lambda_\nu}\right].\end{aligned} \tag{6}$$

The sets lhs_r and rhs_r comprise the nodes or vertices in the left-hand side and right-hand side graphs, G and G', with adjacency matrices g and g', of rule r. The creation and annihilation operators $\hat{a}_\alpha$ and a_α are the 2×2 {0, 1}-valued matrices that add or remove a "particle" (a graph node or link) if possible and, otherwise, yield a probability vector of zero in a many-particle-type Fock space (Mjolsness and Yosiphon, 2006, **Sections 3.2**, **3.3**), simplified from Reed and Simon (1980). They are closely related to the Doi formulation of chemical reaction networks (Doi, 1976a; Doi, 1976b; Mattis and Glasser, 1998) described in **Supplementary Material SC**, as discussed by Mjolsness and Yosiphon (2006), except that the maximum number of identical "particles" of each subscript combination is taken to be one rather than countable infinity. Node labels λ_ν take values in a discrete set or a continuum well approximable in computational implementations by discrete sets such as the set of floating-point numbers. The "probabilistic Fock spaces" comprising probability distributions over graph nodes and edges, on which all these operators act, apply to discrete and/or continuous node labels, including edge information.

The two matrices g and g' share the same consistent numbering of graph nodes (i.e., graph vertices) so that a given node number s can be directionally connected to other nodes t in graph g iff $g_{s\ t} = 1$, graph g' iff $g'_{s\ t} = 1$, or both; and the corresponding individual links (i.e., graph edges) given by nonzero entries in these two matrices can be independently present or absent. Because of the "$\sum_{\langle i_1,\ldots i_k\rangle_{\neq}}\ldots$" form of this operator (**Eq. 5**), each such operator is invariant under any global permutation Σ operating on the object-modeling domain graph nodes indexed by i_s, and it is also invariant under any permutation σ operating on the consistent graph numbering of the graph rule nodes indexed by s, t. This permutation invariance is essential in making the rewrite rule apply to graphs, which do not have an intrinsic ordering to their vertices. However, the permutation symmetry can be and usually is partially broken by graph labels and/or connectivity. The normalizing factor of $1/C_r(N_{\max\ \mathrm{free}})$ in **Eq. 5** may be required to account for the numbering degeneracy of possible new graph nodes added by the right-hand side graph, as shown in **Supplementary Section SA.2**.

The denominator $1/C_r(N_{\max\ \mathrm{free}})$ in **Eq. 5**, like the sum over permutations "$\sum_{\langle i_1,\ldots i_k\rangle_{\neq}}\ldots$," helps account for the change of representation between abstract graphs with their unordered nodes, and computer-representable nodes that are associated with an arbitrary but ordered integer index i_k such as location in computer memory. In particular, the representation of one or more new graph nodes required by the firing of rule r must be drawn from some available pool of one or more available indexed nodes. This is an arbitrary choice. $C_r(N_{\max\ \mathrm{free}})$ counts the number of ways this choice can be made, weighted equally, and ensures their total propensity adds up to what is required by the rest of the expression in **Eq. 5**. The actual count depends on the details of memory management as discussed in **Supplementary Sections SA.2, SA.4.2**; it could be as low as $C_r = 1$, but that may require a serial implementation of the simulation computation.

Undirected graphs can be encoded as a special case in which matrix g is symmetric. Node- and edge-labeled graphs can be encoded as a special case in which node labels come in two colors, the graph is bipartite (alternating node-colored with edge-colored nodes), and all the edge-colored nodes have degree two.

Another useful form of **Eq. 5** is to factor out any graph K that is completely unchanged. This form is exhibited in **Supplementary Section SA.1**.

Returning to **Eqs 5**, **6**, we can combine them to write out more explicitly

$$\begin{aligned}\hat{W}_r &= \frac{1}{C_r\left(N_{\max\,\mathrm{free}}\right)}\int d\mu_r(X)\,\rho_r\left(\boldsymbol{\lambda}(X),\boldsymbol{\lambda}'(X)\right)\\ &\times\sum_{\langle i_1,\ldots i_k\rangle_{\neq}}\left[\prod_{s',t'\in\mathrm{rhs}(r)}\left(\hat{a}_{i_{s'}i_{t'}}\right)^{g'_{s't'}}\right]\left[\prod_{\nu'\in\mathrm{rhs}(r)}\hat{a}_{i_{\nu'}\lambda'_{\nu'}}\right]\\ &\times\left[\prod_{s,t\in\mathrm{lhs}(r)}\left(a_{i_si_t}\right)^{g_{s\ t}}\right]\left[\prod_{\nu\in\mathrm{lhs}(r)}a_{i_\nu\lambda_\nu}\right].\end{aligned} \tag{7}$$

Two models defined by the Master Equation (ME) will be "equivalent" if their state variables can be identified so that solutions of the Master Equation are identical in all statistically observable respects: in all moments of all number operators at all choices of observation times. If α indexes the observable numbers n_α of objects and relationships and N_α is the corresponding number operator, then we can read out a broad range of joint probabilities with the moments of Kronecker delta functions:

$$\Pr_{\mathrm{ME}}\left(\left[n_{\alpha(q)}\left(t_q\right)|q\right]\right) = \left\langle\prod_q\delta\left(N_{\alpha(q)}\left(t_q\right) - n_{\alpha(q)}I_{\alpha(q)}\right)\right\rangle_{\mathrm{ME}} \tag{8}$$

where a collection indexed by q of values $n_{\alpha(q)}$ of number operators $N_{\alpha(q)}$ are measured at times t_q and the ensemble average taken. As the operative definition of equivalence, we demand equality of all such moments. Other observables $\langle f([N_{\alpha(q)}(t_q)|q])\rangle_{\mathrm{ME}}$ (where f is applied component-wise to diagonal matrices) follow from **Eq. 8** as a linear basis.

2.2.1 Application to ODE Rules

There is a natural application of the foregoing class of operator to incorporate ordinary differential equation (ODE) dynamics on parameters appearing in the graph labels, for example, the positions and other continuous state information of particles denoted by labeled graph nodes. We define a stochastic parameterized graph grammar incorporating differential equation bearing rules as dynamical graph grammar (DGG). Suppose the concatenated vector $\boldsymbol{x}$ of real-valued node parameters in a local graph neighborhood matching graph $G^r(\boldsymbol{x})$, which is otherwise unchanged from the left-hand side to right-hand side of the rule, obeys the coupled differential equation system $d\boldsymbol{x}/dt = \boldsymbol{v}(\boldsymbol{x})$. As shown by Eq. 21 in Mjolsness (2013), using Dirac delta functions in a physicist's style of calculation rather than a mathematical analyst's, it suffices to consider an operator of an especially simple form, with the same graph nodes and edges on the left and right sides, and changes only to node labels:

$$\hat{W}_{\mathrm{ODE}\,r} = \hat{W}_r = \int d\mu_r(x) d\mu_r(y)\, \rho_r(\boldsymbol{y},\boldsymbol{x}) \sum_{\langle i_1,\ldots i_k\rangle_{\neq}} \hat{a}_{i_1,\ldots i_k}(G^r(\boldsymbol{y})) a_{i_1,\ldots i_k}(G^r(\boldsymbol{x})), \text{ where} \tag{9a}$$

$$\rho_r(\boldsymbol{y},\boldsymbol{x}) = -\nabla_{\boldsymbol{y}} \cdot (\boldsymbol{v}(\boldsymbol{y})\delta(\boldsymbol{y}-\boldsymbol{x})) = -\sum_a \nabla_{y_a}\left(v_a(\boldsymbol{y}) \prod_b \delta(y_b - x_b)\right). \tag{9b}$$

It is important that the combined definitions of integration measure μ, derivative ∇, and Dirac delta function δ should support integration by parts in **Eq. 9**, as, for example, Lebesgue does with the usual derivative operator and Dirac delta choices. We will assume the same can be said for whatever finite approximation of differential equation solving is to be run on a computer implementation, noting in support of this assumption the extensive literature on summation by parts and its generalization to memetic differential equation solution methods satisfying the identities of vector differential and integral calculus (Corbino and Castillo, 2020); as further support, we have noted the existence of a DGG simulation algorithm with a running implementation (Yosiphon, 2009; Mjolsness, 2013).

Clearly, the top line of **Eq. 9** is a special case of our general algebraic form for $\hat{W}_r$ if Dirac delta functions are admitted into the expressions for ρ_r. Moreover, if not, we can take a suitable $\sigma \to 0$ parametric limit of width-σ Gaussians to approach all the Dirac deltas at the end of all other calculations. This expression (**Eq. 9**) is already flux-balanced, so the corresponding $D_{\mathrm{ODE}\ r} = 0$ and $W_{\mathrm{ODE}\,r} = \hat{W}_{\mathrm{ODE}\,r}$. However, an important mathematical difference is that these ρ functions can no longer be guaranteed to be non-negative because velocities v in the ODEs have no sign restriction. A second important mathematical difference will be encountered in the commutation relations for creation/annihilation operators parameterized by the below real-valued labels: Kronecker deltas become Dirac deltas. The resulting approach based on **Eq. 9** leads to Proposition 1 of **Section 3.6**.

In this way, the proofs of Theorems 1 and 2 remain essentially unchanged, but their function spaces are reinterpreted to yield a nontrivial generalization in the expressive power of the rules, generalizing from stochastic parameterized graph grammars to dynamical graph grammars. A simulation algorithm for dynamic graph grammars is described in Mjolsness (2013). Mjolsness and Yosiphon (2006) and Mjolsness (2010) also show how to further extend this approach of **Eq. 9** to stochastic differential equations (SDEs).

2.2.2 Products and Commutators of Graph Rewrite Operators

From **Eqs 5**, **6**, we can compute the product:

$$\begin{aligned}\hat{W}_{r_2}\hat{W}_{r_1} = {} & \frac{1}{C_{r_1}(N_{\max\text{free}})}\frac{1}{C_{r_2}(N_{\max\text{free}})}\iint d\mu_{r_1}(X_1) d\mu_{r_2}(X_2)\, \rho_{r_1}(\boldsymbol{\lambda}_1(X_1), \boldsymbol{\lambda}'_1(X_1)) \\ & \times \rho_{r_2}(\boldsymbol{\lambda}_2(X_2), \boldsymbol{\lambda}'_2(X_2)) \sum_{\langle j_1,\ldots j_{k_2}\rangle_{\neq}} \sum_{\langle i_1,\ldots i_{k_1}\rangle_{\neq}} \hat{a}_{j_1,\ldots j_{k_2}}(G^{r_2\ \mathrm{out}}_{\mathrm{links}}) \\ & \times \hat{a}_{j_1,\ldots j_{k_2}}(G^{r_2\ \mathrm{out}}_{\mathrm{nodes}}) a_{j_1,\ldots j_{k_2}}(G^{r_2\ \mathrm{in}}_{\mathrm{links}}) a_{j_1,\ldots j_{k_2}}(G^{r_2\ \mathrm{in}}_{\mathrm{nodes}}) \times \hat{a}_{i_1,\ldots i_{k_1}}(G^{r_1\ \mathrm{out}}_{\mathrm{links}}) \\ & \times \hat{a}_{i_1,\ldots i_{k_1}}(G^{r_1\ \mathrm{out}}_{\mathrm{nodes}}) a_{i_1,\ldots i_{k_1}}(G^{r_1\ \mathrm{in}}_{\mathrm{links}}) a_{i_1,\ldots i_{k_1}}(G^{r_1\ \mathrm{in}}_{\mathrm{nodes}}),\end{aligned} \tag{10}$$

and consequently,

$$\begin{aligned}\hat{W}_{r_2}\hat{W}_{r_1} = {} & \frac{1}{C_{r_1}(N_{\max\text{free}})}\frac{1}{C_{r_2}(N_{\max\text{free}})}\iint d\mu_{r_1}(X_1) d\mu_{r_2}(X_2)\, \rho_{r_1}(\boldsymbol{\lambda}_1(X_1), \boldsymbol{\lambda}'_1(X_1)) \\ & \times \rho_{r_2}(\boldsymbol{\lambda}_2(X_2), \boldsymbol{\lambda}'_2(X_2)) \sum_{\langle j_1,\ldots j_{k_2}\rangle_{\neq}} \sum_{\langle i_1,\ldots i_{k_1}\rangle_{\neq}} \hat{a}_{j_1,\ldots j_{k_2}}(G^{r_2\ \mathrm{out}}_{\mathrm{links}}) \\ & \times \left[a_{j_1,\ldots j_{k_2}}(G^{r_2\ \mathrm{in}}_{\mathrm{links}}) \hat{a}_{i_1,\ldots i_{k_1}}(G^{r_1\ \mathrm{out}}_{\mathrm{links}})\right] a_{i_1,\ldots i_{k_1}}(G^{r_1\ \mathrm{in}}_{\mathrm{links}}) \\ & \times \hat{a}_{j_1,\ldots j_{k_2}}(G^{r_2\ \mathrm{out}}_{\mathrm{nodes}}) \left[a_{j_1,\ldots j_{k_2}}(G^{r_2\ \mathrm{in}}_{\mathrm{nodes}}) \hat{a}_{i_1,\ldots i_{k_1}}(G^{r_1\ \mathrm{out}}_{\mathrm{nodes}})\right] a_{i_1,\ldots i_{k_1}}(G^{r_1\ \mathrm{in}}_{\mathrm{nodes}}).\end{aligned} \tag{11}$$

We now discuss the emergence of a new combined propensity function $\rho_{r_{2;1}}(Y_2, Z, X_1)$ for the product of rule operators in **Eq. 11**, which will arise from delta functions that appear in commutators of elementary operators. The form of $\rho_{r_{2;1}}$ is given in **Eq. 14**.

In general, the commutator of elementary operators will either be zero or proportional to a Kronecker or Dirac delta function, which removes one of the multiple summations or integrations over parameters in the foregoing expression. For example, in the case of continuous parameters X, we may have $d\mu(X)$ = Lebesgue measure, encountering Dirac delta functions arising from the operator algebra:

$$\begin{aligned}&\int d\boldsymbol{y}_2 d\boldsymbol{x}_2 \int d\boldsymbol{y}_1 d\boldsymbol{x}_1 \rho_{r_2}(\boldsymbol{y}_2,\boldsymbol{x}_2)\rho_{r_1}(\boldsymbol{y}_1,\boldsymbol{x}_1)\delta^{\mathrm{Dirac}}(\boldsymbol{x}_2 - \boldsymbol{y}_1)\mathcal{O}(\boldsymbol{y}_2,\boldsymbol{x}_2,\boldsymbol{y}_1,\boldsymbol{x}_1) \\ &\quad = \int d\boldsymbol{y}_2 d\boldsymbol{z} d\boldsymbol{x}_1 \rho_{r_{2;1}}(\boldsymbol{y}_2,\boldsymbol{z},\boldsymbol{x}_1)\mathcal{O}(\boldsymbol{y}_2,\boldsymbol{z},\boldsymbol{z},\boldsymbol{x}_1).\end{aligned} \tag{12}$$

Likewise, for discrete label variables, we will have $d\mu(X)$ = a discrete measure so that the integral is a sum, together with Kronecker deltas arising from the operator algebra:

$$\begin{aligned}&\sum_{\alpha_2}\sum_{\beta_2}\sum_{\alpha_1}\sum_{\beta_2} \rho_{r_2}(\beta_2,\alpha_2)\rho_{r_1}(\beta_1,\alpha_1)\delta^{\mathrm{Kronecker}}(\alpha_2,\ \beta_1)\mathcal{O}(\beta_2,\alpha_2,\beta_1,\alpha_1) \\ &\quad = \sum_{\beta_2}\sum_{\gamma}\sum_{\alpha_1} \rho_{r_{2;1}}(\beta_2,\gamma,\alpha_1)\mathcal{O}(\beta_2,\gamma,\gamma,\alpha_1)\end{aligned} \tag{13}$$

where $\mathcal{O}$ is a suitable operator expression and where scalar functions combine simply by multiplication and delta-induced parameter substitution:

$$\rho_{r_{2;1}}(Y_2, Z, X_1) \equiv \rho_{r_2}(Y_2, Z)\rho_{r_1}(Z, X_1), \tag{14}$$

where the capital letter parameters are vectors of discrete and/or continuous parameters. **Eq. 14** preserves the non-negativity of ρ scalar functions if rules r_1 and r_2 have it. Following **Eq. 10**, the variables Z will subsequently be integrated out. This parallelism between discrete and continuous versions of the identity $\int d\mu(x)\delta(x - y)f(x) = f(y)$ is the fundamental reason that Theorems 1 and 2 can be extended to the continuous case described in Proposition 1.

Given a formula for the product $\hat{W}_{r_2}\hat{W}_{r_1}$ of two (in general non-elementary) graph rewrite rule operators, their commutator is of course just

$$\left[\hat{W}_{r_2}, \hat{W}_{r_1}\right] = \hat{W}_{r_2}\hat{W}_{r_1} - \hat{W}_{r_1}\hat{W}_{r_2} \tag{15}$$

The products and commutators of full probability-conserving rule operators of the form $W_r = \hat{W}_r - D_r$ also follow directly. Nevertheless, the operator commutator is mathematically a fundamental object.

2.3 Three Problems to Solve

We can now state the central problems of this study:

(1) Up to equivalence, can the product of two graph grammar rewrite rule operators be expressed in terms of a sum of such operators, and if so, how?
(2) Likewise for the commutator of such operators: up to equivalence, can the commutator of two graph grammar rewrite rule operators be expressed in terms of a sum of such operators, and if so, how?
(3) Do these results extend to dynamical graph grammars, which by definition include rules that bear differential equations?

2.4 Preview of Main Results

After a calculation and several arguments, the main result that answers the foregoing questions will be an operator algebra equivalence that turns a product of graph rewrite operators into a sum of other graph rewrite operators. The required sum is taken over two sets of recognizable combinatorial objects: first, the possible edge-maximal subgraphs H in the output side of rule r_1 that match the structure and labels of some subgraph $\tilde{H}$ of the input side of rule r_2, representing their possible overlap of rule firing action, and second, the one or more possible distinct maps h along which such a one-to-one matching can occur. The equation is

$$\hat{W}_{G'^{2\ \mathrm{in}}\to G'^{2\ \mathrm{out}}}\hat{W}_{G'^{1\ \mathrm{in}}\to G'^{1\ \mathrm{out}}} \simeq \sum_{\substack{H\subseteq G'^{1\ \mathrm{out}} \simeq \tilde{H}\subseteq G'^{2\ \mathrm{in}} \\ |\,\text{edge-maximal}}} \sum_{h: H \overset{1-1}{\hookrightarrow} \tilde{H}} \hat{W}_{G^{1;2\ \mathrm{in}}(\tilde{H}) \underset{h}{\to} G^{1;2\ \mathrm{out}}(H)} \tag{16}$$

where the new labeled graphs, roughly given by

$$\begin{aligned} G^{1;2\ \mathrm{in}}\left(\tilde{H}\right) &= G^{r_1\ \mathrm{in}}\dot{\cup}\left(G^{r_2\ \mathrm{in}}\backslash\tilde{H}\right) \\ G^{1;2\ \mathrm{out}}(H) &= G^{r_2\ \mathrm{out}}\dot{\cup}\left(G^{r_1\ \mathrm{out}}\backslash H\right), \end{aligned} \tag{17}$$

and their labeled graph overlap will be defined more carefully in **Section 3**. The binary set difference "\" and disjoint union "$\dot{\cup}$" operators apply directly to the vertices in the respective graphs but extend to all associated edges to result in valid graphs. Scalar functions ρ_r will combine by multiplication and parameter substitution, as in **Eq. 14**. Note that all integer weights on the left-hand side of **Eq. 16** are nominally zero or one. However, because the same or equivalent operators could arise multiple times, the weights are actually nonnegative integers.

In this way, the operator algebra of graph rewrite rules is "lifted" from the level of creation/annihilation operators on elementary binary random variables to the more abstract and structural level of well-formed labeled graph rewrite rules.

This result will be shown without (Theorem 1, **Section 3.4**, and Supplementary Section SA.5) and with (Theorem 2, **Section 3.5**, and **Supplementary Section SA.6**) hanging edge cleanup semantics. First (**Sections 3.1–3.3** and **Supplementary Sections SA.2–SA.4**), we will discuss some of the used operator algebra calculational techniques and strategies without claiming any optimality for them.

As direct corollaries (Corollaries 1 and 5, **Sections 3.4**, **3.5**), the full operators $W_r = \hat{W}_r - D_r$ obey a similar product $\simeq$ integer-weighted sum operator equivalence, except that the integer-weighted sum over graph rewrite rule operators on the right-hand side can have both positive and negative integer weights. Also, as direct corollaries (Corollaries 2 and 6, **Sections 3.4**, **3.5**), the same is true for the commutators:

$$\begin{aligned} \left[\hat{W}_{G'^{2\ \mathrm{in}}\to G'^{2\ \mathrm{out}}}, \hat{W}_{G'^{1\ \mathrm{in}}\to G'^{1\ \mathrm{out}}}\right] \simeq & \sum_{\substack{H\subseteq G'^{1\ \mathrm{out}} \simeq \tilde{H}\subseteq G'^{2\ \mathrm{in}} \\ H\neq\varnothing\ \wedge\ \text{edge-maximal}}} \sum_{h: H \overset{1-1}{\hookrightarrow} \tilde{H}} \hat{W}_{G^{1;2\ \mathrm{in}}(\tilde{H}) \underset{h}{\to} G^{1;2\ \mathrm{out}}(H)} \\ & - \sum_{\substack{H\subseteq G'^{2\ \mathrm{out}} \simeq \tilde{H}\subseteq G'^{1\ \mathrm{in}} \\ H\neq\varnothing\ \wedge\ \text{edge-maximal}}} \sum_{h: H \overset{1-1}{\hookrightarrow} \tilde{H}} \hat{W}_{G^{2;1\ \mathrm{in}}(\tilde{H}) \underset{h}{\to} G^{2;1\ \mathrm{out}}(H)} \end{aligned} \tag{18}$$

except that the integer-weighted sum over graph rewrite rule operators on the right-hand side can have both positive and negative integer weights, and the $H = \varnothing$ terms always drop out.

In addition, in the course of proving these two theorems, we exhibit in each case a constructive mapping (Corollaries 3 and 7, **Sections 3.4**, **3.5**) from the graph rewrite rule operator algebra semantics to the elementary bitwise (two-state) operator algebras of **Supplementary Section SA.3.1**.

Finally, Corollaries 4 and 8 (**Sections 3.4**, **3.5**) point out that $H = \varnothing$ cancels out all the commutators of Corollaries 2 and 6.

Theorems 1 and 2 will extend straightforwardly, as stated in Proposition 1, to the dynamical graph grammar (DGG) case, in which some rule operators express dynamical systems in the form of systems of ordinary differential equations, as sketched in **Section 2.2.1** and **Eq. 14**. In like manner, some rules could be SDE-bearing rules whose operator expression is given in Mjolsness and Yosiphon (2006) and Mjolsness (2010).

3 RESULTS

In this section, we will sketch the main calculations of this study, which appear in much greater detail in **Supplementary Material**

SA, interleaved with mathematical statements of the results of those calculations. The sketch will take the following form: 1) preliminary definitions and notation, including the two different graph grammar operator semantics that differentiate Theorem 1 from Theorem 2 (**Sections 3.1–3.3**); 2) an operator product problem statement for the first semantics, followed by the statements of Lemma 1 and Theorem 1 each followed by a link to **Supplementary Material SA** for its proof, followed by a series of four corollaries with short proofs (**Section 3.4**); 3) an operator product problem statement for the second semantics, followed by a proof sketch for the removal of hanging edges, followed by the theorem statement of Theorem 2 and a link to **Supplementary Material SA** for its full proof, which expands on but does not depend on the proof sketch, followed by a series of four corollaries with short proofs (**Section 3.5**); 4) further observations based on earlier equations that are gathered together to prove Proposition 1, followed by the statement of Proposition 1 (**Section 3.6**). In addition, we will provide selected example calculations (**Section 3.7**) involving cytoskeleton in plant cells and synapses.

For the sketch, we will set $1/C_r(N_{\max\,\text{free}}) = 1$ by using a choice function for the next-needed unallocated graph node. This choice is, of course, multiplicative, but other ways of achieving that property are discussed in **Supplementary Section SA.2**.

3.1 Algebra of Binary and Mutual Exclusion State Changes

The expressions [...] in square brackets in **Eq. 11** for $\hat{W}_{r_2}\hat{W}_{r_1}$ need to be restored to normal order, with annihilators a_α to the right of (preceding) creation operators $\hat{a}_\alpha$. To this end, we need various operator rules for 2 × 2 elementary operators:

$$\hat{a} = \begin{pmatrix} 0 & 0 \\ 1 & 0 \end{pmatrix}, a = \begin{pmatrix} 0 & 1 \\ 0 & 0 \end{pmatrix} \text{ implies} \tag{19a}$$

$$\hat{a}a = N \equiv \begin{pmatrix} 0 & 0 \\ 0 & 1 \end{pmatrix}, \quad a\hat{a} = Z \equiv I - N = \begin{pmatrix} 1 & 0 \\ 0 & 0 \end{pmatrix}, \text{ and} \tag{19b}$$

$$\left[a_\alpha, \hat{a}_\beta\right] = \delta_{\alpha\beta}(I_\alpha - 2N_\alpha)I \qquad \text{Alternative for normal form calcs :} \tag{19c}$$

$$a_\alpha\hat{a}_\beta = \hat{a}_\beta a_\alpha - 2\delta_{\alpha\beta}\hat{a}_\alpha a_\alpha + \delta_{\alpha\beta}I_\alpha \tag{19d}$$

$$a_\alpha\hat{a}_\beta = \left(1 - \delta_{\alpha\beta}\right)\hat{a}_\beta a_\alpha + \delta_{\alpha\beta}Z_\alpha. \tag{19e}$$

Delta functions $\delta_{\alpha\beta}$ are by default Kronecker deltas or products thereof, but if α indexes a (node, label) pair and the label includes continuous variables, then $\delta_{\alpha\beta}$ for continuous variables should receive Dirac delta factors instead so that the composition rule of **Eq. 14** is equally valid for discrete and continuous variables. It is important not to use anticommutators for these 0/1-valued random state vectors, even though, in the case $\alpha = \beta$, the foregoing commutation relations are equivalent to anticommutation relations for fermions in quantum mechanics because, in the case $\alpha \neq \beta$, the corresponding operators commute and therefore do not anticommute.

For edges at least, we will also need the 2 × 2 "erasure" operator:

$$E_\alpha = Z_\alpha + a_\alpha = \begin{pmatrix} 1 & 1 \\ 0 & 0 \end{pmatrix}, \tag{20}$$

which is a projection operator to the $n_\alpha = 0$ state.

We can enforce a higher-level mutual exclusion ("winner-might-take-all" or "one or zero hot") logic of binary labels by fiat using axioms

$$\begin{aligned} a_{i,\lambda}a_{i,\lambda'} &= 0 \\ \hat{a}_{i,\lambda}\hat{a}_{i,\lambda'} &= 0 \\ a_{i,\lambda}\hat{a}_{i,\lambda'} &= \delta_{\lambda\lambda'}Y_{i,\lambda'}. \end{aligned} \tag{21}$$

where $N^{(a)}_{i,\lambda'}$ and $Y_{i,\lambda'}$ are diagonal in the number basis and idempotent. This leads to a crucially more constraining version of **Eq. 19e** in the case of labels

$$a_{j,\lambda}\hat{a}_{i,\lambda'} = \left(1 - \delta_{ij}\right)\hat{a}_{i,\lambda'}a_{j,\lambda} + \delta_{ij}\delta_{\lambda\lambda'}Y_{j,\lambda}. \tag{22}$$

Here, operator $Y_{j,\lambda}$ has eigenvalue 1 if node j is in the undecided state and also is not in the label λ state; otherwise, it is 0. The detailed mapping from **Eqs 19–22** is discussed in **Supplementary Section SA.4.1**.

3.2 Removal of Hanging Edges

The hanging edge removal variant of graph grammar rule semantics is

$$\begin{aligned} \hat{W}_r = \frac{1}{C_r(N_{\max\,\text{free}})}\int d\mu_r(X)\,\rho_r(\boldsymbol{\lambda}(X), \boldsymbol{\lambda}'(X)) \\ \times \sum_{\langle i_1,\ldots i_k\rangle_{\neq}} E_{\text{cleanup}}(G^r)\hat{a}_{i_1,\ldots i_k}(G^{r\ \text{out}})a_{\,i_1,\ldots i_k}(G^{r\ \text{in}}) \end{aligned} \tag{23}$$

where, as in **Eq. 6**,

$$\begin{aligned} E_{\text{cleanup}}(G^{r\ \text{in}}, G^{r\ \text{out}}) &= \left[\left(\prod_{p\in G^{r\ \text{in}}_{\text{nodes}}\setminus G^{r\ \text{out}}_{\text{nodes}}}\prod_{i\in\mathcal{U}}E_{i_p\ i}\right)\left(\prod_{p\in G^{r\ \text{in}}_{\text{nodes}}\setminus G^{r\ \text{out}}_{\text{nodes}}}\prod_{i\in\mathcal{U}}E_{i\ i_p}\right)\right] \\ \hat{a}_{i_1,\ldots i_k}(G') &= \hat{a}_{i_1,\ldots i_k}(G'_{\text{links}})\hat{a}_{i_1,\ldots i_k}(G'_{\text{nodes}}) \equiv \left[\prod_{(s',t')\in G'_{\text{links}}}\hat{a}_{i_{s'},i_{t'}}\right]\left[\prod_{v'\in G'_{\text{nodes}}}\hat{a}_{i_{v'},\lambda'_{v'}}\right] \\ a_{i_1,\ldots i_k}(G) &= a_{i_1,\ldots i_k}(G_{\text{links}})a_{i_1,\ldots i_k}(G_{\text{nodes}}) \equiv \left[\prod_{(s,t)\in G_{\text{links}}}a_{i_s i_t}\right]\left[\prod_{v\in G_{\text{nodes}}}a_{i_v\lambda_v}\right], \end{aligned} \tag{24}$$

$A \setminus B$ is again the set difference, that is, the subset of A not containing members of B, and $\mathcal{U}$ is the universe of object-modeling domain graph nodes.

3.3 Index Notation

In order to calculate operator products, we introduce systematic index set notation as follows.

Define L_χ, R_χ, $\mathcal{L}_\chi$, $\mathcal{R}_\chi$, for $\chi \in \{1, 2\}$:

$$\begin{aligned} \text{lhs nodes}(r_1) &\overset{\mathcal{I}}{\mapsto} \mathcal{I}(G^{1\ \text{in}}_{\text{nodes}}) \equiv L_1 & \text{rhs nodes}(r_1) &\overset{\mathcal{I}}{\mapsto} \mathcal{I}(G^{1\ \text{out}}_{\text{nodes}}) \equiv R_1 \\ \text{lhs nodes}(r_2) &\overset{\mathcal{J}}{\mapsto} \mathcal{J}(G^{2\ \text{in}}_{\text{nodes}}) \equiv L_2 & \text{rhs nodes}(r_2) &\overset{\mathcal{J}}{\mapsto} \mathcal{I}(G^{2\ \text{out}}_{\text{nodes}}) \equiv R_2; \\ \text{lhs links}(r_1) &\overset{\mathcal{I}}{\mapsto} \mathcal{I}(G^{1\ \text{in}}_{\text{links}}) \equiv \mathcal{L}_1 & \text{rhs links}(r_1) &\overset{\mathcal{I}}{\mapsto} \mathcal{I}(G^{1\ \text{out}}_{\text{links}}) \equiv \mathcal{R}_1 \\ \text{lhs links}(r_2) &\overset{\mathcal{J}}{\mapsto} \mathcal{J}(G^{2\ \text{in}}_{\text{links}}) \equiv \mathcal{L}_2 & \text{rhs links}(r_2) &\overset{\mathcal{J}}{\mapsto} \mathcal{I}(G^{2\ \text{out}}_{\text{links}}) \equiv \mathcal{R}_2. \end{aligned} \tag{25}$$

In this notation, the no-edge-cleanup semantics of **Eq. 6** becomes (making the parameter integrals implicit now, to limit the notational expansion):

$$\hat{W}_{r_\chi} = \frac{1}{C_{r_\chi}(N_{\max \text{free}})}\rho_{r_\chi}\left(\boldsymbol{\lambda}^{(x)},\boldsymbol{\lambda}'^{(x)}\right)\sum_{\mathcal{I}_\chi:\, L_\chi \cup R_\chi \overset{1-1}{\hookrightarrow} \mathcal{U}} \times\left[\prod_{(i_1,i_2)\in\mathcal{R}_\chi}\hat{a}_{i_1 i_2}\right]\left[\prod_{i_5\in R_\chi}\hat{a}_{i_5,\lambda^{(1)}_{\mathcal{I}^{-1}}(i_5)}\right]\left[\prod_{(i_3,i_4)\in\mathcal{L}_\chi}a_{i_3 i_4}\right]\left[\prod_{i_6\in L_\chi}a_{i_6,\lambda^{(1)}_{\mathcal{I}^{-1}}(i_6)}\right] \tag{26}$$

for $\chi \in \{1, 2\}$, where $\mathcal{I}_{\chi=1} \equiv \mathcal{I}$ and $\mathcal{I}_{\chi=2} \equiv \mathcal{J}$. Notation "$\overset{1-1}{\hookrightarrow}$" denotes any one-to-one map from whole of the stated domain into the stated range. Note that the middle square-bracketed terms commute trivially as elementary node and link operators operate in different spaces.

Also in this notation, node maps $\mathcal{I}$ and $\mathcal{J}$ can have overlapping images in $\mathcal{U}$. This relationship is parameterized by a set S (the inverse image of the overlap, under $\mathcal{I}$) and an induced map h from S into the domain of $\mathcal{J}$ (from the inverse image of the overlap under $\mathcal{I}$ to the inverse image of the overlap under $\mathcal{J}$):

$$\begin{aligned} S &= \mathrm{rhs}_1 \cap h^{-1}(\mathrm{lhs}_2) &&= G^{r_1\ \mathrm{out}}_{\mathrm{nodes}} \cap h^{-1}\left(G^{r_2\ \mathrm{in}}_{\mathrm{nodes}}\right)\\ h(S) &= \mathrm{lhs}_2 \cap h(\mathrm{rhs}_1) &&= G^{r_2\ \mathrm{in}}_{\mathrm{nodes}} \cap h^{-1}\left(G^{r_1\ \mathrm{out}}_{\mathrm{nodes}}\right)\\ \mathcal{I}(S) &= \mathcal{J}(h(S)) = L_2 \cap R_1 &&\\ \overline{\mathcal{I}(S)} &= \overline{L_2 \cap R_1} = \overline{L_2} \cup \overline{R_1}. &&\end{aligned} \tag{27}$$

Note also that

$$\mathcal{L}_\chi \subseteq \left[L_\chi \times L_\chi\right] \text{and} \, \mathcal{R}_\chi \subseteq \left[R_\chi \times R_\chi\right] \tag{28}$$

should be preserved inductively by rule firing semantics.

Define $\mathcal{P}_\chi(i_1, i_2)$ = a predicate that determines which edges E_{i_1,i_2} are hanging, if present, and should be deleted, where $\chi \in \{1, 2\}$. It may be a predicate function: $\mathcal{P}_\chi[L_\chi, R_\chi, \ldots, G^{\chi\ \mathrm{in}}_{\mathrm{links}}, G^{\chi\ \mathrm{out}}_{\mathrm{links}}](i_1, i_2)$. Also, $P^T(i_1, i_2) \equiv P(i_2, i_1)$. We will use one of several equivalent possibilities:

$$\mathcal{P}_\chi = \left[\left(L_\chi \backslash R_\chi\right) \times \mathcal{U}\right] \overset{\text{dual}}{\leftrightarrow} \mathcal{P}^\star_\chi = \mathcal{P}^T_\chi = \left[\mathcal{U} \times \left(L_\chi \backslash R_\chi\right)\right] \tag{29}$$

As before, $\mathcal{U}$ = the universe of possible node indices i.

3.4 Sketch of Commutation Calculation: No Edge Cleanup

The product of two such operators is (omitting for now the integral over parameters X)

$$\begin{aligned}\hat{W}_{r_2}\hat{W}_{r_1} = {}& \frac{1}{C_{r_1}(N_{\max \text{free}})}\frac{1}{C_{r_2}(N_{\max \text{free}})}\rho_{r_1}\left(\boldsymbol{\lambda}^{(1)},\boldsymbol{\lambda}'^{(1)}\right)\rho_{r_2}\left(\boldsymbol{\lambda}^{(2)},\boldsymbol{\lambda}'^{(2)}\right)\sum_{\mathcal{J}:\, L_2 \cup R_2 \overset{1-1}{\hookrightarrow} \mathcal{U}}\\ &\times \sum_{\mathcal{I}:\, L_1 \cup R_1 \overset{1-1}{\hookrightarrow} \mathcal{U}}\left[\prod_{(j_1,j_2)\in\mathcal{R}_2}\hat{a}_{j_1 j_2}\right]\left[\prod_{(j_3,j_4)\in\mathcal{L}_2}a_{j_3 j_4}\right]\left[\prod_{j_5\in R_2}\hat{a}_{j_5,\lambda^{(2)}_{\mathcal{J}^{-1}}(j_5)}\right]\\ &\times\left[\prod_{j_6\in L_2}a_{j_6,\lambda^{(2)}_{\mathcal{J}^{-1}}(j_6)}\right]\left[\prod_{(i_1,i_2)\in\mathcal{R}_1}\hat{a}_{i_1 i_2}\right]\left[\prod_{(i_3,i_4)\in\mathcal{L}_1}a_{i_3 i_4}\right]\\ &\times\left[\prod_{i_5\in R_1}\hat{a}_{i_5,\lambda^{(1)}_{\mathcal{I}^{-1}}(i_5)}\right]\left[\prod_{i_6\in L_1}a_{i_6,\lambda^{(1)}_{\mathcal{I}^{-1}}(i_6)}\right]\end{aligned} \tag{30}$$

Then, we will use the relevant commutation relations to calculate the following:

Lemma 1. Let $H(S, h)$ be the maximal common subgraph of both $G^{r_1\ \mathrm{out}}$ and $G^{r_2\ \mathrm{in}}$, for any given choice of nodes S in $G^{r_1\ \mathrm{out}}$ and 1-1 corresponding nodes h(S) in $G^{r_2\ \mathrm{in}}$. We can restrict S to sets of nodes whose labels match in $G^{r_2\ \mathrm{in}}_{\mathrm{nodes}}$ and $G^{r_1\ \mathrm{out}}_{\mathrm{nodes}}$. For any such H, we can commute the link operators as follows:

$$\begin{aligned}&\left[\prod_{(j_3,j_4)\in\mathcal{L}_2}a_{j_3 j_4}\right]\left[\prod_{(i_1,i_2)\in\mathcal{R}_1}\hat{a}_{i_1 i_2}\right]\\ &\quad=\left[\prod_{(i_1,i_2)\in\mathcal{I}\left(G^{r1\ \mathrm{out}}_{\mathrm{links}}\backslash H_{\mathrm{links}}\right)}\hat{a}_{i_1 i_2}\right]\left[\prod_{(j_3,j_4)\in\mathcal{J}\left(G^{r_2\ \mathrm{in}}_{\mathrm{links}}\backslash h^{-1}(H_{\mathrm{links}})\right)}a_{j_3 j_4}\right]\\ &\qquad\times\left[\prod_{(j_7,j_8)\in\mathcal{I}(H_{\mathrm{links}})\equiv\mathcal{L}_2\cap\mathcal{R}_1}Z_{j_7 j_8}\right]\end{aligned} \tag{31}$$

The last factor above implements the edge-checking or link correspondence portion of graph matching between a subgraph H(S, h) of the output graph of rule r_1 and a corresponding subgraph of the input graph of rule r_2.

Note that the 1-1 and onto node map $h: H \to \tilde{H}$ preserves edges and labels of labeled subgraphs H and $\tilde{H}$ and thus is an isomorphism of labeled subgraphs.

By further calculation and careful interpretation of terms, we arrive at the main result, except limited to the case in which hanging edges are not removed by the rule semantics: for the hanging edge permissive semantics of **Eqs 5**, **6**, or equivalently **Eq. 26**,

$$\hat{W}_{G^{r2}\ \mathrm{in}\to G^{r2}\ \mathrm{out}}\hat{W}_{G^{r1}\ \mathrm{in}\to G^{r1}\ \mathrm{out}} \simeq \sum_{\substack{H\subseteq G^{r1}\ \mathrm{out}\simeq\tilde{H}\subseteq G^{r2}\ \mathrm{in}\\ |\,\mathrm{edge-maximal}}}\ \sum_{h:\, H\overset{1-1}{\hookrightarrow}\tilde{H}}\hat{W}_{G^{r1}\ \mathrm{in}\dot{\cup}\left(G^{r2}\ \mathrm{in}\backslash\tilde{H}\right)\underset{h}{\to}G^{r2}\ \mathrm{out}\dot{\cup}\left(G^{r1}\ \mathrm{out}\backslash H\right)} \tag{32}$$

In more detail, the summand graph rewrite rule is then defined by Theorem 1. Under the definitions of the compound label graphs in **Eqs 34**, **35**, one can write the graph rewrite rule algebra as announced in **Section 2.4**.

Theorem 1. For the hanging edge-permissive semantics of **Eqs 5**, **6** or equivalently **Eq. 26** and assuming multiplicative normalization C_r, then

$$\hat{W}_{G^{r2}\ \mathrm{in}\to G^{r2}\ \mathrm{out}}\hat{W}_{G^{r1}\ \mathrm{in}\to G^{r1}\ \mathrm{out}} \simeq \sum_{\substack{H\subseteq G^{r1}\ \mathrm{out}\simeq\tilde{H}\subseteq G^{r2}\ \mathrm{in}\\ |\,\mathrm{edge-maximal}}}\ \sum_{h:\, H\overset{1-1}{\hookrightarrow}\tilde{H}}\hat{W}_{G^{1;2}\ \mathrm{in}\left(\tilde{H}\right)\underset{h}{\to}G^{1;2}\ \mathrm{out}(H)} \tag{33}$$

where the compound labeled graphs $G^{1;2\ \mathrm{in}}(\tilde{H})$ and $G^{1;2\ \mathrm{out}}(H)$ are defined by

$$\begin{aligned} G^{1;2\ in}_{nodes}\left(\tilde{H}_{nodes}\right) &= G^{r_1\ in}_{nodes}\dot{\cup}\left(G^{r_2\ in}_{nodes}\backslash\tilde{H}_{nodes}\right) & G^{1;2\ out}_{nodes}(H_{nodes}) &= G^{r_2\ out}_{nodes}\dot{\cup}\left(G^{r_1\ out}_{nodes}\backslash H_{nodes}\right)\\ &\equiv G^{r_1\ in}_{nodes}\cup h^{-1\star}\left(G^{r_2\ in}_{nodes}\tilde{H}_{nodes}\right) & &\equiv G^{r_2\ out}_{nodes}\cup h^{\star}\left(G^{r_1\ out}_{nodes}\backslash H_{nodes}\right)\\ G^{1;2\ in}_{links}\left(\tilde{H}_{nodes}\right) &= G^{r_1\ in}_{links}\cup h^{-1\star}\left(G^{r_2\ in}_{links}\backslash\tilde{H}_{links}\right) & G^{1;2\ out}_{links}(H_{nodes}) &= G^{r_2\ out}_{links}\cup h^{\star}\left(G^{r_1\ out}_{links}\backslash H_{links}\right)\end{aligned} \tag{34}$$

and their label overlaps $K_{1;2}$ are defined by

$$\begin{aligned} K_a &= G^{r_a\ in}_{nodes}\cap G^{r_a\ out}_{nodes}\\ K_{1;2} &= (K_1\backslash H_{nodes})\cup h^{-1}\left(K_2\backslash\tilde{H}_{nodes}\right)\cup\left(K_1\cap h^{-1\star}(K_2)\right).\end{aligned} \tag{35}$$

The coefficients in **Eq. 33** are all nonnegative integers (as the same graph grammar rule could arise several times by different means). Rate factors ρ multiply with parameter substitution, as in **Eq. 14**. Here, symbol $\dot{\cup}$ denotes disjoint union, and

$h^{\star}$: $G^{r_1\ out} \to G^{1;2\ out}$ extends h: $H \subseteq G^{r_1\ out} \to \tilde{H} \subseteq G^{r_2\ in}$ by remapping the nodes of G^{r_1} along h if possible and to the disjoint union nodes if not, preserving all possible links except those in H_{links}, likewise for h^{-1}: $\tilde{H} \subseteq G^{r_2\ in} \to H \subseteq G^{r_1\ out}$ and $h^{-1\star}$: $G^{r_2\ \mathrm{in}} \to G^{1;2\ \mathrm{in}}$.

Proof: The proof of this theorem is provided in **Supplementary Material SA**, with Theorem 1. It follows the proof sketch above but is written out in detail.

Note that **Eqs 34**, **35** reflect a time-reversal $L \leftrightarrow R$ duality. Examples of graph numbering and disjoint union $\dot{\cup}$ are given in **Section 3.7**. We now derive a series of corollaries presented only here, not in the detailed calculation sections.

Corollary 1. There is an algebraic reduction of operator products to sums, similar to Theorem 1, which applies to the $\mathrm{W_r}$ operators that subtract diagonal operators from $\hat{W}_r$ to conserve probability as in **Eq. 1**, except that the coefficients can be any integer.

Proof: Note that substituting $Z_\alpha = I_\alpha - N_\alpha$ in each elementary operator in Eq. 54 of **Supplementary Section SA.1** and distributing multiplication over addition, yields an integer-weighted sum of operators of the form of Eq. 53 of **Supplementary Section SA.1** or equivalently **Eq. 5**. Therefore, $W_{r_2}W_{r_2}$ is equivalent to a sum of $\hat{W}_s$ operators for a set of labeled graph grammar rules indexed by s. As W_{r_2} preserves probability, $\mathbf{1}\cdot W_{r_2}W_{r_1} = \mathbf{0}\cdot W_{r_1} = \mathbf{0}$. We can therefore subtract zero in the form of $\mathrm{diag}(\mathbf{1}\cdot W_{r_2}W_{r_1})$, applied term by term with the same sum of graph grammar rules substituted in for $W_{r_2}W_{r_1}$, and find that $W_{r_2}W_{r_2}$ is equivalent to a sum of full $W = \hat{W}_s - \mathrm{diag}(\mathbf{1}\cdot\hat{W}_s)$ operators for a set of labeled graph grammar rules indexed by s.

Corollary 2. There is an algebraic reduction of commutators of labeled graph grammar rule state-change operators $\hat{W}_r$ to sums of the same form, similar to Theorem 1, with integer coefficients and cancellation of $H = \varnothing = \tilde{H}$ summands:

$$\left[\hat{W}_{G^{r_2}\ in \to G^{r_2}\ out},\ \hat{W}_{G^{r_1}\ in \to G^{r_1} out}\right] \simeq \sum_{\substack{H\subseteq G^{r_1}\ out \simeq \tilde{H}\subseteq G^{r_2}\ in \\ H\neq\varnothing\ \wedge\ \text{edge-maximal}}} \sum_{h:\ H\overset{1-1}{\hookrightarrow}\tilde{H}} \hat{W}_{G^{1;2}\ in\ (\tilde{H}) \underset{h}{\to} G^{1;2}\ out\ (H)} - \sum_{\substack{H\subseteq G^{r_2}\ out \simeq \tilde{H}\subseteq G^{r_1}\ out \\ H\neq\varnothing\ \wedge\ \text{edge-maximal}}} \sum_{h:\ H\overset{1-1}{\hookrightarrow}\tilde{H}} \hat{W}_{G^{2;1}\ in\ (\tilde{H}) \underset{h}{\to} G^{2;1}\ out\ (H)} \tag{36}$$

Also, there is a similar algebraic reduction of commutators of labeled graph grammar rule full operator W_r commutators to sums of the same form, with integer coefficients.

Proof: As in Corollary 1, but with extra minus signs on some of the rule operators. Cancellation of $H = \varnothing = \tilde{H}$ summands follows from the $r_1 \leftrightarrow r_2$ symmetric definitions of $G^{1;2\ \mathrm{in}}$ and $G^{1;2\ \mathrm{out}}$ in **Eq. 34** in that special case.

Corollary 3. There exists (as exhibited in the proof of Theorem 1) a constructive mapping from the graph rewrite rule operator algebra semantics to the elementary bitwise operator algebras of **Supplementary Section SA.3.1**. Because it depends on an index allocation scheme which can be done in many ways, this mapping is not unique.

Corollary 4. One particular subgraph that always contributes to the product is $H = \varnothing = \tilde{H}$, the empty graph. Its contribution always cancels out of the commutator $[\hat{W}_{r_2}, \hat{W}_{r_1}] = \hat{W}_{r_2}\hat{W}_{r_1} - \hat{W}_{r_1}\hat{W}_{r_2}$ because $H = \varnothing$ and then nothing is shared between the two rule firings so their order does not matter.

3.5 Sketch of Commutation Calculation: With Edge Cleanup

We now turn to the hanging edge cleanup semantics and prove (Theorem 2) that the same algebra as in Theorem 1 and **Eqs 34** and **35**, and **33** still applies.

An elaboration of rule operators $\hat{W}_r$ can clean up hanging edges that may otherwise be left behind by a rule firing:

$$\begin{aligned}\hat{W}_r^{\mathrm{cleaned}} &= \left(\prod_{k_1\in L_r\setminus R_r}\prod_{k_2\in\mathcal{U}} E_{k_1k_2}E_{k_2k_1}\right)\hat{W}_r^{\mathrm{bare}} \\ &\simeq \left(\prod_{(k_1,k_2)\in\mathcal{S}} E_{k_1k_2}\right)\left(\prod_{(k_1,k_2)\in\mathcal{S}} E_{k_2k_1}\right)\hat{W}_r^{\mathrm{bare}}\end{aligned} \tag{37}$$

where $\mathcal{S}$ is the set of indices specified by

$$\mathcal{S} = [(L_r\setminus R_r)\times\mathcal{U}_{A^*}] \tag{38}$$

where $\mathcal{U}_{A^*}$ = all node indices that have ever been allocated in a memory block, hence all memory-live node indices, and $\mathcal{U}$ = the whole universe of node indices, so that $\mathcal{U}_{A^*} \subseteq \mathcal{U}$.

The semantics is now

$$\hat{W}_{r_\chi} = \frac{1}{C_{r_\chi}(N_{\max\mathrm{free}})}\int d\mu_{r_\chi}(X)\,\rho_{r_\chi}(\lambda[X],\lambda'[X]) \sum_{\mathcal{I}_\chi:\ L_\chi\cup R_\chi\overset{1-1}{\hookrightarrow}\mathcal{U}} \left[\left(\prod_{(i',i)\in\mathcal{P}_\chi} E_{i'\,i}\right)\left(\prod_{(\hat{i},\hat{i}')\in\mathcal{P}'_\chi} E_{\hat{i}\,\hat{i}'}\right)\right] \times\left[\prod_{(i_1,i_2)\in\mathcal{R}_\chi}\hat{a}_{i_1i_2}\right]\left[\prod_{(i_3,i_4)\in\mathcal{L}_\chi} a_{i_3i_4}\right]\left[\prod_{i_5\in R_\chi}\hat{a}_{i_5,\lambda'^{-1}_{\mathcal{I}_\chi}(i_5)}\right]\left[\prod_{i_6\in L_\chi} a_{i_6,\lambda^{-1}_{\mathcal{I}_\chi}(i_6)}\right]. \tag{39}$$

We now work to replace the product of E_{ij} factors above with the exponential of a sum:

$$E_\alpha = Z_\alpha + a_\alpha = I_\alpha + (a_\alpha N_\alpha) = I_\alpha + W_{\alpha\to\varnothing} \tag{40}$$

Defining $\epsilon = \tau/m$, we will see that

$$\exp\left(\tau\sum_{\alpha\in\mathcal{S}} W_{\alpha\to\varnothing}\right) = \lim_{m\to+\infty,\epsilon->0^+}\left(\prod_{\alpha\in\mathcal{S}}(I+\epsilon W_{\alpha\to\varnothing})\right)^m. \tag{41}$$

and we will compute that therefore asymptotically as $\tau = \rho_{\mathrm{erase}}t \to +\infty$,

$$\exp\left(\tau\sum_{\alpha\in\mathcal{S}} W_{\alpha\to\varnothing}\right) = \prod_{\alpha\in\mathcal{S}} E_\alpha. \tag{42}$$

So, complete erasure is the limiting behavior of this edge-by-edge stochastic erasure process, and it can be achieved simply by taking the limit $\rho_{\mathrm{erase}} \to +\infty$.

Now, we apply these calculations to the actual hanging edge erasure operator:

$$\exp\left(\tau \sum_{(i_1,i_2)\in\mathcal{S}} W_{(i_1,i_2)\to\varnothing}\right) = \exp\left(\tau \sum_{(i_1,i_2)\in\mathcal{S}} (E_{i_1,i_2} - I_{i_1,i_2}) N_{i_2} Z_{i_1}\right) \tag{43}$$

Here, the node operator Z_i checks for unallocated nodes i with no label.

Then, asymptotically as $\tau = \rho_{\text{erase}} t \to +\infty$,

$$\exp\left(\tau \sum_{\alpha\in\mathcal{S}} W_{\alpha\to\varnothing}\right) = \prod_{(i,j)\in\mathcal{S}} E_{i,j} N_j Z_i \simeq \prod_{(i,j)\in\mathcal{P}} E_{i,j}. \tag{44}$$

So again, we get the product of forward edge erasures by an incremental process of deletion, run for a long effective time τ.

In **Eq. 37**,

$$\begin{aligned}\hat{W}^{\text{cleaned}} &= \left(\prod_{(k_1,k_2)\in\mathcal{S}} E_{k_1k_2}E_{k_2k_1}\right)\hat{W}^{\text{bare}} \\ &= \lim_{n\to+\infty,\epsilon\to 0^+}\left[I + \epsilon \sum_{(k_1,k_2)\in\mathcal{S}} (a_{k_1,k_2}N_{k_1,k_2})N_{k_2}Z_{k_1}\right]^n \\ &\quad\times\left[I + \epsilon \sum_{(k_1,k_2)\in\mathcal{S}} (a_{k_2,k_1}N_{k_2,k_1})N_{k_1}Z_{k_2}\right]^n \hat{W}^{\text{bare}}\end{aligned} \tag{45}$$

The core calculation within $\hat{W}^{\text{cleaned}}_{r_2}\cdot\hat{W}^{\text{cleaned}}_{r_1}$ is thus

$$\begin{aligned}&\hat{W}^{\text{bare}}_{r_2}\left[\epsilon \sum_{(k_1,k_2)\in\mathcal{S}} (a_{k_1,k_2} - N_{k_1,k_2})N_{k_2}Z_{k_1}\right] \\ &= \frac{\epsilon}{C_{r_2}}\sum_{\mathcal{I}}\sum_{(k_1,k_2)\in\mathcal{S}}\left[\prod_{(i_1,i_2)\in\mathcal{R}_2}\hat{a}_{i_1i_2}\right]\left[\prod_{(i_3,i_4)\in\mathcal{L}_2} a_{i_3i_4}\right](a_{k_1,k_2} - N_{k_1,k_2}) \\ &\quad\times\left[\prod_{i_5\in R_2}\hat{a}_{i_5,\lambda_{\mathcal{I}^{-1}}(i_5)}\right]\left[\prod_{i_6\in L_2} a_{i_6,\lambda_{\mathcal{I}^{-1}}(i_6)}\right]N_{k_2}Z_{k_1}\end{aligned} \tag{46}$$

By operator algebra calculation, we find

$$\begin{aligned}&\left[\prod_{(i_1,i_2)\in\mathcal{R}_2}\hat{a}_{i_1i_2}\right]\left[\prod_{(i_3,i_4)\in\mathcal{L}_2} a_{i_3i_4}\right](a_{k_1,k_2}N_{k_1,k_2}) \\ &= \begin{cases} -\left[\prod_{(i_1,i_2)\in\mathcal{R}_2}\hat{a}_{i_1i_2}\right]\left[\prod_{(i_3,i_4)\in\mathcal{L}_2} a_{i_3i_4}\right] & \text{if } (k_1,k_2)\in\mathcal{L}_2 \\ N_{k_1,k_2}\left[\prod_{(i_1,i_2)\in\mathcal{R}_2}\hat{a}_{i_1i_2}\right]\left[\prod_{(i_3,i_4)\in\mathcal{L}_2} a_{i_3i_4}\right] & \text{if } (k_1,k_2)\in\mathcal{R}_2\backslash\mathcal{L}_2 \\ (a_{k_1,k_2}N_{k_1,k_2})\left[\prod_{(i_1,i_2)\in\mathcal{R}_2}\hat{a}_{i_1i_2}\right]\left[\prod_{(i_3,i_4)\in\mathcal{L}_2} a_{i_3i_4}\right] & \text{if } (k_1,k_2)\in\bar{\mathcal{R}}_2\cap\bar{\mathcal{L}}_2. \end{cases}\end{aligned} \tag{47}$$

Further arguments in the detailed calculation section will show that all surviving terms behave as in the third line of **Eq. 47**, and the factor of $a - N$ to the right of the second rule firing simply joins the infinite supply of such factors to its left.

Intuitively, this means that hanging edges can be eliminated nonspecifically by an overactive syntax-checking process rather than surgically in a way that depends on the details of each rule firing because the assumed form of the graph rewrite rules does not recognize or respond to hanging edges; all edges are verified to have two vertices before a rule can fire. As an aside, this explanation would not remain valid if the semantics were changed to allow things like the nonconforming operator $W_{(i_1,i_2)\to\varnothing}$ above, so as to allow hanging edges as part of the normal graph grammar operation. Then, a more complex algebraic operator equation might result.

Thus, we find no change to the algebraic formula of Theorem 1 for the hanging edge removal semantics.

Theorem 2. For the hanging edges removal semantics of **Eqs. 23**, **24**, or equivalently **Eq. 39**, assuming finiteness of rules, index allocation blocks, and number of rule firings, and assuming multiplicative normalization C_r, then

$$\hat{W}_{G'^2\ \text{in}\to G'^2\ \text{out}}\hat{W}_{G'^1\ \text{in}\to G'^1\ \text{out}} \simeq \sum_{\substack{H\subseteq G'^1\ \text{out}\simeq\tilde{H}\subseteq G'^2\ \text{in}\\ |\,\text{edge-maximal}}}\ \sum_{h:\ H\overset{1-1}{\hookrightarrow}\tilde{H}} \hat{W}_{G^{1;2}\ \text{in}(\tilde{H})\ \underset{h}{\to}\ G^{1;2}\ \text{out}(H)} \tag{48}$$

where the compound labeled graphs $G^{1;2\ \text{in}}(\tilde{H})$ and $G^{1;2\ \text{out}}(H)$, and their label overlaps $K_{1;2}$ are defined by **Eqs 34**, **35** in Theorem 1. The coefficients in this expression are all nonnegative integers (as the same graph grammar rule could arise several times by different means). Rate factors ρ multiply with parameter substitution, as in **Eq. 14**.

Proof: The proof of this theorem is provided in **Supplementary Material SA**, with Theorem 2. It follows the proof sketch above but is written out in detail.

We now derive another series of corollaries presented only here, not in the detailed calculation section.

Corollary 5. There is an algebraic reduction of operator products to sums, similar to Theorem 2, that applies to the W_r operators that subtract diagonal operators from $\hat{W}_r$ to conserve probability, except that the coefficients can be any integer.

Proof: Exactly as for Corollary 1.

Corollary 6. There is an algebraic reduction of commutators of labeled graph grammar rule state-change operators $\hat{W}_r$ to sums of the same form, similar to Theorem 2, with integer coefficients. Also, there is a similar algebraic reduction of commutators of labeled graph grammar rule full operator W_r commutators to sums of the same form, with integer coefficients.

Proof: As in Corollary 5 or 1, but with extra minus signs on some of the rule operators.

Corollary 7. There exists (as exhibited in the proofs of Theorems 1 and 2) a constructive mapping from the graph rewrite rule operator algebra semantics to the elementary bitwise operator algebras of **Supplementary Section SA.3.1**. As it depends on an index allocation scheme that can be done in many ways, this mapping is not unique.

Corollary 8. One particular subgraph that always contributes to the product is $H = \varnothing = \tilde{H}$, the empty graph. Its contribution always cancels out of the commutator $[\hat{W}_{r_2}, \hat{W}_{r_1}] = \hat{W}_{r_2}\hat{W}_{r_1} - \hat{W}_{r_1}\hat{W}_{r_2}$ because nothing is shared between the two rule firings so their order does not matter.

We note here that a previous attempt to prove Theorem 2 directly using the large product of E operators and $\mathcal{P}, L, R, \mathcal{L}, R$, among others, by Boolean logic ran aground in notational complexity. The method used here, with the exponential of a sum of $E - I$ operators, seems more tractable.

3.6 Application to ODEs and Dynamical Graph Grammars

In **Section 2.2.1**, we showed that a graph grammar rule that expresses a differential equation by not adding or removing any graph edges and by changing only the node labels, not the presence or absence of graph nodes, can be expressed within the general framework by applying Theorems 1 and 2 using a particular form of rule rate function ρ which, however, may take values of either sign. All steps of Theorems 1 and 2 remain valid. The signs of the commutator-induced coefficients that multiply the rate functions ρ remain as stated in these theorems and their corollaries.

The only change is that when the time to derive a simulation algorithm for these semantics comes, the functions ρ_r for differential equation rules cannot be interpreted as propensities (unnormalized probabilities per unit time) because they can be negative. That is all right because Mjolsness (2013) derived a separate kind of algorithm for stochastic parameterized grammars that contain such rules, calling an ODE solver as a subroutine. Of course, **Section 2.2.1** together with **Eq. 49** below suggests another algorithm under a limiting procedure for small but discrete changes in parameter values.

Thus, we show the following:

Proposition 1. Theorems 1 and 2 extend to rules that express differential equations by way of semantics incorporating Dirac delta functions as in **Eq. 9**.

For example, we will see in **Supplementary Material SB.3** that the operators $[\mathcal{O}_{\mathrm{DE}\,2}, \mathcal{O}_{\mathrm{DE}\,1}]$ of two differential equations for the same variables $d\boldsymbol{x}/dt = \boldsymbol{v}_1(\boldsymbol{x})$ and $d\boldsymbol{x}/dt = \boldsymbol{v}_2(\boldsymbol{x})$ have a commutator $\mathcal{O}_{\mathrm{DE}\,[2,\,1]}$ equivalent to a third differential equation $d\boldsymbol{x}/dt = \boldsymbol{v}_{[2,\,1]}(\boldsymbol{x}) \equiv (\boldsymbol{v}_1 \cdot \mathrm{grad}_{\boldsymbol{x}})\boldsymbol{v}_2(\boldsymbol{x}) - (\boldsymbol{v}_2 \cdot \mathrm{grad}_{\boldsymbol{x}})\boldsymbol{v}_1(\boldsymbol{x})$. In the same section, we will use the notation of Theorem 1 to exhibit the commutator of an ODE rule and a (non-ODE) SPG rule.

Alternatively to **Eq. 9**, one could eschew continuous parameters until the very end of a calculation by taking continuous "motion" of each real-valued parameter component x_a under an ODE to consist of many small discrete uniform-sized steps $\pm\Delta x$, with $\Delta x > 0$, with the sign chosen to be that of v in each component, and each step having a continuous-time propensity to occur given by $|v(\boldsymbol{x})|$. Then, after integration by parts and assuming suitable boundary conditions can be imposed on $\boldsymbol{v}$,

$$\hat{W}_{\mathrm{ODE\,discr}} = \sum_{\boldsymbol{x},a} \frac{|v_a(\boldsymbol{x})|}{\Delta x} \sum_{\langle i_1,\ldots i_k\rangle_{\neq}} [\hat{a}_{i_1,\ldots i_k}(G^r(\boldsymbol{x} + \mathrm{sign}(v_a(\boldsymbol{x}))\Delta x \boldsymbol{e}_a))a_{i_1,\ldots i_k}(G^r(\boldsymbol{x})) - \hat{a}_{i_1,\ldots i_k}(G^r(\boldsymbol{x}))a_{i_1,\ldots i_k}(G^r(\boldsymbol{x}))] \tag{49}$$

where $\boldsymbol{e}_a$ is the unit vector along axis a of the local parameter vector space containing $\boldsymbol{x}$. On timescales $\Delta t \ll \Delta x/\max_a|v_a(\boldsymbol{x})|$, parameter jumps occur one at a time and add up in the expected manner. Again, one would take a parametric limit, this time in the limit $\Delta x \to 0$. This approach has the advantage of non-negative ρ functions and, thus, a probabilistic interpretation of the rule operator.

By either of these means, mixed stochastic graph dynamics and differential equation dynamics can be approximated arbitrarily closely by operators of graph grammar dynamics of the algebraic form we have assumed. **Eq. 49** also hints at a different family of stochastic simulation algorithms, which may or may not lead to something efficient. Alternatively, as in **Eq. 9** and Proposition 1, one can simply admit Dirac delta functions into the allowed expressions for ρ_r and selected commutators, and no parametric limit is needed; this will be our preferred approach.

3.7 Examples

Several biological models have been formulated in terms of structural rewrite rules for graphs and cell complexes (Mjolsness et al., 1991; Spicher and Michel, 2007; Giavitto and Spicher, 2008; Lane, 2015) and the literature on L-systems, all reviewed from the present operator algebra point of view in Mjolsness (2019a).

Here, we will take as a working example a highly simplified stochastic parameterized graph grammar (SPGG) for microtubule dynamics, including treadmilling, bundling/zippering, and katanin-mediated severing in cytoskeleton dynamics as it appears in current plant biology.

3.7.1 MT Stochastic Graph Grammar

A diagrammatic presentation of a small subset of a plant cortical microtubule (MT) graph grammar, with subscripts for the rule-local arbitrary but consistent numbering of vertices in left- and right-hand side graphs of each rule, is shown below. These rules and calculations are a subset of those presented in **Supplementary Material SB**. Discrete parameters will include a four-valued categorical label $s \in \{$*internal*, *grow_end*, *retract_end*, *junct*$\}$ (or $s \in \{\circ, \bullet, \blacksquare, \blacktriangle\}$) for status as interior segment, growth-capable end segment, retraction-capable end segment, or bundling junction segment, respectively:

// Rule 1: Treadmilling growth

$$(\bullet_1)\langle\!\langle (\boldsymbol{x}_1, \boldsymbol{u}_1)\rangle\!\rangle \longrightarrow (\circ_1 \longrightarrow \bullet_2)\langle\!\langle (\boldsymbol{x}_1, \boldsymbol{u}_1), (\boldsymbol{x}_2, \boldsymbol{u}_2)\rangle\!\rangle$$
$$\textbf{with}\ \hat{\rho}_{\mathrm{grow}}([\mathrm{Y}_g])\mathcal{N}(\boldsymbol{x}_1 - \boldsymbol{x}_2; L\boldsymbol{u}_1, \sigma)\mathcal{N}_{|\boldsymbol{u}_2|=1}(\boldsymbol{u}_2; \boldsymbol{u}_1), \epsilon),$$

// Rule 3: Collision-induced bundling or zippering

$$\begin{pmatrix} \circ_1 \longrightarrow \circ_2 \longrightarrow \circ_3 \\ \bullet_4 \end{pmatrix}\langle\!\langle (\boldsymbol{x}_1, \boldsymbol{u}_1), (\boldsymbol{x}_2, \boldsymbol{u}_2), (\boldsymbol{x}_3, \boldsymbol{u}_3), (\boldsymbol{x}_4, \boldsymbol{u}_4)\rangle\!\rangle \tag{50}$$
$$\longrightarrow \begin{pmatrix} \circ_1 \longrightarrow \blacktriangle_2 \longrightarrow \circ_3 \\ \nearrow \\ \circ_4 \end{pmatrix}\langle\!\langle (\boldsymbol{x}_1, \boldsymbol{u}_1), (\boldsymbol{x}_2, \boldsymbol{u}_2), (\boldsymbol{x}_3, \boldsymbol{u}_3), (\boldsymbol{x}_4, \boldsymbol{u}_4)\rangle\!\rangle$$
$$\textbf{with}\ \hat{\rho}_{\mathrm{bundle}}(|\boldsymbol{u}_2 \cdot \boldsymbol{u}_4|/|\cos\theta_{\mathrm{crit}}|)\exp\left(-|\boldsymbol{x}_2 - \boldsymbol{x}_4|^2/2L^2\right)$$

Here, Y_g is a diffusible MT growth factor such as tubulin itself or a catalyst or regulator of tubulin polymerization and/or nucleation, such as (perhaps) XMAP215 (Hamant et al., 2019), and Y_r plays the same role in catastrophe/retraction.

In working out the commutators, we will drop the propensity functions ρ, but they just multiply the results with appropriate variable identifications.

Further MT rules are provided in **Supplementary Section SB.1**.

3.7.2 Example MT Commutator Calculation

The commutator calculations for this minimal MT graph grammar's Lie algebra can be outlined as follows:

$[\hat{W}_3, \hat{W}_1]$:

$\hat{W}_3 \cdot \hat{W}_1$: shared same-label vertex sets run over by H and their mappings under h are $\varnothing$; $\{(1\mapsto 1')\}$; $\{(1\mapsto 2')\}$; $\{(1\mapsto 3')\}$; $\{(1\mapsto 1'), (2\mapsto 4')\}$; $\{(1\mapsto 2'), (2\mapsto 4')\}$; $\{(1\mapsto 3'), (2\mapsto 4')\}$.

$\hat{W}_1 \cdot \hat{W}_3$: shared same-label vertex sets run over by H and their mappings under h are $\varnothing$.

$H = \varnothing$ always cancels in the commutator:

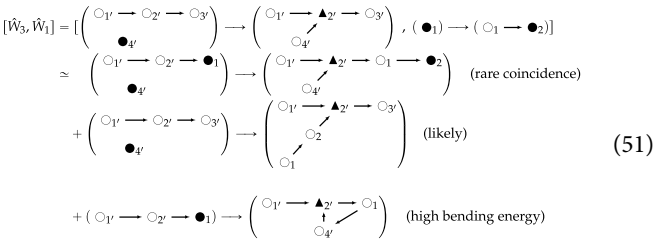

(51)

The reason the second line above involves a "rare coincidence" is that its left-hand side represents a collision of two long MTs very near to the growing end of both, assuming the MTs are generically quite long and thus have many internal nodes (open circles). Likewise, the fourth line requires a high bending energy (can thus be disfavored in a more detailed model) because of the loop of three small MT segments, two interior and one junction, in the RHS graph.

Further commutators are calculated in Theorems 1 and 2 and Proposition 1 in **Supplementary Section SB**.

For the restricted case in which one of the operators is a diagonal "observable," a rule commutator calculation has been exhibited independently in the "double pushout" formalism (**Section 4.2**) for a particular set of basic biochemical binding/unbinding rules expressed in Kappa (Behr et al., 2020). The general combinatorial formula of Theorems 1 and 2 and the extension of Proposition 1 remain unique as far as we know.

The special case in which no graph edges are present, only graph nodes, corresponds to a well-mixed stochastic chemical reaction network. The commutation relations for such models are calculated in **Supplementary Section SC**, in the conventional representation in which all particles of a given type lose their identity and only their population numbers matter.

3.7.3 Actin Cytoskeleton Stochastic Graph Grammar Examples

Actin filament polymerization and depolymerization rules can be analogous to those for MTs. Branching occurs in a different way than the bundling rule for MTs, as for example in this two-dimensional rule:

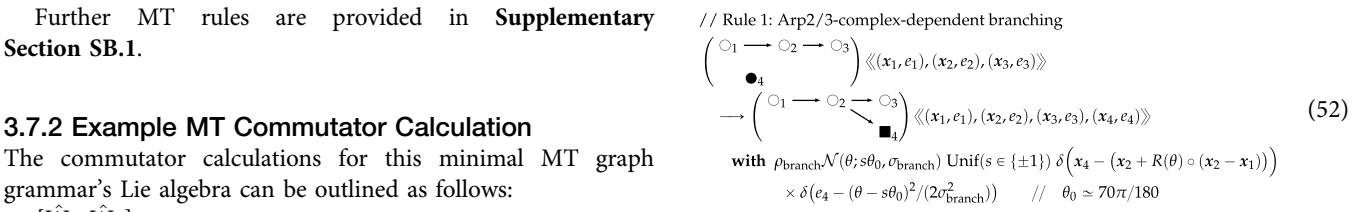

(52)

Here, $\bigcirc_2$ represents actin or short polymers of actin (which have a sense of directionality), $\bullet$ represents the Arp2/3 complex in solution, and $\blacksquare$ represents the Arp2/3 complex bound to actin and can serve as the nucleation site for a new actin filament. Also, the e parameters measure biomechanical energy owing to geometry, which can drive mechanics using differential equation rules. A simple prototype model of this sort has been simulated using the software of Yosiphon (2009).

In fact, MTs also have branching nucleation dynamics facilitated by other molecular players such as the augmin complex.

Other actin grammar rules, including polymerization-driven growth, can be modeled in a very similar manner to MT rules. For example, both kinds of filaments undergo catalyzed severing. Growing actin filaments may also acquire an end-cap, preventing further growth.

3.7.4 Related Kinds of Rewrite Rules

We have analyzed the semantics and given examples of stochastic parameterized graph grammar (SPGG) models.

Mjolsness and Yosiphon (2006) demonstrated how to use integer-valued Object ID (OID) parameters to encode such graph grammars within stochastic parameterized grammars (SPG) comprising parameter-bearing stochastic rewrite rules with operator algebra semantics. This reduction requires the use or dynamical emulation of a source of novel OIDs. Because the reverse inclusion is trivial, SLGGs, SPGGs, and SPGs are essentially different syntactic presentations for the same semantics; SPGGs may be easier to write since the OID encoding step is unnecessary.

Nevertheless, Mjolsness and Yosiphon (2006) showed how to add to SPG rules with ordinary and/or stochastic differential equation syntax and differential operator semantics, obtaining "dynamical grammars" (DGs). DGs can be a continuum limit (in label space and in time) of SPGs. If we allow differential equation rules and stochastic parameterized graph grammar rules, we arrive at dynamical graph grammars (DGGs), as defined here and the subject of Proposition 1.

Many other notational conveniences are possible while maintaining or generalizing the operator algebra semantics.

3.7.5 Cell Complex Rewrite Rules

In Mjolsness (2019a), the operator algebra semantics for a labeled graph rewrite rule is generalized in several ways. One of these generalizations is to cell complexes (each of some maximal dimension d), which have been applied to developmental modeling (Spicher and Michel, 2007; Lane, 2015). Mjolsness (2019a) also provided a constructive implementation mapping from the generalized rewrite rules back to graph grammar rewrite rules. In principle, the graph grammar operator algebra of our Theorems 1 and 2 apply to these generalized settings—but

whether the sum of graph grammar operators resulting from a higher-level product is also a sum of higher-level rewrite rules or not remains to be worked out.

Here, we point out a useful special case for cell complex dynamics: if a graph can be locally embedded in d dimensions (i.e., in d dimensional manifolds with $\mathbb{R}^d$ as the usual case) in such a way that it becomes a Voronoi diagram or a power diagram (weighted Voronoi diagram), then its label set can be augmented by the resulting node positions, and, more importantly, there is a dual d-dimensional cell complex consisting of the boundaries at equal distance (in the Voronoi case) from two or more graph node positions, together with the d-dimensional single-node cells they bound. Then, local graph grammar rewrite rules will generically result in local updates to the embedding and the dual cell complex, inducing local cell complex changes describable as rewrite rules.

As a final point of discussion, in the Lie group theory, the Lie algebra is related to the curvature tensor of a group-invariant metric. Likewise, in differentiable manifolds, commutators of covariant derivatives are related to the manifold curvature tensor. The Lie algebras discussed here are generically in a much higher dimension but, in some cases, may also relate to geometric and/or topological structures.

4 DISCUSSION

4.1 Conclusion

We have computed the product and commutator for any two stochastic parameterized graph rewrite rule operators in a stochastic graph grammar possessing operator algebra semantics, in structural (graph-expressed, combinatorial) form. In this form, the product of the state-changing portions (off-diagonal in the number basis) of two graph rewrite rule operators is a sum, with nonnegative integer coefficients, of other such operators. Non-negative real-valued rate multipliers are also carried along expectedly. The product of the full-graph rewrite rule operators and the commutator of off-diagonal or full-rule operators are likewise expressed as a sum with integer-valued weights of other full-graph rewrite rule operators. The algebra can also be applied to rewrite rules that bear ordinary differential equations for real-valued node parameters. The results are expressed in Theorem 1 and its corollaries for the case of semantics in which hanging edges are left behind and Theorem 2 and its corollaries for the case in which they are not. Proposition 1 demonstrates the application to the differential equation bearing rules. The algebra can be computed explicitly.

There is also a computer-implementable constructive mapping from the resulting graph rewrite rule algebra to many elementary two-state creation/annihilation operators. Because the algebra is expressed in the present work entirely in terms of identities relating to graph rewrite rule operators (up to equivalence) rather than more general expressions built from the underlying elementary two-state creation/annihilation operators, Theorems 1 and 2 are a substantial improvement in utility and perspicuity over the corresponding Propositions 1 and 2 in Mjolsness (2019a). Here, the operator algebra of graph rewrite rules is "lifted" from the concrete level of creation/annihilation operators on elementary binary random variables to the more abstract and structural level of well-formed labeled graph rewrite rules.

As a clarifying test case, the resulting graph-grammar level algebra was applied to an elementary example inspired by the dynamics of cortical microtubules in plant cells, one of many structure-changing dynamical systems in biophysics and other sciences that could be amenable to modeling by stochastic parameterized graph grammars.

4.2 Related Work

The present line of development for operator algebra semantics of chemical reaction networks and graph grammars began with expressivity studies (Mjolsness, 2005; Mjolsness and Yosiphon, 2006), including suitable measure spaces for a probabilistic foundation, followed by a combined SPG and DGG implementation (Yosiphon, 2009), which was applied to growing plant root models with cell division (Mjolsness, 2013), a direct graph semantics without object ID encoding (Mjolsness, 2010), a systematic derivation of stochastic simulation algorithms including differential equations (Mjolsness, 2013), the existence proof for rule product and commutator reduction in (Mjolsness, 2019a), and the calculations reported herein.

The larger context is diverse and includes L-systems (which generate tree-structured graphs without loops) and their generalizations, such as differential L-systems (Prusinkiewicz et al., 1993) and stochastic L-systems (Eichhorst and Walter, 1990; Cieslak and Prusinkiewicz, 2019). The earlier reference (Eichhorst and Walter, 1990) is related to Cieslak and Prusinkiewicz (2019) in part by being applied to computer science rather than biology and by projecting out stochastic event waiting times as described, for example, in Mjolsness and Yosiphon (2006) (Section 3.8), and by the Gillespie algorithm of Cieslak and Prusinkiewicz (2019) is just one possible sampling algorithm for an operator algebra semantics as derived, for example, in Mjolsness (2013). Further context also includes grammar-like "connectionist" models for biological development (Mjolsness et al., 1991) and plant developmental models incorporating cell division (Jönsson et al., 2006; Smith et al., 2006). These include some kind of dynamic graph topology as part of the dynamical system to be modeled. Investigation of more formalized computer support for variable-structure developmental models based on topological cell complexes is shown in Spicher and Michel (2007) and Lane (2015).

Independently, cytoskeletal modeling simulators have been developed, including algorithmic provision for changing topology of filament networks due to, for example, dynamic crosslinking and/or bundling of microtubule or actin fibers, which necessarily change the graph topology that influences further biomechanical dynamics in both microtubule and actin fibers (Nedelec and Dietrich, 2007; Popov et al., 2016; Belmonte et al., 2017; Kim et al., 2022). In such dynamic cytoskeleton codes, there comes a moment when the structure of the graph changes, for example, as a consequence of some molecular binding or unbinding event. At that moment, the problem of biomechanics changes locally but with potentially global

consequences. So, it may be important to explore a more systematic formalization, such as the present operator algebra, of local structure-changing dynamics interacting with differential equation dynamics. Improvements in both algorithms and analyses may result.

There is an alternative category-theory-based approach to graph grammar semantics based on single or double pushout (DPO) commutative diagrams rather than operator algebras and a collection of "independence" conditions for two successive rule firings to have an order-independent result as explained by Ehrig et al. (2006). In our operator algebra language, these conditions would guarantee a zero commutator. The DPO approach was applied to molecular complexes in Danos and Laneve (2004). However, it requires the use of an abstract mathematical language (category theory) that poses a substantial barrier to understanding many biological modelers; direct use of the operator algebra developed by Heisenberg, Von Neumann, and others to formalize quantum mechanics in the 1920s is substantially more accessible, especially when, as in our case, it concerns probability distributions rather than quantum amplitudes.

Behr et al. (2016) and Behr et al. (2019) combined and connected both double-pushout and Master Equation semantics, using a restricted subset of the operator algebra implied by Propositions 1 or 2 in Mjolsness (2019a) or the more powerful Theorems 1 and 2 of this work. Commutators were introduced to this approach in Behr et al. (2016), but, apparently, without computing the explicit combinatorial result in **Eq. 16**, treating only the special case in which one of the operators, an "observable," is diagonal in the number basis, a case which is potentially quite useful for pursuing moment closure approximation methods. They did not address the possibility in Proposition 1 of continuous parameters in the graph node labels or differential equation dynamics on those parameters. This approach has not been applied to the scientific domain of cell- or tissue-level morphodynamics in biological development.

Further discussion of the likely yet unproven relationship between our operator algebra semantics (**Section 2.2**) and the DPO semantics is provided in Mjolsness (2019a) (**Supplementary Section S7.2.10**).

Another work that associates a Lie algebra with a graph grammar is Marcoli and Port (2015). In this case, the basis Fock space over which the Lie algebra operators are defined is a space of labeled graphs G, rather than labeled graph grammar rules $G^{\text{in}} \rightarrow G^{\text{out}}$, so it is a different and smaller operator Lie algebra than ours. It seems closely related to a subalgebra of "graph insertions," comprising rules whose left-hand side graph is a single node.

A hypergraph variant of graph grammars has recently been used as the starting part for a dark-horse attempt to find a fully discrete-mathematical route to fundamental physical theory (Wolfram, 2020). Many evocative examples are given and visualized as evolving graphs embedded in low-dimensional visualization space. Our operator algebra formulation, including Theorems 1 and 2, does not appear, nor is there an integration (e.g., Proposition 1) with continuous-time differential processes we require for efficient simulation of emergent, non-fundamental processes.

4.3 Domain of Applicability

The present line of research began as an approach to multicellular models of biological development that include cell birth, death, and geometry-induced changes in topology (Mjolsness et al., 1991; Jönsson et al., 2006; Mjolsness and Yosiphon, 2006). The graph grammar operator algebra was defined implicitly (by mapping to unique object IDs) in Mjolsness and Yosiphon (2006), a method used to implement general dynamical graph grammar models in Yosiphon (2009), and defined explicitly in Mjolsness (2010).

As discussed in Mjolsness (2019a), operator commutators provide an analytic tool when used with perturbation series expansions such as the Baker–Campbell–Hausdorff (BCH) theorem (as suggested for stochastic chemical reaction networks in Hellander et al. (2014) and rewrite operator algebras in Mjolsness and Yosiphon (2006) and Behr et al. (2019)) underlying operator splitting methods (Jahnke and Altıntan, 2010; MacNamara and Strang, 2016) or the Time-Ordered Product Expansion for Feynman diagrams underlying the Gillespie Stochastic Simulation Algorithm (SSA) and some of its generalizations, including integration with differential equations (Mjolsness, 2013), by which to derive both general and model-specific simulation algorithms and approximations and bound or estimate their errors from the perturbation series remainder terms. For example, operator splitting algorithms, including the exploitation of analytically solvable submodels (Jahnke and Altıntan, 2010) can be formulated and have their errors analyzed by way of commutation relations using BCH. If, for example, two rule firings are simulated out of order for algorithmic efficiency, their commutator (which could be zero) quantifies the error introduced. Operator commutators are also fundamental, of course, for understanding the causal structure of a dynamical model. For example, in the Wightman axioms for quantum field theory in the Minkowski metric, the "Locality" axiom specifies the commutation (or anti-commutation) of operators that act at points separated by spacelike displacements (Glimm and Jaffe, 1981).

Potential applications of dynamical graph grammars (including stochastic parameterized graph grammars) are legion, particularly in multiscale modeling. We claim they comprise a third major scientific computing paradigm on the same level of generality and applicability as 1) partial differential equations (PDEs) or 2) particle methods. These are the two most relevant parallel computing "design patterns" identified for high-performance computing (HPC) in the survey of Asanovic et al. (2009). The same source identifies graph algorithms as a design pattern ubiquitous across parallel computing fields, excluding HPC. This exclusion can now be removed. Dynamical graphs and their operators, optionally expressed by dynamical graph grammars, in principle, bring a third paradigm major into play for generic mathematical and algorithmic tools for computational science.

Examples and categories of examples that would be suitable for DGG description include the following:

- Cytoskeleton: application to plant cortical microtubule dynamics has been described already in Mjolsness (2019a) and will be a running example for **Section 3.7.1** and **Supplementary Material SB.1**. An additional analogous example is the dynamic actin filament network in synapses during learning.
- The originally intended domain for DGGs was multicellular models of biological development that include cell birth, death, and geometry-induced changes in the topology of networks of cells whose adjacency relationships form a graph (Mjolsness et al., 1991), including topology-changing models of plant development in the *Arabidopsis* shoot apical meristems as in Jönsson et al. (2006). An explicit one-dimensional DGG (in textual OID form) for pattern formation and growth in the *Arabidopsis* root apical meristems is presented in Yosiphon (2009) and Mjolsness (2013). DGGs for dynamic developmental topologies such as abstract cell complexes and stratified spaces, *via* graph slice categories, are discussed in Mjolsness (2019a).
- Physical applications may include the dynamics of topological dislocations, defects, and fractures in materials, treated as sparse extended objects in communication with the dense extended object(s) comprising the material [e.g., in "dislocation dynamics" (Devincre et al., 2008; Vattré et al., 2014)].
- Axonal and dendritic arbor growth and retraction in microscope imagery of animal development, under the regulatory influence of key genes such as DSCAM (Santos et al., 2018), comprise a dynamic spatially embedded graph.
- Agent-based systems running on interaction graphs are widely used models in epidemiology (Venkatramanan et al., 2018), social science (Klein et al., 2018), and multiscale biological modeling (Letort et al., 2019). When agent-based systems take agent–agent connectivity to be not only a factor affecting the dynamics of particle-like state-bearing agents but also a time-varying component of the system state governed by its own dynamics, then the underlying mathematics may be well described by the local graph dynamics of DGG rule operators and DGGs are a candidate mathematical formalism (at a higher level of abstraction than computer code) for expressing such models.
- Approximate solution algorithms for partial differential equations frequently proceed by way of spatial discretization first, resulting in a grid or mesh of dynamic variables connected to neighbors that appear on the right-hand sides of a local ordinary differential equation (dynamical system) description. Time is then discretized inside the solution algorithm for the resulting differential equations. If the grid graph is adaptive by local rules, the approximation can be described by a dynamical graph grammar.
- Hypergraph models can also be represented *via* the standard mapping of (labeled) hypergraphs to (labeled) bipartite graphs that connect hypervertex-flavored vertices to hyperedge-flavored vertices and *vice versa*.
- There could be methodological connections to loop quantum gravity.

Most of these applications have in common some form of model reduction from a finer-scale description that does not need dynamical graph description. The standard model of fundamental physics encompasses intertwined particles and fields but not dynamical graphs. On the other hand, coarse-graining or upscaling often introduces dynamical connectivity descriptions suitable for dynamical graphs, so any modeling framework that is to be universal for or invariant under a broad class of model reductions needs something like the rule operators of DGGs.

Universality under model reduction is even better served if DGGs can also encompass partial differential equations (PDEs). As suggested above, DDGs, as described here, can express a wide variety of approximations to PDEs for spatial models, including approximations to continuum models described by PDEs. However, what is missing is the formalization entirely within DGGs of a graph limit that approaches continuous geometries, such as manifolds, cell complexes, and stratified spaces, as discussed in Mjolsness (2019a). Furthermore, a definition of graph limit based on the preservation of graph diffusion across scales was proposed by Scott and Mjolsness (2021). Graph diffusion has the advantage [over, e.g., graphons (Lovász, 2012)] that it is closely related to metric structure in the case of manifolds.

DATA AVAILABILITY STATEMENT

The original contributions presented in the study are included in the article/**Supplementary Material**. Further inquiries can be directed to the corresponding author.

AUTHOR CONTRIBUTIONS

EM did the research and wrote the paper.

FUNDING

This work was funded in part by U.S. NIH NIDA Brain Initiative grant 1RF1DA055668-01, U.S. NIH National Institute of Aging grant R56AG059602, Human Frontiers Science Program grant HFSP—RGP0023/2018, and US NSF grant NSF PHY-1748958. This work was supported in part by the UC Southern California Hub, with funding from the UC National Laboratories division of the University of California Office of the President.

ACKNOWLEDGMENTS

The author wishes to acknowledge the hospitality of the Sainsbury Laboratory Cambridge University, the Center for Nonlinear Studies of the Los Alamos National Laboratory, and

the Kavli Institute for Theoretical Physics at the University of California Santa Barbara. Theorems 1 and 2 of this study and the explicit calculations proving them previously appeared online in preprint form in Mjolsness (2019b). Proposition 1 of this study is new.

SUPPLEMENTARY MATERIAL

The Supplementary Material for this article can be found online at: https://www.frontiersin.org/articles/10.3389/fsysb.2022.898858/full#supplementary-material

REFERENCES

Asanovic, K., Bodik, R., Demmel, J., Keaveny, T., Keutzer, K., Kubiatowicz, J., et al. (2009). A View of the Parallel Computing Landscape. *Commun. ACM* 52 (10), 56–67. doi:10.1145/1562764.1562783

Behr, N., Danos, V., and Garnier, I. (2019). Combinatorial Conversion and Moment Bisimulation for Stochastic Rewriting Systems. arXiv: 1904.07313 April 15, 2019.

Behr, N., Danos, V., and Garnier, I. (2016). "Stochastic Mechanics of Graph Rewriting," in Proceedings of the 31st Annual ACM/IEEE Symposium on Logic in Computer Science, New York City, United States, 05-08 July 2016, 46–55. doi:10.1145/2933575.2934537

Behr, N., and Krivine, J. (2020). "Rewriting Theory for the Life Sciences: A Unifying Theory of CTMC Semantics," in *Lecture Notes in Computer Science*. Editors F. Gadducci and T. Kehrer (Cham: Springer), 12150, 185–202. ICGT 2020, LNCS. doi:10.1007/978-3-030-51372-6_11

Belmonte, J. M., Leptin, M., and Nédélec, F. (2017). A Theory that Predicts Behaviors of Disordered Cytoskeletal Networks. *Mol. Syst. Biol.* 13, 941. doi:10.15252/msb.20177796

Blinov, M. L., Faeder, J. R., Goldstein, B., and Hlavacek, W. S. (2004). BioNetGen: Software for Rule-Based Modeling of Signal Transduction Based on the Interactions of Molecular Domains. *Bioinformatics* 20 (17), 3289–3291. doi:10.1093/bioinformatics/bth378

Bonilla-Quintana, M., Wörgötter, F., Tetzlaff, C., and Fauth, M. (2020). Modeling the Shape of Synaptic Spines by Their Actin Dynamics. *Front. Synaptic Neurosci.* 12. doi:10.3389/fnsyn.2020.00009

Chakrabortty, B., Willemsen, V., de Zeeuw, T., Liao, C.-Y., Weijers, D., Mulder, B., et al. (2018). A Plausible Microtubule-Based Mechanism for Cell Division Orientation in Plant Embryogenesis. *Curr. Biol.* 28, 3031–3043. doi:10.1016/j.cub.2018.07.025

Cieslak, M., and Prusinkiewicz, P. (2019). Gillespie-lindenmayer Systems for Stochastic Simulation of Morphogenesis. *silico Plants* 1 (1), diz009. doi:10.1093/insilicoplants/diz009

Corbino, J., and Castillo, J. E. (2020). High-order Mimetic Finite-Difference Operators Satisfying the Extended Gauss Divergence Theorem. *J. Comput. Appl. Math.* 364, 112326. doi:10.1016/j.cam.2019.06.042

Danos, V., and Laneve, C. (2004). Formal Molecular Biology. *Theor. Comput. Sci.* 325 (1), 69–110. doi:10.1016/j.tcs.2004.03.065

Devincre, B., Hoc, T., and Kubin, L. (2008). Dislocation Mean Free Paths and Strain Hardening of Crystals. *Science* 320 (5884), 1745–1748. (Supplementary Information discusses "local rules" for dislocation dynamics.). doi:10.1126/science.1156101

Doi, M. (1976). Second Quantization Representation for Classical Many-Particle System. *J. Phys. A Math. Gen.* 9, 1465–1477. doi:10.1088/0305-4470/9/9/008

Doi, M. (1976). Stochastic Theory of Diffusion-Controlled Reaction. *J. Phys. A Math. Gen.* 9, 1479–1495. doi:10.1088/0305-4470/9/9/009

Ehrig, H., Ehrig, K., Prange, U., and Taentzer, G. (2006). *Fundamentals of Algebraic Graph Transformation*. Berlin Heidelberg: Springer-Verlag.

Eichhorst, Peter, and Walter, J. (1990). Savitch, "Growth Functions of Stochastic Lindenayer Systems". *Inf. Control* 45, 217–228.

Giavitto, J.-L., and Spicher, A. (2008). Topological Rewriting and the Geometrization of Programming. *Phys. D. Nonlinear Phenom.* 237, 1302–1314. doi:10.1016/j.physd.2008.03.039

Glimm, J., and Jaffe, A. (1981). *Quantum Physics: A Functional Integral Point of View*. New York: Springer-Verlag. Section 6.1.

Hamant, O., Inoue, D., Bouchez, D., Dumais, J., and Mjolsness, E. (2019). Are Microtubules Tension Sensors? *Nat. Commun.* 10, 2360. doi:10.1038/s41467-019-10207-y

Hellander, A., Lawson, M. J., Drawert, B., and Petzold, L. (2014). Local Error Estimates for Adaptive Simulation of the Reaction-Diffusion Master Equation via Operator Splitting. *J. Comp. Phys.* 266, 89–100. doi:10.1016/j.jcp.2014.02.004

Hotulainen, P., and Hoogenraad, C. C. (2010). Actin in Dendritic Spines: Connecting Dynamics to Function. *J. Cell. Biol.* 189 (4), 619–629. doi:10.1083/jcb.201003008

Jahnke, T., and Altıntan, D. (2010). Efficient Simulation of Discrete Stochastic Reaction Systems with a Splitting Method. *Bit Numer. Math.* 50, 797–822. doi:10.1007/s10543-010-0286-0

Jönsson, H., Heisler, M., Shapiro, B. E., Meyerowitz, E. M., and Mjolsness, E. (2006). An Auxin-Driven Polarized Transport Model for Phyllotaxis. *Proc. Natl. Acad. Sci. USA* 103 (5), 1633–1638. doi:10.1073/pnas.0509839103

Kim, M.-C., Li, R., Abeyaratne, R., Kamm, R. D., and Asada, H. H. (2022). A Computational Modeling of Invadopodia Protrusion into an Extracellular Matrix Fiber Network. *Sci. Rep.* 12, 1231. doi:10.1038/s41598-022-05224-9

Klein, D., Marx, J., and Fischbach, K. (2018). Agent-Based Modeling in Social Science, History, and Philosophy: An Introduction. *Hist. Soc. Res.* 43 (1), 7–27.

Lane, B. (2015). *Cell Complexes: The Structure of Space and the Mathematics of Modularity* (University of Calgary). PhD thesis.

Letort, G., Montagud, A., Stoll, G., Heiland, R., Barillot, E., Macklin, P., et al. (2019). PhysiBoSS: A Multi-Scale Agent-Based Modelling Framework Integrating Physical Dimension and Cell Signalling. *Bioinformatics* 35 (7), 1188–1196. doi:10.1093/bioinformatics/bty766

Lovász, L. (2012). *Large Networks and Graph Limits*, Colloquium Publications volume 60. Providence, RI: American Mathematical Soc.

MacNamara, S., and Strang, G. (2016). "Operator Splitting," in *Splitting Methods in Communication, Imaging, Science, and Engineering. Scientific Computation*. Editors R. Glowinski, S. Osher, and W. Yin (Cham, Switzerland: Springer International Publishing). doi:10.1007/978-3-319-41589-5_3

Marcoli, M., and Port, A. (2015). Graph Grammars, Insertion Lie Algebras, and Quantum Field Theory. arXiv:1502.07796.

Mattis, D. C., and Glasser, M. L. (1998). The Uses of Quantum Field Theory in Diffusion-Limited Reactions. *Rev. Mod. Phys.* 70, 979–1001. doi:10.1103/revmodphys.70.979

Mjolsness, E. (2019a). Prospects for Declarative Mathematical Modeling of Complex Biological Systems. *Bull. Math. Biol.* 81 (Issue 8), 3385–3420. Note: For an Earlier Version Integrating Extensive Supplementary Material into the Text Body, See Preprint [24]. doi:10.1007/s11538-019-00628-7

Mjolsness, E. (2019b). Structural Commutation Relations for Stochastic Labelled Graph Grammar Rule Operators. arXiv:1909.04118.

Mjolsness, E. (2010). Towards Measurable Types for Dynamical Process Modeling Languages. *Electron. Notes Theor. Comput. Sci.* 265, 123–144. doi:10.1016/j.entcs.2010.08.008

Mjolsness, E., Sharp, D. H., and Reinitz, J. (1991). A Connectionist Model of Development. *J. Theor. Biol.* 152 (4), 429–453. doi:10.1016/s0022-5193(05)80391-1

Mjolsness, E. (2005). "Stochastic Process Semantics for Dynamical Grammar Syntax: An Overview," in Ninth International Symposium on Artificial Intelligence and Mathematics, Fort Lauderdale, FL, January 4–6, 2006. UCI ICS TR# 05-14 arXiv:cs/0511073 20 November 2005.

Mjolsness, E. (2013). Time-ordered Product Expansions for Computational Stochastic System Biology. *Phys. Biol.* 10, 035009. doi:10.1088/1478-3975/10/3/035009

Mjolsness, E., and Yosiphon, G. (2006). Stochastic Process Semantics for Dynamical Grammars. *Ann. Math. Artif. Intell.* 47, 329–395. doi:10.1007/s10472-006-9034-1

Nedelec, F., and Dietrich, F/(2007). Collective Langevin Dynamics of Flexible Cytoskeletal Fibers" New. *J. Phys.* 9, 427. https://iopscience.iop.org/article/10.1088/1367-2630/9/11/427/meta.

Popov, K., Komianos, J., and Papoian, G. A. (2016). MEDYAN: Mechanochemical Simulations of Contraction and Polarity Alignment in Actomyosin Networks. *PLoS Comput. Biol.* 12, e1004877. doi:10.1371/journal.pcbi.1004877

Prusinkiewicz, P., Hammel, M. S., and Mjolsness, E. (1993). "Animation of Plant Development," in *SIGGRAPH '93 Conference Proceedings* (New York: ACM). doi:10.1145/166117.166161

Reed, M., and Simon, B. (1980). *Methods of Modern Mathematical Physics I: Functional Analysis*. San Diego, CA: Academic Press. Chapter 2.

Sampathkumar, A., Krupinski, P., Wightman, R., Milani, P., Berquand, A., Boudaoud, A., et al. (2014). Subcellular and Supracellular Mechanical Stress Prescribes Cytoskeleton Behavior in Arabidopsis Cotyledon Pavement Cells. *eLife* 3, e01967. doi:10.7554/eLife.01967

Santos, R. A., Fuertes, A. J. C., Short, G., Donohue, K. C., Shao, H., Quintanilla, J., et al. (2018). DSCAM Differentially Modulates Pre- and Postsynaptic Structural and Functional Central Connectivity during Visual System Wiring. *Neural Dev.* 13, 22. doi:10.1186/s13064-018-0118-5

Scott, C. B., and Mjolsness, E. (2021). Graph Diffusion Distance: Properties and Efficient Computation. *PLOS One* 16, e0249624. doi:10.1371/journal.pone.0249624

Smith, R. S., Guyomarc'h, S., Mandel, T., Reinhardt, D., Kuhlemeier, C., and Prusinkiewicz, P. (2006). A Plausible Model of Phyllotaxis. *Proc. Natl. Acad. Sci. U.S.A.* 103 (5), 1301–1306. doi:10.1073/pnas.0510457103

Spicher, A., and Michel, O. (2007). Declarative Modeling of a Neurulation-like Process. *Biosystems* 87 (2-3), 281–288. doi:10.1016/j.biosystems.2006.09.024

Vattré, A., Devincre, B., Feyel, F., Gatti, R., Groh, S., Jamond, O., et al. (2014). Modelling Crystal Plasticity by 3D Dislocation Dynamics and the Finite Element Method: The Discrete-Continuous Model Revisited. *J. Mech. Phys. Solids* 63, 491–505. doi:10.1016/j.jmps.2013.07.003

Venkatramanan, S., Lewis, B., Chen, J., Higdon, D., Vullikanti, A., and Marathe, M. (2018). Using Data-Driven Agent-Based Models for Forecasting Emerging Infectious Diseases. *Epidemics* 22, 43–49. doi:10.1016/j.epidem.2017.02.010

Vos, J. W., Dogterom, M., and Emons, A. M. (2004). Microtubules Become More Dynamic but Not Shorter during Preprophase Band Formation: a Possible "Search-And-Capture" Mechanism for Microtubule Translocation. *Cell. Motil. Cytoskelet.* 57, 246–258. doi:10.1002/cm.10169

Wolfram, S, (2020). *A Project to Find the Fundamental Theory of Physics*. Champaign, IL: Wolfram Media, First Printing.

Yosiphon, G. (2009). Stochastic Parameterized Grammars: Formalization, Inference, and Modeling Applications" PhD Thesis UC Irvine Computer Science Department Thesis and Software. Available at: http://computableplant.ics.uci.edu/theses/guy/downloads/papers/thesis.pdf. Code available at: http://computableplant.ics.uci.edu/theses/guy/ (Accessed July 13, 2022).

Conflict of Interest: The author declares that the research was conducted in the absence of any commercial or financial relationships that could be construed as a potential conflict of interest.

frontiers | Frontiers in Cell and Developmental Biology

TYPE Review
PUBLISHED 16 September 2022
DOI 10.3389/fcell.2022.959468

OPEN ACCESS

EDITED BY
Luis Diambra,
National University of La Plata, Argentina

REVIEWED BY
Paula De Tezanos Pinto,
Consejo Nacional de Investigaciones Científicas y Técnicas (CONICET), Argentina
Laura Corrales-Guerrero,
Sevilla University, Spain
Aidan Ivar Brown,
Ryerson University, Canada

*CORRESPONDENCE
Saúl Ares,
saul.ares@csic.es

SPECIALTY SECTION
This article was submitted to Morphogenesis and Patterning, a section of the journal Frontiers in Cell and Developmental Biology

RECEIVED 01 June 2022
ACCEPTED 25 August 2022
PUBLISHED 16 September 2022

CITATION
Casanova-Ferrer P, Muñoz-García J and Ares S (2022), Mathematical models of nitrogen-fixing cell patterns in filamentous cyanobacteria. *Front. Cell Dev. Biol.* 10:959468. doi: 10.3389/fcell.2022.959468

Mathematical models of nitrogen-fixing cell patterns in filamentous cyanobacteria

Pau Casanova-Ferrer[1,2,3], Javier Muñoz-García[1,2] and Saúl Ares[1,3]*

[1]Grupo Interdisciplinar de Sistemas Complejos (GISC), Madrid, Spain, [2]Departamento de Matemáticas, Universidad Carlos III de Madrid, Leganés, Spain, [3]Centro Nacional de Biotecnologia (CNB), CSIC, Madrid, Spain

The *Anabaena* genus is a model organism of filamentous cyanobacteria whose vegetative cells can differentiate under nitrogen-limited conditions into a type of cell called a heterocyst. These heterocysts lose the possibility to divide and are necessary for the filament because they can fix and share environmental nitrogen. In order to distribute the nitrogen efficiently, heterocysts are arranged to form a quasi-regular pattern whose features are maintained as the filament grows. Recent efforts have allowed advances in the understanding of the interactions and genetic mechanisms underlying this dynamic pattern. Here, we present a systematic review of the existing theoretical models of nitrogen-fixing cell differentiation in filamentous cyanobacteria. These filaments constitute one of the simplest forms of multicellular organization, and this allows for several modeling scales of this emergent pattern. The system has been approached at three different levels. From bigger to smaller scale, the system has been considered as follows: at the population level, by defining a mean-field simplified system to study the ratio of heterocysts and vegetative cells; at the filament level, with a continuous simplification as a reaction-diffusion system; and at the cellular level, by studying the genetic regulation that produces the patterning for each cell. In this review, we compare these different approaches noting both the virtues and shortcomings of each one of them.

KEYWORDS

pattern formation, cyanobacteria, heterocyst differentiation, nitrogen fixation, gene regulatory networks, activator-inhibitor, reaction-diffusion

1 Introduction

Pattern formation is extremely relevant in embryonic development because it allows for precise periodic spatial differentiation of certain cells or groups of cells. An important question is how a pattern, and, therefore, heterogeneity, is produced from a homogeneous state, given that embryos develop from a single cell. Another intriguing feature is that patterning must be robust enough to ensure reliability, given that embryo development is a highly reproducible process. Additionally, the widespread action of pattern formation in

all organisms and different levels of development seems to point to the existence of simple intrinsic mechanisms capable of acting with widely different elements.

The reaction-diffusion system, presented by Turing in his seminal work (Turing, 1952), constitutes a simple model capable of forming spatial patterns starting from a homogeneous state. Turing considers a ring of equivalent cells that generate a couple of diffusible morphogens whose production depends on the concentrations of both of them. He realized, through a linear perturbation analysis, that, while the system starts homogeneous, slight perturbations in the diffusion of morphogens are reinforced and create "waves" of morphogens in the cell ring. This reinforcement is caused because when a cell sends more inhibitor to its neighboring cells than what it receives, the neighboring cells produce less inhibitor. This further reduces the flux of inhibitor that enters the cell, which, in turn, increases inhibitor production and its flux to the neighboring cells. This feedback loop produces waves of morphogens that can drive the system to a heterogeneous state if system parameters are capable of sustaining the perturbation out of the linear regime. Furthermore, if there are more than two diffusible morphogens, the heterogeneous state can be oscillatory. The general condition that allows these instabilities to form is the combination of an activator and a more diffusible inhibitor. The particular ratio between the diffusion rates is highly dependent on the reaction system that regulates these morphogens (Gierer and Meinhardt, 1972). This fine-tuning required for the pattern fixation questions the biological feasibility of this mechanism because it makes the system susceptible to small changes in parameter values that would greatly alter its behavior.

These types of biological pattern–forming systems were further extensively studied by Meinhardt (2008) and fully theoretically fledged out by Murray (2003). A state-of-the-art discussion on Turing's ideas, their development, and some system examples can be found in a research study on this same Special Topic issue (Lacalli, 2022). Subsequently, Murray's analysis has been expanded by considering reaction-diffusion systems in continuous growing domains, observing that depending on the characteristics of the growth, it can produce more robust pattern formation or add difficulties to it (Crampin et al., 1999; Barrass et al., 2006). Finally, the limiting case in which the activator does not diffuse cannot create a stable stationary pattern; therefore, the emergent patterns are always of a dynamical nature (Marciniak-Czochra et al., 2017). The incorporation of mechano-chemical feedback can mediate the reinforcement and consequent fixation of the pattern through a morphological change that affects the diffusion of the inhibitory morphogen (Brinkmann et al., 2018).

When talking about these reaction-diffusion systems, it is important to remember that the insights from linear stability analysis, usually invoked to determine whether a system can form a stable pattern or not, can be deceiving: the dispersion relation close to a homogeneous fixed point can sometimes be very helpful, but also deceiving once full nonlinearities kick in. For this reason, classical rules for pattern formation based on linear analysis are better understood as applying to pattern inception, given that the study of linear perturbations and the stabilization of a final pattern is a process where nonlinearities cannot, in general, be neglected (Smith and Dalchau, 2018). For instance, against classical thinking, systems with equally diffusing signals can make stable patterns (Marcon et al., 2016). In this framework, it is clear that events such as domain growth (Raspopovic et al., 2014), discrete nature of the system (Nakamasu et al., 2009), or separation of timescales for the action of different molecular species can all play a role to shape the formation and maintenance of patterns.

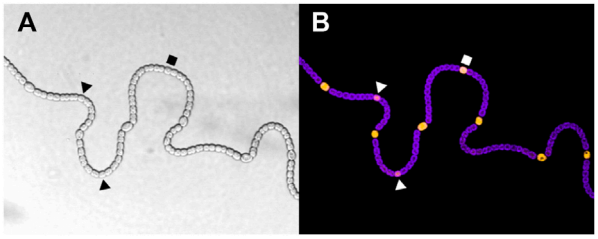

FIGURE 1
(A) Wild type *Anabaena* PCC 7120 filament grown in conditions of nitrogen deprivation showing vegetative cells and heterocysts. **(B)** Florescence images characterize the differentiation stage of each cell. The purple florescence is associated with the thylakoid membranes (and therefore with the photosynthesis), while the yellow florescence marks NsiR1 expression, which is described as an early marker of differentiation in Muro-Pastor (2014). Intermediate stages of developing heterocysts are indicated by polygonal shapes. Images are courtesy of Alicia Muro-Pastor.

All these characteristics are relevant for the study of pattern formation in the filamentous cyanobacterium *Anabaena* (Figure 1). The cells of the filament exchange nutrients and react as a whole to environmental changes. One could argue that, while each cell is still a unicellular organism, the filament is located close to the transition to multicellular organization. This is especially evident when the filament is placed in conditions of nitrogen deprivation. Under these conditions, the filament undergoes a dynamical differentiation process that differentiates roughly one in every ten cells into nitrogen-fixing heterocysts in a quasi-regular pattern that is maintained as the filament keeps growing (Flores and Herrero, 2010). This patterned differentiation constitutes an example of specialization, cooperation, and distribution of labor because, while the vegetative cells keep producing carbon through photosynthesis, the heterocysts fix environmental nitrogen into organic forms that can be assimilated by all cells. Thus, for the filament to subsist, both end products must be shared and diffused through the filament to the cells that are not capable of synthesizing them. While previous reviews have already

compiled the current theories about heterocyst pattern formation (Flores and Herrero, 2010; Herrero et al., 2016; Harish and Seth, 2020; Zeng and Zhang, 2022), in this review, we systematically discuss the different mathematical and computational frameworks that have been used to model the physics of cell differentiation and pattern formation in this system.

2 Diffusion models of an inhibitor exported from heterocysts

First, we present research works that attempted to model the patterned distribution of heterocysts without any explicit genetic regulation. With this aim, these models only considered gradients in nitrogen concentration or some inhibitory signal originating from heterocysts.

An early attempt of modeling the patterning of heterocyst differentiation in cyanobacteria filaments came at a time when, while the biological role of heterocysts was not well-defined (Fay et al., 1968), it was already stated that heterocysts seemed to inhibit the formation of new ones (Wolk, 1967). The model presented by Baker and Herman (1972) consisted of an integer linear cell array simulator which allowed cell-to-cell diffusion of an inhibitory product and division of vegetative cells. Due to computational limitations at the time, concentrations were modeled as integer numbers, setting a discrete minimum change in concentration as a result. This model was used to test the hypothesis that cell division and differentiation are two competing processes in which, at the end of each cell cycle (quantified by a countdown), cells have to choose a fate depending on the inhibitor concentration. This simple model could obtain feasible distributions for heterocyst placement, but the code was heavily limited by having to work with integer concentrations. The model predicted a low threshold of the inhibitor to avoid differentiation, causing integer rounding to be comparable with concentration values. This low threshold was probably caused by the unrealistic assumption of an equal rate for cell–cell and cell–media diffusion, which impeded the formation of a well-defined inhibitory gradient in the filament.

Just a year after this first study, the group responsible for one of the initial experimental studies (Wolk, 1967) also presented theoretical results using a simulation code (Wolk, 1975). The authors considered that heterocyst placement was defined by a diffusible inhibitor whose concentration dynamics was expressed as:

$$\frac{\partial C(x,t)}{\partial t} = D\frac{\partial^2 C(x,t)}{\partial x^2} - k \cdot C(x,t). \quad (1)$$

Here, $C(x, t)$ is the concentration of the diffusible inhibitor at the point x in the time t, D is the diffusion constant, and k is the decay rate.

From this equation, the authors obtained an inhibitor diffusion root mean square distance for the closed ($k = 0$) and general systems by considering a discrete approximation with cells as distance units and the inhibitor generated from a point source. These two distances were used as alternative ways to define the range of inhibition that a heterocyst has over neighboring cells in the simulation. This simulation was a sequential random pick of non-inhibited vegetative cells that continued until all cells were inhibited or heterocysts. The solution for the general system agreed with the experimental distribution of distances between heterocysts better than the closed system. However, the closed system produced a slightly more uniform distribution, while presenting much longer intervals than the experimental data. This led the authors to propose two diffusion-based spacing mechanisms in which a heterocyst would appear on a cell sufficiently distant from preexisting heterocysts so that it has a concentration of the activator higher than some critical level. At the heart of this work was the initial idea that heterocyst differentiation is a purely stochastically driven process. Thus, control is only exerted through desensitization that protects the cells that are close to existent heterocysts against differentiation.

The same diffusive Eq. 1 was studied by De Koster and Lindenmayer (1987), obtaining two different analytical solutions (one continuous and another discrete). These solutions were compared with an improved version of the integer linear cell array simulator discussed previously. This version avoids some problems faced in the study by Baker and Herman (1972) by storing the concentration as a floating-point variable and eliminating the environment with the initialization of the filament already in equilibrium with two heterocysts in the extremes. Through this comparison, two biologically reasonable estimations were made: $D = 0.14–0.39\ \mu m^2/s$ for the inhibitor diffusion constant, and $k = 2.7–7.5 \cdot 10^{-4}\ s^{-1}$ for the degradation rate, and an inaccurate estimation for the cell cycle, 7.25 h, which is known to be around 24 h.

Much later, Allard et al. (2007) proposed a series of models. While the first three models are discussed here, the last one is considered in the following section as it includes some genetic interactions. The initial work (Allard et al., 2007) compares the distribution of heterocysts obtained through random placement with one obtained with a model of nitrogen propagating over a filament with a continuous periplasm. In this model, vegetative cells consume nitrogen to grow, while heterocysts produce nitrogen that diffuses through the filament. When the nitrogen level of a vegetative cell reaches 0, the cell irreversibly commits to differentiation. Additionally, the cells grow at a constant rate and divide at a certain fixed division time for each cell. The model is initialized with a couple of heterocysts at the ends of the filaments and a randomly distributed growth rate for each cell. For this model to be able to reproduce the experimental distributions, the authors have to consider an immediate release of nitrogen after commitment in order to avoid the formation of multiple heterocysts. This work presents an opposing paradigm to the earlier ideas by Wolk (1967): while

in the oldest work, there was a deterministic system of inhibition with a stochastic initiation of differentiation, this work includes a deterministic drive that starts the differentiation to explain *de novo* heterocyst formation. Nevertheless, the need to include a sizable immediate release of nitrogen once a cell is committed to differentiation to avoid the formation of clusters of heterocysts shows that some level of stochasticity is necessary. This stochasticity is represented here by the random distribution of growth rates along the filament. The heterogeneity of growth rates will decide which one of the cells, located in a nitrogen-deprived area, will consume faster its reserves and therefore become a heterocyst. This interplay between deterministic dynamics on a random heterogeneous system seems necessary to recover the observed experimental heterocyst spacing distributions and will be a common trait of most of the models presented below.

This model was expanded by Brown and Rutenberg (2012a) and Brown and Rutenberg (2012b) with the addition of a coupling between the growth and the available nitrogen in the cell and the possibility of nitrogen leakage into the media. Additionally, the commitment condition is also modified, and cells have to remain in complete nitrogen deprivation for a set time before they differentiate into heterocysts. This model is capable of reproducing the experimental placement of heterocysts (with a commitment time of 8 h) considerably better than a random placement and a partially random one where positions adjacent to heterocysts cannot differentiate. Nevertheless, the assumption that a heterocyst is capable of releasing a sizable amount of fixed nitrogen right after commitment is not biologically feasible, and would be substituted by genetic regulation in later research work (Brown and Rutenberg, 2014) (described in Section 3). The authors also obtained a relationship between filament growth rate and heterocyst frequency and found that growth rate presents a maximum for a certain value of heterocyst frequency (Brown and Rutenberg, 2012a). This maximal growth is similar for different placement strategies if nitrogen leakage is not considered in the model. However, if leakage over 1% is considered, the differences in the growth rate between strategies are relevant; the strategy of differentiation by nitrogen-starved cells, that produced the most realistic heterocyst distributions, is also the one that produces maximal growth (Brown and Rutenberg, 2012a).

Alternatively, Ishihara et al. (2015) considered a paracrine inhibitory signal that originated from the heterocysts instead of considering the nitrogen dynamics of the filament. Experimental data obtained from a mutant strain harboring a P*hetR::gfp* reporter cassette (Asai et al., 2009) present delayed heterocyst differentiation, observing the first heterocysts at 63–65 h after nitrogen deprivation instead of the typical 18–24 h (Flores and Herrero, 2010), indicating that the differentiation process is somehow altered in this strain. In their model, the authors continued the idea, first presented by Baker and Herman (1972), that cell division and heterocyst differentiation are two competing mechanisms. They proposed a cellular automaton model where cells have the capacity of aging, dividing, and differentiating into heterocysts (that are immediately functional), and dynamics are simulated with a Gillespie algorithm (Gillespie, 1976). The division and differentiation probabilities are represented by sigmoidal Hill functions of the cell age. Additionally, the differentiation rate is affected by a lateral inhibition produced by existent heterocysts. This effect decreases as the number of vegetative cells to the source heterocysts increases. The initial condition for the simulation is a filament of a random number of cells with random ages flanked by two heterocysts. The model reproduces the experimental distribution of segments between heterocysts but not the age distribution of the cells that differentiate. However, it is worth noting that the filaments in which all vegetative cells differentiate into heterocysts before the filament has grown up to 5,000 cells are discarded. The model predicts that most cells differentiate at an older age, while experimentally, the differentiation happens at a younger age. From this, it is inferred that the model does not properly capture early pattern formation. To solve this disagreement, *hetR* transcription was studied, observing that it was not immediately perturbed by cell division and remained active at the early stage, concluding that *hetR* activity should be considered independent of cell age. Following this, a model was presented, where differentiation is independent of cell age, obtaining a more realistic age distribution of the commitment time. Finally, both early (defined as 63–65 h after nitrogen deprivation) and late (more than 69 h after nitrogen deprivation) differentiation could be explained with the same kinetic parameters by altering the differentiation dependency with cellular age. Given that the commitment time to differentiation is around 7–8 h (Yoon and Golden, 2001; Muro-Pastor and Hess, 2012), it is evident that the reporter strain used introduces artifacts, and any conclusion based on its observation has to be taken with extreme caution.

All the models discussed up to this point are remarkably capable of reproducing the overall experimental interval length distribution of heterocysts; however, they fail to capture the early pattern formation in the filament. In addition, the initial conditions for almost all these studies are filaments with functional heterocysts in the extremes. Therefore, since inhibitors will only reach the cells close to a heterocyst, only the regions far from these heterocysts, if long enough filaments are considered, would properly reflect *de novo* pattern formation. Additionally, all these models only consider an inhibitory signal originating from the heterocysts without including the well-known competitive lateral inhibition between vegetative cells through PatS (Yoon and Golden, 2001; Corrales-Guerrero et al., 2013; Du et al., 2020). Given that the only selection mechanism acting over the vegetative cells during the first round of differentiation is the initial heterogeneity, the authors are forced to add arbitrary mechanisms to avoid the excessive simultaneous differentiation of contiguous cells. In the studies by Allard et al. (2007) and Brown and Rutenberg (2012a,b), the

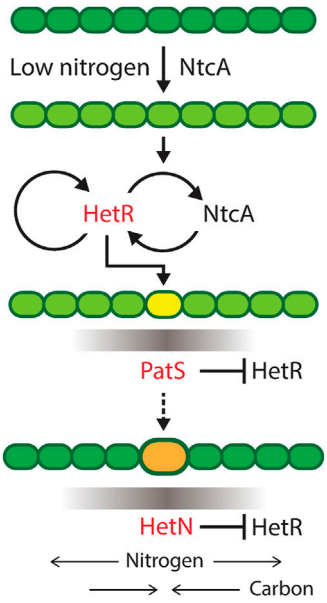

FIGURE 2
Progress of heterocyst differentiation. The scheme represents the process of differentiation of a filament of heterocyst-forming cyanobacteria with the roles of the main genes involved. Darker green means more fixed nitrogen in a cell. Low nitrogen induces NtcA expression, which, in turn, activates HetR, the master regulator of heterocyst differentiation. Yellow is a cell committing to differentiation and producing a gradient of PatS inhibiting the action of HetR in neighboring cells. Orange is a differentiated cell, a heterocyst, producing fixed nitrogen and a gradient of the inhibitor HetN and receiving carbon from vegetative cells. Reproduced from Di Patti et al. (2018), CC BY 4.0 license.

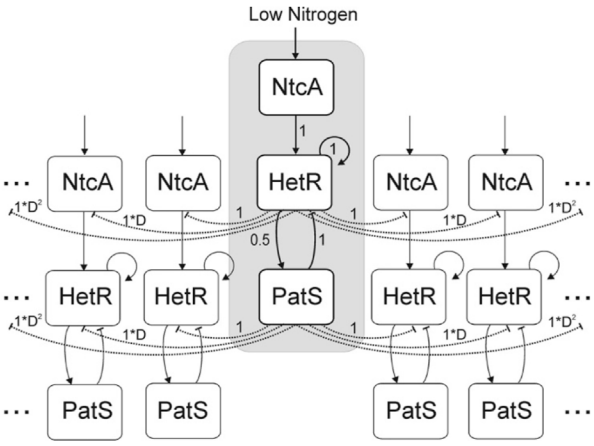

FIGURE 3
Diagram of the network considered in the study by Gerdtzen et al. (2009). Cells are organized in a cyclical manner. Direct interactions are represented by solid lines and, indirect interactions are represented by dashed lines. Arrow heads indicate activation, and vertical lines indicate inhibition. Numbers indicate the strength of the interactions considered among the elements of the network. Reproduced from Gerdtzen et al. (2009), CC BY 2.0 license.

mechanism is an immediate big release of nitrogen from the heterocysts that stops the differentiation of the close neighbors of committed cells. Alternatively, in the study by Ishihara et al. (2015), the model is fitted with a strain with an apparent differentiation impairment in which the first round of differentiation appears almost three times later than the typical appearance time.

As a result of these limitations, it seems necessary to include an inhibitory signal originating from vegetative cells in order to fix the heterocyst pattern. Thus, once this initial pattern is formed, an inhibitory signal originating from the heterocysts, which could be due to the fixed nitrogen (Fogg, 1949; Water and Simon, 1982), to a paracrine inhibitor identified as HetN in Callahan and Buikema (2001) or to a combination of both, could be enough to maintain the preexisting pattern.

3 Genetic regulatory models

The role of the main genes involved in heterocyst differentiation is depicted in Figure 2. The differentiation mechanism is initiated by the upregulation of *ntcA* in nitrogen deficiency conditions. This increase of *ntcA* causes an increase of *hetR* that initiates the production of *patS*. This gene codifies a lateral inhibitor that avoids the differentiation of several contiguous cells into heterocysts. Once the cell has already differentiated, it starts producing both fixed nitrogen and *hetN*, which is another inhibitor of heterocyst formation. *hetR* is the master regulator of the process: in its absence, there is no heterocyst differentiation, consistent with observations in *Cylindrospermopsis*, which is the only Nostocal that lost the ability to develop heterocysts and fix nitrogen.

In the study by Gerdtzen et al. (2009), a deterministic compartmental model was introduced with three genes represented by a vector, with values in the interval [0, 1], that interact between them through an interaction matrix. The genes considered are *ntcA* and *hetR*, and *patS* and *ntcA* are considered to be activated by nitrogen depletion (Vega-Palas et al., 1992) and, in turn, activate *hetR* (Muro-Pastor et al., 2002). *hetR* is considered to activate both itself and *patS* (Huang et al., 2004). Finally, *patS* inhibits *hetR* production (Yoon and Golden, 1998). All these interactions are considered to have the same relative strength, except the *hetR* activation of *patS* which is defined to have half of this strength. An explicative diagram of the model is included in Figure 3.

This model also includes a proxy for *patS* and fixed nitrogen diffusion through a multiplicative factor D^n ($D < 1$). This factor reduces the inhibitory effect of *patS* over the *hetR* expression of a cell located n cells away from the *patS* source. The inhibitory

effect of *ntcA* through fixed nitrogen is characterized as an inhibition from *hetR* expression, given that the cells with *hetR* = 1 will be considered heterocysts.

The simulation is initialized from random conditions, and then state transitions are considered to occur asynchronously, with one gene state on a given cell being updated using the interaction matrix at a time in random order for the whole array of cells. After a certain time, the system converges to a patterned filament, where $\overline{L_H}$, the average interval between heterocysts (cells expressing all genes in the model at the maximum possible level, 1) depends on the value of the diffusion constant D. Increments of D up to a critical value of 0.7 produce an almost linear increase in $\overline{L_H}$ due to the creation of fewer heterocysts. However, from this point onward, the behavior of $\overline{L_H}$ stops being linear, and the system saturates to a state without any heterocyst for $D \geq 0.92$.

The authors set the value of D that produced an $\overline{L_H} = 10 \pm 2$ cells, which is similar to the experimental value observed by Yoon and Golden (1998) to study the system. They presented the histograms for intervals between heterocysts in the case of the wild type, the *patS* deletion mutant, and the *hetR* over-expressed condition. These results show that, while the means $\overline{L_H}$ are compatible with the experimental data, the simulation produces histograms much more skewed towards larger intervals for both the wild type and the over-expression of *hetR*, and a strictly decreasing distribution of interval length for the *patS* mutant. The first discrepancy could be caused due to the reinterpretation of the fixed nitrogen inhibition of *ntcA* through *hetR*. This change would produce an additional inhibitory signal originating from developing cells instead of only from mature heterocysts as it should be. On the other hand, the discrepancy in the *patS* mutant could be just a problem of interpretation. Given that the expression of the variable *patS* is never shut off, one could argue that this variable is a joint representation of the two main inhibitory genes, *patS* and *hetN*. Then the deletion of this variable should result in the complete differentiation observed in the double Δ*patS*Δ*hetN* mutant (Borthakur et al., 2005), but with the additional artificial inhibition of *hetR* described earlier. This inhibition partially rescues this mutant because it fulfills the same dual role. The rescue is not full because it targets *ntcA* instead of *hetR*, which reduces its efficiency.

A continuous representation of a linearly growing one-dimensional filament was presented in Zhu et al. (2010). The system of equations that defines its dynamics is as follows:

$$\frac{dr}{dt} = \alpha_r + \beta_r F(r,s) + G(r,s,n) - \kappa_r r \tag{2}$$

$$\frac{ds}{dt} = \alpha_s + \beta_s F(r,s) + D_s \frac{\partial^2 s}{\partial x^2} - \kappa_s s \tag{3}$$

$$\frac{dn}{dt} = \beta_n F(r,s) + D_n \frac{\partial^2 n}{\partial x^2} - \kappa_n n, \tag{4}$$

where r is the concentration of HetR, s of PatS, and n of HetN. The spatial domain, that is, the filament length L, grows at a constant rate ρ:

$$\frac{dL}{dt} = \rho L. \tag{5}$$

This model considers linear degradation rates (κ_r, κ_s, κ_n) for all the proteins and diffusion of the two inhibitors with rates D_s and D_n. Regarding protein production, the authors considered basal production for both HetR (α_r) and PatS (α_s) and regulated production for all genes through the function

$$F(r,s) \equiv \frac{r^2}{(K_s + s)(K_r^2 + r^2)}, \tag{6}$$

and an additional production term for *hetR*.

$$G(r,s,n) \equiv (r_e - r)^2 (n_c - n - \eta s). \tag{7}$$

Both Eqs 6 and 7 include the HetR homodimer formation described in Huang et al. (2004) through a quadratic *hetR* variable. Eq. 6 models activation of HetR, PatS, and HetN by HetR dimers and inhibition by PatS. Eq. (7) is a phenomenological term affecting HetR: its strength depends on the difference between HetR concentration and an ad hoc level r_e, and its sign is set by the parameter n_c: when the combination of HetN and Pats concentrations given by $n + \eta s$ is larger than n_c, function $G(r, s, n)$ has the effect of a degradation; otherwise, it promotes the production of HetR. Through this term, low levels of inhibitors have the effect of an extra activation that disappears only when the concentration of HetR is r_e. With this model, the goal is to study pattern maintenance; due to this, the initial condition simulates the presence of heterocysts in the borders of the system. This condition is translated into a uniform initial distribution of both HetR and PatS, set to their equilibrium concentration based only on the constitutive production and degradation terms; in the heterocysts, the concentration of HetR is set to the equilibrium value r_e. HetN is initially set to a diffusion-mediated "bowl-shaped" distribution, with the maxima at the heterocysts. In a way akin to Turing patterning (Turing, 1952), the apparition of only one heterocyst in the middle is heavily conditioned by the difference in the two inhibitors' diffusive rates. Particularly, the diffusion of HetN should be lower than the filament growth rate so that there can be HetN depletion in the middle of the filament to induce HetR production. The diffusive rate of PatS must be higher than the one of HetN to reduce the length of the induced region. With these conditions, the model properly reflects the rise of HetR in the middle of the filament that is hypothesized to originate from the new heterocyst (Black et al., 1993) and the reported inhibitory gradients produced by it (Risser and Callahan, 2009).

Low robustness of the pattern to modification of the diffusion parameters is characteristic of Turing-like continuous models. It stems from the requirement that the pattern is an equilibrium

state of the overall regulatory system, and consequently, the interplay of the two inhibitors must be tuned in such a way that the range of the inhibitors is different enough to create steady spatial differences in gene expression that originate the pattern. However, discrete systems such as *Anabaena* filaments can fixate an unstable pattern through the irreversible commitment of a cell that presents a sustained high expression of a given gene, even if that expression is transient and would be reversed without the differentiation. For this reason, in *Anabaena* dynamical stability of the pattern is much less relevant than its establishment.

Brown and Rutenberg (2014) presented the last model of the series discussed in the previous section on diffusion models. In this study, we incorporate a mechanism of genetic inhibition into the nitrogen diffusion model presented by Brown and Rutenberg (2012a). This lateral inhibition through *patS* and *hetN* substitutes the immediate release of nitrogen and allows a more biologically realistic maturation of the heterocysts. Both genes are modeled as Boolean variables that directly prevent the commitment to differentiation of a fixed range of contiguous cells. To replicate the experimental observations, this range is set to five cells. The expression of both *patS* and *hetN* is, in turn, modeled as deterministic switches.

On the one hand, *patS* inhibition starts right after commitment until the complete maturation of the heterocyst (10 h after commitment), and a time τ_S (set to 1 h) after this point, the heterocyst starts producing fixed nitrogen. On the other hand, *hetN* inhibition starts a certain time τ_N (also set to 1 h) after commitment and is never shut off.

The initial condition considered is a lonely cell, which grows for over 7 days in nitrogen-rich conditions in order to get a heterogeneous filament, which will be put under nitrogen-deprived conditions. The model properly reproduces the vegetative interval histograms tendencies for all the mutants but with less noise and without the experimental preference for even-numbered vegetative intervals. Additionally, the authors observe that younger cells are more likely to differentiate, especially on the first round of differentiation (24 h), suggesting an indirect effect of the cell cycle on heterocyst commitment. This work shows that a deterministic model whose only random variable is the growth rate can reproduce some pattern features observed experimentally.

While the Boolean switch-like genetic model is able to reproduce the experimental mutant behaviors, it does it artificially with an immediate complete inhibition over a fixed range. This is arguably hard to justify experimentally. Despite incorporating both *patS* and *hetN* in the model, their roles are completely equivalent to the immediate release of nitrogen presented in their previous works (Allard et al., 2007; Brown and Rutenberg, 2012a,b). Instead of having distinct roles in the pattern formation, one in the pattern formation and the other in its maintenance, as hypothesized by Callahan and Buikema (2001), they are modeled with the same function (which is to avoid the formation of multiple heterocysts). Additionally, the design of the switch-like dynamics

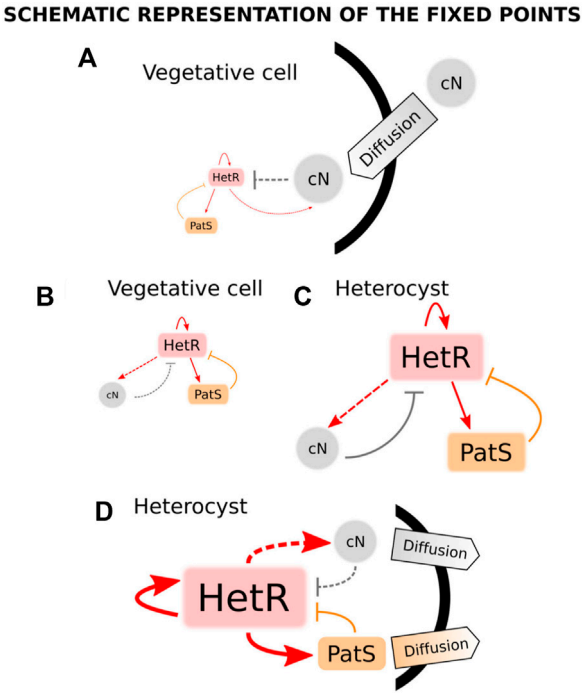

FIGURE 4
States of a cyanobacterium when subjected to different conditions of nitrogen and diffusion in the model in the study by Torres-Sánchez et al. (2015). When combined nitrogen (cN) is provided to the cell, there is only one stable fixed point **(A)**, which corresponds to a state in which the production of both HetR and PatS is minimum (vegetative state). When subjected to nitrogen deprivation, there are two stable fixed points **(B and C)**. The first point **(B)** is a vegetative state in which there exists an equilibrium between a small production of HetR, PatS, and cN. The same kind of equilibrium is present in the second fixed point **(C)** but in this case, the production of all transcription factors and cN is high (heterocyst steady state). When the cell is exposed to nitrogen stress, its trajectory evolves from **(A)** to the steady state **(B)** and, thus, it remains vegetative. Assuming some diffusion of cN and PatS from the cell, the only stable state **(D)** corresponds to a heterocyst state with high levels of production of HetR, cN, and PatS, being the latter transported to the surroundings of the cell. Adapted from Torres-Sánchez et al. (2015), CC BY 4.0 license.

forces the mutant phenotype by providing a window of a duration τ_S (after the cell commitment) and τ_N (after *patS* deactivation) in which there is no inhibition of differentiation in the system for the mutants Δ*patS* and the Δ*hetN*.

A year after this work, a model was presented that used the systems biology framework to study both the stable states of a unicellular system and the pattern formation in a filament (Torres-Sánchez et al., 2015). This model incorporates the nitrogen sensing module of the genetic network with the inclusion of the *nctA* dependence of the GS/GOAT cycle (Muro-Pastor et al., 2001) and *patS*-mediated inhibition. Particularly, *ntcA* production is increased by both HetR and NtcA and inhibited by fixed nitrogen. *hetR* transcription has the same regulation as *ntcA* plus the inhibition from *patS*. In

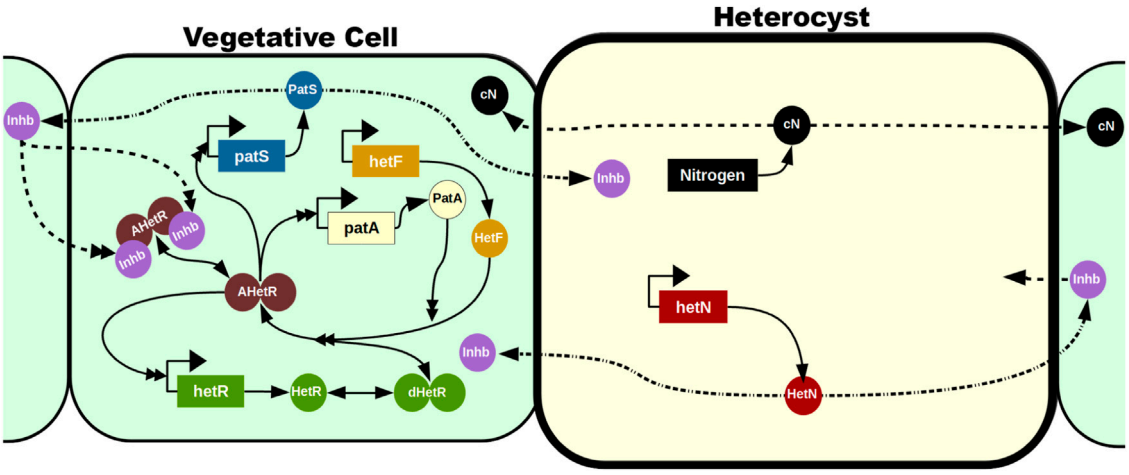

FIGURE 5
Mechanistic model in the study by Casanova-Ferrer et al. (2022). The vegetative cells are represented with a soft green background, while the heterocyst has a soft yellow background and a thicker cell wall. The reactions in the vegetative cell represent all the potential reactions in the model irrespective of the cell's position: in most cells, only a subset of these reactions will be taking place at a given time. This subset is defined by the concentration of the inhibitor *Inhb*. Genes are represented in rectangles and proteins with circles. Dimers are represented with two attached circles and can be inactivated (green), activated (brown), and activated and inhibited (brown with two purple inhibitors attached). Solid lines represent production (with only one simple arrowhead), transformations (with a simple arrowhead on both ends), and interactions (with a double arrowhead). Dashed lines represent intercellular traffic, and dashed–dotted lines represent a transformation when exported to a neighboring cell. The figure does not represent the high expression of *hetR* in heterocysts (as presented by Corrales-Guerrero et al., 2015; Bornikoel et al., 2017; Arbel-Goren et al., 2018): since these cells have already differentiated and HetR localization is restricted to the cells where it is produced, the concentration of HetR in heterocysts is irrelevant for the model's purposes.

addition, both *patS* and fixed nitrogen are positively regulated by HetR. This model considers the dynamics of fixed nitrogen, NtcA, HetR, and PatS concentrations. The authors use both the biological information of the genetic network and statistical mechanics analysis to obtain the regulatory equations of the system. After obtaining a set of parameters that reproduces heterocyst differentiation, the authors assume that there are two temporal scales: one fast, formed by HetR and ntcA, which relaxes to its steady-state much earlier than the slow one, which is due to the dynamics of PatS and fixed nitrogen. Assuming this, one can use an adiabatic argument and consider that the fast variables are in equilibrium when considering the dynamics of the slow ones. Bifurcation analysis for this reduced system is presented: for nitrogen-rich conditions, the system only presents one stable solution, which corresponds to the vegetative state (Figure 4A: low expression of both *hetR* and *patS*). On the other hand, for nitrogen-deprived conditions, the system presents bistability, with a vegetative stage (Figure 4B: with equivalent expressions of *hetR* and *patS*, but higher expression than in nitrogen-rich conditions) and a heterocyst stage (Figure 4C: with high expressions of *hetR*, *patS*, and fixed nitrogen). Additionally, the system presents hysteresis, so after nitrogen deprivation, the system will stay in the vegetative state unless a perturbation pushes it into the heterocyst state. Such a perturbation occurs when considering the diffusion of fixed nitrogen and PatS, which is enough to destabilize the vegetative state and push the dynamics to the heterocyst state (Figure 4D). The study is later expanded to a discrete filament of cells to show that by adding uniform white noise and diffusion of both PatS and fixed nitrogen, the model is capable of forming a patterned differentiation. It is also stated that the appearance of differentiation is considered a pure stochastic event and also that the biological parameters of the model can be tuned to observe the same pattern with different amplitudes of the white noise.

The high dependency on the noise to differentiate seems to contradict previous works that considered deterministic models of nitrogen-mediated inhibition (Brown and Rutenberg, 2012a, 2014) or even the same regulatory network (Gerdtzen et al., 2009). Those models produced a comparable agreement with the experimental data with much lower relevance of the noise; the stochasticity is only present in the initial conditions of the systems and not in their dynamics. In our opinion, this discrepancy can be attributed to the overlapping of the roles of both PatS and fixed nitrogen which saturates the system with inhibitors that stop the increase in HetR production. Particularly, given that the filament model is able to produce fixed nitrogen at a low level once HetR concentration rises in vegetative cells, there is no need for a transition to the high nitrogen production cellular state (heterocyst). Instead, the biological system is not capable of fixing nitrogen until the transition has already occurred, given that nitrogen fixation cannot coexist with photosynthesis. Therefore, the activation of *hetR* transcription

through *ntcA* cannot be shut off until nitrogen is provided to the system. Due to this, the system is forced to maintain the individually unstable state of high expression of both *hetR* and *patS* until a heterocyst is formed in the filament. Additionally, recent experimental works (Higa et al., 2012; Corrales-Guerrero et al., 2013; Rivers et al., 2014, 2018) seem to indicate that both *patS* and *hetN* require a post-translational modification to produce the inhibitory peptide. It has been suggested (Corrales-Guerrero et al., 2014b; Rivers et al., 2018) that this transformation occurs at the cell membrane during cell-to-cell trafficking. This would avoid self-inhibition from the *patS* and *hetN* produced in a given cell and, therefore, would make impossible a unicellular stability study.

A similar systems biology approach was considered in the study by Muñoz-García and Ares (2016), where an alternative three-gene minimal model was presented. This model also included both *hetR* as the main non-diffusive regulator of the system and *patS* as an inhibitor of HetR-mediated activation. Instead of the nitrogen sensing module, the model included *hetN* as an inhibitor produced in the heterocysts. Under such a condition, *hetR* activates both *patS* and its own expression, while *patS* and *hetN* (which are produced at a basal level in the heterocysts) inhibit this activation. Fixed nitrogen is included as a direct inhibitor of HetR regulation. As a substitute for the *ntcA* role as the trigger of *hetR* expression, the model includes a low basal expression of *hetR*. Using mass-action kinetics, the authors obtained a deterministic set of differential equations from the mechanistic information of these interactions. The model considers that, while HetR needs to form a homodimer to promote expression, this activation can also be inhibited with the attachment of just one inhibitor. The stochastic nature of gene expression was considered by adding noise to the equations using Langevin dynamics (Gillespie, 2000). This genetic model was introduced in a agent based simulation of a filament with inhibitor diffusion where each cell has its own noisy dynamical variables, growth rate, and thresholds for both differentiation and cell division. The model was able to reproduce the experimental distribution of vegetative intervals between heterocysts up to the third moment of the distribution for both the wild type and the Δ*patS* mutant, and gave a reasonable prediction for the Δ*hetN* mutant for which it made no comparison with experimental data.

The phenotypical reproduction by the model of the deletion mutants reinforces the role of the two inhibitory genes proposed in the study by Callahan and Buikema (2001). This model also provides additional insight into the interplay between cell division and heterocyst differentiation. Due to the similar timescale between these two processes, the noise on the cell division defines the overall behavior of the filament. If there is low noise and cells divide in a quasi-synchronous way, the filament pattern has an oscillatory behavior with an enlargement and posterior shortening of the mean distance between heterocysts. In this low noise regime, the model also recovers the larger appearance of even-numbered vegetative cell intervals characteristic of heterocyst patterns (Meeks and Elhai, 2002). Instead, for a noisier cell division, the percentage of even intervals always remains close to 50%, and the oscillatory behavior of the mean vegetative cells interval disappears.

A recent follow-up on this model (Casanova-Ferrer et al., 2022) includes the requirement of maturation of HetR in order to act as a transcription factor: HetF is necessary for this maturation (Risser and Callahan, 2008), and PatA enhances it (Figure 5). The product of PatS and HetN modification in the cell membrane is, for simplicity, treated as the same inhibitor (*Inhb* in Figure 5) that can be transported to neighboring cells irrespective of their nature, although only inhibition of mature HetR action in vegetative cells is explicitly modeled. This work focuses especially on the phenotype of the deletion mutant of *patA*. This mutant does not present patterning, and the appearance of heterocysts seems to be purely stochastic, with a huge preference for presenting heterocysts in the filament ends. The model is capable of reproducing this phenotype and predicts a homogenization of the HetR concentration in the filament when PatA is absent due to a reduction in the activation rate of HetR. This homogenization prevents the formation of a pattern and, therefore, internal heterocysts are formed exclusively due to random fluctuations of production rates, inhibitor diffusion, or decision mechanisms. However, if one considers some kind of leak of inhibitor through the filament ends together with the fact that the terminal cells only receive inhibitor from one neighboring cell, terminal cells present a much higher probability to differentiate than internal cells.

This analysis of the *patA* mutant is especially relevant because it is a clear example that one can disrupt the formation of the pattern by affecting the intensity of the feedback loops controlled by HetR. As *patA* is hypothesized to have a supporting role to *hetF*, one could expect that the overall behavior of the network should not be that affected. However, given that without *patA,* the fraction of HetR that gets activated is reduced with respect to the wild type, this mutant seems to lose the compounding effect that allowed the formation of the pattern. This mutant is much less susceptible to sudden spikes of HetR production, and, therefore, most of the stochastic fluctuations get buffered without affecting the overall homogeneity of the filament.

Following the Turing-like characterization, Huang et al. (2004) and Di Patti et al. (2018) present the same three-gene system (*hetR* as an activator and both *patS* and *hetN* as diffusible inhibitors), but, in this case, the inhibitory effect is produced through degradation of HetR dimers mediated by PatS and HetN. The model assumes a basal production in all cells and a linear degradation for the three genes, and an increase in the production of both HetR and PatS activated by HetR. As the model does not enforce any distinction between vegetative and heterocyst cells, all cells actively produce both inhibitors simultaneously. Thus, it does not reflect the temporal differences in the onset of production of PatS and HetN. A

bit surprisingly, the same work presents very nice experimental evidence of this difference through GFP reporters of transcription.

With this set of interactions, the authors obtain a set of differential equations through the van Kampen expansion. Initially, the authors study the linear stability around the homogeneous fixed point of the mean field approximation. Through this analysis, the authors located a set of parameters that allow the formation of instabilities that could originate a pattern in the mean field conditions. As already mentioned during the analysis of Huang et al. (2004), the most relevant parameters are the diffusion constants for both inhibitors. The smaller the ratio $\frac{D_S}{D_N}$ is, the narrower is the instability region. Subsequently, the authors introduce the same interactions in a Gillespie algorithm with the same set of parameters to check how stochasticity affects pattern formation. The authors show that the presence of noise promotes the spontaneous selection of a leading wavelength in the emerging pattern. Due to this the parameter region where the system presents instabilities and, therefore, pattern seeding is considerably larger in the noisy system. The addition of filament growth (cellular division) to the model increases the amount of available unstable modes of the system. Despite this similarity, the patterning is much more stable in the system with deterministic growth than in the noisy one. Without noise, a new high HetR expression region (heterocyst) appears in the midsection of the existing pattern when the filament elongates enough. On the other hand, the addition of growth to the noisy system destabilizes the patterning and allows for the transition between the different unstable modes that arise with the filament growth. This implies that while the pattern formation is enhanced by the addition of noise to the system, its maintenance in a growing domain requires an irreversible fixation of the heterocyst state. Additionally, this model shows that it is possible to form the pattern through the regulation of protein degradation instead of the previously studied regulator inhibition. Nevertheless, it should be tested if this alternative inhibition through HetR degradation reproduces the experimental data for a model with a more realistic temporal separation between the two inhibitors.

After this systematic analysis of the existent genetic models, one can extract some common key ideas. First, the realization that several different configurations of a minimal three-gene network with an activator, *hetR*, and a couple of inhibitors, *patS* and typically *hetN*, but it could also be the fixed nitrogen through *ntcA* regulation, as in Gerdtzen et al. (2009), are capable of reproducing the wild type behavior. Due to this, it seems indispensable to consider other conditions, especially the deletion ones, in order to properly evaluate the regulatory mechanisms proposed. There must be a certain temporal separation between the inhibitory effects in order to originate a pattern. This difference could be either produced due to the relationship between the diffusion coefficients (Zhu et al., 2010; Di Patti et al., 2018), directly imposed (Brown and Rutenberg, 2014) and also (Muñoz-García and Ares, 2016; Casanova-Ferrer et al., 2022) (where *hetN* is exclusively produced in heterocysts), or in the case of fixed nitrogen (Gerdtzen et al., 2009; Torres-Sánchez et al., 2015) acting indirectly through *ntcA* and, therefore, presenting a certain delay.

4 Cyanobacteria population models

An alternative point of view to the study of spatial pattern formation is to consider the cyanobacteria culture as a population problem where the percentage of each cell type is defined by external conditions.

This approach is used in the study by Hense and Beckmann (2006), presenting a deterministic model of the life cycle of cyanobacteria dependent on energy, mainly in the form of light and nitrogen availability. In this formulation, the heterocyst would be the stage with high energy (abundant light) and low nitrogen availability. The model is capable of reproducing the seasonal changes in the cyanobacteria population composition and infers a correlation between summer blooms and cycle velocity, where previous summer conditions strongly affect the possibility of explosive growth. The scope of this work is mostly ecological and does not provide an extensive insight into the mechanisms controlling the vegetative-heterocyst transition.

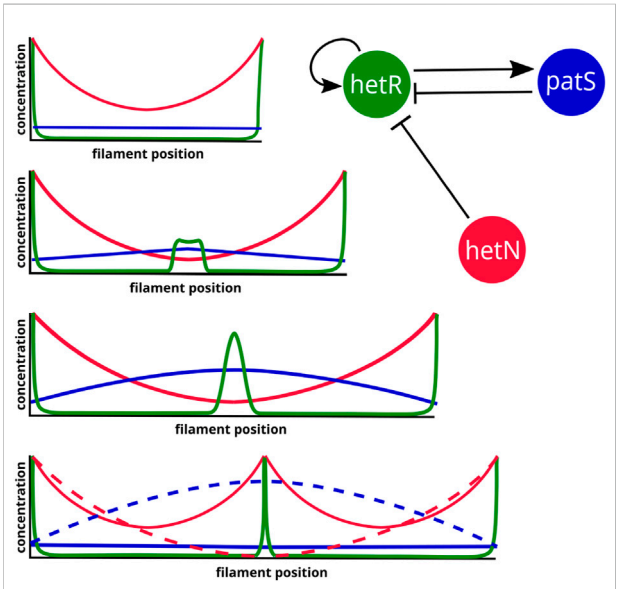

FIGURE 6
Three-gene simplified regulatory system and expected protein concentration dynamics for the emergence of a new intercalary heterocyst in a fully deterministic system. The heterocysts are represented as peaks of HetR that produce HetN. The dashed profiles represent the state right before the transition to a heterocyst.

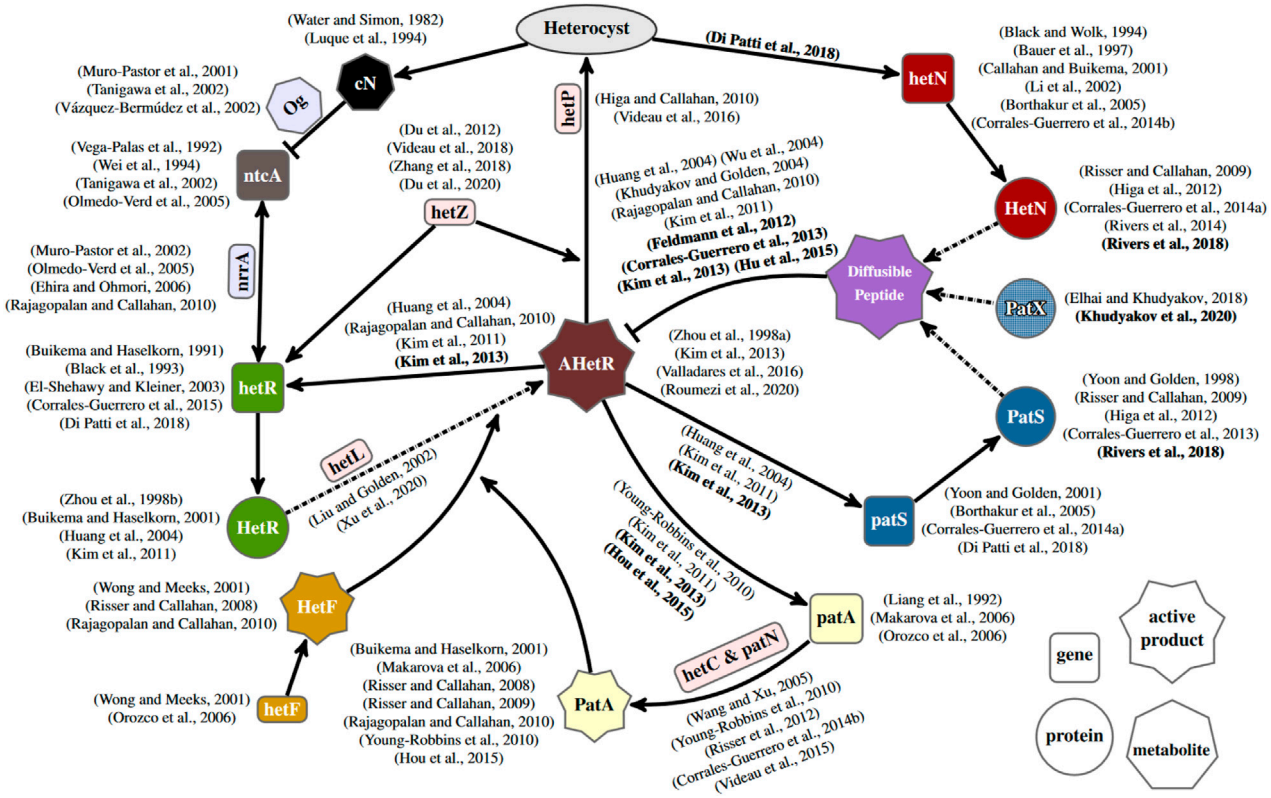

FIGURE 7
Gene regulatory network of heterocyst differentiation. The main elements and their interactions are depicted schematically, together with other relevant elements with either more dubious (in light red background) or oversimplified roles (in light blue background) in the scheme. AHetR stands for the active form of HetR. The ellipse represents the differentiation into a heterocyst. Arrows with solid lines represent interactions between elements. Arrows with dashed–dotted lines represent post-transcriptional changes. Regular and bold formatted references indicate phenotypically inferred and observed molecular interactions, respectively. Discussing all the references contained in this figure, which describe experimental results, is out of the scope of this work. For this reason, a number of them are not cited in the text.

Alternatively, Pinzon and Ju (2006) take the same culture level population approach but with a more biomolecular focus on the cellular processes that modulate the transition from a vegetative cell to a heterocyst. The deterministic model proposed includes photosynthetic growth of vegetative cells, heterocyst differentiation, self-shading effect on light penetration, and nitrogen fixation. The authors hypothesize that heterocyst differentiation is driven by the difference between the required fixed nitrogen to support maximal growth and the available nitrogen. The model describes experimental profiles well and gives reasonable predictions even for the transition from growth over external nitrogen sources to self-sustained growth.

This population point of view was taken again later by Grover et al. (2019). In this work, the authors present a deterministic model where the transition between vegetative and heterocyst cells is controlled by the relationship between the processed and free concentration of both nitrogen and phosphorus in the cells. The model predicts a relationship between the heterocyst to vegetative ratio with the nitrogen to phosphorus ratio of the environment. The authors use this to discuss an evolutionary reason for the regulation of heterocyst differentiation. Given that phosphorus-limited habitats are much more common than nitrogen-limited ones, the costly investments in nitrogen fixation are tightly regulated.

As one can see, this kind of mean-field point of view is more useful for an ecological and evolutionary perspective but does not provide much insight into the regulation of heterocyst differentiation. The patterned differentiation of heterocysts seems relevant to the mechanism controlling the differentiation decision; therefore, the population point of view is less optimal because the pattern information is lost.

5 Conclusion

In the section on inhibitor diffusion models, we have discussed examples of models where just a diffusible

inhibitory signal produced in the heterocysts is enough to maintain an existing pattern in a filament. If one considers the genetic regulatory system (Figure 2), it is easy to see that the role of this inhibitory signal originating from the heterocysts would be taken by HetN and fixed nitrogen. HetN acts directly over HetR and fixed nitrogen indirectly through *ntcA*. With this minimal structure a new heterocyst would arise in the space between heterocysts roughly when the interval doubles its length. Then, as observed when discussing genetic regulatory models, if one also considers *patS*, which is a lateral inhibitor expressed in vegetative cells, the system is capable for creating *de novo* pattern formation. This regulatory system (Figure 6) would be coupled with a switch-like genetic mechanism that initiates differentiation when the HetR concentration is higher than a certain threshold. The three-gene system of an activator and two inhibitors could seem like a Turing pattern, but it presents a key difference, one of the inhibitors *hetN* has its production restricted to the heterocysts. Moreover, this differentiation to heterocysts entails a morphological change and, therefore, is irreversible. This ensures the stability of the pattern that would not be possible in a Turing system.

Different strategies to model these three genes can simulate a heterocyst pattern, so more biological information is necessary to properly define the differentiation mechanism. A powerful tool is constraining models by comparison with different genetic backgrounds. Figure 7 shows a simplified regulatory network of heterocyst differentiation obtained from surveying experimental literature. From this, it is evident that the mechanism controlling heterocyst differentiation is quite more complex than any model discussed in this work. Therefore, incorporating more genes into the models would, on the one hand, deepen the understanding of the regulatory network and, on the other hand, open the possibility to compare with a wider range of genetic backgrounds. Therefore, the way forward is to incorporate into models genes that still have dubious roles, represented in light red rectangles in Figure 7. The research on those genes is still quite brief, and there is not enough information to justify their inclusion in models. There is evidence that both *hetC* and *patN* are connected to *patA* regulation, but there is not enough information to assign a proper role to them. On the other hand, the function of *hetL* seems quite clear: it appears to be involved with HetR activation, but there is no clear link to *hetF* and other genes in the system other than *hetR*. Also, with an apparently clear function but without a clear relation with the other genes are both *hetP* and *hetZ*, which are heavily linked to the heterocyst commitment but without a clear explanation on how they affect the commitment. This patched information is natural given that usually, the first experimental evidence is the effects of the knock-out mutants over the known network. Posterior studies that provide experimental information regarding protein translation, such as studies by Corrales-Guerrero et al. (2015) and Di Patti et al. (2018), could be really useful to properly include the gene in a model of the regulatory network. Modeling of putative mechanisms for these genes could be a useful source of predictions, helping to focus on what experiments should look for. An example is the prediction of inhibitor leakage at the filament extremes as necessary to explain the *patA* phenotype (Casanova-Ferrer et al., 2022). This expansion of the genetic scope of the models would bridge the gap that now exists between this kind of reduced model focusing on heterocyst differentiation and the more general genome-scale frameworks, such as the study by Malatinszky et al. (2017), which model the full metabolism of the *Anabaena* cell and how it changes after the differentiation into a heterocyst.

Author contributions

PC-F, JM-G, and SA contributed to the conception and design of the work. PC-F drafted the manuscript. PC-F, JM-G, and SA edited and revised the manuscript critically for important intellectual content. All authors approved the final version to be published and agreed to be accountable for all aspects of the work.

Funding

This research was supported by MCIN/AEI/10.13039/501100011033 and FEDER *Una manera de hacer Europa* through grant no. FIS2016-78313-P to SA, the associated FPI contract BES-2017-079755 to PC-F, and MCIN/AEI/10.13039/501100011033 through grant BADS, no. PID2019-109320GB-100, to SA and JM-G. The Spanish MICINN has also funded the "Severo Ochoa" Centers of Excellence to CNB, SEV 2017-0712. CSIC Library covers 25% of the APC.

Conflict of interest

The authors declare that the research was conducted in the absence of any commercial or financial relationships that could be construed as a potential conflict of interest.

Publisher's note

References

Allard, J. F., Hill, A. L., and Rutenberg, A. D. (2007). Heterocyst patterns without patterning proteins in cyanobacterial filaments. *Dev. Biol.* 312, 427–434. doi:10.1016/j.ydbio.2007.09.045

Arbel-Goren, R., Di Patti, F., Fanelli, D., and Stavans, J. (2018). Noise–Seeded developmental pattern formation in filamentous cyanobacteria. *Life* 8, 58. doi:10.3390/life8040058

Asai, H., Iwamori, S., Kawai, K., Ehira, S., Ishihara, J. I., Aihara, K., et al. (2009). Cyanobacterial cell lineage analysis of the spatiotemporal *hetR* expression profile during heterocyst pattern formation in *Anabaena* sp. *PCC* 7120. *PLoS ONE* 4, e7371. doi:10.1371/journal.pone.0007371

Baker, R. W., and Herman, G. T. (1972). Simulation of organisms using a developmental model Part 2: The heterocyst formation problem in blue-green algae. *Int. J. Biomed. Comput.* 3, 251–267. doi:10.1016/0020-7101(72)90030-X

Barrass, I., Crampin, E. J., and Maini, P. K. (2006). Mode transitions in a model Reaction–Diffusion system driven by domain growth and noise. *Bull. Math. Biol.* 68, 981–995. doi:10.1007/s11538-006-9106-8

Bauer, C. C., Ramaswamy, K. S., Endley, S., Scappino, L. A., Golden, J. W., and Haselkorn, R. (1997). Suppression of heterocyst differentiation in *Anabaena PCC* 7120 by a cosmid carrying wild-type genes encoding enzymes for fatty acid synthesis. *FEMS Microbiol. Lett.* 151, 23–30. doi:10.1016/S0378-1097(97)00128-6

Black, T. A., Cai, Y., and Wolk, C. P. (1993). Spatial expression and autoregulation of *hetR*, a gene involved in the control of heterocyst development in *Anabaena*. *Mol. Microbiol.* 9, 77–84. doi:10.1111/j.1365-2958.1993.tb01670.x

Black, T. A., and Wolk, C. P. (1994). Analysis of a Het- mutation in *Anabaena* sp. Strain *PCC* 7120 implicates a secondary metabolite in the regulation of heterocyst spacing. *J. Bacteriol.* 176, 2282–2292. doi:10.1128/jb.176.8.2282-2292.1994

Bornikoel, J., Carrión, A., Fan, Q., Flores, E., Forchhammer, K., Mariscal, V., et al. (2017). Role of two cell wall amidases in septal junction and nanopore formation in the multicellular cyanobacterium *Anabaena* sp. *PCC* 7120. *Front. Cell. Infect. Microbiol.* 7, 386–415. doi:10.3389/fcimb.2017.00386

Borthakur, P. B., Orozco, C. C., Young-Robbins, S. S., Haselkorn, R., and Callahan, S. M. (2005). Inactivation of *patS* and *hetN* causes lethal levels of heterocyst differentiation in the filamentous cyanobacterium *Anabaena* sp. *PCC* 7120. *Mol. Microbiol.* 57, 111–123. doi:10.1111/j.1365-2958.2005.04678.x

Brinkmann, F., Mercker, M., Richter, T., and Marciniak-Czochra, A. (2018). Post-Turing tissue pattern formation: Advent of mechanochemistry. *PLoS Comput. Biol.* 14, e1006259. doi:10.1371/journal.pcbi.1006259

Brown, A. I., and Rutenberg, A. D. (2014). A storage-based model of heterocyst commitment and patterning in cyanobacteria. *Phys. Biol.* 11, 016001. doi:10.1088/1478-3975/11/1/016001

Brown, A. I., and Rutenberg, A. D. (2012a). Heterocyst placement strategies to maximize the growth of cyanobacterial filaments. *Phys. Biol.* 9, 046002. doi:10.1088/1478-3975/9/4/046002

Brown, A. I., and Rutenberg, A. D. (2012b). Reconciling cyanobacterial fixed-nitrogen distributions and transport experiments with quantitative modelling. *Phys. Biol.* 9, 016007. doi:10.1088/1478-3975/9/1/016007

Buikema, W. J., and Haselkorn, R. (2001). Expression of the *Anabaena hetR* gene from a copper-regulated promoter leads to heterocyst differentiation under repressing conditions. *Proc. Natl. Acad. Sci. U. S. A.* 98, 2729–2734. doi:10.1073/pnas.051624898

Buikema, W. J., and Haselkorn, R. (1991). Isolation and complementation of nitrogen fixation mutants of the cyanobacterium *Anabaena* sp. Strain *PCC* 7120. *J. Bacteriol.* 173, 1879–1885. doi:10.1128/jb.173.6.1879-1885.1991

Callahan, S. M., and Buikema, W. J. (2001). The role of *hetN* in maintenance of the heterocyst pattern in *Anabaena* sp. *PCC* 7120. *Mol. Microbiol.* 40, 941–950. doi:10.1046/j.1365-2958.2001.02437.x

Casanova-Ferrer, P., Ares, S., and Muñoz-García, J. (2022). Terminal heterocyst differentiation in the *Anabaena patA* mutant as a result of post-transcriptional modifications and molecular leakage. *PLoS Comput. Biol.* 18. doi:10.1371/journal.pcbi.1010359

Corrales-Guerrero, L., Mariscal, V., Flores, E., and Herrero, A. (2013). Functional dissection and evidence for intercellular transfer of the heterocyst-differentiation *patS* morphogen. *Mol. Microbiol.* 88, 1093–1105. doi:10.1111/mmi.12244

Corrales-Guerrero, L., Flores, E., and Herrero, A. (2014a). Relationships between the ABC-exporter *hetC* and peptides that regulate the spatiotemporal pattern of heterocyst distribution in *Anabaena*. *PLoS ONE* 9, e104571. doi:10.1371/journal.pone.0104571

Corrales-Guerrero, L., Mariscal, V., Nürnberg, D. J., Elhai, J., Mullineaux, C. W., Flores, E., et al. (2014b). Subcellular localization and clues for the function of the *hetN* factor influencing heterocyst distribution in *Anabaena* sp. Strain *PCC* 7120. *J. Bacteriol.* 196, 3452–3460. doi:10.1128/JB.01922-14

Corrales-Guerrero, L., Tal, A., Arbel-Goren, R., Mariscal, V., Flores, E., Herrero, A., et al. (2015). Spatial fluctuations in expression of the heterocyst differentiation regulatory gene *hetR* in *Anabaena* filaments. *PLoS Genet.* 11, e1005031. doi:10.1371/journal.pgen.1005031

Crampin, E. J., Gaffney, E. A., and Maini, P. K. (1999). Reaction and diffusion on growing domains: Scenarios for robust pattern formation. *Bull. Math. Biol.* 61, 1093–1120. doi:10.1006/bulm.1999.0131

De Koster, C. G., and Lindenmayer, A. (1987). Discrete and continuous models for heterocyst differentiation in growing filaments of blue-green bacteria. *Acta Biotheor.* 36, 249–273. doi:10.1007/BF02329786

Di Patti, F., Lavacchi, L., Arbel-Goren, R., Schein-Lubomirsky, L., Fanelli, D., and Stavans, J. (2018). Robust stochastic Turing patterns in the development of a one-dimensional cyanobacterial organism. *PLoS Biol.* 16, e2004877. doi:10.1371/journal.pbio.2004877

Du, Y., Cai, Y., Hou, S., and Xu, X. (2012). Identification of the *hetR* recognition sequence upstream of *hetZ* in *Anabaena* sp. Strain *PCC* 7120. *J. Bacteriol.* 194, 2297–2306. doi:10.1128/JB.00119-12

Du, Y., Zhang, H., Wang, H., Wang, S., Lei, Q., Li, C., et al. (2020). Expression from DIF1-motif promoters of *hetR* and *patS* is dependent on *hetZ* and modulated by PatU3 during heterocyst differentiation. *PLoS ONE* 15, e0232383. doi:10.1371/journal.pone.0232383

Ehira, S., and Ohmori, M. (2006). NrrA directly regulates expression of *hetR* during heterocyst differentiation in the cyanobacterium *Anabaena* sp. Strain *PCC* 7120. *J. Bacteriol.* 188, 8520–8525. doi:10.1128/JB.01314-06

El-Shehawy, R. M., and Kleiner, D. (2003). The mystique of irreversibility in cyanobacterial heterocyst formation: Parallels to differentiation and senescence in eukaryotic cells. *Physiol. Plant.* 119, 49–55. doi:10.1034/j.1399-3054.2003.00096.x

Elhai, J., and Khudyakov, I. (2018). Ancient association of cyanobacterial multicellularity with the regulator *hetR* and an RGSGR pentapeptide-containing protein (PatX). *Mol. Microbiol.* 110, 931–954. doi:10.1111/mmi.14003

Fay, P., Stewart, W. D. P., Walsby, A. E., and Fogg, G. E. (1968). Is the heterocyst the site of nitrogen fixation in blue-green algae? *Nature* 220, 810–812. doi:10.1038/220810b0

Feldmann, E. A., Ni, S., Sahu, I. D., Mishler, C. H., Levengood, J. D., Kushnir, Y., et al. (2012). Differential binding between *patS C-Terminal* peptide fragments and *hetR* from *Anabaena* sp. *PCC* 7120. *Biochemistry* 51, 2436–2442. doi:10.1021/bi300228n

Flores, E., and Herrero, A. (2010). Compartmentalized function through cell differentiation in filamentous cyanobacteria. *Nat. Rev. Microbiol.* 8, 39–50. doi:10.1038/nrmicro2242

Fogg, G. E. (1949). Growth and heterocyst production in *Anabaena cylindrica lemm*: II. In relation to carbon and nitrogen metabolism. *Ann. Bot.* 13, 241–259. doi:10.1093/oxfordjournals.aob.a083217

Gerdtzen, Z. P., Salgado, C. J., Osses, A., Asenjo, J. A., Rapaport, I., and Andrews, B. A. (2009). Modeling heterocyst pattern formation in cyanobacteria. *BMC Bioinforma.* 10, S16. doi:10.1186/1471-2105-10-S6-S16

Gierer, A., and Meinhardt, H. (1972). A theory of biological pattern formation. *Kybernetik* 12, 30–39. doi:10.1007/BF00289234

Gillespie, D. T. (1976). A general method for numerically simulating the stochastic time evolution of coupled chemical reactions. *J. Comput. Phys.* 22, 403–434. doi:10.1016/0021-9991(76)90041-3

Gillespie, D. T. (2000). The chemical Langevin equation. *J. Chem. Phys.* 113, 297–306. doi:10.1063/1.481811

Grover, J. P., Scott, J. T., Roelke, D. L., and Brooks, B. W. (2019). Dynamics of nitrogen-fixing cyanobacteria with heterocysts: A stoichiometric model. *Mar. Freshw. Res.* 71, 644–658. doi:10.1071/MF18361

Harish.and Seth, K. (2020). Molecular circuit of heterocyst differentiation in cyanobacteria. *J. Basic Microbiol.* 60, 738–745. doi:10.1002/jobm.202000266

Hense, I., and Beckmann, A. (2006). Towards a model of cyanobacteria life cycle—effects of growing and resting stages on bloom formation of N2-fixing species. *Ecol. Modell.* 195, 205–218. doi:10.1016/j.ecolmodel.2005.11.018

Herrero, A., Stavans, J., and Flores, E. (2016). The multicellular nature of filamentous heterocyst-forming cyanobacteria. *FEMS Microbiol. Rev.* 40, 831–854. doi:10.1093/femsre/fuw029

Higa, K. C., and Callahan, S. M. (2010). Ectopic expression of *hetP* can partially bypass the need for *hetR* in heterocyst differentiation by *Anabaena* sp. Strain *PCC* 7120. *Mol. Microbiol.* 77, 562–574. doi:10.1111/j.1365-2958.2010.07257.x

Higa, K. C., Rajagopalan, R., Risser, D. D., Rivers, O. S., Tom, S. K., Videau, P., et al. (2012). The RGSGR amino acid motif of the intercellular signalling protein, *hetN*, is required for patterning of heterocysts in *Anabaena* sp. Strain *PCC* 7120. *Mol. Microbiol.* 83, 682–693. doi:10.1111/j.1365-2958.2011.07949.x

Hou, S., Zhou, F., Peng, S., Gao, H., and Xu, X. (2015). The *hetR-binding* site that activates expression of *patA* in vegetative cells is required for normal heterocyst patterning in *Anabaena* sp. *PCC* 7120. *Sci. Bull. (Beijing).* 60, 192–201. doi:10.1007/s11434-014-0724-5

Hu, H. X., Jiang, Y. L., Zhao, M. X., Cai, K., Liu, S., Wen, B., et al. (2015). Structural insights into *hetR-patS* interaction involved in cyanobacterial pattern formation. *Sci. Rep.* 5, 16470. doi:10.1038/srep16470

Huang, X., Dong, Y., and Zhao, J. (2004). *hetR* homodimer is a DNA-binding protein required for heterocyst differentiation, and the DNA-binding activity is inhibited by *patS*. *Proc. Natl. Acad. Sci. U. S. A.* 101, 4848–4853. doi:10.1073/pnas.0400429101

Ishihara, J., Tachikawa, M., Iwasaki, H., and Mochizuki, A. (2015). Mathematical study of pattern formation accompanied by heterocyst differentiation in multicellular cyanobacterium. *J. Theor. Biol.* 371, 9–23. doi:10.1016/j.jtbi.2015.01.034

Khudyakov, I., Gladkov, G., and Elhai, J. (2020). Inactivation of three rg(S/t)Gr pentapeptide-containing negative regulators of *hetR* results in lethal differentiation of *Anabaena PCC* 7120. *Life* 10, 3266–E416. doi:10.3390/life10120326

Khudyakov, I. Y., and Golden, J. W. (2004). Different functions of *hetR*, a master regulator of heterocyst differentiation in *Anabaena* sp. *PCC* 7120, can be separated by mutation. *Proc. Natl. Acad. Sci. U. S. A.* 101, 16040–16045. doi:10.1073/pnas.0405572101

Kim, Y., Joachimiak, G., Ye, Z., Binkowski, T. A., Zhang, R., Gornicki, P., et al. (2011). Structure of transcription factor *hetR* required for heterocyst differentiation in cyanobacteria. *Proc. Natl. Acad. Sci. U. S. A.* 108, 10109–10114. doi:10.1073/pnas.1106840108

Kim, Y., Ye, Z., Joachimiak, G., Videau, P., Young, J., Hurd, K., et al. (2013). Structures of complexes comprised of *Fischerella* transcription factor *hetR* with *Anabaena DNA* targets. *Proc. Natl. Acad. Sci. U. S. A.* 110, E1716–E1723. doi:10.1073/pnas.1305971110

Lacalli, T. C. (2022). Patterning, from conifers to consciousness: Turing's theory and order from fluctuations. *Front. Cell Dev. Biol.* 10, 871950. doi:10.3389/fcell.2022.871950

Li, B., Huang, X., and Zhao, J. (2002). Expression of *hetN* during heterocyst differentiation and its inhibition of *hetR* up-regulation in the cyanobacterium *Anabaena* sp. *PCC* 7120. *FEBS Lett.* 517, 87–91. doi:10.1016/S0014-5793(02)02582-6

Liang, J., Scappino, L., and Haselkorn, R. (1992). The *patA* gene product, which contains a region similar to CheY of *Escherichia* coli, controls heterocyst pattern formation in the cyanobacterium *Anabaena* 7120. *Proc. Natl. Acad. Sci. U. S. A.* 89, 5655–5659. doi:10.1073/pnas.89.12.5655

Liu, D., and Golden, J. W. (2002). *hetL* overexpression stimulates heterocyst formation in *Anabaena* sp. Strain *PCC* 7120. *J. Bacteriol.* 184, 6873–6881. doi:10.1128/JB.184.24.6873-6881.2002

Luque, I., Flores, E., and Herrero, A. (1994). Molecular mechanism for the operation of nitrogen control in cyanobacteria. *EMBO J.* 13, 2862–2869. doi:10.1002/j.1460-2075.1994.tb06580.x

Makarova, K. S., Koonin, E. V., Haselkorn, R., and Galperin, M. Y. (2006). Cyanobacterial response regulator *patA* contains a conserved N-terminal domain (PATAN) with an alpha-helical insertion. *Bioinformatics* 22, 1297–1301. doi:10.1093/bioinformatics/btl096

Malatinszky, D., Steuer, R., and Jones, P. R. (2017). A comprehensively curated genome-scale two-cell model for the heterocystous cyanobacterium *Anabaena* sp. *PCC* 7120. *Plant Physiol.* 173, 509–523. doi:10.1104/pp.16.01487

Marciniak-Czochra, A., Karch, G., and Suzuki, K. (2017). Instability of Turing patterns in reaction-diffusion-ODE systems. *J. Math. Biol.* 74, 583–618. doi:10.1007/s00285-016-1035-z

Marcon, L., Diego, X., Sharpe, J., and Müller, P. (2016). High-throughput mathematical analysis identifies turing networks for patterning with equally diffusing signals. *Elife* 5, e14022. doi:10.7554/eLife.14022

Meeks, J. C., and Elhai, J. (2002). Regulation of cellular differentiation in filamentous cyanobacteria in free-living and plant-associated symbiotic growth states. *Microbiol. Mol. Biol. Rev.* 66, 94–121. doi:10.1128/mmbr.66.1.94-121.2002

Meinhardt, H. (2008). Models of biological pattern formation: From elementary steps to the organization of embryonic axes. *Curr. Top. Dev. Biol.* 81, 1–63. doi:10.1016/S0070-2153(07)81001-5

Muñoz-García, J., and Ares, S. (2016). Formation and maintenance of nitrogen-fixing cell patterns in filamentous cyanobacteria. *Proc. Natl. Acad. Sci. U. S. A.* 113, 6218–6223. doi:10.1073/pnas.1524383113

Muro-Pastor, A. M., Valladares, A., Flores, E., and Herrero, A. (2002). Mutual dependence of the expression of the cell differentiation regulatory protein *hetR* and the global nitrogen regulator NtcA during heterocyst development. *Mol. Microbiol.* 44, 1377–1385. doi:10.1046/j.1365-2958.2002.02970.x

Muro-Pastor, A. M. (2014). The heterocyst-specific nsiR1 small RNA is an early marker of cell differentiation in cyanobacterial filaments. *mBio* 5, e01079–e01014. doi:10.1128/mBio.01079-14

Muro-Pastor, A. M., and Hess, W. R. (2012). Heterocyst differentiation: From single mutants to global approaches. *Trends Microbiol.* 20, 548–557. doi:10.1016/j.tim.2012.07.005

Muro-Pastor, M. I., Reyes, J. C., and Florencio, F. J. (2001). Cyanobacteria perceive nitrogen status by sensing intracellular 2-oxoglutarate levels. *J. Biol. Chem.* 276, 38320–38328. doi:10.1074/jbc.m105297200

Murray, J. D. (2003). *Mathematical biology, II: Spatial models and biomedical applications*. Berlin, Germany: Springer.

Nakamasu, A., Takahashi, G., Kanbe, A., and Kondo, S. (2009). Interactions between zebrafish pigment cells responsible for the generation of Turing patterns. *Proc. Natl. Acad. Sci. U. S. A.* 106, 8429–8434. doi:10.1073/pnas.0808622106

Olmedo-Verd, E., Flores, E., Herrero, A., and Muro-Pastor, A. M. (2005). *hetR-dependent* and -Independent expression of heterocyst-related genes in an *Anabaena* strain overproducing the NtcA transcription factor. *J. Bacteriol.* 187, 1985–1991. doi:10.1128/JB.187.6.1985-1991.2005

Orozco, C. C., Risser, D. D., and Callahan, S. M. (2006). Epistasis analysis of four genes from *Anabaena* sp. Strain *PCC* 7120 suggests a connection between *patA* and *patS* in heterocyst pattern formation. *J. Bacteriol.* 188, 1808–1816. doi:10.1128/JB.188.5.1808-1816.2006

Pinzon, N. M., and Ju, L. K. (2006). Modeling culture profiles of the heterocystous N2-fixing cyanobacterium *Anabaena* flos-Aquae. *Biotechnol. Prog.* 22, 1532–1540. doi:10.1021/bp060163c

Rajagopalan, R., and Callahan, S. M. (2010). Temporal and spatial regulation of the four transcription start sites of *hetR* from *Anabaena* sp. Strain *PCC* 7120. *J. Bacteriol.* 192, 1088–1096. doi:10.1128/JB.01297-09

Raspopovic, J., Marcon, L., Russo, L., and Sharpe, J. (2014). Modeling digits. Digit patterning is controlled by a Bmp-Sox9-Wnt Turing network modulated by morphogen gradients. *Science* 345, 566–570. doi:10.1126/science.1252960

Risser, D. D., and Callahan, S. M. (2009). Genetic and cytological evidence that heterocyst patterning is regulated by inhibitor gradients that promote activator decay. *Proc. Natl. Acad. Sci. U. S. A.* 106, 19884–19888. doi:10.1073/pnas.0909152106

Risser, D. D., and Callahan, S. M. (2008). *hetF* and *patA* control levels of *hetR* in *Anabaena* sp. Strain *PCC* 7120. *J. Bacteriol.* 190, 7645–7654. doi:10.1128/JB.01110-08

Risser, D. D., Wong, F. C. Y., and Meeks, J. C. (2012). Biased inheritance of the protein PatN frees vegetative cells to initiate patterned heterocyst differentiation. *Proc. Natl. Acad. Sci. U. S. A.* 109, 15342–15347. doi:10.1073/pnas.1207530109

Rivers, O. S., Beurmann, S., Dow, A., Cozy, L. M., and Videau, P. (2018). Phenotypic assessment suggests multiple start codons for *hetN*, an inhibitor of heterocyst differentiation, in *Anabaena* sp. Strain *PCC* 7120. *J. Bacteriol.* 200, e00220-18–14. doi:10.1128/JB.00220-18

Rivers, O. S., Videau, P., and Callahan, S. M. (2014). Mutation of *sepJ* reduces the intercellular signal range of a *hetN-dependent* paracrine signal, but not of a *patS-dependent* signal, in the filamentous cyanobacterium *Anabaena* sp. Strain *PCC* 7120. *Mol. Microbiol.* 94, 1260–1271. doi:10.1111/mmi.12836

Roumezi, B., Xu, X., Risoul, V., Fan, Y., Lebrun, R., and Latifi, A. (2020). The Pkn22 kinase of *nostoc PCC* 7120 is required for cell differentiation via the phosphorylation of *hetR* on a residue highly conserved in genomes of heterocyst-forming cyanobacteria. *Front. Microbiol.* 10, 3140–3218. doi:10.3389/fmicb.2019.03140

Smith, S., and Dalchau, N. (2018). *Beyond activator-inhibitor networks: The generalised Turing mechanism*. ArXiv Prepr. ArXiv180307886.

Tanigawa, R., Shirokane, M., Maeda, S. I., Omata, T., Tanaka, K., and Takahashi, H. (2002). Transcriptional activation of NtcA-dependent promoters of *synechococcus* sp. *PCC* 7942 by 2-oxoglutarate *in vitro*. *Proc. Natl. Acad. Sci. U. S. A.* 99, 4251–4255. doi:10.1073/pnas.072587199

Torres-Sánchez, A., Gómez-Gardeñes, J., and Falo, F. (2015). An integrative approach for modeling and simulation of heterocyst pattern formation in

cyanobacteria filaments. *PLoS Comput. Biol.* 11, e1004129. doi:10.1371/journal.pcbi.1004129

Turing, A. M. (1952). The chemical basis of morphogenesis. *Philos. Trans. R. Soc. Lond. B. Biol. Sci.* 237, 37–72. doi:10.1098/rstb.1952.0012

Valladares, A., Flores, E., and Herrero, A. (2016). The heterocyst differentiation transcriptional regulator *hetR* of the filamentous cyanobacterium *Anabaena* forms tetramers and can be regulated by phosphorylation. *Mol. Microbiol.* 99, 808–819. doi:10.1111/mmi.13268

Vázquez-Bermúdez, M. F., Herrero, A., and Flores, E. (2002). 2-Oxoglutarate increases the binding affinity of the NtcA (nitrogen control) transcription factor for the *Synechococcus glnA* promoter. *FEBS Lett.* 512, 71–74. doi:10.1016/S0014-5793(02)02219-6

Vega-Palas, M. A., Flores, E., and Herrero, A. (1992). NtcA, a global nitrogen regulator from the cyanobacterium *Synechococcus* that belongs to the Crp family of bacterial regulators. *Mol. Microbiol.* 6, 1853–1859. doi:10.1111/j.1365-2958.1992.tb01357.x

Videau, P., Cozy, L. M., Young, J. E., Ushijima, B., Oshiro, R. T., Rivers, O. S., et al. (2015). The *trpE* gene negatively regulates differentiation of heterocysts at the level of induction in *Anabaena* sp. Strain *PCC* 7120. *J. Bacteriol.* 197, 362–370. doi:10.1128/JB.02145-14

Videau, P., Rivers, O. S., Hurd, K., Ushijima, B., Oshiro, R. T., Ende, R. J., et al. (2016). The heterocyst regulatory protein *hetP* and its homologs modulate heterocyst commitment in *Anabaena* sp. Strain *PCC* 7120. *Proc. Natl. Acad. Sci. U. S. A.* 113, E6984-E6992–E6992. doi:10.1073/pnas.1610533113

Videau, P., Rivers, O. S., Tom, S. K., Oshiro, R. T., Ushijima, B., Swenson, V. A., et al. (2018). The *hetZ* gene indirectly regulates heterocyst development at the level of pattern formation in *Anabaena* sp. Strain *PCC* 7120. *Mol. Microbiol.* 109, 91–104. doi:10.1111/mmi.13974

Wang, Y., and Xu, X. (2005). Regulation by *hetC* of genes required for heterocyst differentiation and cell division in *Anabaena* sp. Strain *PCC* 7120. *J. Bacteriol.* 187, 8489–8493. doi:10.1128/JB.187.24.8489-8493.2005

Water, S. D. V. D., and Simon, R. D. (1982). Induction and differentiation of heterocysts in the filamentous cyanobacterium *Cylindrospermum* licheniforme. *Microbiology* 128, 917–925. doi:10.1099/00221287-128-5-917

Wei, T. F., Ramasubramanian, T. S., and Golden, J. W. (1994). *Anabaena* sp. Strain *PCC* 7120 *ntcA* gene required for growth on nitrate and heterocyst development. *J. Bacteriol.* 176, 4473–4482. doi:10.1128/jb.176.15.4473-4482.1994

Wolk, C. P. (1967). Physiological basis of the pattern of vegetative growth of a blue-green alga. *Proc. Natl. Acad. Sci. U. S. A.* 57, 1246–1251. doi:10.1073/pnas.57.5.1246

Wolk, C. P., and Quine, M. P. (1975). Formation of one-dimensional patterns by stochastic processes and by filamentous blue-green algae. *Dev. Biol.* 46, 370–382. doi:10.1016/0012-1606(75)90113-X

Wong, F. C. Y., and Meeks, J. C. (2001). The *hetF* gene product is essential to heterocyst differentiation and affects *hetR* function in the cyanobacterium *Nostoc* punctiforme. *J. Bacteriol.* 183, 2654–2661. doi:10.1128/JB.183.8.2654-2661.2001

Wu, X., Liu, D., Lee, M. H., and Golden, J. W. (2004). *patS* minigenes inhibit heterocyst development of *Anabaena* sp. Strain *PCC* 7120. *J. Bacteriol.* 186, 6422–6429. doi:10.1128/JB.186.19.6422-6429.2004

Xu, X., Risoul, V., Byrne, D., Champ, S., Douzi, B., and Latifi, A. (2020). *hetL, hetR* and *patS* form a reaction-diffusion system to control pattern formation in the cyanobacterium nostoc *PCC* 7120. *eLife* 9, e59190–48. doi:10.7554/ELIFE.59190

Yoon, H. S., and Golden, J. W. (1998). Heterocyst pattern formation controlled by a diffusible peptide. *Science* 282, 935–938. doi:10.1126/science.282.5390.935

Yoon, H. S., and Golden, J. W. (2001). *patS* and products of nitrogen fixation control heterocyst pattern. *J. Bacteriol.* 183, 2605–2613. doi:10.1128/JB.183.8.2605-2613.2001

Young-Robbins, S. S., Risser, D. D., Moran, J. R., Haselkorn, R., and Callahan, S. M. (2010). Transcriptional regulation of the heterocyst patterning gene *patA* from *Anabaena* sp. Strain *PCC* 7120. *J. Bacteriol.* 192, 4732–4740. doi:10.1128/JB.00577-10

Zeng, X., and Zhang, C.-C. (2022). The making of a heterocyst in cyanobacteria. *Annu. Rev. Microbiol.* 76. doi:10.1146/annurev-micro-041320-093442

Zhang, H., Wang, S., Wang, Y., and Xu, X. (2018). Functional overlap of *hetP* and *hetZ* in regulation of heterocyst differentiation in *Anabaena* sp. Strain *PCC* 7120. *J. Bacteriol.* 200, e00707–17. doi:10.1128/JB.00707-17

Zhou, R., Cao, Z., and Zhao, J. (1998a). Characterization of *hetR* protein turnover in *Anabaena* sp. *PCC* 7120. *Arch. Microbiol.* 169, 417–423. doi:10.1007/s002030050592

Zhou, R., Wei, X., Jiang, N., Li, H., Dong, Y., Hsi, K. L., et al. (1998b). Evidence that *hetR* protein is an unusual serine-type protease. *Proc. Natl. Acad. Sci. U. S. A.* 95, 4959–4963. doi:10.1073/pnas.95.9.4959

Zhu, M., Callahan, S. M., and Allen, J. S. (2010). Maintenance of heterocyst patterning in a filamentous cyanobacterium. *J. Biol. Dyn.* 4, 621–633. doi:10.1080/17513751003777507

frontiers | Frontiers in Physics

TYPE Mini Review
PUBLISHED 04 January 2023
DOI 10.3389/fphy.2022.968409

OPEN ACCESS

EDITED BY
Pau Formosa-Jordan,
Max Planck Institute for Plant Breeding Research, Germany

REVIEWED BY
Yiteng Dang,
Max Planck Institute for the Physics of Complex Systems, Germany
H. Ariel Alvarez,
Universidad Nacional de La Plata, Argentina

*CORRESPONDENCE
Christian Fleck,
christian.fleck@fdm.uni-freiburg.de

SPECIALTY SECTION
This article was submitted to Biophysics, a section of the journal Frontiers in Physics

RECEIVED 13 June 2022
ACCEPTED 09 December 2022
PUBLISHED 04 January 2023

CITATION
Pleyer J and Fleck C (2023), Agent-based models in cellular systems. *Front. Phys.* 10:968409. doi: 10.3389/fphy.2022.968409

Agent-based models in cellular systems

Jonas Pleyer and Christian Fleck*

Freiburg Center for Data Analysis and Modeling (FDM), University of Freiburg, Freiburg im Breisgau, Germany

This mini-review discusses agent-based models as modeling techniques for studying pattern formation of multi-cellular systems in biology. We introduce and compare different agent-based model frameworks with respect to spatial representation, microenvironment, intracellular and extracellular reactions, cellular properties, implementation, and practical use. The guiding criteria for the considered selection of agent-based model frameworks are that they are actively maintained, well documented, and provide a model development workflow.

KEYWORDS

agent-based models (ABM), computer simulation, biological cellular systems, pattern formation, developmental biology

1 Introduction

Interacting cellular biological systems, such as bacterial communities, tissues, organoids, exhibit a plethora of phenomena, which are often not easy to understand intuitively. To explore and analyse cellular systems mathematical equations and/or computer simulations can be powerful tools. Because the fundamental building blocks or units of biological systems are cells, agent-based models with cells as the individual agents are natural simulation tools to study such systems. Pattern formation in cellular systems requires interactions between cells, the exchange of information, and, in case of self-organisation, that cells respond in a sufficiently non-linear manner, including feedback loops [1, 2]. Exchange of information can occur in a multitude of different ways and on different length scales: (short range) mechanical forces [3] and cellular junctions [4], (medium range) diffusing chemicals [5], and (long range) hormones [6]. Due to the individual cell based perspective agent-based models make it easy to implement these interactions and also the signal processing and response of the cells. In this mini-review we consider agent-based software frameworks with individual cells as agents, which are actively maintained and developed, provide documentation beyond a minimum, and provide a model development workflow[1].

Traditionally, pattern formation in biology is studied using Partial Differential Equations (PDEs) that model continuous distribution of cells [7–10]. There is a wealth of literature onhow to solve coupled non-linear PDEs, estimate the parameters

1 An extended list of other agent-based models (ABMs) can be found in the Supplementary material.

from data, and how to explore their behavior, e.g., sensitivity analysis, bifurcation analysis, see, e.g., [11–16]. PDEs are powerful tools, however, in a PDE cells have no spatial extension, ignoring the underlying cellular spatial structure. Although it is possible in a PDE to distinguish between the inside of the cells and their micro-environment, there is no unique or canonical way to handle, e.g., cell proliferation, differentiation, internal cell structure and other properties of the cells, which may be relevant for the questions at hand. This problem can be solved by cellular Automata (CA) [17] which consist of a regular grid with a finite number of states at each grid point and rules, determining how to update them accordingly. A further development of CA introduced ABMs [18–20] where the modeling approach is to handle cells as individual agents with rules, potentially with an internal structure and/or moving in space. By using coarse-graining or homogenization techniques one could derive a system of coupled PDEs from an ABM; there is, however, no unique way to go from a PDE to an ABM [21].

2 Agent-based models

An ABM is a collection of autonomous agents with a predefined set of rules, which depend on the existing state of the agent and external factors [22–25]. The rules can be discrete following logical if-else statements, continuous, i.e., Ordinary Differential Equations (ODEs) for intra-cellular reactions or a combination of both. Also, graphs, neural networks and other intricate algorithms can be implemented [26]. Nevertheless, one usually strives to employ the most simple set of rules sufficient to accurately describe the complexity of the desired system. Compared to macroscopic PDE models, ABMs are considered microscopic modeling, since they deal with agents directly and are thus more common in a bottom-up approach [27]. ABMs should not be seen as a technologically distinct toolset but rather as a mindset for researchers by modeling complex systems from the perspective of individual constituents.

Historically, precursors to ABMs were cellular Automata, which were developed by [17]. They reached widespread recognition even in the general public with the introduction of Conway's "Game of Life" [28, 29]. Not long after, the first ABMs were being envisioned to study a biological system [18]. Up until the break of the century, ABMs were used in many fields of research such as modeling human crowd stampedes [30], bird flocks [19] or the prediction of financial markets [31]. With the rapidly growing accessibility and power of modern computer hardware, the popularity of ABMs kept on increasing, where tools such as NanoHUB [32] or the Systems Biology Markup Language (SBML) [33] further helped to share computational models between researchers. In order to study complex phenomena such as pattern formation ABMs must be able to capture cell-cell communication and cellular response mechanisms [10, 34–37]. In the next section we will compare the available ABM frameworks and discuss how they cover different cellular properties.

2.1 Comparison of ABMs

The effort of writing efficient solving algorithms and data structures in a usable fashion is considerable. Therefore, agent-based model frameworks (ABMFs) have emerged that define a certain workflow and implement a set of features, so that users of the frameworks can focus on their research question instead of having to spend a significant amount of time for design and implementation.

The majority of cell-agent-based model frameworks (CABMFs) evolved as generalizations of solutions to specific problems. BSim [38] was specifically designed to model bacterial populations and has been used to study gene regulatory control [39] and bacterial biofilms [40]. Chaste[2] was designed as a Cancer, Heart and Soft Tissue Environment [41] and has been used in studying growth of epithelial monolayers [42]. CompuCell3D [43] originated from CompuCell [44], which was one of the first frameworks created and originally used to model only simple reaction-diffusion (RD) systems but was since extended considerably to cover a wider range of topics such as angiogenesis [45], cancer [46] and tissue engineering [47]. EPISIM was used to understand how varying proportions of T Cells emerge in different vertebrate taxa [48]. Morpheus [49] was applied to self-organization in neural stem cell divisions in adult zebrafish [50] and polarization of the multiciliated planarian *epidermis* [51]. MultiCellSim [52] resulted from the in-depth analysis of cell-cell communication and was since applied to Immuno-Oncology [53]. PhysiCell [54] is mainly used modeling cancer and tumor dynamics [55, 56]. TiSim/CellSys [57] was applied to liver regeneration processes [58]. VirtualLeaf [59] was specifically designed for modeling plants and emphasizes intercellular connections and details of the mechanical properties of the cell wall. Table 1 displays general characteristics of these modeling frameworks.

2.1.1 Spatial representation

A key distinction between ABMs is given by the difference of the spatial representation of cells and chemicals. ABMs can be separated into lattice-based and lattice-free, the former meaning that cells can only migrate between predefined lattice nodes, while the later permits free movement of cells in a given domain. Frameworks such as Chaste, PhysiCell, TiSim/CellSys and VirtualLeaf utilize off-lattice motion. Chaste[3], CompuCell3D

2 We only consider here the cell-based part of the chaste software environment.

3 Cell-based Chaste supports off-lattice as well as on-lattice representations.

TABLE 1 Comparison of CABMFs in alphabetical order with respect to implementations of spatial representation, dimension, intra- and extracellular processes and cell-cell forces (Supplementary Table S1).

Framework	Spatial representation and dimension	Intracellular	Extracellular	Cell-cell forces
BSim	off-lattice, Arbitrary Meshes 3D	ODEs	PDEs, Molecule-Agents	Micro-Scale Meshing and Collision Detection
Chaste	CPM, off-lattice, CA, Vertex-Model 2D + 3D	ODEs, SBML	RD PDEs, SBML	custom force laws
CompuCell3D	CPM on regular lattice 2D + 3D	ODEs, SBML, PBPK s	RD PDEs, SBML, PBPK s	force terms *via* CPM Hamiltonian
EPISIM	Off-lattice, hexagonal 2D + 3D	ODEs, SBML	SBML	spherical cell potentials
Morpheus	CPM on regular lattice 2D + 3D	ODEs, SBML	RD PDEs, CA lattice ODEs, finite state gradient-based	force terms *via* CPM Hamiltonian
MultiCellSim	CA + Brownian motion	Secretion and uptake	RD PDEs	–
PhysiCell	Off-lattice 2D + 3D	SBML, Boolean Networks, Diffusion Flux Balance Analysis	BioFVM Reaction Kinetics	Spheres with Potential
TiSim/CellSys	Off-lattice 2D + 3D	ODEs, SBML	diffusion + advection	frictional, elastic and stochastic force terms
VirtualLeaf	Vertex model 2D	ODEs	–	polygonal finite elements

and Morpheus utilize lattice-based methods for cell-migration. This also means that no particular cellular shape is modeled explicitly, but rather cells follow rules (often potentials) to determine their respective quantity on lattice points. The disadvantage of the lattice-based approach is that it is limited in the spatial resolution, but in turn as an advantage it can yield considerable performance improvements. Off-lattice models often take a cell centre [60] approach meaning, a cell is defined by a single location vector and a shape (such as sphere, ellipsoid or cylinder) that governs interactions. BSim additionally has the ability to represent microbes as meshed objects thus offering a much higher resolution at micro-scale although at increased computational cost. Another less common modeling choice is to use a vertex model [61, 62] that represents each cell by a polygon, determined by a number of vertices, which can be subject to external forces, pressure, friction, adhesion, chemotaxis and other external and internal contributing factors. Lattice-bound models can utilize different discretizations such as regular Cartesian meshes, hexagonal or triangulated ones. Most of the presented frameworks in Table 1 can be used to simulate two-dimensional (2D) as well as three-dimensional (3D) scenarios. The Cellular Potts Model, also known as Glazier-Graner-Hogeweg (GGH) model [63, 64], is a common choice for many frameworks. Typically, in a Cellular Potts Model a Hamiltonian is formulated which describes the phenomenological "energy" of a given configuration of the system on a Euclidean lattice. Subsequently, the systems is evolved by minimizing the energy. LBIBCell modifies the classical Cellular Potts Model (CPM) approach by representing cells as evolving polygons with the immersed boundary method and thus obtains off-lattice cellular representations [65, 66].

2.1.2 External microenvironment

Transport processes of chemicals typically involve numerically solving (convection-) diffusion equations (67) and (68) with cell to extracellular matrix interaction nodes at the positions of the cellular agents on a (often euclidean) mesh. One exception is presented by VirtualLeaf where intracellular compartments are connected *via* membranes to adjacent cells and model transport through membrane-potentials [59]. Many ABMs utilize PDEs to model intracellular or extracellular transport processes such as convection and diffusion and allow for custom forms of reactions either *via* well-defined user-interfaces like Morpheus [49] or direct implementation into the source code.

2.1.3 Cellular processes

In an agent-based approach the processes occuring inside a cell can naturally be described by giving the agents the required set of functions. Each framework mentioned in Table 1 implements proliferation and cell-death mechanisms as key components. However, predefined and detailed cell-cycle routines such as utilized in PhysiCell [54] are less common, but are important to consider if, e.g., external factors such as growth hormones affect the cell-cycle [69]. In addition, internal chemicals may be released upon cell death. In order to model developmental processes such as embryogenesis, the framework needs to support cell-differentiation with dynamic modifications of the phenotype.

Cell polarity can play an important role in many phenomena such as in ciliary rootlets in planarian *epidermis* [51]. Many frameworks like CompuCell3D, Chaste, Morpheus, VirtualLeaf support this feature. The geometry of the cell includes its spatial representation together with mechanical features such as adhesion and repulsion. PhysiCell utilize spheroid/ellipsoid cellular geometries, meaning each cell is represented by a sphere or ellipsoid and a corresponding potential. Further, adhesion plays an important role in cell-cell interactions and communication. Lattice-free frameworks often model it by choosing a particular form of interaction potential. One sophisticated example is the experimental Johnson-Kendall-Roberts (JKR) potential [70], which was derived from the Hertz contact model [71]. It also models cell separation and is implemented by CellSys. Other frameworks that implement a CPM treat adhesion *via* interaction terms in its Hamiltonian Formulation [72]. In the context of vertex models, force potentials can also be utilized although the implementation is often more complex. All of the above ABMs are able to model stochastic cell migration, excluding VirtualLeaf since almost all plant cells are non-motile. Collectively arising forces and friction which can play an important role in early embryonic development [73] may be harder to simulate if the geometry of the cells is solely implemented as spheroid/ellipsoid. For frameworks such as PhysiCell and TiSim/CellSys who additionally do not support polarity, modeling of force-mitigated spatial effects is difficult. Chemotaxis is a key concept in cell-sorting [74] and can be implemented by any framework that supports migration and can calculate reactant gradients. All of the presented frameworks can capture intracellular reactions by using ODEs ignoring the internal spatial structure of the cells; different reaction compartments can be easily introduced by coupling of ODEs. Some (e.g., Chaste, EPISIM) can also handle intracellular stochastic reactions, using the Gillespie algorithm [75].

2.2 Implementational details

2.2.1 Development, standards and features

Development and design of efficient algorithms and their implementation require knowledge in software engineering and in writing maintainable code, as these frameworks are usually developed by teams rather than by individuals and consist of many thousands of lines of code. The Chaste framework was one of the first projects to follow agile coding principles and other best-practice workflows such as rigorous unit-testing [76]. All presented CABMFs are written in C++ which together with the C and Fortran language have historically served as the *de facto* languages for high-performance software development. In addition to CABMFs, researchers have over the last two decades developed internationally recognized formats to seamlessly share model details (e.g., SMBL). This is utilized in Chaste, CompuCell3D, Morpheus and PhysiCell[4] and allows for rapid model development, implementation and comparison to classical ODE and PDE solvers. CompuCell3D is also able to model physiologically based pharmacokinetics (PBPKs). Additionally, many frameworks come with dedicated [sometimes graphical user interfaces (GUIs)] tools for configuration, analysis, batch-processing, visualization and other workflow-aiding features which are valuable additions. In this regard, EPISIM is special as it utilizes the popular COPASI [77] and Mason [78] software and plugins for the eclipse code editor [79] to build the application.

3 Studying pattern formation with agent-based models

3.1 Applications

Pattern formation in cellular biological systems can occur *via* self-assembly or self-organization and ABMs have been applied to investigate both aspects. Chaste was used to study cell migration in the crypt [80]. Furthermore, CompuCell3D provided examples for self-organization in work on polarization [81] and studies of physical forces [82] in migrating cells. Morpheus was used to describe pattern formations in the telencephalon of adult zebrafish [83] and was also used to study growth of the *Drosophila* wing *via* cell recruitment [84]. PhysiCell recently provided insights to formation of patterns in tumour spheroids [56]. Pattern formation in dicot leaves was modeled using VirtualLeaf [85]. ABMs allow researchers to examine complicated models which would otherwise be hard to study and interpret with classical PDEs.

Figure 1 shows results of a multi-scale model using PhysiCell [54]. We can observe that the pattern changes as the number of patterning cells (type I) increases. This simple example shows, how to readily formulate and explore models in an ABM mindset - by increasing the cell number in this case. Constructing a corresponding PDE model is much harder and not uniquely defined.

3.2 Techniques and challenges

CABMFs allow researchers to investigate biological systems on the cellular level with the option to implement many details, with the downside of substantial computational cost. To combat this issue, all presented frameworks are of multi-scale nature.

4 *Via* an addon libroadrunner and only for intracellular reactions.

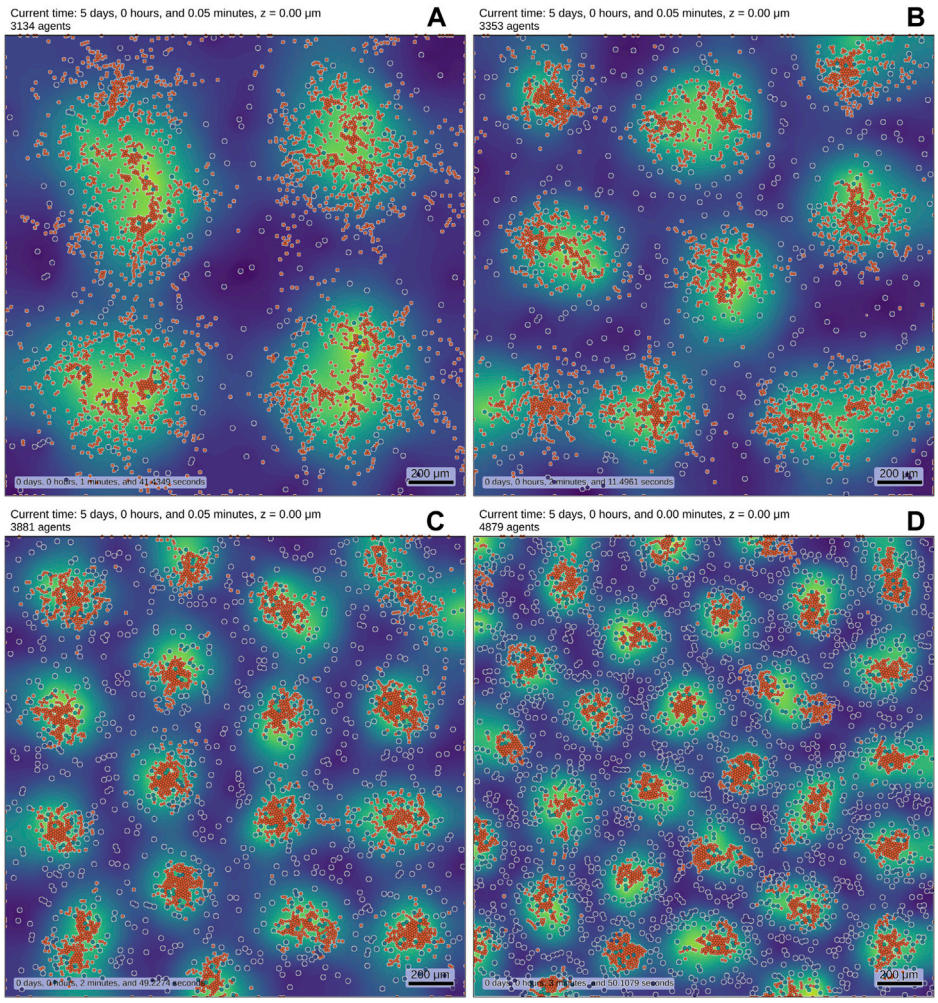

FIGURE 1
We implemented a RD system (see also Supplementary Equation SB1-SB4–Equations) in an ABM to showcase results. The simulation contains two distinct cell types, which are both motile and initially randomly distributed. Cell type I (blue-shaded, white border) obey reaction equations given by a substrate-depletion system [36] and are colored by their internal concentration of the activator. Cell type II (orange) is smaller than cell type I and is chemotactically attracted by the activator which is secreted by cell type I. The background displays the density profile of the secreted activator molecule (yellow: high density, blue: low density). The number of cells I is increased from **(A–D)** (256, 484, 1,024, 2,025), while the number of cells II remains fixed to 3,000. Cell death reduces the overall number of agents. The pictures show the final state of the simulation after reaching (up to statistical fluctuations) a steady-state. The variations in cell number alone lead to different emerging patterns. While these results may be obtainable by a modified purely PDE-based approach, they are much easier to interpret and develop in an ABM. The simulations were carried out using PhysiCell [54].

The relevant time- and length-scales are identified and the corresponding sub-processes are modeled and updated according to their scales. This can greatly improve performance as for example diffusion-driven processes tend to be much faster than cell migrational or phenotypical processes [86]. Other techniques to improve performance are efficient $\mathcal{O}(N_{\text{cells}})$ implementations of algorithms [87] to calculate direct cell-cell interaction partners [], spreading the computational load over multiple processes *via* multiprocessing (for example *via* OpenMP [88]) or on specialized devices such as solving PDEs on a graphics processing unit (GPU) [89]. Due to the stochastic nature of the ABM simulations, appropriate statistical methods need to be applied, which is often challenged by the fact that transient developmental processes are studied not necessarily reaching a stationary state. Analysis of the simulation and comparison with experimental data requires the definition of precise features which are extracted from the simulation results. It is important to define clear goals and questions upfront, as this will guide the process of feature extraction and dimensional reduction. To this end machine learning techniques are becoming more and more popular for analysis of ABM results

[90, 91]. Given current advancements in machine learning, researchers are hopeful that image classification of patterns and self-organizing systems can get more automated in the future [90, 92]. The authors of TiSim/CellSys have explicitly suggested an image-to-model workflow [93]. Neural networks showed promise in partly replacing analysis procedures [94]. Other machine learning techniques can also be used to determine rules for agents and calibrate the model [95]. Auto encoders [96] may provide a way to obtain a dimensionally reduced representation of complex ABM simulation results. Due to the mechanistic and "law-driven" nature of ABMs, often multiple unknown parameters need to be determined or estimated from data. Parameters can be estimated by comparing features extracted from experimental data and from simulation results, which is already a substantial effort. However, this process will usually yield uncertainties, which need to be quantified, as it is not sufficient to evaluate the model locally in parameter space using a sometimes arbitrarily chosen parameter set. In order to focus on the relevant parameters, sensitivity analysis is an important tool, which can also be used for model reduction [15]. Due to highly integrated nature of ABMs sensitivity analysis is demanding and incorporates substantial computational costs [97]. Consequently, it is often only possible to arrive at qualitative statements for complex ABM simulations.

4 Discussion

This review introduced the concepts of agent-based models in cellular systems. We compared different frameworks with respect to their conceptual and implementational differences. To date, a large number of different agent-based model frameworks with different strengths and weaknesses exist and are openly available. The multitude of options is a clear indication for the overall interest in the subject. ABMs provide a unique tool to integrate combinations of processes and study their respective dynamics. Even for the exploration of systems that lack sufficient data, ABMs can be used as they can be developed initially with rather simplified rule sets, by means of which researchers can generate hypotheses, which can in turn guide the design of laboratory experiments. By this cycle of experimental and computational methods, the model and the experiments can be improved and finally increase the conceptual knowledge about the system. Due to this, it is important to understand the challenges of ABMs and their limitations. ABMs can be seen as a mapping of specific rules to spatial configurations. This mapping is non-unique, and the question arises, how the results of the ABM depend on the set of rules and the used parameters. How are the values (or distributions) of the parameters estimated? How does the uncertainty in the system parameters affect the predictions of the simulations? In particular, when analyzing the (often stochastic) results of a simulation, one needs to quantify the influence of the parameter uncertainty which is a considerable challenge. Besides these questions and challenges it can be expected that ABMs are quickly becoming mainstream tools in biology.

Author contributions

CF and JP devised the study. JP wrote the first draft of the manuscript. JP and CF revised, read, and approved the submitted version.

Funding

CF and JP received funding from FET-Open research and innovation actions grant under the European Union's Horizon 2020 (CyGenTiG; grant agreement 801041).

Conflict of interest

The authors declare that the research was conducted in the absence of any commercial or financial relationships that could be construed as a potential conflict of interest.

Publisher's note

All claims expressed in this article are solely those of the authors and do not necessarily represent those of their affiliated organizations, or those of the publisher, the editors and the reviewers. Any product that may be evaluated in this article, or claim that may be made by its manufacturer, is not guaranteed or endorsed by the publisher.

Supplementary material

The Supplementary Material for this article can be found online at: https://www.frontiersin.org/articles/10.3389/fphy.2022.968409/full#supplementary-material

References

1. Mitrophanov AY, Groisman EA. Positive feedback in cellular control systems. *BioEssays : News Rev Mol Cell Dev Biol* (2008) 30:542–55. doi:10.1002/bies.20769

2. Deritei D, Rozum J, Ravasz Regan E, Albert R. A feedback loop of conditionally stable circuits drives the cell cycle from checkpoint to checkpoint. *Scientific Rep* (2019) 9:16430. doi:10.1038/s41598-019-52725-1

3. Vining KH, Mooney DJ. Mechanical forces direct stem cell behaviour in development and regeneration. *Nat Rev Mol Cel Biol* (2017) 18:728–42. doi:10.1038/nrm.2017.108

4. Bloemendal S, Kück U. Cell-to-cell communication in plants, animals, and fungi: A comparative review. *Naturwissenschaften* (2013) 100:3–19. doi:10.1007/s00114-012-0988-z

5. Duester G. Retinoic acid synthesis and signaling during early organogenesis. *Cell* (2008) 134:921–31. doi:10.1016/j.cell.2008.09.002

6. Greenwood FC, Landon J. Growth hormone secretion in response to stress in man. *Nature* (1966) 210:540–1. doi:10.1038/210540a0

7. Kolmogorov A, Petrovsky L, Piskunov N. An investigation of the diffusion equation combined with an increase in mass and its application to a biological problem. *Bull Uni Mosc Ser Int A* (1937) 1:1–26.

8. Turing AM. The chemical basis of morphogenesis. *Philos Trans R Soc Lond Ser B, Biol Sci* (1952) 237:37–72.

9. Koch A, Meinhardt H. Biological pattern formation: From basic mechanisms to complex structures. *Rev Mod Phys* (1994) 66:1481–507. doi:10.1103/revmodphys.66.1481

10. Gierer A, Meinhardt H. A theory of biological pattern formation. *Kybernetik* (1972) 12:30–9. doi:10.1007/bf00289234

11. Browder F. Partial differential equations in the 20th century. *Adv Maths* (1998) 135:76–144. doi:10.1006/aima.1997.1713

12. Müller TG, Timmer J. Parameter identification techniques for partial differential equations. *Int J Bifurcation Chaos* (2004) 14:2053–60. doi:10.1142/S0218127404010424

13. Stavroulakis IP, Tersian SA. Partial differential equations. *An introduction with mathematica and MAPLE*. World Scientific (2004). doi:10.1371/journal.pone.0197666

14. Baker RE, Gaffney EA, Maini PK. Partial differential equations for self-organization in cellular and developmental biology. *Nonlinearity* (2008) 21:R251–90. doi:10.1088/0951-7715/21/11/R05

15. Saltelli A, editor. *Global sensitivity analysis: The primer*. Chichester, England ; Hoboken, NJ: John Wiley (2008).

16. Kielhöfer H. *Bifurcation theory, applied mathematical sciences*, 156. New York, NY: Springer New York (2012). doi:10.1007/978-1-4614-0502-3

17. Von Neumann J, Burks AWAW. *Theory of self-reproducing Automata*. Urbana: University of Illinois Press (1966).

18. Schelling TC. Dynamic models of segregation. *J Math Sociol* (1971) 1:143–86. doi:10.1080/0022250X.1971.9989794

19. Reynolds CW. Flocks, herds and schools: A distributed behavioral model. *ACM SIGGRAPH Comput Graphics* (1987) 21:25–34. doi:10.1145/37402.37406

20. Glen CM, Kemp ML, Voit EO. Agent-based modeling of morphogenetic systems: Advantages and challenges. *PLOS Comput Biol* (2019) 15:e1006577. doi:10.1371/journal.pcbi.1006577

21. Nandakumaran AK. *An Overview of Homogenization* (2007) 87:10.

22. Bodine EN, Panoff RM, Voit EO, Weisstein AE. Agent-based modeling and simulation in mathematics and biology education. *Bull Math Biol* (2020) 82:101. doi:10.1007/s11538-020-00778-z

23. Metzcar J, Wang Y, Heiland R, Macklin P. A review of cell-based computational modeling in cancer biology. *JCO Clin Cancer Inform* (2019) 3:1–13. doi:10.1200/CCI.18.00069

24. Tomlin CJ, Axelrod JD. Biology by numbers: Mathematical modelling in developmental biology. *Nat Rev Genet* (2007) 8:331–40. doi:10.1038/nrg2098

25. Nagarajan K, Ni C, Lu T. Agent-based modeling of microbial communities. *ACS Synth Biol* (2022) 11:3564–74. doi:10.1021/acssynbio.2c00411

26. Haynes T, Sen S. Evolving behavioral strategies in predators and prey. In: Weiß G, Sen S, editors. *Adaption and learning in multi-agent systems*. Berlin, Heidelberg: SpringerLecture Notes in Computer Science (1996). p. 113–26. doi:10.1007/3-540-60923-7_22

27. Bonabeau E. Agent-based modeling: Methods and techniques for simulating human systems. *Proc Natl Acad Sci* (2002) 99:7280–7. doi:10.1073/pnas.082080899

28. Gardner M. Mathematical games. *Scientific Am* (1970) 223:120–3. doi:10.1038/scientificamerican1070-120

29. Berlekamp ER, Conway JH, Guy RK, Peters AK. *Winning Ways for Your Mathematical Plays*. 2nd ed. edn. (Wellesley, MA: A.K. Peters) (2001).

30. Helbing D, Farkas I, Vicsek T. Simulating dynamical features of escape panic. *Nature* (2000) 407:487–90. doi:10.1038/35035023

31. Kephart JO, Hanson JE, Greenwald AR. Dynamic pricing by software agents. *Computer Networks* (2000) 32:731–52. doi:10.1016/S1389-1286(00)00026-8

32. Klimeck G, McLennan M, Brophy SP, Adams GB, III, Lundstrom MS. nanoHUB.org: Advancing education and research in nanotechnology. *Comput Sci Eng* (2008) 10:17–23. doi:10.1109/MCSE.2008.120

33. Keating SM, Waltemath D, König M, Zhang F, Dräger A, Chaouiya C, et al. SBML Level 3: An extensible format for the exchange and reuse of biological models. *Mol Syst Biol* (2020) 16:e9110. doi:10.15252/msb.20199110

34. Bajpai S, Prabhakar R, Chelakkot R, Inamdar MM. Role of cell polarity dynamics and motility in pattern formation due to contact-dependent signalling. *J R Soc Interf* (2021) 18:20200825. doi:10.1098/rsif.2020.0825

35. Nakamasu A, Takahashi G, Kanbe A, Kondo S. Interactions between zebrafish pigment cells responsible for the generation of Turing patterns. *Proc Natl Acad Sci* (2009) 106:8429–34. doi:10.1073/pnas.0808622106

36. Schnakenberg J. Simple chemical reaction systems with limit cycle behaviour. *J Theor Biol* (1979) 81:389–400. doi:10.1016/0022-5193(79)90042-0

37. Wolpert L, Wolpert EPBL, Tickle C, Arias AM. *Principles of development*. USA): Oxford University Press (2015).

38. Gorochowski TE, Matyjaszkiewicz A, Todd T, Oak N, Kowalska K, Reid S, et al. BSim: An agent-based tool for modeling bacterial populations in systems and synthetic biology. *PLOS ONE* (2012) 7:e42790. doi:10.1371/journal.pone.0042790

39. Martinelli V, Salzano D, Fiore D, di Bernardo M. Multicellular PI control for gene regulation in microbial consortia. *IEEE Control Syst Lett* (2022) 6:3373–8. doi:10.1109/LCSYS.2022.3184922

40. Jin X, Marshall JS. Influence of cell interaction forces on growth of bacterial biofilms. *Phys Fluids* (2020) 32:091902. doi:10.1063/5.0021126

41. Cooper F, Baker R, Bernabeu M, Bordas R, Bowler L, Bueno-Orovio A, et al. Chaste: Cancer, Heart and Soft tissue environment. *J Open Source Softw* (2020) 5:1848. doi:10.21105/joss.01848

42. Dunn SJ, Fletcher AG, Chapman SJ, Gavaghan DJ, Osborne JM. Modelling the role of the basement membrane beneath a growing epithelial monolayer. *J Theor Biol* (2012) 298:82–91. doi:10.1016/j.jtbi.2011.12.013

43. Swat MH, Thomas GL, Belmonte JM, Shirinifard A, Hmeljak D, Glazier JA. Chapter 13 - multi-scale modeling of tissues using CompuCell3D. In: *Methods in cell biology* Asthagiri AR, Arkin AP, editors, 110. Academic PressComputational Methods in Cell Biology (2012). p. 325–66. doi:10.1016/B978-0-12-388403-9.00013-8

44. Izaguirre JA, Chaturvedi R, Huang C, Cickovski T, Coffland J, Thomas G, et al. CompuCell, a multi-model framework for simulation of morphogenesis. *Bioinformatics* (2004) 20:1129–37. doi:10.1093/bioinformatics/bth050

45. Nivlouei SJ, Soltani M, Carvalho J, Travasso R, Salimpour MR, Shirani E. Multiscale modeling of tumor growth and angiogenesis: Evaluation of tumor-targeted therapy. *PLOS Comput Biol* (2021) 17:e1009081. doi:10.1371/journal.pcbi.1009081

46. Asadullah KS, Saxena N, Sarkar M, Barai A, Sen S. Combined heterogeneity in cell size and deformability promotes cancer invasiveness. *J Cel Sci* (2021) 134:jcs250225. jcs250225. doi:10.1242/jcs.250225

47. Moldovan NI. Position of the kenzan method in the space-time of tissue engineering. In: Nakayama K, editor. *Kenzan method for scaffold-free biofabrication*. Cham: Springer International Publishing (2021). p. 17–31. doi:10.1007/978-3-030-58688-1_2

48. Aghaallaei N, Dick AM, Tsingos E, Inoue D, Hasel E, Thumberger T, et al. *Aβ*/*Γδ* T cell lineage outcome is regulated by intrathymic cell localization and environmental signals. *Sci Adv* (2021) 7:eabg3613. eabg3613. doi:10.1126/sciadv.abg3613

49. Starruß J, de Back W, Brusch L, Morpheus DA. Morpheus: A user-friendly modeling environment for multiscale and multicellular systems biology. *Bioinformatics* (2014) 30:1331–2. doi:10.1093/bioinformatics/btt772

50. Mulberry N, Edelstein-Keshet L. Self-organized multicellular structures from simple cell signaling: A computational model. *Phys Biol* (2020) 17:066003. doi:10.1088/1478-3975/abb2dc

51. Vu HTK, Mansour S, Kücken M, Blasse C, Basquin C, Azimzadeh J, et al. Dynamic polarization of the multiciliated planarian epidermis between body plan landmarks. *Develop Cel* (2019) 51:526–42.e6. e6. doi:10.1016/j.devcel.2019.10.022

52. Dang Y, Grundel DAJ, Youk H. Cellular dialogues: Cell-cell communication through diffusible molecules yields dynamic spatial patterns. *Cel Syst* (2020) 10:82–98.e7. e7. doi:10.1016/j.cels.2019.12.001

53. Karolak A, Branciamore S, McCune JS, Lee PP, Rodin AS, Rockne RC. Concepts and applications of information theory to immuno-oncology. *Trends Cancer* (2021) 7:335–46. doi:10.1016/j.trecan.2020.12.013

54. Ghaffarizadeh A, Heiland R, Friedman SH, Mumenthaler SM, PhysiCell MP. PhysiCell: An open source physics-based cell simulator for 3-D multicellular systems. *PLOS Comput Biol* (2018) 14:e1005991. doi:10.1371/journal.pcbi.1005991

55. Ponce-de-Leon M, Montagud A, Akasiadis C, Schreiber J, Ntiniakou T, Valencia A. Optimizing dosage-specific treatments in a multi-scale model of a tumor growth. *Front Mol Biosciences* (2022) 9:836794. doi:10.3389/fmolb.2022.836794

56. Gonçalves IG, Garcia-Aznar JM. Extracellular matrix density regulates the formation of tumour spheroids through cell migration. *PLOS Comput Biol* (2021) 17:e1008764. doi:10.1371/journal.pcbi.1008764

57. Hoehme S, Drasdo D. A cell-based simulation software for multi-cellular systems. *Bioinformatics* (2010) 26:2641–2. doi:10.1093/bioinformatics/btq437

58. Hoehme S, Brulport M, Bauer A, Bedawy E, Schormann W, Hermes M, et al. Prediction and validation of cell alignment along microvessels as order principle to restore tissue architecture in liver regeneration. *Proc Natl Acad Sci* (2010) 107:10371–6. doi:10.1073/pnas.0909374107

59. Merks RM, Guravage M, Inzé D, Beemster GT. VirtualLeaf: An open-source framework for cell-based modeling of plant tissue growth and development. *Plant Physiol* (2011) 155:656–66. doi:10.1104/pp.110.167619

60. Drasdo D. Center-based single-cell models: An approach to multi-cellular organization based on a conceptual analogy to colloidal particles. In: Anderson ARA, Chaplain MAJ, Rejniak KA, editors. Single-cell-based Models in Biology and medicine *(basel: Birkhäuser), mathematics and biosciences in interaction* (Basel, CH: Birkhäuser) (2007). p. 171–96. doi:10.1007/978-3-7643-8123-3_8

61. Nagai T, Honda H. A dynamic cell model for the formation of epithelial tissues. *Philosophical Mag B* (2001) 81:699–719. doi:10.1080/13642810108205772

62. Smith C. *On vertex-vertex systems and their use in geometric and biological modelling* Ph.D. thesis, University of Calgary (2006). doi:10.11575/PRISM/439

63. Graner F, Glazier JA. Simulation of biological cell sorting using a two-dimensional extended Potts model. *Phys Rev Lett* (1992) 69:2013–6. doi:10.1103/PhysRevLett.69.2013

64. Savill NJ, Hogeweg P. Modelling morphogenesis: From single cells to crawling slugs. *J Theor Biol* (1997) 184:229–35. doi:10.1006/jtbi.1996.0237

65. Rejniak KA. An immersed boundary framework for modelling the growth of individual cells: An application to the early tumour development. *J Theor Biol* (2007) 247:186–204. doi:10.1016/j.jtbi.2007.02.019

66. Peskin CS. The immersed boundary method. *Acta Numerica* (2002) 11:479–517. doi:10.1017/S0962492902000077

67. Alberts B, Johnson A, Lewis J, Raff M, Roberts K, Walter P. Principles of membrane transport. In: *Molecular Biology of the cell*. 4th ed. (2002).

68. Chandrasekhar S. Stochastic problems in physics and astronomy. *Rev Mod Phys* (1943) 15:1–89. doi:10.1103/RevModPhys.15.1

69. Kassem M, Blum W, Ristelli J, Mosekilde L, Eriksen EF. Growth hormone stimulates proliferation and differentiation of normal human osteoblast-like cells *in vitro*. *Calcified Tissue Int* (1993) 52:222–6. doi:10.1007/BF00298723

70. Johnson KL, Kendall K, Roberts AD. Surface energy and the contact of elastic solids. *Proc R Soc Lond A. Math Phys Sci* (1971) 324:301–13. doi:10.1098/rspa.1971.0141

71. Hertz H. Ueber die Berührung fester elastischer Körper. *J fur die reine und angewandte Mathematik* (1882) 92:156–171. doi:10.1515/crll.1882.92.156

72. Marée AFM, Grieneisen VA, Hogeweg P. The cellular Potts model and biophysical properties of cells, tissues and morphogenesis. In: Anderson ARA, Chaplain MAJ, Rejniak KA, editors. *Single-cell-based models in biology and medicine* (Basel, CH: Birkha user, Mathematics and Biosciences in Interaction) (2007). p. 107–36. doi:10.1007/978-3-7643-8123-3_5

73. Smutny M, Ákos Z, Grigolon S, Shamipour S, Ruprecht V, Čapek D, et al. Friction forces position the neural anlage. *Nat Cel Biol* (2017) 19:306–17. doi:10.1038/ncb3492

74. Vasiev B, Weijer CJ. Modeling chemotactic cell sorting during *Dictyostelium discoideum* mound formation. *Biophysical J* (1999) 76:595–605. doi:10.1016/S0006-3495(99)77228-0

75. Gillespie DT. Stochastic simulation of chemical kinetics. *Annu Rev Phys Chem* (2007) 58:35–55. doi:10.1146/annurev.physchem.58.032806.104637

76. Pitt-Francis J, Bernabeu MO, Cooper J, Garny A, Momtahan L, Osborne J, et al. Chaste: Using agile programming techniques to develop computational biology software. *Philos Trans R Soc A: Math Phys Eng Sci* (2008) 366:3111–36. doi:10.1098/rsta.2008.0096

77. Hoops S, Sahle S, Gauges R, Lee C, Pahle J, Simus N, et al. COPASI—A COmplex PAthway SImulator. *Bioinformatics* (2006) 22:3067–74. doi:10.1093/bioinformatics/btl485

78. Luke S, Cioffi-Revilla C, Panait L, Sullivan K, Mason BG. Mason: A multiagent simulation environment. *SIMULATION* (2005) 81:517–27. doi:10.1177/0037549705058073

79. Burnette E. *Eclipse IDE Pocket Guide: Using the Full-Featured IDE*. Sebastopol, CA: O'Reilly Media, Inc. (2005).

80. Dunn SJ, Näthke IS, Osborne JM. Computational models reveal a passive mechanism for cell migration in the crypt. *PLOS ONE* (2013) 8:e80516. doi:10.1371/journal.pone.0080516

81. Thomas GL, Fortuna I, Perrone GC, Graner F, de Almeida RMC. Shape–velocity correlation defines polarization in migrating cell simulations. *Physica A: Stat Mech its Appl* (2022) 587:126511. doi:10.1016/j.physa.2021.126511

82. Pan M, Yang Y, Liu L. Physical forces influence the self-organization of the leader cell formation during collective cell migration. In: 2021 IEEE 16th International Conference on Nano/Micro Engineered and Molecular Systems (NEMS) (2021). p. 1923. doi:10.1109/NEMS51815.2021.9451315

83. Lupperger V, Marr C, Chapouton P. Reoccurring neural stem cell divisions in the adult zebrafish telencephalon are sufficient for the emergence of aggregated spatiotemporal patterns. *PLOS Biol* (2020) 18:e3000708. doi:10.1371/journal.pbio.3000708

84. Muñoz-Nava LM, Alvarez HA, Flores-Flores M, Chara O, Nahmad M. A dynamic cell recruitment process drives growth of the Drosophila wing by overscaling the vestigial expression pattern. *Develop Biol* (2020) 462:141–51. doi:10.1016/j.ydbio.2020.03.009

85. Holloway DM, Wenzel CL. Polar auxin transport dynamics of primary and secondary vein patterning in dicot leaves. *silico Plants* (2021) 3. diab030. doi:10.1093/insilicoplants/diab030

86. Keener JP, Keizer JE. Fast and slow time scales. In: Fall CP, Marland ES, Wagner JM, Tyson JJ, editors. *Computational cell biology*. New York, NY: SpringerInterdisciplinary Applied Mathematics (2002). p. 77–100. doi:10.1007/978-0-387-22459-6_4

87. Meagher D. Geometric modeling using octree encoding. *Comput Graphics Image Process* (1982) 19:129–47. doi:10.1016/0146-664X(82)90104-6

88. Chandra R, editor. *Parallel programming in OpenMP*. San Francisco, CA: Morgan Kaufmann Publishers (2001).

89. Steuwer M, Kegel P, Gorlatch S. SkelCL - a portable skeleton library for high-level GPU programming. In: 2011 IEEE International Symposium on Parallel and Distributed Processing Workshops and Phd Forum. Anchorage, AK, USA: IEEE (2011). p. 1176–82. doi:10.1109/IPDPS.2011.269

90. Efimenko M, Ignatev A, Koshechkin K. Review of medical image recognition technologies to detect melanomas using neural networks. *BMC Bioinformatics* (2020) 21:270. doi:10.1186/s12859-020-03615-1

91. Caicedo JC, Cooper S, Heigwer F, Warchal S, Qiu P, Molnar C, et al. Data-analysis strategies for image-based cell profiling. *Nat Methods* (2017) 14:849–63. doi:10.1038/nmeth.4397

92. Ker J, Wang L, Rao J, Lim T. Deep learning applications in medical image analysis. *IEEE Access* (2018) 6:9375–89. doi:10.1109/ACCESS.2017.2788044

93. Hoehme S, Friebel A, Hammad S, Drasdo D, Hengstler JG. Creation of three-dimensional liver tissue models from experimental images for systems medicine. In: Stock P, Christ B, editors. *Hepatocyte transplantation: Methods and protocols*. New York, NY: SpringerMethods in Molecular Biology (2017). p. 319–62. doi:10.1007/978-1-4939-6506-9_22

94. Chen SH, Londoño-Larrea P, McGough AS, Bible AN, Gunaratne C, Araujo-Granda PA, et al. Application of machine learning techniques to an agent-based model of pantoea. *Front Microbiol* (2021) 12:726409. doi:10.3389/fmicb.2021.726409

95. Sivakumar N, Mura C, Peirce SM. Combining machine learning and agent-based modeling to study biomedical systems. *Front Sys Biol* (2022) 2.

96. Kramer MA. Nonlinear principal component analysis using autoassociative neural networks. *AIChE J* (1991) 37:233–43. doi:10.1002/aic.690370209

97. Aguilar B, Gibbs DL, Reiss DJ, McConnell M, Danziger SA, Dervan A, et al. A generalizable data-driven multicellular model of pancreatic ductal adenocarcinoma. *GigaScience* (2020) 9:giaa075. giaa075. doi:10.1093/gigascience/giaa075

98. Kang S, Kahan S, McDermott J, Flann N, Shmulevich I. Biocellion : Accelerating computer simulation of multicellular biological system models. *Bioinformatics* (2014) 30:3101–8. doi:10.1093/bioinformatics/btu498

99. Wei G, Bogdan P, Marculescu R. Efficient modeling and simulation of bacteria-based nanonetworks with BNSim. *IEEE J Selected Areas Commun* (2013) 31:868–78. doi:10.1109/JSAC.2013.SUP2.12130019

100. Kaizu K, Nishida K, Sakamoto Y, Kato S, Niina T, Nishida N, et al. *E-Cell System version 4*. Zenodo (2020). doi:10.5281/ZENODO.3865614

101. Sütterlin T, Kolb C, Dickhaus H, Jäger D, Grabe N. Bridging the scales: Semantic integration of quantitative SBML in graphical multi-cellular models and simulations with EPISIM and COPASI. *Bioinformatics (Oxford, England)* (2013) 29:223–9. doi:10.1093/bioinformatics/bts659

102. Gutiérrez M, Gregorio-Godoy P, Pérez del Pulgar G, Muñoz LE, Sáez S, Rodríguez-Patón A. A new improved and extended version of the multicell bacterial simulator gro. *ACS Synth Biol* (2017) 6:1496–508. doi:10.1021/acssynbio.7b00003

103. Lardon LA, Merkey BV, Martins S, Dötsch A, Picioreanu C, Ju K, et al. iDynoMiCS: Next-generation individual-based modelling of biofilms. *Environ Microbiol* (2011) 13:2416–34. doi:10.1111/j.1462-2920.2011.02414.x

104. Tanaka S, Sichau D, Iber D. LBIBCell: A cell-based simulation environment for morphogenetic problems. *Bioinformatics* (2015) 31:2340–7. doi:10.1093/bioinformatics/btv147

105. Delile J, Herrmann M, Peyriéras N, Doursat R. A cell-based computational model of early embryogenesis coupling mechanical behaviour and gene regulation. *Nat Commun* (2017) 8:13929. doi:10.1038/ncomms13929

106. Letort G, Montagud A, Stoll G, Heiland R, Barillot E, Macklin P, et al. PhysiBoSS: A multi-scale agent-based modelling framework integrating physical dimension and cell signalling. *Bioinformatics* (2019) 35:1188–96. doi:10.1093/bioinformatics/bty766

107. Vladimirov N, Løvdok L, Lebiedz D, Sourjik V. Dependence of bacterial chemotaxis on gradient shape and adaptation rate. *PLOS Comput Biol* (2008) 4:e1000242. doi:10.1371/journal.pcbi.1000242

108. Milde F, Tauriello G, Haberkern H, Koumoutsakos P. SEM++: A particle model of cellular growth, signaling and migration. *Comput Part Mech* (2014) 1:211–27. doi:10.1007/s40571-014-0017-4

109. Angermann BR, Klauschen F, Garcia AD, Prustel T, Zhang F, Germain RN, et al. Computational modeling of cellular signaling processes embedded into dynamic spatial contexts. *Nat Methods* (2012) 9:283–9. doi:10.1038/nmeth.1861

110. Canela-Xandri O, Anbari S, TiFoSi BJ. TiFoSi: An efficient tool for mechanobiology simulations of epithelia. *Bioinformatics* (2020) 36:4525–6. doi:10.1093/bioinformatics/btaa592

111. Cytowski M, Szymanska Z. Large-scale parallel simulations of 3D cell colony dynamics: The cellular environment. *Comput Sci Eng* (2015) 17:44–8. doi:10.1109/MCSE.2015.66

112. Hamant O, Heisler MG, Jönsson H, Krupinski P, Uyttewaal M, Bokov P, et al. Developmental patterning by mechanical signals in arabidopsis. *Science* (2008) 322:1650–5. doi:10.1126/science.1165594

113. Jönsson H, Heisler MG, Shapiro BE, Meyerowitz EM, Mjolsness E. An auxin-driven polarized transport model for phyllotaxis. *Proc Natl Acad Sci* (2006) 103:1633–8. doi:10.1073/pnas.0509839103

114. Resasco DC, Gao F, Morgan F, Novak IL, Schaff JC, Slepchenko BM. Virtual Cell: Computational tools for modeling in cell biology. *WIREs Syst Biol Med* (2012) 4:129–40. doi:10.1002/wsbm.165

115. Germann P, Marin-Riera M, Sharpe J. ya||a: GPU-powered spheroid models for mesenchyme and epithelium. *Cel Syst* (2019) 8:261–6.e3. e3. doi:10.1016/j.cels.2019.02.007

frontiers | Frontiers in Physics

TYPE Original Research
PUBLISHED 09 January 2023
DOI 10.3389/fphy.2022.966327

OPEN ACCESS

EDITED BY
Pau Formosa-Jordan,
Max Planck Institute for Plant Breeding Research, Germany

REVIEWED BY
Florian Goirand,
Technical University of Munich, Germany
Raghunath Chelakkot,
Indian Institute of Technology Bombay, India
Luis Diambra,
National University of La Plata, Argentina

*CORRESPONDENCE
Annemiek J. M. Cornelissen,
annemiek.cornelissen@u-paris.fr

SPECIALTY SECTION
This article was submitted to Biophysics, a section of the journal Frontiers in Physics

RECEIVED 10 June 2022
ACCEPTED 30 November 2022
PUBLISHED 09 January 2023

CITATION
Song S, Żukowski S, Gambini C, Dantan P, Mauroy B, Douady S and Cornelissen AJ (2023), Morphogenesis of the gastrovascular canal network in *Aurelia* jellyfish: Variability and possible mechanisms.
Front. Phys. 10:966327.
doi: 10.3389/fphy.2022.966327

Morphogenesis of the gastrovascular canal network in *Aurelia* jellyfish: Variability and possible mechanisms

Solène Song[1], Stanisław Żukowski[1,2], Camille Gambini[1], Philippe Dantan[1], Benjamin Mauroy[3], Stéphane Douady[1] and Annemiek J. M. Cornelissen[1]*

[1]Laboratoire MSC, UMR 7057, Université Paris Cité—CNRS, Paris, France, [2]Faculty of Physics, Institute of Theoretical Physics, University of Warsaw, Warsaw, Poland, [3]Laboratoire J. A. Dieudonné, UMR 7351, Université Côte d'Azur—CNRS, Vader Center, Nice, France

Patterns in biology can be considered as predetermined or arising from a self-organizing instability. Variability in the pattern can, thus, be interpreted as a trace of instability, growing out from noise. Studying this variability can, thus, hint toward an underlying morphogenetic mechanism. Here, we present the variability of the gastrovascular system of the jellyfish *Aurelia*. In this variability emerges a typical biased reconnection between canals and time-correlated reconnections. Both phenomena can be interpreted as traces of mechanistic effects, the swimming contractions on the tissue surrounding the gastrovascular canals, and the mean fluid pressure inside them. This reveals the gastrovascular network as a model system to study the morphogenesis of circulation networks and the morphogenetic mechanisms at play.

KEYWORDS

morphogenesis, gastrovascular, network, jellyfish, instabilities, variability, mechanical constraints

1 Introduction

Morphogenesis remains an important question in biology. Independently of how the phenotype can be selected through natural selection, it remains essential to understand how it can appear, develop from its original fertilized egg, and get its own shape. Since humans observe nature, they classify similar shapes into species. Within one species, the shape is robustly perpetuated across generations. So, biological shapes are constrained enough within one species. Even with the discovery of many genes and produced molecules and their important role in morphogenesis, how these constraints are applied to guarantee a given result is not completely clarified. In particular, how a complex shape can appear while being constrained remains obscure [1]. A complex shape would need much information to be described, thus many regulations to achieve it. However, the unfolding in time of instability can lead to a regulated complex shape from a simple mechanism [2].

In his pioneering work, Alan Turing proposed that even if some morphogenesis can be implemented through the various concentrations of some chemical products, the pattern they present is created by a spatial instability [3]. This means that even if the original distribution of chemicals is homogeneous, this state will be unstable and spontaneously goes into patches of different concentrations. Also, the pattern is spontaneously created, not controlled: only its global characteristics, such as wavelength, which depends on the reactions and diffusion characteristics of the chemicals are set, not its particular position.

This view may seem contradictory with the constrained production of a stereotyped shape. However, many examples of fluctuating shapes can give the intuition of an underlying instability. In this study, this is the case we present for the formation of the gastrovascular network of the jellyfish *Aurelia*. Jellyfishes are very old life-forms that appeared before the "vertebrate" revolution but already present a complex vascular structure. This vascular structure is an open circuit, perfusing the whole body from the open mouth to the stomach pouches and back [4, 5]. The flow in this circuit is due both to the effect of the whole contraction of the body and to the action of many cilia on the internal epithelium. These canals, in a body plan which is basal in the animal tree, can be seen as an early simple model of a network of tubes with a transport function as the later evolved closed vascular networks such as the blood vascular network.

This gastrovascular canal network develops while the jellyfish grows from its first ephyra stage. This ephyra stage emerges from a sessile polyp [5, 6]. During the transformation of the polyp into jellyfish (a process called strobilation), this polyp is subjected to instability that creates many disks along its axial body, each disk being unstable in the radial direction and forming arms (lobes with two marginal lappets), of typical 8-fold symmetry. One after the other, the top disk further transforms and detaches, resulting in a free swimming jellyfish larva, the ephyra. This way of generation ensures that a series of jellyfish appears from a very same polyp, so they are clones. The development of the gastrovascular canal can be followed while the jellyfish goes from a star-like shape ephyra of a few mm diameters to a juvenile jellyfish of approximately 10 mm, which has just reached the circular shape of adult medusa to a mature jellyfish of about 100 mm.

We will focus on the growth of the pattern from juvenile, with few rather stereotyped canals, to adult, with many canals. The formation of the network before the juvenile stage has complex but more regular steps [5] and is not considered in this study. Subsequent growth happens with the sprouting of new canals and their reconnection with the rest of the system. There is a strong tendency for a sprouting canal to reconnect to the younger neighbor, leading in an ideal case to a particular fractal pattern. However, this bias is not absolute, and there are many variations. With the observation of these dynamics and their results of complex and varying shapes, we can get closer to the origin of the morphogenetic process. More precisely, the question of which phenomena can be responsible for the development of these shapes can be studied. In the following, we will present two possible phenomena with both some interests and limitations.

2 Canal network morphogenesis

2.1 Stereotypical morphology

The gastrovascular canal network in juvenile jellyfish can be presented with a stereotypical structure (see Figure 1A). In 1/8th of the jellyfish (an octant), there is radially one gastric pouch of the stomach (or the junction between two pouches) near the center, and a marginal ring canal, circling around the whole rim of the jellyfish. Radially, there are two canals, rather straight and unbranched, joining the side of the pouches to the marginal ring canal, the adradial canals. Between such two straight canals, there is a canal joining the gastric pouch (interradial canal) or directly in the mouth opening at the pouch junction (perradial canal) to the marginal ring canal and a rhopalium (a sensory organ that can be caricatured as an "eye"). These canals present, in the juvenile stage, two secondary side branches connecting the main inter or perradial canal with the ring canal, forming a trifurcation. There is no apparent difference between interradial and perradial morphologies. We will, thus, simply call them "trifurcate" canals (in contrast we can call the adradial canals the "straight" canals). In juveniles, new canals mainly sprout from the marginal ring canal and connect to one of the surrounding already existing radial canals.

After growth, for adult jellyfishes, it is tempting to present its shape as a regular, fractal one. Although a perfect one is rare, it can be sometimes observed in small jellyfish (we found occurrences in nature or in the Cherbourg Aquarium culture). The best way to understand it is, as for fractals, to describe its construction, step by step, with canals connecting to each other in a well-defined and precise order (Figure 1B). In the juvenile stage (Figure 1A) at the ring canal, the trifurcation cut the interval between the two straight canals in four. Roughly four new canals sprout from the ring canal, grow in these intervals, and connect either left or right to the two younger side canals of the fork. The next generation of eight canals would also connect to the last previous generation, leading to a distinctive tree shape (Figure 1B).

There is a strong tendency, around 80% of the cases (Figure 1C and Supplementary Material), for the new sprouting canals to connect to the younger radial canal at proximity. If we look at the distribution of "false" connections, that is, canals not connecting to the younger canal at proximity, per octant, we find the very asymmetric

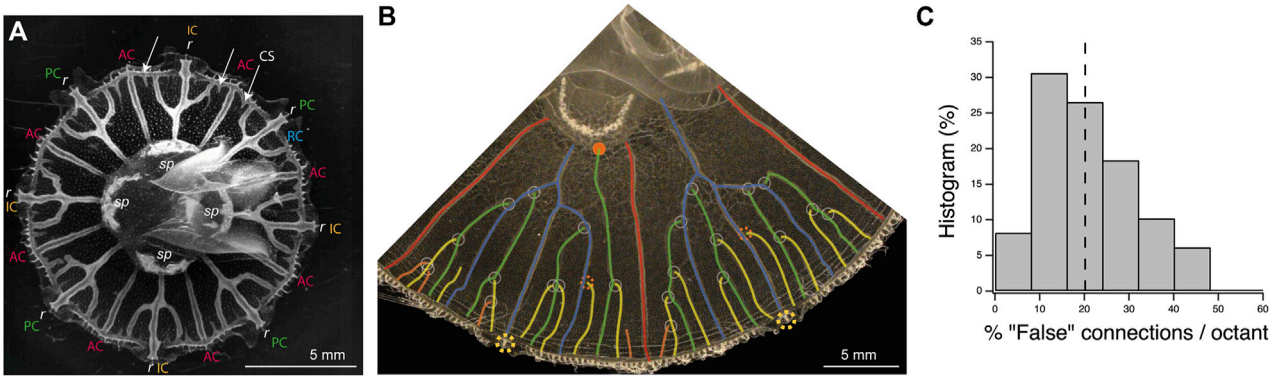

FIGURE 1
Structure and morphogenesis of the canal network of the gastrovascular system of the jellyfish *Aurelia*. **(A)** Picture of a juvenile jellyfish showing the structure of the gastrovascular system. There are typically four stomach pouches (*sp*), eight sensory organs, or rhopalium (*r*). At the periphery of the jellyfish there is a ring canal (RC in blue). Connecting this ring canal, from the sides of the stomach pouches, there are typically eight straight adradial canals (AC in red). Between these adradial canals, other canals connect either the stomach pouch, the perradial canal (PC in green), or the junction between two stomach pouches, the interradial canal (IC in orange), to the rhopalia. New canal sprouts (CS) sprout from the ring canal (arrows). **(B)** Picture of two octants of a later developmental stage (original in Supplementary Figure S2). The sprouting canals have reconnected to older ones, forming branched perradial and interradial canal systems (rhopalia, yellow dashed circles; adradial canals, and red; original trifurcate canals, blue). The sprouting canals have the tendency to reconnect to the youngest side canal (white circles), leading in theory to a specific fractal tree shape. The four (green) canals sprouting in the two intervals between the fork and the two intervals near the side straight canals (red) would connect to side branches of the original (blue) fork. The next eight canals (yellow) would connect to the previous one (green). Also, the next generation (orange) would connect to the previous one (yellow). Some connections do not follow this pattern and either reconnect to older ones (dashed red circles) or even directly to the stomach pouch (red disk). Some irregular growth is also visible on the left (perradial canals), leading to mixing of generations, as some fourth (orange) canals have already appeared, and even connected, while some third order (yellow) generations have not appeared yet or reconnected. **(C)** Histogram of the percentage of "false" connections (i.e., canal connections not made to the closest younger canal) in midsize jellyfish as in B, per octant (seven jellyfish with eight octants and one with nine octants $n = 65$ octants). There are, for instance, 10% of octants present between 32% and 40% of false connections. The median value (dashed line) is 20%.

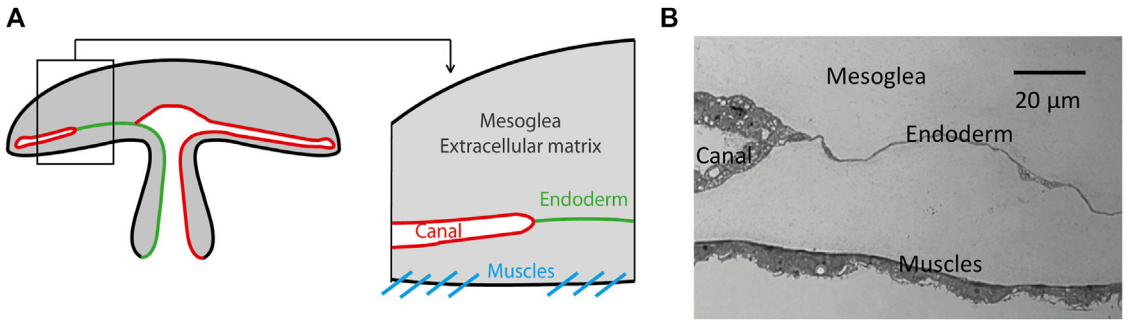

FIGURE 2
Anatomical position of the canals in the jellyfish *Aurelia*. The canals are surrounded by an endodermal layer positioned just above the lower *epidermis* with muscles. **(A)** Schematic representation. **(B)** Optical view of a histological 4 µm thick microtome slice of a fixed jellyfish.

distribution of Figure 1C. This indicates that it is a real bias and that the false connections accumulate independently, making it more probable to have only few false connections (but rare to have none) and rarer to have more false connections. The essential question arising from this structure and its development is to understand why new canals would connect to the younger previous ones.

2.2 Differential contraction

To understand this differential connection of the sprouting canal to the youngest close one, a first observation on the morphology and appearance of the canal itself is helpful. The canals, consisting of a canal wall with a monolayer of dense canal cells around a lumen, are situated inside a monolayer cell

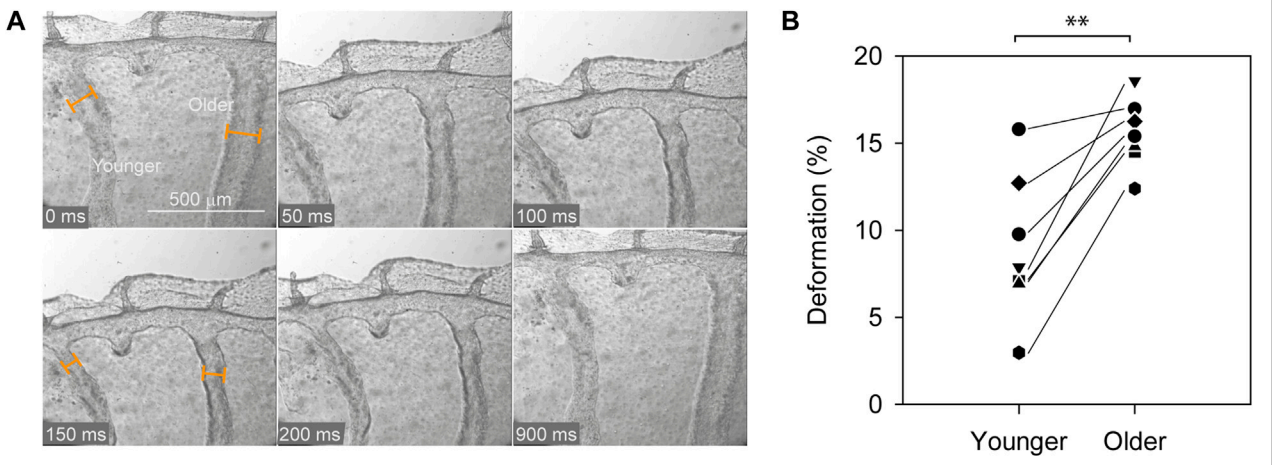

FIGURE 3
Relative contraction of canals during jellyfish swimming contraction. **(A)** A sequence of pictures showing a young and an older canal pictured during a contraction (with also a canal sprout in between). Canal width measurement during the resting phase and the maximum contraction allows measuring the relative contraction of the canals. **(B)** The pairwise measurement shows that the contraction of a young canal is significantly smaller than the one for older canals ($p < 0.01$, one-way repeated measures Anova, followed by a Student–Newman–Keuls test for a pairwise multiple comparison).

sheet with largely spread endodermal cells (see Figure 2). We have observed that the canal sprouts are growing in the endodermal sheet with cell proliferation around the tip of the canal [7].

The second important point for a possible morphogenetic mechanism is that these canals are growing while the jellyfish is growing, and it is growing while being, since the beginning, actively contracting, to swim and gather food. These contractions from a nearly flat state to a bell shape are done by a muscle sheet contracting and reducing the periphery perimeter. These movements then induce a considerable mechanical deformation to the endodermal layer, containing the canals, which is just above this muscle layer (Figure 2).

A proposed mechanism for the bias in connections is that the mechanical response to the contraction during swimming is different for different parts of the tissues. We propose that the endodermal cells which are not part of canals are submitted to a high mechanical stress as they are nearly incompressible, being held by the incompressible, but soft, upper and lower mesoglea [8]. On the contrary, canals are not flat; they enclose a lumen which protrudes out from the endodermal sheet (Figure 2B). Measurements during contractions show that the older the canal, the more deformable it is (Figures 3A,B). We propose this property as the cause of the bias leading growing canals to connect more frequently to younger canals than to older ones.

2.3 Simulating contraction

To see the effect of the differential contractibility of the canals, we analyzed the distribution of the stress in the jellyfish during muscle contractions. To do so, we build a mechanical model of the endoderm and of the canals of the jellyfish. The effects of the mesoglea elasticity and muscle contractions are injected through the boundary conditions.

The model geometry is limited to a slice of the endoderm near the ring canal. The endoderm slice is represented by a ring at the edge of a circular disk (Figure 4A), extending 1/5 of the jellyfish radius. We neglect the local convexity of the endoderm, approximating it with a plane surface. During swimming, the umbrella reduces its radius, increasing the convexity, but we assume it remains flat. The geometry of the canals and sprout were chosen to be coherent with our observations in a juvenile jellyfish of 1 cm diameter (see Supplementary Figure S7A).

The model follows the law of mechanics: $\rho \frac{\partial^2 u}{\partial t^2} - div(\sigma(\epsilon)) = 0$, where ρ is the density of the endoderm (assumed to be similar to that of water), u is the displacement of the material, $\varepsilon = \nabla u$ is the relative displacements of the material (strain), and $\sigma(\varepsilon)$ is its stress–strain relationship. To close the model, we further use the Hooke's law of elasticity to express the stress as a function of the strain. Since we are not interested in the global bell shape of the jellyfish and its change during the muscle contractions and spring back mediated by the mesoglea elasticity [8], we neglect the stress components in the direction normal to the (flat) endoderm surface, that is, $\sigma_z = 0$, $\sigma_{xz} = 0$, and $\sigma_{yz} = 0$. As a consequence, our model is a 2D model and Hooke's law reduces to

$$\sigma_x = \frac{E}{1-\nu^2}\left(\epsilon_{xx} + \nu\epsilon_{yy}\right),$$
$$\sigma_y = \frac{E}{1-\nu^2}\left(\epsilon_{yy} + \nu\epsilon_{xx}\right),$$

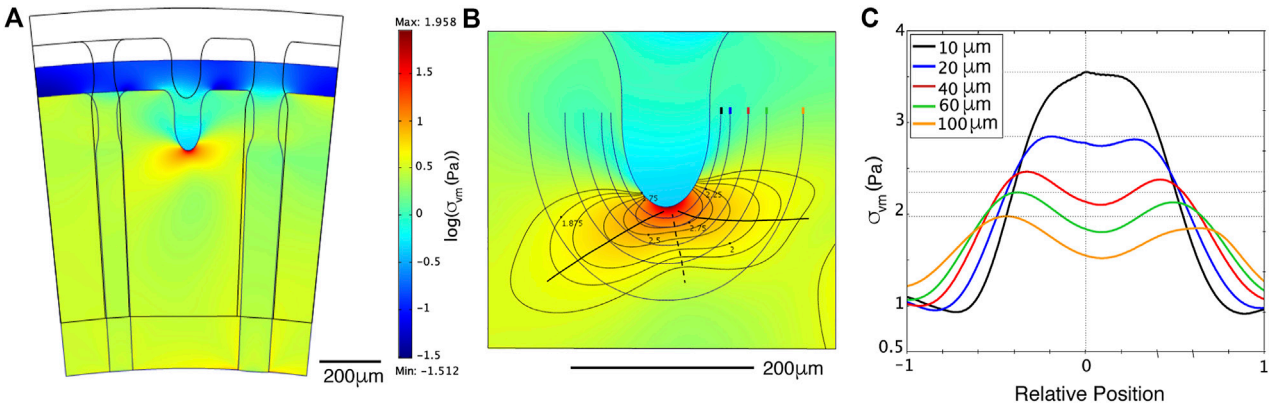

FIGURE 4
Stress distribution predicted by numerical simulations **(A)**: Finite element simulation with stiffer young canal (left) and softer old canal (right). The contraction is reproduced by reducing the radial distance with a constant angle, thus reducing the orthoradial one. The log of the mechanical stress (colored scale) is smaller (blue-green) in the soft right canal, and reduced around the sprouting canal (light blue), but concentrated at its tip (red spot). **(B)**: A zoom of the stress around the tip. Level lines, circling away the red spot reveal two lobes, one forward left to the young canal, one right to the old canal. Lines drawn at fixed distances are drawn with each its color code, to measure the stress along them. The two stress maximums and minimum along these successive lines are indicated by black full and dotted lines, respectively. **(C)**: The stress measured along these lines, centered on the axial position of the tip and rescaled from beginning to end, with their colors, and the distance to the finger indicated. Horizontal dotted lines show that the left maximum toward the young canal is always higher. This will turn the propagation of the new canal sprout toward the younger, stiffer one.

$$\sigma_z = 0,$$
$$\sigma_{xy} = \frac{E}{1+\nu}\epsilon_{xy},$$
$$\sigma_{xz} = 0,$$
$$\sigma_{xz} = 0,$$

with E being Young's modulus and ν Poisson's ratio. The observed difference of deformability (Figure 3) was translated into plausible elastic Young's moduli and Poisson ratio. We assume the endoderm as a flat rigid nearly incompressible elastic sheet. The near incompressibility in the plane is given by Poisson's ratio $\nu_{en} = 0.49$ and the rigidity by Young's modulus $E_{en} = 100\ Pa$. We modeled the canals in 2D by a compressible elastic membrane, with a lower Young's moduli than the endoderm. The chosen Poisson's ratio of the canals of 0.3 ($\nu_{yc} = \nu_{oc} = 0.3$; ν_{yc} being the Poisson's ratio for the young canal and ν_{oc} the Poisson's ratio for the old canal), allows for compression in the plane, translating the vertical expansion of the canals. The Young's modulus of the young canal is assumed to be stiffer with $E_{yc} = 30\ Pa$ than the old canal, for which $E_{oc} = 10\ Pa$.

The muscular orthoradial contraction is mimicked *via* the boundary conditions as shown in the Supplementary Figure S7B. To simplify, instead of compressing the whole two radial borders of the slice, we only reduce the radial position of the outer circular boundary. Following our observations, we typically reduce it by 200 µm in one second. The sides of the ring slice can only slip along the radial axis, and the inner circular boundary is free to move ($\sigma(\epsilon).n = 0$, with n the outer normal of the boundary). As a result, the whole slice compresses after one second. At the end of the contraction, the circular deformation is 4% at the outer edge (top of ring canal) and 5% at the inner edge. With these characteristics, the simulation can be performed quasi-statically. The model of contraction was studied with a numerical simulation based on finite elements.

The results show an accumulation of stress at the tip of a new canal (the stress is partly released at the sprouting canal, and all the residual stress around focuses on the tip), and the stress is slightly different in the two surrounding canals of different age/stiffness (Figure 4A). At the tip, the stress shows two lobes, toward both side canals, the one toward the younger canal being larger and more intense (Figure 4B). The quantitative result is that the maximum of stress is shifting toward the younger stiffer canal (Figure 4C). Based on these observations, we propose that high stress will guide the canal sprout to grow toward the younger stiffer radial side canal.

3 Variability

Since the connection of the sprouting canal to a younger close one is only a strong bias, there are many variations of patterns and only rarely a perfect one. Looking more generally at *Aurelia* jellyfish from different origins and growth conditions (see Section 6) also reveals variable patterns. The observed patterns display more variability than what we would expect from the previously described process based on successive sprouting of new canals from the rim and connection to the youngest neighboring canal.

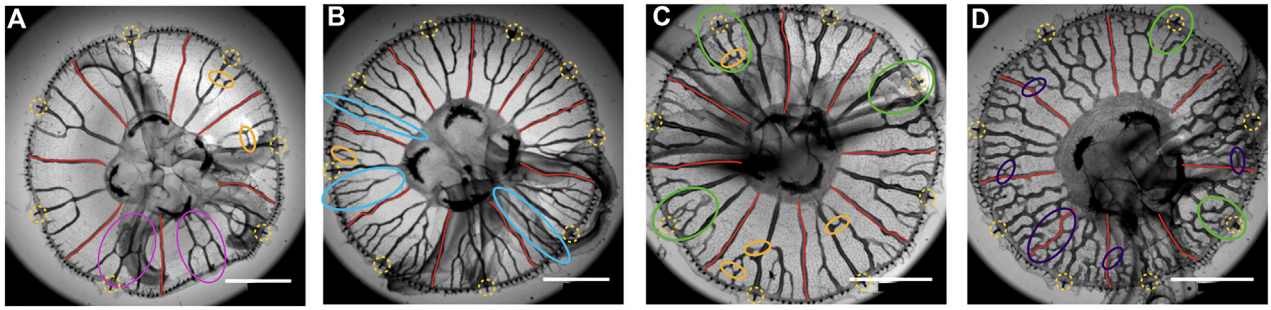

FIGURE 5
Four *Aurelia* specimens of around the same size, from Cherbourg. The rhopalia are surrounded by yellow-dashed circles, and the adradial canals are drawn in red. In **A**, the continuation of canals after connecting to the central one is indicated by pink ellipses. In **(A–C),** some interconnection between canals, forming loops, is indicated (orange ellipses). In **B**, some side canals never reconnect to the central one and connect directly to the stomach pouch (light blue ellipses). In **(C**,**D)**, some rhopalia are not connected to canals (green ellipses). In **D**, there are many meandering canals and reconnections making many loops, in particular reconnections with straight adradial canals (violet ellipses). Scale bar 5 mm.

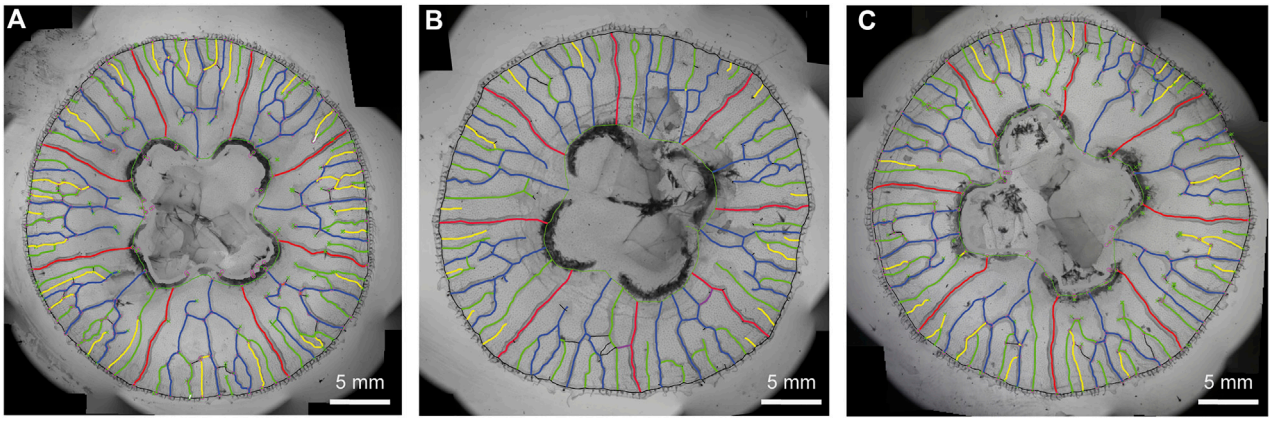

FIGURE 6
Three clones from the same polyp. **(A–C)** The pattern has been interpreted for easier comparison. As in Figure 1B, the adradial canals are drawn in red; the central canal, and the first side canals forming the trifurcation are drawn in blue; the second generation in green; the third in yellow. One can observe many irregularities as in Figure 5: side canals not reconnecting to the central one, reaching (or going to reach) the stomach pouch, interconnections to straight canals [violet, in **(B)**] and to other radial canals (black) making loops. All these irregularities, although similar in the three clones, are in detail different.

Figure 5 shows four cases giving an indication of the large variety of patterns. As a source of variability, one can observe that, even after reconnecting, the side canals would keep growing toward the stomach (pink ovals in Figure 5A). Another variation is the presence of meandering canals that are potential sites for the growth of new canals. Both modes of growth induce the formation of loops on large (old) jellyfish, transforming the gastrovascular network into a foam-like pattern (Figure 5D). This creates patterns much more difficult to analyze.

An interesting point is that since there is a variability in these patterns, one can study where these variations originate from. In the case of ephyrae coming from a single polyp, which means they are clones and grown together, thus in identical conditions, one can look at resulting patterns. Here, we present three such clones grown together (Figure 6). One can observe a similar type of pattern but still differences. This shows that, even for genetically identical jellyfish and an identical environment, there is no strict control of the pattern. This suggests a self-organized pattern formation, relying on instability, amplifying the noise.

4 Canal breakthrough

A particular type of deviation from the stereotypical development is interesting to see dynamically. During development, one can observe that some canal sprouts do not

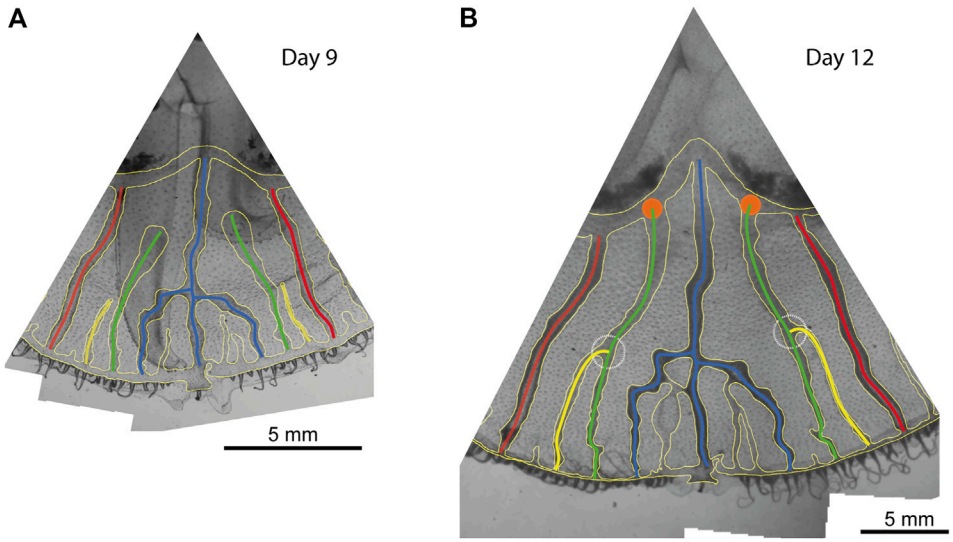

FIGURE 7
Two successive images of a jellyfish octant. **(A)** At day 9 of observation, secondary (green) side canals did not connect to the central ones and are reaching toward the stomach pouches. Similarly, there are two younger (yellow) canals growing aside of them without connecting either. **(B)** 3 days after, the side canals have reached the stomach pouch and connected (orange disks), and in the same period, the younger canals have also connected to these side canals (dashed white circles).

reconnect with the more central canals. Instead, they grow straight toward the stomach, independently from the other canals. It happens for the first-generation canals that sprout between the fork and the side adradial canals (see Figure 1B, Figure 5B), around 17% of the time (see Supplementary Material). Interestingly, in such a case, the next generation of side canals keeps growing independently too as long as the longest canal sprout did not reach the stomach pouch (see Figure 7A). However, as soon as the longest canal sprout reaches the stomach, it is observed that the smaller sprouts connect to the long canal that just got connected to the stomach (Figure 7B).

5 Discussion

When a pattern is constant, it is difficult to describe its origin and what controls it. On the contrary, variability helps get closer to the mechanisms producing these patterns. Here, we see that the pattern can be very variable, even in clonal jellyfish. That points to instabilities being at the origin of the pattern. Since Turing, we understand that instabilities mean that a homogeneous state is unstable, so that tiny inhomogeneities will grow to create a pattern. In this sense, instability starts with the amplification of noise. This first step results in a noisy pattern, which is a source of variability.

The further growth of the instability is often regulated by long-range interactions and global constraints (such as gradient of pressure). This leads to the growth of a regular pattern with a fixed wavelength for instance. This is how regular and reproducible patterns can appear, even if originating from an initial noise. In practice, this noise origin is often overlooked, and only regular patterns are studied theoretically. The most unstable regular pattern will be searched for, as it is the one most growing. Then, after a further restabilization, it will be the one finally observed. However, in some cases, the system keeps growing and being unstable, with no means of reorganization. This happens in physical systems, as in the Saffman–Taylor instability in circular geometry [9] or in biological growth, as in the lungs [10]. In such cases, the noise keeps being amplified, and variability can persist. This seems to be the case with the gastrovascular network of jellyfish.

There is still some regularity: the gastrovascular network can, under some growth conditions, follow a typical asymmetry (bias) and sometimes converge toward a stereotypical pattern. This comes from the interactions between canals, allowing regularization. However, we could guess that not following the bias comes from the presence of more noise, for instance, on the distance between canals, canal growth, and canal stiffness or resistivity. Such noise is well visible on Figure 1B, left, where successive generations of canals appear irregularly. This noise could blur the asymmetry and sometimes allows the sprouting canal to follow the second stress lobe (Figure 4), leading to a non-stereotypical connection. The fact that noise is the origin of these connections escaping the bias can be seen in the asymmetry of the distribution of Figure 1C. Noise leads to independent

misconnections, resulting into stereotypical octants with few mistakes but rarer octants with more numerous ones.

The sprouting of new canals from the circular ring canal also reveals instability of this ring that would be similar to the curving in the meandering canals, leading to local sprouting and later to other reconnections, forming small loops shunting the canals.

The fact that canals reconnect to each other is a particularly interesting phenomenon. The gastrovascular network is a tree structure connected to a ring canal. One would first imagine that it forms as a tree expanding with successive dichotomies of tips or side branching, and finally connecting to the ring canal. Here, we see a reverse growth: the branches appear from the ring canal, separated from each other, and reconnect only later. The reconnection between the canals leads to the formation of loops. The sprouting from other canals than the ring canal that further connect forms even more loops. This is interesting since the usual branching formation of trees, as in Laplacian growth [2], often forbids reconnection, hence the formation of loops [11]. Such reconnection is thus a particular phenomenon that deserves exploration.

This formation of loops by the reconnection of branches has to be differentiated from the case of stabilization and coarsening of loops. As for vascular remodeling from a capillary plexus [12], these systems start from homogeneously connected foam and particular dynamical evolution leads to the stabilization of large hierarchical loops [13–15]. Here, for the formation of loops by reconnection, the first mechanism proposed relates to cracks, which are known to reconnect [16], being related to two-dimensional stress [17], and leading to 2D-reticulated patterns [18, 19]. In this way, canals can be seen as the propagation of cracks in the endoderm. Stress accumulates at the tip of a new crack, and it is guided by the stress around it [16]. Here, too high stress at the tip of a sprout could induce the proliferation of cells [20, 21] and/or their transformation in canals cells, open the canals, and release the stress. The global stress field guides the movement of the tip of a new canal/crack. This relation to stress also explains the observed bias, that the crack is attracted to the larger stress, thus to the still stiff younger canal.

The second mechanism, even if related to Saffman–Taylor and Laplacian growth, would happen in the special case of resistive fingers [22]. This resistance creates gradients of pressure within the fingers. It allows connection of side fingers to a longer one when its pressure is locally lower. This particularly happens when the pressure in the longer one globally drops because of a connection to an outlet (breakthrough). This could explain the coincidence of a canal breaking through the stomach pouch and the reconnection of a side canal to it.

For the jellyfish canals, this would happen with the liquid pressure inside the growing canal sprouts during the muscle contractions in the orthoradial direction. However, when one canal sprout, in analogy with the Saffman–Taylor finger, reconnects directly to the stomach, then this transient high pressure at its tip drops to reach the pressure at the outlet, the stomach pouch. This dropping of pressure happens all along the canal, so that the lateral canal sprout can now perceive a place on the side with low pressure and be attracted to it.

These two mechanisms could be happening in the jellyfish or just be mechanical analogies of other phenomena. However, even from a mechanical point of view, they are not incompatible, being driven by the stress in the endodermal layer and the pressure in the canals, which are complementary parts of the mechanics of the network.

The source of large variability of the patterns, as shown in Figure 5, should also be investigated. Is it due to different growth conditions, growth histories, or also to different strains, revealing a different sensibility to mechanical constraints for instance?

Globally, these first observations show that the gastrovascular network results from a spontaneous organization, or, in other words, that it appears from instabilities, enhancing noise, so that two growths never produce the same result even with settings as close as possible (clones from a single polyp grown together in the same conditions). We consider that blood vascular networks in vertebrates [23–25] and venation in plant leaves [17] could result from similar spontaneous organization, however, with different detailed processes. Here, we show that there are clues that the morphogenesis of the gastrovascular pattern in the jellyfish could be related to mechanical processes, since it grows while the jellyfish is swimming with repetitive contractions. These contractions have clearly a mechanical effect on the tissue either by direct contraction or by a secondary effect on the flow inside the already existing canals.

6 Materials and methods

6.1 Jellyfish culture

Jellyfish *Aurelia aurita* were reared in the laboratory, at room temperature, in artificial seawater, produced by diluting 35 g or 28 g of synthetic sea salt (Instant Ocean; Spectrum Brands, Madison, WI) per liter of osmosis water (osmolarity 1,100 mOsm). Polyps of the Roscoff strain [26] were obtained by courtesy of Konstantin Khalturin from the Marine Genomics Unit, Okinawa Institute of Science and Technology Graduate University, Onna, Okinawa, Japan. Strobilation in polyps was induced by a lowering the temperature down to 10°C [27]. The newborn ephyrae were bred to adult stage. The measurements were performed on jellyfish at different sizes of juvenile jellyfish. Juvenile jellyfish had just reached the circular shape of adult medusas with a diameter of ~1 cm. Juveniles grow out into adult jellyfishes with fully developed stomach pouches.

Juvenile jellyfish (~1 cm in diameter) were obtained from the "Jellyfish Concept" in Cherbourg from their culture. The original polyps are extracted from the North Sea around Cherbourg. Juvenile jellyfish were bred to adults while growing. In the manuscript, we refer to these jellyfish as 'Cherbourg jellyfish'

when they originate from the Roscoff strain, we do not specify it in the manuscript.

6.2 Imaging of the gastrovascular canal network

The gastrovascular network of the jellyfish was observed using a Leica macro zoom (MACROFLUO LEICA Z16 APO S/No: 5763648) and a Photron Fastcam SA3 camera or directly using a Nikon D3300 camera with macro lens AF-S DX Micro NIKKOR 40 mm f/2.8G. Jellyfish were caught from the aquarium approximately 3 h after feeding with artemia when the gastrovascular canals were colored orange from the digested artemia. When they reach about 2.5 cm in diameter, jellyfish were anesthetized with magnesium chloride dissolved in water having the same salinity as the artificial seawater in which they are swimming. To anesthetize the jellyfish, the volume of the jellyfish with seawater was doubled with the magnesium chloride solution. Then, they are placed in a Petri dish in shallow seawater with the sub umbrella facing up. The images are taken by transillumination.

6.3 Histology

The histological section shown in Figure 2B was made for a preparation of observations with transmission electron microscopy. In short, whole juvenile jellyfish are fixed with a 5% glutaraldehyde solution in a 0.1 mol/L cacodylate solution overnight at 4°C [28]. After rinsing with 0.5 mol/L cacodylate solution (overnight at 4°C), the solution is replaced gradually by ethanol 95% after which it is transferred to 95% ethanol containing eosin, in order to stain the jellyfish. Then, the samples are placed in 100% ethanol which is subsequently gradually replaced by a pure molten wax solution. These samples are then cut by a microtome into thin lamellae of about 4 µm thickness. Longitudinal sections of juvenile jellyfish were sliced, starting the sections from the edge of the umbrella, and advancing towards the center of the jellyfish. Figure 2B shows a longitudinal section through a canal and the endoderm of a juvenile jellyfish of approximately 1 cm diameter. The section was visualized under a light microscope (Leica DMI-3000 B), a ×20 magnification objective, and a CCD camera (Andor, iXon3 885).

6.4 Canal diameter deformation measurements

Juvenile jellyfish (n = 7) of about 1 cm in diameter were filmed (30 frames per second) using a Leica inverse microscope (LEICA DMI-3000 B) with a ×20 objective (HCX PL Fluotar L ×20/0.40). The jellyfish were lying flat with the subumbrella facing down. In this position, jellyfish slightly contract occasionally. Two canals were filmed simultaneously. The older and younger canals were identified by looking at the canal network pattern. Off line, diameters were measured before and during contraction at three different positions along the canal and were averaged. Deformation of the canal was calculated by the ratio of the difference in diameter before and during contraction and the diameter before contraction, multiplied by 100. We used one-way repeated measures Anova, followed by a Student–Newman–Keuls test for pairwise multiple comparison to show the statistical difference between the deformation of the older canals versus the younger canals (SigmaPlot 12.5).

6.5 Numerical simulation

Numerical simulations were performed with finite elements toolbox COMSOL Multiphysics 3.5a [29]. We approximated the endoderm and the canals as 2D surface elements with different stiffness.

The simulations were performed on a small piece of a ring at the edge of a circular disk with a radius of 5 mm, with a radial length of 1 mm and with a 12° angle. The geometry of the canals and sprout were chosen to be coherent with our observations in a juvenile jellyfish of 1 cm diameter. The geometry with the simulation mesh is shown in the Supplementary Figure S7A.

We assume the endoderm as a flat rigid incompressible elastic sheet with Young's modulus $E_{en} = 100\,Pa$. The incompressibility of a material corresponds to a Poisson's ratio of 0.5. However, Hooke's law is only valid for Poisson's ratio <0.5. Hence, in our model, we approximate the incompressibility of the endoderm by setting its Poisson's ratio $\nu_{en} = 0.49$. The simulations in 2D imply the absence of out of plane buckling. This assumption is justified for small juveniles at the onset of contraction since the endoderm is held in plane by the mesoglea located above and below.

We modeled the canals in 2D by a slightly compressible elastic membrane, with lower Young's moduli than the endoderm. The young's modulus of the young canal is assumed to be stiffer with $E_{yc} = 30\,Pa$ than the old canal, $E_{oc} = 10\,Pa$. The Poisson's ratio of the canals equals 0.3 ($\nu_{yc} = \nu_{oc} = 0.3$), which allows for compression. It should be noted that the distribution of these stresses does not depend on the values of the Young modulus of the endoderm and the canals but only on the ratio of these values.

We observed that by choosing the elastic modulus of the canals 10 times lower than the endoderm, we obtained rates of reduction of the diameter of the ducts close to those observed *in vivo* (Figure 2B).

To simulate the muscular orthoradial contraction, we impose a reduction of the radial position of the outer circular boundary (at the ring canal). The sides of the ring slice can slip along the radial axis only, and the inner circular boundary is free to move ($\sigma(\epsilon).n = 0$, with n being the outer normal of the boundary).

The simulation was performed quasi-statically, meaning that each simulation step is in a dynamic equilibrium. The relative influence of inertia and elasticity on the system can be determined by computing the Cauchy dimensionless number $C = \frac{\rho V^2}{E}$, with ρ the density of the tissues and V local flow velocity. In our model, $V \approx 200$ µm/s, $\rho = 1{,}000$ kg/m^3 and E ranges from 10 to 100 Pa. Thus, $C<<1$ and the acceleration term $\rho\frac{\partial^2 u}{\partial t^2}$ is always negligible relatively to the elasticity term $div(\sigma(\epsilon))$. As a consequence, we can perform a quasi-static analysis: we solve the static equation $div(\sigma(\epsilon)) = 0$ with a maximal displacement of 200 µm of the outer circular boundary. Then, we reconstruct the time dynamics, thanks to the linearity of the equation relatively to the condition at this boundary.

We selected the mesh size so that a refinement of the mesh did not improve significantly the quality of the results. The mesh consisted in 7,563 triangular elements. The computation time was less than 1 s on an 3.7 GHz 2 Ghz Intel Xeon Gold 6,138.

The different values of the Young's and Poisson's moduli of the different elements under compression results in a distribution of stresses (σ_x, σ_y, σ_{xy}) which are accumulated at the tip of the sprout. The von Mises stresses (σ_{vm}), obtained by combining these different stresses [29], give a satisfactory scalar representation of the stress distribution in the endoderm:

$$\sigma_{vm} = \sqrt{\sigma_x{}^2 - \sigma_x\sigma_y + \sigma_y{}^2 + 3\sigma_{xy}{}^2}.$$

Data availability statement

The original contributions presented in the study are included in the article/Supplementary Material; further inquiries can be directed to the corresponding author.

Author contributions

SS performed the experiments, analyses of the network, in particular for the clones, and wrote the manuscript. SŻ performed the experiments, analyzed the growth dynamics, in particular for the breakthrough event, and wrote the manuscript. CG performed the experiments, in particular for the anatomy, analyses, in particular the contractions, and mechanical modeling and performed mechanical numerical simulations. PD performed mechanical numerical simulations. BM defined the numerical simulations and wrote the manuscript. SD analyzed the patterns and wrote the manuscript. AC directed the work, performed experiments, analyses, and modeling, and wrote the manuscript.

Funding

This work was supported by The LABEX "WHO AM I?" (No. ANR-11-LABX-0071) with a PhD fellowship for SS (doctorants 2015) and a collaborative grant (Projets collaboratifs 2013-II) and by the Mission for Transversal and Interdisciplinary Initiatives (MITI) of the French National Centre of Scientific Research (CNRS), AAP Auto-organisation 2021 and 2022.

Acknowledgments

The authors thank Carine Vias and Léna Zig for their excellent care for the jellyfish. They thank Vincent Fleury for pointing to them this biological system.

Conflict of interest

The authors declare that the research was conducted in the absence of any commercial or financial relationships that could be construed as a potential conflict of interest.

Publisher's note

Supplementary material

The Supplementary Material for this article can be found online at: https://www.frontiersin.org/articles/10.3389/fphy.2022.966327/full#supplementary-material

References

1. Collinet C, Lecuit T. Programmed and self-organized flow of information during morphogenesis. *Nat Rev Mol Cel Biol* (2021) 22(4):245–65. doi:10.1038/s41580-020-00318-6

2. Clément R, Blanc P, Mauroy B, Sapin V, Douady S. Shape self-regulation in early lung morphogenesis. *PLoS ONE* (2012) 7(5):e36925. doi:10.1371/journal.pone.0036925

3. Turing AM. The chemical basis of morphogenesis. *Philos Trans R Soc Lond Ser B, Biol Sci* (1952) 237(641):37–72. doi:10.1098/rstb.1952.0012

4. Southward AJ. Observations on the ciliary currents of the jelly-fish aurelia-aurita L. *J Mar Biol Assoc U K* (1955) 34(2):201–16. doi:10.1017/s0025315400027570

5. Russell FS. *The medusae of the British isles. Vol.Ii - pelagic scyphozoa with a supplement to the firts volume on hydromedusae*. Cambridge: Cambridge University Press (1970).

6. Fuchs B, Wang W, Graspeuntner S, Li Y, Insua S, Herbst E-M, et al. Regulation of polyp-to-jellyfish transition in Aurelia aurita. *Curr Biol* (2014) 24(3):263–73. doi:10.1016/j.cub.2013.12.003

7. Gambini C. *La morphogenaise gastrovasculaire de La méduse Aurelia aurita*. Paris: Université Paris Diderot (2012).

8. Gambini C, Abou B, Ponton A, Cornelissen AJ. Micro- and macrorheology of jellyfish extracellular matrix. *Biophysical J* (2012) 102(1):1–9. doi:10.1016/j.bpj.2011.11.4004

9. Thomé H, Rabaud M, Hakim V, Couder Y. The saffman–taylor instability: From the linear to the circular geometry. *Phys Fluids A: Fluid Dyn* (1989) 1(2):224–40. doi:10.1063/1.857493

10. Clément R, Douady S, Mauroy B. Branching geometry induced by lung self-regulated growth. *Phys Biol* (2012) 9(6):066006. doi:10.1088/1478-3975/9/6/066006

11. Douady S, Lagesse C, Atashinbar M, Bonnin P, Pousse R, Valcke P. A work on reticulated patterns. *Comptes rendus de l'Académie des Sci Série IIb, Mécanique, physique, astronomie* (2020) 348(6-7):659–78. doi:10.5802/crmeca.47

12. Risau W. Mechanisms of angiogenesis. *Nature* (1997) 386(6626):671–4. doi:10.1038/386671a0

13. Katifori E, Szöllősi GJ, Magnasco MO. Damage and fluctuations induce loops in optimal transport networks. *Phys Rev Lett* (2010) 104(4):048704. doi:10.1103/PhysRevLett.104.048704

14. Konkol A, Schwenk J, Katifori E, Shaw JB. Interplay of river and tidal forcings promotes loops in coastal channel networks. *Geophys Res Lett* (2022) 49(10):49. doi:10.1029/2022GL098284

15. Ronellenfitsch H, Katifori E. Phenotypes of vascular flow networks. *Phys Rev Lett* (2019) 123(24):248101. doi:10.1103/PhysRevLett.123.248101

16. Fender ML, Lechenault F, Daniels KE. Universal shapes formed by two interacting cracks. *Phys Rev Lett* (2010) 105(12):125505. doi:10.1103/PhysRevLett.105.125505

17. Couder Y, Pauchard L, Allain C, Adda-Bedia M, Douady S. The leaf venation as formed in a tensorial field. *Eur Phys J B* (2002) 28(2):135–8. doi:10.1140/epjb/e2002-00211-1

18. Bohn S, Pauchard L, Couder Y. Hierarchical crack pattern as formed by successive domain divisions. *Phys Rev E* (2005) 71(4):046214. doi:10.1103/PhysRevE.71.046214

19. Milinkovitch MC, Manukyan L, Debry A, Di-Poï N, Martin S, Singh D, et al. Crocodile head scales are not developmental units but emerge from physical cracking. *Science* (2013) 339(6115):78–81. doi:10.1126/science.1226265

20. Li B, Li F, Puskar KM, Wang JH. Spatial patterning of cell proliferation and differentiation depends on mechanical stress magnitude. *J Biomech* (2009) 42(11):1622–7. Epub 20090530. doi:10.1016/j.jbiomech.2009.04.033

21. Shraiman BI. Mechanical feedback as a possible regulator of tissue growth. *Proc Natl Acad Sci U S A* (2005) 102(9):3318–23. doi:10.1073/pnas.0404782102

22. Budek A, Kwiatkowski K, Szymczak P. Effect of mobility ratio on interaction between the fingers in unstable growth processes. *Phys Rev E* (2017) 96(4):042218. doi:10.1103/PhysRevE.96.042218

23. Al-Kilani A, Lorthois S, Nguyen TH, Le NF, Cornelissen A, Unbekandt M, et al. During vertebrate development, arteries exert a morphological control over the venous pattern through physical factors. *Phys Rev E* (2008) 77(5):051912. doi:10.1103/PhysRevE.77.051912

24. le Noble F, Fleury V, Pries A, Corvol P, Eichmann A, Reneman RS. Control of arterial branching morphogenesis in embryogenesis: Go with the flow. *Cardiovasc Res* (2005) 65(3):619–28. doi:10.1016/j.cardiores.2004.09.018

25. Nguyen TH, Eichmann A, Le NF, Fleury V. Dynamics of vascular branching morphogenesis: The effect of blood and tissue flow. *Phys Rev E* (2006) 73(6):061907. doi:10.1103/PhysRevE.73.061907

26. Khalturin K, Shinzato C, Khalturina M, Hamada M, Fujie M, Koyanagi R, et al. Medusozoan genomes inform the evolution of the jellyfish body plan. *Nat Ecol Evol* (2019) 3(5):811–22. doi:10.1038/s41559-019-0853-y

27. Kroiher M, Siefker B, Berking S. Induction of segmentation in polyps of Aurelia aurita (scyphozoa, Cnidaria) into medusae and formation of mirror-image medusa anlagen. *Int J Dev Biol* (2003) 44(5):485–90. doi:10.2108/zs160161

28. Chapman DM. Microanatomy of the bell rim of Aurelia aurita (Cnidaria: Scyphozoa). *Can J Zool* (1999) 77:34–46. doi:10.1139/z98-193

29. COMSOL. *Comsol Multiphysics®*. 3.5a ed. Stockholm, Sweden: Comsol A.B (2019).

Frontiers in Physics

Investigates complex questions in physics to understand the nature of the physical world

Addresses the biggest questions in physics, from macro to micro, and from theoretical to experimental and applied physics.

Discover the latest Research Topics

See more →

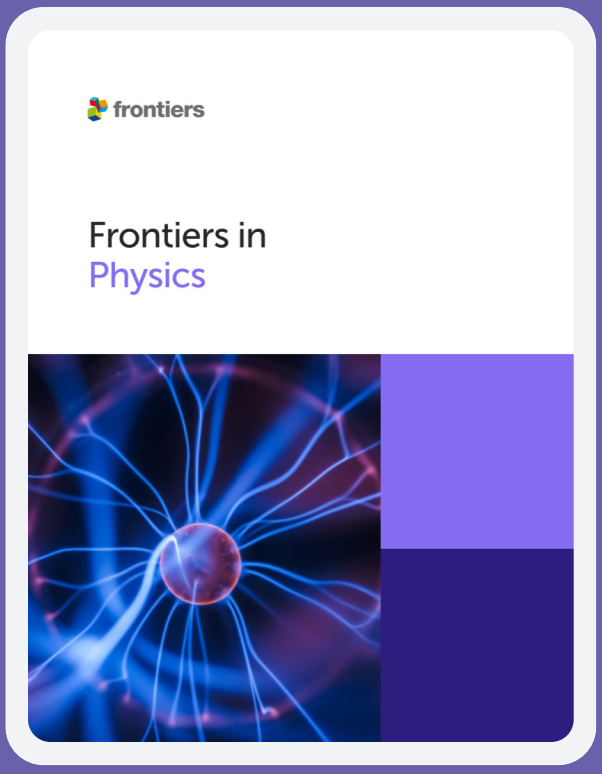

Frontiers

Avenue du Tribunal-Fédéral 34
1005 Lausanne, Switzerland
frontiersin.org

Contact us

+41 (0)21 510 17 00
frontiersin.org/about/contact